



NASA CR-183447

**American Science
and Engineering, Inc.**

Fort Washington
Cambridge, Massachusetts 02139
617-868-1600 Telex 921-458

22 AUGUST 1989

ASE-5568

(NASA-CR-183447) SOLAR X-RAY ASTRONOMY
SOUNDING ROCKET PROGRAM Final Report, 1 Feb.
1979 - 31 Jul. 1989 (American Science and
Engineering) 535 p

CSLT 03A

NPO-1 175

--FISH--

NPO-1 04

Unclad

GA/BR 025484

FINAL REPORT:

**SOLAR X-RAY ASTRONOMY
SOUNDING ROCKET PROGRAM**

PERIOD OF PERFORMANCE:
1 FEBRUARY 1979 TO 31 JULY 1989

CONTRACT: NAS5-25496

PREPARED FOR:

**NATIONAL AERONAUTICS AND SPACE ADMINISTRATION
SOUNDING ROCKET AND BALLOON PROJECT OFFICE
GODDARD SPACE FLIGHT CENTER/WALLOPS FLIGHT FACILITY
WALLOPS ISLAND, VIRGINIA 23337**

22

Final Report

SOLAR X-RAY ASTRONOMY SOUNDING ROCKET PROGRAM

Contract: NAS5-25496

Period of
Performance: 1 February 1979 to 31 July 1989

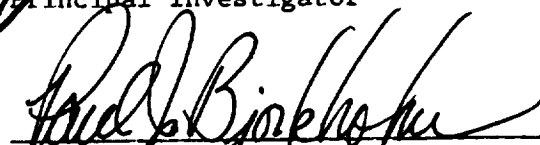
Prepared for: National Aeronautics and Space Administration
Sounding Rocket and Balloon Project Office
Goddard Space Flight Center/Wallops Flight Facility
Wallops Island, Virginia 23337

Prepared by: American Science and Engineering, Inc.
Fort Washington
Cambridge, Massachusetts 02139

Approved by:



J. Daniel Moses
Principal Investigator



Paul J. Bjorkholm
Senior Vice President, Research

22 August 1989

TABLE OF CONTENTS

| | <u>Page</u> |
|---|-------------|
| 1. INTRODUCTION | 1-1 |
| 1.1 Statement of Work | 1-1 |
| 2. PROJECT SUMMARY | 2-1 |
| 2.1 The November 1979 Campaign | 2-1 |
| 2.2 The February 1981 Flight | 2-2 |
| 2.3 Conclusions from the Imaging-Spectroscopy Flight Program | 2-2 |
| 2.4 The AS&E/NRL Campaign | 2-4 |
| 2.5 The 1987 Campaign | 2-4 |
| 3. PRESENTATIONS AND PUBLICATIONS | 3-1 |
| 3.1 Publications | 3-1 |
| 3.2 Abstracts of Presentations | 3-3 |
| 4. SCIENTIFIC RESULTS | 4-1 |
| 4.1 Soft X-Ray Astronomy using Grazing Incidence Optics | 4-1 |
| 4.2 X-Ray Bright Points and the Solar Cycle Dependence of Emerging Magnetic Flux | 4-6 |
| 4.3 Quest for Ultrahigh Resolution in X-Ray Optics | 4-16 |
| 4.4 A Real-Time Electronic Imaging System for Solar X-Ray Observations from Sounding Rockets | 4-30 |
| 4.5 Properties of Coronal Arches | 4-52 |
| 4.6 The Growth of Filaments by the Condensation of Coronal Arches | 4-66 |
| 4.7 X-Ray and Microwave Observations of Active Regions | 4-81 |
| 4.8 Comparison of Coronal Holes Observed in Soft X-Ray and HeI 10830 Angstrom Spectroheliograms | 4-99 |
| 4.9 X-Ray Bright Points and the Sunspot Cycle: Further Results and Predictions | 4-110 |
| 4.10 Observations of the Reappearance of Polar Coronal Holes and the Reversal of the Polar Magnetic Field | 4-117 |
| 4.11 The Detection of Soft X-Rays with Charged Coupled Detectors | 4-142 |
| 4.12 The Design and Evaluation of Grazing Incidence Relay Optics | 4-149 |
| 4.13 The Spatial Distribution of 6 Centimeter Gyroresonance Emission from a Flaring X-Ray Loop | 4-156 |
| 4.14 Small-Scale Flux Emergence and the Evolution of Equatorial Coronal Holes | 4-168 |
| 4.15 The Cyclical Variation of Energy Flux and Photospheric Magnetic Field Strength from Coronal Holes | 4-179 |
| 4.16 The Measured Performance of a Grazing Incidence Relay Optics Telescope for Solar X-Ray Astronomy | 4-194 |
| 4.17 The Plasma and Magnetic Field Properties of Coronal Loops Observed at High Spatial Resolution | 4-204 |

| | <u>Page</u> |
|---|-------------|
| 4.18 The Flight Test of a Grazing Incidence Relay Optics Telescope for Solar X-Ray Astronomy Utilizing a Thinned, Back-Illuminated CCD Detector | 4-219 |
| 4.19 The Correspondence Between Small-Scale Coronal Structures and the Evolving Solar Magnetic Field | 4-229 |
| 4.20 The Observation of Possible Reconnection Events in the Boundary Changes of Solar Coronal Holes | 4-236 |
| 4.21 X-Ray Bright Points and He I 10830 Dark Points | 4-249 |
| 4.22 Advanced in Photographic X-Ray Imaging for Solar Astronomy | 4-258 |
| 4.23 Correspondence Between Solar Fine-Scale Structures in the Corona, Transition Region, and Lower Atmosphere from Collaborative Observations | 4-267 |

1. INTRODUCTION

For over two decades, NASA has supported a continuous effort in solar coronal studies based on high resolution X-ray imaging, through a series of research contracts with AS&E. This report describes the work performed under the latest of these contracts, which extends the set of synoptic solar X-ray images through a full 22-year (magnetic) solar cycle. Specifically, the interval of time covered by this work extends from the maximum of Solar Cycle 21 to the beginning of the ascending phase of Solar Cycle 22.

Each flight of the X-ray imaging payload has provided an observation of at least one previously unknown process or structure in the solar corona. Overall, the result of this contract has been a clarification of, instead of a revolution in, our understanding of coronal processes. Coordinated, multispectral observations have played a dramatically increasing role in this research, indicating the maturing of this field. The major new results from this work are the limits placed on models of coronal heating based on impulsive heating ("nanoflares") of coronal loops as obtained through coordinated observations with the NRL HRTS Sounding Rocket payload as well as through the high time resolution X-ray images obtained with the ultra-high resolution payload CCD camera.

A summary of the research activity in this project is given in Section 2. The results of this research are presented in the form of 23 papers contained in Section 4.

1.1 Statement of Work

The overall scientific program consists of several broad objectives which are pursued by the development and flight of the AS&E High Resolution Soft X-Ray Imaging Sounding Rocket Payload followed by the analysis of the resulting data and by the comparison with both ground-based and space-based observations performed by other investigators (including archival and synoptic data). The major scientific objectives are:

1. Study the thermal equilibrium of active region loop systems by analyzing the X-ray observations to determine electron temperatures, densities and pressures, by comparing these measurements with coordinated multispectral observations, and by developing physical and mathematical models to explain the data.
2. Record the changes in the large scale coronal structures from the maximum and descending phases of Cycle 21 through the beginning of the ascending phase of Cycle 22 and correlate these observations with the photospheric magnetic field.
3. Extend our study of small scale coronal structures through the minimum of Cycle 21 with a new emphasis on correlative observations.

The detailed approach to these objectives is presented in Section 4, Scientific Results. Instrument innovations and developments required for this research include:

1. Grazing Incidence Imaging Telescope
2. Photographic X-Ray Sensitometry
3. Two-Crystal Collimated Bragg Spectrometer
4. Multichannel Plate/Vidicon Real-Time X-Ray Imaging and Aspect Control System
5. Magnifying Grazing Incidence Relay Optic
6. X-Ray Sensitive CCD Camera
7. Sequential, Coordinated Sounding Rocket Flights Utilizing the Saab S-19 Boost Phase Guidance System

To meet these scientific objectives, AS&E furnished the personnel, equipment, materials and facilities, except where furnished by the Government, which were necessary to design, fabricate and support sounding rocket integrations and launches; and analyze and publish the solar X-ray data from six sounding rocket flights. The specific tasks included:

1. Payload Modification and Refurbishment. AS&E modified, refurbished, tested, calibrated and prepared for flight the X-Ray Imaging and Imaging-Spectrometer payloads.
2. Launch Support. AS&E provided the necessary resources for payload integration and flight support up to rocket lift-off for three sounding rocket flights.
3. Data Reduction and Analysis. AS&E reduced, analyzed and interpreted the data obtained from the three flights and continued the interpretation of the data obtained from earlier flights in order to satisfy the scientific objectives of the program. Where applicable these results were reported to the scientific community in the form of talks presented at scientific meetings and articles published in refereed journals.

The activities undertaken by AS&E in completing this statement of work are described below in the form of brief descriptions of the six rocket flights and of reproductions of the scientific papers written under the contract.

2. PROJECT SUMMARY

During the period of performance of the contract, six sounding rocket flights were supported and the new ultra-high resolution payload was developed. The rocket flights fall into three groups: three flights at or near the maximum of solar cycle 21; a flight conducted simultaneously with the flight of Spacelab 2; two flights of the new payload launched in conjunction with the Naval Research Laboratory's (NRL) HRTS payload. With the exception of the Spacelab 2 flight, which was terminated by the White Sands Missile Range (WSMR) Safety Officer before reaching altitude, all the other flights were successful in meeting the majority of the comprehensive success criteria established at the Pre-Integration Review.

2.1 The November 1979 Campaign

The campaign's objectives were to observe the corona at or near the sunspot maximum. The launches were scheduled for November 1979 and sunspot maximum was eventually determined to have occurred in December 1979. The campaign consisted of two flights to occur 9 to 14 days apart so that the hemisphere hidden from view at the time of the first flight would have rotated into view for the second. The experiment configuration for the first flight, 27.030 CS, consisted of the grazing incidence telescope with both film and microchannel plate/Vidicon cameras. The Nike-Brant VB launch occurred on 7 November 1979, and the mission success criteria were met. The second flight, 4.337 CS, was launched successfully on 16 November 1979 by an Aerobee 150 rocket. The payload contained the original high resolution X-ray mirror with a film camera. The two flights recorded approximately 90 percent of the corona at the time of solar maximum and the campaign was considered extremely successful as it provided an important data point for our studies of the cyclical behavior of small scale magnetic field emergence. The images from the two flights allowed a global average to be constructed which was less sensitive to possible longitudinal variations in the field emergence patterns.

2.2 The February 1981 Flight

This campaign was the final flight of the imaging spectrometer payload. It was initially viewed as a collaborative effort with the Solar Maximum Mission (SMM). Unfortunately, SMM, which was launched in February 1980, lost the ability to solar point in November 1980. The experiment configuration for this flight consisted of the grazing incidence telescope with both film and MCP/Vidicon cameras and a two-crystal collimated Bragg spectrometer. The sounding rocket, 27.050 CS, was launched 13 February 1981. All the mission success criteria were met with the exception of the acquisition of the correct roll angle, which resulted in the spectrometers acquiring data from a quiet, rather than an active, region of the corona.

2.3 Conclusions from the Imaging-Spectroscopy Flight Program

As this was the last flight of the imaging spectrometer payload, it is useful to summarize the practical results of this project. The objectives of the program were to obtain simultaneous high-resolution X-ray full disk images and high-resolution spectra of restricted regions, i.e., regions which contained only a single coronal feature. The imaging spectroscopy payload was flown in its various forms a total of nine times between 1972 and 1981. Of this total, two failed to point to the sun and of the remaining seven all were successful to a greater or lesser extent. In general, the imaging objectives which were the first priority, were always met. In the process, we experimented with different types of photographic emulsions and broad band filters. In the performance of this program we established a unique record of the variation of the solar corona over a period spanning a full solar cycle.

In retrospect, the spectroscopy program was too ambitious for the resources that were available. Prior to SMM, all solar X-ray spectra had been obtained with large field of view instruments, either the whole sun or, at best, complete active regions. Consequently, emission from a wide range of features, which we knew from the X-ray images to have different temperature and density characteristics, were mixed together. By narrowing the field of view to 30 arc sec FWHM, we hoped to be able to isolate the spectra from a single feature.

Further, through the aid of a fiducial system, we planned to locate the field of view directly into a solar image taken through the X-ray telescope.

The first difficulties we encountered were that by reducing the field of view, we had to point the collimators very precisely to obtain statistically significant counts during the short time available in a rocket flight. To compound this difficulty, we learned that H-alpha images upon which we relied for our pre-launch pointing coordinate selection were not a good proxy for the X-ray corona. To counter this, we developed a real time imaging and control system. We were not able to use the SPARCS ASCL system, which uses pitch and yaw offsets to control the location of the pointing axis, since we were simultaneously taking X-ray images through the grazing incidence telescope and this required the pointing axis to remain sun-centered if the image was not to fall outside the film frame. We developed a system based upon an (r, θ) transformation in which r (the radial offset from sun center) was mechanically set into the collimators, and θ was the roll angle acquired by SPARCS. Although we had some success with this system, there was never sufficient time within a rocket flight to interpret the X-ray image which one was seeing for the first time, select a target, determine its coordinates in r and θ , calculate the commands and transmit them to the payload in flight, and verify their implementation.

Nevertheless, we were able to develop and test operationally all these systems. An investigation based on this hardware was proposed and selected in August 1979 as a candidate for flight as part of the second Spacelab solicitation. Unfortunately, as a result of budget constraints, the investigation was never funded beyond the extended Definition Phase.

However, this was not known in February 1981 and following the flight of 27.050 CS, we initiated an instrument upgrade which involved the development of two new technologies: (1) secondary grazing incidence optics, to obtain a magnified secondary image and (2) an X-ray sensitive CCD camera, to record these secondary images. These systems were incorporated into the payload to form the Ultra-High Resolution Telescope which has flown twice, August 1987 and December 1987.

2.4 The AS&E/NRL Campaign

One of the scientific objectives of the Naval Research Laboratory High Resolution Telescope Spectrograph (NRL HRTS) investigation on Spacelab 2 was to locate the high velocity jets which they had observed on a series of rocket flights with coronal features, especially X-ray bright points. Consequently, a collaboration was formed and flight 21.094 CS was approved to make simultaneous observations in the soft X-ray regime with the HRTS observations being made from Spacelab 2. Amid various distractions on the ground, difficulties in commencing the observation sequence on Spacelab, and deteriorating weather conditions, the payload was launched at 1600 MDT and terminated by Missile Flight Safety approximately 30 seconds later. The payload was recovered more or less intact, the major damage was the separation of the mirror from the optical bench. Subsequent calculations showed that this joint must have experienced a force greater than 115 Gs. Amazingly, the mirror was not damaged apart from two small chips and a coating of smoke particles.

Since the scientific objectives were not met, a new collaboration involving joint rocket flights was established.

2.5 The 1987 Campaign

The campaign was organized for a flight on 8 June 1987 to pursue three objectives: (1) a second attempt at the aborted 1985 AS&E/NRL campaign to study small scale coronal structure utilizing sounding rocket platforms for both instruments, (2) the first flight of the Ultra-High Resolution Telescope configuration of the payload incorporating the first use in X-ray astronomy of either an X-ray sensitive CCD camera or secondary grazing incidence optics, and (3) a collaborative effort with the Solar Maximum Mission X-Ray Polychromator and ground-based observers to study hot coronal loops. Critical to the success of dual rocket launches within the temporal constraint of the mean lifetime of small scale coronal structures (< 90 minutes) was the use of the Saab S-19 boost phase guidance system. With an S-19 the anticipated dispersion of the rocket trajectories becomes small enough so that launches can be held during a very wide range of wind conditions, even without obtaining the extended range

option. However, the application of S-19 units to the two sounding rockets in this campaign resulted in a number of launch aborts and cancellations.

After a series of attempts, the first launch of the AS&E payload, labeled 36.021 CS, finally occurred on 15 August 1987. The launch of the NRL HRTS V payload, which was scheduled 30 minutes later, was aborted at T-2 seconds by yet another S-19 failure. The performance of 36.021 CS was nominal and all success criteria were satisfied except those involving coordinated observation with HRTS V. Due to a lack of solar activity, the SMM XRP low temperature spectrometers were turned off to conserve counter gas. Due to the cumulative effect of all the previous launch cancellations, VLA observations were also unobtainable. Big Bear Solar Observatory, Kitt Peak National Solar Observatory, Owens Valley Radio Observatory, and Sacramento Peak Solar Observatory all obtained coordinated observations.

Following the 15 August 1987 failure of the S-19 system for the NRL payload, a redesign was made substituting an electromechanical valve for a squib operated device that controlled the regulator for the canard control gas. An analysis of the 36.021 CS photographic X-ray images indicated throughput problems with the grazing incidence optics persisted due to an invisible remnant of the residue deposited during the termination of the 1985 flight 21.094 CS. A more intrusive cleaning procedure was executed which brought the throughput back up to the level obtained when the optic was new without degrading any other aspect of X-ray performance.

After an intense interval of refurbishment activity, the AS&E payload, now labeled 36.038 CS, was returned to WSMR for a successful launch on 11 December 1987. The NRL HRTS V payload, labeled 36.020 DS, was also successfully launched exactly 30 minutes after 36.038 CS. Good observations were made at all the observatories which participated in the 15 August launch. SMM XRP and VLA radio observations were also made as part of an expanded multispectral observing campaign called CoMStOC (Coronal Magnetic Structures Observing Campaign).

The simultaneous observations with the improved temporal resolution of ground-based magnetographs obtained during both of the flights have changed our view

of the magnetic nature of XBP. Previous work initiated in the Skylab era implied that XBPs were associated with emerging magnetic flux regions while the recent observations show an association with submerging or cancelling magnetic flux. The interpretation of XBPs as signatures of surface magnetic field reconnection is reinforced by the out of phase variation in XBP population with the weekly average sunspot number through the 11-year solar cycle, which was shown to persist through Cycle 21 and into Cycle 22 by these flights. This interpretation also spurred an investigation into archival Skylab data which resulted in the discovery of an apparent role of XBPs in mediating the change in coronal hole boundaries.

The comparison of the X-ray images from 36.038 CS with NRL EUV observations provided the surprising result that the XBPs do not appear to be associated with the smallest scale high velocity transition region features. The XBPs are associated with lower velocity (on the order of 20 km/sec) transition region features with spatial scales very similar to the coronal structures (10,000 km). The smallest scale high velocity transition region features are found predominantly in regions of the lowest X-ray emission, adding another clue to the still unsolved puzzle of the nature of these seemingly ubiquitous energetic solar features.

The data from this campaign are far from exhausted by these analysis efforts. Further work will be accomplished under the analysis section of the follow-on contract NAS5-31619.

3. PRESENTATIONS AND PUBLICATIONS

The results of the sounding rocket flights and the subsequent analyses performed under this contract have been presented to the scientific community as presentations at scientific meetings and as papers published in the scientific literature.

3.1 Publications

- "Soft X-Ray Astronomy using Grazing Incidence Optics," J.M. Davis, Symp. of High Energy Solar Physics, Inst. Space and Aeronautical Sci., Tokyo, Japan, 1979.
- "X-Ray Bright Points and the Solar Cycle Dependence of Emerging Magnetic Flux," J.M. Davis, NASA Conf. Publication 2098, Study of the Solar Cycle from Space, p. 65-73, 1979.
- "Quest for Ultrahigh Resolution in X-Ray Optics," J.M. Davis, A.S. Krieger, J.K. Silk and R.C. Chase, SPIE 184, 96, 1979.
- "A Real-Time Electronic Imaging System for Solar X-Ray Observations from Sounding Rockets," J.M. Davis, J.W. Ting and M. Gerassimenko, Space Sci. Instrum. 5, 51, 1979.
- "Properties of Coronal Arches," J.M. Davis and A.S. Krieger, Solar Phys. 80, 295, 1982.
- "The Growth of Filaments by the Condensation of Coronal Arches," J.M. Davis and A.S. Krieger, Solar Phys. 81, 325, 1982.
- "X-Ray and Microwave Observations of Active Regions," D.F. Webb J.M. Davis, M.R. Kundu and T. Velusamy, Solar Phys. 85, 267, 1983.
- "Comparison of Coronal Holes Observed in Soft X-Ray and HeI 10830 Angstrom Spectroheliograms," S.W. Kahler J.M. Davis, and J.W. Harvey, Solar Phys. 87, 47, 1983.
- "X-Ray Bright Points and the Sunspot Cycle: Further Results and Predictions," J.M. Davis, Solar Phys. 88, 337, 1983.
- "Observations of the Reappearance of Polar Coronal Holes and the Reversal of the Polar Magnetic Field," D.F. Webb J.M. Davis and P.S. McIntosh, Solar Phys. 92, 109, 1984.
- "The Detection of Soft X-Rays with Charged Coupled Detectors," P. Burstein and J.M. Davis, X-Ray Microscopy, G. Schmahl and D. Rudolph (eds.), Springer-Verlag, Berlin, 1984.

- "The Design and Evaluation of Grazing Incidence Relay Optics," J.M. Davis, R.C. Chase, J.K. Silk, and A.S. Krieger, Nuclear Instrum. Methods in Phys. Res. 221, 20, 1984.
- "The Spatial Distribution of 6 Centimeter Gyroresonance Emission from a Flaring X-Ray Loop," S.W. Kahler, D.F. Webb, J.M. Davis and M.R. Kundu, Solar Phys. 92, 271, 1984.
- "Small-Scale Flux Emergence and the Evolution of Equatorial Coronal Holes," J.M. Davis, Solar Phys. 95, 73, 1985.
- "The Cyclical Variation of Energy Flux and Photospheric Magnetic Field Strength from Coronal Holes," D.F. Webb and J.M. Davis, Solar Phys. 102, 177, 1985.
- "The Measured Performance of a Grazing Incidence Relay Optics Telescope for Solar X-Ray Astronomy," D. Moses, A.S. Krieger, and J.M. Davis, SPIE 691, 138, 1986.
- "The Plasma and Magnetic Field Properties of Coronal Loops Observed at High Spatial Resolution," D.F. Webb, G.D. Holman, J.M. Davis M.R. Kundu and R.K. Shevgaonkar, Astrophys. J. 315, 716, 1987.
- "The Flight Test of a Grazing Incidence Relay Optics Telescope for Solar X-Ray Astronomy Utilizing a Thinned, Back-Illuminated CCD Detector," J.D. Moses and J.M. Davis, SPIE 982, 22, 1988.
- "The Correspondence Between Small-Scale Coronal Structures and the Evolving Solar Magnetic Field," D.F. Webb and D. Moses, Advances in Space Research, Proceedings of the XXVII COSPAR, 1988
- "Characteristics of Energetic Solar Flare Electron Spectra," D. Moses, W. Droege, P.Meyer, and P. Evenson, Ap. J. 346, 1989..
- "The Observation of Possible Reconnection Events in the Boundary Changes of Solar Coronal Holes," S.W. Kahler and D. Moses, Proceedings of the Chapman Conf. on the Physics of Magnetic Flux Ropes, Hamilton, Bermuda, March 1989.
- "Advanced in Photographic X-Ray Imaging for Solar Astronomy," D. Moses, R. Schueller, K. Waljeski, and J.M. Davis, SPIE 1159, 1989.
- "X-Ray Bright Points and He I 10830 Dark Points ," L. Golub, K.L. Harvey, M. Herant, and D.F. Webb, Solar Phys. (submitted), 1989.
- "Correspondence Between Solar Fine-Scale Structures in the Corona, Transition Region, and Lower Atmosphere from Collaborative Observations," D. Moses, J.W. Cook, J.-D.F. Bartoe, G.E. Brueckner, K.P. Dere, D. Webb, and J.M. Davis, F. Recely, S.F. Martin and H. Zirin, Astrophys. J. (in preparation), 1989.
- "Discrete Changes in Solar Coronal Hole Boundaries," S.W. Kahler and D. Moses, Ap. J. (submitted), 1989.

3.2 Abstracts of Presentations

(Following pages)

ORIGINAL PAGE IS
OF POOR QUALITY

Bull. AAS, 11, 409 (1979).

03.08.03 Establishing the Radiative Instability in Coronal Loops and the Formation of Filaments. J. M. DAVIS, AS&E - Observational evidence exists that strongly suggests that filaments form as the result of the condensation of coronal arches. To explore the validity of this hypothesis, analyses have been performed to determine

(1) the conditions required to establish the radiative instability in the face of the assumed steady state energy supply and conduction along the arch and (2) whether the conversion into internal energy of the potential energy released by the collapse of the material of the arch could result in sufficient material being evaporated into the arch to establish the required conditions.

The analysis enables limits to be set on the physical parameters of arches which are capable of forming filaments by this mechanism. The times required for these arches to cool from coronal to typical filament temperatures have been evaluated.

Bull. AAS, 12, 518 (1980).

25.07.03 Observations Linking X-Ray Bright Points with the Source of the Mass Input to the Solar Wind, J.M. DAVIS, AS&E - Davis and Golub (Bull. AAS, 8, 326, 1976) have shown that the evolution of equatorial coronal holes is accompanied by an increase in the areal density of X-ray Bright Points (XBP). Ahmad and Webb (Solar Phys., 58, 323, 1978) have observed polar plumes located above XBPs, or XBP-like structures, and have hypothesized that XBP/plume combinations could be the source of mass injection into the solar wind. If this hypothesis is correct, then the plasma density of recurrent high speed solar wind streams, whose sources are located within equatorial coronal holes, should be found to increase as the streams are observed on successive rotations. Skylab and corresponding solar wind data have been analyzed and support this prediction. The result appears to be a special case of a more general relationship. For over this time period (May - December 1973) the global averages of the solar wind density and XBP number per unit area (27-day running averages) are surprisingly well correlated. Preliminary analysis suggests that the correlation holds over the whole solar cycle with the average solar wind density showing the same anticorrelation with sunspot number as XBPs. If the correlation holds over three separate time scales, it increases the likelihood that we are observing a direct cause and effect relation.

This work was supported by NASA under contract NAS5-25496.

Bull. AAS, 12, 916 (1980).

H.1 Correlated Soft X-Ray and Microwave Observations of Active Region Loops. D.F. WEBB and J.M. DAVIS, AS&E; M.R. KUNDU and T. VELUSAMY, Univ. of Maryland - Correlated observations of solar soft X-rays and microwaves provide information on the density, temperature and geometry, scale height and strength and direction of the magnetic field of individual loops at coronal heights. We report on the analysis of near simultaneous soft X-ray and microwave observations with equivalent high spatial resolution (1 - 3 arc-sec) of CaK regions 16421 and 16419 on 16 November 1979. The X-ray data were obtained during a sounding rocket flight at 1700 UT and the radio data with the VLA at 6 cm from 1500 - 1645 UT. Coaligned photospheric magnetograms from Kitt Peak and Big Bear Observatories and H α filtergrams from Big Bear are also compared with these data. The plasma and field parameters are estimated and used to deduce the relative contribution of thermal bremsstrahlung and gyroresonance absorption to the microwave emission within specific structures. This work was supported, at AS&E, by NASA under contract NAS5-25496 and at Maryland by NSF Grant ATM 78-21762 and NASA Grant NGR 21-002-199.

Bull. AAS, 13, 821 (1981).

15.11 The Radiative Instability as a Mechanism for
Bright Point Flares. J.M. DAVIS and D.F. WEBB, AS&E -
X-ray images of a small, isolated, bright loop were ob-
tained during a sounding rocket flight on 31 January 1978.
Improved recording techniques enabled the loop to be re-
solved and its dimensions, diameter: 1 arc second,
length: 12 arc seconds, were measured. Its physical
properties were determined using broadband filter analysis
and it was found to be relatively cool and dense
($N_e \sim 7 \times 10^{10} \text{ cm}^{-3}$) for a coronal loop. The same analy-
sis indicates that the material surrounding the loop is
at a slightly higher temperature. This combination of
circumstances suggests that the loop is cooling and that
the bright emission is a consequence of the radiative
instability. A model for this behavior has been de-
veloped. The implication of the result as an explanation
of bright point flares in terms of the radiative insta-
bility is discussed. The work has been supported by NASA
under contract NAS5-25496.

Bull. AAS, 13, 906 (1981).

47.06 Rebirth of the Polar Holes at Solar Maximum.
D.F. WEBB and J.M. DAVIS, AS&E - We examine observations relating to the evolution of the global solar magnetic field following sunspot maximum, when the net polar flux switches polarity and coronal holes redevelop around the poles. Sufficient data are now available to permit a study of this process through two consecutive solar cycles. Synoptic H α , He I - 10830 Å, Mg X - 625 Å, magnetogram, and white light K-coronameter data are compared with X-ray coronal images obtained from sounding rockets at the maxima of cycles 20 and 21. We find that the polar holes redevelop only a few solar rotations after the time of the field reversal. The general field evolution following maximum is similar for both cycles, despite a marked contrast in their sunspot activity. These results will be discussed in the context of Babcock-type models for the solar cycle evolution of the solar dynamo. This work was supported by NASA under contract NAS5-25496.

Fifth International Symposium on Solar-Terrestrial Physics,
COSPAR XXIV, 1982.

STP.II.2.4 DAVIS J.M. and KRIEGER A.S. (American Science and Engineering, Inc., Cambridge, MA, USA). Cyclical Variations in Coronal Structure and Their Influence on the Solar Wind.

A decade of solar X-ray observations has demonstrated the existence of a cyclical variability in large and small scale coronal structures, which contrast to the classical pattern of the sunspot cycle. These structures appear, certainly under specific circumstances and perhaps more generally, to control the parameters of the solar wind. Observations during the declining phase of the 11-year cycle have shown that the evolution of coronal holes is accompanied by an increase, within the hole boundary, of the areal density of X-ray Bright Points, which are small, magnetically bipolar, coronal features. This increase is reflected in a similar increase in the plasma density of the high speed stream associated with the coronal hole. This result appears to be a special case of a more general relationship. For over a nine-month period the global averages of solar wind density and bright point number per unit area are surprisingly well correlated. Explanations for this correlation range from the hypothesis that the bright points are themselves sources of mass flow into the solar wind to a more general interpretation as a reflection of the dominant effect of the evolution of the solar magnetic field upon both parameters. This work has been supported by NASA.

10.10 The Spatial Distribution of 6 cm Gyroresonance Emission from a Flaring X-Ray Loop. D.F. WEBB, J.M. DAVIS and S. KAHLER, AS&E; and M. KUNDU, U. MD - We compare simultaneous high resolution soft X-ray and 6 cm images of a flaring region to deduce the microwave emission mechanisms in that region. The photographic X-ray images were obtained from an AS&E sounding rocket payload flown on 7 November 1979. At 2050 UT the decay phase of an M3 X-ray flare in Hale Region 16413 was observed.

During this time 6 cm observations of the region were made with the VLA. Synthesis maps of radio brightness temperature with a spatial resolution of about 5 arc sec were then obtained. The X-ray images were converted to deconvolved energy arrays which were used to obtain line-of-sight emission integrals and average temperatures throughout the region. The X-ray flare structure consisted of a large loop system of length ~ 2 arc min and average temperature $\sim 8 \times 10^6$ K. Comparison of these data to the aligned radio image showed that the peak 6 cm emission appeared to come from a region below the X-ray loop. The predicted 6 cm flux due to thermal bremsstrahlung calculated on the basis of the X-ray parameters was about an order of magnitude less than the observed flux. We model the loop geometry to examine emission expected from gyroresonance absorption along the loop. Since the loop presents a wide range of angles between the presumed magnetic field direction and the line of sight, and gyroresonance emission is strongly dependent on this angle, these data provide a stringent test of this mechanism.

34.08

Grazing Incidence Relay Optics for X-Ray Astronomy

J.M. Davis and A.S. Krieger (AS&E)

Progress in solar and celestial X-ray astronomy is keyed to the acquisition of high spatial resolution electronic images. If the resolution is not to be detector limited above 1 arc sec, plate scales in excess of $25\mu\text{m arc sec}^{-1}$, corresponding to focal lengths greater than 5m are required. In situations where the physical size of the instrument is restricted, large plate scales can be obtained using grazing incidence relay optics to magnify the image. We have developed such a secondary mirror with externally polished hyperboloid-hyperboloid surfaces to be used in conjunction with an existing Wolter-Schwarzschild primary. The optic is located in front of the primary focus and provides a magnification of 4. This results in a plate scale of $28\mu\text{m arc sec}^{-1}$ within an instrument length of 1.9m. The design, specification, fabrication and performance at visible and X-ray wavelengths of the system is described.

Trans. Am. Geophys. Union, EOS, 67, 331 (1986).

SC/SS31B-10 0830h POSTER
High-Spatial-Resolution Microwave and Soft
X-ray Observations as Diagnostics of Solar
Magnetic Loops

G. D. HOLMAN (NASA/GSFC, LASP, Code 682,
Greenbelt, MD 20771)
D. F. WEBB and J. M. DAVIS (AS&E, Fort
Washington, Cambridge, MA 02139)
M. R. KUNDU (Astronomy Program, Univ. of
Maryland, College Park, MD 20742)

Simultaneous high-spatial-resolution microwave and soft X-ray observations of solar magnetic loops, together with theoretical models for the loop emission, can provide detailed information about the temperature, density, and magnetic field within the loop, as well as the environment around the loop. VLA maps at 5 and 1.5 GHz, and soft X-ray images obtained with a rocket payload, of active region loops are analyzed. Models for the microwave emission, which can be either thermal gyroresonance (cyclotron) or free-free emission, are developed and compared with the observational results. In addition to average physical parameters, information about the magnetic and plasma structure of the loops is obtained. The 1.5 GHz observations require the presence of an external plasma around the 3×10^6 K X-ray loops with a temperature $\sim 10^5$ K or less. These results emphasize the value of obtaining high-spatial-resolution microwave and simultaneous soft X-ray, and EUV, observations of magnetic loops on the sun.

26.03

The Energy Spectra of Solar Flare Electrons

D. Moses (AS&E), P. Evenson (Bartol Res. Foundation),
P. Meyer (Enrico Fermi Inst./U. Chicago), and D. Hovestadt
(MPI for Extraterrestrial Phys.)

A survey of 45 interplanetary electron energy spectra from 0.1 to 100 MeV originating from solar flares has been made by the combination of data from two spectrometers onboard the ISEE-3 (ICE) spacecraft. The observed spectral shapes can be divided into two classes through the criteria of fit to the so-called "standard" two step acceleration model. This model involves an impulsive step that accelerates particles up to 100 keV and a second step that further accelerates these particles up to 100 MeV by a single shock. The spectral shape exhibited by one class of flares is well fit by the model predictions while the spectral shape of the second class of flares can be characterized as being excessively hard above 1 MeV relative to the model predictions. A correlation is found between the electron spectral class of the observed flares and the duration of the associated soft X-ray emission. Correlations with soft X-ray and meter radio observations have implications for the relative importance of the impulsive phase as well as energy losses during the shock acceleration phase of the second class of flares.

This work was supported in part by NASA Contracts NAS5-26680 and NAS5-25496 and NASA Grant NGL-14-001-005.

Bull. AAS, 19, 944, 1987.

10.08

High Resolution Soft X-Ray Solar Imaging Observations
During the Minimum Activity Phase of Solar Cycle 21

D. Moses, K. Hester (AS&E, Inc.), J. Davis (MSFC)

The new American Science and Engineering, Inc. High Resolution Soft X-Ray Imaging Solar Rocket Payload is scheduled for a sounding rocket flight in early June, 1987. Part of the rocket observation program includes the first attempted use of grazing incidence relay optics and a CCD detector for soft X-ray solar astronomy. Additionally, two programs of coordinated simultaneous multispectral observations with ground, rocket, and spacecraft based instrumentation are planned to investigate active region loops and small scale coronal structure. Preliminary results from these observations will be presented.

19.04

Boundary Changes in Coronal Holes

S.W. Kahler (Emmanuel College) and J.D. Moses (American Science and Engineering, Inc.)

Coronal holes are large scale regions of magnetically open fields which are easily observed in solar soft X-ray images. The properties of holes were extensively studied using images from the AS&E X-ray telescope on Skylab. The boundaries of coronal holes separate large-scale regions of open and closed magnetic fields. Photospheric motion of the field lines and magnetic reconnection will both contribute to changes in the hole boundaries. Previous studies by Nolte and colleagues using Skylab images established that large scale ($> 9 \times 10^4$ km) changes in coronal hole boundaries were due to coronal processes, i.e., magnetic reconnection, and not to photospheric motions. Those studies were limited to sequences of images separated in time by about one day, and no conclusion could be drawn about the size and time scales of the reconnection process at hole boundaries. However, sequences of appropriate Skylab images with a time resolution of about 90 min (one orbit) over periods of 6-10 hours are available for times of the central meridian passages of coronal holes 1 and 2. We are using these images to search for hole boundary changes which can yield the spatial and temporal scales of coronal magnetic reconnection.

31.03

The Correspondence Between Fine-Scale Structures in the
Solar Corona and Transition Region

J.D. Moses (American Science and Engineering, Inc.), J.-
D.F. Bartoe, G.E. Brueckner, J.W. Cook, K.P. Dere (Naval
Research Lab), J.M. Davis (Marshall Space Flight Center),
and D. Webb (Emmanuel College)

Fine-scale structures at the 2 arc sec spatial scale have previously been observed from space by soft x-ray instruments viewing the corona and by EUV spectrographs viewing transition region and chromospheric plasmas. Transient phenomena with lifetimes from 20 s up to the order of an hour are present. The lack of near simultaneous x-ray and EUV observations has left the correspondence between these coronal and transition region fine-scale transient structures unclear. In an effort to determine this correspondence, coordinated sounding rocket flights were made by the AS&E High Resolution Soft X-Ray Imaging Payload and the NRL High Resolution Telescope and Spectrograph (HRTS) experiment from White Sands on 11 December 1987, with launches at 1815 UT (AS&E) and 1845 UT (NRL).

The AS&E experiment obtained full disk coronal images over the wavelength range 2-64 Å, emitted by 10^6 K plasmas, with a spatial resolution of approximately 2 arc sec. The HRTS spectrograph slit length of 920 arc sec was rastered in 2 arc sec steps across an approximately 3 arc min wide area in the northwest quadrant, covering a quiet area out to the solar limb. HRTS spectra were obtained of the C IV 1548 Å and 1550 Å lines, emitted by transition region plasmas at 10^5 K. We will present the co-registered observations from the two experiments and discuss their correspondence and interpretation.

31.04

The Correspondence Between Small-Scale Coronal Structures
and the Evolving Solar Magnetic Field

D.F. Webb (Emmanuel Col.), J.D. Moses (A.S.&E.), J.M.
Davis (NASA/MSFC), J.W. Harvey (NSO/Tucson), S.F. Martin
and H. Zirin (Caltech)

Coronal bright points were first identified in soft X-ray images. Such X-ray Bright Points (XBPs) are compact, short-lived and associated with small bipolar magnetic flux. Similar compact emission features have also been detected at other coronal wavelengths, in the transition region, and in the chromosphere. XBPs are globally distributed and anticorrelated with the sunspot cycle. Contradictory studies have suggested either that XBPs are a primary signature of the emerging flux spectrum of the sun, or that they are representative of the annihilation (reconnection) of preexisting flux. We present results using coordinated data obtained during recent X-ray rocket flights on 15 August and 11 December 1987 to determine the correspondence of XBPs with ground-based observations of He-I dark points, bipolar magnetic structures, and the network. Time-series observations of the photospheric magnetic field enable us to better understand the evolution of the global solar magnetic flux spectrum and its signatures higher in the atmosphere.

50.05

A Grazing Incidence Relay Optics Telescope for Solar X-Ray Astronomy Utilizing an X-Ray Sensitive CCD Detector

J.D. Moses (American Science and Engineering) and
J.M. Davis (Marshall Space Flight Center)

The first use in X-ray astronomy of a grazing incidence relay optic or an X-ray sensitive CCD detector has been demonstrated by the new AS&E Ultrahigh Resolution Soft X-Ray Solar Research Rocket Payload during successful sounding rocket flights on 15 August 1987 and 11 December 1987. These flights provided the first implementation of the new X-ray secondary mirror which consists of 3.8X magnifying hyperboloid-hyperboloid grazing incidence relay optic used in conjunction with an existing Wolter-I primary mirror. An RCA CID series CCD detector was utilized in a thinned, backside-illuminated configuration for this payload. The 5.4 m effective focal length of the compound optics system resulted in a plate scale of 1 arc second per pixel which is comparable to the inherent resolution of the primary mirror. These observations and the preliminary results of our data analysis will be presented.

Bull. AAS, 20, 1008, 1988.

25.03

Solar Cycle Variation of the X-Ray Bright Point
Population: New Observations

J.D. Moses (American Science and Engineering) and
J.M. Davis (NASA/MSFC)

New observations from flights of the AS&E High Resolution Soft X-Ray Imaging Solar Research Rocket Payload on 15 August 1987 and 11 December 1987 provide an extension of the previous X-ray bright point population data set into the ascent to maximum of solar cycle 22. Soft X-ray observations from Skylab and rocket flights over the period 1970-1981 show that the number of X-ray bright points varies inversely with the sunspot index (J.M. Davis, 1983, Solar Phys. 88, 337). The new X-ray bright point counts will be compared with the first order prediction extrapolated from solar cycles 20 and 21: $N_{XBP} = 421.1 N_{SS}^{-2/3}$ where N_{XBP} is the corrected X-ray bright point count and N_{SS} is the weekly average international sunspot number. This result will be discussed in terms of the solar cycle evolution of the structure of the coronal magnetic field.

32.08

Comparison of Soft X-Ray Broadband and Emission Line
Temperature Diagnostics for Active Region Loops in the
Solar Corona

K. Waljeski (Brandeis University), J.D. Moses (American Science and Engineering, Inc.), J.R.L. Saba and K.T. Strong (Lockheed Palo Alto Research Laboratory)

Simultaneous observations of solar active region AR 4901 were made on 11 December 1987 by the Solar Maximum Mission X-Ray Polychromator and the AS&E Soft X-Ray High Resolution Imaging Sounding Rocket Payload. From these observations, a comparison is made of coronal plasma temperature diagnostics by two techniques: (1) broadband X-ray spectroscopy and (2) emission-line X-ray spectroscopy. A first order comparison is made assuming that the plasma in the emitting region is isothermal. The line intensity ratios of Fe XVII:Fe XVIII, Fe XVII:Mg XI, O VIII:Ne IX, Mg XI:Ne IX, O VIII:Fe XVIII, Mg XI:Fe XVIII, and Fe XVIII:Ne IX are used as temperature diagnostics for the line spectra. The ratio of the energy flux through an organic filter and a beryllium filter is used as a temperature diagnostic for the broadband images.

14.03

Soft X-Ray Transmission Grating Spectroscopy for Solar Observations Revisited

J.D. Moses (AS&E) and J.M. Davis (NASA/MSFC)

Recent advances in soft X-ray objective grating design and fabrication as well as X-ray detector technology have dramatically improved the potential performance of soft X-ray transmission grating spectrographs. Transmission grating spectrographs have previously been used for solar physics on an AS&E sounding rocket flight (Vaiana et al., 1968, Science 161, 564) and the AS&E Skylab instrument (Silk et al., 1974, Oss. Mem. Oss. di Arcetri 104, 143). The success of these applications was limited by a lack of spectral and spatial resolution due to the aberrations inherent in the optical design. A practical optical design described Beuermann, Brauning, and Trumper (1978, App. Opt. 17, 2304) based on a grating consisting of a group of individual facets can be optimized to reduce primary coma and astigmatism to levels below the resolution of X-ray telescopes. The AXAF High Energy Transmission Grating (HETG) instrument uses this design and, through HETG development, gratings which will give spectral resolution of about 1000 have been developed and tested (e.g., Schattenburg et al., 1988, SPIE 982, 210). We will present instrument simulations of HETG quality facet transmission gratings in combination with both the existing AS&E High Resolution Soft X-Ray Imaging Sounding Rocket Payload and a "new technology" Wolter-I mirror (at the level of the AXAF Test Mirror Assembly). We find for the existing optics that the O VII triplet (22 Angstroms) can be resolved for objects smaller than 20 arc seconds (e.g., X-ray Bright Points) directly provide a plasma density diagnostic. We find for optics with 0.5 arc second resolution that Doppler velocities of 100 km/sec can be observed.

4. SCIENTIFIC RESULTS

4.1 Soft X-Ray Astronomy using Grazing Incidence Optics

John M. Davis

American Science and Engineering, Inc.
Cambridge, Massachusetts 02139

ORIGINAL PAGE IS
OF POOR QUALITY

Symposium of High Energy Solar Physics
Institute of Space and Aeronautical Science
Tokyo, Japan

SOFT X-RAY ASTRONOMY USING
GRAZING INCIDENCE OPTICS

John M. Davis
American Science and Engineering, Inc.
Cambridge, Massachusetts 02139 USA

ABSTRACT

The instrumental background of X-ray astronomy with an emphasis on high resolution imagery is outlined. Optical and system performance, in terms of resolution, are compared and methods for improving the latter in finite length instruments described. The method of analysis of broadband images to obtain diagnostic information is described and is applied to the analysis of coronal structures.

1. Instrumental Background

Although X-rays are characterized by their ability to penetrate matter classical dispersion theory shows that below a critical angle, X-rays, incident on a denser medium will undergo total external reflection. The critical angle, defined in terms of atomic constants, is

$$\theta_c = \left[\frac{e^2}{\pi m c^2} \frac{Z \rho N}{A} \right]^{1/2} \lambda$$

and is shown for a variety of materials in Figure 1. These angles fall in the range of a few degrees and therefore X-ray optical systems have to be designed with their reflecting surfaces nearly parallel to their optical axis. For a parabola, this means using the far zone of the surface. However, this region of the surface does not satisfy the Abbe sine condition and the image suffers from coma, i.e., a point source will be imaged as a circle having an angular radius equal to the displacement of the point source from the optical axis. This can be minimized by introducing a second reflecting surface (Wolter, 1952) and in the X-ray region a paraboloid-hyperboloid combination is most commonly used.

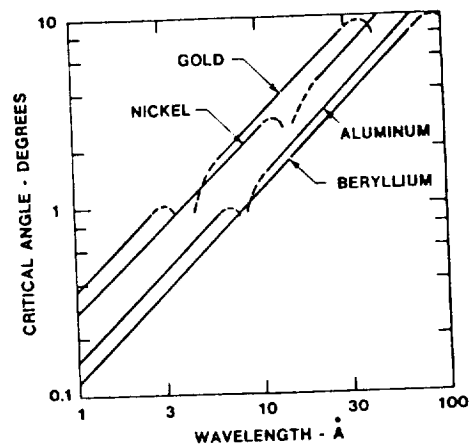


Figure 1. The variation of the critical angle with wavelength for several materials.

For the past 20 years we, at AS&E, have stressed the importance of high resolution imagery. The resolution of a particular system is a combination of the resolution of the optics, which is established by the manufacturing tolerances, and of the detecting system. X-ray mirrors can be made with angular

resolution of 1 arc second. However, even when film has been used, most X-ray images have been limited by the detector. In the future, when the missions dictate the use of electronic imaging detectors, with relative coarse picture elements, compared to film, the situation will be worse unless the images can be made correspondingly larger. If longer focal lengths are prohibited, magnifying optics provide the only alternative. Two types of systems are shown in Figure 2. We are developing the second, which uses hyperboloid-hyperboloid

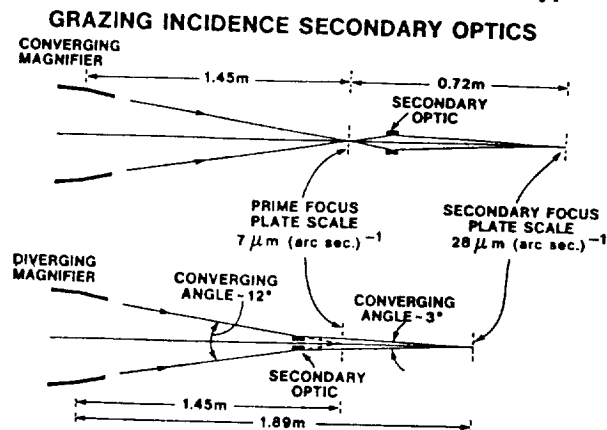


Figure 2. Diagrams of the two possible designs for secondary grazing incidence optics. The dimensions refer to systems based on an existing primary mirror and a magnification of 4.

optics (Davis *et al.*, 1984) since it combines the greatest magnification in the shortest length. Currently magnifications of 4 are near the practical limit set by the tolerance on the axial slope. The difficulties in this approach are that it adds two extra reflections, requiring extra smooth surfaces, and provides images with a field of view limited to a few square arc minutes.

2. Method of Analysis

To extract the properties of the coronal plasma (temperature, density and pressure) from the images, we relate them to the focal plane irradiance through the use of a model spectrum (Vaiana *et al.*, 1977). The spectrum gives the power emitted by unit volume of plasma with density N_e at temperature T in the wavelength range $\Delta\lambda$. If this incident spectrum is focussed by a telescope and the beam passed through a filter, the instrument will detect a spectrum that has been modified by the reflection efficiency of the mirrors and the transmission of the filter. By using more than one filter, different integrals of the spectrum will be sampled. Using the model spectrum, we can form ratios of the filter transmissions to create spectral hardness indices as a function of temperatures. These allow pairs of images to be converted into temperature maps and once the temperature is known, the focal plane irradiance can be converted into emission measure, or the $\int N_e^2 dl$, along the line of sight. Finally, if the geometry of the emitting structure is known, a density can be evaluated. Since the spectrum consists of a large number of lines and continuum, this method has the advantage of averaging and, since in general no single line, ion or continuum process is dominant, the impact of uncertainties in atomic parameters and element abundances is minimized.

3. Physical Properties of Loops

Soft X-ray observations have dispelled the idea of a vertically layered corona and have replaced it by a view dominated by magnetic loops on all spatial scales. The loops are long lived and therefore must exist in an equilibrium state where the power losses, though conduction and radiation, must balance the power inputs. The sources and mechanisms of the latter remain a mystery. Figure 3 is a schematic representation of the power loss as a function of temperature for a coronal loop.

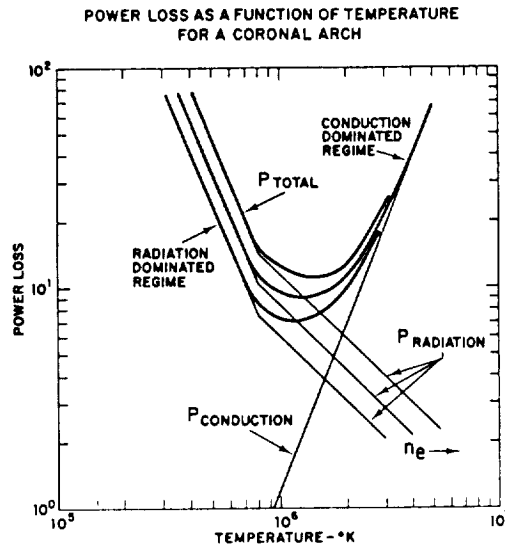


Figure 3. A schematic diagram showing the dependence of the power losses of a coronal arch on its temperature.

Shown are the conductive losses which are proportional to $T^{5/2}$ and the radiative losses which are proportional to $n_e T$ at coronal temperatures. The total power loss is the sum of these curves which has a minimum at a certain temperature. An equilibrium will exist when the power supply heating the loop balances the radiative and conductive losses. For the equilibrium to be stable the loop must exist on the conduction dominated branch of the total loss curve where small fluctuations in the power supply can be compensated by moving to a new equilibrium state. For instance if the heating supply decreases, the temperature will fall and although the radiation losses increase with falling temperature the conduction losses which are the dominant loss mechanism at these temperatures decrease sufficiently to allow a new equilibrium to be established at a slightly lower temperature. An increase in the heating supply will result in a new equilibrium at a higher temperature.

This is not the case if the loop exists on the radiation dominated branch of the total loss curve. Here where the radiation losses dominate the conduction losses a reduction in the heating supply leading to a decrease in temperature will result in an increase in the total losses which cannot be conduction stabilized at coronal temperatures and the loop will cool. This phenomenon is known as the radiative instability.

To reach this equilibrium state chromospheric 'evaporation' is invoked to fill the magnetic loop with coronal material. The process can be visualized by realizing that if power is dissipated in a magnetic structure, it will cause the material within the structure to rise rapidly in temperature because of its low thermal capacity, its low radiation losses and the negative temperature coefficient of the loss term. The eventual result will be that the majority of the dissipated power will be conducted to the chromosphere/transition region where it will heat that material to coronal temperatures which will allow it to rise and fill the loop. The increased radiation losses of the now dense loop will allow an equilibrium state to be reached. These ideas are discussed by Pye *et al.* (1978).

They have been used by Davis and Krieger (1982) to show how filaments could condense from coronal loops. This hypothesis was based on the observation that filament channels, i.e., regions in which the H-alpha data show a field structure identical to that surrounding the filament but where no filament exists, are located beneath arcades of coronal loops and that the quantity of material within the arcade is sufficient to form the filament.

In another study where we had obtained images using a finer grain emulsion than used on Skylab, we were able to evaluate the plasma parameters of a small bright loop, tentatively identified as a flaring bright point. The loop was 10 arc sec long by 1 arc sec wide and we found a density in excess of $2 \times 10^{11} \text{ cm}^{-3}$ at a temperature of $2 \times 10^6 \text{ K}$. This low temperature is uncharacteristic of typical flare phenomena. Since the dimensions of the loop were known, we were able to calculate the total loss curves as a function of temperature. When the loop was located on the appropriate curve, it was found to exist on the radiation dominated branch of the curve and thus to be radiatively unstable. It is unlikely that the temperature determination could be in error by the amount necessary to place the arch on the conduction dominated branch for this would require temperatures above $6 \times 10^6 \text{ K}$ which are ruled out by the observation.

Therefore, we appear to have an example of a bright loop cooling through the radiative instability. This identification depended critically on our ability, through the availability of high resolution images, to define the dimensions of the loop which allowed us to convert an emission measure into density.

This example and many others have confirmed our firmly held belief in the importance of obtaining images with the highest possible resolution if the secrets of the corona are to be revealed.

References

- Davis, J.M. and Krieger, A.S., Solar Phys. 81, 325 (1982)
- Davis, J.M. *et. al.*, Nuc. Instrum. and Methods 221, 20 (1984)
- Pye, J.P. *et. al.*, Astron. & Astrophys. 65, 123 (1978)
- Vaiana, G.S. *et. al.*, Space Sci. Instrum. 3, 19 (1977)
- Wolter, H., Ann. Physik 10, 94 (1952)

4.2 X-Ray Bright Points and the Solar Cycle Dependence of Emerging Magnetic Flux

John M. Davis

American Science and Engineering, Inc.
Cambridge, Massachusetts 02139

ORIGINAL PAGE IS
OF POOR QUALITY

— — — — —

X-RAY BRIGHT POINTS AND THE SOLAR CYCLE DEPENDENCE OF EMERGING MAGNETIC FLUX

John M. Davis

American Science and Engineering, Inc.
955 Massachusetts Avenue
Cambridge, Massachusetts 02139

ABSTRACT

Soft X-ray imaging of the solar corona during the period 1970 to 1978 has resulted in significant modifications to our view of the solar cycle with respect to both the properties of the large scale (coronal holes) and small scale (X-ray Bright Points) solar magnetic field. In the latter case the particular contribution is to the emerging magnetic flux. Sounding rocket observations combined with the Skylab data indicate that the XBP are anticorrelated with sunspot number and are the dominant contributors to the total emerging flux spectrum during all but the maximum phase of the solar cycle. A continuous data set covering a complete cycle would enable the validity of this result, which has serious implications for the nature of the solar dynamo, to be confirmed.

1.0 INTRODUCTION

Since the early sixties NASA has supported a program of high spatial resolution solar X-ray astronomy at AS&E. One of the prime objectives of this program has been the study of both the large and small scale variations occurring in the corona during the 11-year solar cycle. The studies have used the data from sounding rocket flights and Skylab; the latter providing a major contribution by establishing a baseline against which the sounding rocket observations can be compared.

During the first decade of the program major advances were made in the fabrication of the X-ray optics, in the preparation of the broadband filters used to select the various soft X-ray wavelength ranges and in the development of suitable photographic emulsions which are used as the recording medium. These three areas of development had all reached fruition by 1970 and produced for the first time the high quality X-ray images to which we have now grown accustomed. A panoramic representation of these data is shown in Figure 1 where images from 6 rocket

flights and 3 representative Skylab photographs are combined. The images cover the period 1970 to 1978 and show all the phases of the solar cycle except solar maximum, for which period no images of comparable quality exist. The combination of high resolution and sensitivity has revealed many new phenomena of which two have a direct bearing on the cyclical behavior of the solar magnetic field. The unique contribution of the X-ray images has been to clearly and unambiguously identify phenomena whose signatures, although present in the records of the photospheric magnetic field, tend to be obscured by a wealth of confusing detail.

2. CORONAL HOLES AND X-RAY BRIGHT POINTS

Historically the first major result of the program was the unambiguous identification of coronal holes followed by the recognition that equatorial coronal holes were the elusive 'M-Regions' which give rise to geomagnetic storms by their influence on the velocity pattern of the solar wind. Although coronal holes had been tentatively identified earlier on the basis of ground-based observations (Waldmeier, 1957) and low resolution X-ray pinhole and XUV heliograms (Russell and Pounds, 1966; Austin et al., 1967), they attracted little interest primarily because they were not clearly defined entities. However, three different groups reintroduced the subject almost simultaneously (Altschuler et al., 1972; Munro and Withbroe, 1972; Krieger et al., 1973) just prior to Skylab. The subsequent high resolution X-ray images obtained during Skylab ignited a general interest in the study of these indicators of the large scale structure of the solar magnetic field. Several categories, based on their heliographic location, are known each having a characteristic relationship to the solar cycle; for instance, the recurrent equatorial holes are present only during the declining phase of the solar cycle, while the polar holes are always present except perhaps during solar maximum. Although coronal holes can now be identified from ground-based observations, notably the He 10830 line, the reconfiguration of the magnetic field which occurs as their boundaries expand or recede is best studied with X-ray or XUV observations.

The X-ray observations have also shed light on the small scale structure of the magnetic field following the observation and classification of the features known

as X-ray Bright Points (XBP). XBPs are small, compact, short-lived, magnetically bipolar regions whose size and lifetime spectra blend into the corresponding active region spectra.

Their major significance results from their identification as sources of emerging magnetic flux. The relationship of XBPs to the general solar field is still not understood. However what is clear is that the emerging magnetic flux associated with XBPs differs radically from that associated with active regions in at least two ways. The first, discovered from the Skylab observations, is that the XBP are distributed more or less uniformly over the solar surface in sharp contrast to the active regions which are limited to the equatorial band (Golub et al., 1974, 1975). The observations do suggest that there are two components to the bright point distribution, one associated with the active region latitudes and the second uniformly distributed over the entire disk.

The second difference is their variation with the solar cycle which appears to run counter to the well-known sunspot cycle.

3. THE SOLAR CYCLE VARIATION

A basic limitation of the Skylab study was that it covered only a short period (8 months) of the solar cycle and consequently the conclusions drawn from this period may not be typical of solar conditions throughout the 11-year cycle. To augment these data, four sounding rockets have been flown since Skylab and in particular two flights were made in September and November 1976 close to solar minimum. On both these occasions the X-ray images revealed that the corona was composed of low-lying weakly emitting structures, interspersed with very large numbers of XBPs. Coronal holes were visible at both poles, however, there was no evidence of the large equatorial holes which were so characteristic of the declining phase.

The most obvious and striking difference was the large number of XBPs. In order to compare their number with those from the Skylab period, the relative efficiencies of the two rocket telescopes were evaluated and compared to the Skylab

telescope. Using these ratios the closest comparable rocket exposures were selected and were used to establish the bright point counts.

The major result of the investigation is shown in Figure 2 where the relative numbers of XBP in 1973 and 1976 are compared (Davis et al., 1977). The 124 daily averages from 1973 are plotted in the form of a histogram showing the frequency of occurrence of each number count. The histogram approximates to a Gaussian distribution, even though there were persistent non-random variations during the eight rotations observed, and the mean (39) and its standard deviation (± 3) have been used to characterize the distribution. The values observed in 1976 are indicated by arrows and lie well outside the range of values recorded in 1973.

After scaling the 1976 values are 90 ± 8 and 75 ± 9 . They are both consistent with a substantial increase in the number of bright points occurring between 1973 and 1976. In fact the average of the two 1976 observations, 83, is 110 percent higher than the combined average, 39, of the 1973 data. Under the assumption that the data from both 1973 and 1976 belongs to the same Gaussian frequency distribution, the probability that two random observations will result in the 1976 value is found to be 1 in 5×10^6 . Even using the lower bounds for the 1976 observations, thus maximizing the probability, the chance of making the observations is still only 1 in 2×10^5 . We realize that because of deviations from a Gaussian distribution these probabilities are not strictly true but even so the inescapable conclusion remains that the 1976 data belong to a different frequency distribution with a higher mean value.

In Figure 3 we show the latitude distribution of XBP seen on the two 1976 images, compared with the 1973 average. The 1976 data show much larger error bars since only two photographs were available. However, it is clear from the figure that there were more XBP at all latitudes in 1976 than in 1973, with the possible exception of the extreme polar latitudes where the statistical sample is small. Thus it is clear that the emergence of small-scale magnetic flux regions at solar minimum does not follow the pattern set by the larger active regions. Unfortunately, further details of the behavior within restricted latitude intervals cannot be deduced because of the limited statistics of the data sample.

The increase in the number of XBP is even more significant when compared to the changes in the other indices of solar activity between 1973 and 1976. For instance the average relative sunspot number, R_z , for the Skylab period, May to November 1973, was 35 whereas the index for January to December 1976 averaged 13. Thus while the sunspot number has declined by a factor of 3, the number of XBPs has increased by over a factor of 2. The implication of this result is that XBPs vary out of phase with the solar cycle as measured by the usual indicators of activity.

To explore this possibility further we have reexamined data from the older rocket flights going back to 1970 and the two other post-Skylab flights. Following a careful calibration program to compensate for the instrumental differences, a consistent pattern of anticorrelation between sunspot number and bright point count is found. The data are summarized in Figure 4 where we show the variation with time of R_z and XBP number, both normalized to maximum values of 100, over the last sunspot cycle. It is apparent that the variation in XBP count is close to 180° out of phase with R_z . This demonstrates that XBP must represent magnetic flux which emerges independently of the active regions. For if the emergence of XBPs was somehow associated with the emergence of the larger active regions (e.g., if the XBP represented either precursors or remnants of the larger active regions), then the bright point count could not lead or lag R_z by much more than the characteristic lifetime of the flux associated with the active regions (~ 6 months). Instead the observed phase lag is closer to 6 years. Therefore, in order to determine the total magnetic flux emerging at the solar surface at any time, it is necessary to sum the magnetic flux represented by the XBPs with that represented by the active regions.

4. IMPORTANCE OF THE RESULT

The last conclusion, that in order to determine the total magnetic flux emerging from the solar surface, it is necessary to sum both the XBP and active region components, provides the significance to the observations. For now, the possibility exists that the amount of magnetic flux emerging throughout the cycle is constant or even that the total increases at solar minimum.

Comparison of the X-ray data with high resolution magnetograms shows that on average XBP emerge with $2 - 3 \times 10^{19}$ Mx of flux (Harvey et al., 1975; Golub et al., 1977). Although this is more than an order of magnitude less than for active regions, because of their large number, XBP contributed 80 percent of the total of all emerging magnetic flux at the time of the Skylab observations. Under the assumptions that the XBPs seen in all of the rocket flights are physically the same so that the characteristic value of 3×10^{19} M_x per bright point can be used for all the data, and that the sunspot index R_z may be used as a relative indicator of the amount of flux emerging in the form of active regions throughout the solar cycle, it is possible to proceed to estimate the relative contributions of XBP and active regions to the total magnetic flux spectrum of the sun during the period 1970 to 1978. By taking the 1973 fraction of 80 percent as a base, we estimate that ~40 percent of the total magnetic flux in 1970 emerged in the form of XBP. The contribution of XBPs to the total reached a peak of ~95 percent in 1976 and has since declined to about 70 percent in early 1978. From this analysis we conclude that XBPs make a substantial contribution to the total emerging magnetic flux spectrum throughout the entire solar cycle and are the dominant contributors throughout the declining, minimum and ascending phases.

5. CONCLUSIONS

High resolution X-ray images of the solar corona contribute to the study of the solar magnetic field by revealing, in a unique manner, the topology of the extension of that field into the corona. It is extremely difficult, if not impossible, to obtain this information in other ways, for instance by extrapolating the measurements of the photospheric magnetic field because this requires theoretical modelling, e.g., potential field calculations, which results in, at best, an approximation to the real situation.

The X-ray images, although recorded only during brief intervals over the last decade, have revealed two new facets of the behavior of the solar magnetic field which must be explained in any comprehensive theory of its origin and variability. In particular it has been learned that XBPs represent a dominant feature of the

emerging magnetic flux spectrum through the majority of the solar cycle. In fact they display a counter cycle to the better known sunspot cycle and at this time the relative importance of the two cycles to the actual description of the solar dynamo is not known. Because of the limited number of data samples, the statistics of the observations over a solar cycle are not high and other contributions of XBPs to the complete picture of the solar magnetic field almost certainly remain to be discovered. An example is their latitude distribution which is known to differ markedly from that of active regions but whose possible cyclical variation is completely unknown.

In this context the SCADM mission presents a unique and valuable opportunity to obtain an uninterrupted, long duration sample of coronal observations. In the recording of these data, the value of high sensitivity, high resolution observations cannot be overemphasized. For although both XBPs and coronal holes are visible, in retrospect, in the X-ray images made prior to 1970 their importance was not realized at the time because the lack of definition in the observations did not allow a positive and unambiguous identification to be made. Since the coronal observations will still be to some extent exploratory, the preliminary planning for the SCADM spacecraft must reflect the requirement for imaging data with comparable quality to those of current rocket programs.

ACKNOWLEDGMENTS

The work described in this report has been supported in part by NASA under contracts NAS2-8683, NAS5-25496, and NAS8-27758.

REFERENCES

- Altschuler, M.D., Trotter, D.E., and Orrall, F.Q.: Solar Phys. 26, 354, 1972.
- Austin, W.E., Purcell, J.D., Snider, C.B., Tousey, R., and Widing, K.G.: Space Research VII, 1252, 1966.
- Davis, J.M., Golub, L., and Krieger, A.S.: Astrophys. J. 214, L141, 1977.
- Golub, L., Krieger, A.S., Silk, J.K., Timothy, A.F., and Vaiana, G.S.: Astrophys. J. 189, L93, 1974.
- Golub, L., Krieger, A.S., and Vaiana, G.S.: Solar Phys. 42, 131, 1975.
- Golub, L., Harvey, J.W., Krieger, A.S., and Vaiana, G.S.: Solar Phys. 53, 111, 1977.

Harvey, K. L., Harvey, J. W., and Martin, S. F.: Solar Phys. 40, 87, 1975.
Krieger, A. S., Timothy, A. F., and Roelof, E. C.: Solar Phys. 29, 505, 1973.
Munro, R. H. and Withbroe, G. L.: Astrophys. J. 176, 511, 1972.
Russell, P. C. and Pounds, K. A.: Nature 109, 490, 1966.
Waldmeier, M.: Die Sonnenkorona 2, Verlag Birkhauser, Basel, 1957.



7 March 1970



24 November 1970



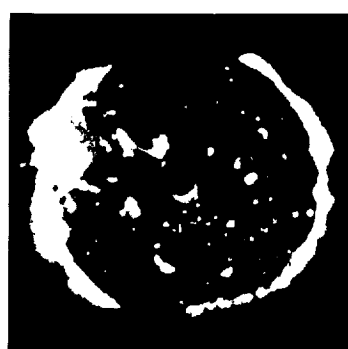
8 March 1973



1 June 1973



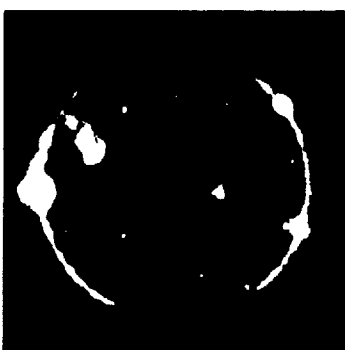
2 September 1973



14 November 1973



27 June 1974



17 November 1976



31 January 1978

Figure 1. Coronal X-ray observations during the period 1970-1978.
A collection of images from sounding rockets and Skylab.

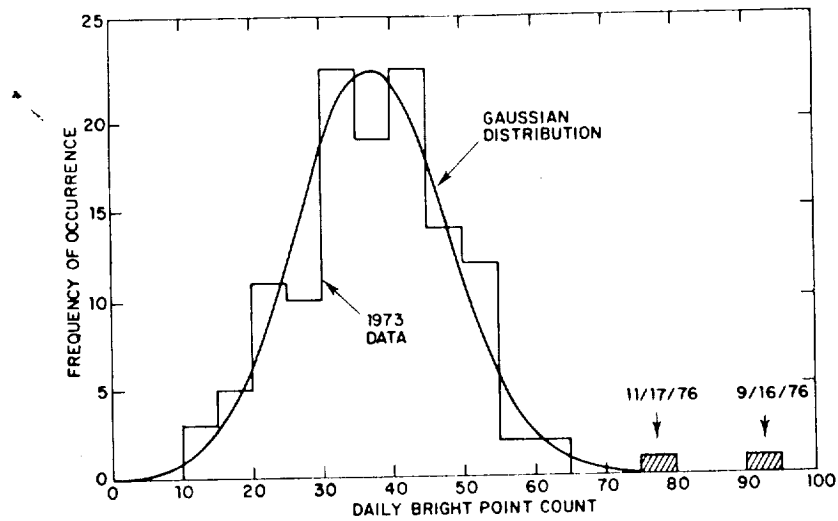


Figure 2. Daily X-ray bright point counts. The curve is a Gaussian distribution fitted to the 1973 data.

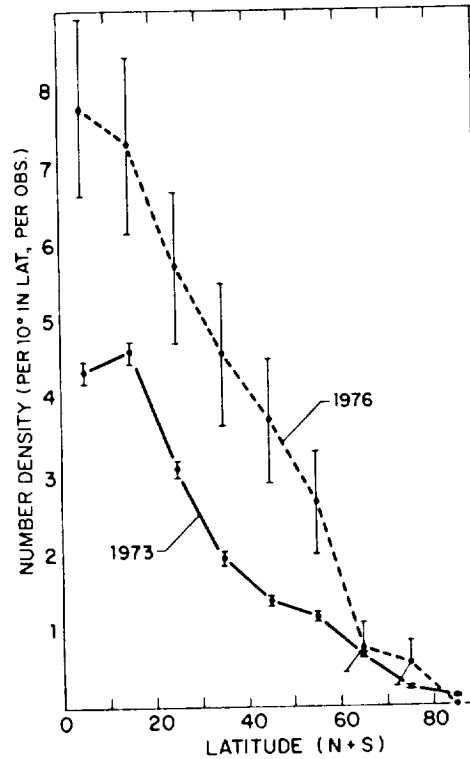


Figure 3. The latitude distribution of X-ray bright points in 1973 and 1976.

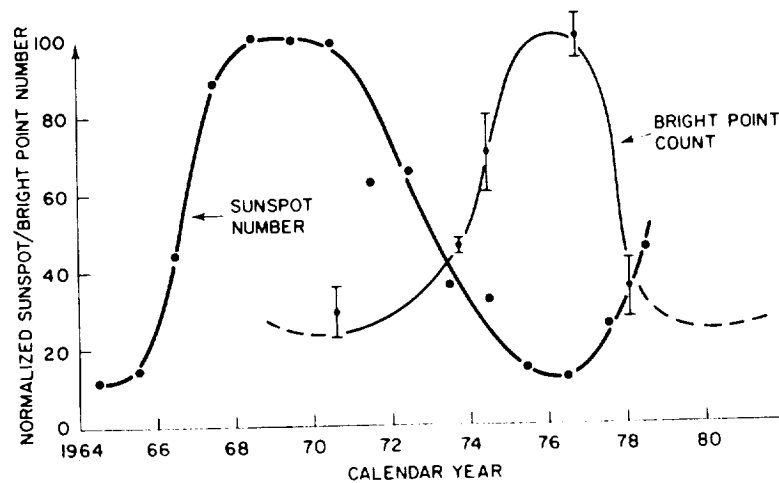
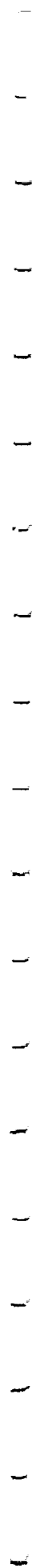


Figure 4. Variation of the number of X-ray bright points with the solar cycle.



4.3 Quest for Ultrahigh Resolution in X-Ray Optics

John M. Davis, Allen S. Krieger, J. Kevin Silk and Richard C. Chase

American Science and Engineering, Inc.
Cambridge, Massachusetts 02139

ORIGINAL PAGE IS
OF POOR QUALITY

Quest for ultrahigh resolution in x-ray optics

John M. Davis, Allen S. Krieger, J. Kevin Silk, and Richard C. Chase

American Science and Engineering, Inc.
955 Massachusetts Avenue
Cambridge, Massachusetts 02139

Abstract

A program of solar X-ray astronomy using grazing incidence optics has culminated in X-ray images of the corona having one arc second spatial resolution. These images have demonstrated that in general X-ray optics can be fabricated to their specifications and can provide the level of resolution for which they are designed. Several aspects of these programs relating to the performance of X-ray optics in regard to resolution, including the point response function, the variation of resolution with off-axis position and the recognition that nearly all solar X-ray images have been film limited, are discussed. By extending the experience gained on this and other programs it is clearly possible to design and fabricate X-ray optics with sub-arc second resolution. The performance required to meet the scientific objectives for the remainder of the century are discussed in relation to AXIO, an Advanced X-Ray Imaging Observatory for solar observations which is proposed for flight on the space shuttle. Several configurations of AXIO are described, each of which would be a major step in the quest for ultra-high resolution observations.

Introduction

The majority of the contributions to this workshop have described the application of grazing incidence optics to celestial X-ray astronomy. Although this is not surprising, in light of the dramatic results from the HEAO-2/Einstein mission, it should not be allowed to completely overshadow either the achievements or the requirements of that branch of X-ray astronomy devoted to the study of the solar corona. Our current abilities in this field represent the culmination of fifteen to twenty years of experimentation at several laboratories throughout the United States and Europe. The scientific results from these studies have suggested that the understanding and detailed interpretation of the physics of the corona will require observations with a much higher spatial resolution than has been achieved to date; which fact provides the incentive for this paper.

Any discussion of the design and performance specifications of grazing incidence telescopes must recognize that there exist significant differences in the requirements placed on the observations by the objectives of solar and celestial X-ray astronomy. These differences are reflected in the way the performance of the instruments is described. Solar X-ray images are views of a highly structured object of considerable extent. Point to point variations of intensity within the image, which after analysis can be converted into electron temperature, density and pressure measurements, are important. In contrast celestial observations are frequently limited to the study of one or more, but never very many, point sources within the field of view, whose internal structure is unresolved. Consequently for solar observations, the requirement of high spatial resolution reflects the more general optical application in which the performance of an imaging system is represented by its modulation transfer function (MTF). In contrast the advantage of high resolution in celestial imaging systems is to improve the sensitivity of the instrument by concentrating the flux from a particular object within a single image element. This improves the sensitivity by increasing the signal to noise ratio of the observation thus allowing the detection of fainter and presumably more distant and hence cosmologically interesting objects. In the celestial case it is convenient to describe the performance of the grazing incidence mirror in terms of the RMS blur circle radius of the image of a point source, since this indicates the efficiency with which the reflected energy is concentrated in the image plane.

Since the objective in solar physics is to distinguish discrete structures, identify their boundaries, describe their geometry and differentiate between the plasma conditions inside and outside these structures, it is possible to define the level of resolution achieved in practice by reference to the observations. The Skylab telescopes and the mirror used in our current rocket program produce images having a realistic resolution when defined in this way of a few (2-5) arc seconds. However it must be realized that the observed resolution of these instruments is the result of folding together the transfer functions of both the optics and the detector. The latter has usually been photographic film and, as we will show later, all the recent solar images, but one, recorded to date have been limited by the film rather than by the optics. This type of performance, i.e., the ability to resolve structures at the 2-5 arc second level will be referred to as high resolution. The term ultra-high will refer to roughly an order of magnitude improvement over existing instruments, that is, to sub-arc second resolution with limiting values of 0.1 to 0.2 arc second.

We believe that this level of resolution is necessary if further significant advances in our understanding of coronal physics are to be made. Moreover, we are confident that the technology now exists, not only for the fabrication of ultra-high performance grazing incidence mirrors, but also with the development of the space shuttle to carry these large instruments into orbit. Together these facts make the serious consideration of the next generation of solar X-ray telescopes both meaningful and worthwhile.

Characterizing the Performance of Grazing Incidence Optics

The Point Response Function

The performance of X-ray grazing incidence optics is usually described in terms of two quantities: the point response function (PRF) of the mirror, and the variation of the RMS blur circle radius as a function of off-axis position. The PRF describes the fraction of the reflected intensity which falls within a given radius of the central maximum and it is determined experimentally. In general the PRF can be considered as the sum of two separate distributions which are composed of the specularly reflected rays and of the surface scattered rays respectively. The specularly reflected component forms a narrow central peak which is characterized by its HWHM. It is a measure of the accuracy of the figure of the mirror surfaces and its magnitude can be directly related to their tolerances. The scattered distribution tends to be broad and flat and it can be described by the half power radius, i.e., by the radius within which 50 percent of the reflected energy is contained. The presence of the broad 'wings' of the scattering distribution, which extend out to at least 15 arc minutes, means that the power in the image is spread out over a large angular area. These terms can be demonstrated by the comparison of the PRFs of the Skylab and rocket mirrors which are shown in Figure 1.

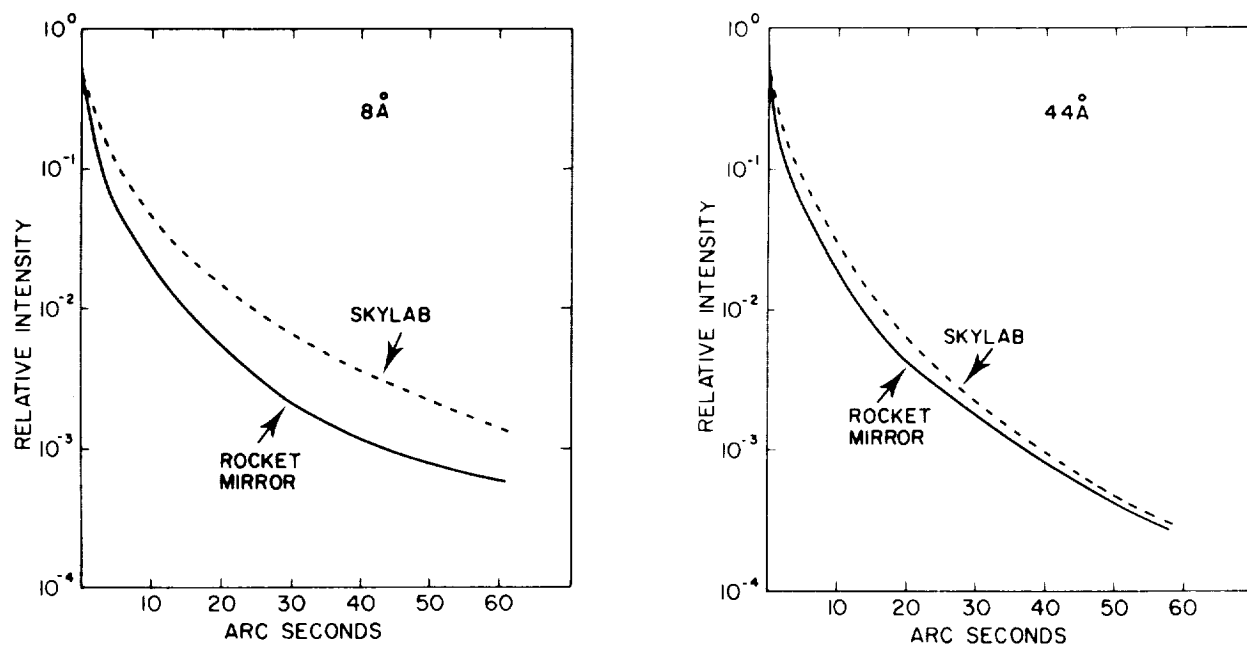


Fig. 1. A comparison of the inner region of the PRFs of the rocket and Skylab mirrors at 8 and 44 \AA .

The Skylab mirrors⁽¹⁾ are a nested pair of Wolter Type I paraboloid-hyperboloids. They were fabricated from beryllium with superpolished⁽²⁾ electroless nickel (Kanigen) reflecting surfaces. The rocket mirror is also a Wolter Type I design, but it has Wolter Schwarzschild surfaces which, although more difficult to fabricate, were chosen over the more normal paraboloid-hyperboloid surfaces since they satisfy the Abbé sine condition and therefore eliminate the coma aberration for paraxial rays⁽³⁾. It was chosen to fabricate the mirror from fused silica on the basis of a test program which evaluated the scattering of X-rays from highly polished flats. The results of this program indicated that fused silica was superior to all other metals and glasses available at that time.

The HWHM of the rocket mirror PRF is approximately 1 arc second while the corresponding value for the Skylab mirror is roughly twice as large. The half power radii are respectively 31 and 48 arc seconds at 8 \AA and 18 arc seconds for both mirrors at 44 \AA . Inspection of the data recorded in Figure 1 shows that the rocket mirror PRFs have very little dependence on wavelength and further that the PRFs of the two mirrors are quite

similar at 44 Å. These data can be interpreted as an indication that the surface roughness for the Skylab mirror is small compared to 44 Å but not to 8 Å while the surface roughness of the rocket mirror which is beginning to affect the PRF at 8 Å may be of this order.

Both these mirrors were fabricated over seven years ago and represent a rather early stage of surface polishing technology. In particular our ability to measure surface smoothness was limited and this was reflected in the mirror specification for surface smoothness. In contrast the HEAO-2 mirrors⁽⁴⁾ are the latest stage in this technology and demonstrate the improvements in our ability not only to make mirrors of very large size but more importantly with very smooth reflecting surfaces. By comparison the half power radii for 8 and 44 Å radiation are respectively 6 and 4 arc seconds⁽⁵⁾. These values reflect the average smoothness for all the mirrors in the nested set and the surface achieved on the smoothest mirror would be adequate for the next generation sub-arc second telescope.

The Off-Axis Resolution of Grazing Incidence Optics

In order to introduce the topic of the off-axis response of grazing incidence mirrors we will first discuss a method we have developed for determining the location of the focal plane. In the past modified Focault tests, Hartmann cameras or other techniques which determine the focus for on-axis rays have been used. However, the focal plane of an X-ray mirror is not flat but is curved and when the objective is to image a broad source, such as the sun, an adjustment has to be made from the measured position to compensate for the different focus of the off-axis rays. In general the optimum focus for an on-axis ray is located behind the same position for an off-axis ray (Figure 2). To overcome the need for an adjustment we have developed a simple procedure which allows us to specify the optimum focal plane for a broad source.

The procedure uses a star pattern of resolution targets. Each block in the star contains 5 groups (II through VI) of a USAF resolution target. Each group contains 6 patterns containing 3 vertical and 3 horizontal bars with each pattern reduced in size by $6\sqrt{2}$ from its predecessor. A set of focus plates is taken with the flight camera as its position is varied along the optical axis and the resulting images are observed with a microscope. Rather than obtaining the best focal position by inspection, we have placed the procedure on a numerical basis by calculating a Figure of Merit (FoM) which reflects the resolution across the field of view.

The FoM is determined in the following way:

- (i) Each pattern in each group is assigned a numerical value starting with II-1, which is set equal to unity, and increasing by one for each succeeding (i.e., decreasing) pattern. Thus,

$$\begin{aligned} \text{II-1} &= 1 \\ \text{II-2} &= 2 \\ &\dots \\ \text{II-6} &= 6 \\ \text{III-1} &= 7, \text{ etc.} \end{aligned}$$

i.e., the patterns with better resolution are assigned higher numbers.

- (ii) Three exposures of the star pattern are taken at each focal position to eliminate (or minimize) the effects of Schlieren due to air turbulence. The smallest horizontal and vertical patterns, which are resolvable in each exposure, are recorded for each position in the star. The average of the smallest horizontal and vertical pattern resolved is computed and recorded for each position (Figure 3).
- (iii) The sum of the averages from each position in the star is recorded and is used as an indicator or FoM for the resolution across the field of view at that focal position.

A typical set of data obtained with the fused silica rocket mirror is shown in Figure 4. The two sets of points correspond to the orthogonal directions in the focal plane formed by the star pattern. The data shows a

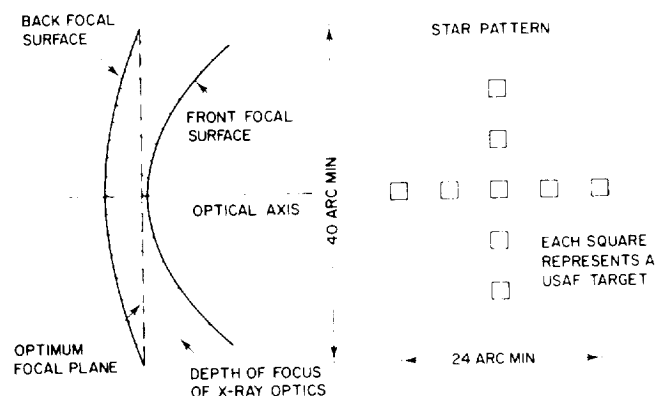


Fig. 2. Schematic representation of the mirror focal plane and the star pattern used in its location.

| Focal Position | Star Position | | | | | | | | | | Figure of Merit |
|----------------|---------------|------|------|------|------|------|------|------|-----------------------------------|------|----------------------|
| | 1 | | 2 | | 3 | | 4 | | 5 | | |
| | H | V | H | V | H | V | H | V | H | V | |
| 550 | IV-5 | IV-3 | IV-4 | IV-3 | IV-4 | IV-4 | IV-3 | IV-4 | IV-3 | IV-2 | 81 ← Sum of averages |
| | IV-4 | IV-4 | IV-4 | IV-3 | IV-5 | IV-3 | IV-4 | IV-3 | IV-4 | IV-4 | |
| | IV-4 | IV-4 | IV-4 | IV-4 | IV-5 | IV-4 | IV-4 | IV-4 | IV-4 | IV-4 | |
| | 16.5 | | 16 | | 16.5 | | 16 | | 16 ← average within each position | | |

1/2 (IV-5 + IV-4)

= 1/2 (17 + 16) = 16.5

H & V are the horizontal and vertical sets within a pattern

Fig. 3. An example of the data used in the determination of the Figure of Merit.

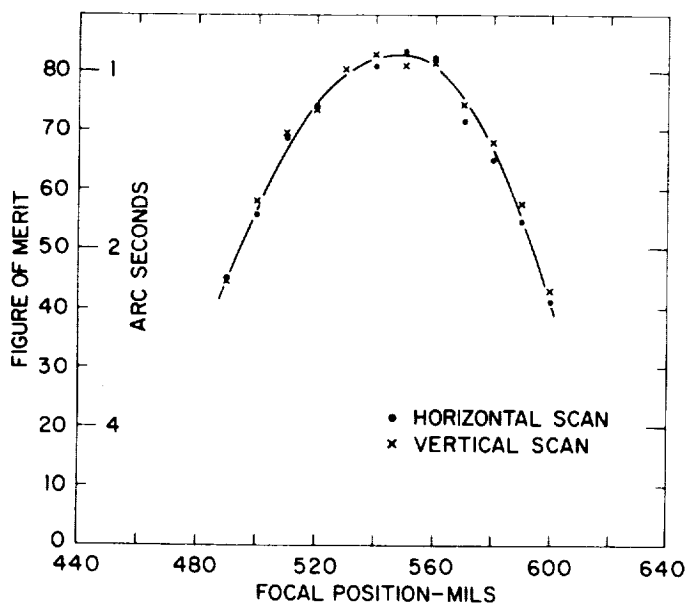


Fig. 4. Experimental data showing the location of the focal plane by the figure of merit method.

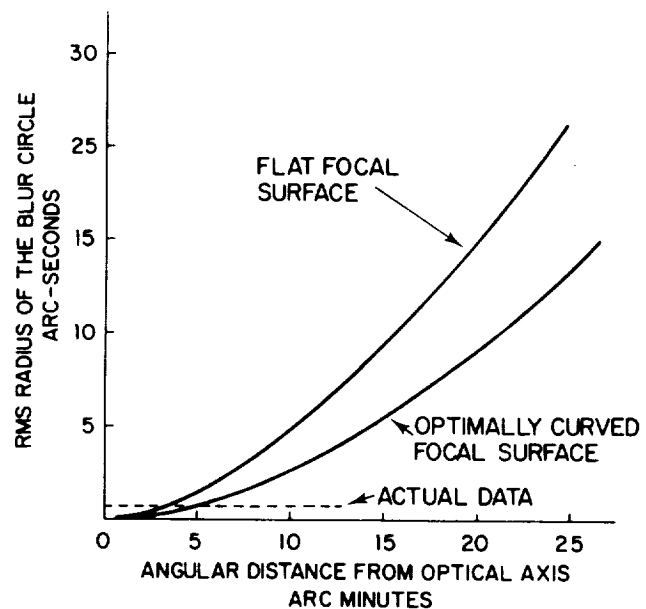


Fig. 5. The variation of the RMS blur circle radius with off-axis position. The broken line represents the observed resolution using USAF resolution charts.

plateau where the average resolution is better than 1 arc second ($FoM > 80$) which we interpret as the effective depth of field. The 1 arc second level of resolution at the plateau is predominantly a function of the recording medium for, if a finer grain film is used, the effective resolution improves to close to 0.5 arc second ($FoM = 116$) which is near the diffraction limit for visible light for this mirror.

Although we believe that this is a useful method for determining the focal plane of grazing incidence mirrors, we have introduced it to illustrate a different point; namely, the off-axis response of the mirror or the variation of resolution with distance from the optical axis. In general our knowledge of the off-axis performance of grazing incidence mirrors is obtained from ray-tracing calculations. These calculations are based on purely geometrical optics and make no allowance for diffraction effects or for the X-ray PRF. They describe the off-axis response in terms of the RMS radius of the blur circle formed of a point object. In general this radius increases monotonically with the angular distance of the source from the optical axis for both flat and curved focal surfaces. However, when we analyze the focus plates, as described above, it is immediately apparent

that the variation of resolution with off-axis position is far less severe than predicted by the calculations of the RMS blur circle radius. In fact out to 12 arc minutes no fall off in resolution is observed for the rocket mirror while the ray tracings indicate that the RMS radius has increased from essentially zero to 4 arc seconds in the best case (Figure 5).

The conclusion that we draw from this result is that the RMS blur circle radius is a poor indicator of actual mirror performance when applied to angular resolution. Consequently the various figures which can be found in the literature describing the off-axis performance of mirrors are probably misleading when considered in the context of solar observations. A more serious consideration is their use in those solar applications which call for both high resolution and large collecting areas. To increase collecting area, for a fixed focal length, there are usually three options available, to increase the diameter of the mirror, to use nested sets, or to increase the length of the mirror element. When the application calls for high resolution over a wide field, the third option is usually rejected because of the loss in off-axis resolution predicted by the ray tracing programs. Our observations would suggest that this conclusion may be overly restrictive and we would be interested to learn of the experience of other groups in this area.

To conclude this section we would like to illustrate the two points that we have raised, namely that there is little degradation in image quality as one goes off-axis and secondly that most of the observations made to date have been limited by the film rather than by the optics and its corollary that the current generation of X-ray optics have in fact met their design goals of one arc second imaging, by using actual data recorded during a rocket flight. Figure 6 shows the solar X-ray corona on 31 January 1978 photographed with the fused silica rocket mirror. The box encloses a feature which has been tentatively identified as a flaring bright point. It is located a little over 14 arc minutes from sun center at which the optical axis of the telescope was directed. The two lower frames of Figure 6 are magnified views of the same region taken with different exposures and recorded on two different emulsions. The left hand frame was recorded on Eastman Kodak SO-212, the Skylab film. The effect of the grain noise is obvious and the feature is unresolved. However, in the right hand frame, which was recorded on Eastman Kodak SO-253, a fine grain holographic emulsion, the structure is clearly revealed as a single loop 12 arc seconds long and slightly in excess of 1 arc second wide. The photograph, which of course includes the effect of the PRF which is neglected in the ray tracing treatment, clearly demonstrates that even at relatively large angles from the optical axis the angular resolution of the mirror for X-rays is on the order of one second of arc. Note: Essentially the same conclusion can be drawn from the HEAO-2 calibration data which shows that the HWHM is essentially independent of off-axis position⁽⁵⁾.

The Scientific Rationale for Improved Resolution Imaging

Given the fact that our current observational capability is on the order of one arc second, we must ask the question: Are there valid scientific objectives that will justify the effort to improve the resolution of X-ray telescopes by an order magnitude? Clearly we believe the answer to this question is yes. During the last decade our knowledge of the solar corona has been vastly increased due, in large part, to observations made with grazing incidence optics in the soft X-ray region of the spectrum. The classical view of the corona, as uniform and symmetrical with a radially outward decreasing density which expanded and contracted with the solar cycle, has been replaced by a picture dominated by plasma filled magnetic loops of all dimensions down to the limit of resolution (Figure 7). Similarly the description of the physics of the corona, of its energy balance, of the method of its heating, of the mass exchange between it and the lower levels of the solar atmosphere and of the nature of the instabilities which give rise to solar flares and other transient phenomena, has evolved into an explanation of these phenomena within the framework of magnetic loops.

This change in perspective has developed in concert with improvements in the spatial resolution of X-ray telescopes and in particular as a result of the long duration observations obtained from Skylab. However, the latter were limited in general to a spatial resolution of a few arc seconds, except for certain objects which have very high contrast. Nor, because of the high level of scattering produced by the mirror surfaces, were the Skylab X-ray instruments well suited for distinguishing between subtle changes in intensity from adjacent image elements. For many of the more fundamental problems outlined above, this has proved to be a particularly severe limitation to the Skylab data.

Observationally the requirement is not simply to resolve loops, or other structures, of smaller and smaller size, but rather to resolve the internal structure of individual loops which are themselves of moderate dimensions. For instance typical active region loops have widths on the order of 5-30 arc seconds and lengths of 1-4 arc minutes. The Skylab telescopes, with their realistic resolution of something in excess of 3 arc seconds, had sufficient resolution to resolve these loops but were unable to unravel the characteristic structure of individual loops. In particular it has not proved possible to specify the radial variations of the plasma properties of loops. This question is crucial because the high transport coefficients along the direction of the magnetic field (i.e., along the loop) tend to smooth out longitudinal pressure and temperature variations. In contrast the magnetic field inhibits the transport properties perpendicular to the field and gradients can be

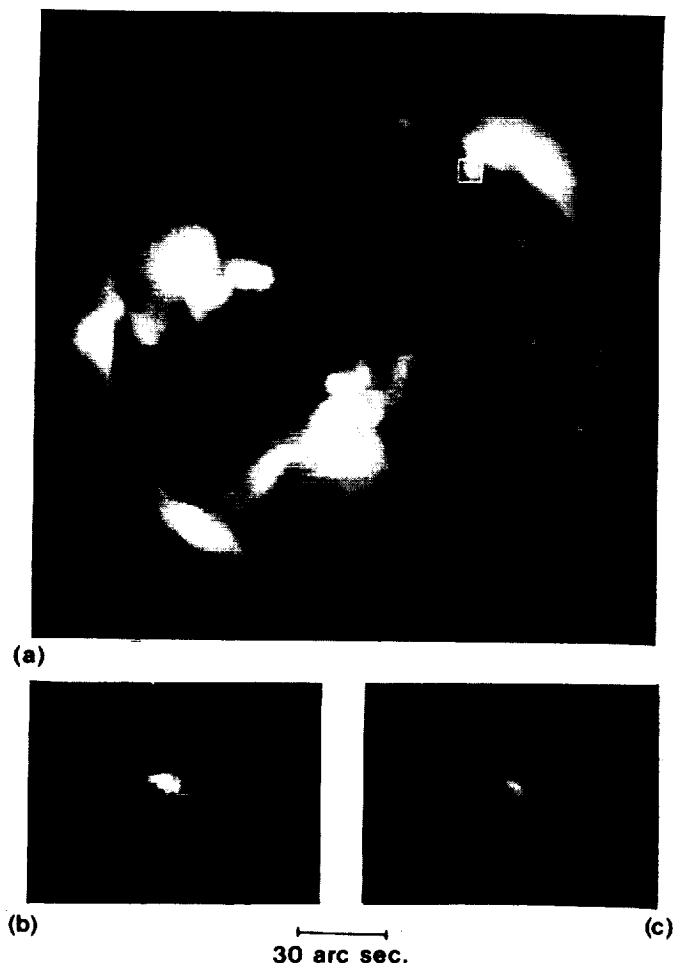


Fig. 6. The X-ray corona on 31 January 1978 showing the location of a flaring bright point (a). Magnification of the feature seen in different exposures shows the improvement in resolution between Eastman Kodak SO-212, the Skylab film (b) and the fine grain SO-253 (c). In the latter a single loop with a width slightly in excess of 1 arc sec and 12 arc sec long is clearly revealed.

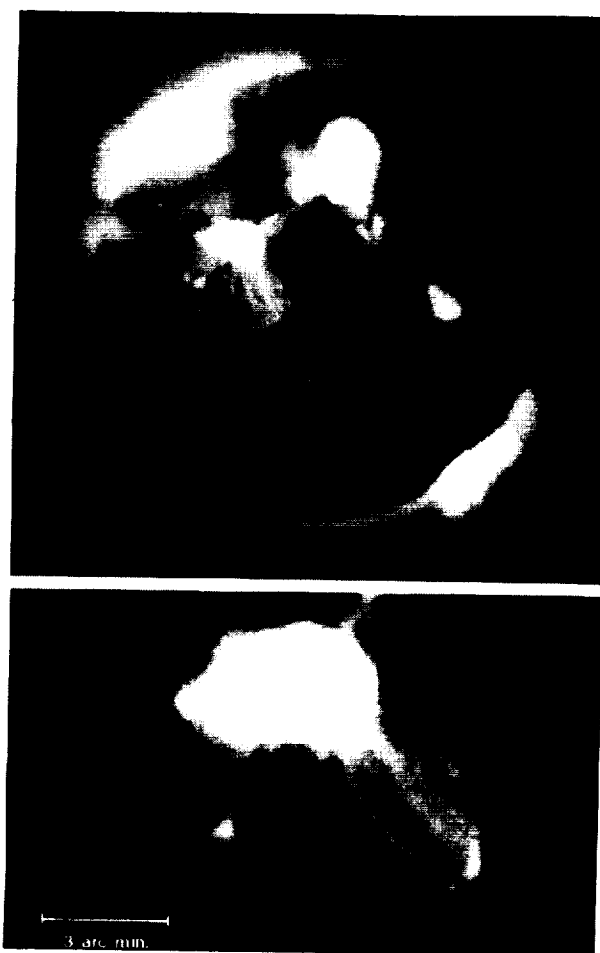


Fig. 7. The X-ray corona on 8 March 1973 showing the predominance of loop-like structures throughout the corona. The magnified image shows the loops associated with one of the active regions. The loops are several arc minutes long and 15–25 arc sec wide. They are too narrow to have their radial structure clearly resolved at the 2–3 arc sec resolution level of this image.

established in this direction. Consequently the different models of loop heating can be characterized by their description of the variations that can be expected across the loop. For instance, does loop heating take place only in a thin surface layer which surrounds a cool core or are loops bundles of individual flux strands each with its own temperature and pressure regime? It is difficult to see how a rationale choice can be made between the various theoretical models without observations with much higher spatial resolution than is currently available.

A second fundamental and largely unexplored area deals with the stability of loops. Here the important question is why many loops remain relatively quiescent while others undergo large transient brightenings and flaring. Recent theoretical work indicates that the initial instabilities in loops are almost certainly the long wavelength macroscopic instabilities. The pressure, or temperature, perturbations corresponding to these instabilities will show up as brightness fluctuations at or below the arc second level.

An estimate of the time resolution required for the study of transient or flaring phenomena can be obtained from the time taken for a plasma disturbance moving at the coronal sound speed ($2-3 \times 10^2 \text{ km s}^{-1}$) to cross one arc second, that is the distance over which independent determinations of the plasma characteristics can be made. Since this distance corresponds to $\sim 700 \text{ km}$ at the center of the solar disk then a time resolution of 1 s or less is necessary. Further, since the small loops frequently found at the centers of flaring regions

have lengths on the order of 10 arc seconds, it is obvious that a combination of both high spatial and temporal resolution is essential if the propagation of disturbances through this type of structure is to be studied. A recent review by Wentzel⁽⁶⁾ provides a more detailed discussion of the current problems of coronal physics with particular emphasis on coronal loops.

The Next Generation of X-Ray Imaging Instruments for Solar Observations

The observational goals that would justify the development of a new generation instrument are:

- (i) A real spatial resolution of less than half an arc second. In light of the earlier discussion, this resolution is the resultant of folding together the MTFs of both the optics and the detector; and
- (ii) A temporal resolution on the order of one second.

The first stage in achieving this goal would be the fabrication of a very high quality grazing incidence mirror and such a program forms the basis of our proposal for AXIO - An Advanced X-Ray Imaging Observatory.

An Advanced X-Ray Imaging Observatory

Our concept of AXIO is based on a single Wolter Type I grazing incidence mirror with Wolter Schwarzschild reflecting surfaces. We believe that only minor advances in current technology are required to permit the fabrication of the reflecting surfaces with sufficient accuracy to provide a resolving power of better than 0.2 arc seconds. The instrument concept provides for a group of four interchangeable focal plane detectors which would be selected for specific scientific objectives. An initial configuration, designed specifically for imaging observations would consist of pairs of 70 mm photographic cameras for ultra-high spatial resolution and electronic cameras for high time resolution observations. Many other configurations are possible and would undoubtedly be implemented in the expected 20-year operational life of the mirror and one rather exciting example is discussed later.

AXIO is projected as a candidate for flight on the Space Shuttle where it would be mounted to the instrument pointing system (IPS). Consequently it has been sized to be contained within a cylindrical volume roughly 7 m long and 1 m in diameter and weighing approximately 1000 kg. This size was chosen specifically to allow AXIO to be flown as part of a solar instrument cluster. For although AXIO is designed to operate alone the range of problems which it is proposed to study would benefit from the simultaneous acquisition of data by other solar instruments, many of which are already planned for flight.

An indication of the improvements in observational capability that AXIO will provide can be found by reference to Table I. In this table the various instrument parameters are compared with those of the Skylab telescope and in general reflect an order of magnitude improvement.

We have chosen a single mirror for AXIO rather than a nested set for three main reasons:

- (i) In a nested set the final imaging properties tend to be governed by the worst mirror in the set rather than by the best.
- (ii) The mechanics of nesting large mirror assemblies inevitably leads to some degradation in image quality arising from distortions introduced in the mounting plane, slight differences in focal lengths, etc., and these degradations are likely to be relatively more severe for large, ultra-high resolution mirrors.
- (iii) For solar observations the requirement for very large collecting areas is not quite as overriding as it is for celestial astronomy.

Obviously a single mirror design of rather modest dimensions, as AXIO is, will also be less expensive to fabricate than, for instance, the larger and more mechanically complex nested assembly proposed for the Advanced X-Ray Astrophysical Facility (AXAF). However, even if cost were not a consideration, for those applications where ultra-high resolution is of paramount importance we believe that the single mirror approach is the best solution.

The AXIO Mirror Fabrication Tolerances

The goal of sub-arc-second resolution for the AXIO mirrors can be met with carefully figured and very smooth reflecting surfaces. The tolerances on the surface figure are generally tighter than those specified for

TABLE I INSTRUMENT PARAMETERS
A Comparison Between AXIO and Skylab

| | <u>AXIO</u> | <u>Skylab</u> |
|--------------------------------|---|--|
| Wavelength Range | 6 - 300 Å | 2 - 60 Å |
| Spectral Resolution | Broadband 10 ranges | Broadband 6 ranges |
| Field of View | 40 x 40 (arc min) ² | 48 x 48 (arc min) ² |
| <u>X-Ray Mirrors</u> | | |
| Figure | Wolter Schwarzschild | Paraboloid-Hyperboloid |
| Material | Fused Silica | Nickel Coated Beryllium |
| Diameter | 80 cm | 30 cm and 23 cm nested pair |
| Effective Collecting Area | 175 cm ² | 20 cm ² |
| Focal Length | 475 cm | 213 cm |
| Plate Scale | 23 microns (arc sec) ⁻¹ | 10 microns (arc sec) ⁻¹ |
| Solar Image Size | 4.4 cm | 2.0 cm |
| Resolving Power (X-ray) | 0.2 arc sec | 2 arc sec |
| Diffraction Limit 5600 Å | 0.1 arc sec | 0.4 arc sec |
| 20 Å | 4 x 10 ⁻⁴ arc sec | 2 x 10 ⁻³ arc sec |
| Point Response Function (FWHM) | 0.5 arc sec | 3.4 arc sec |
| <u>Focal Plane Detectors</u> | | |
| <u>Film</u> | | |
| Type (Eastman Kodak) | 3414 | SO-212 |
| Spatial Frequency 20% MTF | 9 cycles (arc sec) ⁻¹ | 1 cycle (arc sec) ⁻¹ |
| Exposure Times | 1/4, 1, 4, 16, 64, 256 sec | 1/64, 1/16, 1/4, 1, 4, 16, 64, 256 sec |
| Time Resolution | 0.5 sec | 6.5 sec |
| <u>Photoelectric</u> | | |
| Types | Microchannel Plate & CCD | -- |
| Pixel Center to Center Spacing | 15 microns (0.65 arc sec) | -- |
| Wavelength Range | 6 - 300 Å | -- |
| Spectral Resolution | Broadband 4 ranges | -- |
| Time Resolution | -- | -- |
| for 4 x 4 arc min field | 1 sec (for data rate of 1 M bits s ⁻¹) | -- |
| for 40 x 40 arc min field | 15 sec (for data rate of 1 M bits s ⁻¹) | -- |

the HEAO-2 mirrors by approximately a factor of 2. Not surprisingly they are very similar to the tolerances proposed for the AXAF mirrors⁽⁵⁾. However the latter are physically larger and consist of a nested set of mirrors and consequently in assessing the ultimate resolution of the AXAF mirrors the tolerances which describe the achievement of confocality between the individual mirrors of the set have to be included.

In general the fabrication methods that were used for the HEAO mirrors will be adequate to achieve the specifications required for AXIO. However, the in-process metrology must be improved since the current limitations in our ability to figure very accurate surfaces, is not in actually figuring the surface but rather in knowing when the required figure has been achieved. In this respect we believe that a laser scanning technique developed for the fabrication of a high resolution X-ray microscope could be adapted successfully to the metrology of the AXIO mirrors. The technique is capable of measuring displacements of less than one microinch or slopes of less than one microinch per inch in real time and without the removal of the piece under fabrication from its production fixture. The tolerances on the microscope figure were in general tighter than required by AXIO and its successful fabrication⁽⁷⁾ demonstrates the soundness of the basic concepts and gives us confidence that the tolerances for the larger AXIO mirror can be achieved.

The tolerances on the mirror surfaces required to achieve AXIO's stated goal are shown in Table II where they are compared with the specifications for the HEAO-2 mirrors. Definitions of these tolerances can be found in the description of AXAF presented by Zombeck⁽⁵⁾ at this conference. It is more instructive to compare the AXIO requirements with the tolerances actually achieved on HEAO-2. From this comparison it can be seen that

TABLE II MIRROR TOLERANCES*
A Comparison Between AXIO and HEAO-2

| <u>Tolerance</u> | <u>HEAO-2</u> | | <u>AXIO</u> | |
|--|-------------------------|------------------------|-------------------------|--------------------------|
| | <u>Specification</u> | <u>Achieved</u> | <u>Specification</u> | <u>Design Goal</u> |
| 1. Out of Roundness $\Delta R = (R_{\max} - R_{\min})$ | 200×10^{-6} | 40×10^{-6} | 100×10^{-6} | -- |
| 2. $\Delta (\Delta R)$ | 50×10^{-6} | 43×10^{-6} | 20×10^{-6} | 8×10^{-6} |
| 3. $\overline{\Delta R}$ | 250×10^{-6} | | 250×10^{-6} | -- |
| 4. $\overline{\Delta R (\phi)}$ per inch of Circumference | $\pm 25 \times 10^{-6}$ | 5×10^{-6} | $\pm 10 \times 10^{-6}$ | $\pm 5 \times 10^{-6}$ |
| 5. Sagittal Depth | $\pm 5 \times 10^{-6}$ | $\pm 3 \times 10^{-6}$ | $\pm 3 \times 10^{-6}$ | -- |
| 6. Δ Slope per Axial Length of One Inch | $\pm 3 \times 10^{-6}$ | $\pm 4 \times 10^{-6}$ | $\pm 3 \times 10^{-6}$ | $\pm 0.5 \times 10^{-6}$ |
| 7. Surface Finish RMS Roughness | 30 \AA | $14-25 \text{ \AA}$ | 20 \AA | 10 \AA |

* All specifications are in inches unless otherwise stated.

the major problem area is the axial slope error (Δ slope per axial length). However it is precisely this tolerance that the laser scanning method was developed to measure. Since with its use we have demonstrated a capability to figure and measure surface slopes to better than one microinch per inch we feel confident that the AXIO design tolerance can be met.

Finally the surface smoothness actually achieved for several of the HEAO mirrors is better than the required specification for AXIO and very close to the design goal. The HEAO mirrors were finished using the submerged polish technique and, provided that sufficient time is available for final polishing, this technique appears to be adequate to achieve our goals.

In concluding this section we would like to reiterate the point that the achievement of the fine tolerances required by AXIO lies not so much in improvement of the fabrication techniques themselves, but rather in the in-process metrology which must be capable of monitoring the progress in near real time.

Expected Performance

To visualize the improvement in the observations that we expect to obtain with the AXIO system, we have compared several indicators of its predicted performance with the known performance of the Skylab telescope. The two characteristics that we will compare here are the PRF, which is the ultimate indicator of resolution and the ERF or edge response function which demonstrates how well the system, i.e., the optics and the detector can reproduce an infinitely sharp brightness edge.

The central maximum of the AXIO PRF has been calculated on the basis of the tolerances placed on the surface figure while the wings are based on the achieved scattering function of the HEAO mirrors. The Skylab PRF is actual experimental data and the two curves are shown in Figure 8. Compared to Skylab, the AXIO PRF is very sharply peaked within a few arc seconds of the central maximum. It has a HWHM of ~ 0.25 arc seconds and a half power radius of ~ 3 arc seconds. The latter figure is quite conservative since it can be obtained without any improvement in surface finish over that which has already been achieved with the HEAO mirrors.

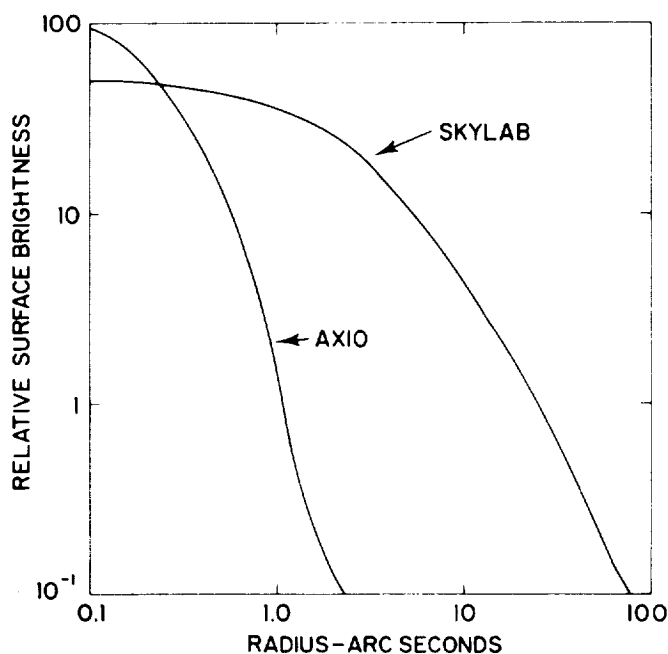


Fig. 8. A comparison of the calculated PRF for AXIO with the measured PRF of Skylab.

However, even if no further technological advances in fabrication are made and the calculated AXIO PRF is realistic, the ability to resolve the fine details of solar structure will be greatly improved compared to Skylab whose PRF within 2-3 arc seconds of the central maximum is nearly flat.

In order to obtain the maximum performance from AXIO the resolution of the mirrors and the detection system must be carefully matched. For the highest resolution observations, we plan to use a fine grain emulsion film as the prime detector. Unfortunately, there is a penalty for the use of these emulsions, namely their poor sensitivity. For instance we have found that it requires fifty times more deposited energy to obtain a net photographic density of 1.0 for SO-253 than for SO-212, the two emulsions compared in Figure 6. Therefore before we can calculate the ERF we have to make certain that the choice of emulsion will not limit the observations by making the exposure times too long. To check this, we have defined a criterion based on our Skylab experience. For instance we wish to record bright features, e.g., flares and active region cores, with exposure times not exceeding 4 s while we are prepared to make synoptic observations of large scale structures, coronal holes, etc., with exposures up to but not exceeding 256 s. Now the effective speed (f-number)

of an X-ray mirror can be defined as the ratio of the effective collecting area to the focal length squared and using the values in Table I, AXIO shows an improvement in speed of a factor of 2 over Skylab. This is insufficient to compensate for the difference in film speed; however, because of the increase in focal length, and hence image size, it is not necessary to use SO-253 to achieve the 0.2 arc second resolution design goal. A review of available Eastman Kodak emulsions suggests that 3414, a high definition aerial film with an intermediate grain size, is a good compromise.

Experimentally 3414 is a factor of 10 slower than SO-212 which would still leave AXIO with only 1/5 the speed of the Skylab telescope. However we have not compensated for the effect of AXIO's greatly improved PRF. The narrowing of the PRF means that more of the reflected energy will fall on the central image location, thus increasing the speed, at least for small scale features. By modelling various size features we have estimated the magnitude of this effect based on the measured results from Skylab. For cylindrical features with a source radius of 1.5 arc seconds the increase is a factor of 12, which falls to 6 for a 4 arc second radius and levels off around a factor of 3 for features larger than 10 arc seconds in radius. Taking all factors into account the speed of the AXIO mirrors together with 3414 film should be roughly equal to Skylab for large scale features and over twice as fast for the smallest features.

Having decided on the emulsion that will be used for AXIO we can now evaluate the ERFs for both AXIO and Skylab. They are calculated by integrating the PRF to form the line spread function of the mirror. This is then convolved with the line spread function of the film and the resultant is integrated to form the ERF. The results are shown in Figure 9 and the superiority of AXIO over Skylab at both high and low frequencies is obvious. To quantify the smoothing introduced by the system we find that a ± 10 percent change in the ERF at the center of the edge occurs over a spatial separation of 0.16 arc seconds for AXIO and 2.0 arc seconds for Skylab while a ± 50 percent change in the ERF reflects spatial separations of 0.82 and 14 arc seconds, respectively. Consequently, we believe that the AXIO system as presently configured will be capable of meeting the design resolution goal of 0.2 arc second.

The Use of Grazing Incidence Relay Optics

The previous discussion has been directed towards ultra-high spatial resolution observations using film placed at the primary focus of the grazing incidence objective mirror. However, an equally important scientific objective outlined earlier was for high time resolution observations and these almost certainly imply electronic imaging. The likely candidates for focal plane detectors, e.g., CCDs or microchannel plates, have resolution elements with center to center spacings of no less than 15 microns. Since the plate scale for AXIO is 23 microns/arc second, these devices will severely limit the spatial resolution of the observations. As an

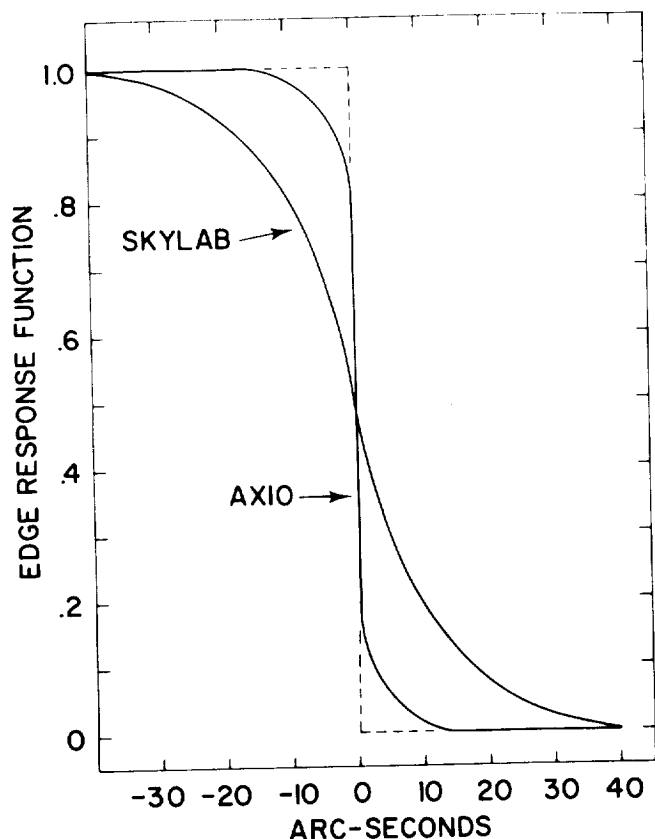


Fig. 9. A comparison of the ERFs for the Skylab and AXIO systems.

alternative to increasing the plate scale by increasing the focal length, we believe that the level of technology is sufficiently advanced to consider the development of relay optics to magnify the primary image.

In particular a grazing incidence microscope of the type described by Silk⁽⁷⁾ could, with suitable modification, be used to image the primary focus of the AXIO mirrors to form a grazing incidence astronomical telescope, an arrangement shown in Figure 10. The secondary grazing incidence mirror has hyperboloid-ellipsoid reflecting surfaces with the forward surface designed to collect the cone of rays leaving the primary focus of the objective. Since the microscope has achieved a spatial resolution of ~ 1 micron in the object plane, it will not deteriorate the resolution of the secondary image, for the design goal of 0.2 arc seconds corresponds to 5 microns at the primary focus. The factor of 10 magnification will expand the plate scale in the secondary image to 230 microns/arc second and consequently the 15 micron center to center spacing of the CCD resolution elements would not be a limiting factor.

The price paid for the increased magnification is a restriction of the field of view. However, if the instrument is baselined with an 800×800 CCD, which corresponds to a (52×52) arc second² field of view, the transmission of this field every second would require a data rate in excess of 5 M bit s^{-1} for 8 bits of intensity information per resolution element.

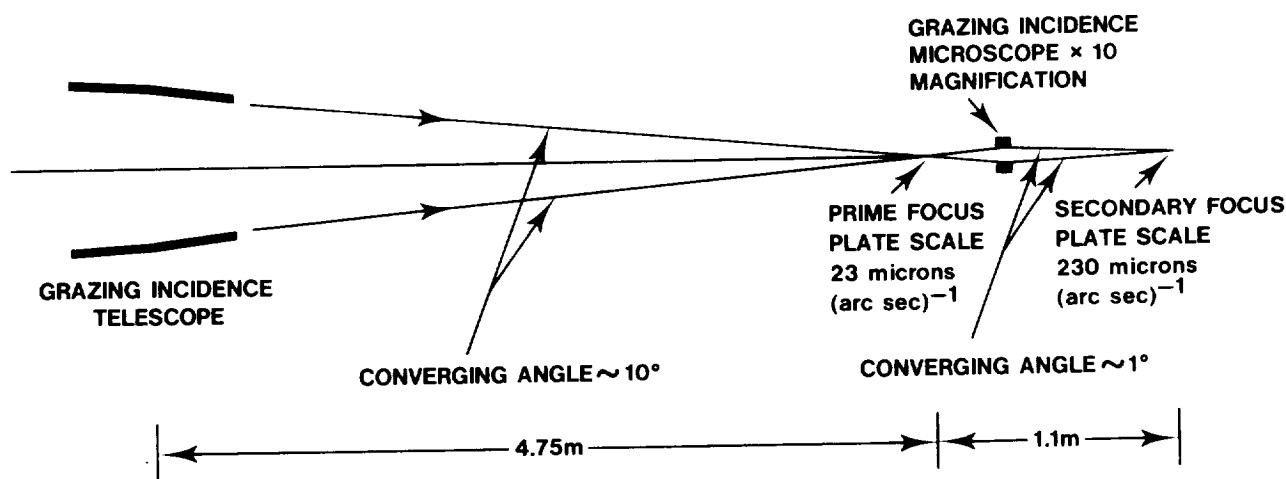


Fig. 10. A grazing incidence astronomical telescope employing two separate grazing incidence optical elements.

Therefore in the near future, the very high information content of the images is likely to restrict the area sampled to (20×20) arc second² which, based on our experience, is compatible with the field of view of the X-ray microscope.

Other advantages of the use of relay optics are that:

- (i) It provides the increase in magnification with only a modest increase in the total length of the instrument compared with the alternative of increasing the focal length of the objective; a difference

between 6 and 47.5 m in the example described above.

- (ii) Since the primary focus is not obstructed film cameras could be inserted there without disturbing the location of the secondary optic which is rather critical because of its small depth of focus.
- (iii) The addition of the relay optics also decreases the divergence of the X-ray beam which has a major impact when the grazing incidence mirror is used as a flux collector for a grating spectrograph. In the design shown in Figure 10 the convergence of the beam has been reduced from 10° after the primary to 1° after the secondary mirror with the result that the secondary beam is much more attractive for illuminating gratings. For now the grazing angles of the secondary beam, with respect to the grating, are below the critical angle and the reflection coefficients for the X-ray lines have reasonable values.

Although these designs are still in their infancy we believe that the progress already made indicates their feasibility and their realization will be a great assist in the quest for ultra-high resolution.

Conclusion

In summary, the notable success of the HEAO-2/Einstein mission has demonstrated that the technology for fabricating ultra-high resolution mirrors exists. The scientific uses of such an instrument are clearly defined and extremely important to the understanding of the physics of the solar corona. When coupled with the imminent availability of the Space Shuttle Transportation System to carry large instruments into orbit, the time seems opportune for the development of a large ultra-high resolution grazing incidence mirror to serve the needs of the solar physics community.

Finally by illustrating (Figure 11) how our view of the corona has changed as the resolution of X-ray telescopes has improved, from 20-30 arc seconds in the early sixties to 2-3 arc seconds during the Skylab mission in 1973, we hope to convey the feeling of excitement that we have about this project. At the poorer resolution the areas of bright emission were isolated and found to be located above active regions. With a factor of 10 improvement in resolution, the bright emitting regions are resolved into individual loops, the basic building blocks of the corona. The improved resolution and sensitivity also reveals the presence of X-ray bright points and coronal holes. We expect that a further factor of 10 improvement will reveal the internal structure of the loops, will enable propagating wavefronts arising from energy released in localized instabilities to be tracked and perhaps allow us to observe the reconnection of magnetic field lines.

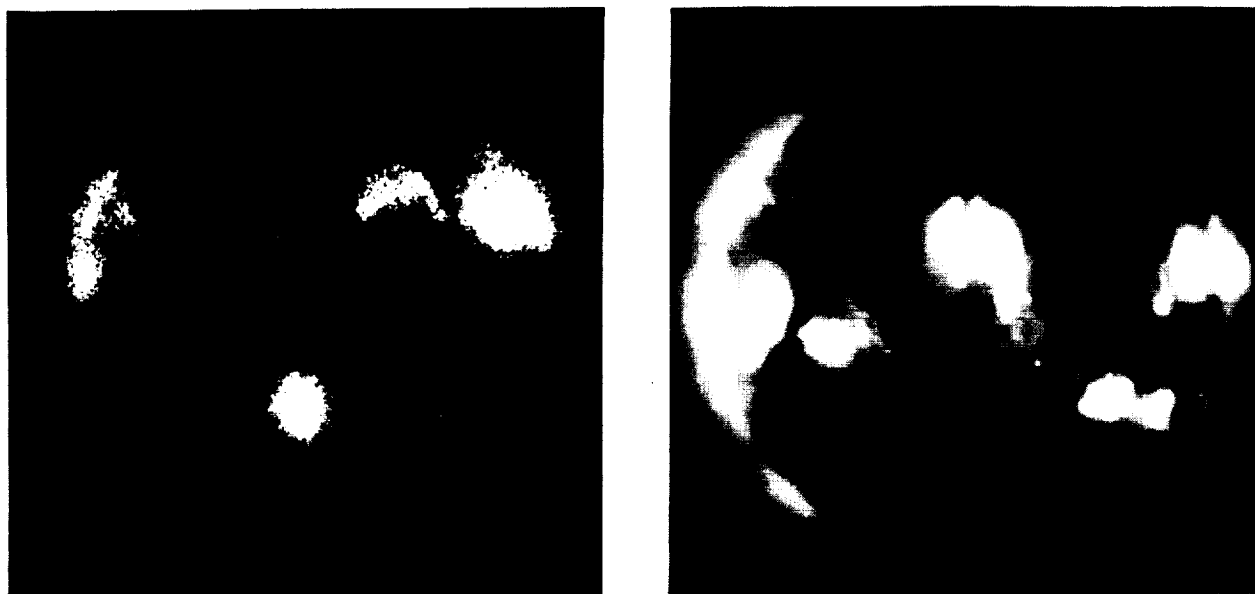


Fig. 11. Images demonstrating the effect of improving resolution on our knowledge of the structure of the corona. (a) A rocket photograph from May 1966 and (b) a Skylab image from June 1973.

Acknowledgments

It is a great pleasure to acknowledge the contributions of the many engineers and technicians at Diffraction Limited, Perkin Elmer, Applied Optics and Random Devices whose skill in fabricating grazing incidence optics has been largely responsible for our success.

The work described in this review has been supported in part by NASA under contracts NAS5-9041, NASW-2347, NAS2-7424, NAS2-8683, NAS5-25496, and NAS8-27758.

References

1. Vaiana, G.S., VanSpeybroeck, L., Zombeck, M.V., Krieger, A.S., Silk, J.K., and Timothy, A.F.: "The S-054 X-Ray Telescope Experiment on Skylab," Space Sci. Instr. 3, 19, 1977.
2. DelCarlo, C.: "Low-Scatter Metal Optics," Electro-Opt. Syst. Desgn. 3, 32, 1970.
3. Chase, R.C. and VanSpeybroeck, L.P.: "Wolter-Schwarzschild Telescopes for X-Ray Astronomy," Applied Opt. 12, 1042, 1973.
4. VanSpeybroeck, L.P.: "The Einstein Observatory Telescope - Design and Performance," Proc. SPIE 184, 1979.
5. Zombeck, M.V.: "The Advanced X-Ray Astrophysics Facility - Performance Requirements and Design Considerations," Proc. SPIE 184, 1979.
6. Wentzel, D.G.: "Heating of the Solar Corona: A New Outlook," Rev. Geophys. Space Phys. 16, 757, 1978.
7. Silk, J.K.: "Laboratory Evaluation of the High Resolution X-Ray Microscope," Proc. SPIE 184, 1979.

Questions from the Floor

Question 1: What is the projected curvature of field for AXIO?

Answer 1: The AXIO mirror design employs Wolter Schwarzschild surfaces and the expression for the curvature of field for such a mirror can be found in Reference 3. Substituting the parameters for AXIO, the deviation from a flat surface is 60 microns at 5 arc min and 480 microns at 15 arc min from the optical axis. If AXIO is coupled with a grazing incidence microscope to form a two element system, the curvature of field of the primary focus would not be the limiting factor. The primary focal plane would be within the depth of field of the microscope over an angle of $\pm 2\frac{1}{2}$ arc min, which is very large compared to the useful field at the secondary focus which is of order $1/2$ arc min.

Question 2: At 0.1 arc seconds, might you not require more light (x-rays) to make exposures rapidly (~ 1 sec) to prevent smearing of the image by actual motions on the Sun's surface?

Answer 2: It is quite true that there is little advantage to be gained by improving the spatial resolution for dynamic events if the temporal resolution is limited to a time which is long compared to the characteristic time, defined by the quotient of the resolution element and the velocity of the process to be observed. However, AXIO is designed to observe both static and dynamic events and the highest resolution observations will be associated with the former. The dynamic events will require electronic imaging and here the resolution will be limited to ~ 0.5 arc sec, at least initially. For a sound speed of 200 km sec^{-1} the characteristic time for 0.5 arc sec resolution at the center of the solar disk is ~ 2 sec, i.e., longer than the temporal resolution and therefore the image will not be smeared. As the observations are improved, we will undoubtedly run into limits imposed by the photon statistics. However, there is one saving grace, namely that at least one class of dynamic events, solar flares, have very high emissions and will allow an increase in temporal resolution of at least an order of magnitude above the one second level.

4.4 A Real-Time Electronic Imaging System for Solar X-Ray Observations from
Sounding Rockets

John M. Davis, Joseph W. Ting and Michael Gerassimenko

American Science and Engineering, Inc.
Cambridge, Massachusetts 02139

ORIGINAL PAGE IS
OF POOR QUALITY



A REAL-TIME ELECTRONIC IMAGING SYSTEM FOR SOLAR X-RAY OBSERVATIONS FROM SOUNDING ROCKETS

JOHN M. DAVIS, JOSEPH W. TING and MICHEL GERASSIMENKO

*American Science and Engineering, Inc., 955 Massachusetts Avenue, Cambridge,
Massachusetts 02139, U.S.A.*

(Received 2 February, 1979)

Abstract. A real-time imaging system for displaying the solar coronal soft X-ray emission, focussed by a grazing incidence telescope, is described. The design parameters of the system, which is to be used primarily as part of a real-time control system for a sounding rocket experiment, are identified. Their achievement with a system consisting of a microchannel plate, for the conversion of X-rays into visible light, and a slow-scan vidicon, for recording and transmission of the integrated images, is described in detail. The system has a quantum efficiency better than 8% above 8 Å, a dynamic range of 1000 coupled with a sensitivity to single photoelectrons, and provides a spatial resolution of 15 arc seconds over a field of view of 40×40 square arc minutes. The incident radiation is filtered to eliminate wavelengths longer than 100 Å. Each image contains 3.93×10^5 bits of information and is transmitted to the ground where it is processed by a mini-computer and displayed in real time on a standard TV monitor.

1. Introduction

During the past decade high spatial resolution X-ray images of the Sun's corona have been obtained using grazing incidence optics and photographic film [1-4]. Although there have been major advances in the recording techniques and in the analysis of the images [5], the use of film as the detector has so far limited their application to sounding rockets and manned spacecraft, where recovery of the film is possible. However, photoelectric detection of the X-rays and subsequent electronic imaging would allow the techniques to be extended to non-manned satellites and would in addition permit real-time control of the experiment either from the ground or in the case of the Space Shuttle from the Payload Specialist Station. The imaging capability would also enable non-imaging X-ray diagnostic instrumentation with narrow fields of view to be directed at targets on the solar disk selected on the basis of their X-ray rather than their visible light (e.g., H α) signature. In this way several classes of coronal phenomena, for example X-ray bright points, coronal arches or coronal hole boundaries, which in general cannot be observed at longer wavelengths, can be studied directly. Primarily to meet this objective but also to provide experience for eventually replacing film entirely, an electronic X-ray imaging system has been developed for flight on a sounding rocket as part of a target acquisition system for a narrow field, plane crystal, X-ray spectrometer. Since electronic cameras cannot yet provide the same spatial resolution as film, the rocket instrument also included a photographic camera to record data for post flight analysis. Since there is only a single X-ray mirror, the experiment

was designed so that the two cameras could be interchanged in the focal plane either automatically or as a result of a ground command.

The scientific objectives of the experiment and the characteristics of the X-ray emission from the Sun establish the specifications of the electronic imaging system. They are:

- (1) A spatial resolution of better than 15 arc sec which corresponds to 9 line pairs per millimeter at the focal plane detector.
- (2) A dynamic range in excess of 100 coupled with the capability of detecting single photons and of withstanding 5 orders of magnitude above this minimum level without permanent damage.
- (3) A capacity to integrate signals for periods up to tens of seconds.
- (4) Stable photometric accuracy under varying environmental exposure conditions and freedom from geometrical distortions.

To meet these requirements we have developed a system which uses a micro-channel plate (MCP) to convert the X-rays into visible light and a slow scan vidicon for signal recording and readout. The two units are coupled together using coherent fiber optics. This solution was chosen over relay optics to simplify the design of the interchangeable focal plane assembly.

To match the image size formed on the front plate of the MCP to the scanned area on the vidicon faceplate, the MCP phosphor is deposited directly onto the surface of a reducing fiber optic which reduces the image size by a factor of 1.5 (linear dimension). The demagnified image is transmitted to the fiber optic faceplate of the vidicon through a flexible coherent fiber bundle, or imagescope. The fibers in the optic and the vidicon are grouped in hexagonal arrays, whereas those in the imagescope form square arrays to minimize the Moiré patterns arising at the interfaces. For the same reason the individual fiber diameters change from 6 microns in the optic to 10 microns in the imagescope and back to 6 microns in the vidicon faceplate.

The detailed instrument description which follows is divided into sections devoted to the X-ray detector, the video camera, various circuit details and system performance.

2. The X-ray Detector

The solar X-ray corona viewed from the Earth subtends an angle of approximately 40 arc min. The image of this field produced by the rocket grazing incidence telescope has a diameter of 17 mm. Of the photoelectric detectors currently available, only the microchannel plate (MCP) combines high spatial resolution with a sufficiently large sensitive area to detect this image.

MCPs consist of close-packed arrays of geometrically uniform, semiconducting glass channels. The channel diameters may be chosen from within the range 8–50 microns, depending upon the application, and typically the channel diameter is 80% of the center-to-center spacing. When X-rays strike the inner surface of one

of the channels they are either reflected or absorbed. Since the work function of the glass is a few electron volts, the absorbed X-rays release one or more electrons. The application of an electric field between the ends of the plate accelerates the electrons and an electron avalanche forms as a result of further collisions with the channel walls. Upon exiting from the channels the electrons are proximity-focussed onto a phosphor screen. The overall gain of the system is limited to 10^4 by a process called ion feedback which arises because of the linear geometry of the channels. The effective gain can be increased by mounting plates in tandem in such a way that the channels of one plate are set at a small angle, or geometrical bias, to the plane of the MCP. This eliminates the straight path through the combined plate and the ions, because of their mass, are trapped at the junction of the plates [6]. This configuration which is called a chevron plate allows gains in excess of 10^7 to be obtained and chevron plates, manufactured by Galileo Electro-Optics [7], were used in the present instrument. For the flight unit we chose a chevron plate with a circular sensitive area of 25-mm diameter with 25-micron-diameter channels arrayed on 31-micron centers. This geometry provided a suitable match to the image size and resolution requirements; however, the more advanced projects that we have planned will need both smaller channels and larger sensitive areas.

The quantum efficiency of the MCP is a function of the angle at which the incident X-rays strike the channels [8], which in turn is set by the f -number of the imaging system. Because of the finite size of the solar image and the fact that grazing incidence optics produce an annular bundle of rays, the striking angle varies between

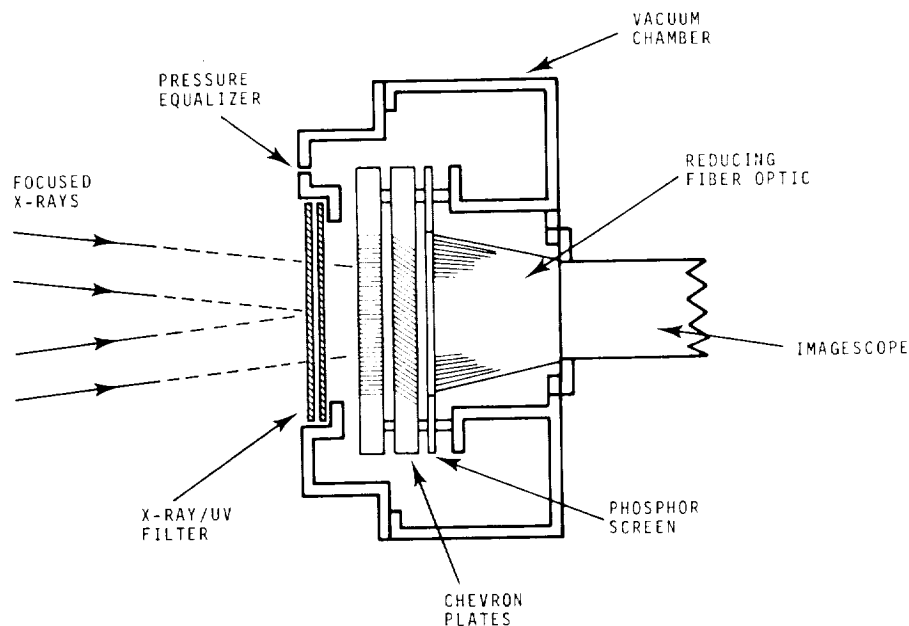


Fig. 1. Schematic diagram of the MCP focal plane assembly.

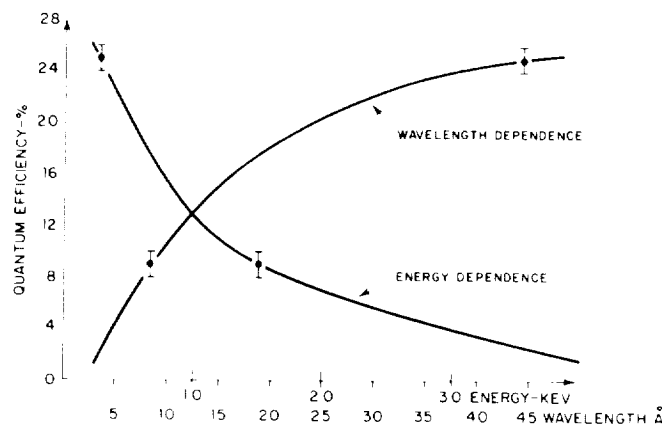


Fig. 2. The variation of the quantum efficiency of the MCP with wavelength (energy) for a fixed glancing angle.

5.5 and 6 degrees in the present instrument. As the quantum efficiency peaks close to this angle the channels of the first plate are aligned parallel to the optical axis of the imaging system and the second plate set at a bias of 15° (Figure 1), i.e. the reverse of the normal arrangement. This geometry provides approximately uniform quantum efficiency across the image. Actual measurements were performed at 8.3 and 43.4 Å and are shown in Figure 2 where the solid line represents the theoretical efficiency calculated using the model of Bjorkholm *et al.* [8] and normalized to the experimental data at 8.3 Å. The required passband of the detector is from 7 to 60 Å and the data show that the quantum efficiency increases monotonically from 7% to 25% across this range.

2.1. MOUNTING ASSEMBLY

Since the MCP can only be operated below 2×10^{-6} torr and must be conditioned for several hours at or below this pressure before the voltage is applied, it was enclosed in a stainless steel vacuum chamber (Figure 3). Copper gaskets were used throughout and the chamber was continuously pumped using a 2 l s^{-1} titanium cathode ion-pump [9]. To save weight the standard iron magnet was replaced by a magnet made from cerium cobalt [10] which has provided excellent performance at less than one fifth of the total weight. Typical operating pressures of 5×10^{-7} torr have been obtained.

The front port of the vacuum chamber contains a quartz window which allows the MCP to be operated in the payload during ground testing. The front port releases and swings forward when the MCP is driven into the focal plane. This action exposes a thin aluminized organic X-ray filter which now forms the forward vacuum seal. To minimize the pressure differential across the filter this event is timed to occur above an altitude of 120 km.

We have chosen not to operate the pump during flight to avoid the possibility

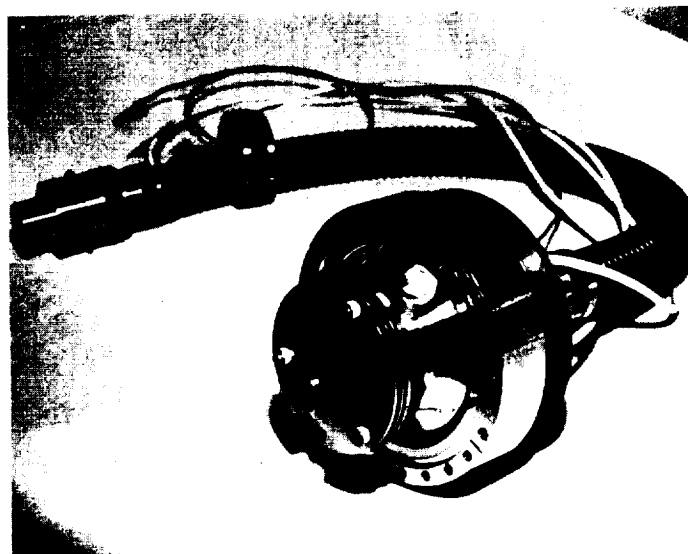


Fig. 3. A photograph of the MCP mounted in its stainless steel vacuum chamber with the front cover removed. The imageoscope is also shown.

of ion contamination of the MCP; this was never a major problem on the ground although its operation could be detected at the highest gain settings as a slight increase in the noise. However, the ion-pump is also used as a diagnostic aid to measure the chamber pressure and for this function its in-flight operation can be controlled from the ground.

2.2. X-RAY AND EUV FILTERING

The solar EUV and UV radiations, to which the plate is sensitive, are prevented from reaching it by a composite filter of 3000 Å of aluminum and 5 microns of polypropylene (C_3H_6). The most critical wavelength region for the filter lies just beyond the aluminum L-edge between 170 and 250 Å. The transmission of the filter can be calculated using the mass absorption coefficients of Caruso [11] and Henke and Elgin [12]. It was found that increasing the thickness of polypropylene will reduce the transmission in the 170-250 Å waveband faster than the transmission at the shorter X-ray wavelengths. The actual thickness of the filter was chosen so that it would reduce the number of photons in the incident spectrum in the longer waveband to less than 5% of the number between 7-60 Å.

The filter is made in a sandwich; the first layer consists of 2.5 microns of polypropylene with 1500 Å of aluminum on either side and is followed by a separate film containing the balance of the polypropylene. The use of two layers of aluminum has been found to produce a much higher yield of pinhole-free filters and the sandwich construction isolates the second aluminum layer from the MCP and prevents UV-produced photoelectrons from producing noise counts.

2.3. THE MCP GAIN

Although the MCP can be operated at gains up to 10^7 there is a distinct advantage to operating at lower gains as this will reduce the noise contribution from spurious events. The required gain can be estimated from a knowledge of the sensitivity of the vidicon and the requirement that the system be able to detect single photoelectrons.

Typical slow scan vidicons are sensitive to a faceplate illumination of 0.01 foot-candles per second which corresponds to approximately $0.17 \text{ erg s}^{-1} \text{ cm}^{-2}$. If the sensitive area ($\sim 1 \text{ cm}^2$) is divided into a 256×256 pixel matrix (see Section 3.1), the energy required per pixel is on the order of $3 \times 10^{-6} \text{ erg s}^{-1}$. The maximum spectral response of the vidicon and the peak output of the MCP phosphor were matched at 4200 Å. Using this wavelength the number of photons required to produce a useable signal is 6.3×10^5 . Under normal operation the phosphor provides a gain of 100; consequently to detect single X-ray photons the MCP need only provide a gain of 10^4 . On the basis of the manufacturer's gain characteristics this requires operating the plate under a potential difference of 1350 volts. This is well below the maximum recommended operating voltage (2200 V) and ensures that the operation of the plate is essentially noise free.

Because of the wide range in intrinsic brightness of the X-ray corona (10^3 – 10^4), the imaging system was provided with three time exposures by electronically shuttering the MCP. The three exposures were nominally 1/4, 1 and 4 s and were obtained by gating the plate voltage. Thus each exposure duration is defined by the time the high voltage is maintained across the plate allowing electron multiplication to take place. When the exposure is over, the gating pulse is turned off and the plate is returned to a lower voltage where multiplication does not occur. The rise and fall time of the power supply was approximately 20 ms which is adequate for defining even the shortest exposure.

The three time exposures coupled with the intrinsic dynamic range of the vidicon (~ 100) provide a total dynamic range of 1.6×10^3 . This value is marginal for detecting the range of phenomena on the sun and leaves little room for error in selecting the flight settings. The first alternative of adding further exposures, e.g. 16, 64 s, etc., was rejected as their addition to the sequence would take up too great a fraction of the observing time (approximately 100 s of the flight was all that could be allotted to the operation of the X-ray video system). An alternative approach is to vary the gain of the MCP by controlling the voltage applied across it. For instance if the gain is increased by a factor of 64 then the signal recorded by the vidicon during the shortest exposure will now be equivalent to four times the signal recorded during the longest exposure at the low gain setting, for a source of constant illumination. Thus the combination of the three exposure sequences and the two gains will provide a total system dynamic range in excess of 10^5 . This increase in gain can be achieved with a potential difference across the plates of 2000 V, which is still well below the maximum operating voltage. The instrument is launched in the low gain config-

uration and if the picture displayed on the ground monitor is too faint, the gain of the MCP can be increased by activating a relay closure, by way of a radio link, to select a second biasing resistance on the low voltage side of the MCP high voltage power supply.

3. The Video Camera

3.1. DESIGN CONSIDERATIONS

The video camera is designed to meet the scientific requirements of the experiment within the constraints set by the capabilities of the telemetry and ground data handling and display systems. To recapitulate, it must possess a dynamic range of at least 100, a spatial resolution corresponding to 15 arc seconds and a capacity to integrate signals for a few tens of seconds. To interpret the spatial resolution requirement consider a square field of view of 40×40 square arc minutes which satisfactorily contains the solar image. For such a field a picture format of 256×256 pixels provides 10 arc second resolution elements. The incident flux within each pixel is represented by one of 64 intensity levels (6 bits) which our experience, gained with the computer display of digitized photographic images, has shown to provide an adequate visual representation of the corona and also suitably matches the dynamic range of the imaging system.

As it is necessary to integrate the X-ray signal for several seconds to obtain sufficient intensity the vidicon tube must combine image storage and high resolution during operation at room temperature. Although secondary electron conduction (SEC) vidicons have excellent storage capabilities, their spatial resolution and dynamic range are severely limited. The best available tubes at the time (1975) had a resolution, at the center of the frame, of only 250 TV lines with a 50% modulation transfer function (MTF). Comparable figures for slow scan vidicons are in excess of 800 TV lines and under slow scan operation, vidicons have been developed which retain over 90% of their signal for periods in excess of 20 s. They operate at room temperature, have dynamic ranges over twice as wide as SEC vidicons and are much less susceptible to burn out, being able to withstand signals in excess of 10^5 times the minimum without suffering damage. Both types of tube have similar photometric accuracy and are capable of providing an absolute accuracy of approximately 10%, which is adequate for the present application. Therefore, because resolution and dynamic range were of primary importance, a slow scan vidicon was selected as the basis of the camera design.

A pulse coded modulation (PCM) transmitter is used to relay the video pictures and additional scientific data to the ground. Each telemetry data frame is divided into 32 twelve-bit words and the repetition frequency is $1024 \text{ frames s}^{-1}$. Ten words of the 32-word frame are used to transmit the video data. Of these ten, 8 contain pixel intensity coded into 6 bits, or 64 grey levels; the remaining two bits of each intensity word are used for housekeeping or other low bit rate data. The sixth word identifies the vertical and horizontal locations, within the image array, of the first intensity

word of the group of 8 and the tenth word indicates the presence of TV data. This last word is used to alert the computer, which displays the data, that a time exposure has been completed and that a readout cycle is underway. Each picture is composed of 2^{16} pixels and takes 8 s to be transmitted; therefore, the greatest storage time for an image will be 12 s, i.e., the sum of the longest exposure plus the transmission time, and signal losses from the vidicon target will be minimal. The TV information is presented to the transmitter in parallel form through a cable of 8 wires, one for each bit of the data word. All the bits are clocked together and synchronized with the telemetry system so that after each word is sampled a new complete word is shifted into the transmitter buffer.

We have used a camera readout technique which we call 'dot scanning.' In contrast to the continuous sweeps used in standard cameras, each pixel in the 256×256 square format is read by turning the electron beam on and off at each location. While the beam is off, the magnetic deflection fields are changed to select the next pixel location (see Figure 4 for a timing diagram of the read cycle). After a picture is read out, the charge pattern left on the target is the whole picture less the partially filled 'dotted holes.' The erasure scan that follows must charge the target uniformly, thereby reconditioning it for the next exposure. In order to assure complete erasure, the electron beam makes continuous sweeps during the erase cycle. To minimize the time between exposures, erasure is limited to a single scan and consequently a

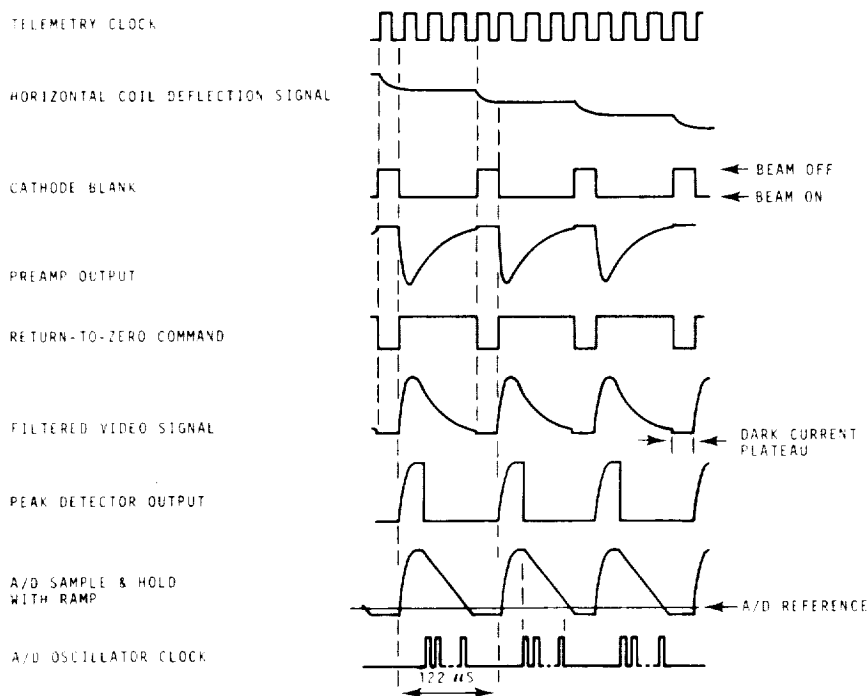


Fig. 4. The read cycle timing diagram.

small residual image may remain after the completion of the read-erase cycle. The residual image is a result of a combination of effects arising from the surface impedance of the photoconductor, the impedance of the scanning beam and the capacitance of the target. Several methods of improving the efficiency of the erase scan were investigated. They included increasing the beam current by increasing the target potential during the erase cycle and the superposition of a vertical 'dither' to the horizontal scan with an amplitude equal to the separation of the scan lines. Although the first method removed the residual traces of the highlights from the previous exposure, it substantially decreased the dynamic range by cutting off the low level signals. The dither system made only marginal improvements to the picture; therefore, in the interest of simplicity and reliability the changes in the erase scan were limited to the adoption of a continuous sweep cycle.

Although power consumption is not usually a severe problem on short duration rocket flights, low power circuits were used whenever possible and CMOS was chosen for the logic family. The total power required by the camera is 12 W which is supplied by 3 packs of high rate silver zinc batteries. The packs are mounted within pressurized battery boxes and are assembled to provide +28 V and ± 18 V. The +28 V supply is used for the vidicon heaters and for the focussing coil, in each case being independently current regulated. The ± 18 V packs are voltage regulated to +15 V and ± 12 V and are used for the biasing of the vidicon and the control of the logic circuits.

Finally, past experience has shown that electronic memory devices, such as flip flops, often reset, without any apparent reason, during typical rocket flights. We believe the cause to be momentary power interruptions, perhaps resulting from relay contact bounce, and to prevent this possibility affecting the camera operation, a diode capacitor network, capable of holding enough charge to maintain the circuit for a few milliseconds, has been built into the system wherever necessary.

3.2. THE VIDICON

To implement the design, several slow scan vidicons manufactured by General Electrodynamics [13] were tested. The tubes are part of a series of space qualified designs which have been used successfully on several Mariner missions. The preliminary tests resulted in the selection of a model 7290 vidicon. It has a custom-fitted fiber optic faceplate and combines magnetic focussing and deflection. The material of the target is amorphous red selenium. It has a dark resistivity of $10^{13} \Omega \text{ cm}^{-1}$ which permits slow scan operation at room temperature. This particular model is not ruggedized, but since it was planned to launch the experiment with power off, it was considered to be mechanically adequate and this decision has been justified by flight experience.

The slow scan vidicon can be visualized as a special tetrode tube. Its essential elements are an electron gun, an electric field free region and a target (Figure 5). The electrons are generated in the gun by thermionic emission from the indirectly heated cathode. The number of free electrons, or beam current, is regulated by the

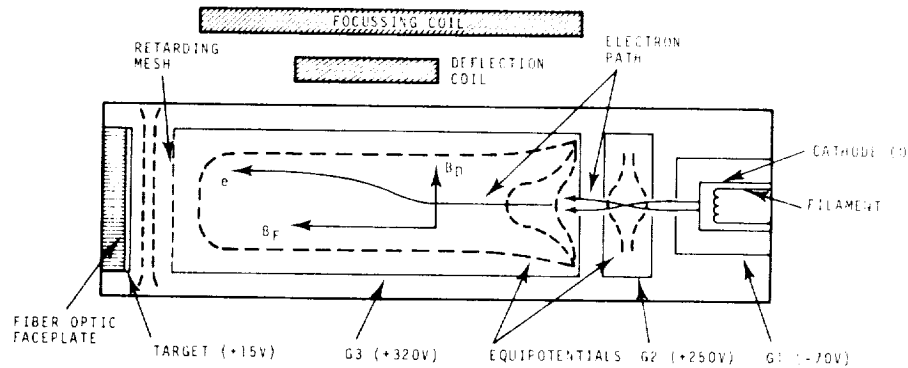


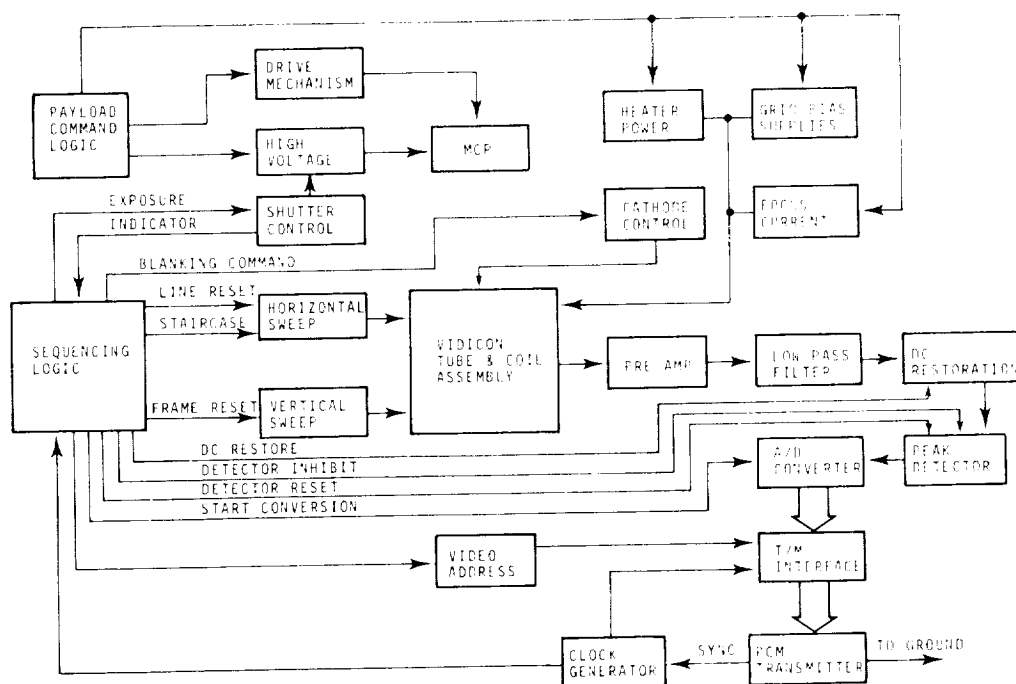
Fig. 5. Schematic diagram of the vidicon tube.

G1 electrode which plays the same role as the control grid in a triode. Leaving G1, the energy of the electrons is increased to +250 V by the accelerating grid G2. At this energy the electrons can be deflected without substantial dispersion arising from their Coulomb repulsion. This grid also acts as an electrostatic lens and focusses the beam into its first crossover point which occurs within the lens. The slightly divergent beam exiting from G2 is refocussed by the action of G3 which is set at +320 V. This grid provides a region free of electric fields where the beam can be magnetically deflected using coils aligned such that their field is normal to the electron beam. At the far end of G3 is a fine wire mesh placed directly in front of the target and held at the same potential as G3. The uniform electric field between the mesh and the target decelerates the electrons so that they strike the target at near-zero velocity. This 'soft landing' prevents the generation of secondary electrons which are a source of 'blooming'. Beam focussing, as in most high-resolution tubes, is achieved by using a separate coil to produce a uniform magnetic field aligned parallel to the electron beam. The field causes the electrons to spiral around their direction of motion and by adjusting its strength a node can be located at the target where the displacement due to the random perpendicular component of the velocity of the electrons is zero. Thus the field has the effect of focussing the first beam crossover point onto the target.

The control grid voltages are supplied from two separate d.c. to d.c. converters that operate on +28 V d.c. power. A custom made MIL power supply [14] provides the -70 V for G1 and the +250 V for G2. A separate Velonex [15] supply provides the +320 V for G3. The high audio chopping frequency of the converters was a significant source of noise and it would have been preferable if they had been synchronized to the basic camera clock frequency of 9.192 kHz or its first harmonic.

4. Circuit Details

A functional block diagram of the camera electronics is shown in Figure 6. It consists of three major elements:



(i) The video chain, which takes the signal output from the vidicon and processes it for transmission. It contains a preamplifier, a two-pole low-pass filter, a d.c. restoration circuit, a peak detector and an analog to digital converter.

(ii) The vidicon deflection circuitry which controls the vertical and horizontal sweeps.

(iii) The control logic which generates all the clock and timing signals in the camera. The circuitry is of standard design built around binary counters and monostable multivibrators. The CMOS logic family, operating at +12 V, is used throughout the camera because of its low power and high noise immunity characteristics. The input clock is derived from the PCM transmitter and the start of every read cycle is synchronized with the PCM frame encoding. A special feature of the design ensures that the exposure cycle always starts at the shortest exposure and cycles through to the longest exposure. A summary of the various functions is given in Table I.

4.1. THE VIDEO CHAIN

The video chain takes the signal output from the vidicon and processes it for transmission. It consists of a preamplifier which is a.c. coupled to the tube target, a two-pole low-pass filter to remove high frequency noise, a d.c. restoration circuit which provides a base level for the peak detector and finally an analog to digital converter.

The signal pulse from the tube target, resulting from the discharge of a target

TABLE 1
Logic functions for the video camera

| Mnemonic | Function |
|-----------|--|
| ZRZ | Video d.c. restoration command. |
| PDR | Peak Detector Reset; discharges the peak holding capacitor. |
| PIB | Peak Detector Inhibit; disables the input to the peak detector at the same time PDR is exercised. |
| ZSH | ADC sample and hold command. |
| HSH | Sampling command for the horizontal sweep sample and hold converts the linear ramp into a staircase. |
| CBK | Blanking signal for the tube cathode. It holds the beam off during the time when the beam is being switched from one pixel to the next and during exposure and beam retrace times. |
| HOR | Horizontal sweep integrator reset. |
| VER | Vertical sweep integrator reset. |
| IIG | Image intensifier gating; this is the electronic shutter command. |
| HAD & VAD | 8-bit counters that are synchronized with the horizontal and vertical sweeps. They indicate the X and Y addresses of the pixel being read out. |
| EXS | Exposure sequence indicator; shows which one of the three exposures is being read out. |
| CIN | Input clock derived from the PCM transmitter. |
| FIN | Synchronizes the start of every read cycle with the PCM frame encoding. Its presence simplifies the frame decoding by the ground computer. |

pixel, is due to the induced charge flow from that pixel through the target bias and preamplifier circuitry. To detect this charge flow a current-to-voltage preamplifier (Figure 7) was chosen because it reproduces the physical target discharge more directly and has high speed because of its relative independence of source and stray capacitances. Because the input is a virtual a.c. ground, almost all of the signal current goes to develop the output voltage. If a true current-to-voltage conversion is to be made, the input bias current to the preamplifier must be much less than the minimum signal current that is to be measured. The detectable signal above the dark noise, during a typical beam gating read cycle, is on the order of a few nano-amperes and therefore the bias current of the preamplifier input has to be lower than this value, which calls for an FET input stage.

The minimum dynamic range of the tube is specified by the manufacturer as 200 and therefore the preamplifier should not significantly degrade this value. The best compromise in terms of dynamic range and low bias is a pair of discrete low

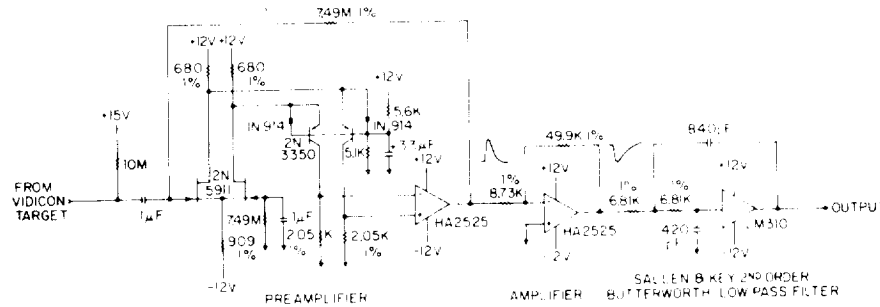


Fig. 7. The front end of the video chain showing the details of the preamplifier and the low pass filter.

noise FETs at the input of a fast, good quality, operational amplifier. This arrangement was preferred over an FET operational amplifier because discrete FETs offer much better noise characteristics. Secondly, a balanced differential configuration is preferred over a single FET input circuit because such an arrangement rejects common mode noise. However, the high frequency response is degraded because of the Miller effect which reflects the gate to drain capacitance back to the input, multiplied by the gain of the FET.

The addition of a pair of bipolar transistors connected in cascode with the FETs improves the high frequency response; however, in the present design a 'folded cascode' differential pair is used. The advantages it presents over the simple cascode are several: (a) it allows a larger input voltage swing; (b) the quiescent current of the FET and bipolar transistor can be biased separately; and (c) the output voltage of the stage swings closer to halfway between the supply voltages. Its gain expression is identical to a simple cascode, provided $R_d > Z_e$ where Z_e is the input impedance of the common-base bipolar transistor and R_d is the drain resistor. This condition is easily met, because $Z_e \approx 50 \Omega$. The input differential FET pair used is a 2N5911 and the bipolars are implemented by a 2N3350, a dual PNP in a single can. The operational amplifier is the high slew-rate, dielectrically isolated Harris HA-2525. The closed-loop Bode plot of the preamplifier response is shown in Figure 8. The measured noise was $120 \mu V_{rms}$.

The second stage in the chain is the two-pole low-pass filter which is added to remove all high frequency noise from the video signal, especially that arising in the vidicon bias power supplies. It consists of a two-pole Butterworth-type active filter [16], built around a high-input impedance unity-gain buffer (Figure 7). Since all the time constants of the vidicon tube are invariant with the signal strength, some of the higher-frequency components can be attenuated without impairing the linearity of the amplitude response. It is important that the filter does not alter the dark current plateau (see Figure 4) from which the d.c. restoration is made. The minimum breakpoint frequency to meet this requirement was found experimentally to be 40 kHz.

As the target is a.c. coupled to the preamplifier it produces a signal with average

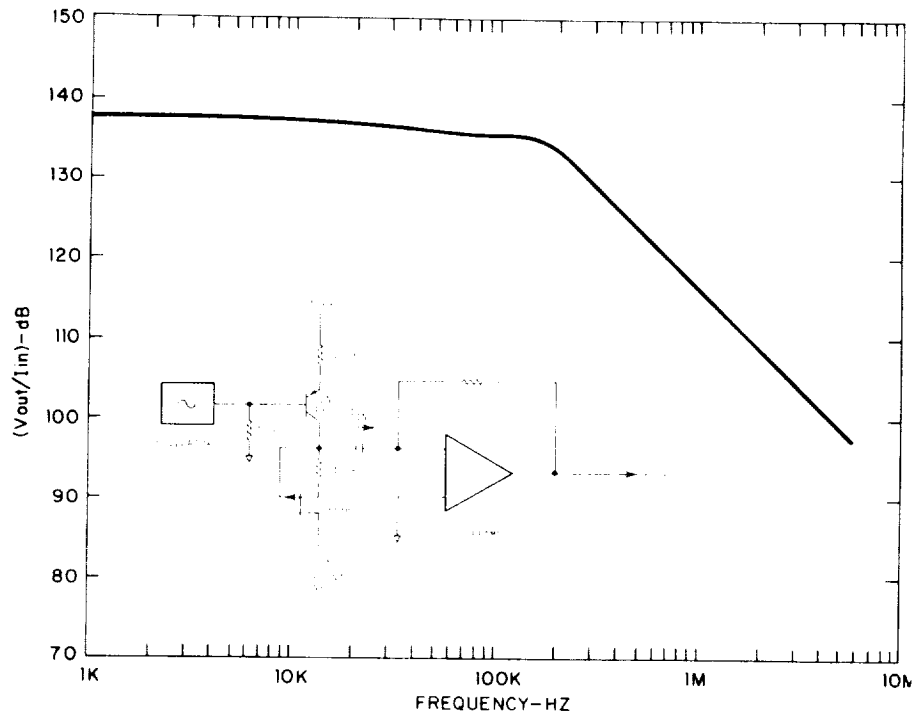


Fig. 8. The experimentally measured Bode plot of the video preamplifier. The insert shows the circuit used to obtain the result.

charge balanced around zero volts. Consequently d.c. restoration is required to bring the dark current plateau of the signal back to zero volts and is accomplished by subtracting the preamplifier signal from the continuous dark current level of the tube with the help of a sample and hold circuit.

Following d.c. restoration the peak amplitude voltage of the signal, within a specified time interval, is detected and held. Conceptually, a capacitor and a perfect diode are sufficient to perform this function; however, it is obvious that a real diode cannot provide good peak transfer linearity because diodes exhibit voltage drops in the forward biased condition. If instead, the diode capacitor combination is placed inside a negative feedback loop of an operational-amplifier, the offset is divided by the open loop gain of the operational-amplifier, thereby reducing it to a negligible error. A circuit based on this concept was built with the peak holding capacitor connected as the load of an emitter follower. The base to emitter junction of this transistor, besides replacing the diode, also supplied extra current gain in the forward direction. A discrete operational-amplifier is used, because integrated types are too slow. When the circuit was initially tested for fast rise input signals, the output carried a large overshoot. As this deviation disappeared when the input was slowed down, high frequency peaking, with a low damping ratio, was suspected

and a suitable two-pole, one-zero shunt filter designed for the appropriate frequencies cured the peaking problem without sacrificing the speed.

After each pulse detection, the holding capacitor is reset by a shorting switch. This switch is placed inside the feedback loop of an operational-amplifier so that the reset voltage remains constant. An input clamping switch protects the output stage of the circuit from being shorted to ground.

Finally the analog signal voltage is measured and converted, using a single-slope open loop circuit, into a digital output signal. This design was chosen because of its simplicity and because it provides sufficient accuracy for 6-bit resolution. It is accomplished by connecting the output of the peak detector to a constant discharge sample and hold. As long as the switch of this sample and hold is closed, the peak level of the signal is reproduced. But as soon as the switch opens the signal starts to decay at a constant rate. The decay time to a reference level is measured against a digital clock.

4.2. THE DEFLECTION CIRCUITRY

This circuitry drives the horizontal and vertical deflection coils which produce the magnetic fields and which in turn control the sweep of the electron beam across the target. Two integrators generate the horizontal and vertical sweeps under logic control. The linear vertical sweep is applied directly to the vertical coil driver while the horizontal linear sweep is first transformed into a voltage staircase through the action of a sample and hold. Each step, when converted into coil current, deflects the beam into a particular horizontal pixel location. The block diagram of the deflection circuitry is shown in Figure 9.

During the reset, the capacitors of the integrators are discharged by JFET analog switches. Care was taken to assure stable operation. All critical resistors are precision types and the integrating capacitors are made of low leakage polycarbonate material.

Originally, instead of analog integrators, a natural binary counter followed by a CMOS digital to analog converter (DAC) generated the horizontal staircase signal. Unfortunately the DAC exhibited excessive differential non-linearities, which meant the distances between pixels were not always constant. As an example, in the camera, there are 8 pixel bits in each direction. If a 5% maximum differential linearity is allowed, then the DAC must have at least 13 bits. Such a DAC was not available in a low power version at the time the camera's design was completed.

Before the deflection coil drivers, the horizontal and vertical reference signals go through adjustable amplifiers in which both gains and offsets can be varied. The coil drivers are essentially closed loop voltage to current converters. The peak deflection currents for the horizontal coil driver are ± 90 mA. An integrated power operational-amplifier, the Fairchild μ A 791, was used for this purpose. The peak vertical deflection coil currents are only ± 10 mA, and here a monolithic LM301A operational-amplifier was employed.

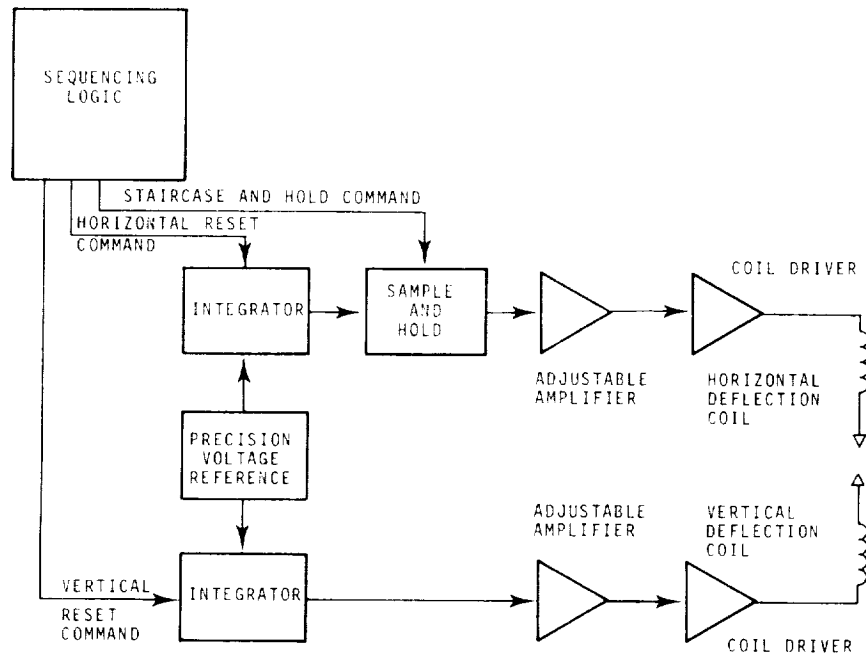


Fig. 9. Functional block diagram of the deflection circuits.

5. Performance

In the current application the parameters of major interest are the sensitivity, dynamic range and spatial resolution of the system and their evaluation was carried out in two stages. In the first stage the performance of the vidicon camera and electronics was optimized using visible light illumination of the camera. Once this was accomplished the performance of the whole system was studied using either X-ray or UV illumination.

5.1. DYNAMIC RANGE MEASUREMENTS

Since the solar X-ray corona has an intrinsic brightness variation in excess of 4 orders of magnitude it is most important that the dynamic range of the system be as large as possible in order to minimize the range of exposure times required to display the different phenomena. Consequently particular attention was paid, during the design of the video chain, to maintaining the inherent dynamic range of the vidicon. Once the camera was assembled the dynamic range was measured and the measurements repeated as the various parameters and circuits were adjusted and modified. The procedure followed consisted of illuminating the vidicon with a diffuse halogen light source operated at constant voltage. While the incident light intensity was held constant, the length of the exposure was varied using a com-

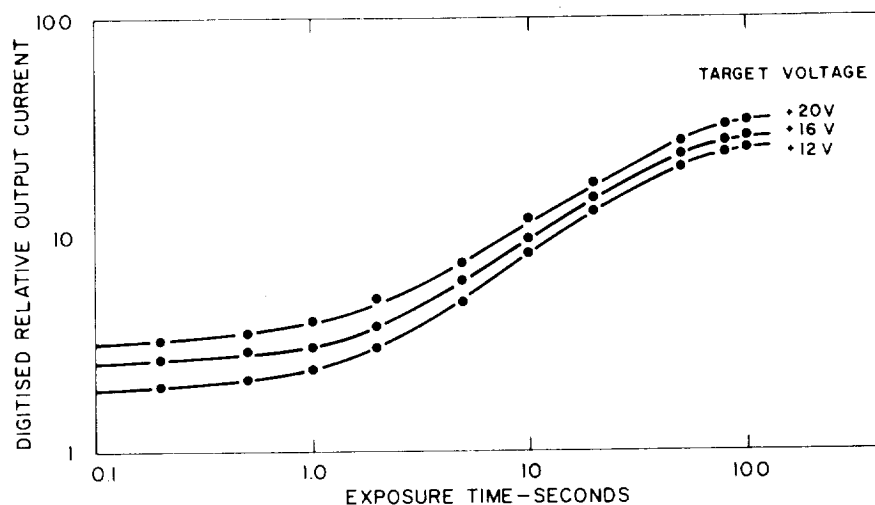


Fig. 10. The dependence of the dynamic range on the target bias voltage.

puter controlled shutter. The computer recorded the data and the integrated light output was formed from an average of the central 50×50 point pixel array.

Typical response curves, for several values of the target bias voltage, are shown in Figure 10. Contrary to expectation the dynamic range is insensitive to this voltage, which controls the gain of the vidicon, and in all cases the dynamic range, defined as the ratio of the incident light required to saturate the tube to the noise signal, is in excess of 1000. A target bias of 15 V was ultimately chosen for the vidicon as this provides an optimum system gain. Too high a gain results in the formation of 'bright spots' caused by electrical breakdown in target surface non-uniformities.

These curves are only valid for exposure times which are sufficiently short for the integrated dark current to be negligible. Experimental data showed that, at room temperature (21 °C), the dark current increased monotonically with time. However, for exposures of less than 15 s the noise contribution was at or below the level of detectability and therefore, since the longest exposure planned for the flight sequence was 4 s, the dark current does not limit the dynamic range of the system.

The total system response was measured in an analogous fashion except that 8.3 Å X-rays were used instead of visible light. The MCP was operated in vacuum at a pressure below 1×10^{-6} torr and was illuminated by a uniform monochromatic source of X-rays obtained by filtering a beam generated by electron bombardment of an aluminum anode. The instantaneous flux incident on the MCP was measured with a calibrated proportional counter. The measurements were performed using the flight program which generated exposures of 1/4, 1 and 4 s by using the MCP as a shutter and the average integrated intensity over the central 50×50 pixel array was calculated by the computer as before. The response curves were generated by varying the incident X-ray flux and typical values are shown in Figure 11. It

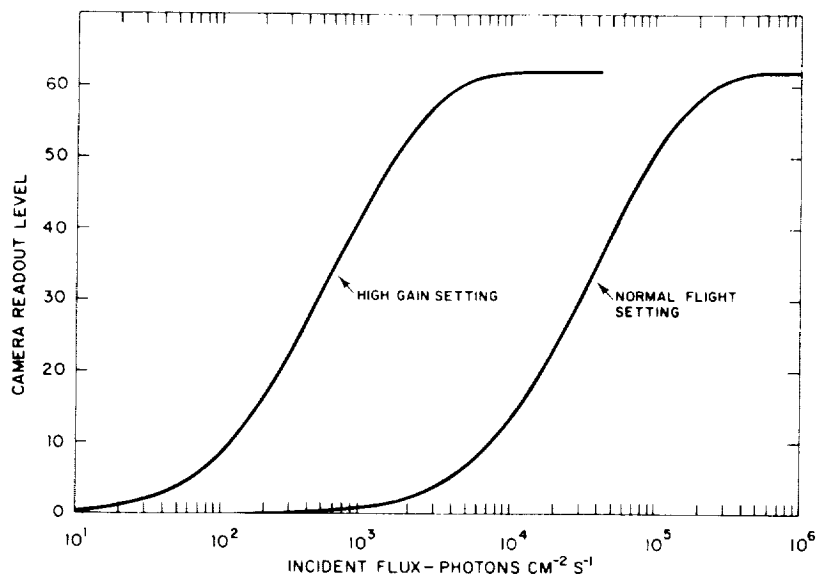


Fig. 11. The dynamic range of the electronic imaging system irradiated with 8.3 Å X-rays at the two flight MCP gain settings.

can be seen that the dynamic range of the system is approximately 1000. Note that even at the highest gains, where single photons are being detected, the noise contribution from the MCP itself is small. The curves for the two flight settings of the MCP gain are shown and inspection shows that a total range in incident energy of 5 orders of magnitude can be observed.

5.2. SPATIAL RESOLUTION

The spatial resolution of the total system is a result of folding together the modulation transfer functions (MTF) of the individual elements of the imaging system. These are the X-ray mirror, the MCP, the fiber optic and imagescope and the TV camera. Of these components only the camera is capable of adjustment and consequently its evaluation was performed first using visible light illumination.

Slow scan vidicons are inherently capable of much higher resolution than standard TV rate vidicons and for the tube chosen modulations of 50% at 800 TV lines are typical. However, because of telemetry limitations, the video picture was limited during flight to 256 lines per frame and this format was used throughout the test program. The MTF was evaluated using a Limansky mask [17, 18] and the computed maximum and minimum sine wave responses, which depend on the relative positions of the sampling elements and the lines in the Limansky mask, are shown in Figure 12. The result indicates that 50% modulation occurs at 12 line pairs/mm which is within the required specification.

Since our experimental apparatus did not permit us to reproduce this test at

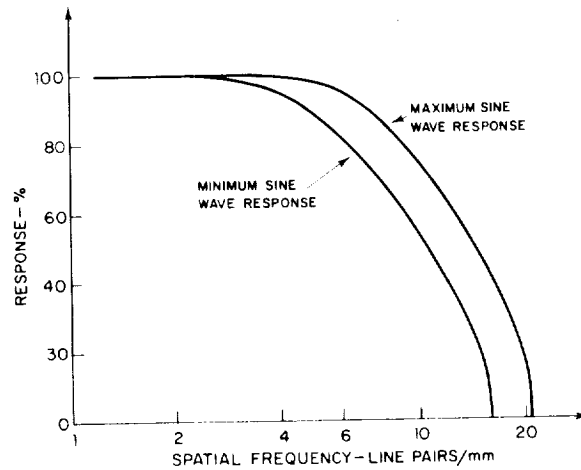


Fig. 12. The computed sine wave response of the vidicon.

X-ray wavelengths, we limited our studies of the total system response to the observation of its capability to resolve UV illuminated pinholes arranged in star patterns of varying sizes. The star patterns were placed at the focus of a 40-cm-diameter parabolic reflector to produce a collimated beam which was focussed by the X-ray mirror onto the MCP. The resulting images were displayed on a TV monitor. The tests showed that 3 arc second pinholes on 12 arc second centers could be resolved.

6. Conclusions

An electronic imaging system with a spatial resolution of better than 15 arc seconds has been designed and built from commercially available components for the observation of solar X-rays. The system was flown as part of a sounding rocket payload on 31 January, 1978. Unfortunately an interlock system, designed to prevent the MCP and the photographic camera from entering the focal plane at the same time, was activated during powered flight and prevented the MCP from leaving its stowed position. Consequently, no X-ray data were recorded. The images that were received showed the dark current patterns to be normal at both gain settings, and there is every reason to believe that satisfactory solar images would have been obtained if the MCP had been translated into the focal plane. The payload is scheduled for reflight in November, 1979.

In the introduction we indicated that one of the objectives of the development of electronic imaging systems was to replace the use of film as the recording medium in satellite experiments. If that goal is to be realized the resolution of the electronic imaging systems has to be improved by roughly an order of magnitude from that reported here, i.e., from approximately 10 to 1 arc second. This improvement is

essential because the detailed study of coronal phenomena requires a knowledge of the physical parameters of the plasma at this level.

The major factor limiting the resolution of systems of this type is the physical dimensions of the microchannels in the MCP. Although the technology exists for making glass channels with diameters down to 6 microns (a factor of 4 improvement over the present system), MCPs made with this size channel are reported by the manufacturers to have low gains. One suspects that within the immediate future 10 micron channels may be a practical limit. Charge coupled devices (CCDs) have also been proposed for X-ray detectors [19]. The most promising versions have square pixels with sides of 15 microns. CCDs have the advantage of a negligible dead space between pixels. However their sensitive areas are rather small; the largest CCDs currently planned, for instance, being 800×800 arrays occupying an area of 1.44 cm^2 [20]. In contrast MCPs are commercially available with circular sensitive areas in excess of 44 cm^2 .

In the event that a limit to the pixel size exists at around 10 microns, the only alternative is to increase the focal length of the X-ray optical system. For instance the large space platforms, envisaged for the Shuttle era, will be capable of accommodating an instrument with a 5 m focal length. Such an instrument would have a plate scale of 24 microns per arc second and thus, with a channel size of 10 microns, angular resolution on the order of 1 arc second should be possible.

In conclusion, our experience indicates that even though electronic imaging systems are practical, if they are to replace film as the prime detector in the focal plane of high resolution solar X-ray imaging experiments, there will have to be modest improvements in the geometry of the detectors coupled with an increase in focal length of the optics. Our studies have shown that the sensitivity of electronic systems for X-ray detection is equal or superior to film. Therefore observations with improved time resolution will be possible since there will be no limitations on the number of images that can be recorded, provided that the telemetry systems are capable of handling the data rates. In summary, if the technological conditions are met, then the techniques of high resolution imaging using electronic detection will significantly augment our observational capabilities and will be extremely helpful in expanding our knowledge of coronal transient phenomena.

Acknowledgements

This project could not have been completed without the help of many individuals both within AS&E and throughout the industry. From among this large group we would, however, like to single out Dr Ann Hutchinson of GEC for her patience and her many helpful explanations, Mr Gary Bailey of JPL whose suggestions led to the preamplifier design and Mr Frank Hills of AS&E who developed the computer interface and software which formed an integral part of the instrument. One of us (JWT) would also like to thank Professor Denis Fermentat of Tufts University for

his guidance and encouragement. The work was supported by NASA under contract NAS2 8683.

References

1. Vaiana, G. S., Reidy, W. P., Zehnpfennig, T., Van Speybroeck, L., and Giacconi, R.: *Science* **161**, 564 (1968).
2. Van Speybroeck, L. P., Krieger, A. S., and Vaiana, G. S.: *Nature* **227**, 818 (1970).
3. Vaiana, G. S., Krieger, A. S., and Timothy, A. F.: *Solar Phys.* **32**, 81 (1973).
4. Krieger, A. S., Davis, J. M., and Haggerty, R.: *Bull. AAS* **10**, 439 (1978).
5. Vaiana, G. S., Van Speybroeck, L. P., Zombeck, M. V., Krieger, A. S., Silk, J. K., and Timothy, A. F.: *Space Sci. Instrum.* **3**, 19 (1977).
6. Timothy, J. G.: *Space Sci. Instrum.* **2**, 289 (1976).
7. Galileo Electro-Optics Corp., Sturbridge, MA 01518, U. S. A.
8. Bjorkholm, P. J., Van Speybroeck, L. P., and Hecht, M.: *SPIE Proc.* **106**, 195 (1977).
9. Varian Vacuum Division, Waltham, MA 02154, U. S. A.
10. Raytheon Company, Microwave and Power Tube Division, Waltham, MA 02154, U. S. A.
11. Caruso, A. J.: *Applied Optics* **13**, 1744 (1974).
12. Henke, B. L., and Elgin, R. L.: *Advances in X-ray Analysis* **13**, 639 (1970).
13. General Electrodynamics Corp., Garland, TX 75042, U. S. A.
14. MIL Electronics, Inc., Lowell, MA 01854, U. S. A.
15. Velonex Division of Varian, Santa Clara, CA 95050, U. S. A.
16. Sallen, R. P., and Key, E. L.: *IRE Trans. Circuit Theory*, CT-2, 74 (1955).
17. Limansky, I.: 'A New Resolution Chart for Imaging Systems', *The Electronic Engineer*, June (1968).
18. Hall, J. A.: *Photoelectronic Imaging Devices*, Biberman, L. M. and Nudelman, S. (Eds.), Plenum Press, Vol. 2, 1971, p. 53.
19. Burstein, P., Krieger, A. S., Vanderhill, M. J., and Wattson, R. B.: *Proc. SPIE* **143**, 114 (1978).
20. Texas Instruments, Inc., Dallas, TX 75222, U. S. A.

[illegible]

4.5 Properties of Coronal Arches

John M. Davis and Allen S. Krieger

American Science and Engineering, Inc.
Arlington, Massachusetts 02174

ORIGINAL PAGE IS
OF POOR QUALITY

PROPERTIES OF CORONAL ARCHES

JOHN M. DAVIS and ALLEN S. KRIEGER

*American Science and Engineering, Inc., Space Systems Division,
37 Broadway, Arlington, MA 02174, U.S.A.*

(Received 6 May, 1980; in revised form 11 December, 1981)

Abstract. The properties of coronal arches located on the peripheries of active regions, observed during a sounding rocket flight on March 8, 1973, are discussed. The arches are found to overlie filament channels and their footpoints are traced to locations on the perimeters of supergranulation cells. The arches have a wide range of lengths although their widths are well approximated by the value 2.2×10^9 cm. Comparison of the size of the chromospheric footprint with the arch width indicates that arches do not always expand as they ascend into the corona. The electron temperatures and densities of the plasma contained in the arches were measured and the pressure calculated; typical values are 2×10^6 K, 1×10^9 cm $^{-3}$, and 2×10^{-1} dyne cm $^{-2}$, respectively. The variation of these parameters with position along the length of the arch indicates that the arches are not in hydrostatic equilibrium.

1. Introduction

Observations of coronal X-ray and EUV emission (Vaiana *et al.*, 1973a, b; Tousey *et al.*, 1973; Noyes *et al.*, 1975) have shown that the topography of active regions can be described in terms of a hierarchy of loops or arches. Classified by their location within the active region they are:

(I) Loops of the active region core which connect regions of opposite polarity across the neutral line (Krieger *et al.*, 1971).

(II) Compact volume loops which surround the core and occupy a region somewhat larger in size than the H α or calcium plage (Švestka, 1976). The average pressure within this region decreases uniformly outward from the center (Davis *et al.*, 1975). The topography of such higher, often unresolved loops is well approximated by an extrapolation of the photospheric magnetic field using a potential field model (Poletto *et al.*, 1975).

(III) Loops which extend outward from the active region to form arcades that connect the compact volume to the surrounding photospheric field. The loops may provide connections between active regions (Chase *et al.*, 1976) or even between active regions on opposite sides of the equator (Švestka *et al.*, 1977).

A series of images which contained excellent examples of loops in category (III) were obtained on March 8, 1973, during a sounding rocket flight of a grazing-incidence X-ray telescope. The wavelength range of the images differs slightly from those obtained later with the S-054 experiment on Skylab (Vaiana *et al.*, 1974) for the short wavelength cutoff occurs at 8 rather than 3 Å. This is a characteristic of the surface material of the grazing incidence mirror (fused silica, chosen for its low scattering) and has the effect of reducing the contribution of the radiation from higher temperature material. The point response function of the mirror at 8 Å has a FWHM of about 2 arc sec while 50% of the energy

of the image of an on-axis point source is contained within a radius of 31 arc sec. The comparable values for the S-054 mirrors are 4 and 48 arc sec respectively and the difference between these two sets of specifications indicates the decreased scattering of the new mirror. The images were recorded on Eastman Kodak SO 212 film.

2. Morphological Properties of the Coronal Arcades

2.1. DETAILS OF THE ANALYSIS

The arcades containing the bright X-ray loops (identified by arrows in Figure 1a) are associated with the two active regions McMath 12259 and 12261. Their appearance at different exposure levels and through different wavelength filters is shown in Figure 1.

The X-ray images have been compared with both chromospheric spectroheliograms and photospheric magnetic field observations, using photographic overlay techniques, to study the correspondence between the structures seen at different levels in the solar atmosphere. The X-ray and H α observations were made at 18:00 UT on March 8 and the Ca K observations at 16:46 UT. The images can be overlaid either from a knowledge of the orientation of the X-ray images with respect to heliocentric north, determined from the measured roll orientation of the rocket payload, or by using features on the solar disk which are well separated and visible in all sets of images to manually align pairs of images. Both techniques allow pairs of images to be superimposed to an accuracy of $\pm 1^\circ$ in rotation. The corresponding point to point uncertainty between different images then depends on their distance from Sun center. For features located in the McMath 12259 and 12261 active region complex, this uncertainty varies from ± 3 to ± 12 arc sec. To this must be added the uncertainty in superposing the solar limbs on the different images which is typically no worse than ± 5 arc sec. Adding the uncertainties quadratically leads to a range in the point to point uncertainties between ± 6 to ± 13 arc sec.

Efforts to obtain simultaneous magnetograms from a ground based observatory were foiled by inclement weather across the western United States. Although some data were obtained, no full disk magnetic field measurements were recorded before 17:00 UT on March 9, at which time data from the Mt. Wilson observatory are available. In an attempt to compare the X-ray observations with the photospheric magnetic field, the data from March 9 were used to reconstruct the photospheric magnetic field at the time of the rocket flight by correcting for solar rotation. Where information from KPNO exists it was used to cross-check the extrapolation. Since the magnetic field and X-ray data were obtained 23 hr apart any conclusions drawn from their comparison assume that the large scale features did not change significantly during that interval.

2.2. MORPHOLOGY OF CATEGORY (III) LOOPS

The category (III) loops occur in groups or arcades with the loops in each arcade separated from adjacent loops by a distance approximately equal to the loop's width. Comparison of the X-ray images with magnetograms (Figure 2) shows that the loops

ORIGINAL PAGE
BLACK AND WHITE PHOTOGRAPH

PROPERTIES OF CORONAL ARCHES

297

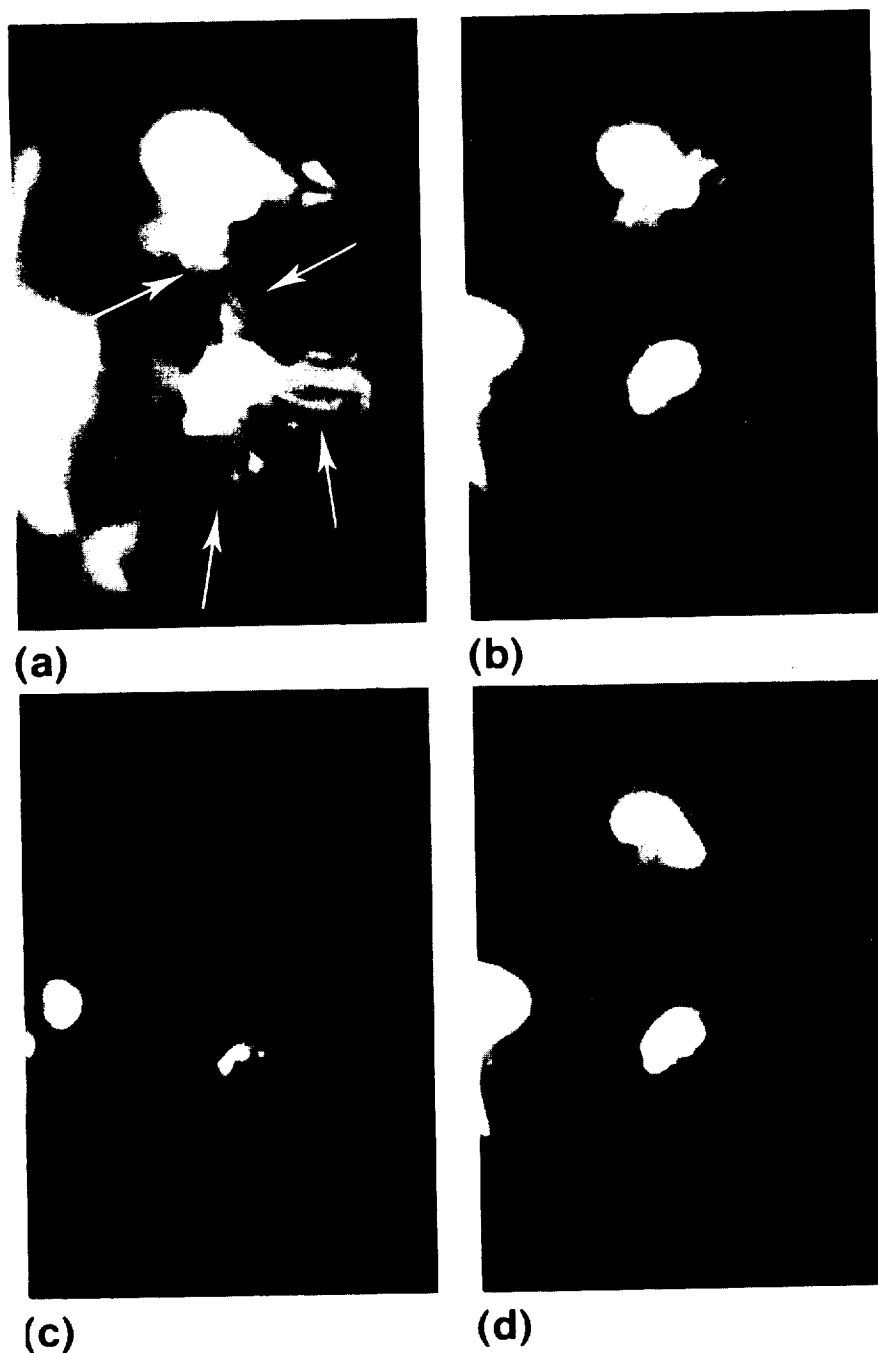


Fig. 1. The active region complex consisting of McMath 12259 (upper) and McMath 12261 (lower) observed at 18:00 UT on March 8, 1973. The coronal arcs are indicated by arrows. The waveband and exposure levels are (a) 8-37, 44-60 Å, and 58.6 s; (b) 8-37, 44-60 Å, and 20.3 s; (c) 8-37, 44-60 Å, and 0.8 s; (d) 8-20 Å and 58.6 s.

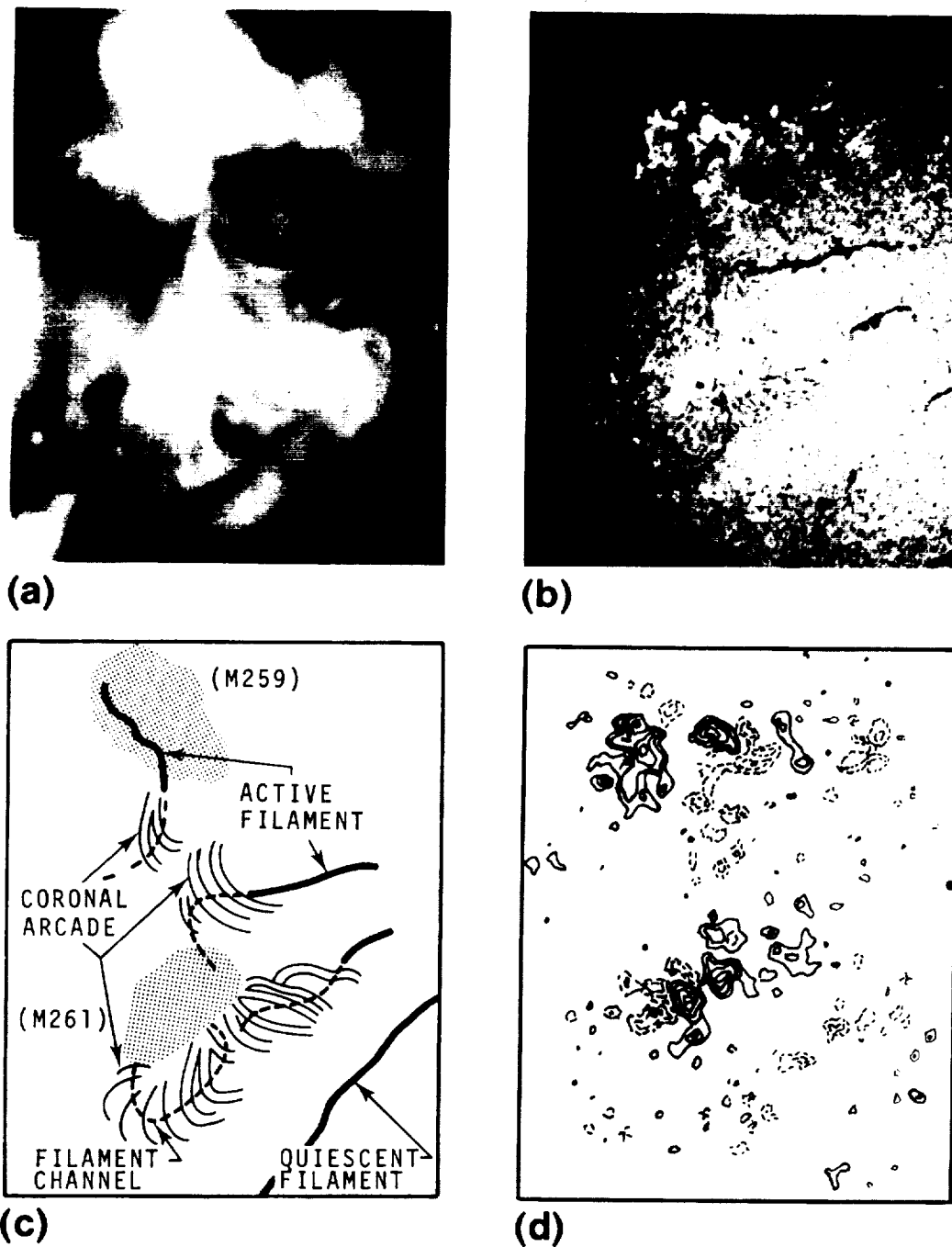


Fig. 2. The association of X-ray, H α and magnetic features. (a) X-ray image showing the arcades of bright loops and filament cavities. (b) Simultaneous H α photograph showing the location of the filaments and filament channels. (c) A schematic showing the location of coronal arcades above active filament channels. (d) The photospheric magnetic field obtained by correcting the Mt. Wilson magnetogram from 17:00 UT on March 9, 1973 for solar rotation.

emerge from localized areas within the active region where the field magnitude and gradients are high. The loops connect the field at the center of the active region to the surrounding background field and these connections are not restricted to fields originating on the same side of the equator. There is no preference for connecting to preceding or following polarity within the active region nor does the age of the active region appear to have any influence on the presence of arcades.

When the X-ray and H α images are overlaid the arcades of category (III) loops are found to be associated with active filaments. In particular the loops of each arcade span a particular filament thus forming a connection between areas which are separated by the neutral line of the longitudinal magnetic field.

The presence of these arcades creates a marked difference in the X-ray morphology of active and quiescent filaments. The latter, when seen in projection against the disk, appear as long, dark cavities surrounded by diffuse X-ray structures (Figure 2). Observations at limb crossings (Serio *et al.*, 1978) show that the cavities are closed by faint loops. The cavities contain little, if any, material at a high enough temperature to emit soft X-rays and have an average height of 5×10^9 cm. In contrast the corresponding regions above the active filaments are the sites of the arcades of bright X-ray loops which are of a comparable height to the quiescent filament cavities.

In general the active filaments, seen in these images, extend into filament channels which show little or no H α absorption. However the channels do contain a neutral line around which the photospheric field shows the same orientation, interpreted from the fibril alignments, as the region surrounding the active filament. Close inspection of the overlaid images shows that the loops are located either above a filament channel or over a segment of the active filament where the H α absorption is weak. Loops are not present above strongly absorbing sections of the filament which are located beneath X-ray cavities similar to those found above quiescent filaments.

This contrast in X-ray morphology between the cavities observed above absorbing filaments and the bright loops above filament channels, with the loops occupying the same general volume as the cavities, provides circumstantial evidence for a connection between the appearance of bright X-ray loops and the subsequent development of a filament (Davis and Krieger, 1978, 1982).

The outer footpoints of the arches can be traced to localized brightenings in both the Ca K and H α spectroheliograms. Since adjacent loops have separations on the order of one arc minute and the images can be aligned to ± 10 arc sec, the identification of each loop with a specific brightening is relatively unambiguous even though the X-ray loops cannot be traced directly to the chromosphere. In Ca K the brightenings appear as enhancements of the normally bright boundaries of the supergranulation network (Figures 3 and 4). Only a segment of the network perimeter is enhanced suggesting that the loops are anchored to localized areas where the magnetic flux, concentrated by the convective motions in the cell, is dense, well ordered or both. In H α the brightenings appear as groups of bright convection cells with the surrounding fibrils aligned perpendicularly to their major axes, confirming that the footpoints are localized sections of the cell boundary. In one case (McMath 12259) two arches appear to originate from

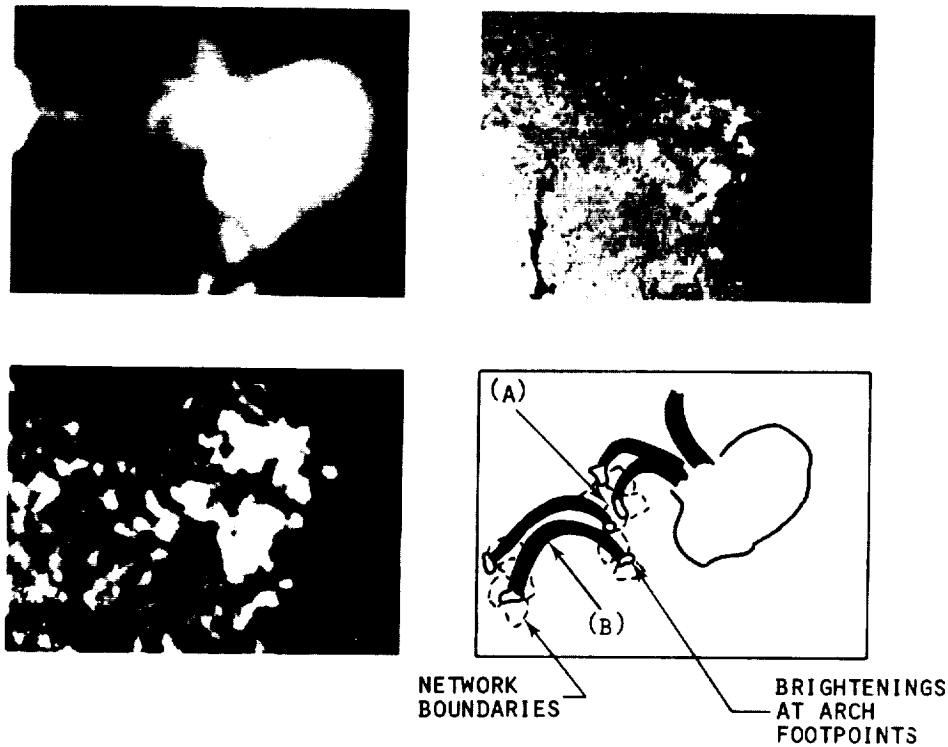


Fig. 3. X-ray, H α and Ca K images of McMath 12259 showing the termination of loops from different arcades in the same supergranulation cell (A) and the X-ray loop (B) which has neither termination within the compact volume of an active region.

opposite sides of the same network cell (identified as A in Figure 3). These arches are components of two separate arcades and there appear to be no cases where arches from the same system terminate in the same cell.

3. Properties of Individual Arches

3.1. PHYSICAL DIMENSIONS

The physical dimensions, length and breadth, of individual category (III) arches were measured from the X-ray images. The arch lengths were measured directly and were corrected for projection effects resulting from both their position on the solar surface and their vertical extension. To determine the widths, the images were digitized, using a 3 arc sec square aperture, converted into incident energy and deconvolved to remove the effect of the telescope point response function. Sections were made across each arch at several locations and an average made of the measured full widths. The cross-sections

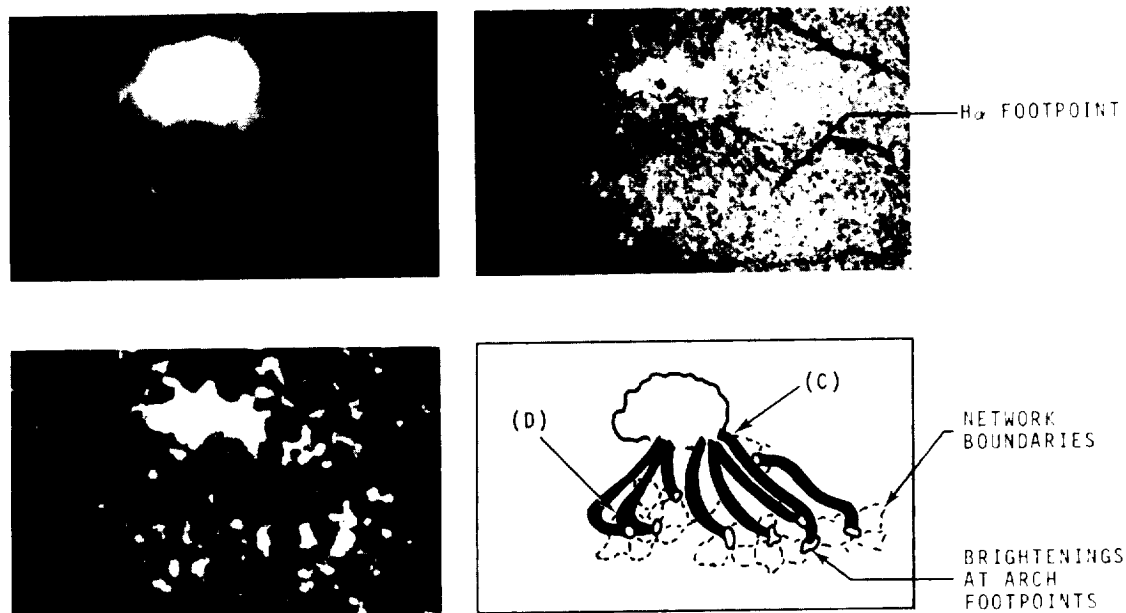


Fig. 4. X-ray, H α , and Ca K images of McMath 12261 showing the location of the arch footpoints in network brightenings and identifying the arches (C) and (D) whose properties are described in the text.

did not show any evidence of structure within the arch; however, the resolution of the telescope-film system is marginal for revealing the structure of emitting features at or below 15 arc sec unless they are accompanied by substantial intensity or temperature gradients.

Inspection of the data reveals the following points:

(i) The width and length distribution of the individual arches have lower limits of 1.5×10^9 and 5×10^9 cm, respectively. The dimensions of the arches are comparable to those of loop-prominence systems.

(ii) Arch widths appear to be independent of their lengths and are well approximated by a single, average, value of $2.2 \pm 0.3 \times 10^9$ cm.

By comparison the loops of categories (I) and (II) are typically both shorter and narrower. The ranges of values of all three categories are summarized in Table I.

TABLE I
Dimensions of active region loops

| | Category (I) Active region cores | Category (II) Compact volume loops | Category (III) Outward extending loops |
|-----------|-------------------------------------|---------------------------------------|---|
| Width-cm | $7 \times 10^7 - 5 \times 10^8$ | $5 \times 10^8 - 1.5 \times 10^9$ | $1 \times 10^9 - 3 \times 10^9$ |
| Length-cm | $7 \times 10^8 - 2 \times 10^9$ | $1 \times 10^9 - 1 \times 10^{10}$ | $5 \times 10^9 - 5 \times 10^{10}$ |

It has been suggested that the lengths of individual arches may be governed by a stability condition which equates the time scales for conduction and radiation (Tucker, 1973). By expressing the time scale for conduction in terms of the thermal diffusion coefficient for Coulomb collisions parallel to the magnetic field (Spitzer, 1962), and following Tucker and Koren (1971) for the radiative energy loss, the maximum length, L_{\max} , of an arch can be written as

$$L_{\max} \simeq 2.9 \times 10^5 \frac{T^{9/4}}{n_e} \text{ cm},$$

where T is the temperature in degrees K and n_e is the electron density in cm^{-3} .

The arches have observed densities between 0.7 and $1.2 \times 10^9 \text{ cm}^{-3}$ and temperatures between 1.8 and $2.5 \times 10^6 \text{ K}$. These values correspond to maximum lengths ranging from 2×10^{10} to $1 \times 10^{11} \text{ cm}$. None of the observed arches exceed this limit and in general their measured lengths are less, by a factor of 2, than their respective limit.

3.2. THE STRUCTURE OF THE BASE OF CORONAL ARCHES

If the area of enhanced network identified with the footpoints of the coronal arches defines the chromospheric cross-section of the loop, then the change in the cross-section of the loop as it rises into the corona can be determined. Although the chromospheric brightenings have rather irregular shapes they are elongated along the network boundary. Consequently their cross-sections can be characterized by major and minor axes. The measured lengths of each set of axes, after correction for their projection on the solar disk, were found to vary over a factor of three. Since the X-ray cross-sections are roughly constant for all loops, the expansion of the loops from the chromosphere into the corona, for this data set, is inversely proportional to the size of the chromospheric major axis, when this parameter is used to characterize the size of the footpoint. Expansion factors varied from 0.8 to 3.2 with 40% of the loops showing a contraction rather than an expansion. Therefore we conclude that on average the loops tend to maintain the same cross-section as they ascend into the corona.

This result is contrary to the generally accepted view that the field lines at supergranule boundaries and hence by inference the field lines within loops diverge as they ascend into the corona (Pneuman and Kopp, 1978; Kopp and Kuperus, 1968). The observational results might be in error if the downward conducted energy from the coronal arch, which is assumed to be responsible for the chromospheric brightening, is greater than the energy density at this level of the chromosphere. In this case the excess energy may be transported into adjacent convection cells, creating an apparent increase in the size of the footpoint. The evaluation of conductive fluxes in the transition zone is difficult (see Athay, 1976), however the steep temperature gradient will have substantially reduced the flux at the level corresponding to H α emission, say $T = 10^4 \text{ K}$, compared to the flux at the base of the corona. An order of magnitude calculation indicates that the conductive flux is not a significant fraction of the energy density and since at 10^4 K the radiative loss function has an extremely steep temperature dependence (Cox and

Tucker, 1969) the plasma at the base of the arch will easily adjust to a small increase in the energy input. Therefore we feel justified in assuming that the network brightening reflects the true loop cross-section and therefore that ascending loops are not automatically characterized by an increasing diameter.

3.3. PLASMA PARAMETERS AND HYDROSTATIC EQUILIBRIUM

When images are obtained through two filters with different wavelength passbands, it is possible to determine an average line of sight electron temperature, T , and emission measure, $\int n_e^2 dl$ (Vaiana *et al.*, 1973b; Davis *et al.*, 1975). In the present study the images were converted into deconvolved energy arrays consisting of 3 arc sec by 3 arc sec image elements. The ratio, at any element point, of two such array values taken through different filters, provides a measure of the average line of sight temperature which can then be used to evaluate the emission measure at the same location from one of the images.

To evaluate the electron density, it is necessary to make assumptions about the structure of the emitting region along the line of sight. For the X-ray arches we have assumed that the emitting material is distributed uniformly within a circular cross-section and that the integrated line of sight density of the material emitting X-rays either above or below the arch is negligible. The electron density, n_e , can then be evaluated from the emission measure by dividing the latter quantity by the measured width of the arch at each point.

Where the parameters are presented as a function of position along the longitudinal axis of the arch, average energy arrays were formed from the pairs of image elements on either side of the axis. Ratios of these averaged arrays were used to obtain temperatures and densities which were then smoothed by forming the running average, along the axis, of pairs of values. Thus each value corresponds to a 6 arc sec by 6 arc sec area. Although the absolute values of the points may be subject to unknown systematic errors, the relative uncertainty between adjacent points is of the order of 2 to 3% and consequently the trends that are evident in the data are significant.

The measurements show that the loops have average temperatures of $2.1 \pm 0.2 \times 10^6$ K and densities of $1.0 \pm 0.2 \times 10^9 \text{ cm}^{-3}$. The material between the arches is both cooler and less dense. The upper limits placed on the temperature and density are 1.5×10^6 K and $1 \times 10^8 \text{ cm}^{-3}$. When the variation of the temperature with position along the longitudinal axis of the arches is studied, the arches are found to fall into two groups distinguished by temperature variations which are either approximately constant with position or which decrease steadily with distance from one termination; the latter temperature distributions are directly correlated with the location of the higher temperature termination within the compact volume of the active region.

When both footpoints lie outside the compact volume the data has the form shown in Figure 5 which shows the variation with position of the electron density and temperature for the arch identified as *B* in Figure 3. The pressure, $n_e kT$, has been calculated from the measured quantities and increases smoothly to a maximum, approximately 20% above the base value, at the center of the arch before decreasing. The pressure maximum

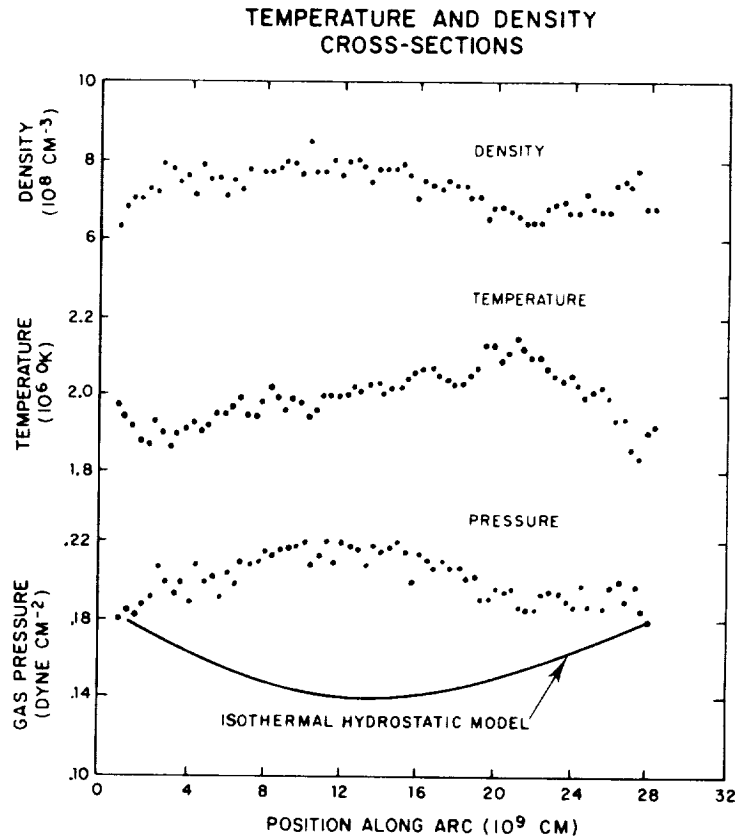


Fig. 5. The observed temperature, density and pressure profiles along the arch (*B*) of Figure 3. The solid curve depicts the pressure profile that would be obtained if the arch was isothermal and in hydrostatic equilibrium.

occurs in the vicinity of the peak, or highest vertical extension, of the arch which is estimated to be 5×10^4 km above the base of the corona.

If the arch were in hydrostatic equilibrium and its temperature distribution were truly isothermal, the pressure within the arch would decrease exponentially with a scale height

$$H_0 = \frac{2kT}{\mu m_H g_0},$$

where μ is the mean molecular weight of the plasma and the other constants have their usual meaning. Substituting the measured altitude profile of the arch into the exponential model and using an average temperature of 2×10^6 K to calculate the scale height, the solid curve of Figure 5 is obtained. The difference between the predicted curve and the actual data is quite dramatic and illustrates that even seemingly stable arches do not necessarily exist in hydrostatic equilibrium.

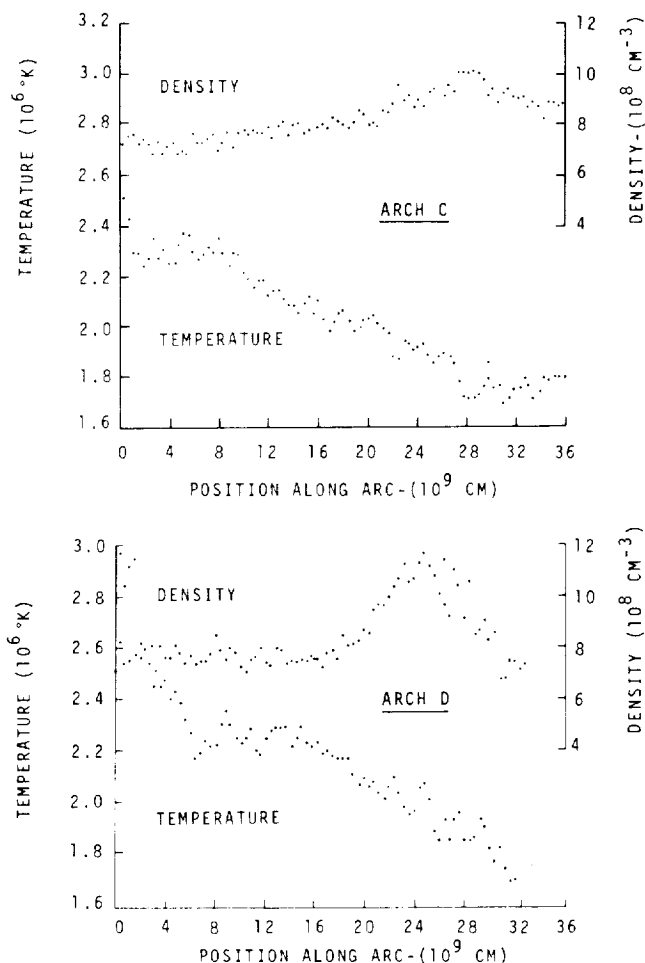


Fig. 6. Temperature and density profiles along the arches (C) and (D) of Figure 4 showing (a) the linear temperature decline with distance from the active region and (b) the density enhancement described in the text.

The observation that loops exist in non-hydrostatic equilibrium agrees with the observations of Foukal (1976) for the much cooler loops ($10^4 < T < 10^6$ K) associated with sunspots, but is in contrast to the assumption made in several theoretical papers (e.g., Rosner *et al.*, 1978) where hydrostatic equilibrium has been used as the starting point in the development of a theoretical description of the geometry and thermal stability of X-ray loops.

When one of the footpoints lies within the active region the longitudinal variations of the temperature and density are similar to Figure 6 which shows the data for the loops identified as (C) and (D) in Figure 4. In both cases the temperature decreases linearly outward from the active region with a longitudinal temperature gradient between $2-3 \times 10^{-3}$ deg K m $^{-1}$. In general the density increases slightly over the same distance

(Figure 6, above) although not sufficiently to compensate for the falling temperature in the pressure term which also decreases from one end of the arch to the other.

The second example (Figure 6, below) belongs to an arcade where several of the arches have bright knots at or near their apexes. The analysis shows that the knots owe their increased brightness to a substantial increase in density. The knot in the example shown has a volume of $1.5 \times 10^{28} \text{ cm}^3$, a density of $1.2 \times 10^9 \text{ cm}^{-3}$, which is 50% above the value for the rest of the arch, and a mass of $3 \times 10^{13} \text{ g}$. We have rejected the hypothesis that the density increase is simply a projection effect because we are unable to duplicate the observed intensity distribution by numerically modelling the expected distribution for a variety of possible geometries. If this identification is correct then the violation of hydrostatic equilibrium is even more severe in this arch and its neighbors in the arcade which show the same characteristic.

4. Conclusions and Discussion

Observations have been made of a category of coronal arches found on the periphery of active regions. The arches are associated with active filaments and they occur above filament channels rather than above regions where the $\text{H}\alpha$ absorbing filament is clearly defined.

The terminations of the arches, where they are visible outside the active region, have been projected to locations on the boundaries of supergranulation cells. These locations are characterized by brightenings in $\text{H}\alpha$ and if the bright areas are an accurate representations of the cross-section of the arch at this level in the solar atmosphere there is no clear evidence for a general expansion of arches as they ascend into the corona.

The arches were found to have a wide range of lengths coupled with a narrow distribution of widths which is well approximated by a single average value of $2.2 \times 10^9 \text{ cm}$.

The electron temperature, density and pressure of the material in the arches has been measured and typical average values are $2 \times 10^6 \text{ K}$, $1 \times 10^9 \text{ cm}^{-3}$ and $2 \times 10^{-1} \text{ dyne cm}^{-2}$, respectively. The coronal material surrounding and between arches is less dense, cooler and at a lower pressure than the material within arches. By determining the variation of these parameters along the longitudinal axis of the arch, i.e., as a function of altitude and in some cases as a function of distance from the active region, it was found that, in general, the material within the arches was not in hydrostatic equilibrium. Secondly, for those arches with one of their terminations lying within the compact volume of the active region, there existed an outward temperature gradient which is perhaps indicative of outward energy conduction from the center of the active region.

Arches were also observed with substantial density enhancements at their apexes. It is tempting to interpret the enhancements as evidence of coronal condensations occurring within loops. Since the same arches are located above filament channels the obvious corollary is that the condensations are responsible for the subsequent development of a filament. This possibility has been explored in a companion paper (Davis and Krieger, 1982).

Acknowledgements

The help and assistance of the AS & E Rocket Group and of the Sounding Rocket Division of the Goddard Space Flight Center in the launch of research rocket 13.027 is gratefully acknowledged. It is also a pleasure to acknowledge the help and encouragement provided by Dr Giuseppe Vaiana during the early stages of the work and the assistance of Ms Jadwiga Zmijewski in the photographic analysis.

The experimental observations were supported by NASA under contract NAS2-7424 and the analysis by NASA under contracts NAS2-8683 and NAS5-25496.

References

- Athay, R. G.: 1976, *The Solar Chromosphere and Corona: Quiet Sun*, D. Reidel Publ. Co., Dordrecht, Holland, p. 406.
- Chase, R. C., Krieger, A. S., Švestka, Z., and Vaiana, G. S.: 1976, *Space Res.* **16**, 917.
- Cox, D. P. and Tucker, W. H.: 1969, *Astrophys. J.* **157**, 1157.
- Davis, J. M. and Krieger, A. S.: 1978, *Bull. Am. Astron. Soc.* **10**, 439.
- Davis, J. M. and Krieger, A. S.: 1982, *Solar Phys.*, (in press).
- Davis, J. M., Gerassimenko, M., Krieger, A. S., and Vaiana, G. S.: 1975, *Solar Phys.* **45**, 393.
- Foukal, P. V.: 1976, *Astrophys. J.* **210**, 575.
- Kopp, R. A. and Kuperus, M.: 1968, *Solar Phys.* **4**, 212.
- Krieger, A. S., Vaiana, G. S., and Van Speybroeck, L. P.: 1971, in R. Howard (ed.), 'Solar Magnetic Fields', *IAU Symp.* **43**, 397.
- Landini, M., Monsignori-Fossi, B. C., Krieger, A. S., and Vaiana, G. S.: 1975, *Solar Phys.* **44**, 69.
- Noyes, R. W., Foukal, P. V., Huber, M. C. E., Reeves, E. M., Schmahl, E. J., Timothy, J. G., Vernazza, J. E., and Withbroe, G. L.: 1975, in S. Kane (ed.), 'Solar Gamma, X-, and EUV Radiation', *IAU Symp.* **68**, 3.
- Pneuman, G. W. and Kopp, R. A.: 1978, *Solar Phys.* **57**, 49.
- Poletto, G., Vaiana, G. S., Zombeck, M. V., Krieger, A. S., and Timothy, A. F.: 1975, *Solar Phys.* **41**, 83.
- Rosner, R., Tucker, W. H., and Vaiana, G. S.: 1978, *Astrophys. J.* **220**, 643.
- Serio, S., Vaiana, G. S., Godoli, G., Motta, S., Pirronello, V., and Zappala, R. A.: 1978, *Solar Phys.* **59**, 65.
- Spitzer, L.: 1962, *Physics of Fully Ionized Gases*, (2nd edition), Interscience, New York.
- Švestka, Z.: 1976, in 'International Symp. on Solar-Terrestrial Physics', *Physics of Solar Planetary Environments*, Vol. I, p. 129.
- Švestka, Z., Krieger, A. S., and Chase, R. C.: 1977, *Solar Phys.* **52**, 69.
- Tousey, R., Bartoe, J. D. F., Bohlin, J. D., Bruechner, G. E., Purcell, J. D., Scherrer, V. F., Sheeley, N. R., Schumacher, R. J., and Van Hoosier, M. E.: 1973, *Solar Phys.* **33**, 265.
- Tucker, W. H.: 1973, *Astrophys. J.* **186**, 285.
- Tucker, W. H. and Koren, M.: 1971, *Astrophys. J.* **168**, 283.
- Vaiana, G. S., Davis, J. M., Giacconi, R., Krieger, A. S., Silk, J. K., Timothy, A. F., and Zombeck, M.: 1973a, *Astrophys. J.* **185**, L47.
- Vaiana, G. S., Krieger, A. S., and Timothy, A. F.: 1973b, *Solar Phys.* **32**, 31.
- Vaiana, G. S., Krieger, A. S., Petrasso, R., Silk, J. K., and Timothy, A. F.: 1974, *Proc. SPIE* **44**, 185.



4.6 The Growth of Filaments by the Condensation of Coronal Arches

John M. Davis and Allen S. Krieger

American Science and Engineering, Inc.
Cambridge, Massachusetts 02139

ORIGINAL PAGE IS
OF POOR QUALITY

THE GROWTH OF FILAMENTS BY THE CONDENSATION OF CORONAL ARCHES

JOHN M. DAVIS and ALLEN S. KRIEGER

American Science and Engineering, Inc., Cambridge, Mass. 02139, U.S.A.

(Received 11 December, 1980; in revised form 16 April, 1982)

Abstract. A model of filament formation based on the condensation of coronal arches is described. The condensation results from initiating the radiative instability within an arch by superimposing a transient energy supply upon the steady state heating mechanism. The transient energy supply increases the density within the arch so that when it is removed the radiative losses are sufficient to lead to cooling below the minimum in the power loss curve.

Times from the initial formation of the condensation to its temperature stabilization as a cool filament have been calculated for various initial conditions. They lie in the range 10^4 to 10^5 s with the majority of the time spent above a temperature of 1×10^6 K.

Under the assumption that the condensation of a single arch forms an element of the filament, a complete filament requires the condensation of an arcade of loops. Using experimentally derived parameters, filament densities of 10^{11} to 10^{12} cm^{-3} can be obtained.

1. Introduction

1.1. BACKGROUND

X-ray observations of the solar corona have shown that arcades of X-ray loops situated on the boundaries of active regions are frequently located above active filament channels (Davis and Krieger, 1982). The archetypal example is the active filament complex, consisting of filaments and filament channels, observed to the SE of McMath 12261 between 7 and 9 March 1973 (Figure 1). At the start of the observations the filament channel has an elliptical shape which shows little change for 24 hr. The X-ray observations, taken at this time, show that the filament channel is located directly beneath an arcade of loops having bright knots at their summits, which are the result of a local increase in the electron density. During the following 24 hours a filament is observed to develop within the channel. The observations suggest that filaments form out of coronal arches and it is tempting to identify the bright knots with the density perturbations proposed by Hildner (1974), Raadu and Kuperus (1973), and others (see Tandberg-Hanssen, 1974) to describe the initial stage of filament formation.

In these models a density perturbation grows and cools because the radiative losses are proportional to n_e^2 and T^{-1} ; thus, the cooling produces a decrease in pressure, and the resulting compression by the surrounding medium will produce a further increase in density and increased cooling. The additional energy needed to halt this cycle cannot be supplied by the surrounding medium because conduction across the field lines, running through the perturbation, is inhibited. These models require a large initial compression to start the cooling cycle so that it will proceed fast enough to account for

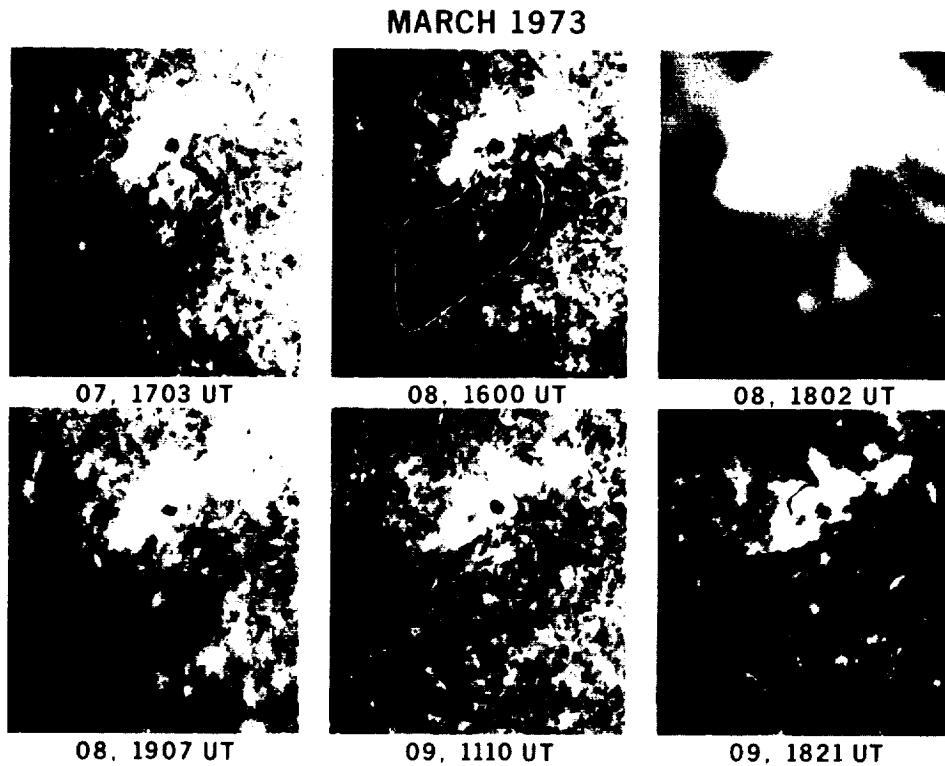


Fig. 1. The growth of an active filament associated with McMath 12261. The H α images show the development of the filament, outlined in frame 2, between 17:03 UT on 7 March 1973 and 18:21 UT on 9 March. (H α images courtesy of NOAA, Boulder, USAF Palehua, and the Canary Islands Observatories.)

the time scale of formation of active filaments (Tandberg-Hanssen, 1974). As an empirical alternative we have investigated a model based on initiating the radiative instability within a coronal arch by providing a transient increase in the energy supplied to the arch.

1.2. MODEL

The model is based on the thermal equilibrium of active region arches described by Pye *et al.* (1978). They considered arches in their initial state to be essentially empty flux tubes which undergo a rapid rise in temperature when energy is deposited within the tube. Since their low density limits radiation, conduction becomes the dominant loss mechanism. The result is a transfer of the energy to the arch footpoints located in the lower atmosphere. The material at the footpoints responds to this conductive energy input by 'evaporating' into the flux tube, i.e., its increase in temperature, and therefore in scale height, allows it to rise into the flux tube (Rosner *et al.*, 1978). The subsequent increase in density within the arch increases the radiative losses and leads to an

ORIGINAL PAGE
BLACK AND WHITE PHOTOGRAPH

equilibrium or steady state condition in which the radiative and conductive losses balance the rate of energy deposition.

Now consider the effect on the equilibrium condition of an additional, transient energy input. Initially the temperature of the arch will rise and the radiative losses, P_{rad} , which are inversely proportional to temperature under coronal conditions (Cox and Tucker, 1969; McWhirter *et al.*, 1975), will decrease while the conductive losses, $P_{\text{cond}} \sim T^{5/2}$, increase. Thus the energy of the transient source will be transferred via conduction to the lower atmosphere which will respond by evaporating additional material into the arch until a new equilibrium is reached in which the increase in the radiative losses balances the power supplied by the transient source. After the transient supply is turned off, the arch will be losing more energy than it is receiving and its temperature will start to fall; but since $P_{\text{rad}} \sim T^{-1}$ at coronal temperatures, the classical conditions for the

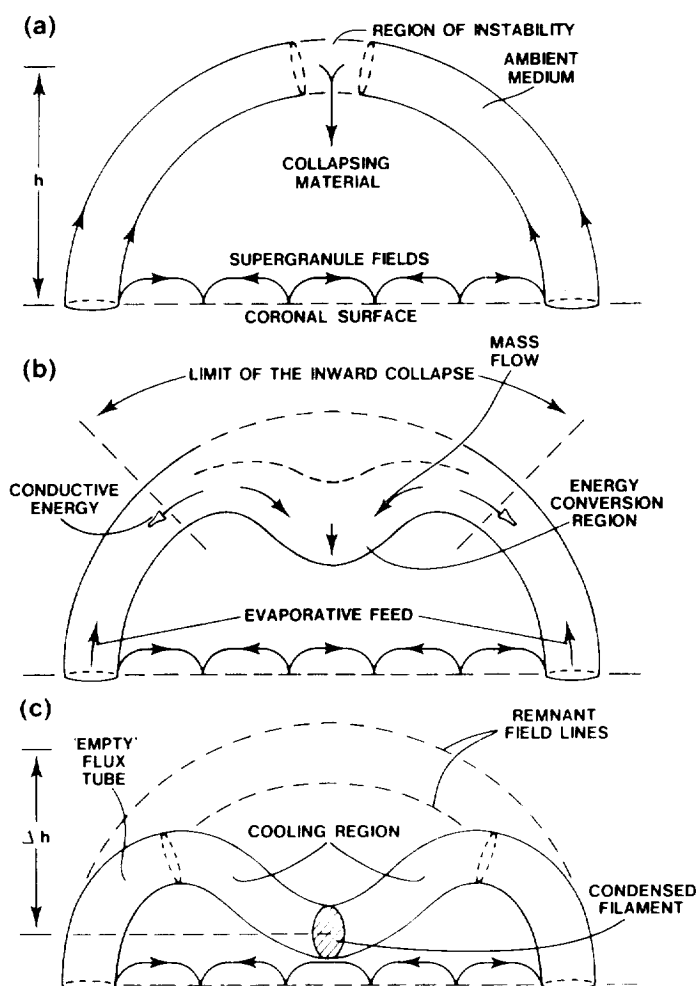


Fig. 2. A pictorial representation of the sequence of events which lead to the condensation of a coronal arch into an element of a filament.

radiative instability *may* be met. If they are, the temperature will continue to fall until a new balance is established. This occurs when the radiative losses equal the energy supply for as the temperature falls P_{cond} tends to zero.

To establish this sequence of events the arch must have a geometry which prevents the cooling material from immediately dissipating. For instance, if the radiative instability is established within the original magnetic configuration of the arch, the cooling material could return directly to the lower atmosphere without destroying the magnetic configuration of the arch (Pye *et al.*, 1978). The arch could then refill with material at a later time (Levine and Withbroe, 1977). Therefore the relationship between the transient supply and the geometry within which it is dissipated is important to the success of the model.

Observations have not identified the transient energy source. However the arches proposed as the source of the filament material extend to much greater heights than the resulting filaments. If the final configuration of the filament has the form proposed by Kippenhahn and Schlüter (1957) the arches must at least partially collapse to reach this state. If the collapse *precedes* the condensation, the release of potential energy during the collapse is itself a transient energy source and this assumption has been used to quantify the model. These ideas are shown schematically in Figure 2.

2. The Energetics and Time Scales for Filament Formation

To calculate the properties of a filament formed by this mechanism and to predict the time scales of formation as a function of the incremental density provided by the transient supply, the equations governing the initiation of the radiative instability in the presence of the external supply and conduction along the arch have been developed. To evaluate these equations, a standard arch has been defined (Table I) using experimentally determined values for the plasma parameters.

2.1. THE INCREMENTAL DENSITY REQUIRED TO OVERCOME CONDUCTION STABILIZATION

Coronal arches exist in a state of dynamic equilibrium in which a balance is maintained between the heating supply and the conductive and radiative losses. The balance is

TABLE I
Physical parameters of the standard isothermal arch based on the observations of Davis and Krieger (1982)

| | | |
|----------------------|-------|--------------------------------------|
| Length | l | 3.0×10^{10} cm |
| Radius | r | 1.1×10^9 cm |
| Electron density | n_e | 1.2×10^9 cm $^{-3}$ |
| Electron temperature | T_e | 2.0×10^6 K |
| Electron pressure | P_e | 3.3×10^{-1} dyne cm $^{-2}$ |
| Cross section area | A | 3.8×10^{18} cm 2 |
| Volume | V | 1.1×10^{29} cm 3 |
| Height | h | 5.0×10^9 cm |
| Scale height | H_0 | 2.0×10^{10} cm |
| Sound speed | V_s | 1.3×10^8 cm s $^{-1}$ |

maintained by adjusting the density of the arch by either evaporating from, or returning material to the lower atmosphere (Pye *et al.*, 1978). Once the arch is established within a conduction dominated regime, the equilibrium can be maintained by slight adjustments of its temperature. Consequently, if a positive density perturbation develops within an arch and attempts to cool due to its increased radiative losses, the cooling will be limited because conduction from adjacent regions in the arch connected by the same field lines will compensate for the increased radiative losses. This can be visualized with the aid of Figure 3 which is a schematic representation of the power loss of a coronal arch as a function of temperature. The major loss terms are radiation and conduction and the total loss curve is defined by the relation

$$P_{\text{total}}(T) = P_{\text{cond}}(T) + P_{\text{rad}}(T), \quad (1)$$

where $P_{\text{rad}}(T)$ is the energy radiated by the whole arch and $P_{\text{cond}}(T)$ is the energy lost through both footpoints when the material in the arch is at temperature T . When the arch is maintained in equilibrium by the steady state energy supply, it will exist on the conduction dominated branch of the total loss curve where an increase in temperature is accompanied by an increase in total losses. Increasing the arch density will increase the radiative losses at any temperature, thus moving the minimum loss point of the curve toward higher temperatures. However if $P_{\text{total}} = P_{\text{source}} = \text{constant}$, then if P_{rad} in-

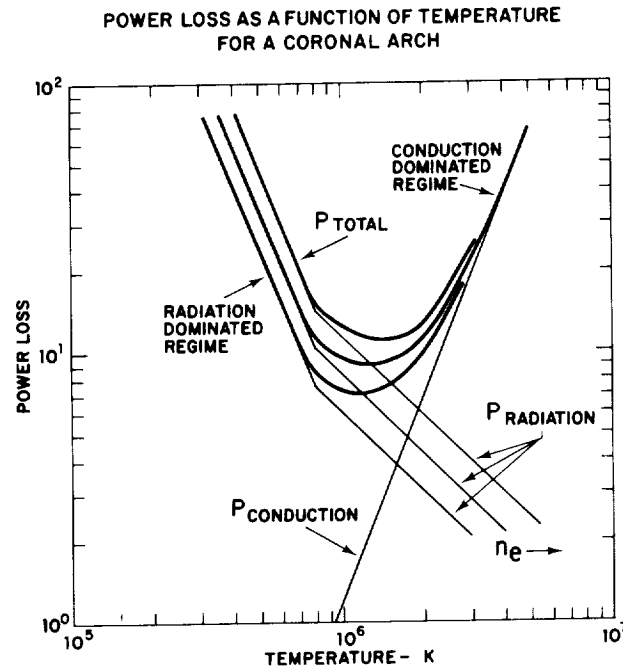


Fig. 3. A schematic diagram showing the dependence of the power losses of a coronal arch on its temperature. Since the functional dependence of the conductive and radiative losses have different signs, the total power loss curve exhibits a minimum at a temperature given by Equation (5).

creases, due to an increase in density, P_{cond} must decrease. This implies a reduction in temperature of the arch. Thus the net result of an increase in density will be a slight cooling of the whole loop. The new equilibrium temperature will be closer to the minimum loss temperature since the latter will have moved to a higher temperature. To establish the radiative instability, the increase in density must be sufficient to drive the arch through the minimum in the total power loss curve onto the radiation dominated branch, where a decrease in temperature increases the total losses, thus precipitating further decreases in temperature.

Following Jordan (1976) and assuming that conduction occurs uniformly across the cross-section of the arch, the conduction losses through both ends of the arch are given by

$$P_{\text{cond}}(T) = 1.6 \times 10^{-10} (2\pi r^2) (T^{5/2} - T_b^{5/2}) \approx k_c T^{5/2}, \quad (2)$$

where T_b is the temperature at the base of the arch and is on the order of $2-5 \times 10^4$ K. Although Equation (2) is strictly valid only for $T_b \geq 10^5$ K, the effect of neglecting T_b has little impact on P_{total} for, by the time a temperature is reached where the value of T_b has any effect on the magnitude of the conductive losses, the latter are less than 1 percent of the radiative losses.

Above 8×10^5 K the radiative losses (Hildner, 1974) are

$$\begin{aligned} P_{\text{rad}}(T) &= 5.5 \times 10^{-17} n_e^2 V T^{-1} \\ &= k_r T^{-1}. \end{aligned} \quad (3)$$

Therefore the total loss curve is given by

$$P_{\text{total}}(T) = k_c T^{5/2} + k_r T^{-1}. \quad (4)$$

This function will have a minimum at a temperature given by

$$T_{\text{min}} = \left(\frac{2k_r}{5k_c} \right)^{2/7} = (6.9 \times 10^{-8} n_e^2 l)^{2/7}. \quad (5)$$

Consequently, to establish the radiative instability and cool the arch below T_{min} , the added density, Δn_e , must be sufficient to increase the radiative losses so that the total losses at T_{min} , i.e., $P_{\text{total}}(T_{\text{min}})$, exceed the energy input to the arch evaluated at the steady state condition. Thus

$$P_{\text{rad}}(n_e + \Delta n_e, T_{\text{min}}) + P_{\text{cond}}(T)_{\text{min}} \geq P_{\text{source}}(n_e, T). \quad (6)$$

By expressing P_{source} in terms of the conductive and radiative losses at the steady state temperature, and evaluating the LHS of Equation (6) using Equations (4) and (5), Equation (6) can be solved for Δn_e . Thus

$$\begin{aligned} \Delta n_e \geq [n_e^{4/7} l^{-5/7} (9.0 \times 10^{-3} n_e^2 l T^{-1} + 5.2 \times 10^4 T^{5/2} - \\ - 0.4 n_e^{10/7} l^{5/7})]^{1/2} - n_e. \end{aligned} \quad (7)$$

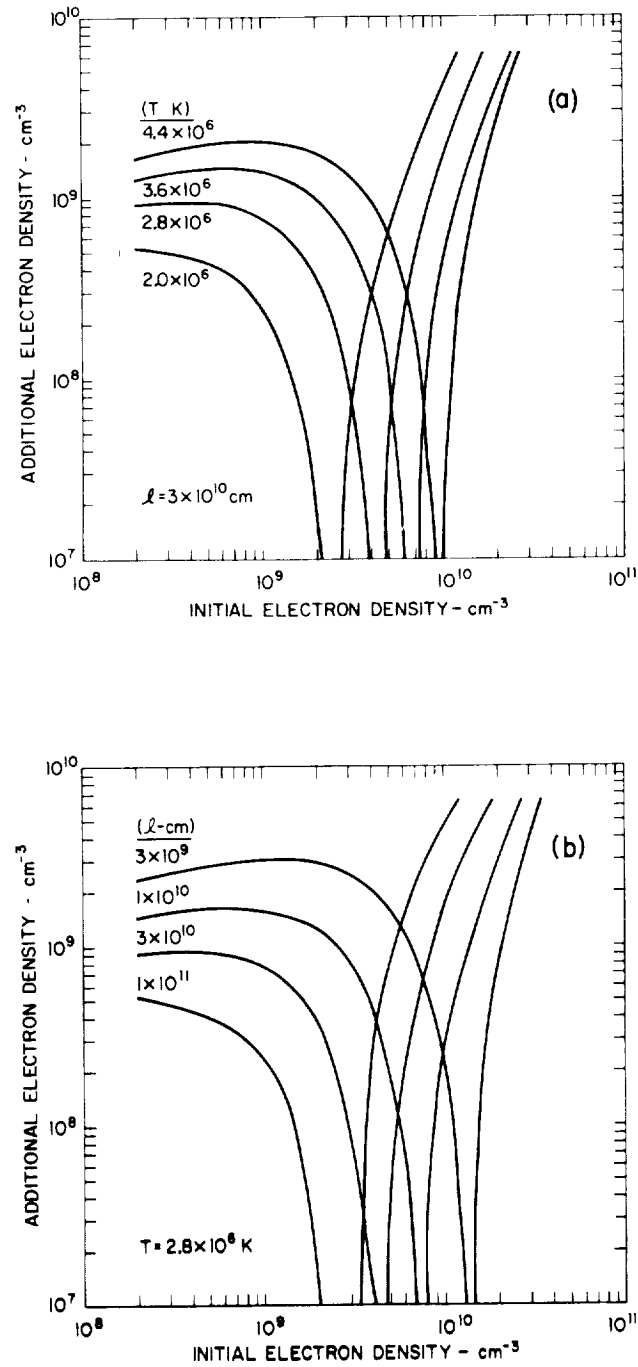


Fig. 4. The increase in density required to establish the radiative instability in a coronal arch as a function of the steady state density n_e , for (a) a constant length and various electron temperatures and (b) a constant electron temperature and various lengths.

By substituting the parameters for the standard arch (Table I), we find that Δn_e must exceed $2.5 \times 10^8 \text{ cm}^{-3}$ if a new equilibrium is not to be established at some lower temperature which is above the temperature of the minimum of the power loss curve. For greater values of Δn_e , conduction will not be able to stabilize the temperature and cooling will continue until typical filament temperatures are reached.

Equation (7) has been evaluated to determine the dependence of Δn_e on the initial density for various values of the length l and initial temperature T . Inspection of the resulting curves (Figure 4) shows that: (1) For all arches there exist specific values of n_e and T for which the density perturbation required to initiate the radiative instability becomes very small. For constant l (Figure 4a) the value of the initial density for which this occurs is a positive function of temperature, while for constant T (Figure 4b) the critical value of the initial density is proportional to a negative power of the length. (2) For constant l and T , as the ambient density increases, corresponding to an increase in the loop heating supply, the density perturbation Δn_e required to drive the arch through the minimum in the loss curve remains fairly constant for ambient densities below $1 \times 10^9 \text{ cm}^{-3}$ but falls off rapidly above this value.

From these results and the measured distribution of n_e , l , and T among active filament arches the cooling mechanism can be expected to occur preferentially among the longer, cooler loops of the observed distribution. They require a smaller increase in density to establish the radiative instability which in turn places less stringent requirements on the transient supply.

2.2. THE RELEASE OF POTENTIAL ENERGY AS THE TRANSIENT ENERGY SUPPLY

Our model considers filaments to be supported in a Kippenhahn-Schlüter configuration which has been reached through the collapse of a coronal arch. If the collapse is the initial stage in this sequence, the release of potential energy during the collapse would appear as a transient energy source. For this particular mechanism to establish the radiative instability the energy released must be sufficient to increase the density of the whole arch to the required level and in the process to raise the temperature (i.e., the internal energy) of the material to coronal values.

To estimate the latter quantity the material is assumed to reach the temperature characteristic of the minimum of the power loss curve for the particular arch. This allows the energy required to be expressed in terms of n_e and l by using Equation (5) to eliminate temperature.

The integral energy equation has the form

$$\Delta PE_{\text{arch}} \geq \Delta PE_{\text{evap}} + \Delta IE_{\text{evap}} + Q_{(\text{rad} + \text{cond})}, \quad (8)$$

where ΔPE_{arch} is the change in potential energy of the collapsed material, ΔPE_{evap} and ΔIE_{evap} are the increase in potential and internal energy of the evaporated material respectively, and $Q_{(\text{rad} + \text{cond})}$ is the sum of the radiative and conductive losses of the evaporated material as it ascends into the arch. The second term dominates the RHS of the equality and in comparison the radiative and conductive loss term can be

neglected for evaporation times less than 10^4 s. In this limit their inclusion would change the result by less than 10%.

Based on the energy equation, the maximum increase in density provided by the collapse of an arch can be evaluated in terms of h , the height of the arch, and Δh , the distance fallen during the collapse. Thus,

$$n'_e = \frac{m_p n_e \bar{g}_h \Delta h}{1.5 m_p \bar{g}_h (h - \Delta h) + 6k(T_{\min} - T_b)} \quad (9)$$

and \bar{g}_h is the acceleration due to gravity averaged over height. By setting $h = 5 \times 10^9$ cm and $\Delta h = 3.5 \times 10^9$ cm, values which are typical of experimental observations, and evaluating the coefficients, Equation (9) can be reduced to

$$n'_e = n_e (5.0 \times 10^{-8} n_e^{4/7} l^{2/7} - 0.1)^{-1}. \quad (10)$$

Equation (10) has been evaluated for arches of three sizes which cover the range of

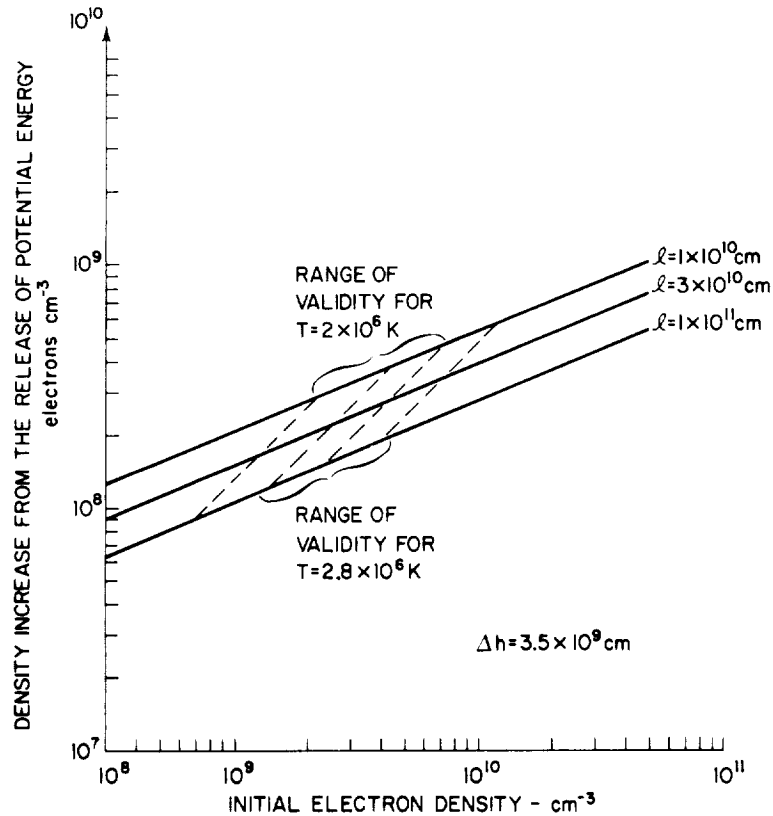


Fig. 5. The density increase to be expected from the release of potential energy in the collapse of arches of various lengths through a height of 3.5×10^9 cm as a function of the initial arch density. The broken lines show the range in added density needed to initiate the radiative instability for various temperature arches. For arches whose parameters lie within these limits, the proposed model of filament formation is energetically feasible.

observed values and the results are shown in Figure 5. By comparing the result for the maximum density obtainable by this mechanism with the evaluation of Equation (7) (Figure 4) for the density increase necessary to initiate the radiative instability, one can specify the ranges of values of n_e , l , and T for which the model is energetically feasible. Ranges for two coronal temperatures are superimposed on Figure 5, and it can be seen that the arches for which the model is successful are quite typical of coronal observations.

2.3. THE TIME SCALES OF FILAMENT FORMATION

Two times are relevant for comparing the model with observation. They are the time for establishing the radiative instability, τ_1 , which consists of the duration of the transient energy supply and its subsequent conversion into increased density within the arch, and the time, τ_2 , once this has happened for the arch to cool and condense into a filament.

A lower limit can be placed on τ_1 by considering the collapse occurs instantaneously throughout the arch, that the material then falls freely under gravity during which time the conversion of potential energy to internal energy occurs and that the energy conduction and the evaporated return are governed by the sound speed. The free-fall time through 3.5×10^9 cm is approximately 5×10^2 s. The sound speed, $V_s = (kT/m_p)^{1/2}$, for the plasma within the standard arch is 1.3×10^2 km s $^{-1}$ and therefore the conduction-evaporation time will be approximately 2.0×10^3 s. Thus, the minimum time required to establish the radiative instability will be on the order of 2.5×10^3 s.

Once the transient source ceases, the new material which has entered the arch will cause the arch to cool. The cooling time τ_2 is defined as the time taken for the arch to cool from its ambient, precollapse, temperature T_1 to the final temperature T_2 reached by the filament. T_2 has been chosen for the purpose of calculation as 2×10^4 K. The cooling time can be estimated by evaluating the integral

$$\tau_2 = \int_{T_1}^{T_2} \frac{E_{\text{total}} dT}{P_r(T) + P_c(T) - Q_{ss}} \quad (11)$$

Q_{ss} is the steady state energy supply which is assumed to be directly proportional to the total electron density and its magnitude has been evaluated by assuming that, in the pre-collapse condition, the heating supply is in equilibrium with the conductive and radiative losses.

Substituting for the various quantities the cooling time integral becomes

$$\tau_2 = \int_{T_1}^{T_2} \frac{3(n_e + n'_e)kl dt}{k_r(T)l(n_e + n'_e)^2 + 2k_c T^{5/2} - n_e^{-1}(n_e + n'_e) [k_r n_e^2 l T_1^{-1} + 2k_c T_1^{5/2}]} \quad (12)$$

Numerical evaluations using the temperature dependence of the radiative loss function proposed by Hildner (1974) for several values of n'_e/n_e , l , and T_1 , which are within the range of permissible values, are shown in Figure 6. The cooling times generally fall in the range of 10^4 to 10^5 s (3 to 30 hr) with the longer times being more realistic since they require smaller increases in density and are therefore energetically preferred.

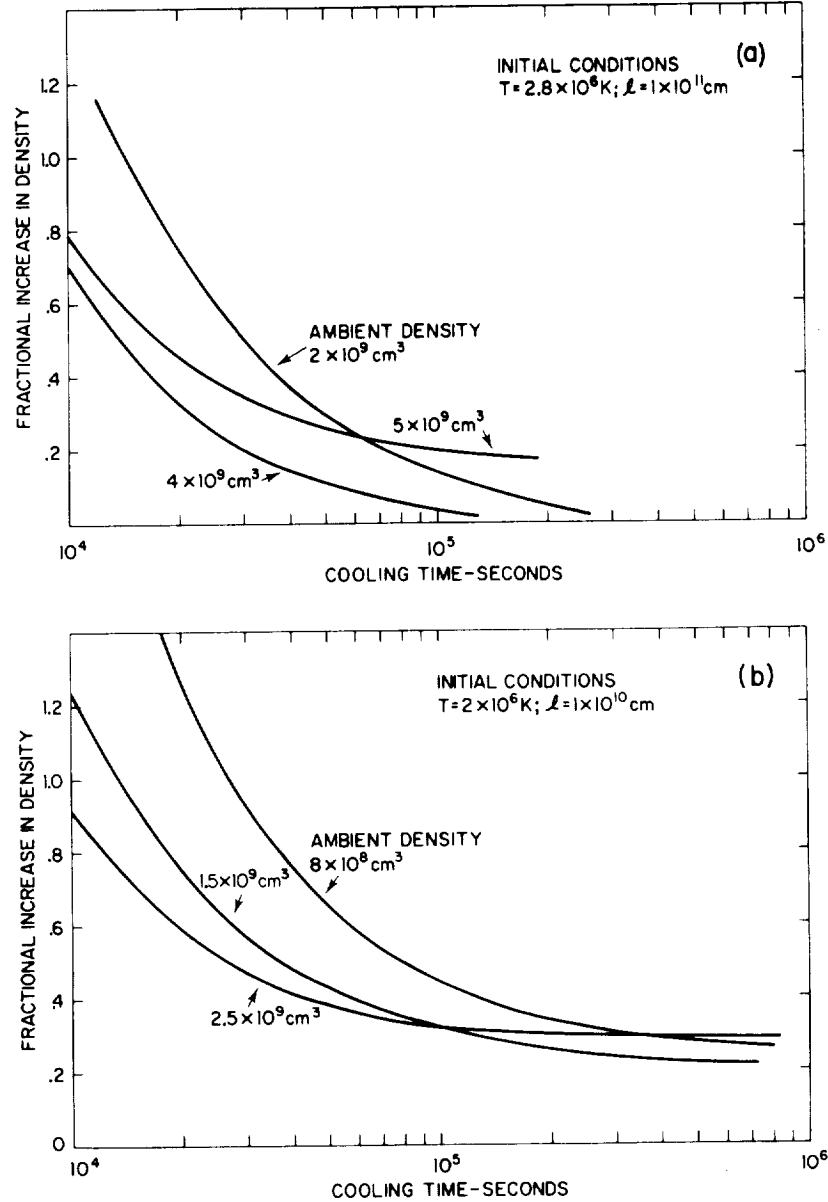


Fig. 6. The dependence of the cooling times of the proposed coronal condensations on the fractional increase in density produced by the transient energy supply. (a) For $T = 2 \times 10^6$ K and $l = 1 \times 10^{10}$ cm. (b) For $T = 2.8 \times 10^6$ K and $l = 10^{11}$ cm.

Inspection of the cooling curves shows that the condensations cool rather slowly above 1×10^6 K and very rapidly below. For example the two typical condensations, shown in Figure 7, spend 98% of their time above one million degrees which, in the higher temperature case corresponds to 12 hr, compared to 14 min below. Although inclusion of dynamic effects may well alter these values, observations at the wavelengths associated with temperatures below 1×10^6 K are unlikely to yield information about the formation of the condensation which occurs at much higher temperatures.

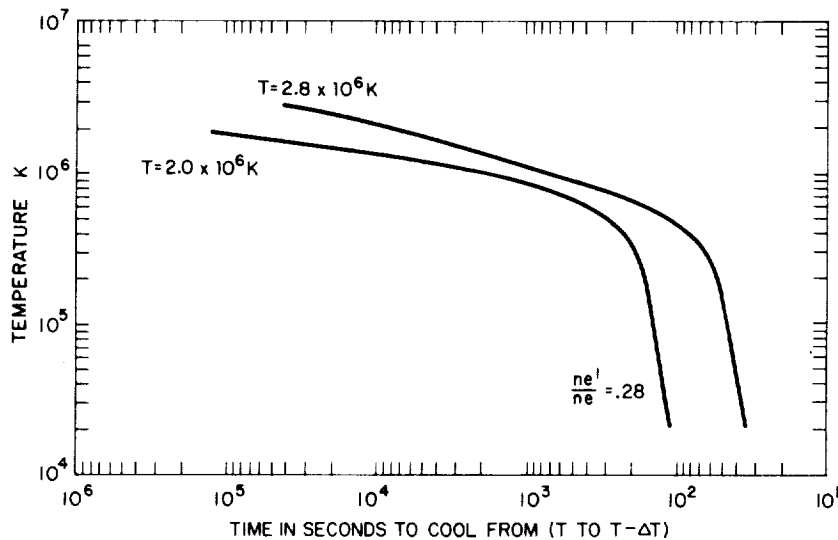


Fig. 7. Cooling curves for two coronal condensations starting from different temperatures. The curves show the length of time required to cool between two temperatures and demonstrate that the condensations cool slowly above 1×10^6 K.

The length of time spent at the higher temperatures provides an explanation for the current failure to have observed filament appearances and associated changes in the structure of X-ray arches. Such a study was performed by one of the authors (JMD) using the S-054 Skylab data. It was restricted to single orbits (10^3 – 4×10^3 s) since this was the period over which sequences of good time resolved images were available. If the present model is realistic correlations would be expected only over much longer periods. Ideally such a study requires observations from the intermediate temperatures, for otherwise the association of the filament appearance in H α with a short lived X-ray event occurring 20–30 hr earlier may be unconvincing.

2.4. THE MASS AND DENSITY OF THE FILAMENT

The model is based on the assumption that the condensation of a single arch will form an element of length of a filament. This assumption is derived from the experimental observations which show *arcades* of loops above filament channels, their absence over existing filaments and, for irregular filaments, the location of arches only above sections

of the filament where the $H\alpha$ absorption is weak or missing (Davis and Krieger, 1982). Since the arches within an arcade are separated by distances roughly equal to their diameters (Figure 1), the length of the element is assumed to be twice the diameter of the original arch.

It is also assumed that material from only half of the precollapse arch flows into the condensation, under the action of both gravity and the pressure differential generated by the falling temperature of the condensation. Therefore the mass of material that will condense into an element of the filament will be

$$M_c = m_p \rho_a \pi r_a^2 \frac{l_a}{2} + \Delta M, \quad (13)$$

where the subscript a refers to the parameters of the arch in its pre-collapse condition and ΔM is the added mass required to initiate the radiative instability. On the basis of Figure 6, ΔM is set equal to $0.3M_c$. If the filament has an elliptical cross-section with a ratio between major and minor axes of $\frac{5}{3}$, the mass of the filament will be given by

$$M_f = m_p \rho_f \frac{3\pi}{5} r_f^2 4r_a, \quad (14)$$

where $4r_a$ is the length of the element of the filament formed by the condensation of the arch of radius r_a . Thus since $M_f = 1.3M_c$, if no mass is lost,

$$r_f = \left[0.271 r_a l_a \frac{\rho_a}{\rho_f} \right]^{1/2}. \quad (15)$$

Thus for density ratios (ρ_f/ρ_a) in the range 10^2 to 10^3 corresponding to filament densities from 10^{11} to 10^{12} cm^{-3} the thickness of the filament would vary from 8×10^3 to $3 \times 10^3 \text{ km}$. Condensation of the five individual arches seen in Figure 1 would result in a filament with a mass of $6 \times 10^{14} \text{ g}$. These values are in reasonable agreement with observation and indicate that sufficient material exists within coronal arches to form filaments.

Finally the remaining material in the arms of the arch may either fall back into the lower atmosphere or by a siphon action (Pikel'ner, 1971; Serio *et al.*, 1978) flow into the condensation. In either case the result will be a dense, cool condensation supported in a virtually empty flux tube. If the steady state heating mechanism continues to operate, the energy dissipated in the empty tube will continue to be available for evaporating material into the arch providing a continuous mass feed to the filament. This will compensate for the material that is frequently observed draining from the filament because of the imperfect nature of the supporting mechanism and may explain the long lifetimes of quiescent filaments.

3. Conclusions

A model has been proposed to condense filaments from coronal arches by invoking a transient energy source to establish the radiative instability. The model provides a

mechanism for cooling the arch through the minimum in the power loss curve ensuring that the arch will cool to the temperature associated with filaments. The energy required for this is not large and the parameters of coronal arches observed above filament channels are adequate to generate the requisite density. Time scales for cooling the condensation are quite long, ranging from 10^4 to 10^5 s with the majority of the time spent above 1×10^6 K. Establishing a direct connection between the X-ray arch and the appearance of the filament will require observations over a broad spectral range.

Since the X-ray observations have demonstrated that arcades of loops occur above filament channels, the model assumes that the formation of a complete filament requires the condensation of the arcade. In this way sufficiently massive filaments can be obtained.

A logical extension of the basic concept suggests that the mechanism which originally maintained the X-ray arches may continue to operate thus providing a method for continually feeding material into the filament. Such a mechanism would explain the extended existence of quiescent filaments.

Although the model successfully describes the broader aspects of filament formation it is still in a very preliminary stage. In particular the identification of the transient energy source with the release of potential energy of the collapsing arch is open to question.

However the basic premise of the model that transient heating can lead to cooling is not affected by these questions and hopefully will provide a useful addition to the continued studies of filament formation.

Acknowledgements

It is a pleasure to acknowledge the many useful discussions held with our colleagues at AS&E since the inception of this project in 1973. The work has been supported by NASA under contracts NAS2-7424, NAS2-8683 and NAS5-25496.

References

- Cox, D. P. and Tucker, W. H.: 1969, *Astrophys. J.* **157**, 1157.
Davis, J. M. and Krieger, A. S.: 1982, *Solar Phys.* **80**, 295.
Hildner, E.: 1974, *Solar Phys.* **35**, 123.
Jordan, C.: 1976, *Phil. Trans. Roy. Soc.* **A281**, 391.
Kippenhahn, R. and Schlüter, A.: 1957, *Z. Astrophys.* **43**, 36.
Levine, R. H. and Withbroe, G. L.: 1977, *Solar Phys.* **51**, 83.
McWhirter, R. W. P., Thonemann, P. C., and Wilson, R.: 1975, *Astron. Astrophys.* **40**, 63.
Pikel'ner, S. B.: 1971, *Solar Phys.* **17**, 44.
Pye, J. P., Evans, K. D., Hutcheon, R. J., Gerassimenko, M., Davis, J. M., Krieger, A. S., and Vesecky, J. F.: 1978, *Astron. Astrophys.* **65**, 123.
Raadu, M. A. and Kuperus, M.: 1973, *Solar Phys.* **28**, 77.
Rosner, R., Tucker, W. H., and Vaiana, G. S.: 1978, *Astrophys. J.* **220**, 643.
Serio, S., Vaiana, G. S., Godoli, G., Motta, S., Pirronello, V., and Zappala, R. A.: 1978, *Solar Phys.* **59**, 65.
Tandberg-Hanssen, E.: 1974, *Solar Prominences*, D. Reidel Publ. Co., Dordrecht, Holland.

4.7 X-Ray and Microwave Observations of Active Regions

D.F. Webb and J.M. Davis

American Science and Engineering, Inc.
Cambridge, Massachusetts 02139

and

M.R. Kundu and T. Velusamy

Astronomy Program
University of Maryland
College Park, Maryland 20742

ORIGINAL PAGE IS
OF POOR QUALITY

X-RAY AND MICROWAVE OBSERVATIONS OF ACTIVE REGIONS

D. F. WEBB and J. M. DAVIS

American Science and Engineering, Inc., Cambridge, MA 02139, U.S.A.

and

M. R. KUNDU and T. VELUSAMY*

Astronomy Program, University of Maryland, College Park, MD 20742, U.S.A.

(Received 30 March; in revised form 15 October, 1982)

Abstract. We compare coordinated, high spatial resolution (2–3 arc sec) observations at 6 cm and in soft X-rays with photospheric magnetograms and optical filtergrams of two active regions. The correspondence of the brightest centimetric components in these regions with coronal loops, sunspots and pores, chromospheric structures and the photospheric magnetic field was determined. Our principal results are: The association between the microwave components and coronal X-ray and photospheric magnetic field structures is complex; in general X-ray emission was not associated with the microwave components. A majority of the components were *not* associated with sunspots, although the brightest ($T_b \geq 4 \times 10^6$ K) components overlay regions of strong photospheric field or high field gradients. Several of the components coincided with the apparent bases of shorter coronal loops and 4 with the tops of X-ray loops.

The X-ray and magnetic field observations are used to constrain possible centimetric emission mechanisms. Thermal bremsstrahlung can not be a significant contributor to this bright microwave emission. Thermal gyro-resonance absorption is consistent with some of the observations, but untenable for those components which are bright in microwaves, lack X-ray emission, and overlie regions of weak magnetic field. As an explanation for the brightest ($T_b \geq 4 \times 10^6$ K) components, the g-r theory requires coronal loops with significant currents but very low densities. Alternatively, a nonthermal mechanism implies that the emission arises from the transition region and suggests that discrete regions of continuous particle acceleration may be common in active regions.

1. Introduction

Much recent work in solar physics has focussed on the problem of the structure of active regions (ARs) in the transition region and low corona. This study has been paced by observations from rockets and satellites, which can observe X-ray and EUV emission with high spatial and spectral resolution, and with large ground-based arrays at centimeter radio wavelengths. The high spatial resolution (a few arc sec) of the instruments has substantially altered our view of the transition region and corona, and prompted the development of more realistic models of active regions.

The slowly varying component of the radio emission over ARs has a spectral maximum at centimeter wavelengths. Only recently has this emission been examined with sensitivity and spatial resolution approaching that of other wavelengths. Observations have shown that the brightest centimetric components are associated with structures near sunspots, transverse fields over neutral lines or filaments (Kundu, 1977,

* Presently at the Tata Institute of Fundamental Research, Bombay, India.

1980, 1981), and emerging flux regions (Kundu and Velusamy, 1980). The fact that these latter features are also associated with X-ray loops and that thermal bremsstrahlung can produce emission at both microwave and X-ray wavelengths leads us to suspect that at least part of the microwave emission in active regions arises in coronal loops. Recent high resolution centimeter observations with the Very Large Array (VLA) have revealed loop-like structures reminiscent of those observed in X-rays and EUV (Kundu and Velusamy, 1980). Previous comparisons of imaging observations in soft X-rays and microwaves have shown that most of the general plage-related emission in ARs is due to thermal bremsstrahlung (Gerassimenko *et al.*, 1976; Pallavicini *et al.*, 1979). The brighter centimetric components require an explanation in terms of low harmonic gyromagnetic emission (e.g., Kundu *et al.*, 1980; Alissandrakis *et al.*, 1980; Felli *et al.*, 1981).

This paper presents the initial results of a long term study whose purpose is to measure the plasma parameters and the properties of the magnetic field in coronal structures through the use of combined high spatial resolution X-ray, magnetogram and microwave data. Although this first paper is primarily observational, the results are sufficient to constrain possible centimetric emission mechanisms. In particular we conjecture that the results imply a significant small-scale, nonthermal component to the slowly varying radiation from ARs.

We describe the analysis of two active regions observed on 16 November 1979. The data include soft X-ray filtergrams from a sounding rocket flight, microwave radio maps of total intensity and circular polarization obtained with the VLA, photospheric magnetograms and optical filtergrams, all of comparable high spatial resolution (1–3 arc sec). This is the first time that such coordinated, high spatial resolution observations in microwaves and X-rays of active regions have been available. In the next section we describe the observational data. In Section 3 we discuss the observational results. The key results are summarized in Section 4 and discussed in the last section.

2. The Observations and Data Analysis

2.1. SOFT X-RAY DATA

On 16 November 1979 American Science and Engineering (AS&E) launched the second of two rocket flights designed to obtain a complete view of the solar corona at solar maximum. This payload utilized a metallic mirror previously flown many times (Vaiana *et al.*, 1973). Full-disk images of the corona with an on-axis spatial resolution of 2–3 arc sec were obtained between 17:02 and 17:05 UT. The images were recorded with two Kodak emulsions, SO-212, a moderate-speed emulsion, and SO-253, a fine-grain holographic emulsion which permits improved definition of coronal features (Davis *et al.*, 1979).

2.2. MICROWAVE DATA

The radio observations were made at 6 cm with the VLA of the National Radio Astronomy Observatory between 15:00 and 16:45 UT on 16 November 1979. Seven-

teen antennas were available during the observations, providing good determination of the two-dimensional brightness distribution. The system was sensitive to structures smaller than 3 arc min because the shortest spacing used for these maps was 1200λ . The observing procedure and calibration and cleaning methods were similar to those discussed by Kundu and Velusamy (1980). The observations alternated between two active regions, Hale Nos. 16419 and 16421. The centers of the regions used for continuous tracking were located at N10 W23 and N32 W33 in heliographic coordinates at 00 UT. Synthesized maps of total intensity and circular polarization were obtained of a field of view of 6.4×6.4 arc min around each active region. The synthesized beam was 3×6 arc sec with the long axis oriented in the north-south direction. The dynamic range on these maps was greater than a factor of 10.

2.3. CHROMOSPHERIC AND PHOTOSPHERIC DATA

Full-disk photospheric magnetograms were obtained at Kitt Peak National Observatory (KPNO). The magnetograms used for our study were obtained at 15:43, 17:43, 18:28, 19:17, 20:07, and 21:00 UT. In addition, a full disk He I – 10830 Å filtergram was obtained at KPNO at 16:47 UT. The magnetograms at 15:43 and 17:43 UT bracketed the times of the X-ray and radio observations and therefore were used in our detailed analysis. No significant changes in the general magnetic field in either of the two ARs was observed on the magnetograms. In addition, video magnetograph (VMG) images were obtained from Big Bear Solar Observatory (BBSO) and used to verify the KPNO data.

Chromospheric data were obtained in collaboration with BBSO. Nearly continuous H α observations with time resolution of 10 s of both active regions were obtained on 16 November from 15:55 to 22:00 UT. Most of these images were centered on H419; only 5 min of high resolution data were taken of H421 starting at 21:54 UT. A cine version of these data was used to select individual frames for enlargement and to study the evolution of chromospheric and photospheric structures in H419. Frames enlarged for the detailed study were recorded at 16:58, 19:35, and 19:37 UT in H α , H α wings and continuum, respectively, and in H α at 21:57 UT for H421. Full-disk patrol H α data obtained at 19:37 UT (H α) and 21:40 UT (near-H α continuum) were used in the alignment scheme.

2.4. METHOD OF COMPARISON

A selection of the X-ray and visible light images, the microwave maps, and the optical images were converted to transparencies with a scale of $4.8 \text{ arc sec mm}^{-1}$ (40.6 cm solar disk diameter). To compare the locations of the X-ray and microwave features, the heliographic positions of the centroids of the sunspots that lay within the field of the radio maps were determined, using a Mt. Wilson sunspot chart and an H α image from NOAA-Boulder. These positions were converted to celestial coordinates at 17:00 UT and plotted on the radio maps. Visible light images from the AS&E experiment revealed sunspots which were used as an intermediary to coalign the X-ray, radio and optical data. The magnetograms were coaligned by using the fact that H α plage emission tends

to occur in areas of strong vertical magnetic fields. Up to 6 spot groups were used for alignment. The alignment accuracy between the X-ray data and the radio maps was about 5 arc sec. The overall accuracy including the optical data was 5–10 arc sec.

3. Observational Results

Figure 1 presents the 6 cm maps in total intensity (left) and circular polarization (right) of active region H421 (top) and H419 (bottom), observed on 16 November, 15:00–16:45 UT. The crosses denote the centers of the large sunspots lying within the area of the radio maps. To illustrate the relation of the microwave emission to hot ($T_e > 10^6$ K) coronal loops and to the photospheric magnetic field, we show the radio intensity contours of AR H421 (Figure 2) and AR H419 (Figure 3) superimposed on a soft X-ray image (top) and on a photospheric magnetogram (bottom).

Table I lists the brightest microwave components in each region in approximately decreasing order of brightness temperature (T_b). For each source its estimated size, dominant polarity and degree of polarization (V/I), and possible physical association are also listed. For each active region the source components are indicated on the intensity maps in Figure 1. It should be emphasized that we studied only the *brightest* microwave components in these regions. The VLA configuration used was not sensitive to large structures or low brightness sources (e.g., plages), but was optimal for observation of the compact, bright coronal structures typical of ARs. The noise level of the maps was about $T_b = 4 \times 10^5$ K. We concluded that the X-ray and microwave sources in these two regions were quiescent, i.e. that no obvious flares or bursts occurred there during the period of observation. The limitations of this statement are discussed in the final section.

3.1. ACTIVE REGION H421

Active region H421 was closer to disk center than H419 ($r \sim 0.75$ from Sun center) on 16 November and therefore suffered less from projection effects and off-axis vignetting and scattering in X-rays. It was apparently evolving rapidly, because BBSO observations on 18 November showed a dramatic change in the region with considerable emerging flux in the area to the northwest of the main spot. Region H421 contained one dominant sunspot with penumbra of negative polarity and many small spots or pores. The large spot had an area of 50 millionths of a solar hemisphere and a field strength ≤ 2000 G (*Solar Geophysical Data*, 1980).

The bright coronal X-ray structure of AR H421 consisted of two loop arcades crossing the N–S magnetic inversion lines of the region. The arcades were potential-like, with their loops oriented orthogonally to the inversion line. The salient X-ray feature was a short, bright loop (arrow, Figure 2a) which bridged the inversion line in an area of high field gradient near the spot. The western foot of the loop ended at the edge of the spot penumbra. The length ($\sim 2 \times 10^4$ km), shape and location of this loop are typical of a class of X-ray loops called penumbral loops (Webb and Zirin, 1981). The inversion line swung in toward the spot and was marked by a short $H\alpha$ filament; the

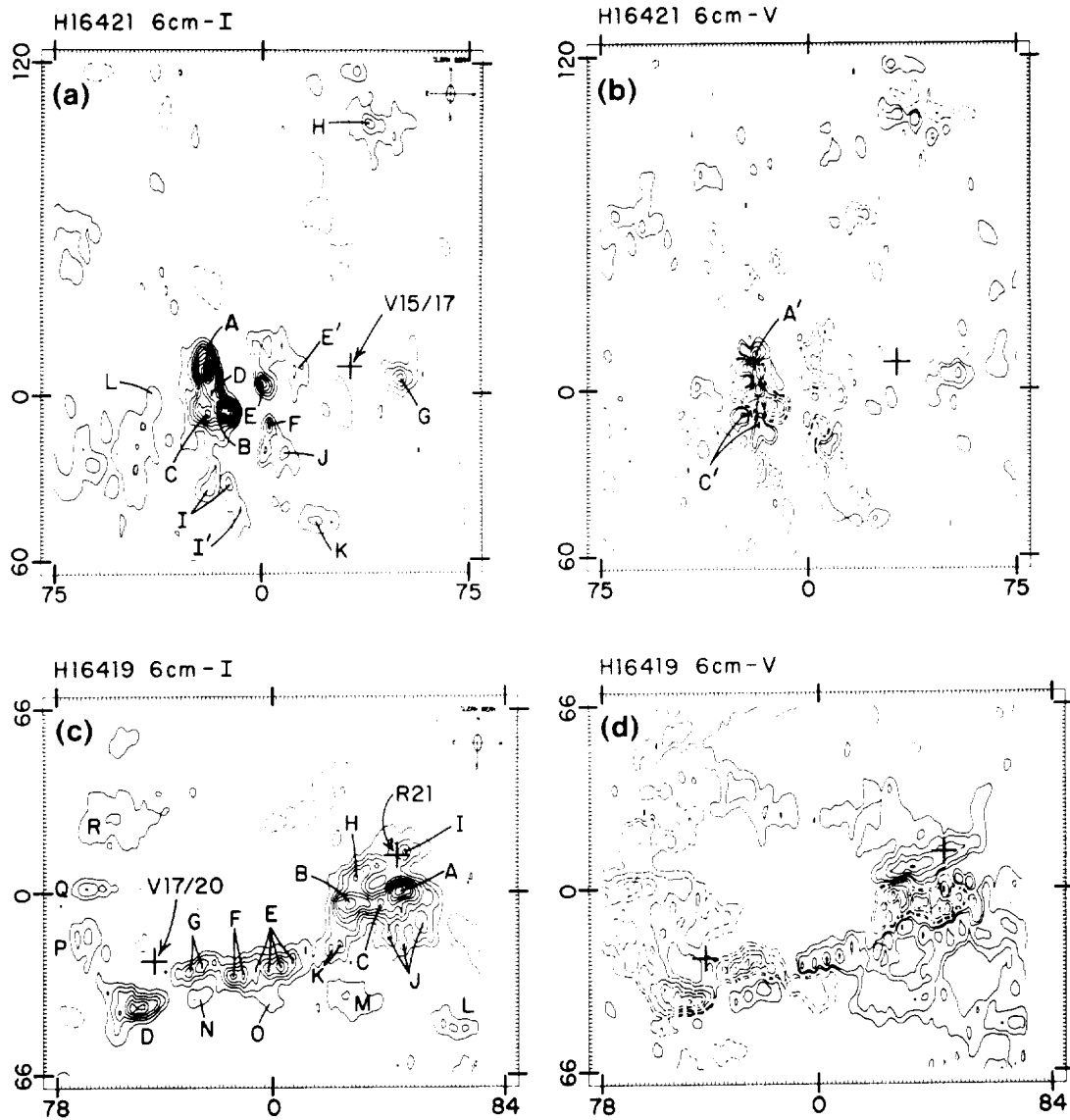


Fig. 1. 6 cm VLA maps of active regions H 16421 (top) and H 16419 (bottom) on 16 November 1979. The size of the synthesized beam was 6×3 arc sec. Geocentric north is at the top and east to the left. The center (0, 0) of the H 16421 map was at 263 arc sec north and 316 arc sec west of disk center at 16:00 UT, and the center (0, 0) of the H 16419 map was at 660 arc sec north and 342 arc sec west of disk center. (a) Total intensity ($R + L$) map of H 16421. The lowest contour and the contour interval is 8×10^5 K. The cross shows the centroid of the large sunspot V15/17 in Mt. Wilson group No. 21042; the length of the arms of the cross is 10 arc sec, which is representative of the alignment uncertainties. The letters designate individual microwave components. (b) Circularly polarized ($R - L$) intensity map of H 16421. The first two contours are 4 and 8×10^5 K, respectively, and the contour interval for the higher contours is 8×10^5 K. The solid (broken) contours represent positive (negative) values. (c) Total intensity map of H 16419. The contour levels are the same as (a). The crosses show the centroids of sunspots V17/20 and R21 in the Mt. Wilson group No. 21041. (d) Circularly polarized intensity map of H 16419. The contour levels are the same as (b).

TABLE I

List of the brightest microwave components in the ARs H16421 and H16419

| Source | Peak T_b (10 ⁶ K) | Size ^a (arc sec) | Polarity ^b | Reversed? ^c | Polarization (%) ^d | Association |
|--------|-----------------------------------|--------------------------------|-----------------------|------------------------|-------------------------------|---|
| 421 A | 10.5 | 7 × 9 | L | R | 23 | Photospheric pores – emerging flux loops |
| 421 B | 8 | 7 × 5 | L | R | ~30 | Foot of bright loop? |
| 421 C | 6.5 | 6 × 6 | L | R | 30 | ? |
| 421 D | 6.5 | < 2 | L | R | 62 | ? |
| 421 E | 4.8 | 4 × 5 | L | ? | 33 | Foot of bright loop? |
| 421 E' | 1.5 | 4 × 5 | L | S | – | Top of bright loop |
| 421 F | 3.2 | 3 × 11 | L | R | 25 | Foot of bright loop or of arcade loop |
| 412 G | 3.2 | 5 × 5 | R | ? | 25 | Penumbra or neutral line |
| 421 H | 2.5 | 8 × 6 | R | S? | 33 | Top of coronal arcade |
| 421 I | 1.5 | 3 × 9 | L | R? | 100 | Foot of filament arcade loop |
| 421 I' | 1.5 | 3 × 12 | L | – | – | Top of filament arcade loop |
| 421 J | 1.5 | 3 × 4 | R | ? | 50 | Foot of arcade loops |
| 421 K | 1.5 | 3 × 5 | R? | R? | – | Foot of filament arcade loop |
| 421 L | ~1 | diffuse | R | R | – | Small loop over magnetic cell |
| 419 A | 7.2 | 7 × 5 | L | R | 22 | Photospheric pore and/or penumbra |
| 419 B | 6.5 | 11 × 6 | L | R | 50 | Photospheric pore and/or penumbra |
| 419 C | 4.8 | 2 × 3 | L | R | 40 | Photospheric pore and/or penumbra |
| 419 D | 4.8 | 12 × 6 | L | S | 83 | Penumbral loops |
| 419 E | 1.5–4.8 | 15 × 7 | R | S and R | 40–100 | Neutral line with high field gradients |
| 419 F | 4 | 7 × 4 | L? | S? | ? | Top of loop? |
| 419 G | 4 | 12 × 5 | L | S | 80 | Penumbral loops |
| 419 H | 4 | 6 × 4 | R | S | 60–80 | Photospheric pore and/or penumbra |
| 419 I | 3.2 | 4 × 5 | R | S? | 50 | Sunspot umbra |
| 419 J | 1.5–2.5 | 15 × 8 | R | S | 33–100 | Loop arcade crossing NL. |
| 419 K | 2.5 | 5 × 3 | R | S | 33 | ? |
| 419 L | 1.5 | 10 × 3 | R | ? | 50 | ? |
| 419 M | 1.5 | 12 × 6 | R | ? | 50 | Top of long X-ray loop |
| 419 N | 1.5 | 6 × 3 | R | S or R | – | Magnetic cell or foot of penumbral loops |
| 419 O | ~1 | diffuse | L | ? | – | Foot of loops |
| 419 P | 1.5 | 6 × 5 | L | ? | 100 | Foot of X-ray loop? |
| 419 Q | 2.5 | 9 × 5 | L | R? | 100 | Foot of X-ray loop? |
| 419 R | 1.5 | diffuse | L | ? | ? | Foot of filament arcade loop? |

^a The approximate FWHM dimensions of the total intensity along the short and long axis of each component. These have not been corrected for the beam shape.

^b The sense of circular polarization at the peak intensity of the component. L is left CP (negative) and R is right CP (positive).

^c Whether the sense of circular polarization (b) is the same (S) or reversed (R) with respect to the underlying photospheric magnetic field. This assignment does not account for projection effects.

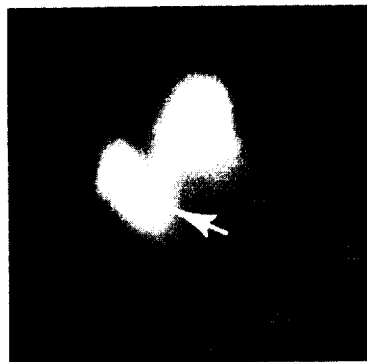
^d Degree of polarization %_v(V/I) at the peak intensity of the component.

ORIGINAL PAGE
BLACK AND WHITE PHOTOGRAPH

X-RAY AND MICROWAVE OBSERVATIONS OF ACTIVE REGIONS

273

H 421



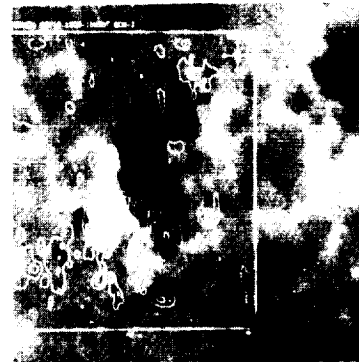
a) X-RAY: 1704 UT



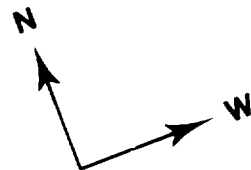
b) X-RAY + 6 CM



c) MAG: 1742 UT

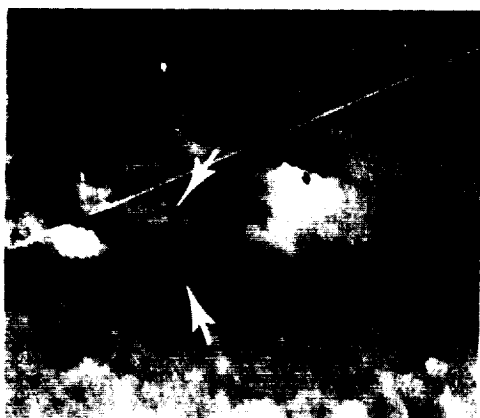
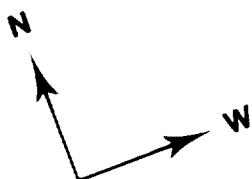


d) MAG + 6 CM



2 arc min.

Fig. 2. Coaligned, high resolution images in soft X-rays (top), of the photospheric magnetic field (bottom) and at 6 cm of active region H 16421 on 16 November 1979. The X-ray image is a 60 s exposure on Kodak SO-253 emulsion. The 6 cm total intensity map from Figure 1a is superimposed on the X-ray and magnetogram images (b and d, respectively), which are shown separately on the left side for clarity. The direction arrows at the bottom denote heliographic directions.

H 419**a) X-RAY: 1704 UT****b) X-RAY + 6 CM****c) MAG: 1742 UT****d) MAG + 6 CM**

2 arc min.

Fig. 3. Coaligned images similar to Figure 2 for active region H 16419 on 16 November 1979.

ORIGINAL PAGE
BLACK AND WHITE PHOTOGRAPH

bright loop appeared to cross over this structure at a small angle, indicative of a high degree of shear in the coronal magnetic field. The bright loop and the eastern arcade crossed the area of the highest field gradients in the region.

In order to determine parameters of the coronal magnetic field, it is important to identify components of the bright X-ray loop in the microwave map (e.g., Kundu *et al.*, 1980). Unfortunately, the 6 cm components in this region were tightly clustered precluding an unambiguous identification. The component 421E appeared to be coincident with the eastern foot of the loop, and the weak component *E'* to the west with the top of the loop. But component *E*, left circularly polarized (LCP), also appeared to straddle the photospheric inversion line. If *E* was at the loop footpoint, then it lay east of the inversion line but was of reversed polarity to the photospheric field. Alternatively *E* might have marked the location of a neutral sheet or arcades crossing the inversion line.

The brightest microwave components in AR H 421 were < 2 to 7 arc sec in diameter. Components *A*, *B*, *C*, and *D* lay south of the eastern X-ray arcade and well east of the inversion line (Figure 2). The photospheric field, especially underlying *A*, was strong and of positive polarity. Although the central polarization of this group was LCP, it was surrounded by islands of RCP indicating the bipolar nature of the group (Figure 1b). The component *A*, which had the brightest peak ($T_b = 10.5 \times 10^6$ K) observed in either active region, was of LCP, weakly polarized ($\sim 20\%$) and was coincident with an H α patch which later brightened and with several pores. Just north of *A* was a region of strong RCP (*A'*). This suggests that *A* and *A'* were at the feet of an arcade of short loops. The proximity of the pores and the H α brightening suggests that strong emission around *A* might have been associated with neutral sheets in the corona over emerging flux (Kundu and Velusamy, 1980). The optical coverage was not adequate to definitely identify such emerging flux.

There were no obvious features underlying components *B* and *C* in the southern part of this group. *C* was flanked by two compact sources of RCP (*C'* in Figure 1b) suggesting bipolarity. All of the brightest sources in H 421 had lower circular polarization (20–30%) except for *D* which was highly polarized ($\geq 60\%$).

An inclusion of negative photospheric polarity east of the neutral line (arrow, Figure 2c) was adjacent to an area of H α brightening and faint X-ray and microwave emission, but the alignment accuracy precluded a definite association.

The components *I*, *J*, and *K* straddled a large, quiescent filament which ran generally E–W and bounded the active region to the south. Since large coronal arcades are known to overlie filaments and filament channels (McIntosh *et al.*, 1976; Webb and Zirin, 1981), the radio sources *I* and *K* probably were emission from the legs or feet of loops crossing the filament. Component *I'*, the southern extension of *I*, overlay the filament; its emission probably came from the top of an arcade loop. The opposite polarization of the components *J* and *F* indicates that they outlined compact loop structures crossing a second inversion line north of the filament. The proximity of these two inversion lines suggests that this area was magnetically complex with high field gradients.

North of the sunspot was a classic arcade structure with X-ray loops joining opposite

polarity plage divided by a faint filament. The brightest X-ray structure was a large, diffuse arch defining the northern limit of the arcade. Superimposed near the top of this arch was component *H*, a bipolar source with peak $T_b \sim 2.5 \times 10^6$ K. The component was of predominantly RCP.

Finally, the component *G* was compact, bright and entirely of RCP. It was ~ 25 arc sec west of the center of the spot in an area of mixed photospheric polarity. It could have been associated with the penumbral field, especially since there were no bright X-ray or H α structures in the vicinity.

3.2. ACTIVE REGION H419

Region H419 was 2–3 rotations old and appeared stable. However, it was magnetically more complex than region H421 with a dominant preceding spot with a large penumbra and some pores, and two trailing spots. The large *p* spot, numbered R21 by Mt. Wilson, had an area of 270 millionths and a field strength of ~ 2500 G. The smaller central negative spot, V17/20, and the trailing positive spot, R20, were of nearly equal size. Two of the sunspots (R21 and V17/20) lay within the field of the radio map (Figures 1 and 3). The large leading spot had many, bright microwave components clustered nearby.

The AR was characterized by diffuse X-ray emission spreading linearly in an E–W band. The most notable X-ray feature was a bright, compact structure, which was *not* associated with 6 cm emission, on the perimeter of the central spot penumbra. Several bright loops to the west were just outside of the field of view of the radio observations. Within this field of view the coronal emission generally bridged inversion lines.

We first discuss the microwave components surrounding the leader sunspot. Figure 4a shows details of the spot structure as seen in the continuum at 19:35 UT. A small spot lay within the southeast border of the penumbra, and several pores lay just outside the penumbra. The BBSO film revealed no appreciable changes in the leader sunspot and the pores around it between about 16:00 UT, when the radio and X-ray data were obtained, and 19:35 UT.

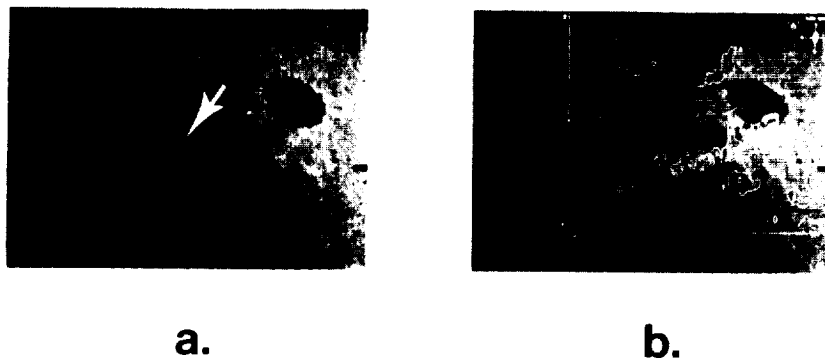


Fig. 4. (a) Near-H α continuum image of AR H16419 at 19:35 UT on 16 November 1979 showing the sunspot structure. The arrow points to a pore that appeared after 17:00 UT. (b) The same image with the 6 cm total intensity map of Figure 1c superimposed on it.

Figure 4b shows the microwave components superimposed over the same continuum image. This comparison illustrates the following points: (1) The brightest components (*A*, *B*, *C*, and *H* with $T_b = 4 - 7.2 \times 10^6$ K) were clustered in the vicinity of the penumbral spot and pores about 20–25 arc sec south of the umbral center; the spots and pores were all of the same polarity; (2) The strongest components (*A*, *B*, and *C*) were all LCP or of reversed polarity to the photosphere; (3) The small penumbral spot was associated with a region of low T_b , i.e., a 'hole' surrounded by bright emission. The components *A*, *B*, and *C* were in areas devoid of significant H α or X-ray emission. Their higher T_b , lower polarization (20–50%), and association with the high field strengths and gradients of the penumbra and pores suggest that this emission was due to a gyromagnetic mechanism.

About 30 arc sec south of the sunspot umbra was a bright V-shaped area of X-ray emission associated with H α fibrils. The multiple, elongated radio components *J* overlay this area. The N–S orientation of this microwave pattern, the X-ray structure, and the H α fibrils suggest that the emission arose from an arcade of low-lying loops crossing the inversion line.

The central sunspot in AR H419 (Figure 4a) like the spot in AR H421, had a well developed penumbra with no X-ray or microwave emission above it. The nearest radio components were *D* and *G*, 15–20 arc sec away, at the perimeter of the penumbra.

The area surrounding this spot was the scene of significant activity in the visible in the H α film. The brightest X-ray feature coincided with a negative magnetic spot in a moat of positive flux at the northern edge of the penumbra (top arrow; Figure 3c). Of flare-like brightness in H α from 16:50 to 17:20 UT, this area was active all day and reminiscent of the hot transient penumbral spots studied by Webb and Zirin (1981). This spot was not bright in microwaves, a point we will discuss later. A pore (arrow; Figure 4a) adjacent to the location of the magnetic knot emerged after our observing period.

The small positive polarity arc visible south of the sunspot (bottom arrow; Figure 3c) represents an inclusion of opposite polarity in the general field of the spot. It coincided with dark H α fibrils emanating from the edge of the spot and was located between the microwave components *D* and *N*. The arc was more likely associated with *N* because this component was RCP, of the same polarity as the magnetic arc, and projection effects would have shifted it to the northwest.

The component *D* was a bright ($T_b \sim 5 \times 10^6$ K), compact source which lay just south of the sunspot penumbra. It was highly polarized (83%) in LCP, the same sense as the nearby spot polarity. Component *G* was a double source which overlay the penumbra. Both components *D* and *G* were likely associated with penumbral loops.

The chain of components labelled *E* in Figure 1c overlay an area of negative polarity to the east and positive polarity to the west, an area of high field gradients. The component *F* was bright and overlay a patch of H α emission, but was weakly polarized or unpolarized. This suggests emission from the top of a loop.

Three fainter components, *M*, *P*, and *Q*, appeared to be associated with X-ray loops. The large component *M* coincided with the top of a long, narrow X-ray loop, in a manner

similar to that of component *H* in AR H 421. The X-ray loop may have been evolving since its feet were brighter than its midsection (Figure 3a); most quiescent X-ray loops are isobaric.

4. Summary

The key results of our comparative study for 16 November 1979 are:

(1) The association between the microwave components and coronal X-ray structures is complex. In general X-ray emitting structures were *not* associated with the microwave components. This result is supported by Schmahl *et al.* (1982).

(2) The association between the microwave components and photospheric magnetic fields is likewise complex. Although about half of the radio components were associated with strong photospheric fields, such strong fields did not always produce centimetric emission. The *brightest* microwave components were associated with areas of strong longitudinal magnetic fields or high field gradients, but *not* with sunspot umbrae.

(3) About one-third of the sources appeared to be associated with only the feet or legs of coronal loops of size $\leq 5 \times 10^4$ km. However, only some of these loops were observed in X-rays. The existence of others was deduced from the geometry of the surrounding magnetic field.

(4) There were five cases of possible microwave emission from the tops of coronal loops (Table II). Four of these loops, or loop arcades were identified by their emission in X-rays. These components were fainter ($T_b \leq 2.5 \times 10^6$ K) and more diffuse than the other components, but had one dominant polarization.

TABLE II
Sources at tops of coronal loops

| Source | Peak T_b (10^6 K) | Peak polarity | X-radiation | Association |
|---------------|---------------------------|------------------|-------------|---|
| 421 <i>E'</i> | 1.5 | L | yes | Bright penumbral loop |
| 421 <i>H</i> | 2.5 | R | yes | Bright loop arcade over neutral line |
| 419 <i>J</i> | 1.5–2.5 | R | yes | Loop arcade over neutral line |
| 419 <i>M</i> | 1.5 | R | yes | Long single loop |
| 421 <i>I'</i> | 1.5 | L | no | Possible filament arcade loop |

(5) None of the sunspot umbrae studied had overlying X-ray emission; i.e., there is little if any material at coronal temperatures over spots. This agrees with previous coronal observations (Pallavicini *et al.*, 1979; Webb and Zirin, 1981; Webb, 1981; Nicolas *et al.*, 1981). Two of the 3 sunspot umbrae and the largest pore for which we had radio observations had no significant microwave emission over them. This result is also supported by other recent measurements at high spatial resolution (Kundu and Velusamy, 1980; Kundu *et al.*, 1981; Pallavicini *et al.*, 1981). The one sunspot with associated microwave emission (component 419I) was also the largest in both area and

magnetic field strength. This observation is consistent with the recent model of Pallavicini *et al.* (1981), which shows that thermal g-r emission may arise only over umbrae of sufficiently large size.

(6) Finally, the sense of 6 cm circular polarization was often reversed with respect to the underlying photospheric field, especially for the bright components. Also, in nearly every case where we interpreted the centimetric components as denoting the legs or feet of loops, one or both components had reversed polarization. We believe that these reversals are related to mode coupling in a quasi-transverse region (Kundu *et al.*, 1977; Bandeira, 1982).

5. Discussion

A major result of this study is that a *majority* of the individual bright microwave components we identified were *not* associated with sunspots. This result is contrary to the low resolution radio observations, i.e., that the centimetric core emission from ARs is *only* associated with spot umbrae. To quantify our assertion we drew circles with diameters equal to the largest measured diameters of the penumbra and centered on the umbra of each of the 3 spots we observed. In addition we drew concentric circles 10 arc sec in diameter larger to allow for alignment uncertainties. Sources which lay within or touched these circles were defined to be 'associated' with the sunspot. Thirty-two components for both ARs are listed in Table I. Of these only seven lay within the three inner circles and a total of 13 lay within the three outer circles. Therefore, 19, or 59% of the components were definitely *not* associated with sunspots using our criteria. This number is conservative because we did not correct for penumbral foreshortening and we grouped similarly structured sources together (e.g., 419E).

The existence of such a large number of strong components, not all associated with regions of strong photospheric magnetic field, and with a low correlation with X-ray structures means that mechanisms invoked to explain the radio sources must apply over a large range of magnetic field strengths and outside of the range of plasma parameters typical of ARs.

We can use the X-ray observations to constrain these emission mechanisms. First, although low brightness temperatures suggestive of thermal bremsstrahlung may be typical of the extended, plage-associated component of active regions (Kundu *et al.*, 1977; Pallavicini *et al.*, 1981; Felli *et al.*, 1981), we can rule out bremsstrahlung as a significant contributor to the bright radio emission studied here. Most of the material in a typical active region is at coronal temperatures ($T_e > 10^6$ K), and is visible in broadband X-rays (see Webb, 1981 for a review). Therefore, since the corona is optically thin to bremsstrahlung in both broadband X-rays and at 6 cm, we can estimate the contribution of bremsstrahlung to the observed brightness temperature, T_b , of those centimetric components associated with X-ray structures. The 4 components associated with the X-ray loops (Table II) have brightness temperatures consistent with their being optically thin to bremsstrahlung (quiescent X-ray loops invariably have

$T_e = 2-3 \times 10^6$ K). In the optically thin case the predicted T_b is

$$T_b = \frac{\xi}{\nu^2 T_e^{1/2}} \int n_e^2 dl,$$

where $\int n_e^2 dl$ is the thermal emission measure along the line of sight derived from X-ray observations, ν is the frequency of the radio observations, and ξ has a value of 0.16 in the corona (Kundu, 1965). Using an appropriate value for $n_e^2 dl$ in X-ray loops of $\sim 10^{28} \text{ cm}^{-5}$, $T_b \sim 5 \times 10^4$ K at 5 GHz, a value too low to explain the bright radio emission.

Gyromagnetic emission mechanisms provide the only known alternative explanation to bremsstrahlung for the bright components of the slowly varying radiation. Nonthermal gyrosynchrotron processes have been invoked, but these require continuous acceleration of electrons to explain the long lifetime of the bright components and more polarization diversity than observed. The fact that the radio brightness temperatures and the coronal electron temperatures are often nearly equal argues for a thermal mechanism (e.g., Kundu *et al.*, 1980), such as resonance absorption at harmonics of the gyrofrequency.

This theory predicts that in coronal loops, which should be optically thin to bremsstrahlung, the gyroresonance (g-r) absorption process makes the radio emission optically thick where the magnetic field strength is high and where the angle θ between the magnetic field direction and the line of sight is large (Kundu *et al.*, 1977; Gel'freikh and Lubyshev, 1979). This mechanism has been invoked in an interpretation of bright

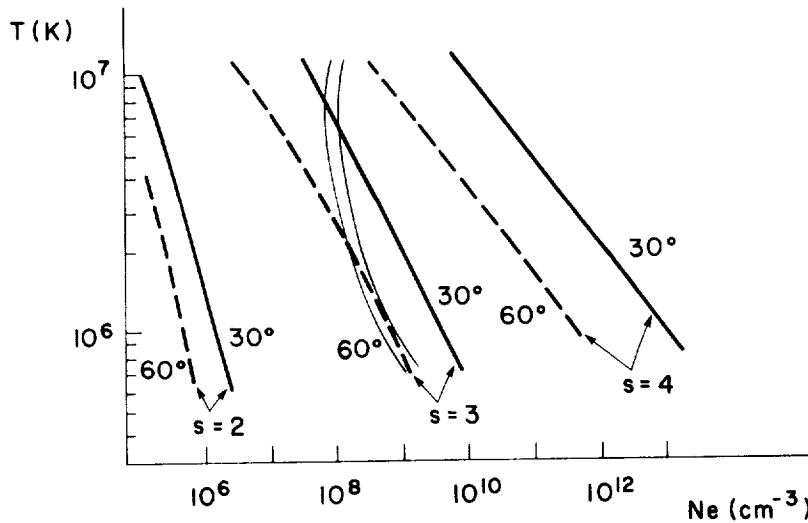


Fig. 5. Loop temperatures and electron densities required to reach unit optical depth at resonant harmonics, s , of the gyrofrequency. The observing frequency is 5 GHz and the scale length of the magnetic field strength is assumed to be 10^9 cm. The optical depth is larger (smaller) than unity on the right (left) side of each curve. The curved lines represent the limiting sensitivity to X-ray structures and are discussed in the text. (After Kundu *et al.*, 1980, Figure 2.)

non-sunspot components in terms of neutral sheets overlying emerging flux (Kundu and Velusamy, 1980), or emission from the tops of loops bridging magnetic inversion lines (e.g., Kundu *et al.*, 1977). In support of these interpretations, we find that generally the microwave components we observed were in regions where strong magnetic fields or high field gradients might be expected.

Figure 5 is a plot of the resonant optically thick layers as a function of temperature and electron density from the g-r theory. The curved lines indicate the limiting sensitivity of the AS&E X-ray rocket experiment for the detection of coronal loops at two fixed diameters, the maximum diameter (left) of typical AR X-ray loops and the average diameter (right) of loops in one well-studied AR (Pye *et al.*, 1978). Structures which lie to the left of these curves in terms of their electron temperature and density could not be detected in X-rays. Figure 5 implies that for those components lacking significant X-ray emission, resonance emission can only occur at the second harmonic or at high values of θ at the third harmonic. Six cm emission at these harmonics requires fields of 900 and 600 G, respectively, in the corona. But about half of the components overlie regions where the *photospheric* magnetic field is less than these values. Even for those components with possible, faint X-ray emission (e.g., 421F) it is very unlikely that harmonics higher than 3 (and therefore lower field strengths) can be responsible for the g-r emission. Therefore, for many of the microwave components, the g-r theory implies unreasonably high magnetic field strengths in the corona.

A different problem arises in interpreting the emission from the brightest ($T_b > 4 \times 10^6$ K) components in each region. Most of these components were associated with reasonably strong photospheric magnetic fields, but not with X-ray emission or sunspot umbrae. For a thermal interpretation of the radio emission, $T_b \leq T_e$. Therefore, a g-r explanation demands very high electron temperatures, low densities ($< 10^8 \text{ cm}^{-3}$) and high coronal field strengths. We speculate on two possible explanations for this emission. High field strengths could be produced in coronal loops with significant currents. But it is difficult to understand why such currents would not also heat the loops sufficiently to emit in X-rays unless they have very low density. Hollweg (1981) recently reviewed mechanisms for producing nonthermal radio emission from runaway electrons in the corona. But 'hot' loops, which were not observed here, and high electric fields are requirements for such *coronal* radio emission. It is possible that such large electric fields are produced in the transition region, where the large temperature gradient and strong magnetic fields can readily accelerate electrons (J. Ionson, private communication). If such an interpretation for the bright, non-sunspot microwave sources is correct, then our observation of numerous, nonvarying bright sources in two undistinguished ARs suggests that continuous acceleration of particles may be common in ARs.

It is possible that we failed to detect small-scale transient or burst activity in these sources. We did not observe such activity within the limitations of our study. For instance, no H α flares were reported in the *Solar Geophysical Data* bulletins in either region on 16 November nor were any detected in H419 on the BBSO film. There were no significant fluctuations observed in soft X-rays between 10:00 and 20:30 UT by the NOAA/GOES satellite at 1–8 Å. There were no changes observed on the six KPNO

magnetograms obtained between 15:43 and 21:00 UT. Finally, no statistically significant time variations in the *integrated* microwave flux were observed during continuous scanning from 15:00–16:45 UT. However, we cannot rule out the possibility of some significant variability in one or more of the bright components. In addition, the spectral characteristics of the radiation useful in distinguishing thermal and nonthermal contributions were unknown.

We find that the presence of strong, longitudinal magnetic fields is not a sufficient condition for bright microwave emission. Although many of the brightest microwave components were associated with regions of strong photospheric fields, there were other regions of apparently strong field that had no bright emission. For example, in AR H 421 single pores and clusters of pores north of the main sunspot had no associated microwave emission. Also, the presence of an isolated magnetic knot north of the central sunspot of AR H 419 was cospatial with bright, flare-like patches in $H\alpha$ and X-rays, but was void of microwave emission. The dependence of g-r emission on the geometry of the magnetic field and the plasma distribution apparently restricts this emission to only a limited number of coronal structures with high magnetic fields.

If the microwave emission at $T_b = 1\text{--}4 \times 10^6$ K is due primarily to the g-r process, we can understand the lack of association between the X-ray emitting structures and the bright centimetric components. High g-r opacity is a function of a strong magnetic field and the angle θ . If the field is too weak, the resonance layer will not be optically thick and no emission will be observed. Since X-ray emitting plasma is confined by the magnetic field in loops and the corona is highly conducting, the internal loop field strength should be low. For instance, the equipartition field strength in typical AR loops is only a few gauss and potential field extrapolations yield values of a few to tens of gauss in some AR loops (e.g., Poletto *et al.*, 1975; Levine and Withbroe, 1977). Although X-ray emission certainly arises from some loops associated with strong field regions (e.g., Webb and Zirin, 1981), most quiescent AR X-ray loops do not terminate in such regions. Therefore, we should not necessarily expect bright centimeter emission from typical AR X-ray loops.

Acknowledgements

The authors are grateful to the following individuals for participating in and providing data for the observations discussed in this paper: J. Harvey of KPNO for the magnetograms, H. Zirin and A. Patterson of BBSO for the optical filtergrams, R. Howard of the Mt. Wilson Observatory for sunspot positions, and P. McIntosh of the NOAA Space Environment Laboratory for an $H\alpha$ image. We thank S. Bichisecci of the AS&E photographic laboratory for his assistance with the imagery used in this study. We benefited from discussions with E. Schmahl, S. Kahler, and A. Krieger. DFW and JMD were supported at AS&E by NASA Contract NAS5-25496. MRK and TV were supported at the University of Maryland by NSF Grant ATM 81-030839, NASA Grant NGR 21-002-199, and NASA Contract NSG 5320.

References

- Alissandrakis, C. E., Kundu, M. R., and Lantos, P.: 1980, *Astron. Astrophys.* **82**, 30.
- Bandeira, R.: 1982, *Astron. Astrophys.* **112**, 52.
- Davis, J. M., Krieger, A. S., Silk, J. K., and Chase, R. C.: 1979, *SPIE* **184**, 96.
- Felli, M., Lang, K. R., and Willson, R. F.: 1981, *Astrophys. J.* **247**, 325.
- Gelfreikh, G. B. and Lubyshv, B. I.: 1979, *Soviet Astron.* **23**, 316.
- Gerassimenko, M., Nolte, J. T., and Petrasso, R. D.: 1976, *Solar Phys.* **48**, 121.
- Hollweg, J. V.: 1981, in F. Q. Orrall (ed.), *Solar Active Regions*, Colorado Associated University Press, Boulder, Colorado.
- Kundu, M. R.: 1965, *Solar Radio Astronomy*, Interscience, New York.
- Kundu, M. R. and Velusamy, T.: 1980, *Astrophys. J.* **240**, L63.
- Kundu, M. R., Alissandrakis, C. E., Bregman, J. D., and Hin, A. C.: 1977, *Astrophys. J.* **213**, 278.
- Kundu, M. R., Schmahl, E. J., and Gerassimenko, M.: 1980, *Astron. Astrophys.* **82**, 265.
- Kundu, M. R., Schmahl, E. J., and Rao, A. P.: 1981, *Astron. Astrophys.* **94**, 72.
- Levine, R. H. and Withbroe, G. L.: 1977, *Solar Phys.* **51**, 83.
- McIntosh, P. S., Krieger, A. S., Nolte, J. T., and Vaiana, G.: 1976, *Solar Phys.* **49**, 57.
- Nicolas, K. R., Kjeldseth-Moe, O., Bartoe, J.-D., and Brueckner, G. E.: 1982, *Solar Phys.* **81**, 253.
- Pallavicini, R., Sakurai, T., and Vaiana, G. S.: 1981, *Astron. Astrophys.* **98**, 316.
- Pallavicini, R., Vaiana, G. S., Tofani, G., and Felli, M.: 1979, *Astrophys. J.* **229**, 375.
- Poletto, G., Vaiana, G. S., Zombeck, M. V., Krieger, A. S., and Timothy, A. F.: 1975, *Solar Phys.* **44**, 83.
- Pye, J. P., Evans, K. D., Hutcheon, R. J., Gerassimenko, M., Davis, J. M., Krieger, A. S., and Vesecky, J. F.: 1978, *Astron. Astrophys.* **65**, 123.
- Schmahl, E. J., Kundu, M. R., Strong, K. T., Bentley, R. D., Smith, J. B., Jr., and Krall, K. R.: 1982, *Solar Phys.* **80**, 233.
- Solar Geophysical Data*, 1980, U.S. Department of Commerce, NOAA, Boulder, Colorado.
- Vaiana, G. S., Krieger, A. S., and Timothy, A. F.: 1973, *Solar Phys.* **32**, 81.
- Webb, D. F.: 1981, in F. Q. Orrall (ed.), *Solar Active Regions*, Colorado Associated University Press, Boulder, Colorado.
- Webb, D. F. and Zirin, H.: 1981, *Solar Phys.* **69**, 99.

4.8 Comparison of Coronal Holes Observed in Soft X-Ray and HeI 10830 Angstrom Spectroheliograms

S.W. Kahler and J.M. Davis

American Science and Engineering, Inc.
Cambridge, Massachusetts 02139

and

J.W. Harvey

Kitt Peak National Observatory
Tucson, Arizona 85726

ORIGINAL PAGE IS
OF POOR QUALITY

COMPARISON OF CORONAL HOLES OBSERVED IN SOFT X-RAY AND HE I 10830 Å SPECTROHELIOGRAMS

S. W. KAHLER and J. M. DAVIS

American Science and Engineering, Inc., Fort Washington, Cambridge, MA 02139, U.S.A.

and

J. W. HARVEY

Kitt Peak National Observatory, Tucson, AZ 85726, U.S.A.*

(Received 31 December, 1982)

Abstract. We compare coronal holes observed in solar soft X-ray images obtained with rocket-borne telescopes during 1974 to 1981 with holes observed on nearly simultaneous 10830 Å maps. Hole boundaries are frequently poorly defined, and after 1974 the brightness contrast between the large scale structure and holes appears substantially diminished in both X-rays and 10830 Å. We find good agreement between soft X-rays and 10830 Å for large area holes but poor agreement for mid and low latitude small area holes, which are generally of low contrast. These results appear inconsistent with the popular view that the quiet corona is sharply separated into open magnetic field regions consisting of coronal holes and closed field regions consisting of the large scale structure.

1. Introduction

Coronal hole research was greatly stimulated by the solar soft X-ray and XUV observations during the Skylab mission in 1973–1974. High resolution images showing coronal holes devoid of coronal emission were available on at least a daily basis and over many solar rotations. The holes were found to be regions of magnetic field open to the interplanetary medium and inferred to be the sources of high speed wind streams. The Skylab results of coronal hole studies were summarized by Zirker (1977).

The end of the Skylab mission stimulated a search for alternative sources of information to identify coronal holes. During the mission a number of full disk spectroheliograms were obtained at Kitt Peak National Observatory in the D₃ line of He I at 5876 Å. A qualitative comparison by Harvey *et al.* (1974) of the KPNO D₃ spectroheliograms with the AS&E soft X-ray images from Skylab showed promising results for detecting coronal holes in the D₃ line. Improved signal-to-noise ratio observations, using He I 10830 Å, became possible at KPNO by the end of the Skylab mission. One such observation was compared with a Skylab He II 304 Å observation by Harvey and Sheeley (1977) and confirmed that a coronal hole was indeed detectable with 10830 Å. However, because routine 10830 Å observations were started just after the Skylab mission, no direct comparisons between the 10830 Å and Skylab soft X-ray data could be made.

* Operated by the Association of Universities for Research in Astronomy, Inc., under contract with the National Science Foundation.

The contrast between coronal holes and the quiet corona viewed in the 10830 Å line is due to the enhanced population in the quiet corona of the triplet state of He I, which absorbs the continuum radiation from below. The physical problem posed by the observations is why the excited 1s2s ground state of the 10830 Å transition should be so abundant when it is 19.7 eV above the ground state in an ion formed at chromospheric temperatures. Helium is unique in this respect since coronal holes cannot be discerned in lines of other abundant elements formed at chromospheric or transition region temperatures (Huber *et al.*, 1974). Goldberg (1939) suggested that an excess of ultra-violet radiation in the 500 Å region could ionize He I from its ground state. This enhanced ionization mechanism, together with the metastability of the 1s2s triplet state, would thus explain the depleted population of singlet levels.

Zirin (1975) found that calculations of a model in which He is photoionized by coronal radiation and then recombines to populate the upper states were in good agreement with line intensity observations. He dismissed attempts to explain the He lines with collisional excitation models, specifically that of Milkey *et al.* (1973), as hopeless. His model as the dominant process for He line formation was soon attacked by Milkey (1975) on the grounds of an incompatibility with the observed line profiles. Shortly afterwards, Shine *et al.* (1975) developed a model of thermal diffusion of He ions into the transition region resulting in an enhanced rate of excitational collisions with high temperature electrons. Although Skylab XUV observations of the center-to-limb variations of He lines by Mango *et al.* (1978) and Glackin *et al.* (1978) suggested collisional excitation of the He I 1s2s triplet state, the question of the primary excitation process still remains unsettled.

For our purposes the important fact is that the presence of the triplet state and consequent 10830 Å absorption in the chromosphere is closely coupled to the presence of overlying hot coronal material. Because of this, the distinction between active regions and the quiet corona is sharp in the 10830 Å images as it is in X-ray images. However, the correspondence between X-ray coronal holes and holes inferred from the 10830 Å maps has been examined only for the 27 June, 1974 X-ray image obtained with an AS&E rocket observation (Harvey and Sheeley, 1979). In that case only one large hole near central meridian was seen, and no detailed comparisons of the 10830 Å and X-ray hole boundaries was made. Since the 10830 Å images are now widely used to infer coronal holes (Sheeley and Harvey, 1981), it is appropriate to compare in detail the coronal holes observed in the X-ray images obtained in the AS&E solar rocket program with those of the corresponding KPNO 10830 Å images.

2. Data Analysis

2.1. INSTRUMENTATION

Since the Skylab period the X-ray Sun has been observed with AS&E grazing incidence telescopes on seven rocket flights. On each flight full disk solar X-ray images were recorded on Kodak SO-212 film using a combination of filters and exposure times.

During this time daily He I 10830 Å spectroheliograms have been recorded continually at KPNO, except for some coverage gaps ranging from several days to several months in extent. A large coverage gap occurred at the time of the 17 November, 1976 flight, so that observation, described by Nolte *et al.* (1977), is not used in this analysis. Each 10830 Å observation was taken during a 40 min period by scanning the Sun in 4 swaths each 512 arc sec wide. Except for 27 June, 1974, the scans were made in the solar east-west direction. Times shown in the figures are the midpoints of the observing periods. Details of the observations are presented in Harvey and Sheeley (1977).

The dates and times of the rocket images are listed in Table I. Two sets of paraboloid-hyperboloid mirrors have been used in the X-ray rocket program. The reflecting surfaces of the older mirrors, used primarily in pre-Skylab observations, are layers of a nickel alloy, Kanigen, deposited on beryllium. The details of that telescope were discussed by Vaiana *et al.* (1968) and Giacconi *et al.* (1969). The newer mirrors, consisting of fused silica (glass), are compared with the Kanigen mirrors in Table 1 of Davis *et al.* (1977).

TABLE I
Rocket X-ray images

| Date | Time (UT) | Mirror | Exposure and filter ^a | Wavelength (Å) |
|----------------|-----------|---------|----------------------------------|--------------------|
| 27 June, 1974 | 19:48 | glass | 59 s pp | 8-39, 44-64 |
| 16 Sept., 1976 | 18:03 | Kanigen | 59 s pp | 3-37, 44-60 |
| 31 Jan., 1978 | 18:41 | glass | 60 s pp | 8-39, 44-64 |
| 7 Nov., 1979 | 20:53 | glass | 3 s Al | 8-100 ^b |
| 16 Nov., 1979 | 17:03 | Kanigen | 3 s Al | 3-100 ^b |
| 13 Feb., 1981 | 19:16 | glass | 45 s pp | 8-39, 44-64 |

^a pp is nominally 1 micron of polypropylene (C₃H₆) coated with 1500 Å of Al plus a 1500 Å Al prefilter. Al is 1500 Å of aluminium without a prefilter.

^b The sensitivity of the photographic emulsion at the long wavelength cut-off is unknown and may well limit the bandpass to shorter wavelengths.

The principal differences between the two sets of mirrors are that the glass mirrors are characterized by a factor of 2.6 larger effective collecting area at 44 Å and by a substantially reduced point spread function.

Variations among the rocket images in mirrors, filters, and exposure times preclude the use of a uniform set of X-ray images for this study. For each flight, the exposure duration and filter of the image judged best for showing coronal holes is listed in the fourth column of Table I. Images obtained through the polypropylene (pp) filter during the Skylab mission (Vaiana *et al.*, 1977) were normally used to study coronal holes. Images were obtained through a similar filter on each rocket flight and are used here except for the two cases shown in Table I where images obtained through an ultra-thin aluminium filter were used. On 7 November, 1979 instrumental scattering from a flare at S 13 E 20 washed out the faint regions in the pp image, while the optimum 16 November, 1979 pp image was blurred from a pointing rotation. The wavelength

passbands at the 1% transmission levels for the chosen filters are given in the last column of the table.

2.2. DETERMINATION OF BOUNDARIES

Using transparencies overlaid on 10830 Å full disk prints, one of us (JWH) traced the apparent boundaries of inferred coronal holes. In some cases the low brightness intensity rendered the identification of the hole questionable, and these boundaries are indicated in the figures by dashed lines. In a similar manner one of us (SWK) traced the boundaries of coronal holes on transparencies overlaid on high contrast X-ray transparencies. These boundaries were first drawn to include all possible hole areas. Shaded regions were used to indicate areas where the existence of an X-ray coronal hole was questionable. These shaded regions encompassed both entire small hole candidates and the diffuse boundaries of well established holes. The high contrast of the X-ray features in and around holes allowed the X-ray hole boundaries to be traced in greater detail than those of the 10830 Å maps. Each set of hole boundaries was independently traced on images with 10.8 cm disk diameters before the comparisons were made. It should be appreciated that this determination of the position of holes and hole boundaries in both the X-ray and 10830 Å data is a subjective process. One can anticipate differences in hole boundaries determined by different observers or by the same observer at different times.

For two dates the daily 10830 Å maps were not obtained, and it was necessary to project hole boundaries from adjacent dates forward or backward in time to compare with the X-ray hole boundaries. Boundaries from the 2 February, 1978 map were projected back to 31 January, 1978, and those of 5 November, 1979 and 9 November, 1979 were projected forward and backward respectively to 7 November, 1979. In each case the Newton–Nunn rotation rates (Allen, 1963) determined the displacements traced with Stonyhurst disks.

The 10830 Å and X-ray images were aligned to within an estimated 10 arc sec by means of the active region features which were bright on the X-ray transparencies and dark on the 10830 Å prints. In the three figures the X-ray and 10830 Å boundaries are superposed for each set of images.

2.3. DETAILED COMPARISONS OF HOLE BOUNDARIES

Large coronal holes show a general correlation in the X-ray and 10830 Å images. The best case is that of 27 June, 1974 shown in Figure 1a. The prominent X-ray hole extends from the north pole to about 25° S in latitude and about 50° in longitude at the equator. The eastern boundaries of the X-ray and 10830 Å holes are in good agreement, but elsewhere the X-ray hole is larger, generally by several heliocentric degrees. A small but distinct neck connecting the polar and equatorial X-ray holes is absent in the 10830 Å image. The brightness contrast between the hole and the background corona is higher in this X-ray image than in the others shown here, but even so, we see that extensive parts of the hole boundaries are indistinct as indicated by shaded areas in Figure 1a.

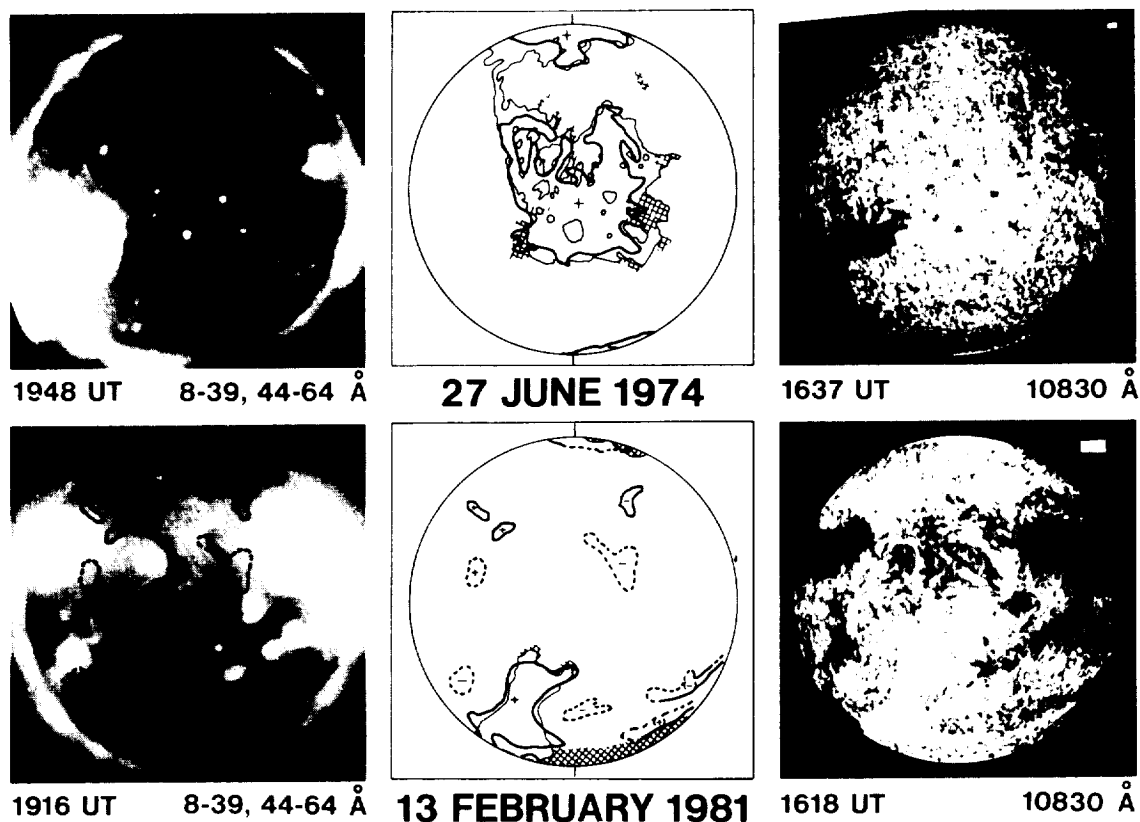


Fig. 1. *Top:* The comparison of the aligned X-ray and 10830 Å images and coronal hole boundaries for 27 June, 1974. The 10830 Å boundaries are shown in the middle panel by heavy lines, the X-ray boundaries by light lines. Hatched areas indicate uncertain X-ray holes. The north and south poles are indicated by the vertical marks on the limbs in the middle panel. *Bottom:* The same for 13 February, 1981. The heavy dotted lines are uncertain boundaries of 10830 Å holes. The 10830 Å boundaries are projected on the X-ray image.

X-ray and 10830 Å boundaries of the large polar holes observed on 13 February, 1981 (Figure 1) and 31 January, 1978 and 7 November, 1979, shown in Figure 2, also agree well to first order. The best agreement in detail is that of 13 February, 1981, but that is the only one of the three dates for which simultaneous X-ray and 10830 Å data exist.

The worst agreement between hole boundaries appears in the mid and low latitude small holes of 13 February, 1981 (Figure 1) and 7 November, 1979 (Figure 2). In the first case no evidence of the five northern latitude holes appears in the X-ray image. Similarly, there is no X-ray analog of the negative polarity hole in the southeast, but the east-west 10830 Å holes near the south pole do correspond to regions of decreased X-ray brightness. However, these latter features appear to be empty filament channels (McIntosh *et al.*, 1976), rather than holes, when compared to H α synoptic maps published in *Solar-Geophysical Data*.

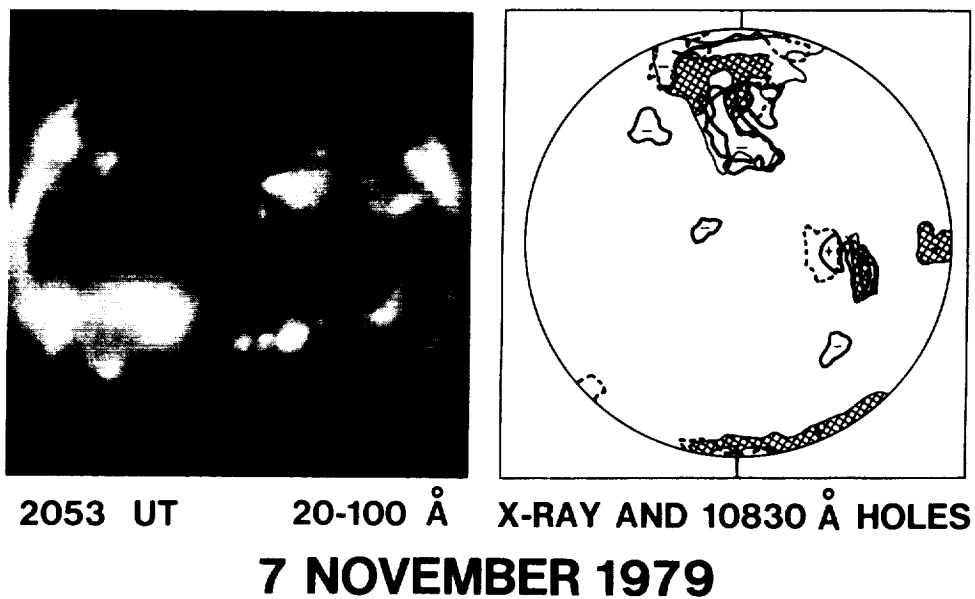
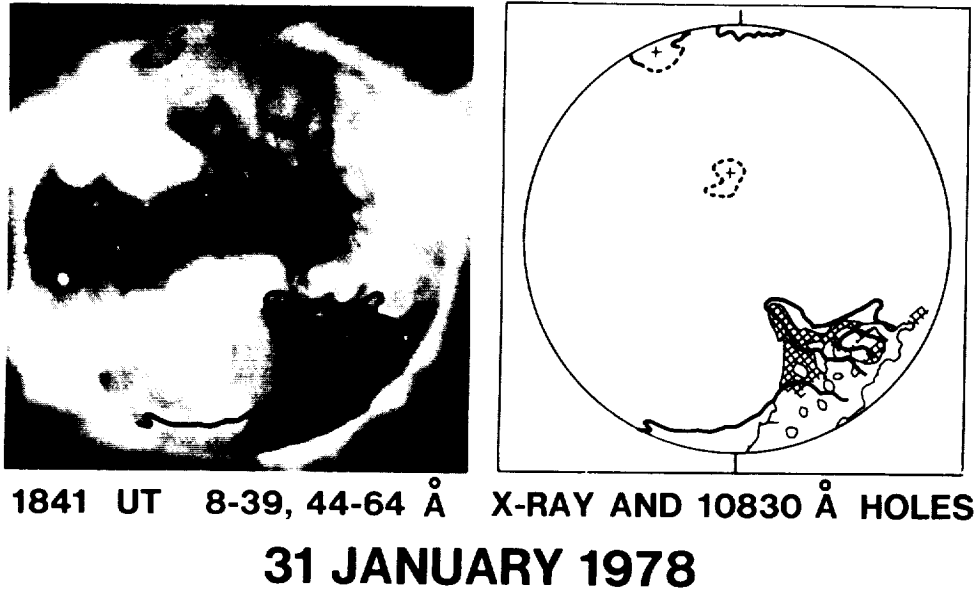


Fig. 2. *Top*: The X-ray image and comparison of X-ray and 10830 Å coronal hole boundaries for 31 January, 1978. The 10830 Å boundaries are projected back in time from the 17:29 UT image of 2 February, 1978 using the Newton–Nunn differential rotation rate. The 10830 Å hole boundaries are projected on the X-ray image. *Bottom*: The same for 7 November, 1979. The 10830 Å hole boundaries have been projected forward from the 18:25 UT image of 5 November, 1979 and backward from the 17:32 UT image of 9 November, 1979 using the Newton–Nunn rotation rate. Both sets of boundaries are shown.

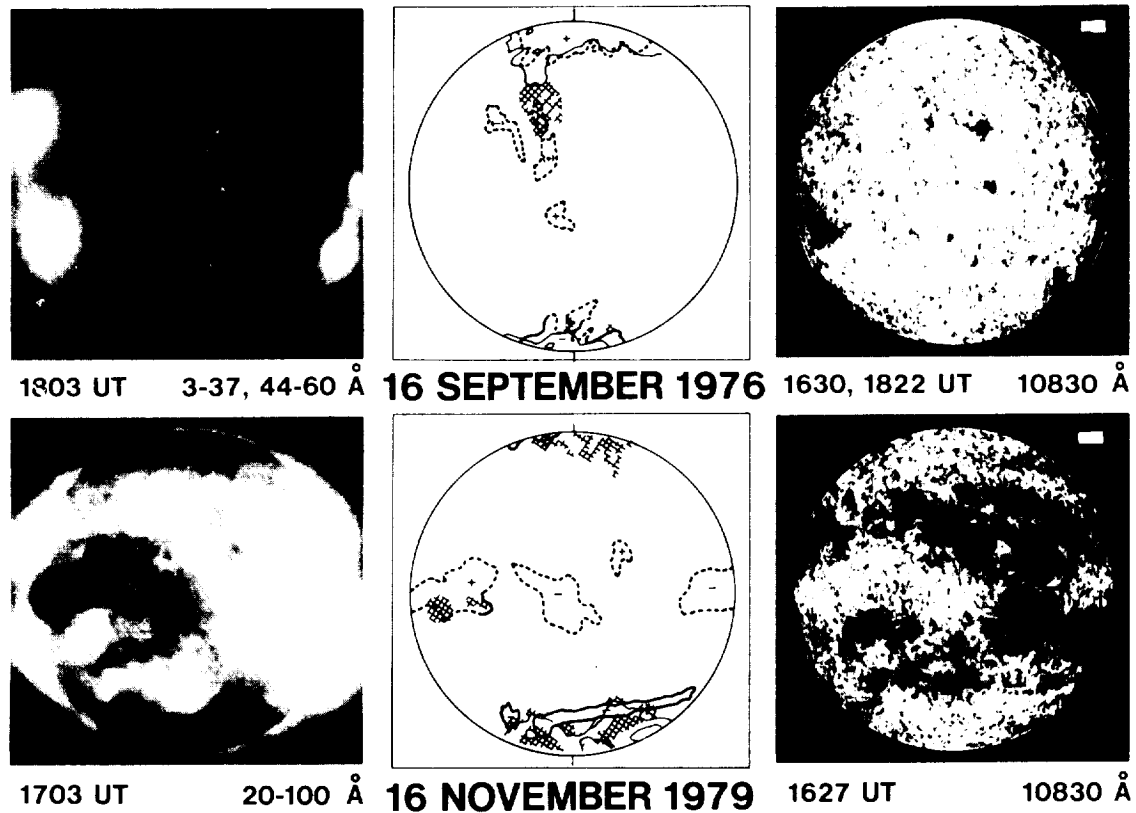


Fig. 3. The same as Figure 1 for 16 September, 1976 (*top*) and 16 November, 1979 (*bottom*). The 16 November, 1979 image is a composite of two images at the times shown.

The 7 November, 1979 comparison is compromised by the lack of simultaneous data, but here again, four small 10830 \AA holes within 40° of central meridian are not associated with obvious holes in the X-ray image, although they do lie in regions of relatively low emission. In addition, an X-ray hole on the equator at the west limb was not associated with a 10830 \AA hole.

To a lesser degree the data of Figure 3 also illustrate the poor correspondence of the mid and low latitude holes. The four such holes observed in 10830 \AA on 16 September, 1976 are all faint and uncertain, as indicated by the dashed lines, and while they correspond to regions of low X-ray brightness, other regions of the X-ray corona are of comparable or lesser brightness. This X-ray image was obtained near solar minimum and shows a generally faint corona. The 16 November, 1979 X-ray image reflects a more active Sun, and here again the uncertain 10830 \AA hole boundaries correspond only roughly to regions of low X-ray brightness. Only two small, doubtful regions appeared as low latitude X-ray holes in that image. The region of 10830 \AA emission elongated in the east-west direction at $S 40^\circ$ is a filament channel seen in the H α synoptic charts of *Solar-Geophysical Data*.

One might expect to detect polar holes more easily in 10830 Å than in X-rays as a result of the obscuration of X-ray polar holes by adjacent bright coronal features such as loop arcades (McIntosh *et al.*, 1976). This does appear to be the case in the 31 January, 1978 north and south polar holes (Figure 2), but in general the X-ray holes appear larger at the poles than do the 10830 Å holes. The best example of this is the 27 June, 1974 north polar hole in which the X-ray eastern boundary is substantially farther from the pole than is that of the 10830 Å boundary. The X-ray polar hole is also substantially larger than the 10830 Å hole in those cases where we consider the hatched (uncertain) area of the X-ray hole. The south pole of 13 February, 1981, the north pole of 16 September, 1976, and both poles of 7 and 16 November, 1979 all illustrate this result.

3. Discussion

The Skylab X-ray images have formed the observational basis for the implicit assumption that coronal hole (CH) boundaries are sharp and well defined. Bohlin (1977) has briefly discussed the displacement of apparent hole boundaries due to foreground coronal emission, and Nolte *et al.* (1976) pointed out the occasional presence of faintly emitting X-ray regions within or near the hole boundaries which rendered those boundaries uncertain, but otherwise no indication of ambiguity in hole boundaries is found in the literature. In fact, in their quantitative Skylab X-ray study of CH1, Maxson and Vaiana (1977) concluded that the transition from coronal hole to large scale structure is sharp. However, they offered no quantitative definition of 'sharp', and both their contour plots of the boundaries and histograms of photographic density in and around hole areas suggest that the uncertainties in hole areas are large fractions of the areas themselves. Thus, past studies provide no support for the usual assumption that coronal hole boundaries are well defined.

The contrast between the X-ray brightness of the large coronal hole and that of the large scale structure in the 27 June, 1974 image (Figure 1) appears comparable to that of the Skylab images (cf. Zirker, 1977). This contrast appears considerably diminished in the X-ray images of later dates as shown in the figures. Without a quantitative photometric analysis of the X-ray holes and large-scale structures of these images, a definitive statement about possible brightness changes can not be made. However, this apparent decrease in X-ray contrast is accompanied by a comparable contrast decrease in the 10830 Å data, as indicated by the dashed 10830 Å hole boundaries in the figures. It therefore appears that non-polar holes appearing near solar minimum and during the rise phase of the current cycle are not so clearly discerned from the large scale structure as was the case during the declining phase in 1973–1974. This result, coupled with the observation that the hole boundaries are often diffuse, implies that drawing hole boundaries with either X-ray or 10830 Å data is a far more subjective process than previously believed.

Even with the above caveats, we have found a good correlation between the X-ray and 10830 Å data for the presence of large area coronal holes. In two cases (31 January,

1978 and 13 February, 1981) the large holes were at the south pole and in the other at the equator (27 June, 1974). Since the 10830 Å data allows one to infer holes at the chromospheric level, and intervening coronal emission renders polar holes less visible in X-rays, we might expect that these holes would be larger in the 10830 Å data. Evidence of this effect can be seen in the 31 January, 1978 polar hole, but it is not the rule. The dominant X-ray polar hole is distinctly larger than the corresponding 10830 Å hole on 27 June, 1974, 7 and 16 November, 1979, and 13 February, 1981, although in the last three cases the excess X-ray hole areas are uncertain as indicated by hatched areas.

We have found the worst agreement between the X-ray and 10830 Å holes at low and mid latitudes. For the period 1976 to 1981, these holes, generally seen in the 10830 Å data as weak holes, were small in diameter (10–20 solar degrees) and usually did not correspond to obvious X-ray holes. In the cases of 16 November, 1979 and 13 February, 1981 there are weak holes well away from central meridian, so the poor agreement with X-ray holes could be due to projection effects of foreground coronal material. However, all the 10830 Å maps except that of 27 June, 1974 have weak holes near central meridian with poor agreement in X-rays, so this effect is not due to projection problems.

Weak 10830 Å holes were reported by Sheeley and Harvey (1981) and appeared most often in their Bartels display during 1976–1977. They also found that the correlation between coronal holes and solar wind streams established during the Skylab period (cf. Zirker, 1977) degraded since 1976. Some recurrent holes had no observed associated wind streams, and in other cases the recurrent streams had lower peak velocities than those of Skylab. Nolte *et al.* (1977) had also found similar results using the 1976 rocket X-ray images. The role of the weak holes in the deterioration of the wind stream correlation is unclear. Most of the Sheeley and Harvey recurrent holes, confined to $\pm 40^\circ$ latitude, were well defined, whereas in this study the low and mid latitude holes are mostly weak. On the other hand, some of the well defined holes of the Sheeley and Harvey study may well correspond to the weak holes of this study.

On the basis of the Skylab X-ray images Maxson and Vaiana (1977) have claimed that the quiet solar corona is sharply separated into two different components – the open magnetic field regions associated with coronal holes and closed field regions associated with the large scale structure. The existence of low contrast holes and indistinct hole boundaries in both the 10830 Å and X-ray images of this study is difficult to understand in the context of this two component description. These results suggest the presence of regions where closed and open field lines may be mixed. Evidence for this more complex picture was presented by Levine *et al.* (1977) based on a comparison of a harmonic analysis of the solar magnetic field with the Skylab X-ray pictures. They found evidence that the formation of open field regions preceded the occurrence of coronal holes by as much as a solar rotation. They also concluded that closed magnetic fields occupied a significant part of the area of coronal holes. More recently, Levine (1982) has presented examples of apparently open magnetic structures which cannot be identified unambiguously in He I 10830 Å spectroheliograms. Their results and ours suggest that the magnetic field in the quiet corona is complex in a way that is not yet understood.

Acknowledgements

We are pleased to acknowledge many helpful discussions with D. F. Webb and the assistance of M. Rizza in the preparation of the photographic evidence. Support for the study at AS&E was provided by NASA under contracts NASW-3586 and NAS5-25496.

References

- Allen, C. W.: 1963, *Astrophysical Quantities*, Athlone Press, London, p. 179.
- Bohlin, J. D.: 1977, in J. B. Zirker (ed.) *Coronal Holes and High Speed Wind Streams*, Colorado Associated University Press, Boulder, p. 27.
- Davis, J. M., Golub, L., and Krieger, A. S.: 1977, *Astrophys. J.* **214**, L141.
- Giacconi, R., Reidy, W. P., Vaiana, G. S., Van Speybroeck, L. P., and Zehnpfennig, T. F.: 1969, *Space Sci. Rev.* **9**, 3.
- Glackin, D. L., Linsky, J. L., Mango, S. A., and Bohlin, J. D.: 1978, *Astrophys. J.* **222**, 707.
- Goldberg, L.: 1939, *Astrophys. J.* **89**, 673.
- Harvey, J. W. and Sheeley, N. R., Jr.: 1977, *Solar Phys.* **54**, 343.
- Harvey, J. W. and Sheeley, N. R., Jr.: 1979, *Space Sci. Rev.* **23**, 139.
- Harvey, J., Krieger, A. S., Timothy, A. F., and Vaiana, G. S.: 1974, *Osserv. Mem. Oss. Arcetri* **104**, 50.
- Huber, M. C. E., Foukal, P. V., Noyes, R. W., Reeves, E. M., Schmahl, E. J., Timothy, J. G., Vernazza, J. E., and Withbroe, G. L.: 1974, *Astrophys. J.* **194**, L115.
- Levine, R. H.: 1982, *Solar Phys.* **79**, 203.
- Levine, R. H., Altschuler, M. D., Harvey, J. W., and Jackson, B. V.: 1977, *Astrophys. J.* **215**, 636.
- Mango, S. A., Bohlin, J. D., Glackin, D. L., and Linsky, J. L.: 1978, *Astrophys. J.* **220**, 683.
- Maxson, C. W. and Vaiana, G. S.: 1977, *Astrophys. J.* **215**, 919.
- McIntosh, P. S., Krieger, A. S., Nolte, J. T., and Vaiana, G.: 1976, *Solar Phys.* **49**, 57.
- Milkey, R. W.: 1975, *Astrophys. J.* **199**, L131.
- Milkey, R. W., Heasley, J. N., and Beebe, H. A.: 1973, *Astrophys. J.* **186**, 1043.
- Nolte, J. T., Krieger, A. S., Timothy, A. F., Vaiana, G. S., and Zombeck, M. V.: 1976, *Solar Phys.* **46**, 291.
- Nolte, J. T., Davis, J. M., Gerassimenko, M., Lazarus, A., and Sullivan, J. D.: 1977, *Geophys. Res. Letters* **4**, 291.
- Sheeley, N. R., Jr. and Harvey, J. W.: 1981, *Solar Phys.* **70**, 237.
- Shine, R., Gerola, H., and Linsky, J. L.: 1975, *Astrophys. J.* **202**, L101.
- Vaiana, G. S., Reidy, W. P., Zehnpfennig, T., Van Speybroeck, L., and Giacconi, R.: 1968, *Science* **161**, 564.
- Vaiana, G. S., Van Speybroeck, L., Zombeck, M. V., Krieger, A. S., Silk, J. K., and Timothy, A.: 1977, *Space Sci. Instr.* **3**, 19.
- Zirin, H.: 1975, *Astrophys. J.* **199**, L63.
- Zirker, J. B. (ed.): 1977, *Coronal Holes and High-Speed Wind Streams*, Colorado Associated University Press, Boulder.

4.9 X-Ray Bright Points and the Sunspot Cycle: Further Results and Predictions

John M. Davis

American Science and Engineering, Inc.
Cambridge, Massachusetts 02139

ORIGINAL PAGE IS
OF POOR QUALITY

X-RAY BRIGHT POINTS AND THE SUNSPOT CYCLE: FURTHER RESULTS AND PREDICTIONS

JOHN M. DAVIS

American Science and Engineering, Inc., Fort Washington, Cambridge, MA 02139, U.S.A.

(Received 28 January; accepted 26 April, 1983)

Abstract. X-ray images obtained during two rocket flights near the maximum of sunspot cycle 21 now allow the study of the variation of X-ray bright point number over an eleven-year period covering the maxima of the last two cycles. The new data are consistent with the earlier conclusion that the temporal variation of bright point and sunspot number are out of phase. The quantities are related through a power law with a negative exponent of $2/3$.

1. Introduction

The current interest in solar variability and the solar terrestrial connection has focused attention on the Sun's magnetic activity cycle both as a source for, and as a baseline against which the variability of other phenomena can be compared. Recent studies have been wide ranging and have included the variation of the total UV flux (Cook *et al.*, 1980; Torr *et al.*, 1980), the large scale coronal structure and the solar wind (Sheeley and Harvey, 1978, 1981) and the polar solar wind (Coles *et al.*, 1980). Our efforts have been directed at understanding the behavior of regions of small scale flux emergence known as coronal or X-ray bright points (XBP). Their interest lies both in their direct relation to the solar magnetic field and in their identification as a possible source for the solar wind (Akasofu, 1983; Davis and Krieger, 1982; Mullan and Ahmad, 1982; Pneuman, 1983).

It will be remembered that bright points appear as small emission features in soft X-ray spectroheliograms. Comparison with photospheric magnetograms (Golub *et al.*, 1977) has revealed their bipolar nature and thus their similarity to ephemeral active regions (Harvey and Martin, 1973). However both this and a more recent study (Tang *et al.*, 1983) have indicated the lack of a one-to-one correspondence between bright points and ephemeral regions. For although all bright points can be directly associated with a magnetic bipole, the reverse is not true. The particular characteristics which distinguish those magnetic bipoles which are also coronal bright points from the general class of ephemeral regions remain unclear.

Davis *et al.* (1977) and Golub *et al.* (1979) have shown that the frequency of occurrence of coronal bright points is periodic and varies out of phase with sunspot number. The phase difference is close to 180° , i.e., the two quantities appear to be anticorrelated. This result was based upon X-ray observations made during the Skylab mission and during six sounding rocket flights covering the period 1970–1978. The Skylab data covering a six-month period in 1973, provided a continuous set of observations against which the single data points obtained during each rocket flight can be

judged. Results are now available from two further rocket flights, launched on 16 November, 1979 and 13 February, 1981, respectively, during the maximum phase of sunspot cycle 21. The addition of these two points to the data set extends the coverage to an eleven-year period containing the maxima of cycles 20 and 21.

2. Results and Discussion

Representative images from the two flights are shown in Figure 1. Inspection shows that there are few coronal bright points and that the background corona appears brighter than found in images taken at other times of the sunspot cycle. The increased background emission is important because of the problem of obscuration (Golub *et al.*, 1976). This governs the difference in visibility of a small feature when viewed against a background of either the weakly emitting, large scale structure or the essentially emissionless background of a coronal hole. To eliminate this difference the standard procedure for counting bright points uses short exposures where the background is at or below the threshold of detection. Although this lowers the number of bright points that are observed, it removes the bias between regions containing different structures. For the Skylab data a 4 s exposure was used.

7 NOVEMBER 1979



13 FEBRUARY 1981



Fig. 1. Full-disk X-ray images recorded on 16 November, 1979 and 13 February, 1981.

The relevant instrumental parameters for the two rocket experiments are collected in Table I. On each flight nominal exposure times of 1, 3, 9, and 27 s are available. To normalize the rocket data the bright points were counted on exposures where the product of the relative efficiency and exposure time approximates 4 s. The relative efficiency is defined as the product of the filter and prefilter transmissions and the mirror's effective collecting area at 44 Å. For these two flights 9 and 3 s images were

selected and the values listed in Table I are the actual exposure times measured from the telemetry record.

Although an understanding of the origin of the increased background is not essential to this study, it is useful in providing a quantitative estimate for the obscuration correction. Analysis suggests that the background arises from the presence of extended, low density loops associated with, and having temperatures typical of, active regions. This conclusion is based upon interpretation of the images and a preliminary analysis of coronal spectra recorded during the second of the two flights. The spectra came from a 1 arc min^2 field centered at S03 W42. The field was located between three active regions and contained emission only from the large-scale structure. A line ratio analysis of various hydrogen-like and helium-like ions leads to a plasma temperature of $2.5 \times 10^6 \text{ K}$. This is above the range of 1.5 to $2.1 \times 10^6 \text{ K}$ previously reported for the quiet Sun (Withbroe, 1975; Maxson and Vaiana, 1977; Mariska and Withbroe, 1978) and which has at other phases of the sunspot cycle formed the background against which the earlier bright point counts were made.

For X-ray telescopes the power emitted by a plasma in the temperature range 1 to $6 \times 10^6 \text{ K}$, integrated over all wavelengths, reaching the focal plane is proportional to the second power of the electron temperature (see Vaiana *et al.*, 1977, Figure 32). Thus an increase in coronal temperature from 2.0 to $2.5 \times 10^6 \text{ K}$ will raise the detected emission by a factor of 1.5 . That is, the background on a 4 s exposure from the rocket flights at solar maximum should be comparable to that on a 6 s exposure from the earlier period. This is found to be the case, and although this analysis is almost certainly an oversimplification, it has been used as the basis for correcting the data for the increased obscuration. The approach can be justified by noting that the temperature of the large-scale structure is likely to vary over the solar surface and will almost certainly be lower outside the active region zone. Thus the correction factor should be conservative. However one might also expect an accompanying increase in the amount of material at these temperatures with the increased background arising from a combination of both these factors. The increase in density of the large-scale structure must be rather modest for the emission measure, estimated from the spectrometer data, is not inconsistent with the results of Maxson and Vaiana (1977). Thus the higher temperature appears to make the dominant contribution to the increased background and applying the correction factor of 1.5 to the observations from the whole disk is more likely to cause the number of bright points to be over- rather than underestimated.

On balance the factor of 1.5 is believed to be a reasonable correction for the increased obscuration. Using this value the corresponding decrease in bright point visibility is approximately 30% (see Golub *et al.*, 1976, Figure 1). Therefore the measured values have been increased accordingly by a factor of 1.3 . A final correction was applied to compensate for the fraction of the observable disk occupied by active regions at the time of the observations and which were therefore excluded from the area in which bright points were counted. The data are summarized in Table I.

The variation with time over sunspot cycles 20 and 21 of the corrected bright point counts is shown in Figure 2 where they are compared with the yearly averaged sunspot

TABLE I
Instrumental characteristics and bright point statistics

| Date | Relative efficiency at 44 Å | Exposure (s) | $N_{\text{mens.}}$ | Active region correction | $N_{\text{corrected}}$ |
|---------------|-----------------------------|--------------|--------------------|--------------------------|------------------------|
| 16 Nov., 1979 | 0.433 | 8.94 | 9 | 1.16 | 13.6 ± 3.5 |
| 13 Feb., 1981 | 1.233 | 2.84 | 7 | 1.27 | 11.6 ± 3.4 |

number. The new data provide additional support to our previous conclusion that the temporal variation of large and small scale flux emergence is out-of-phase. Both sets of measurements have been normalized to their greatest values which occur for sunspots at the maximum of cycle 21 and for bright points at the minimum between the two cycles. It is possible that this presentation overemphasizes the single peak in the bright point data and the absolute amplitude of the bright point curve should be viewed with this in mind since we do not yet know whether the magnitude of the peak is typical of bright point behavior.

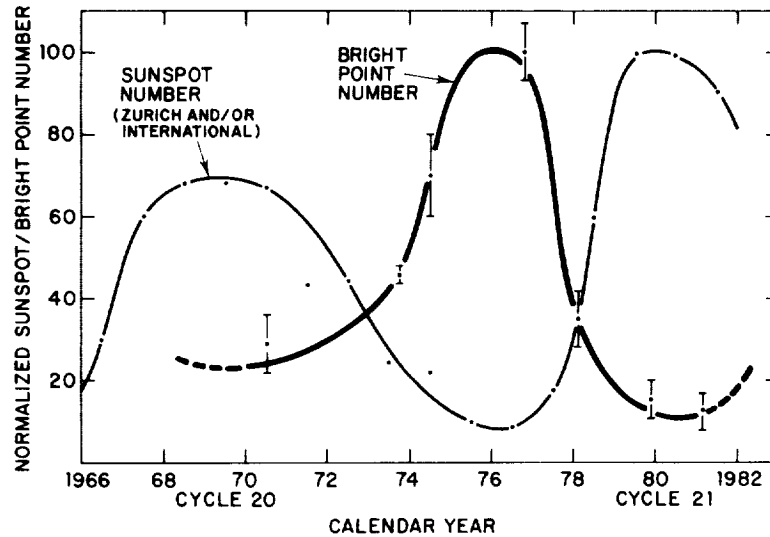


Fig. 2. Variation of the number of X-ray bright points over sunspot cycles 20 and 21.

To test for interdependence between these indicators of large and small scale flux emergence we have compared the corrected bright point counts with the weekly average sunspot number, centered on the day of the bright point observation (Figure 3). A weekly sunspot average was used to provide a measure of global, rather than local activity. The data fit a power law of the form

$$N_{\text{XBP}} = 421.1 N_{\text{SS}}^{-0.662}.$$

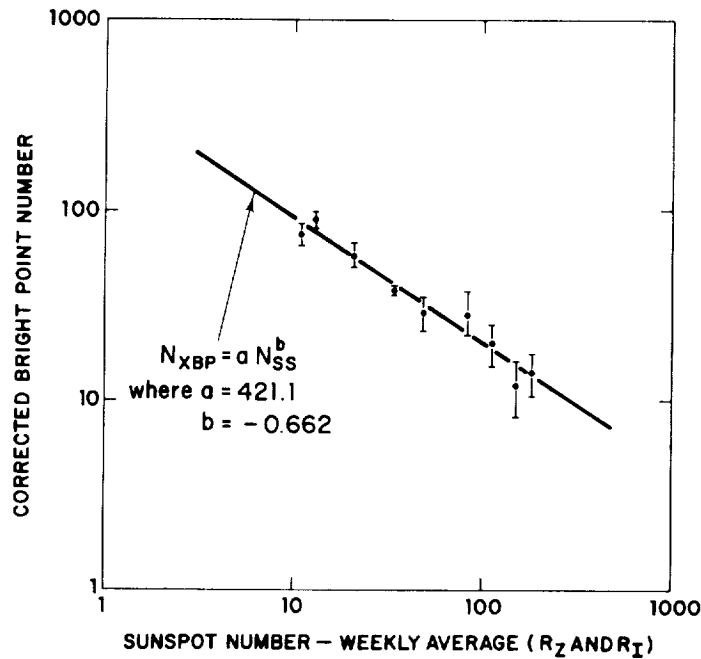


Fig. 3. The dependence of the number of bright points on the weekly average sunspot number.

The reduced χ^2 for the fitted curve is 0.9 and $P(\chi^2)$ is 0.5 indicating an acceptable fit to the data. The fact that the data points are from two sunspot cycles suggest that this relation could be used successfully as a first order predictor of future bright point behavior.

The anticorrelation of the small and large-scale components of the emerging flux spectrum has been interpreted as evidence of a constant pattern of flux emergence over a solar cycle (Golub *et al.*, 1979). This hypothesis has been questioned (Bonnet, 1981) in light of the result of Howard and LaBonte (1981) who find that considerably more flux is emerging during cycle 21, than emerged during cycle 20. However, the constant flux hypothesis was based on the observations over a single cycle, for which the result is still valid. It did not exclude inter-cycle variations in the total flux emergence. However, bright point data now exist from the maximum phase of two cycles. The comparison of these data show that the bright point minimum at the maximum of cycle 21 falls approximately a factor of 2 below the value at the previous maximum. Interpretation of this result in terms of the power law relationship suggests that the higher level of small scale flux at the cycle 20 maximum is compensating for the lower level of large scale flux and vice versa at the maximum of cycle 21.

The implication of this result is that the amplitude of the bright point maximum at the next solar minimum will depend more on the depth of the sunspot minimum than on the difference in the total flux between cycle 20 and 21. Since the 1976 minimum was not deep by historical standards, the observed numbers being over twice the mean of

cycles 8–20, the possibility exists for even more dramatic XBP increases at future solar minima.

Finally, many aspects of the behavior of XBP remain enigmatic. The reason for the lack of correspondence, for instance, between the temporal behavior of bright points and ephemeral regions, which do not appear to show the dramatic out-of-phase variation with sunspots (Martin and Harvey, 1979), is still not known. All studies have shown that ephemeral regions are more numerous than bright points but no study has yet elucidated the particular characteristics which distinguish the two phenomena. We support the conclusion of Tang *et al.* (1983) that joint simultaneous, high spatial resolution, observations (soft X-ray and magnetograms) of several days duration are necessary to resolve this problem and suggest that the observation period provided by a space shuttle flight, scheduled late in the declining phase of the current cycle, would be ideal for this test.

Acknowledgement

This work has been supported by NASA under contract NAS5–25496.

References

- Akasofu, S.-I.: 1983, *Solar Wind Five* (in press).
 Bonnet, R. M.: 1981, *Solar Phys.* **74**, 485.
 Coles, W. A., Rickett, B. J., Rumsey, V. H., Kaufman, J. J., Turley, D. G., Ananthakrishnan, S., Armstrong, J. W., Harmons, J. K., Scott, S. L., and Sime, D. G.: 1980, *Nature* **286**, 239.
 Cook, J. W., Brueckner, G. E., and Van Hoosier, M. E.: 1980, *J. Geophys. Res.* **85**, 2257.
 Davis, J. M., Golub, L., and Krieger, A. S.: 1977, *Astrophys. J.* **214**, L141.
 Davis, J. M. and Krieger, A. S.: 1982, *Fifth International Symposium on Solar Terrestrial Physics*, COSPAR XXIV, Ottawa, Canada, p. 25.
 Golub, L., Krieger, A. S., and Vaiana, G. S.: 1976, *Solar Phys.* **50**, 311.
 Golub, L., Krieger, A. S., Vaiana, G. S., and Harvey, J. W.: 1977, *Solar Phys.* **53**, 111.
 Golub, L., Davis, J. M., and Krieger, A. S.: 1979, *Astrophys. J.* **229**, L145.
 Harvey, K. L. and Martin, S. F.: 1973, *Solar Phys.* **32**, 389.
 Howard, R. and LaBonte, B. J.: 1981, *Solar Phys.* **74**, 131.
 Mariska, J. T. and Withbroe, G. L.: 1978, *Solar Phys.* **60**, 67.
 Martin, S. F. and Harvey, K. L.: 1979, *Solar Phys.* **64**, 93.
 Maxson, C. W. and Vaiana, G. S.: 1977, *Astrophys. J.* **215**, 919.
 Mullan, D. J. and Ahmad, I. A.: 1982, *Solar Phys.* **75**, 347.
 Pneuman, G. W.: 1983, *Astrophys. J.* **265**, 468.
 Sheeley, Jr., N. R. and Harvey, J. W.: 1978, *Solar Phys.* **59**, 159.
 Sheeley, Jr., N. R. and Harvey, J. W.: 1981, *Solar Phys.* **70**, 237.
 Torr, M. R., Torr, D. G., and Hinteregger, H. E.: 1980, *J. Geophys. Res.* **85**, 6063.
 Tang, F., Harvey, K., Bruner, M., Kent, B., and Antonucci, E.: 1983, *Adv. Space Res.* **2**, No. 11, 65.
 Vaiana, G. S., Van Speybroeck, L., Zombeck, M. V., Krieger, A. S., Silk, J. K., and Timothy, A.: 1977, *Space Sci. Instr.* **3**, 19.
 Withbroe, G. L.: 1975, *Solar Phys.* **45**, 301.

4.10 Observations of the Reappearance of Polar Coronal Holes and the Reversal
of the Polar Magnetic Field

D.F. Webb and J.M. Davis

American Science and Engineering, Inc.
Cambridge, Massachusetts 02139

and

P.S. McIntosh

Space Environment Laboratory
National Oceanic and Atmospheric Administration
Boulder, Colorado 80303

ORIGINAL PAGE IS
OF POOR QUALITY

—

OBSERVATIONS OF THE REAPPEARANCE OF POLAR CORONAL HOLES AND THE REVERSAL OF THE POLAR MAGNETIC FIELD

D. F. WEBB and J. M. DAVIS

American Science and Engineering, Inc., Cambridge, MA 02139, U.S.A.

and

P. S. McINTOSH

*Space Environment Laboratory, National Oceanic and Atmospheric Administration,
Boulder, CO 80303, U.S.A.*

(Received 28 September, 1983; in revised form 9 January, 1984)

Abstract. We examine observations relating to the evolution of the polar magnetic field around sunspot maximum, when the net polar flux reverses polarity and coronal holes redevelop around the poles. Coronal hole observations during the last two solar maxima are examined in detail. Long-term averages of the latitudinal dependence of the photospheric magnetic field and the evolutionary pattern of the polar crown filaments are used to trace the poleward motion of the reversal of the large-scale surface field, and are compared to the redevelopment of the polar holes. The polar holes evolve from small, mid-latitude holes of new-cycle polarity which expand poleward until they join and cover the pole. We find that the appearance of these mid-latitude holes, the peak of flux emergence at low latitudes, and the polar polarity reversal all occur within a few solar rotations. Lagging 6 months to $1\frac{1}{2}$ yr after this time, the polar crown disappears and the polar holes redevelop.

These results are examined in the context of phenomenological models of the solar cycle. We believe the following results in particular must be accounted for in successful models of the solar cycle: (1) The process of polarity reversal and redevelopment of the polar holes is discontinuous, occurring in 2 or 3 longitude bands, with surges of flux of old-cycle polarity interrupting the poleward migration of new-cycle flux. There is a persistent asymmetry in these processes between the two hemispheres; the polarity reversal in the two hemispheres is offset by 6 months to $1\frac{1}{2}$ yr. (2) Contrary to the Babcock hypothesis, the polar crown disappears months *after* the magnetic polar reversal. We suggest one possible scenario to explain this effect. (3) Our observations support suggestions of a poleward meridional flow around solar maximum that cannot be accounted for by Leighton-type diffusion.

1. Introduction

The simplest description of the solar magnetic field is as a dipole oriented along the rotation axis with radial, unipolar fields at the poles. These polar fields are strongest and of maximum area at solar minimum. Because coronal holes form in regions where the large-scale field is unipolar, we expect the poles to be covered by holes at solar minimum and this has been consistently observed (Waldmeier, 1981; Sheeley, 1980; Nolte *et al.*, 1977).

Recent phenomenological concepts of the formation and development of coronal holes (e.g., Bohlin and Sheeley, 1978; Hundhausen, 1977) have generally invoked the ideas originally outlined by Babcock (1961) and Leighton (1964) for the explanation of the solar cycle. The Babcock and Leighton models are qualitative descriptions of the evolution of surface magnetic fields placed in the context of a dynamo theory. In these

models a weak initial poloidal field is amplified by the solar differential rotation to form a strong toroidal field. This field rises to the surface by magnetic buoyancy where it forms bipolar magnetic regions (BMRs). The BMRs are dispersed by random walk diffusion which preferentially directs the following polarity fields poleward. During this period cyclonic convection, acting on the toroidal field, produces a toroidal current and an associated poloidal field of reverse polarity to the initial field. Eventually this new poloidal field becomes dominant and the cycle reverses. Models based on these ideas are called kinematic, or $\alpha - \omega$ dynamos (e.g., Stix, 1981). However their basic assumptions are not universally accepted and models called oscillator theories exist which are based on the existence of a deep-seated, primordial field (e.g., Layzer *et al.*, 1979). These models are generally not as well developed, mathematically, as the kinematic dynamos.

Obviously the period of the reversal of the polar fields contains information which must be explained by any successful theory. In this study we examine new observations relating to the evolution of the high latitude and polar magnetic field around solar maximum to provide a firm observational context for the development of solar cycle models. For this purpose we will derive the relative timing near the maxima of solar cycles 20 and 21 of five specific events in each solar hemisphere. These are the peak of the sunspot number, the magnetic polarity reversal above 70° latitude, the disappearance of the polar crown of filaments, the first appearance of a small, mid-latitude coronal hole(s) of new-cycle polarity, and the earliest coverage of the pole by a hole. It will be shown that the data set allows each of these events to be determined within a few solar rotations.

The data set emphasizes high spatial resolution synoptic coronal observations which were not previously available. Coronal hole studies have shown an intimate spatial relationship between coronal holes and large-scale unipolar areas; therefore, we expect the development of high-latitude and polar coronal holes to provide insight into the process of the polarity reversal of the polar fields. Sufficient synoptic data have now been accumulated to permit the study of two consecutive cycles of polar hole development around sunspot maximum.

Hundhausen *et al.* (1981, hereafter HHH) and Broussard *et al.* (1978) have shown that 'mid-latitude' holes (those centered at latitudes roughly between 20 and 60°) were a feature of the corona during the maximum of cycle 20. In Section 2 we describe the high-latitude evolution of coronal holes around the maxima of cycles 20 and 21, and show that one of the characteristics of this evolution was the areal increase and poleward growth of particular mid-latitude holes of new-cycle polarity, to eventually cover the poles. In Section 3 we describe the evolution of the high-latitude magnetic field using observations of the migration of the polarity reversal of the photospheric field and of the migration and dissolution of the polar crown. In Section 4 we summarize our results with the goal of guiding the development of future models of the solar cycle.

2. High-Latitude Coronal Hole Evolution around Sunspot Maximum

The coronal data used for this study included AS & E X-ray rocket images, Harvard OSO-6 Mg X maps for cycle 20, eclipse data on 7 March, 1970, synoptic High Altitude Observatory (HAO) white light K -coronameter charts for cycle 20, and synoptic He I -10830 Å coronal hole boundaries for cycle 21. Various formats of H α synoptic charts from the NOAA Space Environment Laboratory were used to trace the poleward migration of filaments and of the large-scale magnetic field. Graphs of the latitudinally averaged photospheric field from Mt. Wilson were used to trace the poleward migration of the polarity reversals at the times of maxima. In Figure 1, the times of the rocket and OSO-6 data are superposed on the sunspot data for cycles 20 and 21 using smoothed values of R_Z , the Zürich sunspot number, normalized to the starting minima of the cycles in October 1964 and June 1976, respectively.

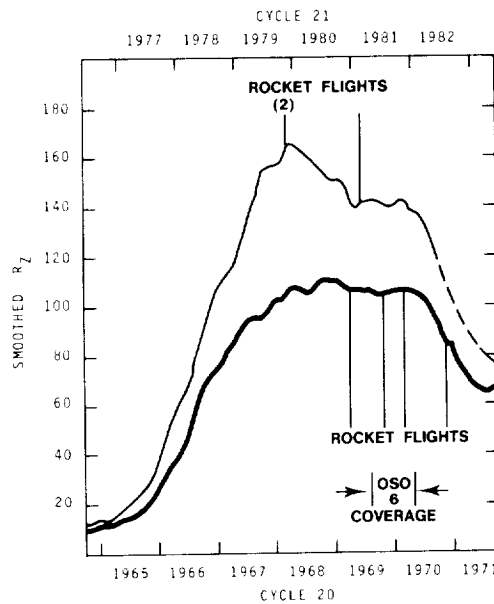


Fig. 1. The rise, maximum and early decline phases of solar sunspot cycles 20 (bottom curve) and 21 (top). The curves show smoothed values of R_Z , the Zürich sunspot number, normalized to their starting minima in October 1964 (bottom) and June 1976 (top). The dashed line represents predicted R_Z through late 1982 and early 1983. These data are adapted from the *Solar-Geophysical Data Bulletin*. The vertical lines denote the times of AS & E X-ray rocket flights (there were 2 in November 1979), and the arrows indicate the time coverage of the Harvard OSO-6 Mg X movie.

The maximum of cycle 20 was broad, with shape and peak similar to the average profile of the previous 12 cycles. In contrast, cycle 21 was the second most active sunspot cycle in recorded history. Compared to cycle 20 it had a steeper rise and an earlier and narrower peak. It is important to compare the patterns of evolution in the polar regions for these two cycles, which have such different levels and distributions of

magnetic activity. In this section we will examine the evolution of the high-latitude coronal holes which lead to the reformation of the polar holes.

2.1. THE REDEVELOPMENT OF THE POLAR HOLES IN CYCLE 20

The structure of the corona during the maximum of cycle 20 was observed in 1969 with the use of *K*-coronal observations (HHH) and EUV and soft X-ray images obtained by rocket flights (Krieger *et al.*, 1971, Figure 6; Broussard *et al.*, 1978). The rocket images corroborate the description given by HHH: that the corona was characterized by the absence of polar holes and the presence of elongated mid-latitude holes. In particular, the AS & E X-ray image on 4 November, 1969 (Carrington Rotation 1554) showed that there was no polar coronal hole in the south. The magnetic field data showed no dominant polarity at high latitudes until 1970.

For this cycle the exact time of reappearance of polar coronal holes is difficult to determine because of the low resolution of the *K*-corona data and the infrequent rocket X-ray images, as well as the cyclical tilting of the solar poles toward and away from our line of sight. HHH noted that by mid-1970 (CR 1561–63) dominance by a single polarity had begun to appear in both hemispheres. The polarities (positive in the north, negative in the south) were those expected for the new cycle following sunspot maximum.

Our interpretations of the timing of the coverage, or encirclement of the polar caps by coronal holes from the *K*-coronameter maps differ from those of HHH. Using a more conservative approach to the data, they claimed that the southern polar hole did not appear until early 1971 (CR 1572). The earliest indication in the *K*-coronameter data of a large coronal hole extension to the southern pole was in July 1970 (CR 1563). By October (CR 1567) a coronal hole could be observed poleward of S 70° latitude at all solar longitudes. Although there were gaps in the *K*-coronameter data during this period, we believe that these data imply complete coverage of the polar cap by a hole at this time. An unambiguous southern polar hole was visible on the AS & E X-ray image taken on 24 November, 1970 (CR 1568) (Krieger *et al.*, 1973). This asymmetric hole extended to the equator at about $L = 270^\circ$, and could be traced as a continuous feature of the corona back to July 1970.*

The critical period of late 1969 to mid-1970 was studied with the use of a cine presentation of the corona obtained with the Harvard spectroheliograph on the OSO-6 satellite (Withbroe 1981; Withbroe *et al.*, 1971), $H\alpha$ synoptic charts (McIntosh, 1979), and coronal data obtained on 7 March, 1970, the date of a total solar eclipse at Earth. The OSO-6 movie revealed the gradual development of three coronal holes which we believe were the earliest indication of the new-cycle magnetic organization leading to the formation of the southern polar hole. These holes appeared at mid-latitude and expanded in longitude and toward the south until they reached the pole. All were of negative polarity, in agreement with the subsequent polarity of the south pole.

* It was identified with the first long-lived, recurrent high speed wind stream following solar maximum (Krieger *et al.*, 1973; Sheeley *et al.*, 1977). The stream first appeared on August 1970 (CR 1564), in agreement in time, polarity, and longitude with the southern coronal hole.

The centroids of the holes were relatively stationary in longitude, with average Carrington longitudes of 20, 110, and 220°. The hole at $L \simeq 110^\circ$ stretched across the central meridian on the day of the 7 March, 1970 eclipse and, hence, was well observed. It was bordered in the south by the polar crown of filaments prior to March 1970 (CR 1558), implying that the hole did not extend to the pole prior to that rotation. The polar crown began to break up on CR 1558.

The eclipse data clarify these observations. Figure 2 is a superposition of the 7 March AS & E X-ray image of the inner corona and the HAO ground-based image of the white-light outer corona. The X-ray image revealed large areas of low emission, similar in appearance to coronal holes, surrounding both poles. The solar B_0 angle, denoting the tilt of the solar equator to the ecliptic, had its maximum negative value, exposing the south pole to our view. Gaps in the X-ray limb emission at position angles of 180° and $215\text{--}240^\circ$ (measured CCW from north) corresponded to gaps in the white-light emission (Van Speybroeck *et al.*, 1970; HHH). These corresponded to the small hole near the south pole and the large hole at $L = 220^\circ$ observed by OSO-6. In X-rays the region between these two 'accepted' holes contained similar low emission, suggesting that there were no intervening bright arcades that would indicate changes of magnetic polarity. Thus, the high southern latitudes appeared to be dominated by a single polarity.*

Figure 3 shows the H α synoptic map which includes the date of the eclipse (CR 1558). The top map has superimposed on it the boundaries of the coronal holes carefully drawn from the 7 March, 1970 X-ray image (Figure 2). Although the boundaries are subjective (e.g., Kahler *et al.*, 1983), our determinations are based on the use of film transparencies, which reveal subtle contrast differences not visible on prints. The double dashed lines mark regions where filament arcades may cause obscuration of the hole boundaries. The bottom map shows the 2 and 3×10^{-8} pB K -coronameter contours from the west-limb data of HHH. Comparison of these maps reveals that: (1) in the southern hemisphere the 3×10^{-8} pB contour lies within the negative polarity cell; (2) part of the southern coronal hole visible on the X-ray image is of uniform darkness and its boundary generally follows that of the 3×10^{-8} contour; (3) the small positive-polarity hole near the center of the X-ray disk (S 25, 135° L) is not visible in the white light data.

These observations suggest that by March 1970 the large-scale south polar field was dominated by the polarity of the new cycle, with a small area of the south polar region possibly covered by an asymmetric hole. The south polar region did not become completely encircled by a hole until about October 1970.

The above comparison indicates that, at this time of the solar cycle, the 3×10^{-8} pB contour of the K -coronameter data may be a better approximation for the boundaries of high latitude coronal holes. We believe that HHH's interpretation of the timing of the reappearance of the polar holes was overly conservative. Their use of a single, average contour (2×10^{-8}) to define hole boundaries over the entire cycle and their

* We believe that the white-light helmet streamer lying at $180\text{--}215^\circ$ had its base in the hidden hemisphere, contrary to HHH's interpretation.

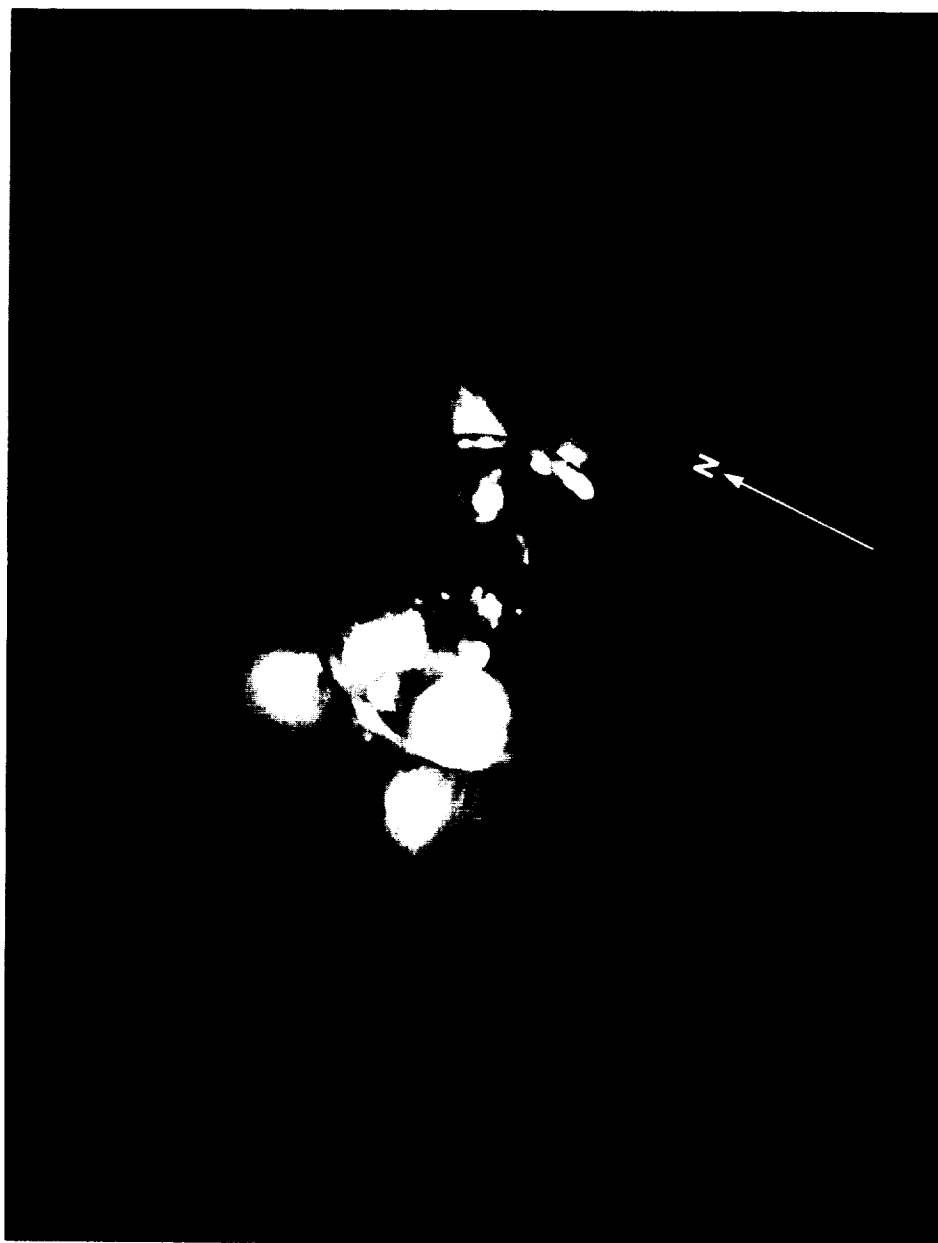
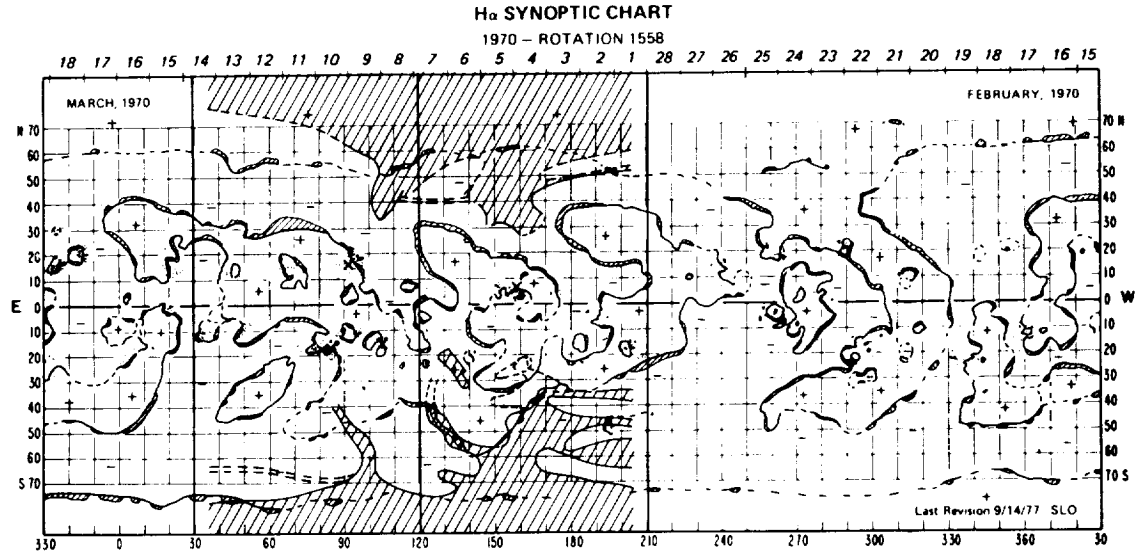
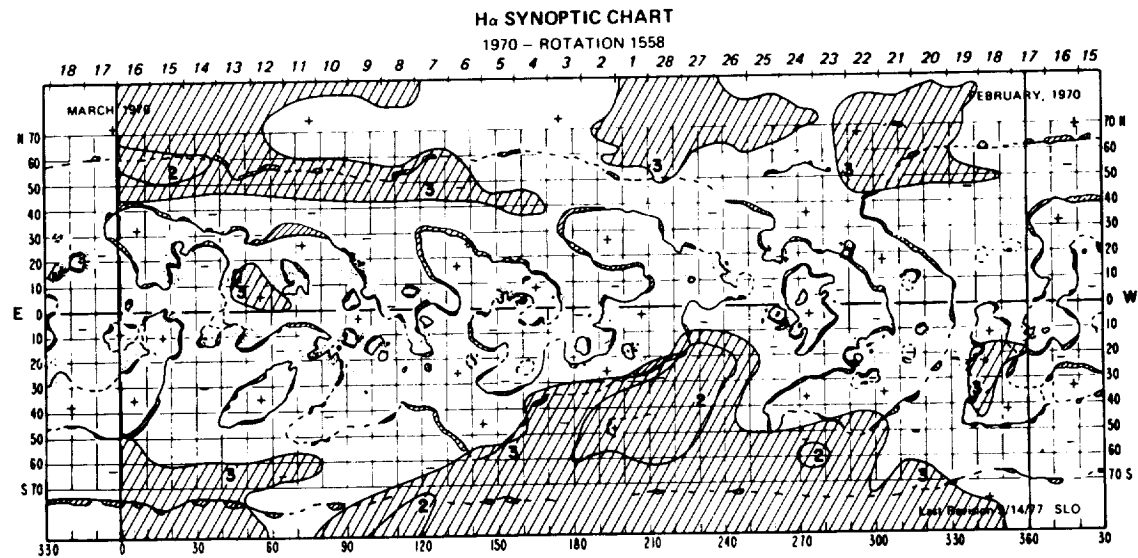


Fig. 2. A superposition of an AS & E X-ray image of the inner corona obtained during a rocket flight and a ground-based HAO white light image of the outer corona. Both were taken during the solar eclipse of 7 March, 1970. The X-ray image had passbands of 3–30 and 44–55 Å. The arrow indicates solar north.

ORIGINAL PAGE
BLACK AND WHITE PHOTOGRAPH



(a)



(b)

Fig. 3. Coronal data superimposed on an H α synoptic chart for CR 1558 (McIntosh, 1979). (a) Boundaries of coronal holes drawn from the 7 March, 1970 X-ray image in Figure 2. The three vertical lines represent the positions of the east limb (left), CMP (center) and west limb (right) on that day. Single dashed lines indicate uncertain boundaries; double dashed lines indicate the locations of coronal filament cavities. The 'x's mark the location of sunspots observed with the X-ray experiment, and provide a benchmark of the accuracy of transferring the X-ray data to the rectangular format. (b) The 2 and 3×10^{-8} pB contours of the white light K-corona adapted from the west limb synoptic data of HHH.

TABLE I
Polar events associated with sunspot maximum

| Cycle No. | Pole ⁽¹⁾ | Sunspot peak ⁽²⁾ | Polarity reversal above 70° lat. | Mid-latitude hole appearance | Polar crown disappearance | Earliest polar coverage by a hole |
|-----------|---------------------|--|---|--|---|--|
| 21 | N | July–Nov. 1979 1684–88 ⁽³⁾ | Mar. 1980 1692–93 (Feb.–Mar. 1982 1719) | Dec. 1979–Jan. 1980 1690 May 1980 1695 | Oct.–Nov. 1980 1701 | July–Aug. 1981 1711–12 |
| | S | Mar.–July 1980 1692–97 | Sept. 1980 1699 | May 1980 1695 Nov.–Dec. 1981 1715 | Apr.–May 1981 1707 | June 1981–Jan. 1982 1710–16 |
| 20 | S | Oct. 1969 1553 | Sept. 1969 1552 | ≥ Oct. 1969 ≥ 1553 | May 1970 1561 | July–Oct. 1970 1563–67 |
| | N | June 1970 1562 | July 1970 ⁽⁴⁾ 1563 (Aug. 1971 1577) | ≤ May 1970 ⁽⁵⁾ ≤ 1561 Jan. 1971 1570 | Sept. 1969 ⁽⁶⁾ 1552 June–July 1971 1576 | Mar.–Apr. 1971 ⁽⁷⁾ 1572–73 |
| 19 | S | Aug. 1957 | Mar.–July 1957 ⁽⁸⁾ | – | Jan. 1959 ⁽⁹⁾ | – |
| | N | Jan. 1959 | Nov. 1958 ⁽⁸⁾ | – | Oct. 1959 ⁽⁹⁾ | – |

(1) The first pole listed in each cycle switched polarity earliest.

(2) Peak in each hemisphere. Data for cycles 19 and 20 are from White and Trotter (1977). Data for cycle 21 were derived from NOAA–SESC sunspot group numbers (see text).

(3) Carrington rotation number.

(4) From Howard (1974). The earliest time was the first reversal to positive polarity. The second time was the 'final' reversal to positive polarity.

(5) From the data of Hundhausen *et al.* (1981). The earliest time is our estimate of the hole's original time of formation. The last time is HHH's time when the hole 'reformed'.

(6) The earliest time was when the polar crown preceding positive polarity disappeared. The second time was when the 'final' polar crown preceding positive polarity disappeared.

(7) From the data of HHH.

(8) From Babcock (1959).

(9) Estimated from Waldmeier (1981); Figure 5.

definition of polar encirclement only when the pole appeared to be surrounded by a uniform band of low emission separated from the 'equatorial corona by a steep brightness gradient' yields estimates of polar hole rebirths which are, consistently, several rotations later than our estimates of the earliest coverage. It is important to emphasize that in our data set we seek the earliest time when we can be reasonably certain that each pole is covered by a hole, no matter how small or asymmetric, and which will persist in subsequent rotations. This time, or a window of times, will appear in Table I under the column 'Earliest Polar Coverage by a Hole'.

HHH's conservative approach is understandable, given the limitations of the *K*-coronameter data, which they discuss in detail. We note that these data are particularly insensitive to the detection of small coronal holes and cannot give accurate locations of the boundaries of large holes, especially those obscured by brighter structures in the line of sight. These problems are more severe near the poles at solar maximum where the pB signal contains a large contribution due to numerous bright structures in the mid-latitudes.

The evolution of the high-latitude holes in the northern hemisphere followed a similar, but more complicated pattern. HHH noted that redevelopment of the north polar hole occurred in a manner similar to that in the south. A small positive-polarity (new-cycle) hole developed at mid-latitudes and expanded towards the pole to eventually cover it; however, this process lagged that of the south and took longer. The delay in establishing a persistent polar hole was apparently related to an anomalous 'wave' of poleward-moving flux which caused the north pole to reverse its polarity twice more after the initial reversal (e.g., Waldmeier, 1973).

Our independent interpretation of the *K*-coronameter data indicates that north polar coverage by a hole occurred 1 to 2 rotations earlier than HHH's suggestion (i.e. CR 1572-73 rather than 1574). This event was preceded by the growth of a high-latitude, positive-polarity hole which developed on or before CR 1561 (May 1970). HHH thought this hole disappeared then reappeared between CR 1567 and 1570, but we believe that the hole only fluctuated in area, possibly because of a surge of negative flux which swept through the northern mid-latitudes (Howard and LaBonte, 1981). The X-ray image for 7 March, 1970 (Figures 2 and 3) revealed low emission over the north pole although that pole was tilted away from our view. Bright arcades overlying the broken polar crown at N 50-60° likely obscured the north pole in the *K*-corona data.

2.2. THE REDEVELOPMENT OF THE POLAR HOLES IN CYCLE 21

The study of the birth and evolution of coronal holes in the present solar cycle is improved because of the availability of continuous synoptic He I-10830 Å data from KPNO. Advantages to the 10830 Å data are their high spatial resolution and the minimal obscuration of hole boundaries due to overlying structures. Disadvantages include a poor understanding of the close correspondence between He I absorption and hot coronal material (Kahler *et al.*, 1983), and limb darkening in coronal holes (Harvey and Sheeley, 1977). Additional data available included AS & E X-ray rocket images obtained at the maximum and early decline of the solar cycle (as marked in Figure 1)

7 NOVEMBER 1979

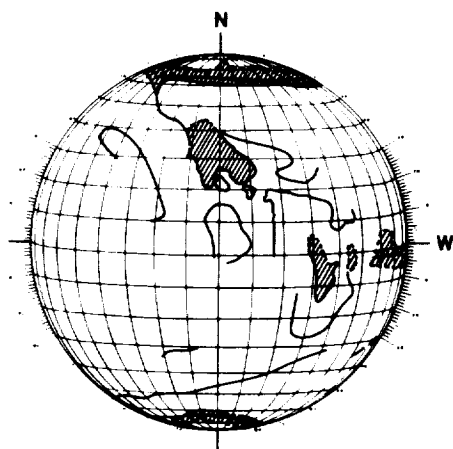
13 FEBRUARY 1981



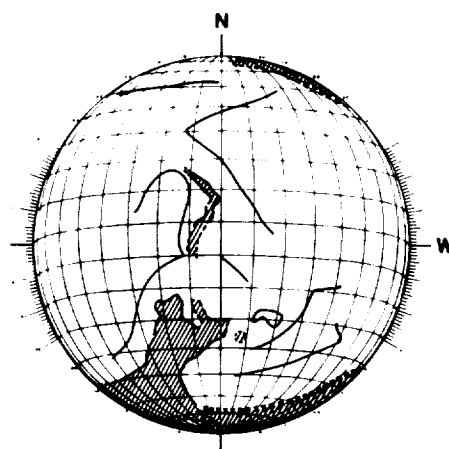
(a)



(c)



(b)



(d)

Fig. 4. *Top*: AS & E X-ray rocket images of the corona obtained on 7 November, 1979 (a) and 13 February, 1981 (c). The passbands of the images were $8 \approx 100 \text{ \AA}$ and $8-39, 44-64 \text{ \AA}$, respectively. *Bottom*: Tracings on Stonyhurst disks of the boundaries of the darkest areas on the 7 November, 1979 (b) and 13 February, 1981 (d) X-ray images. Dashed lines indicate less well defined boundaries. Also shown are the principal (solid lines) neutral lines and filaments transferred from the synoptic charts for CR 1688 and 1705.

and a complete atlas of $H\alpha$ synoptic charts with 10830 \AA coronal holes superimposed.

Figure 4 presents the AS & E X-ray images obtained on 7 November, 1979 (a), near solar maximum, and on 13 February, 1981 (c), 14 months after maximum. These images had similar sensitivities at the film plane and covered similar solar longitudes ($\text{CMP} \approx 300^\circ \text{ L}$ for both images). At the bottom of the figure are tracings of the

boundaries of the darkest areas on the X-ray images, and tracings from $H\alpha$ synoptic charts for CR 1688 and 1705 of the definite (solid) neutral lines and filaments which were located near the dark X-ray features. Since neutral lines tend to border coronal holes and lie within coronal cavities (e.g., McIntosh *et al.*, 1976), they help us to separate these two types of dark X-ray features. Again, we used high contrast transparencies to make the X-ray drawings. We believe that the low contrast of the solar corona near maximum is physically real (Kahler *et al.*, 1983).

No polar holes are evident on the 7 November, 1979 image, nor on another X-ray rocket image obtained on 16 November, 1979. Together these images provided coverage of approximately $2/3$ of the solar disk near solar maximum. The dark lanes near the poles corresponded to polar crown or high-latitude filament channels. A small hole may have appeared near the south pole on 16 November, but it was probably of negative polarity, i.e., indicative of old-cycle flux. Small mid- and high-latitude coronal holes appeared on both images. We conclude that the overall appearance of the low corona at the maximum of cycle 21 was similar to that of cycle 20. Examination of the X-ray images and the $H\alpha$ charts showed that there were small mid-latitude holes but no conspicuous polar holes, and no large-scale organization of 'new-cycle' polarity at high latitudes.

By February 1981, early in the decline of cycle 21, the X-ray image revealed a large, asymmetric coronal hole extending to near the south pole. The solar south pole was visible on the disk just as in March 1970. A coronal hole may have been present near the north pole, but this is uncertain because that pole was tilted away from Earth.

Spectroheliograms taken in the $He I - 10830 \text{ \AA}$ line have been obtained daily at the KPNO since mid-1974 and have been used to map the boundaries of the coronal holes onto $H\alpha$ synoptic charts, which places the coronal holes in context with the patterns of large-scale solar magnetic fields, active regions and filaments. The accuracy of this mapping depends on observer bias in determining the hole boundary from daily images, day to day contrast variations between the hole and its surroundings, and the transfer of the data to a rectangular grid. As is the case for the $H\alpha$ data, subjective variations in the mapping are minimized by only mapping features which persist from day to day. We have assumed that for our study of large-scale evolutionary patterns the location of hole boundaries, mapped in this way, is sufficiently reliable. This assumption is supported by the observation of consistent and persistent patterns on the charts from one rotation to another.

The visibility of coronal holes in 10830 \AA is a separate question. Kahler *et al.* (1983) have recently reviewed the comparisons of coronal holes seen in 10830 \AA with $He II - 304 \text{ \AA}$ and soft X-ray images. They compared six AS & E rocket X-ray images with 10830 \AA images and found good agreement between the boundaries of large holes but poor agreement for mid- and low-latitude small holes, which were of low contrast, from 1976 to 1981. Limb darkening in coronal holes is also more pronounced in the 10830 \AA line (Harvey and Sheeley, 1977). Combined with foreshortening and the variation of the solar B_0 angle, these factors somewhat compromise the use of the 10830 \AA data for detecting polar holes. However, although the boundaries of high-latitude holes are uncertain, the existence and large-scale evolution of these holes are

well observed in the synoptic data. Also, Fisher (1982) has shown that around solar maximum 10830 Å coronal holes of sufficient size and lifetime were always detected by the HAO M-III K-coronameter.

The relationships between coronal holes and the large-scale magnetic field patterns displayed on the H α synoptic charts have been examined by McIntosh *et al.* (1976) and Bohlin and Sheeley (1978). Coronal holes consistently lie near the center of unipolar magnetic areas whose dimensions usually exceed 30 heliographic degrees. The hole boundaries generally parallel the paths of adjacent neutral lines, with a constant separation between hole and neutral line. The shapes of coronal holes, therefore, mimic the forms of the surrounding magnetic cells as bounded by the H α neutral lines.

These relationships can be illustrated using charts where the areas of negative polarity are shaded dark, and coronal holes are crosshatched. The relationships are temporal as well as spatial, so a time series of charts, made by dividing the shaded synoptic charts into narrow zones of latitude and then assembling the zones in time series (McIntosh, 1980, 1981), is used. Figure 5 displays the zone for the southern high latitudes (south at the bottom) for the period encompassing solar cycle maximum, the polar polarity reversal and early decline of the solar cycle (May 1979–April 1982; CR 1682–1720). Although these zones extend only to 70° latitude, the original H α synoptic charts and daily 10830 Å images were used to confirm the boundaries of coronal holes above 70° latitude.

During the period shown in Figure 5a, a high-latitude, negative-polarity (black) coronal hole disappeared about the time of sunspot maximum. This hole was within a polar crown gap (PCG – McIntosh, 1980), seen as a dark diagonal sloping to the left with time. The PCG closed rapidly in late 1979 during the apparent deceleration of the positive-polarity (white) area to the west (right) and the demise of the coronal hole. These observations mimic those of cycle 20, when the closure of the PCG occurred exactly 11 years earlier, in late 1968 (McIntosh, 1980).

After this time the south polar region gradually became dominated by positive, new-cycle polarity. The reversal of polarity in the polar regions evidenced by the movement of the polar crown beyond the lower border (S 70) of this zone by CR 1701 (Figure 5b), followed the closure of the PCG by at least six months.

The first persistent mid-latitude coronal hole appeared on CR 1695. Figure 5b shows that this hole formed near the center of a growing positive-polarity area which encircled the Sun by early 1981. The hole grew in size and expanded poleward until it dominated the polar region by mid-1981 (after CR 1710, Figure 5c).

This episode was followed by a poleward surge of negative polarity flux from CR 1709 to 1722 which coincided with a large reduction in the high latitude hole area. The surge is seen as increased black polarity at high latitudes in Figure 5c and as a prolonged negative downturn in the magnetic field averages at mid- to high-latitudes (Section 3.1). This surge began at lower latitudes, progressed poleward and was contemporary with the development of a second mid-latitude hole on about CR 1714 at L 260°. Like the first such hole, this hole grew in size and expanded poleward until it connected to the first coronal hole at the pole on CR 1721.

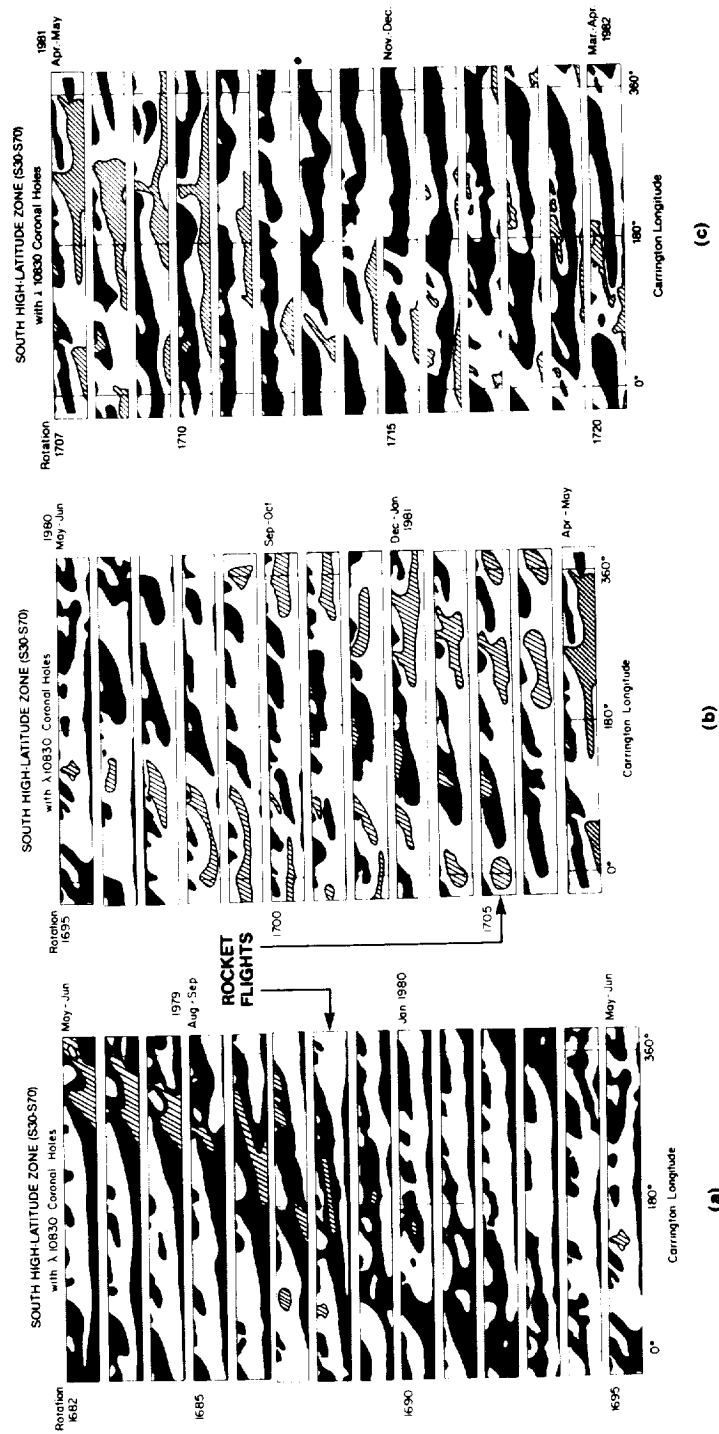


Fig. 5. A time series of portions of H α synoptic charts for high solar latitudes encompassing the period of sunspot maximum, polar polarity reversal and early decline of solar cycle 21 (May, 1979 - April, 1982). The upper border of each strip is at S 30° and the lower border at S 70°. Black areas are negative polarity; white areas are positive polarity; grey and cross-hatched areas are coronal holes mapped from KPNO He I-10830 Å images. The bottom strip of each column is repeated at the top of the next column. The rotations during which the AS & E rocket images of Figure 4 were obtained are indicated.

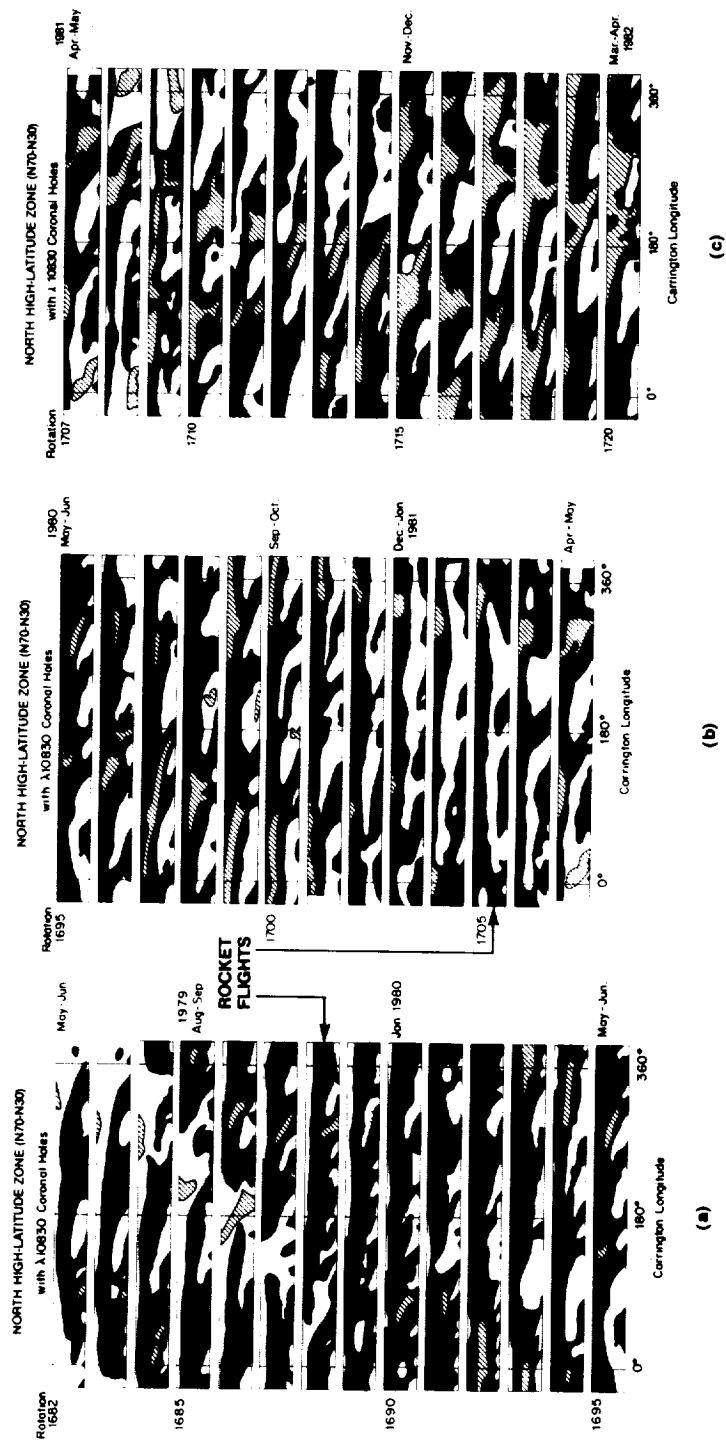


Fig. 6. High-latitude zones for the northern hemisphere for the same period as in Figure 5. The upper border of each strip is at N 70° and the lower border at N 30°.

The time when the south pole became covered by a coronal hole is uncertain because of the changing solar B_0 angle and the reduction of the high latitude hole area through late 1981 and 1982. By CR 1717, when the B_0 angle was favorable, the pole appeared to be covered over all longitudes to a latitude of at least $S 80^\circ$.

The evolutionary process in the northern hemisphere during solar cycle 21 was similar to that in the south, but more complicated, just as in the previous solar cycle. Figure 6 displays the northern high-latitude zone (north at the top) for the same period as Figure 5. The PCG is white (positive-polarity) and closed rapidly from CR 1687 to 1689, identical with the time of closure of the southern PCG. The polar crown is the upper border of the large black (negative-polarity) area centered within the zone for CR 1682 at the top of Figure 6a. The movement of the polar crown past the $N 70$ border occurred by CR 1695, two rotations earlier than the southern polar crown.

By CR 1690 the northern hemisphere was encircled at high latitudes by negative (new-cycle) polarity flux. Within this belt the first persistent mid-latitude hole formed on CR 1690, very soon after the PCG closure and five rotations earlier than for the southern hemisphere. A second, persistent, mid-latitude hole formed on CR 1695 at 130° L. The first failed to grow and did not move to the pole. The second hole expanded rapidly on CR 1697 (Figure 6b) both toward the pole (top) and toward the equator. It extended beyond $N 70$ by CR 1699. Its lower-latitude portion could be identified continuously through CR 1719 (March 1982).

By CR 1712 the pole appeared completely covered by a hole. But in the interval CR 1700–1712 the situation was confused, probably because of another poleward surge of flux. This surge occurred from about CR 1708 to 1714 and is seen as increased white (positive) polarity at high latitudes (Figure 6b, c) and as a positive poleward-moving peak in the magnetic field averages (Figure 7). The earliest time of coronal hole coverage of the north pole was as much as a year earlier than for the southern hemisphere. This time was better established than for the south because the coverage of the pole occurred during the time when the solar B_0 angle favored viewing of the north pole.

3. The Polar Magnetic Field Evolution Around Maximum

There are two other specific observational tracers of the evolutionary pattern of the magnetic flux that can be related to polar hole evolution near sunspot maximum. They are the dependence of the time of reversal of the long-term average photospheric field strength as a function of latitude, and the evolution of the polar crown of filaments.

3.1. THE MAGNETIC POLARITY REVERSAL

The most detailed discussion of the polar polarity reversal during cycle 20 was given by Howard (1972, 1974). Using Mt. Wilson magnetograph data, he observed successive reversals of the sign of the field to the new-cycle polarity starting at $40\text{--}50^\circ$ latitude and proceeding to the pole. The time for this 'migration' was 1 to $1\frac{1}{2}$ yr and similar patterns were observed at both poles, although not in phase. The reversal occurred at least 11 rotations earlier in the south than in the north, in agreement with the pattern of the development of the high-latitude and polar coronal holes.

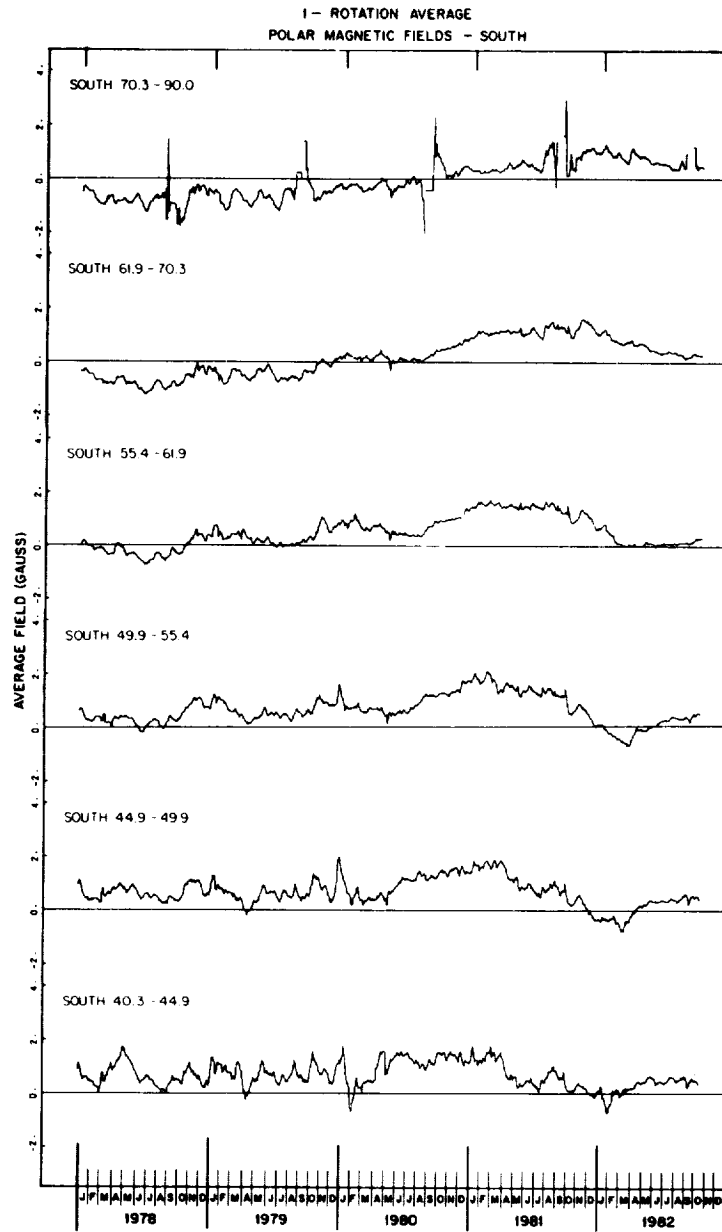


Fig. 7a.

Fig. 7a-b. The variation of the southern (a) and northern (b) photospheric magnetic field strength averaged over six latitude intervals from 1978 through October 1982. The zero level is drawn for each latitude interval. The field averages are 27-day running means. The large excursions in the data above 70° are related to data gaps and instrument recalibrations at times when the respective poles had their maximum tilt away from the Earth. These data are from Mt. Wilson Observatory, courtesy of R. Howard.

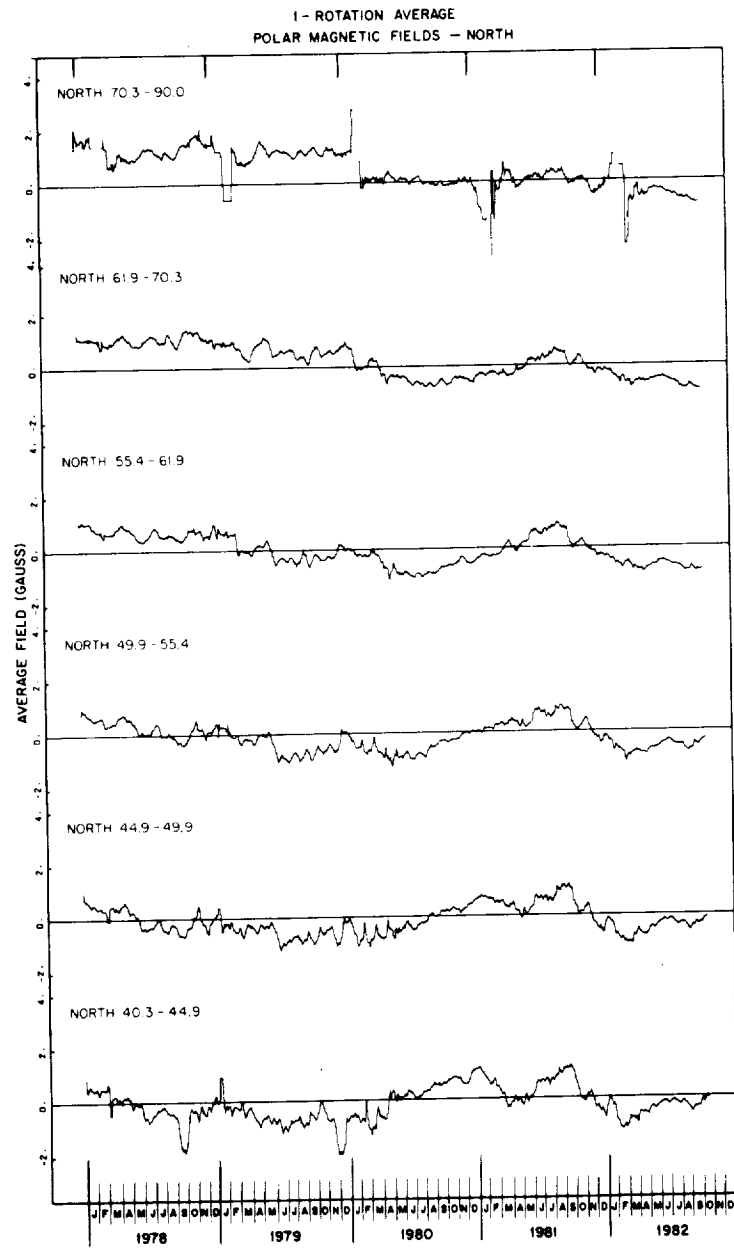


Fig. 7b.

R. Howard has kindly provided Figures 7a, b, which are plots of the north and south photospheric field, respectively, averaged over six latitude intervals from 1978 to 1982. We can see that a long-term reversal to new-cycle polarity (negative in the north, positive in the south) occurred above latitudes 70° around March 1980 in the north and about 6 months later in the south, although the data contain significant fluctuations and the zero level is uncertain. Because the polemost latitude band that the magnetograph samples is large, these measurements underestimate the time of reversal at the pole. However, the poleward reversal 'wave' moves so rapidly in each hemisphere that the actual polar reversal is anticipated by, at most, 1–2 rotations. (A tendency for earlier reversal at successively lower latitudes is also apparent.)

As mentioned earlier, the timing of the reversals in cycle 21 was complicated by apparent poleward movement of old-cycle polarity flux in both hemispheres. This occurred earlier and was more clearly delineated in the north. The northern surge also produced a clear but temporary positive shift in the long-term, increasingly negative polar field (Figure 7b, mid-1981). However, the effect of this shift in the polar field was very weak and the second 'reversal' was out-of-phase with the timing of the other tracers. Therefore, although in Table I we have listed two times when the northern field above 70° reversed polarity from positive to negative, we conclude that the earliest reversal was the 'true' one.

The southern surge did not appear to be strong enough to reestablish negative flux above 70° S, so we list only one reversal time for the southern hemisphere.

Table I list the times of the sunspot peak in each hemisphere (column 3) and the times of polarity reversals above latitudes 70° (column 4), both for cycles 20 and 21. It follows from dynamo models that the differences in the time of the polarity reversal for the two poles should depend on the differences in flux production in the two hemispheres. A crude, but commonly used measure of the amount of flux appearing on the solar surface is the sunspot number, which has been plotted separately for each hemisphere by White and Trotter (1977) through cycle 20. Such segregated counts were not available for the present cycle, so we used counts of the number of SESC regions (active regions assigned a serial number by NOAA Space Environment Services Center) occurring in each hemisphere during cycle 21. This estimate was made from the weekly NOAA *Preliminary Report and Forecast of Solar-Geophysical Activity*, without resorting to counting the number of groups on individual sunspot drawings. More regions formed in the northern hemisphere throughout the rising portion of the solar cycle. The northern hemisphere strongly dominated during the 6 months just prior to sunspot maximum. The southern hemisphere then dominated for the six months ending in August 1980. The lag time and the order of dominance between the two hemisphere mimicked that between reversals of the northern and southern poles for the last two cycles, suggesting that the amount of flux generated in each solar hemisphere determines the order and timing of the polar magnetic field reversal.

We see that in cycle 20 the south pole reversed at least $\frac{3}{4}$ of a year before the north, and in cycle 21 the north pole reversed first, about $\frac{1}{2}$ a year before the south. For both cycles the general pattern of development of new-cycle polarity coronal holes followed

these reversals in this same sequence. These observations are therefore consistent with our expectation for the general evolution of the polar field following sunspot maximum, as set forth in the Introduction. For completeness we have included in Table I Babcock's (1959) estimate of the time of reversal during cycle 19, when the south reversed about $1\frac{1}{2}$ yr before the north.

3.2. THE DISAPPEARANCE OF THE POLAR CROWN

The final observational parameter that must be accounted for in models of the solar cycle is the poleward migration of the polar crown of filaments (e.g., Leighton, 1964). After sunspot minimum filaments in the mid-latitudes begin to move toward their respective poles. The locus of filaments maintains a nearly constant distance of 20° from the boundary of the shrinking polar hole (Waldmeier, 1981); in fact the coronal arcades overlying the filaments form the physical boundary of the polar hole (McIntosh *et al.*, 1976). For the past several cycles the reappearance of the polar holes has occurred close to the time of arrival near the pole, and disappearance, of the polar crown (Waldmeier, 1981).

We have determined the time of disappearance of the polar crowns for cycles 20 and 21 through the use of H α synoptic charts (McIntosh, 1979; *Solar Geophysical Data*) and high-latitude zonal diagrams derived from the H α charts (like Figures 5 and 6). This method permits us to observe the systematic motions of features on the maps. Integration of daily measurements of filaments at latitudes higher than 60° minimizes the uncertainties in the position of the polar crown.

Using mean values of the latitude distribution of prominence areas, Waldmeier (1973) was able to determine the poleward migration rate and time of arrival at the pole of the polar crown for cycle 20. Using the H α synoptic charts, we have developed similar curves for cycles 20 and 21 which show the maximum latitude reached by the polar crown on each solar rotation. The times of polar crown disappearance listed in column 6 of Table I were determined to be the rotation on which the last conspicuous polar crown filament was observed.* The disappearance times for cycle 19 were estimated from Waldmeier's (1981) Figure 5.

4. Summary and Discussion

4.1. SUMMARY OF RESULTS

We will now attempt to synthesize these observations in order to learn more about the polar evolution of the solar magnetic field. Several caveats are required for the interpretation of these data: (1) Like other solar synoptic observations, the data are noisy and

* From Waldmeier's (1973) data on the evolution of the northern polar crown in cycle 20 one would infer an earlier disappearance time than ours. This is because his 'anomalous' polar crown (also referred to by Howard, 1974) was not the final one. Following the passage of the 'anomalous' front the polar field was of negative polarity. It then switched to the new-cycle (positive) polarity after the passage of the final polar crown.

best used to discern longer term trends. This is especially true of the polar observations which are effected by foreshortening and the tilt of the solar axis with regard to the ecliptic. (2) As noted by Howard (1974) the timing of the magnetic polarity reversal is uncertain, requiring several years of data around solar maximum to ascertain its actual occurrence. (3) Coronal hole boundaries were determined from different sets of data in cycles 20 and 21. In cycle 20 we used higher altitude *K*-coronameter, X-ray and EUV data and in cycle 21 we used primarily lower altitude He I-10830 Å data. The detailed intercomparison of hole boundaries determined at these different wavelengths is not well understood, but knowledge of the general location and evolution of the larger holes should be sufficiently accurate for our purposes. (4) Because of these limitations we estimate that the uncertainties in the timings of Tables I and II are of the order ± 2 rotations.

First we summarize the high-latitude magnetic evolution near the maxima of the last two cycles. In cycle 20 the polar polarity reversal and polar hole redevelopment occurred first in the south. Mid-latitude holes developed in late-1969 and evolved into three holes which joined at the south pole in mid-1970. The polar crown disappeared in the spring of 1970. This process took longer in the north, lagged that of the south and was more complicated. A persistent, mid-latitude hole did not appear in the north until mid-1970, following by half a year the development of such a hole in the south. The polar hole redeveloped in the spring of 1971. In both hemispheres, polar hole development lagged the appearance of the mid-latitude holes by about one year. In cycle 21 a similar pattern was followed except that all of the key events, including the peak of flux emergence, occurred first in the north. The northern polar hole redeveloped in mid-1981 and the southern in late 1981. These holes lagged the appearance of persistent mid-latitude holes of new-cycle polarity by 1–2 yr. The magnetic reversal process in the north preceeded that of the south by about 6 months, as did the polar crown disappearance. In each hemisphere the complete coverage of the pole by a hole was delayed by poleward surges of late-emergent flux.

These observations can be organized by relating the timing of the key high latitude events to the polarity reversals. Table II is adapted from Table I and shows the lag times in Carrington rotations from the time of the earliest indication of the polarity reversal

TABLE II
Lag times from polar polarity reversal (Carrington rotations)

| Cycle No. | Pole | Mid-latitude hole appearance | Polar crown disappearance | Polar hole encirclement |
|-----------|------|------------------------------|---------------------------|-------------------------|
| 21 | N | -3 to +3 | +(8 to 9) | +(18 to 20) |
| 21 | S | -4 | +8 | +(11 to 17) |
| 20 | N | $\geq +1$ | +9 | +(11 to 15) |
| 20 | S | $\geq (-2 \text{ to } +7)$ | +13 | +(9 to 10) |
| 19 | S | - | +(20 to 25) | - |
| 19 | N | - | +12 | - |

above 70° in each hemisphere to the time of the following events: the development of the mid-latitude hole of new-cycle polarity, the disappearance of the last conspicuous polar crown filament, and the earliest coverage of the pole by a hole. We summarize these results as follows: In each hemisphere the peak of the flux emergence (in terms of sunspot number), the appearance of the mid-latitude hole(s), and the polarity reversal at the pole all occurred within a few months of each other. This is particularly true if we compare the time of the earliest indication of the polar reversal and the earliest birth of a mid-latitude hole. The polar crown disappearance and the redevelopment of the polar hole occurred between 8 months and $1\frac{1}{2}$ yr after the polar reversal. Polar hole coverage occurred at or after the time of polar crown disappearance in both cycles, lagging by about one year in both hemispheres in cycle 21.

4.2 DISCUSSION

We have examined the observations relating to the evolution of the high-latitude solar magnetic field around sunspot maximum, when the net polar flux switches polarity and coronal holes redevelop around the poles. We now integrate our results with the phenomenological concepts of coronal hole evolution near maximum mentioned in the Introduction. Before activity maximum, flux in the form of BMRs emerges at mid-latitudes. The trailing part of this flux, of opposite polarity to that of the old cycle at the poles, moves toward the poles, canceling the unipolar field there and reducing or eliminating the area of the pole occupied by a coronal hole. Near sunspot maximum a sufficient amount of trailing polarity flux has arrived at the poles to switch the polarity of the net flux, although a large amount of mixed polarity remains. In the mid-latitudes at this same time the field has reversed and the unipolar area of trailing polarity field is sufficiently large for small holes to form. After maximum, as the amount of new flux brought to the surface begins to decline, large unipolar areas of new-cycle (following) polarity begin to dominate the mid- to high-latitude region. In two or three longitude zones the small holes begin to enlarge. Although they can spread very rapidly, for a period of time they are prevented from encircling the Sun at high latitudes because of residual flux emergence and poleward flows of net old-cycle flux. The unipolar cells and the holes within them persist and grow larger until they join at high latitudes to cover the pole. At about this time the polar crown, which is supposed to form the boundary between the old-cycle (or mixed) polarity of the pole and the new-cycle, high-latitude polarity, begins to break up and disappear as it nears the pole. Although the development time of the new-cycle, high-latitude holes for these two cycles varied from 6 months to $1\frac{1}{2}$ yr, the appearance of the polar hole occurred within several rotations of the disappearance of the polar crown in both cycles.

A major goal of our study is to provide a firmer observational context for the development of models of the solar cycle. Toward this end we comment below on the following results of our analysis which we believe must be taken into account in future models of the solar cycle.

First, the process of polarity reversal accompanying the redevelopment of the polar

holes is not a smooth process that sweeps the trailing flux from the emerging flux belts to the pole. Instead it is discontinuous, occurring in equally-spaced longitude bands. These patterns are apparent in the zonal charts (Figures 5 and 6) as diagonals formed by the large-scale magnetic cells and the coronal holes within them. The slopes of these diagonals indicate the rate of rotation of the features relative to the Carrington rate. These rates suggest a slowing of the large-scale features around the time of the cycle 21 polarity reversal, similar to that found for cycle 20 (McIntosh, 1980).

These patterns are reflected in all of the magnetic tracers that we have examined; i.e., coronal holes, latitudinally averaged photospheric magnetic fields, and the polar crown. This process is perhaps best seen in the coronal hole evolution. Small mid-latitude holes form when the magnetic cells at that latitude become large enough. Eventually one or more of them continues to grow in area and to move poleward until a segment reaches the pole. This latter process yields the large, asymmetric, high-latitude holes discussed earlier and found to be typical of high-latitude holes soon after maximum. The ultimate development of a symmetrical polar hole does not occur until a second poleward thrust of unipolar new-cycle field, as evidenced by the growth of a second magnetic cell and mid-latitude hole. This second hole develops at a longitude 180° from the first, and lags the first by 5–10 rotations. The observed poleward movement of the old-cycle field (Figure 7), after the early polar reversal and mid-latitude hole appearance, tends to disrupt the growth of new-cycle field, to maintain the asymmetry of the high-latitude holes, and to diminish the hole area. If the surge reaches the polar zone, the polar crown will be reestablished in that longitude band. This yields the kind of 'anomalous' polar crown first reported by Waldmeier (1973) in the north in cycle 20.

There is a persistent asymmetry between the two solar hemispheres in the timing of the processes discussed above. For instance, in any given cycle the magnetic polarity reversal between hemispheres is offset by 6 months to $1\frac{1}{2}$ yr. Our results have confirmed such an asymmetry for the present cycle and indicate that the polar crown and high-latitude coronal hole evolution also follow this pattern for cycles 20 and 21 (Table I). Our sunspot group data for cycle 21 and the extensive sunspot number data of White and Trotter (1977) suggest that such an asymmetry is a characteristic of the maximum of the solar cycle.

Our second result concerns the relationship between the polar field reversal and the polar crown disappearance. The polar crown is hypothesized to form the boundary between the poleward-receding old-cycle flux and the advancing new-cycle flux. If this idea were correct, then we could use the time of disappearance of the polar crown to infer the time of polarity reversal at the pole. We can predict that this inferred time should be approximately the same as that implied by magnetograph polarity measurements. If the strongest new-cycle field lay $15\text{--}20^\circ$ equatorward of the polar filaments, we might expect the measured reversal to lag the inferred reversal by several rotations. Howard (1974) first noted that for cycle 20 this relationship was not as good as expected. We have found that, for the last two cycles, the *opposite* actually occurred; i.e., the polar crown consistently disappeared 6 months to 1 year *after* the magnetic polar reversal.

It is possible to explain this sequence in terms of the presence of the poloidal field of the new cycle, which, in $\alpha - \omega$ dynamo models, is generated by the toroidal current associated with the toroidal field component. The poloidal field, although essential to the regeneration of the dynamo, is much weaker than the toroidal field and would therefore be difficult to observe. In fact, doubt has been cast on its existence and subsequently used as argument against the $\alpha - \omega$ mechanism (Layzer *et al.*, 1979). However, at the time of the polar field reversal, the toroidal components of the old and new cycle flux might be expected to cancel, thus allowing the poloidal field to be observed. Our observations suggest the following scenario: With the appearance of new-cycle flux at mid-latitudes, the quantity of old-cycle flux migrating poleward will gradually diminish. If a point in time is reached, before the new-cycle flux reaches the polar zone, when the polar zone flux from the old cycle falls below the level of the poloidal component arising from the new cycle, a reversal in the measured average field strength in the polar zone would occur. Thus the apparent contradiction in the observations would be removed; the polar crown would still form the boundary between the *toroidal* fields of the old and new cycle. As the new cycle builds and its flux migrates poleward, the polar crown will dissipate and the toroidal component will again dominate the field measurements. If this interpretation is correct, it provides the first evidence for the existence of a reversing poloidal field component which is critical for kinematic models of the solar dynamo.

Finally, our observations appear to support recent studies of the magnetic field (Howard and LaBonte, 1981) and polar filaments (Topka *et al.*, 1982) which suggest that there is a poleward meridional flow averaging about 10 m s^{-1} . These authors have interpreted this flow as the result of a large-scale poleward circulation that cannot be accounted for by Leighton (1964) - type diffusion. In the Mt. Wilson data the strongest flows originated in the sunspot belts near solar maximum and moved to the poles in 2-3 yr. We see apparent poleward flows of this magnitude in our data at high latitudes near maximum. For instance, in the south in cycle 21 the polarity reversal wave and the subsequent surge of old-cycle flux moved poleward at about 13 m s^{-1} . We estimate that the poleward movement of the high-latitude coronal holes was about $10-15 \text{ m s}^{-1}$, but with a large uncertainty due to the difficulty of measuring the coronal hole boundaries at high latitudes.

We can ask if we see any differences in the timing of these events that can be understood in terms of the different levels and distributions of magnetic activity between the last two cycles. Interestingly, the answer is generally no. The polarity reversal occurred first in the south for two consecutive cycles (19 and 20), then in the north in this cycle. A persistent phase lag between hemispheres of 6 months to 1 year was observed. In accordance with the more rapid rate of flux emergence, the polar reversals occurred faster in cycle 21 than cycle 20. On the other hand, the timing of the development of the high-latitude, new-cycle field and the polar crown migration and disappearance were similar during these two cycles. Polar hole coverage appeared to be retarded in cycle 21. This latter result could be due to the increased amount of total flux emergence in cycle 21 and the subsequent disruption in the development of the high-lati-

tude unipolar fields from poleward movement of old-cycle flux. In conclusion, there seems to be no strong correlation between the levels of solar cycle-dependent magnetic activity and the timing of events around the time of the polar polarity reversal.

Acknowledgements

The authors would like to thank R. Howard, of the Mt. Wilson and Las Campanas Observatories, for providing the magnetograph data and A. Krieger for helpful discussions. We thank the AS & E and NOAA technical publication groups for their assistance with the figures. DFW and JMD were supported at AS & E by NASA Contracts NAS5-25496 and NASW-3586.

References

- Babcock, H. D.: 1959, *Astrophys. J.* **130**, 364.
 Babcock, H. D.: 1961, *Astrophys. J.* **133**, 572.
 Bohlin, J. D. and Sheeley, N. R., Jr.: 1978, *Solar Phys.* **56**, 125.
 Broussar, R. M., Sheeley, N. R., Jr., Tousey, R., and Underwood, J. H.: 1978, *Solar Phys.* **56**, 161.
 Fisher, R. R.: 1982, *Astrophys. J.* **259**, 431.
 Harvey, J. W. and Sheeley, N. R., Jr.: 1977, *Solar Phys.* **54**, 343.
 Howard, R.: 1972, *Solar Phys.* **25**, 5.
 Howard, R.: 1974, *Solar Phys.* **38**, 283.
 Howard, R. and LaBonte, B. J.: 1981, *Solar Phys.* **74**, 131.
 Hundhausen, A. J.: 1977, in J. Zirker (ed.), *Coronal Holes and High-Speed Wind Streams*, Colorado Associated Univ. Press, Boulder, Colorado, p. 225.
 Hundhausen, A. J., Hansen, R. T., and Hansen, S. F.: 1981, *J. Geophys. Res.* **86**, 2079.
 Kahler, S. W., Davis, J. M., and Harvey, J. W.: 1983, *Solar Phys.* **87**, 47.
 Krieger, A. S., Vaiana, G. S., and van Speybroeck, L. P.: 1971, in R. Howard (ed.), *Solar Magnetic Fields*, D. Reidel Publ. Co., Dordrecht, Holland, p. 397.
 Krieger, A. S., Timothy, A. F., and Roelof, E. G.: 1973, *Solar Phys.* **29**, 505.
 Layzer, D., Rosner, R., and Doyle, H. T.: 1979, *Astrophys. J.* **229**, 1126.
 Leighton, R. B.: 1964, *Astrophys. J.* **140**, 1547.
 McIntosh, P. S.: 1979, UAG Report 70, World Data Center A for Solar-Terrestrial Physics, NOAA, Boulder, Colorado.
 McIntosh, P. S.: 1980, in M. Dryer and E. Tandberg-Hanssen (eds.), *Solar and Interplanetary Dynamics*, D. Reidel Publ. Co., Dordrecht, Holland, p. 25.
 McIntosh, P. S.: 1981, in L. E. Cram and J. H. Thomas (eds.), *The Physics of Sunspots*, Sacramento Peak National Observatory, Sunspot, New Mexico, p. 7.
 McIntosh, P. S., Krieger, A. S., Nolte, J. T., and Vaiana, G.: 1976, *Solar Phys.* **49**, 57.
 Nolte, J. T., Davis, J. M., Gerassimenko, M., Lazarus, A. J., and Sullivan, J. D.: 1977, *Geophys. Res. Letters* **4**, 291.
 Sheeley, N. R., Jr.: 1980, *Solar Phys.* **65**, 229.
 Sheeley, N. R., Jr., Asbridge, J. R., Bame, S. J., and Harvey, J. W.: 1977, *Solar Phys.* **52**, 1977.
Solar Geophysical Data Bulletins: U.S. Department of Commerce, NOAA, Boulder, Colorado.
 Stix, M.: 1981, *Solar Phys.* **74**, 79.
 Topka, K., Moore, R., LaBonte, B. J., and Howard, R.: 1982, *Solar Phys.* **79**, 231.
 Van Speybroeck, L. P., Krieger, A. S., and Vaiana, G. S.: 1970, *Nature* **227**, 818.
 Waldmeier, M.: 1973, *Solar Phys.* **28**, 389.
 Waldmeier, M.: 1981, *Solar Phys.* **70**, 251.
 White, O. R. and Trotter, D. E.: 1977, *Astrophys. J. Suppl.* **33**, 391.
 Withbroe, G. L.: 1981, private communication of 16-mm OSO-6 movie.
 Withbroe, G. L., Dupree, A. K., Goldberg, L., Huber, M. C. E., Noyes, R. W., Parkinson, W. H., and Reeves, E. M.: 1971, *Solar Phys.* **21**, 272.

4.11 The Detection of Soft X-Rays with Charged Coupled Detectors

P. Burstein and J.M. Davis

American Science and Engineering, Inc.
Cambridge, Massachusetts 02139

ORIGINAL PAGE IS
OF POOR QUALITY

19. The Detection of Soft X-Rays with Charged Coupled Detectors

P. Burstein and J. M. Davis

American Science and Engineering, Inc., Fort Washington
Cambridge, MA 02139, USA

The characteristics of an ideal soft x-ray imaging detector are enumerated. Of recent technical developments the CCD or charge coupled device goes furthest to meeting these requirements. Several properties of CCDs are described with reference to experimental work and their application to practical instruments is reviewed.

19.1 Introduction

The development of soft x-ray sensitive, electronic imaging detectors for scientific applications is a major concern of laboratories worldwide. In contrast to purely imaging applications scientific observations require quantitative, intensity and position information from the image. Therefore the characteristics of an ideal detector must include:

(1) A spatial resolution comparable to photographic film which implies a format with a large number of picture elements. In this case a large number is of the order 10^6 to 10^7 .

(2) A high sensitivity, to achieve the efficient detection of single, incident photons, to minimize the degradation caused by system noise and to provide high temporal resolution.

(3) A stable transfer function between input and output in order to achieve a photometric accuracy of 1%.

(4) Broad spectral response, or quantum efficiency, covering the energy range from 0.2 to 20 keV coupled with energy resolution for single photons over the same range.

The search for a single detector which completely satisfies all these conditions has been largely unsuccessful. It has included imaging proportional counters [19.1], which combine very large areas, good energy resolution, but only moderate spatial resolution, microchannel plates with a variety of readout systems which have large areas, good spatial resolution but extremely limited energy resolution [19.2,3], and more recently and quite promisingly charge coupled devices or CCDs.

In the following paragraphs the properties of CCDs as they apply to soft x-ray detection and their application to scientific investigations is discussed.

19.2 Properties of Charge Coupled Devices

CCDs are closely spaced, two-dimensional arrays of MOS capacitors which are laid down on a silicon substrate, shown schematically in Fig.19.1. The capacitors are electrically isolated from each other by the p- and n-type archi-

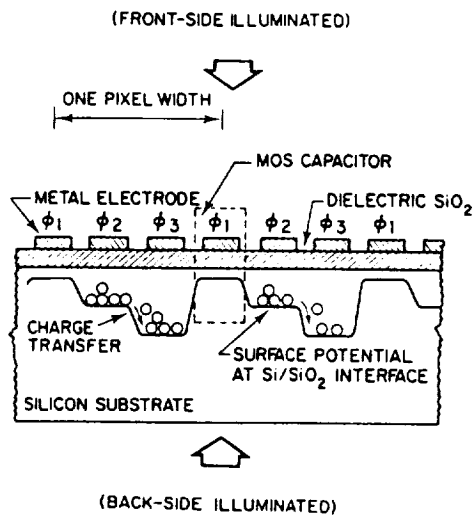


Fig.19.1 Functional description of a typical three-phase CCD architecture illustrating front and back illumination, taken from MELEN and BUSS [19.7]

texture of the device and by the applied voltages. A photosite, or picture element (pixel), consists of a set of three adjacent capacitors grouped in the columns of the array. The electrodes of the capacitors are independently controlled by "clock" or "gate" voltages. Because of this arrangement this type of CCD is known as a three-phase device.

When an incident x-ray is absorbed in the silicon substrate it excites electrons into the conduction band which then diffuse into a depletion layer formed by the positive voltages applied to the electrodes. These applied voltages form a potential well which traps charge at a particular photosite. To read out the device the applied voltages are changed, or clocked, so that the charge at each photosite along a row is transferred vertically to the adjacent site in its column. The charges in the row formed by the lowest site in each column are transferred into a shift register where they are read out serially following on-chip amplification.

The key to the operation of the CCD as an x-ray detector is the use of the interaction site as the storage site. It can be thought of as an array of solid-state detectors each with its own memory for the CCD can accept photons over its entire surface simultaneously.

In "conventional x-ray detection" by the CCD [19.4,5] the detector is used exactly as for visible light detection, as a total energy detector. The output of a particular pixel is a charge which is proportional to the total amount of energy deposited in the pixel.

The spatial resolution can be determined largely on the basis of pixel-to-pixel spacing and charge localization between pixels.

When only one x-ray photon is known to have interacted in an element of the array, then the charge in that element will be a function of the photon energy, as in a solid-state detector. Thus, each pixel will have an associated energy to charge transfer curve, and hence an energy resolution curve. The energy resolution, to a first approximation, is that of a tiny solid state detector.

On the average one electron-hole pair is created in the pixel for every 3.6 eV of energy in the x-ray photon. This is a very small amount of energy when compared with other soft x-ray detectors. Thus, a proportionally greater number of electrons will be created for each photon interaction, and the associated Poisson (or Poisson-like) statistics become more precise.

Since all pixels have a similar type of response, the CCD may be used as a nondispersive x-ray spectrometer [19.5,6]. The only requirement is that the probability of any single pixel receiving more than one photon during an integration period be small.

CCDs have several important characteristics which influence their operation as x-ray imaging detectors which we will briefly describe. First the quantum efficiency, defined as the probability of detecting an incident photon, is a function of x-ray energy and is close to unity for energies between 1 and 10 kilovolts. At the higher energies the efficiency falls off because the photons pass through the device without interacting while at the lower energies the efficiency falls off because when the CCD is illuminated in the so-called front-illuminated mode the x-ray photons are absorbed by the electrode and insulating structures on the front surface. These structures form a dead layer between 0.5 to 2 microns thick, and to overcome their effect CCDs have been operated in a back-illuminated mode. In this case the silicon substrate is illuminated directly, and to maximize the efficiency its thickness is tailored to the particular application, a process known as thinning. This leads to a considerable improvement in sensitivity, and we have been able to detect carbon K_{α} x rays at 250 eV with RCA CCDs manufactured in this fashion.

An alternative approach has been developed by Texas Instruments, who have developed a virtual phase CCD [19.8,9]. In this device the three applied voltages of the three-phase CCD have been reduced to one. The steplike potential is created through the use of ion implants in the n-type buried channel. By reducing the number of polysilicon gates per pixel from three to one, the thickness of the dead layer can be substantially reduced. However, in our tests of such a front-illuminated device, we were unable to detect carbon K_{α} x rays, and so in this respect, the modification is not an adequate substitution for back illumination.

The intrinsic noise of a CCD limits both the energy resolution and the length of time a picture can be integrated. Noise levels of 30 electrons rms can be achieved corresponding to energy resolution of 250 eV. The energy resolution is essentially independent of energy [19.10], and therefore CCDs are better than proportional counters at energies above 500 eV and marginally worse at lower energies. The ultimate noise goal is of the order of 10 electrons rms, which would be set by the stray capacitance of a few hundred pFs between the on-chip preamplifier and the last transfer gate. Noise levels approaching this have been reported in the literature [19.11] which makes their energy resolution superior to proportional counters.

To achieve these noise levels, the CCD and the on-chip amplifier have been cooled. Typical operating temperatures are around -100 °C. However, the operating temperature can be made too low for there are other completing factors, of which the most important are the charge transfer efficiency and the leakage current, which are also functions of temperature. The charge transfer efficiency is the fraction of the original charge transferred from one pixel to the next during the readout process. Incomplete charge transfer results in a loss of both photometric accuracy and dynamic range and introduces smearing of the image. The leakage current is a measure of the charge of

the spills from an illuminated pixel to adjacent dark pixels. In our tests with RCA CCDs we have found that an ideal operating temperature must be determined for each device, which is warm enough so that charge transfer efficiency is adequate (~ 0.99995 to 0.99999) while still cool enough to keep the leakage current acceptably low. This tradeoff has to be made on a device by device basis.

In principle the dynamic range of the CCD is limited by the readout noise and the full well capacity. The latter scales roughly as the pixel area, and for $30\text{ }\mu\text{m}$ square pixels the well capacity is $\sim 250,000$ electrons. The typical dc level for the three-phase CCDs we have tested is several hundred electrons, which corresponds to a dynamic range of the order of or less than 10^3 .

Although one should be able to extend the dynamic range by improving the noise characteristics of the preamplifier this is not necessarily true in the x-ray region. For a single x-ray photon produces a large number of electrons, e.g., a one kilovolt x ray will contribute in excess of 300 electrons, and if this value is greater than the noise it will place the limit on the dynamic range which is thus energy dependent varying inversely with the incident photon energy.

Finally, CCDs have excellent linearity to increases in the incident x-ray intensity characteristics of solid-state detectors and pixel nonuniformities arising from processing variations and mask alignment errors during fabrication are generally quite small.

19.3 Applications

Although the primary incentive for our studies of CCDs has been their application to astronomical observations there are many other scientific investigations in which their sensitivity and excellent spatial resolution can be used to advantage. Examples are the in vivo examination, in real time, of biological specimens and the recording of the x-ray emission arising during the collapse of the fuel pellets used in inertial confinement fusion experiments.

In x-ray astronomy a heavy emphasis has been placed on obtaining observations with the highest spatial resolution. In this regard most electronic detectors have compared poorly to film. However, since film requires recovery which is impossible in most missions, astronomers have had to be satisfied with observations which were limited by the detector. As a numerical example, if we require one arc second resolution and we use a CCD with $15\text{ }\mu\text{m}$ pixels, a focal length in excess of 6 m is required for the optical system. Such arguments have lead to the choice of a 10 m focal length for the Advanced x-ray Astronomical Facility. The increased image size resulting from a large focal length is something of a mixed blessing. First, the field of view subtended by the detector is correspondingly reduced. For instance an 800×800 array of 1 arc second pixels subtends a field of just over 13 arc minutes. This can be compared with the diameter of the sun which is 32 arc minutes. Secondly, such an image contains a tremendous amount of information which has to be processed digitally. If the intensity scale is divided into 256 gray levels, the number of bits required to specify the image is in excess of half a million. Thus unless very high data rates are available, the transmission time for the image can be very much greater than the exposure time. This difficulty tends to negate the advantage provided by the high sensitivity of the CCD which is roughly three orders of magnitude better

than photographic emulsions and, for solar observation, allows exposure times of a few to a few tens of milliseconds. In principle this should open up a new field of coronal observations involving the dynamics of the coronal structures, changes at boundaries due to magnetic reconnection and the mechanisms of flaring events at high spatial resolutions. However, because of the high telemetry rates that are required the full potential of these studies has yet to be realized.

An added advantage of the CCD which results directly from its ability to detect single x-ray photons is its ability to minimize the effects of blooming. Blooming is the spreading of charge which has accumulated in overexposed areas to adjacent pixels of the CCD and is common to all electronic imaging systems. In many astronomical applications, the source object has a very large dynamic range and thus the average flux from the region might dictate an optimum exposure which causes blooming somewhere else on the chip. However, if the CCD is used in the single photon or spectrometric mode, many short exposures which will not cause blooming can be summed electronically, without losing spatial resolution because of the digital nature of the device, to provide a single image with an effective dynamic range larger than that of the CCD.

19.4 Conclusions

CCDs used for the detection of soft x rays are a relatively new technology. They hold great promise as astronomical x-ray imaging detectors combining high spatial resolution and energy sensitivity. In practical applications CCDs have both advantages and disadvantages over competing technologies. On the plus side, they are compact, low-power devices whose operation requires neither the use of high voltages or hard vacuums. On the negative side they have to be cooled to temperatures on the order of -100 °C for optimum performance.

It is almost certain that in the next few years they will see wide application in a variety of space missions and their success will determine their future development.

Acknowledgements

This work has been supported by NASA through several contracts.

References

- 19.1 P. Gorenstein, H. Gursky, F.R. Harnden, Jr., A. DeCaprio, and P. Bjorkholm: IEEE Trans. NS-22, 616 (1975)
- 19.2 R. Giacconi et al.: Astrophys. J. 230, 540 (1979)
- 19.3 J.M. Davis, J.W. Ting, and M. Gerassimenko: Space Sci. Instrum. 5, 17 (1979)
- 19.4 G. Renda and J.L. Lowrance: Proc. Symp. on CCD Technology, JPL SP 43-21, 91 (1975)
- 19.5 P. Burstein, A.S. Krieger, M.J. Vanderhill, and R.B. Wattson: Proc. SPIE 143, 114 (1978)
- 19.6 R.E. Griffiths, G. Polluci, A. Mak, S.S. Murray, D.A. Schwartz, and M.V. Zombeck: Proc. SPIE 244, 57 (1980)
- 19.7 R. Melen and D. Buss: Charge-Coupled Devices: Technology and Applications, IEEE Press (1977)

- 19.8 J. Janesick, J. Hynecek, and M.M. Blouke: Proc. SPIE 290, 165 (1981)
- 19.9 R.A. Stern, K. Liewer, and J.R. Janesick: Rev. Sci. Instrum. 54, 198 (1983)
- 19.10 D.A. Schwartz, R.E. Griffiths, S.S. Murray, M.V. Zombeck, and W. Bradley: Proc. SPIE 184, 247 (1979)
- 19.11 S. Marcus, R. Nelson, and R. Lynds: Proc. SPIE 172, 207 (1979)

4.12 The Design and Evaluation of Grazing Incidence Relay Optics

J.M. Davis, R.C. Chase, J.K. Silk, and A.S. Krieger

American Science and Engineering, Inc.
Cambridge, Massachusetts 02139

ORIGINAL PAGE IS
OF POOR QUALITY

THE DESIGN AND EVALUATION OF GRAZING INCIDENCE RELAY OPTICS

J.M. DAVIS, R.C. CHASE *, J.K. SILK and A.S. KRIEGER

American Science and Engineering, Inc., Cambridge, MA 02139, USA

X-ray astronomy, both solar and celestial, has many needs for high spatial resolution observations which have to be performed with electronic detectors. If the resolution is not to be detector limited, plate scales in excess of $25 \mu\text{m arc sec}^{-1}$, corresponding to focal lengths greater than 5 m, are required. In situations where the physical size is restricted, the problem can be solved by the use of grazing incidence relay optics. We have developed a system which employs externally polished hyperboloid-hyperboloid surfaces to be used in conjunction with a Wolter-Schwarzschild primary. The secondary is located in front of the primary focus and provides a magnification of 4, while the system has a plate scale of $28 \mu\text{m arc sec}^{-1}$ and a length of 1.9 m. The design, tolerance specification, fabrication and performance at visible and X-ray wavelengths of this optical system are described.

1. Introduction

Our understanding of the physical conditions existing in the solar corona and in particular of the importance of the interaction between the coronal gas and the solar magnetic field has increased rapidly during the past decade. This is a direct result of the technical achievements in the fabrication of grazing incidence optics which have enabled the spatial structures of the corona to be imaged at high resolution in soft X-rays. The visual identification of a diverse population of coronal structures has provided both a new framework for the reformulation of the more classical concepts of solar physics and an incentive for new ideas. Since many of the theoretical descriptions describe processes which occur over very small spatial scales, future advances will depend on the acquisition of even higher resolution observations.

In practice resolution is a function both of the intrinsic resolution of the optical system and the relationship of the size of the image to that of the detector pixel. In the past even images recorded on photographic emulsions have been detector limited [1] and the situation is much worse when solid state detectors are used. However, for space instruments, electronic imagery has several advantages over film. It provides better temporal resolution, it is easier to calibrate, and instrument recovery is not required. These are strong incentives for the development of electronic imaging systems and new techniques for improving resolution must be found.

When a system is limited by the detector, the two factors that affect the system angular resolution are the instrument's focal length and the dimensions of the

detector pixel. Although considerable efforts are being made to improve the latter, which will undoubtedly prove fruitful, they are unlikely to surpass the performance of photographic film. Therefore, it is essential to simultaneously explore the alternative of increasing the focal length of the X-ray telescope.

As a numerical example, if we baseline the pixel dimensions at $25 \mu\text{m}$, the focal length required to subtend an angle of 1 arc sec across a pixel is in excess of 5 m. Even this modest goal, which corresponds to a system resolution of order 2.8 arc sec (where we have defined the system resolution as $2\sqrt{2}$ pixel size), results in an instrument size which is sufficiently large to make it impractical for any but major programs. In normal incidence systems the solution to this problem would be to use secondary optics to increase the effective focal length by magnifying the primary image. Until recently this approach had not been followed for X-ray imaging because of the difficulties anticipated in the figuring of small grazing incidence optical elements and in the loss of signal to noise associated with the increased scattering from four reflections instead of the customary two. However, recent advances in fabrication technology, in particular in the in-process metrology and in the preparation of low-scatter surfaces, have made their development realistic. Consequently, under NASA sponsorship, we have designed a grazing incidence magnifier to be used in conjunction with an existing grazing incidence primarily to be used for solar studies.

1.1. Design considerations

Two distinct designs [2] for the magnifier are possible. Their principle of operation is shown in fig. 1 in which the focal distances are based on using an existing primary and a secondary magnification of 4. In the first

* Present address: Itek Optical Systems Division, Lexington, Massachusetts 02173, USA

GRAZING INCIDENCE SECONDARY OPTICS

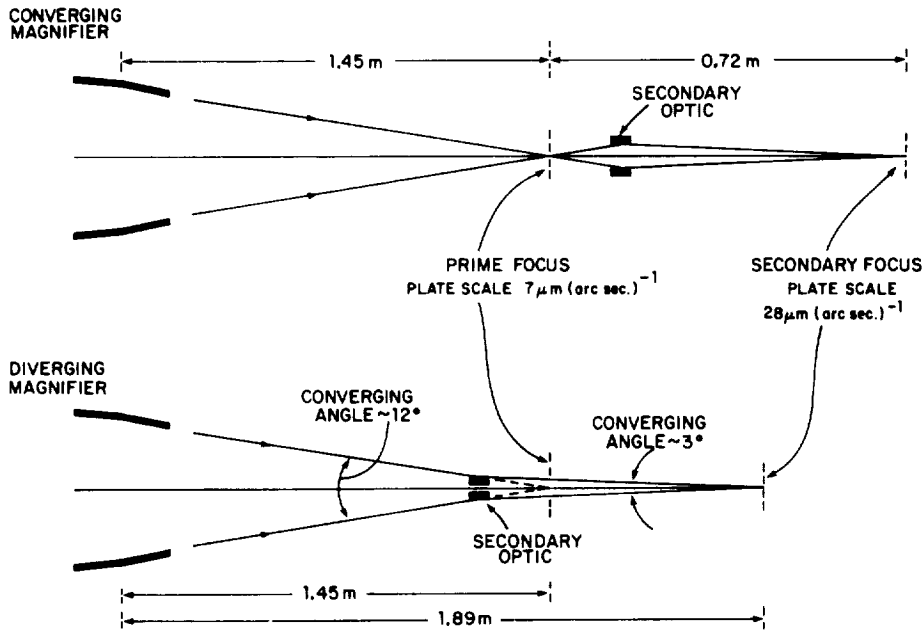


Fig. 1. Diagrams of the two possible designs for secondary grazing incidence optics. The dimensions refer to systems based on an existing primary mirror and a magnification of 4.

design the secondary optic acts as a microscope and is located behind the primary focal plane. It is known as a converging magnifier and has internally reflecting hyperboloid and ellipsoid surfaces. Alternatively the mirror can be placed in front of the focal plane where it acts as a Barlow lens. This configuration is known as a diverging magnifier and the mirror has externally reflecting hyperboloid-hyperboloid surfaces.

In both cases a considerable reduction in system length required for a given plate scale is achieved, the examples shown being roughly one third of the single mirror equivalent. In the present program, this param-

eter is of critical importance as the telescope will be flown as a sounding rocket payload. Of the two designs, for a given object distance and magnification, the diverging magnifier is the shorter and was selected. An additional benefit of this design is that the primary focused X-rays are bent through a smaller angle to reach the secondary focus, thus minimizing reflection losses and maximizing collecting area. In principle the design is fixed by choosing the magnification and the object distance. In practice increasing magnification lowers the system's speed, and increasing object distance, for a given magnification, lengthens the overall

Table 1
General properties of the X-ray mirrors

| | Primary | Secondary |
|-------------------------|--------------------------------|---------------------------------|
| Figure | Wolter-Schwarzschild | hyperboloid-hyperboloid |
| Material | fused silica | nickel coated beryllium |
| Principal diameter | 30.48 cm | 3.15 cm |
| Focal length | 144.9 cm | -19.4 cm |
| Geometrical area | | |
| On-axis | 41.5 cm ² | 20.2 cm ² |
| 3 arc min | 41.1 cm ² | 2.7 cm ² |
| Plate scale | 7.0 μm (arc sec) ⁻¹ | 28.1 μm (arc sec) ⁻¹ |
| Field of view | 60 × 60 (arc min) ² | 5 × 5 (arc min) ² |
| Resolving power (X-ray) | 1 arc sec | 1 arc sec |

instrument and also increases the physical size of the polished area and a compromise has to be made. We chose a magnification of 4 which provides a plate scale of $28 \mu\text{m arc sec}^{-1}$ while retaining reasonable exposure times. The object distance, which is the separation between the principal plane of the diverging magnifier and the primary focus, is 14.55 cm. This leads to an overall length for the imaging system of 189 cm which is within the 2 m limit established for the experiment. The general properties of the primary and secondary mirrors are summarized for reference in table 1.

2. Specification and fabrication

The equations for the external mirror surfaces of the diverging magnifier are:

1st Hyperboloid:

$$\frac{(z+c)^2}{c^2-b^2} - \frac{x^2}{b^2} = 1,$$

2nd Hyperboloid:

$$\frac{(z+2c+f)^2}{f^2-e^2} - \frac{x^2}{e^2} = 1,$$

where $c = 1.726981$, $b = 0.147002$, $e = 0.293203$, $f = 6.870371$.

The constants are defined in fig. 2, which shows the geometrical properties of the surfaces and their relation to the primary mirror. The first hyperboloid is located

so that one of its foci is co-spatial with the focus of the primary mirror. Its second focus is confocal with the first focus of the second hyperboloid. The second focus of this last surface forms, in turn, the secondary focus of the telescope. Since hyperboloids have two foci, small deviations from the design surface can be compensated for by axial displacements with no drawbacks other than a slight change in the overall focal length.

The mirror is fabricated, in two pieces, from optical grade beryllium. The reflective surfaces are electroless nickel which is applied to a depth of 0.13 mm over all the surfaces of the two elements. Each section is separately mounted to a central plate made of high-strength stainless steel. It is supported by four fingers which together intercept less than 3% of the open aperture. The steel chosen, 17-4PH, heat treated to condition H1150, provides a very close thermal match to the beryllium, which is essential to avoid radial distortions of the mirror surfaces under changing temperature conditions.

Although the primary mirror is made of uncoated fused quartz, there appear to be no scientific reasons for expecting the dissimilar surfaces to adversely affect performance. It will of course modify the passband of the instrument. The choice was made primarily for practical (e.g. cost, manufacturing capabilities of the local area) rather than scientific considerations. On the positive side it results in a lighter optic which allows the supporting fingers to be made narrower than would otherwise have been the case.

The dimensions of the pieces are shown in table 2.

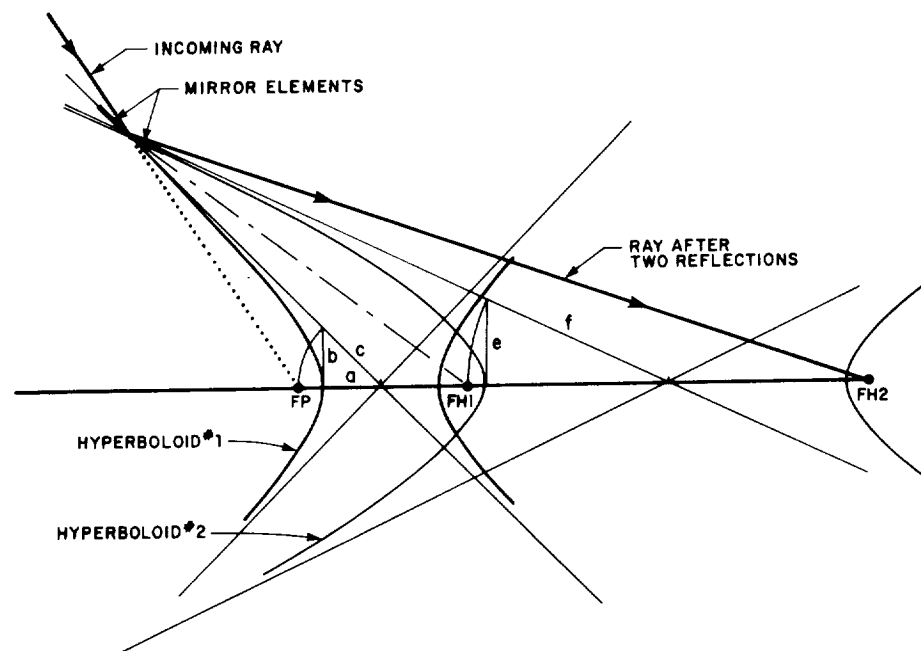


Fig. 2. The geometric relationships for hyperboloid-hyperboloid external surface mirrors.

Table 2

Secondary mirror demensions (Note: dimensions are in inches).

| | |
|--------------------------------------|---------|
| Diameter at front of 1st hyperboloid | 1.40804 |
| Diameter at rear of 1st hyperboloid | 1.24878 |
| Calculated diameter at mid-plane | 1.24000 |
| Diameter at front of 2nd hyperboloid | 1.23527 |
| Diameter at rear of 2nd hyperboloid | 1.16433 |
| Length of 1st hyperboloid | 0.91006 |
| Length of 2nd hyperboloid | 0.74605 |
| Gap for center plate | 0.10000 |

and the tolerances placed on the reflecting surfaces are shown in table 3. The most demanding tolerances that must be met during the fabrication of the mirror are the roundness of the elements and the deviation of the local slope from that predicted by the design curve. The principal roundness criterion is the variation in the difference between the forward and aft radii of each piece as a function of azimuth. This tolerance is referred to as $\Delta(\Delta R)$ and for this mirror has to be less than 1.5 μm . This is a tighter specification than usual for grazing incidence mirrors and is a consequence of their small size. However, the tolerance was met in the fabrication of an X-ray microscope [3] which had similar dimensions, and depends on the precision of the turning machine, for which this is not an unreasonable requirement. The axial slope error is 0.05 μm per cm. Achievement of this tolerance depends more on the sensitivity of the in-process metrology than on the figuring techniques. Recent improvements using laser scanning instruments make this possible. A typical observation, after reduction, is shown in fig. 3. The observations are repeatable and demonstrate the ability to measure the surface at the nanometer level.

Fabrication [4] of the secondary mirrors takes place in the following steps. First, the selected beryllium blanks are diamond turned to the approximate dimensions of the mirror elements. Since the polished area is relatively small, roll over at the ends will have a major negative effect. Therefore the blanks are turned and



Fig. 3. Analyzed data recorded during acceptance testing of an X-ray microscope [5]. In practice the data are continuous and deviations from the true surface of 1.0 nm or less are easily detectable.

lapped with removeable end pieces in place. The machined blanks are nickel plated and the surfaces are again diamond turned, lapped and the surface profile measured in-situ. The work is being performed in a modified Random [5] machine utilizing linear, air bearing slides to define tangents to the best fit circle. This circle is used to guide the lathe head which holds the mirror during turning and lapping. The radii of curvature, which in our case are on the order of 40 m, are determined with an accuracy of ± 2 cm and the location of the center of curvature with respect to the surface is known to be better than 1 part in 4000.

The in-process metrology uses a laser beam which is scanned over the surface in a controlled way and the local slope is determined from the reflected beam using a position-sensitive detector. The difference between the slope of the required surface and the best fit circle is corrected optically before display and the signal can also be integrated electronically to obtain the sagittal depth as a function of position. Once a satisfactory surface has been obtained the end pieces are removed from the finished mirror and the radial dimensions measured. Finally, the surfaces are superpolished to provide a low-scatter finish.

3. Expected performance

The design was based on optimizing the resolution and effective collecting area of the secondary mirror which are the most important performance parameters. Resolution depends strongly on off-axis angle, and collecting area is, in addition, a function of wavelength. The results of ray-tracing calculations are shown in figs. 4 and 5. NOTE: Resolution is defined in this case as the rms blur circle radius which in general underestimates the practical resolution except for on-axis rays.

Our ray tracing indicated that a trade-off had to be made between effective area, resolution and field of view. The design goal was to keep the rms blur circle

Table 3

Mirror tolerances (Note: tolerances are in inches).

| Optical tolerance | Specification |
|---|---|
| Out of roundness $\Delta R = (R_{\max} - R_{\min})$ | 40×10^{-6} |
| $\Delta \bar{R}$ | 200×10^{-6} |
| $\Delta(\Delta R)$ | 6×10^{-6} |
| Sagittal depth | 3×10^{-6} |
| Δ slope per axial length of one inch | 5×10^{-6} |
| Surface finish rms roughness | $< 10 \text{ \AA}$ |
| <i>Performance tolerance</i> | |
| Resolution | 2 arc sec with a one arc sec design goal |

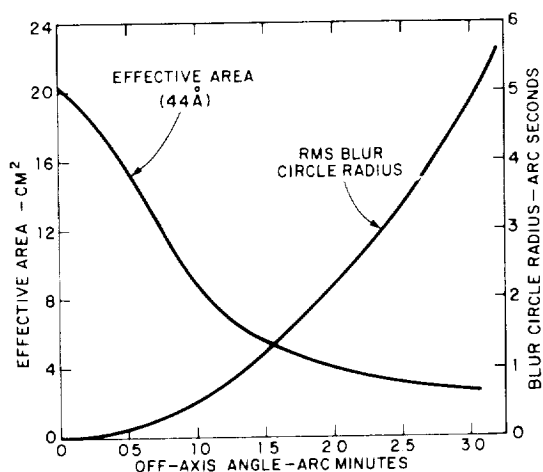


Fig. 4. The dependence of the effective area and the rms blur circle radius of the combined mirror system on the deviation from the optical axis of the incident ray.

radius below one arc second. This criterion limits the field of view to about 1 arc min. From fig. 4 it can be seen that even this restricted field is vignetted around the perimeter. The vignetting results in part from our choice of element length, for not all the primary rays which can contribute to the image are refocused. However, the rays that are missed are in fact poorly focused by the secondary mirror. Therefore, increasing the element length to catch these rays, although increasing the off-axis area, does so only at the expense of greatly increasing the blur circle radius. We have chosen to deliberately sacrifice some collecting area and accept the vignetting in order to maintain the highest image quality.

Alternatively, the field of view could be defined at the position where the effective area has dropped to one-tenth of its maximum value. This occurs a little beyond 3 arc min from the central axis. In practice solar active regions, which will typically be the target for this instrument, occupy areas of order (5×5) arc min²; and the vignetting at the edge of the field of view will be about 80%. It remains to be seen how severe an impact this will have on the observations. However, since recording and display will be performed electronically, if the system is properly calibrated, it should be possible to remove the effect of the vignetting during display processing. The field of view has to be matched to the physical size of the detector. At the secondary focus, an angular displacement of 5 arc min corresponds to 0.84 cm which provides a reasonable fit to typical CCDs suitable for use in the soft X-ray region.

The on-axis effective area of the combined system is approximately 20 cm² which is approximately 50% of the primary alone. This is a result of the combination of reflection losses and the limit set on the element lengths

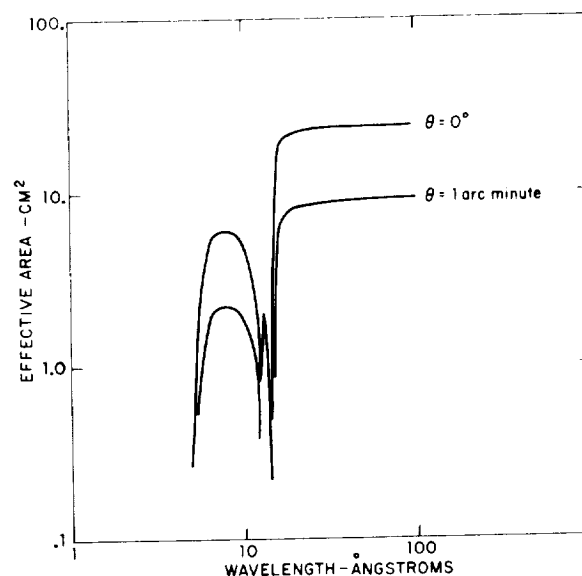


Fig. 5. The wavelength dependence of the effective area for on-axis ($\theta = 0^\circ$) and off-axis ($\theta = 1$ arc min) rays.

by the resolution criterion. The increase in image size reduces the secondary image brightness by a further factor of 16; therefore, the brightness at the center of the secondary image will be reduced by a factor of 30 from the brightness of the same feature viewed in the primary image. Since imaging bright solar features on photographic emulsions requires exposure times of 1–3 s at the primary focus, exposure times up to 100 s will be required at the secondary focus. Although this is possible, the temporal resolution would be poor and it is obvious that secondary optics and solid state detectors make natural partners. The increased sensitivity to soft X-rays of the latter, which is on the order of 1000, will allow exposure times of less than one second at the secondary focus. In this situation, time resolution is more likely to be limited by the data handling capability of the telemetry system than by the sensitivity of the detector.

4. Program status

Although it had been expected that the secondary optic would have been completed by the time of this workshop, this has not been the case. At this time turning and polishing of the first hyperboloid has just started. All the procedures that will be used have been tested on an aluminum blank and we have a high degree of confidence that the finished optic will meet our specifications.

Upon completion of the first hyperboloid the metrology will be reviewed and the surface of the second

hyperboloid recalculated if necessary. Following final assembly the spatial resolution of the optic will be tested in visible light using a USAF 1951 resolution target placed at the focus of a converging beam with an f -number of 4.6 and 97% occulted, the acceptance criterion at this stage is 2 arc sec resolution with 1 arc sec as a design goal.

Upon acceptance the optics performance will be tested in both visible light and X-rays in conjunction with the primary. Since the alignment of the two mirrors will be critical, we have designed a special alignment and holding mechanism which will be used for both flight and ground testing. The mechanism permits independent translation along three orthogonal axes together with rotations in pitch and yaw. Adjustment in increments of $2.54\text{ }\mu\text{m}$ is possible along the optical axis, in increments of $25\text{ }\mu\text{m}$ along the two orthogonal axes and of 1 arc sec about the two axes of rotation.

X-ray testing will be performed in AS&E's recently extended 100 m vacuum facility. Parameters measured will include spatial resolution, collecting area and point response function, both on- and off-axis and at several wavelengths including as a minimum 8.3 and $44\text{ }\text{\AA}$.

The revised delivery schedule has the optics being

delivered in August 1983. The complete testing program will take a further six months. The results of these tests will be reported in a subsequent paper.

It is a pleasure to acknowledge the help of the staff of the Applied Optics Center where the secondary optic is being fabricated. We would also like to thank Alan DeCew who has contributed to the fabrication procedures.

The work is being performed under NASA contract NAS5-25496.

References

- [1] J.M. Davis, A.S. Krieger, J.K. Silk and R.C. Chase, *Proc. Soc. Photo-Opt. Instr. Eng.* 184 (1979) 96.
- [2] R.C. Chase, A.S. Krieger and J.H. Underwood, *Appl. Opt.* 21 (1982) 4446.
- [3] J.K. Silk, *Proc. Soc. Photo-Opt. Instr. Eng.* 184 (1979) 40.
- [4] Applied Optics Center, Burlington, Massachusetts 01803, USA.
- [5] Random Devices Inc., Newbury, Massachusetts 01950, USA.

4.13 The Spatial Distribution of 6 Centimeter Gyroresonance Emission from a Flaring X-Ray Loop

S.W. Kahler, D.F. Webb, and J.M. Davis

American Science and Engineering, Inc.
Cambridge, Massachusetts 02139

and

M.R. Kundu

Astronomy Program
University of Maryland
College Park, Maryland 20742

ORIGINAL PAGE IS
OF POOR QUALITY

— — — — —

THE SPATIAL DISTRIBUTION OF 6 CENTIMETER GYRORESONANCE EMISSION FROM A FLARING X-RAY LOOP

S. W. KAHLER, D. F. WEBB, and J. M. DAVIS

American Science and Engineering, Inc., Cambridge, MA 02139, U.S.A.

M. R. KUNDU

Astronomy Program, University of Maryland, College Park, MD 20742, U.S.A.

(Received 5 September, 1983; in final form 12 March, 1984)

Abstract. We compare simultaneous high resolution soft X-ray and 6 cm images of the decay phase of an M3 X-ray flare in Hale Region 16413. The photographic X-ray images were obtained on an AS & E sounding rocket flown 7 November, 1979, and the 6 cm observations were made with the VLA. The X-ray images were converted to arrays of line-of-sight emission integrals and average temperature throughout the region. The X-ray flare structure consisted of a large loop system of length ~ 1.3 arc min and average temperature $\sim 8 \times 10^6$ K. The peak 6 cm emission appeared to come from a region below the X-ray loop. The predicted 6 cm flux due to thermal bremsstrahlung calculated on the basis of the X-ray parameters along the loop was about an order of magnitude less than observed. We model the loop geometry to examine the expected gyroresonance absorption along the loop. We find that thermal gyroresonance emission requiring rather large azimuthal or radial field components, or nonthermal gyrosynchrotron emission involving continual acceleration of electrons can explain the observations. However, we cannot choose between these possibilities because of our poor knowledge of the loop magnetic field.

1. Introduction

Recently advances have been made in mapping the microwave emission of both the flaring (Kundu and Vlahos, 1982) and the quiet (Kundu, 1982) Sun with high temporal and spatial resolution. While gyrosynchrotron emission from nonthermal electrons appears to be the obvious radiation mechanism for the flaring case, thermal mechanisms involving bremsstrahlung and gyroresonance emission at harmonics of the gyro-frequency are the best candidates in the non-flaring case. In the latter case the gyroresonance absorption process has been invoked for strong sunspot-associated magnetic fields and bremsstrahlung for the plage regions of weaker fields (Kundu *et al.*, 1977; Alissandrakis *et al.*, 1980; Felli *et al.*, 1981).

The combination of simultaneous X-ray observations and microwave maps has constrained the range of possible microwave emission mechanisms by allowing a determination of the electron thermal temperature T_e , linear emission integral $\int n_e^2 dl$, and, perhaps, electron density n_e , independently of the microwave observations. Some observers (Chiuderi-Drago *et al.*, 1982; Lang *et al.*, 1983; Shibasaki *et al.*, 1983) have found good agreement between the combined X-ray and microwave observations and the accepted radiation mechanisms for quiescent active region features. Others (Webb *et al.*, 1983; Schmahl *et al.*, 1982) have found some significant differences between the detailed locations of the active region X-ray and microwave sources. In cases of high

microwave brightness temperature, T_b , but low X-ray brightness, thermal bremsstrahlung is not a viable microwave emission mechanism, and gyroresonance absorption theory may require unrealistically large magnetic fields.

An interesting long-lasting burst on 19 May, 1979 was mapped at 20 cm by Velusamy and Kundu (1981). The 20 cm emission occurred in three looplike structures and was interpreted as either thermal gyroradiation or as nonthermal gyrosynchrotron emission. Subsequent comparison of these maps with soft X-ray images from the P78-1 satellite revealed that only one of the three 20 cm sources coincided with an X-ray source, leading Schmahl *et al.* (1983) to favor the nonthermal interpretation. The observations discussed here are similar to that event in that we have simultaneous 6 cm microwave maps and soft X-ray images during the decay of an M3/1B flare on 7 November, 1979. We find that the region of peak 6 cm emission is not spatially coincident with the bright soft X-ray loop responsible for the bulk of the X-ray emission. The mechanism of the 6 cm radiation emitted by the X-ray loop is discussed in detail using gyroresonance absorption theory and a simple model of the loop magnetic field.

2. Observations and Data Analysis

2.1. SOFT X-RAY DATA

The American Science and Engineering (AS & E) rocket flight of 7 November, 1979 was the first of two flights to observe the X-ray Sun at solar maximum. The grazing incidence X-ray telescope payload included a Wolter-Schwarzschild fused quartz mirror and four different filters. Full-disk images with a spatial resolution of approximately 2 arc sec were obtained on Kodak SO-212 film between 20:51 and 20:56 UT.

The brightest feature of these images was a flare loop in Hale Region 16413. For our quantitative analysis of this loop we used two adjacent exposures through a 1/2 mil beryllium filter and similar exposures through a 1 micron aluminized polypropylene filter, both obtained at about 20:52 UT. The images were converted to arrays of film density with pixels of size 2.8 arc sec square. The analytic procedure given in Vaiana *et al.* (1977) for conversion of film density to effective temperature and linear emission integral was followed closely. Calibrations of film density to energy flux and point spread functions at 8.3 Å and 44 Å were used in the analysis of the beryllium and polypropylene images, respectively. The deconvolved energy flux density image obtained with the polypropylene filter is shown in Figure 1. Arrays of 4 × 4 pixel averages (11.4 arc sec square) were used to obtain maps of effective temperatures and linear emission integrals at points along the loop.

2.2. MICROWAVE DATA

The radio observations were made of Hale Region 16413 at 6 cm with the Very Large Array (VLA) of the National Radio Astronomy Observatory between 19:50 and 20:37 and then 20:50 and 21:18 UT. Seventeen antennas were available during the observations, providing good $u-v$ coverage. The system was sensitive to structures smaller than 3 arc min because the shortest spacing used for these maps was 1200 λ.

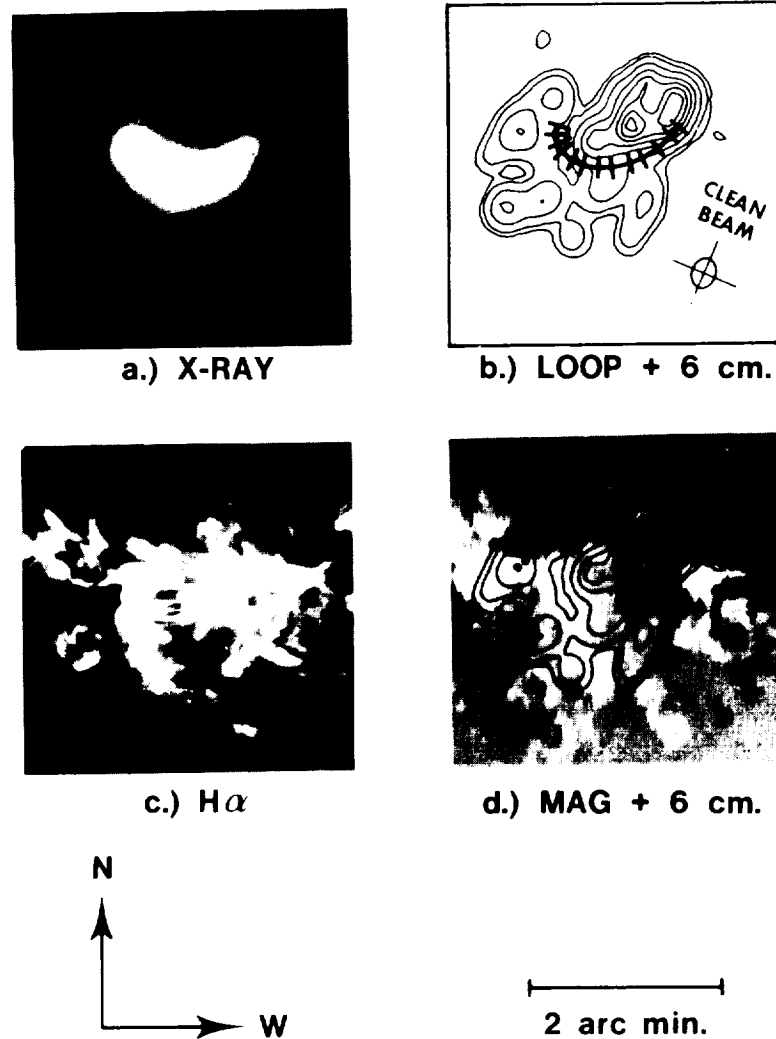


Fig. 1. (a) Deconvolved soft X-ray image of flaring loops in Hale plage region 16413 at 20:52 UT on 7 November, 1979. The original image was obtained on SO-212 film through a 1 micron polypropylene filter with a passband of 8-39, 44-64 Å. (b) Axis of the X-ray loop with every 15° positions of angle α indicated. 6 cm brightness temperature contours are superimposed. The temperature of the lowest contour is 10^6 K with successively higher contours separated by levels of 10^6 K. The radio map is an integration over 20:50-20:55 UT. The 6 cm beam resolution is shown; the long axis lies along celestial N-S. (c) Simultaneous H α image from the Holloman SOON station. (d) KPNO magnetogram at 19:18 UT with the superimposed 6 cm contours. All images are aligned to within ~ 10 arc sec.

Synthesized maps of total intensity were obtained of a field of view of 7.2×7.2 arc min with a synthesized beam of 19 arc sec by 15 arc sec. The observing procedure, calibration, and cleaning methods were similar to those discussed by Kundu and Velusamy (1980).

2.3. CHROMOSPHERIC AND PHOTOSPHERIC DATA

Hale Region 16413 was a new active region first observed near the east limb at S 15 on 3 November. Over the next several days the plage grew in area and intensity, reaching an area of 5000 millionths of a solar hemisphere on 7 November (*Solar-Geophysical Data*, 1980). Over this same period, the magnetic configuration became more complex; on 7 November it was a bipolar group with a delta configuration and peak fields exceeding 2000 G. This region was the brightest feature on the Sun in the 2.0 cm La Posta daily map.

A 1B H α flare occurred in region 16413 at S 13 E 22 beginning at approximately 20:00 UT with a maximum at $\sim 20:34$ UT. The associated GOES 1–8 Å X-ray flare reached a peak flux density of $3 \times 10^{-5} \text{ W m}^{-2}$ (M3) at about the same time. By 20:52 UT, the time of the observations reported here, the 1–8 Å flux density had declined to $1 \times 10^{-5} \text{ W m}^{-2}$ (M1). The 2.8 GHz Ottawa burst reported for this event was a gradual rise and fall burst with a peak flux of 14 sfu at 20:38 UT. The H α image from the Holloman Solar Optical Observatory Network (SOON) station is shown in Figure 1 along with the Kitt Peak National Observatory (KPNO) magnetogram obtained that day. The position of the H α image and magnetogram relative to the 6 cm map was found by converting the solar positions of the sunspots to celestial coordinates and matching those with the radio map. The X-ray, H α , and magnetogram images were aligned using sunspots as an intermediary. The resulting H α and X-ray images, magnetogram, and radio map are all aligned to within about 10 arc sec.

2.4. COMPARISON OF THE X-RAY AND MICROWAVE DATA

The images of Figure 1 show that the peak of the 6 cm emission is displaced from the X-ray loop by about 20 arc sec. It appears to be associated with a lower-lying compact H α flare region on the magnetic inversion line. The earlier radio maps near the peak of the event also show that the centroid of the emitting region coincides with the peak of Figure 1. The peak 6 cm region appears to have no well defined X-ray counterpart although the region is not devoid of X-ray emission. Unfortunately, lack of a well defined X-ray structure has precluded a detailed analysis of that feature. Our interest here is in using the plasma parameters deduced for the X-ray loop to determine the mechanism of the 6 cm radiation from the loop. There are three generally accepted candidate mechanisms: (1) thermal bremsstrahlung; (2) thermal gyroresonance emission; and (3) nonthermal gyrosynchrotron emission.

The length of the X-ray loop is about 80 arc sec, measured linearly between the footpoints while its diameter varies between ~ 35 –45 arc sec, depending upon where it is measured. The longest dimensions of the H α flare regions at each footpoint of the loop are ~ 35 –45 arc sec. Since these are in agreement with the X-ray observations, we have used an average diameter of 40 arc sec. The temperature distribution of the X-ray loop is confined to the narrow range $T_e \approx 6.5$ – 8.5×10^6 K. The temperature of the top of the loop averaged over an area 57 arc sec along the loop by 34 arc sec across the loop is $T_e = 8.2 \pm 0.2 \times 10^6$ K and for the larger region of 120 arc sec by 80 arc sec, encom-

passing the entire loop and surrounding area, is $T_e = 7.6 \pm 0.3 \times 10^6$ K. The peak linear emission integral along the line of sight near the axis of the loop is $\int n_e^2 dl = 1.4 \times 10^{29} \text{ cm}^{-5}$. For a loop thickness of $l = 40 \text{ arc sec} \approx 3 \times 10^9 \text{ cm}$, $n_e = 7 \times 10^9 \text{ cm}^{-3}$.

To estimate the importance of thermal bremsstrahlung to the radio emission, we first calculate the optical depth at 6 cm using the derived X-ray parameters in the equation from Kundu (1965),

$$\tau_x = \frac{0.16}{\nu^2 T_e^{3/2}} \int n_e^2 dl, \quad (1)$$

where ν is the frequency of the radio observations. For $\int n_e^2 dl = 1.4 \times 10^{29} \text{ cm}^{-5}$, $\nu = 5.0 \text{ GHz}$, and a lower limit of $T_e = 6 \times 10^6 \text{ K}$, we get an upper limit of $\tau_x = 6.1 \times 10^{-2}$. Therefore, for these conditions the corona is optically thin and $T_b = \tau_x T_e = 3.7 \times 10^5 \text{ K}$. This value is about an order of magnitude less than the observed values along the loop. Thermal bremsstrahlung may therefore make a small contribution to the observed T_b , but it cannot be the dominant emitting mechanism.

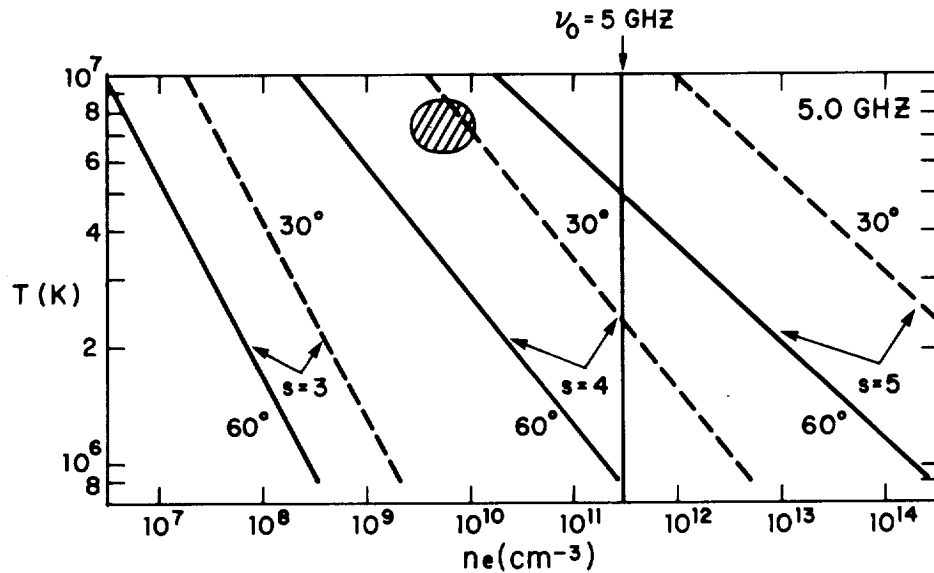


Fig. 2. Loop electron densities and thermal temperatures required to achieve an optical depth of unity in the extraordinary modes of the $s = 3, 4$, and 5 resonant harmonics of the gyrofrequency. The assumed frequency is 5.0 GHz (6 cm) and the e -folding length of the magnetic field magnitude is 10^9 cm . The optical depth scales linearly with both this length and with n_e , being less than unity to the left and greater than unity to the right of each curve. Dashed and solid lines show unity optical depths for values of θ , the angle between the magnetic field and the line of sight, equal to 30° and 60° . The magnetic field intensities required for each harmonic are 600 G for $s = 3$, 450 G for $s = 4$, and 360 G for $s = 5$. Vertical line indicates the density corresponding to the plasma frequency of 5.0 GHz , to the right of which wave propagation does not occur. The shaded oval corresponds to the range of X-ray loop parameters deduced for the 7 November, 1979 flare.

After Kundu *et al.* (1980).

Another obvious candidate for the 6 cm emission mechanism is thermal emission due to the enhanced absorption at low harmonics of the gyrofrequency ν_H . Following Kundu *et al.* (1980), we show in Figure 2 the loop densities and temperatures required to achieve an optical depth of $\tau = 1$. We assume, as they did, an e -folding length of 10^9 cm for the magnetic field scale length. For the density and temperature range characteristic of the X-ray loop (shown by the shaded oval) we see that only the fourth and fifth ($s = 4, 5$) harmonics are viable emission mechanism candidates to produce $\tau \leq 1$. These harmonics require magnetic fields of 450 and 360 G, respectively, which do not seem unreasonable in view of the fact that the loop footpoints are in the vicinity of the strong spot fields of the active region.

The optical depth due to gyroresonance absorption is a strong function of θ , the angle between the magnetic field direction and the line of sight. Using the expression for the absorption coefficient of the extraordinary mode and the e -folding thickness of the resonance region of 10^9 cm given by Takakura and Scalise (1970) and by Kundu *et al.* (1980), we have

$$\tau_{\text{res}} = 0.030 \Phi n_e \left(\frac{2kT_e}{m_0 c^2} \right)^{s-1} (\sin \theta)^{2s-2} (c_1 + c_2 \cos \theta) \frac{l}{\nu_H}, \quad (2)$$

where $\Phi = 10.7$ and 63.6 for $s = 4$ and 5 , $\nu_H = s^{-1} \times 5.0$ GHz, l is the scale length of the magnetic field, and c_1 and c_2 are functions of s and θ given explicitly in Takakura

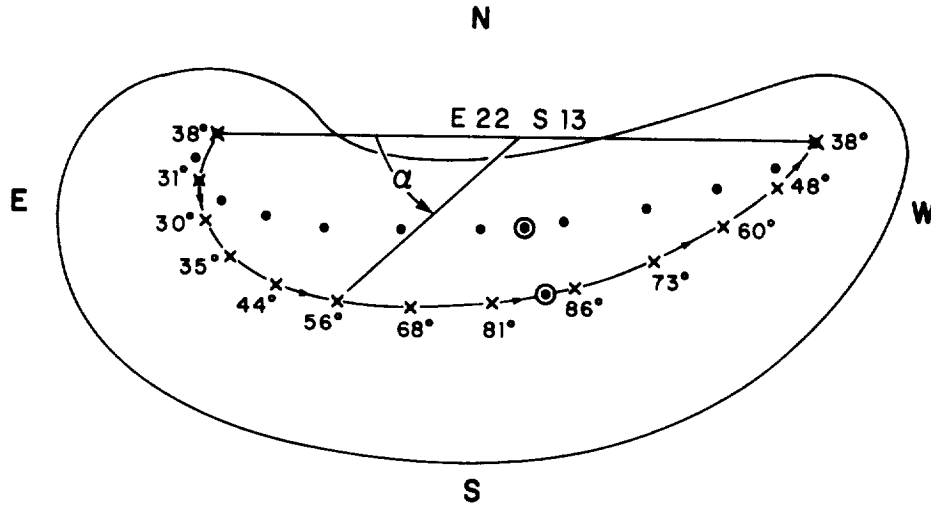


Fig. 3. Schematic model of the X-ray flare loop shown in Figure 1(a). The flare center is taken as E 22 S 13 on the solar disk, but with the loop endpoints assumed to lie in an east-west direction. Curved line is the semicircular loop axis projected onto the plane of the sky with crosses at every 15° increment of α , the angle subtended to the axis of the loop by the arc length, increasing westward from the eastern footpoint. The angle given at each cross is that of θ , the angle between the magnetic field direction and the line of sight. The plane of the loop lies 32° south of the line of sight. A similar semicircular loop lying in a plane in the local solar vertical is shown by the dots; this gave a poor match to the observed loop perspective and was not used. Points with circles indicate positions where $\theta = 90^\circ$ for each loop. The outer line shows approximate outline of loop edges for loop diameter of 40 arc sec or $\sim 3 \times 10^9$ cm.

and Scalise (1970). We can use Equation (2) to calculate τ_{res} for $s = 4$ or 5 at any part of the loop by using the values of n_e and T_e derived from the X-ray observations, assuming an l consistent with those observations, and knowing θ .

In order to find θ at points along the axis of the loop, we have modelled the X-ray loop as a simple semicircular structure as shown in projection in Figure 3. Since the flare position was E22, we assume a 22° angle between the line of sight and the meridional plane bisecting the loop. The flare was 13° south of the solar equator, which places it about 17° south of the Sun–Earth line. We assumed the loop plane to project radially from Sun center and then calculated the shape of the projected loop axis shown by the dots of Figure 3. The ratio of the projected loop height to the projected loop length was far too small to match the values observed for the X-ray loop. A good match was achieved by letting the plane of the loop be 32° south of the plane containing the Earth–Sun line, which means the loop plane lay 15° south of the local solar vertical. The angle α is defined by the eastern footpoint, the center of curvature of the loop and the point of interest along the loop. Assuming the B field parallel to the loop axis, we have calculated the corresponding values of θ and τ_{res} for 15° increments in α and plotted them in Figure 4. A value of $l = 10^9$ cm, about one third of the apparent loop diameter derived from the X-ray measurement was used. The measured X-ray temperature was used at each point, and $n_e = 7 \times 10^9 \text{ cm}^{-3}$ was assumed for all points. It is known (Kundu, 1965) that the quasi-longitudinal approximation used here is only valid for $\sin^4 \theta \ll 4s^2 \cos^2 \theta$, which limits θ to values less than $\sim 80^\circ$. A substantial decrease in τ is expected at $\theta > 80^\circ$, the region between the dashed lines in Figure 4 (Holman, private communication). With increasing α , θ would become greater than 90° on the west side of the loop, but we have assumed a polarization change and use $\theta = 180^\circ - \theta$ for the extraordinary mode calculation in that region. The 6 cm polarization maps obtained at the VLA were too noisy to be used as a test of this assumption.

The observed 6 cm optical depths along the loop axis derived from the radio brightness temperature maps using $T_b = T_e (1 - e^{-\tau})$ are compared with the calculated gyroresonance optical depths in Figure 4. The $s = 5$ optical depths are in fair agreement with the observed values for large angles near the loop top, and the $s = 4$ depths are in fair agreement near the footpoints, but neither individual curve matches the relatively flat distribution of τ with θ over the entire loop. Qualitatively, it is conceivable that the loop magnetic field intensity could be around 450 G at the footpoints, decreasing to around 360 G at the top in just such a way that the sum of the $s = 4$ and $s = 5$ fortunately, the photospheric magnetic field observations were severely degraded due to poor observing conditions, so that no quantitative estimates of the magnetic field intensity along the loop could be made. In addition, since the assumed value of l could be in error by a factor of 3 or more, this scenario seems unlikely.

The comparisons of Figure 4 are further limited by our lack of detailed knowledge of the topology of the loop magnetic field. If the ratio of the loop height to the distance between footpoints is larger or smaller than assumed, the range of θ will be somewhat larger or smaller, respectively, than that shown in Figure 4. However, a lower assumed loop height would require that the plane of the loop be inclined at more than 15° to the

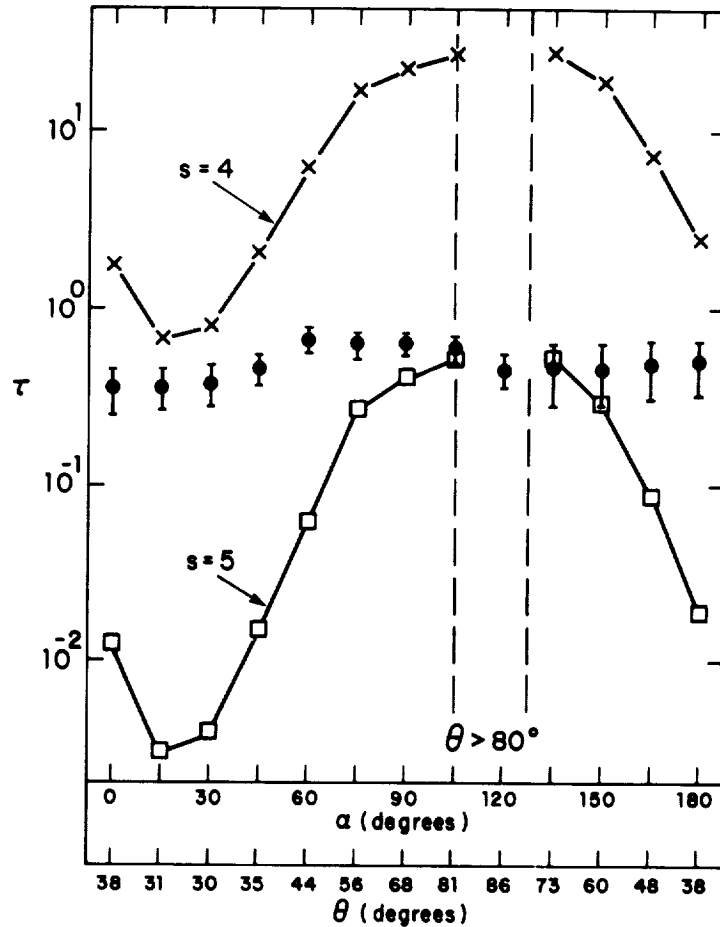


Fig. 4. Crosses and squares show optical depth τ calculated for the fourth and fifth harmonics of the gyrofrequency as a function of both α and θ for the loop model of Figure 3. The quasi-longitudinal approximation is not valid for $\theta \geq 80^\circ$, the region between the dashed lines; a drop in τ is expected there. A density of $n_e = 7 \times 10^9 \text{ cm}^{-3}$ and a magnetic field scale length of $l = 10^9 \text{ cm}$ was assumed for 5.0 GHz; temperatures were then calculated from X-ray measurements for each point along the loop. Filled circles show the values of τ deduced from the measured radio brightness temperatures at corresponding points along the loop.

local solar vertical direction. Another possibility is that the loop field lines are helical, rather than parallel to the loop axis. If so, a range of θ would be associated with each angle α of Figure 4, resulting in a flatter distribution of τ with θ . We calculate that an angle of about 40° between an azimuthal field component B_ϕ and the longitudinal component B_z , both assumed constant throughout the loop, will result in fair agreement between the $s = 5$ curve and the observed values of τ shown in Figure 4. For example, in this case the values of τ at $\theta = 30^\circ$ and 40° are 0.13 and 0.21, respectively, which are only slightly lower than the observed values. Furthermore, the lack of any drop in

τ for $\theta > 80^\circ$ is also expected in this model. Because the observed loop is thick, with $L/a = 4$, where a is the loop radius and L the loop length, the threshold for the external kink instability (Spicer and Brown, 1981)

$$B_\phi^2 \ln(L/a) > B_z^2 \quad (3)$$

is not satisfied, and the loop is stable. A similar range of θ might also result from a spreading of the cross section of the loop with height, particularly near the footpoints. Thus we see that the assumption of large azimuthal or radial field components can result in much better agreement between the observed and calculated values of τ than that shown in Figure 4.

A final candidate to explain the optical depth of at least part of the loop is gyrosynchrotron emission. Petrosian (1982) has modelled the gyrosynchrotron emission expected from a flaring semicircular magnetic loop similar to our model shown in Figure 3. For loops near the center of the solar disk his uniform trap model, in which the magnetic field is nearly uniform and the electron pitch angle distribution isotropic, yields maximum microwave emission near the loop top and a minimum at the footpoints. In his nonuniform trap model, in which the magnetic field intensity decreases rapidly with height and the pitch angle distribution is broadest at the footpoints, the strongest emission arises from the footpoints. The uniform trap model was preferred to account for the observations (cf., Kundu *et al.*, 1982) of the impulsive phase peak flare emission at the tops of loops, but in our case, if gyroresonance absorption from either the $s = 4$ or $s = 5$ harmonic is effective at the loop top as shown in Figure 4, the nonuniform trap model better fits the data.

Any nonthermal electrons responsible for the 6 cm emission observed at 20:52 UT cannot have been accelerated tens of minutes earlier near the flare maximum. Using the equation of Kundu and Vlahos (1982) for the collisional deflection time of energetic electrons,

$$\tau_D = 2 \times 10^8 E^{3/2} (\text{keV}) n_e^{-1} \text{ s}, \quad (4)$$

we find that τ_D is only 30 s for the derived loop density and for $E = 100$ keV electrons. Thus, the gyrosynchrotron explanation for the 6 cm emission from the X-ray loop requires continuous or continual acceleration of electrons of $E \geq 100$ keV, the energy range required for microwave gyrosynchrotron emission (Takakura, 1972).

3. Discussion and Conclusion

We have used the plasma parameters deduced from X-ray observations to infer the 6 cm radiation mechanisms of the bright flare loop in its decay phase. The apparently simple geometry of the X-ray loop has allowed us to test gyroresonance absorption theory using a semicircular loop model to look for the strong dependence of τ on θ . Earlier studies (e.g., Schmahl *et al.*, 1982) had invoked gyroresonance harmonics only as high as the fourth ($s = 4$) to explain the 6 cm emission from active regions, but in our study the large values of T_e and n_e combined with the low 6 cm values of τ have made $s = 5$ harmonic

emission a possibility. For a uniform axial field we find that no single gyroresonance harmonic can account for the relatively flat distribution of τ vs θ , but an unlikely combination of the $s = 5$ harmonic at the top of the loop and the $s = 4$ harmonic at the loop footpoints is consistent with the observations. Magnetic fields in the range of 360 to 450 G are required for these harmonics. We also investigated the effect of non-parallel field distributions on the gyroresonance model and find that azimuthal or radial field components at an angle of about 40° to the axial field can explain the observations.

We also investigated qualitatively gyrosynchrotron emission from nonthermal electrons to explain the 6 cm emission mechanism along at least the lower part of the loop. Gyrosynchrotron emission as an alternative to thermal gyroradiation had earlier been suggested by Velusamy and Kundu (1981) as the radiation mechanism for 20 cm postflare loops they observed with the VLA. They used the ≥ 2.5 hr lifetime of the observed burst to infer the loop magnetic field strength on the assumption that this lifetime was the radiative decay time of mildly relativistic electrons. Their calculation is valid, however, only if the radiative loss time is shorter than the collisional loss time, which, in their case, requires $n_e \leq 10^8 \text{ cm}^{-3}$. This condition is definitely not fulfilled in our case, where $n_e \sim 7 \times 10^9 \text{ cm}^{-3}$. Thus if the 6 cm emission is nonthermal, it must be from newly accelerated electrons and not from electrons surviving from the earlier flare maximum.

Nonthermal emission has also been suggested for some 6 cm quiescent active region loops by Webb *et al.* (1983). In their case the 6 cm components were not associated with any X-ray emission. The low temperatures and/or densities inferred from the X-ray observations permitted only low harmonics ($s = 2$ or 3) with their associated unrealistically large magnetic fields (900 or 600 G, respectively) as acceptable gyroresonance absorption mechanisms. Schmahl *et al.* (1982), faced with essentially the same dilemma in a similar study, suggested localized current systems to enhance the coronal magnetic fields and retain the gyroresonance mechanism. In our case the fifth harmonic of gyroresonance emission requires a field of only 360 G, which is not unreasonable in view of the presumed strong fields of the flare region. We find that such thermal emission can explain the observations over the whole loop only if there are rather large azimuthal or radial field components. Alternatively, the gyrosynchrotron hypothesis can account, at least in part, for the observations if a continuous supply of energetic electrons is available. We conclude that one or a combination of these mechanisms is the likely source of the microwave emission, but that we cannot choose among them because of our poor knowledge of the loop magnetic field.

This lack of more detailed knowledge of the loop magnetic field intensity and geometry has been a serious obstacle in our effort to assess the role of gyroresonance emission as the 6 cm radiation mechanism. Although the X-ray loop was large, with fairly uniform brightness and well determined longitudinal temperature and density distributions, important assumptions about the shape and orientation of the loop and the helicity and scale length of the magnetic field were required to calculate the gyroresonance optical depth. We find that models based on either gyroresonance or gyrosynchrotron mechanisms can be made to fit the observations by a suitable choice

of poorly known parameters. Complete microwave polarization and multi-frequency observations are required to better infer the coronal magnetic field. Future tests of gyroresonance theory will benefit greatly from a combination of such high-resolution microwave observations and X-ray and photospheric magnetogram images, and should allow us to confirm or eliminate one of these mechanisms from consideration.

Acknowledgements

We are grateful to J. Harvey of KPNO for providing the magnetogram and white-light images and to D. Rust for the Holloman H α film. We acknowledge the useful comments of the referee and helpful discussions with E. Schmahl and G. Holman about gyroresonance absorption. The work at AS & E was supported by NASA contracts NAS5-25496 and NASW-3586. SWK thanks M. Shea of AFGL for her generous support. The work of MRK at the University of Maryland was supported by NASA contract NSG 5320, NASA grant NGR 21-002-199 and NSF grant ATM 81-03089.

References

- Alissandrakis, C. E., Kundu, M. R., and Lantos, P.: 1980, *Astron. Astrophys.* **82**, 30.
 Chiuderi-Drago, F., Bandiera, R., Falciani, R., Antonucci, E., Lang, K. R., Willson, R. F., Shibasaki, K., and Slottje, C.: 1982, *Solar Phys.* **80**, 71.
 Felli, M., Lang, K. R., and Willson, R. F.: 1981, *Astrophys. J.* **247**, 325.
 Kundu, M. R.: 1965, *Solar Radio Astronomy*, Interscience, New York.
 Kundu, M. R.: 1982, *Rep. Prog. Phys.* **45**, 1435.
 Kundu, M. R. and Velusamy, T.: 1980, *Astrophys. J.* **240**, L63.
 Kundu, M. R. and Vlahos, L.: 1982, *Space Sci. Rev.* **32**, 405.
 Kundu, M. R., Alissandrakis, C. E., Bregman, J. D., and Hin, A. C.: 1977, *Astrophys. J.* **213**, 278.
 Kundu, M. R., Schmahl, E. J., and Gerassimenko, M.: 1980, *Astron. Astrophys.* **82**, 265; Erratum, 1980, *Astron. Astrophys.* **91**, 377.
 Kundu, M. R., Schmahl, E. J., and Velusamy, T.: 1982, *Astrophys. J.* **253**, 963.
 Lang, K. R., Willson, R. F., and Gaizauskas, V.: 1983, *Astrophys. J.* **267**, 455.
 Petrosian, V.: 1982, *Astrophys. J.* **255**, L85.
 Schmahl, E. J., Kundu, M. R., Strong, K. T., Bentley, R. D., Smith, J. B., Jr., and Krall, K. R.: 1982, *Solar Phys.* **80**, 233.
 Schmahl, E. J., Kundu, M. R., Landecker, P. B., and McKenzie, D. L.: 1983, *Solar Phys.* **83**, 3.
 Shibasaki, K., Chiuderi-Drago, F., Melozzi, M., Slottje, C., and Antonucci, E.: 1983, *Solar Phys.* **89**, 307.
Solar-Geophysical Data Bulletins: 1980, published by WDC-A for Solar-Terrestrial Physics, NOAA, Boulder, Colorado, U.S.A.
 Spicer, D. S. and Brown, J. C.: 1981, in S. Jordan (ed.), *The Sun as a Star*, NASA SP-450, Washington, D.C., p. 413.
 Takakura, T.: 1972, *Solar Phys.* **26**, 151.
 Takakura, T. and Scalise, E., Jr.: 1970, *Solar Phys.* **11**, 434.
 Vaiana, G. S., Van Speybroeck, L., Zombeck, M. V., Krieger, A. S., Silk, J. K., and Timothy, A.: 1977, *Space Sci. Instr.* **3**, 19.
 Velusamy, T. and Kundu, M. R.: 1981, *Astrophys. J.* **243**, L103.
 Webb, D. F., Davis, J. M., Kundu, M. R., and Velusamy, T.: 1983, *Solar Phys.* **85**, 267.



4.14 Small-Scale Flux Emergence and the Evolution of Equatorial Coronal Holes

John M. Davis

American Science and Engineering, Inc.
Cambridge, Massachusetts 02139

ORIGINAL PAGE IS
OF POOR QUALITY

SMALL-SCALE FLUX EMERGENCE AND THE EVOLUTION OF EQUATORIAL CORONAL HOLES

JOHN M. DAVIS

American Science and Engineering, Inc., Fort Washington, Cambridge, MA 02139, U.S.A.

(Received 18 October, 1982; in final form 4 September, 1984)

Abstract. To study the formation and development of coronal holes, their association with X-ray bright points has been investigated. The areal density of X-ray bright points was measured within the boundaries of coronal holes and was found to increase linearly with time for each of the three, long-lived, equatorial coronal holes of the Skylab era. Analysis of the data shows that the effect is not the result of global changes in bright point number and is therefore a property of the restricted longitude region which contains the coronal hole. The bright point density at the time of the hole's formation was also measured and, although the result is more uncertain, was found to be similar to the bright point number over the solar surface. No association was found between bright points and the rate of change of coronal hole area.

1. Introduction

Coronal holes are regions of exceptionally low density in the inner corona, which have been observed at both soft X-ray and He I 10830 Å wavelengths for over a decade. However, a definitive explanation of their formation and subsequent evolution is still missing. For example, X-ray observations exist for the birth of only a single coronal hole (Solodyna *et al.*, 1977). In this case the hole developed rapidly, i.e., in less than a day and with a growth rate three times faster than the long term average of all holes; a result which is consistent with the He I 10830 Å coronal hole observations (Harvey and Sheeley, 1979). This behavior led Nolte *et al.* (1978a) to conclude that the conditions for coronal hole development are built up over a longer period of time and the actual birth is triggered by an event (or events) which leads to the rapid opening of field lines. This hypothesis is supported by the observations of the photospheric magnetic field beneath the hole which shows little if any change during the period of the hole's rapid growth (Harvey and Sheeley, 1979).

The subsequent development of coronal holes has been linked to the process of random walk diffusion, proposed by Leighton (1964) to explain the transport of surface magnetic fields. This phenomenological description is known generically as the model of locally unbalanced flux (Timothy *et al.*, 1975; Bohlin, 1976; Bohlin and Sheeley, 1978; Broussard *et al.*, 1978). In it the flux from an emerging bipolar magnetic region (BMR) reconnects to opposite but pre-existing flux in its immediate environment. The reconnection results from the separation, through diffusion of the original BMR, and leads to regions of a single polarity with field lines that are open rather than closed.

Observational support for the model was provided by the results of several studies (Timothy *et al.*, 1975; Bohlin, 1977; Nolte *et al.*, 1978a) which measured the areal growth and decay rates of coronal holes. They found that on average $(dA/dt)_{ch}$ is

approximately $1.5 \times 10^4 \text{ km}^2 \text{ s}^{-1}$. In Leighton's (1964) model for the transport of surface magnetic fields, this rate can be related to the diffusion coefficient, D , through the equation (Mosher, 1977)

$$D = \frac{1}{4} \frac{L^2}{t} = \frac{1}{4\pi} \left(\frac{dA}{dt} \right),$$

where L^2 is the mean square displacement over the time interval t . The coronal hole measurements lead to a value for D of $1.2 \times 10^3 \text{ km}^2 \text{ s}^{-1}$ which, although somewhat larger, is still consistent with Leighton's value of $800 \text{ km}^2 \text{ s}^{-1}$. However, Mosher (1977), who repeated Leighton's analysis using more recent observations and analytical techniques, concluded that the most probable value of D is of order $200 \text{ km}^2 \text{ s}^{-1}$ and that values as high as $1000 \text{ km}^2 \text{ s}^{-1}$ can definitely be excluded. Thus the coronal hole observations join the growing body of evidence, e.g., measurements of the supergranule velocity fields (Worden and Simon, 1976) and the background and large-scale magnetic fields (Stenflo, 1976; Howard and LaBonte, 1981; Topka *et al.*, 1982) which cast doubt on the general applicability of the random walk process to the transport of surface fields.

Sheeley and Harvey (1981) have interpreted their most recent He I 10830 Å observations of mid-latitude holes in terms of their diffusion and regeneration by the organizing action of differential rotation. While their model still retains random walk diffusion as the basic mechanism, apparent growth rates which differ from the canonical value can be explained. However, differential rotation as an organizing force has obvious limitations when applied to the equatorial coronal holes whose boundaries rotate rigidly (Timothy *et al.*, 1975; Wagner, 1975).

An alternative approach would be to supplement the Leighton mechanism by adopting the suggestion of Marsh (1978). He showed that the interaction of ephemeral regions (*ER*) with elements of the supergranulation network could increase the apparent rate of magnetic diffusion, measured over large scales, by superposing large discrete changes upon the random walk mechanism. The changes have the characteristic length of the *ER* pole separation and by integrating over their observed size spectrum Marsh obtained a value for D of $830 \text{ km}^2 \text{ s}^{-1}$. This is close to the value required to explain coronal hole growth and therefore *ERs* might be expected to play a role in their development.

Inspection of the X-ray images of the Skylab coronal holes (see, e.g., Zombeck *et al.*, 1978) suggests that coronal holes are formed with few X-ray bright points (*XBP*), the X-ray analogue of an ephemeral region, within their boundaries but that their number increases on successive appearances of the hole. To quantify this impression and to amplify our knowledge of the formation and development of coronal holes, we have sought answers to the following questions. (1) Is the evolution of coronal holes accompanied by an increase in the bright point areal density? (2) Do coronal holes form in regions where the bright point areal density is enhanced? (3) Is the bright point areal density related to changes in the growth and/or decay of coronal holes?

2. Analysis and Results

X-ray bright points (XBPs) are tracers of the emergence patterns of small scale activity. They are clearly identified, discrete sites of emerging magnetic flux with a relatively high frequency of occurrence. They possess two other characteristics which are important for a statistical study; namely, they are shortlived with a mean lifetime of 8 hr and they possess a wide latitude distribution which is not restricted to the active region zone (Golub *et al.*, 1974). Although a more detailed analysis of the observations suggest that their latitude distribution during the period of the Skylab studies was bimodal (Golub *et al.*, 1975), the current study is restricted to the near-equatorial latitudes over which their distribution is approximately flat. Consequently, it was not considered necessary to correct for non-uniformities in the bright point latitude distribution and an equal weight is attributed to the occurrence of an XBP anywhere within a coronal hole.

The coronal hole set used for the study is based on the Skylab atlas prepared by Nolte *et al.* (1976). Six X-ray holes were identified. Of these two have been excluded from the following analysis because they document only the final stages of the hole's existence. The excluded holes are, in the standard nomenclature, CH5, which was observed only during the first rotation, and CH3. The latter, although visible on three rotations, appeared as a badly fragmented extension of the northern polar hole which is consistent with its identification by Timothy *et al.* (1975), using Fe xv observations, as the remnant of a hole formed at least seven rotations before being observed from Skylab. Of the remaining holes CH1 also connects, at times, to the northern polar hole. When this occurs the measurements have been restricted to latitudes below 40°N. The restriction is designed to remove any influence that the northern polar hole, which was a continuous but evolving feature during the Skylab period (Bohlin, 1977; Sheeley, 1980), may have on the data.

To maximize the statistics of each XBP observation, the longest exposure (256 s) through the long wavelength filter (3–32; 43–54 Å bandpass) was used to count the bright points. In the following analysis these numbers will be compared with a global bright point average based on the statistics of Golub *et al.* (1976) which reflect the number of XBPs observed on a 4 s exposure. Different exposures are used because of the difference in visibility of bright points when observed against backgrounds of either the weakly emitting, large scale structure or emissionless, coronal holes. To remove any bias introduced by the background, bright points are generally counted using an exposure which is short enough to suppress the emission from the large scale structure and which for the Skylab instrument was 4 s. This of course reduces the number of XBPs which are observed and increases the statistical uncertainty in any single observation.

In this study we are counting bright points *only* in coronal holes where the obscuration is negligible and are therefore free to use the longest available exposure to maximize the number of counts and minimize the statistical variations. When the two data sets are compared the observations have been normalized following the procedure of Golub *et al.* (1974). They demonstrated that as the exposure was lengthened the

number of XBP observed increased, asymptotically approaching a value ten times that on a 4 s exposure at 256 s. This result suggests that all XBPs belong to the same size distribution and that at the longest exposure all the bright points are being seen. Therefore the numbers of bright points observed on the 256 s exposures should be the total number. The numerical values of bright point areal density quoted in this paper will always refer to this total number. When comparisons are made, the bright point averages of Golub *et al.* (1976) have been normalized to correspond to the same total number.

The simplest procedure for our study would be to straightforwardly count the numbers of XBPs within each hole. However, since the area of each hole changes considerably from one rotation to the next, we have instead determined the number of bright points per unit area. This areal density has been obtained by measuring both the area of the coronal hole and the average number of XBPs it contains at central meridian passage. To improve the precision of the areal measurements an average coronal hole area was derived from nine observations made at approximately 12-hr intervals between ± 48 hr of CMP, when suitable images were available. The bright point average was based on five counts made over the same period but at 24 rather than 12-hr intervals to allow the points in the earlier sample to decay below the visibility threshold. The longer interval between observations is necessary because the bright point lifetime is a function of the exposure and increases to 15 hr at 256 s. The 24-hr interval between bright point counts was chosen as a compromise between the need to obtain as many measurements as possible but to have the measurements statistically independent.

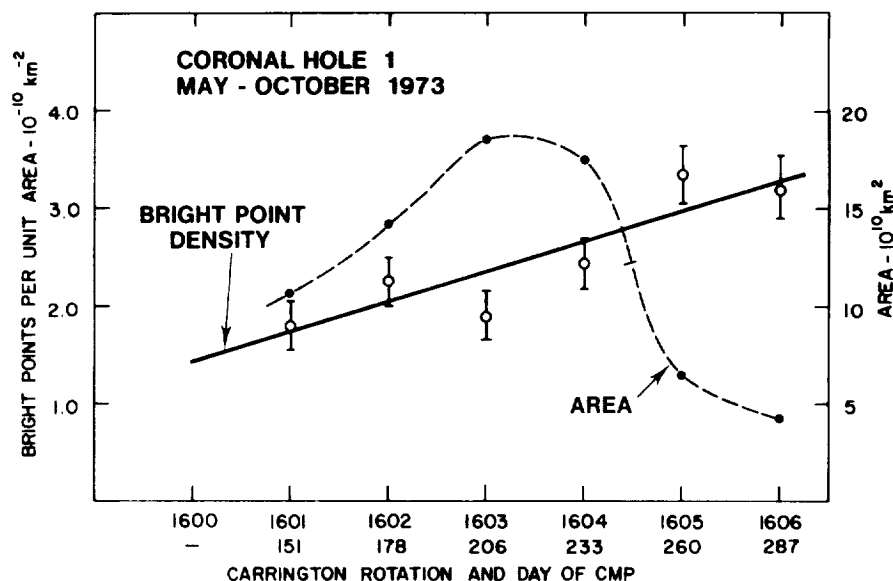


Fig. 1. The variation with time of the X-ray bright point areal density, within CH1. The solid line is a least squares fit to the data points which were measured at successive CMPs. The area of the coronal hole is shown by the broken line.

Of the questions posed in the introduction, the first, namely, whether there exists an increase in the bright point areal density within coronal holes as a function of time, is most easily answered. CH1 was investigated first and the results are shown in Figure 1. The open circles show the bright point areal density measured at each central meridian passage; the error bars represent only the statistical uncertainty in the number of points. Over the six-month interval the bright point density shows a steady increase with no apparent correlation with either the area of the hole, which varies considerably from rotation to rotation (broken line), or its rate of change. A least squares fit to the XBP data produces the solid line shown which has a correlation coefficient of 0.88.

Of the remaining holes in the data set, two, CH2, and CH4, last for more than 3 rotations. The same analysis was applied to these holes and produced similar results (Figure 2 and 3). In all three cases as the hole evolves, the bright point areal density, and therefore the rate of new flux emergence increases linearly, reaching several times its initial value before the coronal hole loses its identity.

The initial density and rate of increase for the four measured holes are summarized in Table I. The first observation of CH1 had a measured areal density of $1.6 \times 10^{-10} \text{ km}^{-2}$. However, CH1 had existed for at least two rotations before it was observed by Skylab (Bohlin, 1977). Using the least squares fit to extrapolate over these two rotations, we obtain an estimated value of $1.16 \times 10^{-10} \text{ km}^{-2}$ for the initial density. For CH6, which was the only hole to actually be observed forming on the disk, the initial density, which is the highest of the four, is the average value measured over the first three days of its existence.

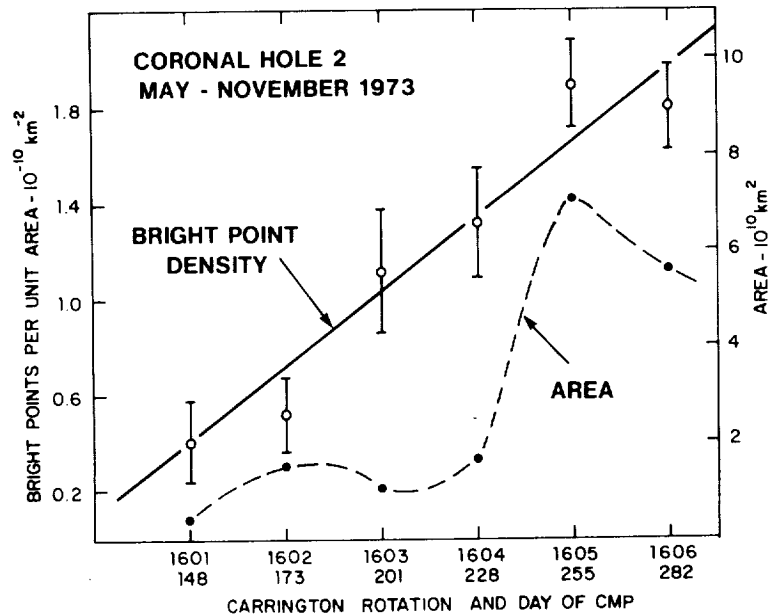


Fig. 2. The temporal variation of the bright point areal density and coronal hole area for CH2 in the same format as Figure 1.

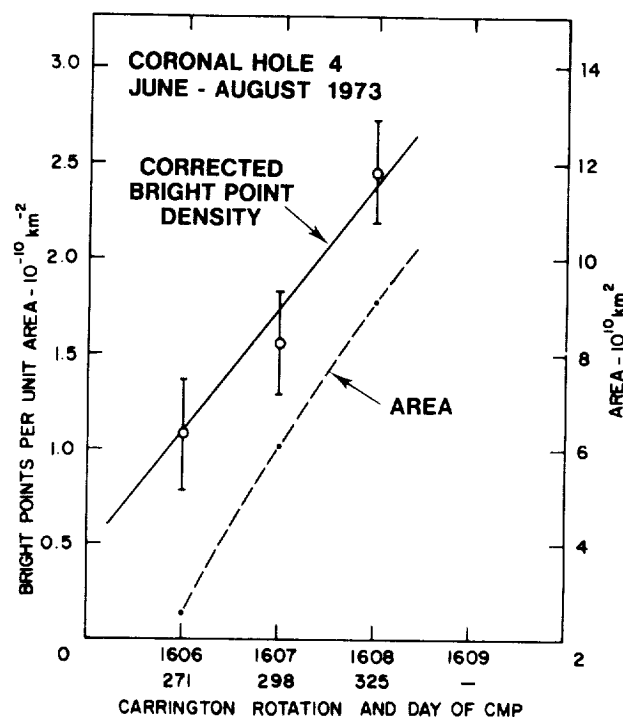


Fig. 3. The temporal variation of the bright point areal density and coronal hole area for CH4. The data points have been corrected by subtracting the globally averaged density from the values measured within the coronal hole.

TABLE I
X-ray bright point data

| Coronal hole identification | Bright point density XBP km^{-2} | | Rate of increase XBP $\text{day}^{-1} \text{km}^{-2}$ |
|-----------------------------|---|---------------------------------|---|
| | Initial | Global average | |
| CH1* | 1.16×10^{-10} | 0.90×10^{-10} | 1.14×10^{-12} |
| CH2 | 0.41×10^{-10} | 0.95×10^{-10} | 1.17×10^{-12} |
| CH4 | 1.43×10^{-10} | 1.14×10^{-10} | 1.67×10^{-12} |
| CH6 | 1.65×10^{-10} | 1.61×10^{-10} | — |
| Mean | $1.16 \pm 0.54 \times 10^{-10}$ | $1.15 \pm 0.32 \times 10^{-10}$ | $1.33 \pm 0.30 \times 10^{-12}$ |

* Values for CH1 have been extrapolated back two rotations.

To determine whether holes form in regions which are characterized by an enhanced bright point areal density, it is necessary to establish a global average for use as a baseline against which the initial densities can be compared. During Skylab the number of bright points on the Sun at any instant of time ranged from 400 ± 90 to 1200 ± 160 (Golub

et al., 1976). The average is usually taken as 500 corresponding to an areal density of $8.3 \times 10^{-11} \text{ km}^{-2}$. However, the bright point statistics suggest an excess within the equatorial latitudes (Golub *et al.*, 1975). The excess is such that two thirds of the bright points lie between $\pm 30^\circ$ latitude. Consequently, an average areal density of $1.1 \times 10^{-10} \text{ km}^{-2}$ is more appropriate for the region containing the equatorial coronal holes.

To compare the data against a single global average is questionable because it makes no allowance for the wide variation in the average bright point number over this period. Therefore, we have attempted to construct a more realistic average which reflects the temporal variation of the bright point density and allows one to assign a value to the density existing at the actual time of the formation of the coronal hole. Since the individual observations are restricted to a single hemisphere, the global average has been calculated in the form of a 360-degree running mean using the data set of Golub *et al.* (1976). They compiled averages of XBP observed between latitudes 30° N and 30° S in 10° longitude intervals on 4 s exposures. The data have been normalized as described earlier and a 36-point or 360° running average computed. The eight-month curve is reproduced in Figure 4. Each point is centered on the position of the CMP of the particular Carrington longitude interval and the data are displayed as number per unit area so that they can be compared directly with the results from the earlier analyses. It can be seen that the temporal variation is aperiodic with a magnitude ranging between $0.72 \times 10^{-10} \text{ km}^{-2}$ to $1.71 \times 10^{-10} \text{ km}^{-2}$. There are at least two distinct episodes of enhanced bright point emergence; however, the central meridian passages of the coronal holes appear to fall randomly across the distribution.

Comparison of the initial bright point density with the corresponding global average (Table I) shows that they are essentially identical, and one concludes that there is no evidence for coronal hole formation in regions where the small scale flux emergence is either enhanced or reduced. This conclusion is based, however, on only four data points

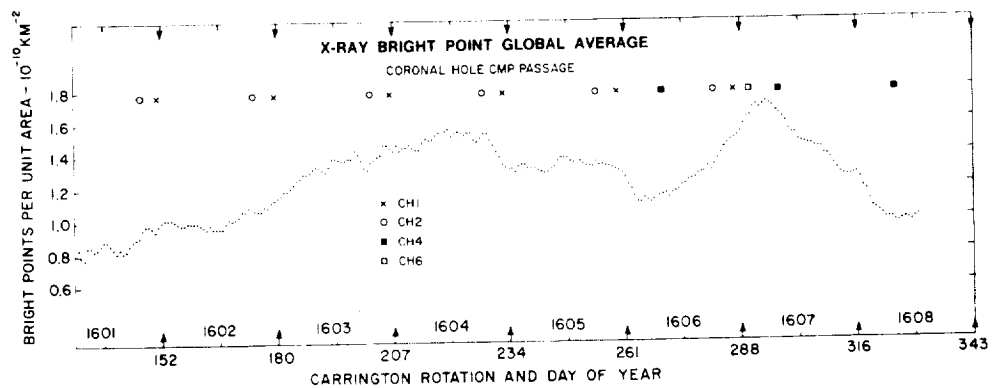


Fig. 4. The variation of the global bright point density with time for the period of the Skylab mission (May–November 1973). The curve is a 360° running average of the bright points counted between latitudes 30° N and 30° S and normalized to include all the points visible on the longest X-ray exposure (256 s). The CMPs of the four coronal holes are indicated.

of which one point (CH1) is based upon a linear extrapolation of the data. The validity of this extrapolation is open to question, since the detailed behavior of the XBP distribution prior to 28 May, 1973 is unknown, with one exception. The exception was a rocket flight which occurred on 8 March, 1973 (Davis and Krieger, 1982) precisely three rotations (81 days) before the first observed CMP of CH1. The corresponding global bright point density for this observation was $0.95 \times 10^{-10} \text{ km}^{-2}$ which is similar to the density observed at the start of the Skylab period. Therefore the data are consistent with a constant level of XBP emergence over this period, which justifies the use of the extrapolation.

Finally, by subtracting the global background evaluated at the time of the coronal hole's CMP, a set of points are obtained which give the density excess above the global average. These points can be used to repeat the evolutionary study of the areal density. Apart from an offset, neither the corrected points nor the slopes of the fitted lines exhibit any but minor differences when compared to the original data (Figure 3). This implies that a global variation can be ruled out as being responsible for the steady increase in bright point density found within coronal holes.

3. Conclusions

From a study of the association between X-ray bright points and coronal holes, a linear relationship has been discovered between coronal hole evolution and the emergence of small-scale magnetic flux. The relationship has the form of a steady growth in the emergence of the small scale flux which is maintained throughout the hole's life and reaches levels 3 to 4 times the global average before the hole disappears. Our analysis has ruled out global variations in the bright point emergence patterns as an explanation of this result, which implies that this is a local property of the longitude region which contains the coronal hole. We also found that the initial appearance of coronal holes with an apparent absence of bright points within their boundaries is misleading. Instead the data indicate that coronal holes are born in regions where the XBP density is not suppressed below the global average. In fact, the data show a very slight excess in the rate at which the magnetic flux is emerging. The first result supports and extends the work of Nolte *et al.* (1978b), who found that the number of XBP located near the boundaries of coronal holes also increased as the hole aged.

In the introduction the need for modifying Leighton's model of random walk diffusion in order to explain the rate of growth of coronal holes was described and Marsh's hypothesis (1978) was identified as a candidate for this role. If his hypothesis is valid, one would expect to find a relationship between bright point density and the rate of change of coronal hole area. To test for the latter a comparison between the long term average rate of change of coronal hole area, defined as the difference in area measured on subsequent rotations, and the areal density was made. A scatter plot constructed from the data from all the holes had a random appearance indicating the poor correlation ($r \sim -0.3$) between the two variables. Before dismissing Marsh's hypothesis we should realize the limitations of the present study. Only time-averaged data have been used, and

the averaging period is long compared to bright point life times. Although the use of long-term averages for studying the rate of change of hole area was justified by Nolte *et al.* (1978a), who found excellent agreement between short (~ 2 days) and long-term rates of change, there may be subtleties which have been missed, for instance, perhaps only bright points close to the boundary influence the growth rate. Unfortunately, the present data are insufficient to test this hypothesis.

To summarize the answers to the three questions posed in the introduction, we have found that the evolution of coronal holes is accompanied by a substantial increase in the bright point density, but this increase is not related to the rates of growth or decay. The statistical evidence provides only weak support for the formation of coronal holes in regions of above normal bright point density. Where it is possible to study the formation of a hole in detail, as in the case of CH6 (see Solodyna *et al.*, 1977, Figure 3), a bright point is present at, or close to, the birth of the hole. This could be a random association, and since the subsequent changes in coronal hole area are not directly coupled to the small-scale flux emergence, our observations suggest that the XBP acts only as the catalyst which triggers the birth of the coronal hole within a larger region, in which the conditions for hole formation have been preset by a systematic, widespread mechanism (Frankenthal and Krieger, 1977; Nolte *et al.*, 1978a).

Acknowledgements

It is a pleasure to acknowledge the many useful discussions held with my colleagues D. Webb and A. Krieger of AS&E since the inception of this project and the assistance of Ms. Jadwiga Zmijewski in the counting of bright points. The author also wishes to thank an anonymous referee for his critical review of the original draft of this paper.

The work has been supported by NASA under contract NAS5-25496.

References

- Bohlin, J. D.: 1976, in D. J. Williams (ed.), *Physics of Solar Planetary Environments*, Vol. I, Am. Geophys. Union, p. 114.
- Bohlin, J. D.: 1977, *Solar Phys.* **51**, 377.
- Bohlin, J. D. and Sheeley, Jr., N. R.: 1978, *Solar Phys.* **56**, 125.
- Broussard, R. M., Sheeley, Jr., N. R., Tousey, R., and Underwood, J. H.: 1978, *Solar Phys.* **56**, 161.
- Davis, J. M. and Krieger, A. S.: 1982, *Solar Phys.* **80**, 295.
- Frankenthal, S. and Krieger, A. S.: 1977, *Solar Phys.* **55**, 83.
- Golub, L., Krieger, A. S., Silk, J. K., Timothy, A. F., and Vaiana, G. S.: 1974, *Astrophys. J.* **189**, L93.
- Golub, L., Krieger, A. S., and Vaiana, G. S.: 1975, *Solar Phys.* **42**, 131.
- Golub, L., Krieger, A. S., and Vaiana, G. S.: 1976, *Solar Phys.* **50**, 311.
- Harvey, J. W. and Sheeley, Jr., N. R.: 1979, *Space Sci. Rev.* **23**, 139.
- Howard, R. and LaBonte, B. J.: 1981, *Solar Phys.* **74**, 131.
- Leighton, R. B.: 1964, *Astrophys. J.* **140**, 1547.
- Marsh, K. A.: 1978, *Solar Phys.* **59**, 105.
- Mosher, J. M.: 1977, Ph.D. Thesis, California Institute of Technology, Pasadena, California.
- Nolte, J. T., Krieger, A. S., Timothy, A. F., Vaiana, G. S., and Zombeck, M. V.: 1976, *Solar Phys.* **46**, 291.
- Nolte, J. T., Gerassimenko, M., Krieger, A. S., and Solodyna, C. V.: 1978a, *Solar Phys.* **56**, 153.

- Nolte, J. T., Davis, J. M., Gerassimenko, M., Krieger, A. S., Solodyna, C. V., and Golub, L.: 1978b, *Solar Phys.* **60**, 143.
- Sheeley, Jr., N. R.: 1980, *Solar Phys.* **65**, 229.
- Sheeley, Jr., N. R. and Harvey, J. W.: 1981, *Solar Phys.* **70**, 237.
- Solodyna, C. V., Krieger, A. S., and Nolte, J. T.: 1977, *Solar Phys.* **54**, 123.
- Stenflo, J. O.: 1976, in V. Bumba and J. Kleczek (eds.), 'Basic Mechanisms of Solar Activity', *IAU Symp.* **71**, 69.
- Timothy, A. F., Krieger, A. S., and Vaiana, G. S.: 1975, *Solar Phys.* **42**, 135.
- Topka, K., Moore, R., LaBonte, B. J., and Howard, R.: 1982, *Solar Phys.* **79**, 231.
- Wagner, W. J.: 1975, *Astrophys. J.* **198**, L141.
- Worden, S. P. and Simon, G. W.: 1976, in V. Bumba and J. Kleczek (eds.), *IAU Symp.* **71**, 121.
- Zombeck, M. V., Vaiana, G. S., Haggerty, R., Krieger, A. S., Silk, J. K., and Timothy, A.: 1978, *Astrophys. J. Suppl.* **38**, 69.

4.15 The Cyclical Variation of Energy Flux and Photospheric Magnetic Field
Strength from Coronal Holes

David F. Webb and John M. Davis

American Science and Engineering, Inc.
Cambridge, Massachusetts 02139

ORIGINAL PAGE IS
OF POOR QUALITY

1000
 900
 800
 700
 600
 500
 400
 300
 200
 100
 0

THE CYCLICAL VARIATION OF ENERGY FLUX AND PHOTOSPHERIC MAGNETIC FIELD STRENGTH FROM CORONAL HOLES

DAVID F. WEBB and JOHN M. DAVIS

American Science and Engineering, Inc., Fort Washington, Cambridge, MA 02139, U.S.A.

(Received 5 August, 1985)

Abstract. We measured the average soft X-ray emission from coronal holes observed on images obtained during AS & E rocket flights from 1974 to 1981. The variation of this emission over the solar cycle was then compared with photospheric magnetic flux measurements within coronal holes over the same period. We found that coronal hole soft X-ray emission could be detected and that this emission appeared to increase with the rise of the sunspot cycle from activity minimum to maximum. Our quantitative results confirmed previous suggestions that the coronal brightness contrast between holes and large-scale structure decreased during this period of the cycle. Gas pressures at the hole base were estimated for assumed temperatures and found to vary from about $0.03 \text{ dyne cm}^{-2}$ in 1974 to $0.35 \text{ dyne cm}^{-2}$ in 1981. The increase in coronal hole X-ray emission was accompanied by a similar trend in the surface magnetic flux of near-equatorial holes between 1975 and 1980 (Harvey *et al.*, 1982).

1. Introduction

Coronal holes were first and most easily identified in soft X-ray and XUV images as regions of very low brightness in comparison to surrounding active regions or other large-scale structures. They were first studied in detail during the Skylab period and their observational characteristics at that phase of the solar cycle were well established. These characteristics included nearly rigid rotation, large, low-latitude extensions of polar holes, near-zero X-ray emission and a strong correlation between the low-latitude portions of holes and high speed solar wind streams (Krieger *et al.*, 1973; Nolte *et al.*, 1976; Zirker, 1977; Sheeley and Harvey, 1978, 1981). Also during this period a nearly one-to-one association was established between coronal holes and regions of open field lines derived from potential magnetic field calculations using observed photospheric line-of-sight fields (Altschuler and Newkirk, 1969; Levine, 1977, 1982). However, it has been suggested that these relationships are less clear during other parts of the cycle. For instance, Levine (1977, 1982) showed that during Skylab and around solar maximum open fields also emanate from active regions, and Nolte *et al.* (1977) and Sheeley and Harvey (1978, 1981) showed that during solar minimum and the rise to maximum of cycle 21 there were solar wind sources that could not be identified with low-latitude coronal holes.

Since the Skylab mission, ground-based He I 10830 Å images have been used (e.g., Sheeley and Harvey, 1978, 1981) for determining coronal hole positions and areas and their relationships to solar wind speeds and geomagnetic activity indices. In addition, rocket flights have provided us with high resolution, full-disk solar X-ray images at

approximately 18-month intervals. At AS & E these images have been used in a program to study the evolutionary characteristics of coronal holes over the solar cycle, including the degree of their correspondence to open field configurations. As part of this program, Kahler *et al.* (1983) compared coronal hole boundaries determined from both AS & E X-ray and Kitt Peak 10830 Å images. During their study, they found what appeared to be a decrease in the brightness contrast between the coronal holes and large-scale coronal structure in the period after 1974. Such a 'weakening' of holes was also observed in the 10830 Å data alone during 1976–1977 by Sheeley and Harvey (1978). Also, Levine (1982) determined that the association between predicted open magnetic structures and 10830 Å coronal holes was less clear after the Skylab period.

Finally, Harvey *et al.* (1982) found that low-latitude coronal holes contained three times more flux near sunspot maximum than near minimum even though their areas were comparable. Taken together, these results suggest that the distinction in terms of open and closed fields between coronal holes and large-scale structure is not always as clear as during the declining phase of solar cycle 20.

This paper describes the next phase of our program, the photometric analysis of the soft X-ray energy flux from coronal holes from 1974 to 1981 and the comparison of this flux with measurements of photospheric magnetic field strength. We have addressed two questions: (1) In terms of apparently contradictory results using Skylab X-ray data, is X-ray emission from coronal holes detectable above background, and if so does it vary over the solar cycle? (2) Can a change in the plasma conditions within low-contrast coronal holes explain the difference in visibility, and are these conditions in turn related to the increased photospheric field strength found in the coronal holes of the new cycle?

2. Observational Analysis

Our approach to this study involved three phases. First, we selected those X-ray images which most clearly showed coronal holes for calibration and measurement of hole emission. The minimum average energy flux within the coronal hole boundaries as determined by Kahler *et al.* (1983) was measured and variations in this emission over the solar cycle were examined. Second, the average magnetic field strength within the same X-ray coronal hole boundaries was measured. Finally, the X-ray and magnetic flux measurements were compared to each other and to the magnetic flux measurements of Harvey *et al.* (1982).

2.1. CALIBRATION AND ANALYSIS OF THE X-RAY DATA

Since Skylab, full-disk soft X-ray images of the solar corona have been obtained on seven AS & E rocket flights in 1974, 1976, 1978, 1979, and 1981. Kahler *et al.* (1983) provided details on the dates, times, and instrumentation of the flights (except for 17 November, 1976). Images on these flights were obtained with two mirror systems, a Kanigen metal mirror and a fused silica mirror. To minimize the relative uncertainties between flights and the background from scattering effects, we restricted our analysis to images obtained with the fused silica mirror and through aluminized polypropylene

TABLE I
Selected X-ray images and magnetograms

| X-ray images | Time (UT) | Carrington rot. | CR ^a | Mt. Wilson daily maps ^b | Kitt Peak synoptic maps |
|---------------|-----------|-----------------|-----------------|---|-------------------------|
| 27 June, 1974 | 1948 | 1616 | 6 | 26 June; 1456 27 June; 1652 28 June; 1715 | No |
| 17 Nov., 1976 | 1827 | 1648 | 32 | 16 Nov.; 1659 17 Nov.; 2243 18 Nov.; 1751 | No |
| 31 Jan., 1978 | 1841 | 1664 | 16 | 31 Jan. 1 Feb.; 1846 | Yes (gap) |
| 13 Feb., 1981 | 1916 | 1705 | 41 | 14 Feb.; 2326 | Yes |

^a The interval in Carrington rotations between rocket observations. The 1974 observations occurred six rotations after Skylab.

^b Times are UT at the midpoint of the mapping interval.

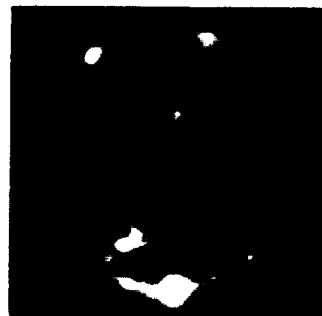
TABLE II
X-ray energy flux in coronal holes

| Date | Coronal hole subareas | PP exposure time (s) | Average PDS density | Net intensity (erg cm ⁻² s ⁻¹) |
|---------------|-----------------------------|----------------------|---------------------|---|
| 27 June, 1974 | Large hole: center | 19.7 | 21.6 ± 1.2 | 2.2 ± 0.8 × 10 ⁻³ |
| | | 59.2 | 32.6 ± 2.2 | 2.1 ± 0.7 × 10 ⁻³ |
| | Large hole: northwest | 19.7 | 19.5 ± 0.8 | 1.7 ± 1.3 × 10 ⁻³ |
| | | 59.2 | 27.8 ± 1.9 | 1.4 ± 0.5 × 10 ⁻³ |
| | North polar hole | 19.7 | 21.0 ± 2.1 | 2.1 ± 1.6 × 10 ⁻³ |
| | | 59.2 | 30.3 ± 4.1 | 1.8 ± 1.2 × 10 ⁻³ |
| 17 Nov., 1976 | Equatorial extension of SPH | 3.7 | 13.0 ± 0.7 | 7.5 ± 3.3 × 10 ⁻³ |
| | | 16.5 | 18.8 ± 1.2 | 5.6 ± 2.0 × 10 ⁻³ |
| | South polar hole | 3.7 | 12.6 ± 0.8 | 6.4 ± 3.0 × 10 ⁻³ |
| | | 16.5 | 17.4 ± 1.1 | 4.6 ± 1.7 × 10 ⁻³ |
| | North polar hole | 3.7 | 13.5 ± 0.8 | 8.3 ± 3.8 × 10 ⁻³ |
| | | 16.5 | 19.7 ± 1.3 | 6.1 ± 2.2 × 10 ⁻³ |
| 31 Jan., 1978 | Southwest hole: center | 2.6 | 18.6 ± 0.9 | 1.7 ± 0.9 × 10 ⁻² |
| | | 8.7 | 25.8 ± 1.3 | 1.6 ± 0.9 × 10 ⁻² |
| | Southwest hole: limb | 2.6 | 18.1 ± 1.0 | 1.6 ± 0.8 × 10 ⁻² |
| | | 8.7 | 25.4 ± 0.8 | 1.5 ± 0.9 × 10 ⁻² |
| 13 Feb., 1981 | Southern hole: limb | 2.8 | 24.3 ± 1.4 | 1.5 ± 1.2 × 10 ⁻¹ |
| | | 9.6 | 39.2 ± 1.6 | 1.3 ± 1.0 × 10 ⁻¹ |
| | Southern hole: center | 2.8 | 26.6 ± 1.7 | 1.8 ± 1.3 × 10 ⁻¹ |
| | | 9.6 | 41.8 ± 1.5 | 1.5 ± 1.2 × 10 ⁻¹ |

CORONAL X-RAY OBSERVATIONS 1974 - 1981



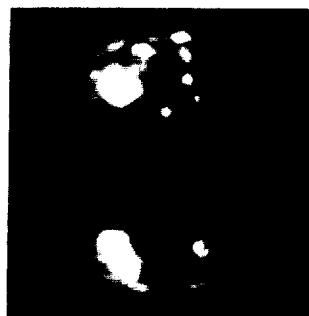
27 JUNE 1974



17 NOVEMBER 1976



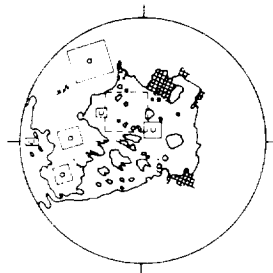
31 JANUARY 1978



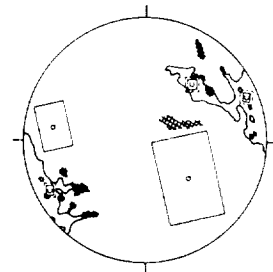
13 FEBRUARY 1981

Fig. 1. Soft X-ray images of the solar corona for the four dates analyzed in this study. All images were obtained with the AS & E fused silica mirror and with polypropylene filters. The exposure times vary. Solar north is up and east to the left for all images. The central meridian longitudes L_0 for the four images in time order were: 237, 220, 175, and 298°.

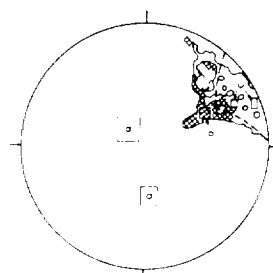
CORONAL HOLE BOUNDARIES



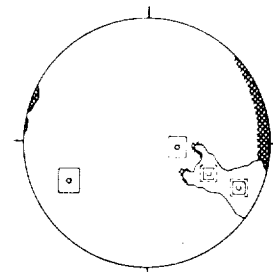
27 JUNE 1974



17 NOVEMBER 1976



31 JANUARY 1978



13 FEBRUARY 1981

Fig. 2. Tracings of X-ray coronal hole boundaries from Kahler *et al.* (1983) to the same scale as Figure 1. Hatched areas indicate uncertain X-ray holes. See Kahler *et al.* for details on the boundary determinations. The solid boxes indicate the subareas in which the X-ray measurements of emission from coronal holes ('C') and the diffuse background corona ('Q') were made. The dashed subareas indicate where the magnetic flux was measured.

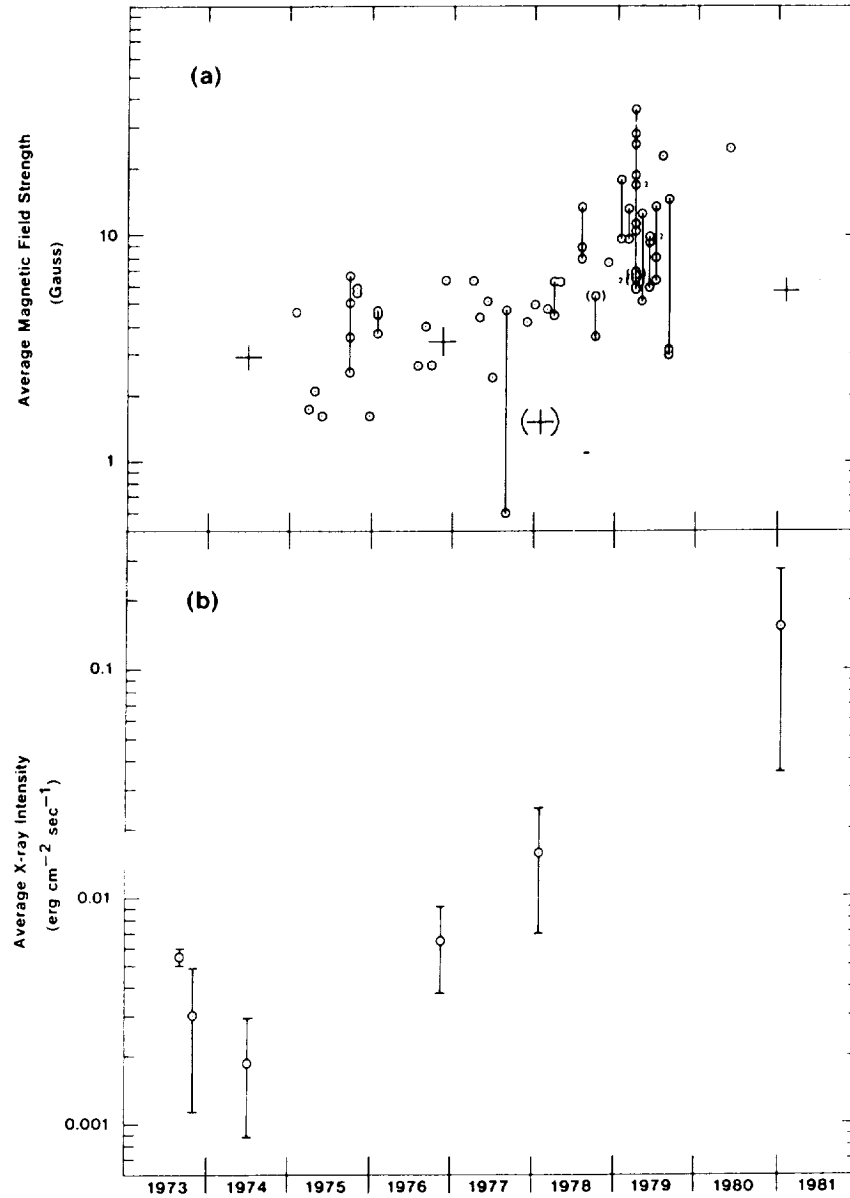


Fig. 3. Overall comparison of the magnetic field strength and X-ray flux of coronal holes from 1974 to 1981. (a) Semi-log plot of magnetic field strengths from Kitt Peak synoptic maps within 10830 Å coronal hole boundaries from 1975 to 1980 (from Table I of Harvey *et al.*, 1982). Points joined by vertical lines represent measurements of different holes made during the same month. The crosses indicate the averaged Mt. Wilson measurements for the X-ray equatorward holes (see text). (b) Semi-log plot to the same timescale as (a) of the X-ray energy fluxes of the Skylab and rocket coronal holes listed in Table II. For each flight all of the measurements have been averaged together and plotted as a single point. Each error bar is a simple average of the measurement uncertainties for each flight.

(PP) and beryllium (BE) filters. The passbands of the PP filters used in these flights are similar to Filter 3 used with the Skylab S-054 instrument (Vaiana *et al.*, 1977) to study coronal holes. Table I lists the dates, times, and Carrington rotations of the X-ray data from the four rocket flights analyzed for this study*, and the dates and times of the magnetogram data we used. Representative PP images from the four flights are shown in Figure 1 and the X-ray coronal hole boundaries from Kahler *et al.* (1983) are reproduced in Figure 2 to the same scale. The 17 November, 1976 boundaries, though not included in their paper, were drawn by Kahler *et al.* during their analysis. Their 1976 and 1981 boundaries compare favorably with those determined independently by Nolte *et al.* (1977) and Webb *et al.* (1984), respectively.

To determine coronal plasma parameters, the X-ray photographic density images must be calibrated and reduced to arrays of energy flux deposited on the film plane. Details of the reduction and calibration of the rocket images are discussed by Davis and Webb (1985). Since the rocket images were obtained with the same film emulsion, Eastman Kodak SO-212, used with the AS&E Skylab telescope, we followed the general calibration procedures developed for the Skylab analysis (Vaiana *et al.*, 1977). Each flight image was scanned with AS&E's PDS microdensitometer to produce a digitized density array with 20 micron pixels, equivalent to 2.8 arc sec spatial resolution. Because of difficulties with laboratory calibration of the wavelength dependence of the X-ray sensitivity of SO-212 film, we used a synthesized calibration procedure based on the image data themselves (cf. Maxson and Vaiana, 1977) to provide absolute energy calibrations for each flight. The uncertainties in the film calibration lead to relatively large error ranges in the measured coronal hole energy fluxes. However, as we will show, our results still provide meaningful limits on the cyclical dependence of energy flux from coronal holes.

Subareas were chosen to encompass areas of minimum brightness in the holes and are indicated on Figure 2 by the boxes labelled 'C'. These subareas were carefully chosen to exclude regions of brighter diffuse emission and bright point-like features within each hole boundary, and to be distant from active regions so as to minimize scattering effects. Generally the average density and statistical error at at least two subareas per hole and on two adjacent PP images was measured. The resulting average X-ray intensities and uncertainties derived for the coronal hole subareas shown in Figure 2 are listed in Table II.

In Figure 3(b) the X-ray coronal hole flux measurements are presented as a function of time over nine years of solar cycles 20 and 21. The two 1973 points are averages of the two sets of published Skylab X-ray measurements of the emission from coronal holes. The first point is the average of six measurements of two areas in Coronal Hole 1 (CH 1) made in August 1973 using two low-density calibration methods (Maxson and Vaiana, 1977). The second point is the average of three measurements of the emission

* Although small coronal holes were visible on the day of our rocket flight on 7 November, 1979 (see Figure 4 in Webb *et al.*, 1984), that data could not be used for this study because scattered radiation from a flare precluded photometric measurements in faint areas.

from CH 6 shortly after its birth on the disk in October 1973 (Solodyna *et al.*, 1977). From 1974 to 1981 the X-ray measurements for each rocket flight in Table II have been averaged together and plotted as a single point. This procedure is justified because the uncertainties of each point are larger than the variations of the intensities between exposures or among the different coronal holes observed on each flight.

A clear trend in the X-ray emission is apparent. The coronal hole emission in 1973, 1974, and 1976 was similar and low, but rose to a maximum in 1981. Examining only the rocket data, average coronal hole emission was lowest in June 1974, a factor of 3 higher in November 1976 near solar minimum, and a factor of 8 higher in January 1978. The emission from the large southern hole in February 1981 near solar maximum was an order of magnitude higher than in 1978, although with larger uncertainties due to the film calibration and possible scattering problems.

We derived gas pressure from the average coronal hole X-ray intensities using the technique developed by Kahler (1976). This method is applicable over the temperature range where a single filter's response is temperature insensitive. Therefore, the method is especially useful when the plasma temperature and density cannot be uniquely determined, as in our case. For the fused silica mirror the pressure, in dyne cm^{-2} , is given by:

$$P_i^2 = 3.49 \times 10^{-14} I_i/L\alpha,$$

where I_i is the focal plane intensity through filter i in $\text{erg cm}^{-2} \text{s}^{-1}$, L is the pathlength in cm, and α is a function of the assumed filtered solar spectrum, corrected for film speed, and T^2 . For L we assumed the constant density scale height of 6.5×10^9 cm derived by Vaiana *et al.* (1973) for an X-ray coronal hole observed in 1970. Table III presents the results for the PP images from each rocket flight under two temperature assumptions. Column 2 shows the hole pressures for an assumed constant temperature of 1.3×10^6 K, i.e., the barometric temperature for the 1970 coronal hole (Vaiana *et al.*, 1973). In column 4 are given the pressures derived using an average value of α over the full temperature range over which the PP filter is temperature insensitive to within $\pm 33\%$ (for the rocket PP filter this occurs from 0.7 to 5×10^6 K). Pressures derived

TABLE III
Derived coronal hole pressures^a

| Date | $P (1.3 \times 10^6 \text{ K})^b$ (dyn cm ⁻²) | ΔP (above 1974 level) | $P (\langle \alpha(T) \rangle)^b$ (dyn cm ⁻²) | ΔP (above 1974 level) |
|--------|--|----------------------------------|--|----------------------------------|
| Skylab | 0.050 | 1.8 | 0.029 – 0.081 ($0.9 < T_6 < 3.0$) | |
| 1974 | 0.027 ± 0.003 | – | 0.031 ± 0.004 | – |
| 1976 | 0.054 ± 0.003 | 2.0 | 0.063 ± 0.003 | 2.0 |
| 1978 | 0.078 ± 0.008 | 2.9 | 0.090 ± 0.010 | 2.9 |
| 1981 | 0.310 ± 0.068 | 11.5 | 0.352 ± 0.072 | 11.3 |

^a For an assumed density scale height of 6.5×10^9 cm.

^b The uncertainties represent the ranges in pressures due only to the uncertainties in the film calibration.

by Maxson and Vaiana for Skylab CH 1 are given as a reference. Shown in columns 3 and 5 are the ratios of the hole pressures with respect to 1974, showing a tenfold increase between activity minimum and maximum.

We also estimated the emission measure, $\int n_e^2 dl$ (Vaiana *et al.*, 1977), from the average coronal hole intensities. We assumed a constant $T_e = 1.3 \times 10^6$ K and derived average emission measures ranging from about $4 \times 10^{25} \text{ cm}^{-5}$ in June 1974 to $5 \times 10^{27} \text{ cm}^{-5}$ in February 1981. The values derived from the average hole intensities for 1974, 1976, and 1978 are within a factor of 3 of the emission measure at 1.3×10^6 K for CH 1 of $1.3 \times 10^{26} \text{ cm}^{-5}$ (Maxson and Vaiana, 1977).

Because coronal hole fluxes are very small, an understanding of the X-ray calibration and reduction procedures is important. Of particular concern in X-ray measurements are scattering effects arising from surface roughness of the mirrors, which can contribute an important source of background 'noise'. Thus, our decision to make no corrections for scattering in our analysis must be justified. In analyzing the Skylab data, Maxson and Vaiana concluded that CH 1 had significant emission over background. They made no corrections for scattering, claiming that such effects were minimized by choosing subareas far from bright sources, and because CH 1 had a large area and cross sections through the hole revealed flat-bottomed profiles inconsistent with scattering effects. To the contrary, Solodyna *et al.* (1977) estimated significant scattering contributions from individual sources and concluded that the CH 6 emission after its development 'was consistent with zero within our assessment of the experimental uncertainties'. However, unlike CH 1, CH 6 at the time of Solodyna *et al.*'s measurement was a very small hole surrounded by large-scale structures (LSS) and active regions, and flaring occurred in a limb region during some of the observations. Like Maxson and Vaiana we attempted to minimize the effects of scattering by choosing subareas away from bright regions and checking cross-sectional profiles through the holes. More importantly, we only used rocket data obtained with the fused silica mirror, which has improved scattering characteristics compared with the Skylab mirror (Davis *et al.*, 1977). For instance, the scattering is substantially reduced at shorter wavelengths and is nearly wavelength

TABLE IV

Contrast ratios:

diffuse coronal emission / coronal hole emission

| Date | Ratio |
|----------------------------|-----------------|
| 21 Aug., 1973 ^a | 8.4 ± 1.2^b |
| 27 June, 1974 | 11.1 ± 6.8 |
| 17 Nov., 1976 | 5.4 ± 3.0 |
| 31 Jan., 1978 | 3.5 ± 2.8 |
| 13 Feb., 1981 | 3.0 ± 3.2 |

^a Skylab from Maxson and Vaiana (1977). The ratio of the LSS emission from their region 'D' divided by the emission from CH 1.

^b The errors are the statistical errors of the ratios of the uncertainties discussed in the text.

independent. It must be emphasized that neither the Skylab nor rocket coronal hole measurements include the effects of systematic errors which might arise from uncertainties in the calibration data, including the wavelength dependence of film aging, and the absolute source spectrum.

We measured average intensities of diffuse background coronal subareas as a means of comparing the coronal hole flux variations with overall cyclical variations in coronal plasma conditions and to cross-check the data from each rocket flight. These subareas, labelled 'Q' in Figure 2, were chosen to include large-scale areas of minimal coronal emission on the disk *away* from coronal holes, active regions and bright LSS. For each image these subareas were averaged together and compared with the averaged coronal hole fluxes plotted in Figure 3(b). Table IV shows for each date the coronal contrast ratio between the diffuse emission and the coronal hole emission. This ratio decreased from 1974 to 1981, thereby quantitatively confirming the previous suggestions from both X-ray and 10830 Å observations that the brightness contrast between holes and large-scale structure decreased during the rise to solar activity maximum.

2.2. ANALYSIS OF THE PHOTOSPHERIC MAGNETIC FIELD STRENGTH DATA

In the next phase of the analysis we compared as a function of time the X-ray emission and the photospheric magnetic flux density from the coronal holes, using the boundaries determined by Kahler *et al.* (1983). For the magnetic field data we used daily averaged magnetic flux maps from Mt. Wilson Observatory and Kitt Peak synoptic flux maps constructed for each Carrington rotation (Harvey *et al.*, 1980). Table I lists the dates and times of the Mt. Wilson magnetograms. Kitt Peak data were not available for long periods around the dates of the rocket flights in 1974 and 1976, and contained a three-day gap centered on 31 January, 1978, the date of the third flight. However, the Mt. Wilson daily maps were available on or within one day of each of the four rocket flights analyzed. To check for day-to-day variations in the maps, we required maps on the day of the flight, the day before and the day after. However, for the 1978 flight only maps on the day of the flight and the day after were available, and in 1981 only one map was available on the day after the flight. Fortunately, good Kitt Peak data were obtained for the 1981 period.

We obtained the Mt. Wilson data in the form of averaged pixels in Gauss integrated over 34×34 equal intervals of sine longitude and sine latitude, therefore representing large area averages of flux density. The magnetograph measures the longitudinal component of the photospheric field in the 5250 Å line of Fe I. Because of line weakening, the values measured are on the order of a factor of two too low, although the magnitude of this effect varies across the disk (Howard and Stenflo, 1972). Our results were corrected for this effect and for foreshortening as described below.

We obtained the Kitt Peak synoptic maps in the form of digitized equal-area pixels in Gauss of one degree longitude by (1/90) unit of sine latitude of the mean field strength. The data were obtained with the 512-channel magnetograph which measures the longitudinal field in the 8688 Å line of Fe I and requires no correction outside of

sunspots. Where necessary a cosine weighting function in longitude has been applied to the synoptic data to merge it across daily data gaps.

We selected rectangular subareas on the magnetic maps that corresponded spatially with the coronal hole subareas in which the X-ray measurements were made. These subareas are shown by the dashed outlines on Figure 2. For the 1976 and 1981 data the subareas coincided with the X-ray subareas, but for 1974 and 1978, we used single large subareas to increase the statistical accuracy of the measurements. Because of the large area of the holes in 1974 and 1978 and the coarse spatial resolution of the Mt. Wilson data, we feel that the integration of the X-ray and magnetic data over dissimilar areas did not significantly effect the results. The results of our analysis of the coronal hole magnetic field strengths are given in Table V. The table lists the dates and subareas measured in terms of the X-ray coronal hole designations used in Table II.

TABLE V
Average magnetic field strength in coronal holes

| Date | Coronal hole subareas | Polarity | Observatory | Net B_T (G) | θ_c (deg) |
|---------------|-----------------------|----------|-------------|---------------|------------------|
| 26 June, 1974 | Large hole: center | + | MW daily | + 2.87 | 14.5 |
| 27 June, 1974 | Large hole: center | + | MW daily | + 3.06 | 19 |
| 28 June, 1974 | Large hole: center | + | MW daily | + 2.88 | 31.5 |
| 16 Nov., 1976 | Equatorial ext. | - | MW daily | - 2.51 | 27.6 |
| 17 Nov., 1976 | Equatorial ext. | - | MW daily | - 3.23 | 34.8 |
| 17 Nov., 1976 | South polar hole | - | MW daily | - 3.68 | 59.8 |
| 17 Nov., 1976 | South polar hole | + | MW daily | - 0.34 | 59.8 |
| 18 Nov., 1976 | Equatorial ext. | - | MW daily | - 4.53 | 44.5 |
| 31 Jan., 1978 | Southwest hole | - | KP synoptic | - 1.28 | (55)* |
| 31 Jan., 1978 | Southwest hole | - | MW daily | - 2.23 | 64.6 |
| 1 Feb., 1978 | Southwest hole | - | MW daily | - 0.80 | 68.4 |
| 13 Feb., 1981 | Southern hole: limb | + | KP synoptic | + 1.55 | (58)* |
| 13 Feb., 1981 | Southern hole: center | + | KP synoptic | + 5.60 | (40)* |
| 14 Feb., 1981 | Southern hole: limb | + | MW daily | + 4.50 | 66.4 |
| 14 Feb., 1981 | Southern hole: center | + | MW daily | + 5.74 | 40.1 |

* The average longitudes for the coronal hole locations on the Kitt Peak maps are estimates only.

Column 3 gives the known polarity of the hole as determined by $H\alpha$ synoptic charts in *Solar-Geophysical Data* and the magnetic field/solar wind observations of Sheeley and Harvey (1981). With one exception (i.e., the north polar hole on 17 November, 1976) the measured polarities agreed with the expected ones.

The average longitudinal field strength B_m for each hole subarea was calculated by computing the algebraic sum of all pixels within the chosen subarea and dividing by the number of pixels. The Mt. Wilson data were then corrected for line weakening and foreshortening by using the form given by Howard (1977) to derive the 'true' field strength B_T :

$$B_T = B_m \frac{0.48 + 1.33 \cos \theta}{\cos \theta},$$

where θ is the great-circle distance from Sun center to the center of the subarea. In Table V the value B_T is given in column 5 and θ in column 6. In addition, the June 1974 Mt. Wilson measurements were increased by 20% to account for a change in the magnetograph aperture in 1975 (R. Howard, private communication). The Kitt Peak synoptic data are already corrected for the longitude projection effect, so we applied a latitude correction of the form $B_c = B_m/\cos \theta$. The Mt. Wilson and Kitt Peak measurements within the February 1981 hole equatorial extension suffer least from foreshortening and agree with 3%.

Harvey *et al.* (1982) used Kitt Peak synoptic images to determine the magnetic fluxes in thirty-three 10830 Å coronal holes from 1975 to 1980. They only analyzed holes below a latitude of 50° and made no corrections for projection effects. In Figure 3(a) we have plotted their field strength data from their Table I. This plot illustrates their result that during this phase of solar cycle 21, low-latitude holes contained three times more flux near activity maximum than at minimum.

The corrected Mt. Wilson flux values (B_T) shown in Table V for the days centered on the rocket flights have been averaged together and plotted as crosses on Figure 3(a). We included the single Mt. Wilson measurement on 14 February, 1981 the day after the rocket flight. One of the Harvey *et al.* measurements (coronal hole No. 18 on 19 October, 1976) was from the southern equatorial extension that we measured one rotation later on 16–18 November, 1976. Our averaged measurement for this hole of –3.4 G agrees favorably with their value of –2.7 G. In general, our coronal hole fluxes are consistent with the trend of the Harvey *et al.* data (note: the 1978 value was subject to considerable foreshortening).

3. Discussion

We now summarize our observational results in terms of the questions posed in the Introduction. First, we conclude that the rocket results confirm earlier Skylab results that detectable X-ray emission arises from coronal holes. In addition we find that this emission appears to increase as the cycle evolves from activity minimum to maximum. One can take the view that despite the uncertainties arising from differing calibration procedures, and the diversity in coronal hole area, location on the disk and evolutionary characteristics, the four independent data sets from 1973 to 1976 reveal remarkably consistent X-ray hole emission values varying over this period near sunspot minimum by only about a factor of three. The 1974 rocket measurements are also consistent with Solodyna *et al.*'s (1977) measurements of CH 6 made only 8 months earlier. However, when the data over this entire 9-year period of the solar cycle is examined, the observed X-ray coronal hole emission appears to vary roughly with the sunspot cycle, reaching minimum flux in 1974 just before sunspot minimum*, then increasing through 1981, about one year after sunspot maximum. Finally, because the rate of intensity increase

* We cannot rule out that coronal hole emission in October 1973 (Skylab) and June 1974 (rocket) was below the detection threshold and, therefore, that these values are upper limits.

of the X-ray hole flux was greater than that of the background flux (Table IV), our photometric results confirm the qualitative suggestion of Kahler *et al.* (1983) and Sheeley and Harvey (1978, 1981) that the brightness contrast between coronal holes and large-scale structure decreased during the rise to activity maximum.

Figure 3 provides a partial answer to our second question, namely does a relationship exist between increasing X-ray emission and increasing magnetic field strength from coronal holes over this period of the cycle? The data of Harvey *et al.* (1982; our Figure 3(a)) show an increase of a factor of three in the field strength of near-equatorial coronal holes between 1975 and 1980. Our calculations of field strength within the X-ray hole boundaries are sparse but consistent with the Harvey *et al.* data. The X-ray emission (Figure 3(b)) shows an increasing trend with the cycle, in general agreement with the magnetic flux but with greater amplitude. Comparison of these two data sets over the same time period reveals that they appear to have a power law dependence. The relationship is such that the coronal hole X-ray intensity, which is proportional to the gas pressure (Table III), is consistent with being proportional to B^2 . Thus, the data lend support to coronal heating models in which the corona is directly heated by the dissipation of magnetic energy (e.g., Rosner *et al.*, 1978). We may speculate from our results that such magnetic heating occurs routinely in coronal holes over the solar cycle.

It is important to attempt to relate the observed change in coronal hole contrast over the cycle with the degree to which the underlying magnetic fields were open or closed. We examined two approaches to this question: (1) by directly comparing the location and contrast of our holes with regions of open fields as deduced from potential field models, and (2) by examining the interplanetary effects of the low-latitude holes or extensions of holes observed in our data.

Regarding the first approach, Levine compared regions of open fields with the Skylab data on coronal holes (e.g., Levine, 1977) and with 10830 Å holes observed in 1975 and 1978–1979 (Levine, 1982). However, his comparisons were made during periods when we had no rocket observations and, therefore, we are unable to make any direct comparisons. However, our observation of the southern hole extension in January 1978 could be indirectly compared with Levine's (1982) results starting in May 1978. Levine's Figures 3–6 confirm that this lobe was detected as a strong open field region of similar size and shape and persisting through the period of Levine's study.

Concerning the second approach, we decided to examine the interplanetary effects of our holes because of the well-known, strong correlation during Skylab between low-latitude holes and, therefore, apparently open field regions, and high speed solar wind streams. In addition, we sought assurance that our holes were reasonably typical of each epoch with regard to their evolutionary characteristics and effects on the solar wind. We compared the locations and timing of our low-latitude holes with the Bartels displays and discussions of Sheeley and Harvey (1978, 1981).

The large coronal hole in June 1974 was the only one in our data which extended over the equatorial region. This hole evolved from a separate, small equatorial hole during Skylab (CH 4) to join with the north polar hole by mid-January 1974 (Solodyna *et al.*, 1975). The Bartels display shows that in June 1974 this hole was midway through its

lifetime. Through mid-1975 this hole and another of opposite polarity formed a two-sector structure of strong, recurrent solar wind. These holes, and their associated wind streams, had a 27-day recurrence period. These characteristics were typical of equatorial holes observed during Skylab (e.g., Zirker, 1977).

The equatorial extension holes observed on the rocket images on 17 November, 1976 and 31 January, 1978 represented the early development of long-lived, slowly rotating (28–29 day periods) but weak holes. Sheeley and Harvey (1978) described the 1976 hole as follows: "Despite its weak appearance, this hole was associated with one of the most prominent recurrence patterns of high-speed solar wind and enhanced geomagnetic activity that occurred during 1976–1977." Finally, on 13 February, 1981 the large, high-latitude coronal hole was embedded in the first new-cycle polarity region (Webb *et al.*, 1984) and was probably associated with a recurrent wind stream. All of the near-equatorial X-ray holes were associated with IMF polarity of the same sign (Sheeley and Harvey, 1981).

Taken together, these facts suggest that these holes were strongly connected with the interplanetary medium flow by open field lines emanating from the base of the holes. These indirect comparisons support a general correspondence between open field regions and the X-ray coronal holes of our study. But the variation of X-ray flux from coronal holes does not appear to be strongly dependent on the degree of the open field structures. We hope to extend this inference by directly comparing the X-ray coronal hole data with open field structures as deduced from potential field calculations.

In conclusion, our limited X-ray results provide evidence for a solar cycle variation in overall coronal hole emission and gas pressure, which is supported by the qualitative, but more frequent observations of a 'weakening' or decreased contrast of 10830 Å holes and an increase in the surface magnetic flux within holes over the same period. The variation of the coronal pressure is consistent with being proportional to the square of the magnetic flux, suggesting the importance of magnetic energy dissipation to heating at the base of coronal holes.

Acknowledgements

We would like to thank J. Harvey and R. Howard of the National Solar Observatory for providing the photospheric magnetic field data used in this study and for helpful discussions. We also acknowledge useful discussions on calibration of the X-ray data with C. Maxson of the Center for Astrophysics and S. Kahler of Emmanuel College. We appreciate the assistance of M. Rizza and F. Simpson of AS & E in the preparation of the figures. This study was funded by the Air Force Geophysics Laboratory/PHS, Air Force Systems Command, under contract F19628-84-C-0037. The acquisition and initial reduction of the rocket data was supported by NASA under contracts NAS5-25496 and NAS2-8683.

References

- Altschuler, M. D. and Newkirk, G., Jr.: 1969, *Solar Phys.* **46**, 185.
- Davis, J. M. and Webb, D. F.: 1985, 'A Study of the Cyclical Variations of Coronal Holes and Their Relation to Open Magnetic Fields', AFGL-TR-85-0003.
- Davis, J. M., Golub, L., and Krieger, A. S.: 1977, *Astrophys. J.* **214**, L141.
- Harvey, J., Gillespie, B., Miedaner, P., and Slaughter, C.: 1980, *Report UAG-77*, World Data Center A, NOAA, Boulder, CO.
- Harvey, K. L., Sheeley, N. R., Jr., and Harvey, J. W.: 1982, *Solar Phys.* **79**, 149.
- Howard, R.: 1977, *Solar Phys.* **52**, 243.
- Howard, R. and Stenflo, J. O.: 1972, *Solar Phys.* **22**, 402.
- Kahler, S.: 1976, *Solar Phys.* **48**, 255.
- Kahler, S. W., Davis, J. M., and Harvey, J. W.: 1983, *Solar Phys.* **87**, 47.
- Krieger, A. S., Timothy, A. F., and Roelof, E. C.: 1973, *Solar Phys.* **29**, 505.
- Levine, R. H.: 1977, in J. B. Zirker (ed.), *Coronal Holes and High Speed Wind Streams*, Colorado Associated University Press, Boulder, Colo., p. 103.
- Levine, R. H.: 1982, *Solar Phys.* **79**, 203.
- Maxson, C. W. and Vaiana, G. S.: 1977, *Astrophys. J.* **215**, 919.
- Nolte, J. T., Krieger, A. S., Timothy, A. F., Gold, R. E., Roelof, E. C., Vaiana, G. S., Lazarus, A. J., Sullivan, J. D., and McIntosh, P. S.: 1976, *Solar Phys.* **46**, 303.
- Nolte, J. T., Davis, J. M., Gerassimenko, M., Lazarus, A. J., and Sullivan, J. D.: 1977, *Geophys. Res. Letters* **4**, 291.
- Rosner, R., Tucker, W. H., and Vaiana, G. S.: 1978, *Astrophys. J.* **220**, 643.
- Sheeley, N. R., Jr. and Harvey, J. W.: 1978, *Solar Phys.* **59**, 159.
- Sheeley, N. R., Jr. and Harvey, J. W.: 1981, *Solar Phys.* **70**, 237.
- Solodyna, C. V., Nolte, J. T., and Krieger, A. S.: 1975, memo to Skylab Solar Workshop Participants.
- Solodyna, C. V., Krieger, A. S., and Nolte, J. T.: 1977, *Solar Phys.* **54**, 123.
- Vaiana, G. S., Krieger, A. S., and Timothy, A. F.: 1973, *Solar Phys.* **32**, 81.
- Vaiana, G. S., Van Speybroeck, L., Zombeck, M. V., Krieger, A. S., Silk, J. K., and Timothy, A.: 1977, *Space Sci. Instr.* **3**, 19.
- Webb, D. F., Davis, J. M., and McIntosh, P. S.: 1984, *Solar Phys.* **92**, 109.
- Zirker, J. B. (ed.): 1977, *Coronal Holes and High Speed Wind Streams*, Colorado Associated University Press, Boulder, Colo.

4.16 The Measured Performance of a Grazing Incidence Relay Optics Telescope
for Solar X-Ray Astronomy

Dan Moses, Allen S. Krieger, and John M. Davis

American Science and Engineering, Inc.
Cambridge, Massachusetts 02139

ORIGINAL PAGE IS
OF POOR QUALITY

— — — — —

The measured performance of a grazing incidence relay optics telescope for solar X-ray astronomy

Dan Moses, Allen S. Krieger, and John M. Davis*

American Science and Engineering, Inc., Fort Washington
Cambridge, Massachusetts 02139

Abstract

X-ray astronomy, both solar and celestial, requires long focal length optical systems to provide high spatial resolution images and to be used as feeds for spectrometers. In typical experimental situations, the physical size is restricted and grazing angles must be kept at or below one degree. Grazing incidence secondary optics are an alternative to long focal length primary mirrors. We have designed, fabricated and tested a system which employs a secondary with externally polished hyperboloid-hyperboloid surfaces. It is to be used in conjunction with an existing Wolter-I primary. The system has been designed for high resolution imaging of the solar corona with the goal of producing images electronically with the same spatial resolution as achieved at the primary focus with film. The secondary optic is located in front of the primary focus, as in a Galilean telescope, and provides a magnification of approximately four. The combined system has a plate scale of $26.0 \mu\text{m}$ (arc sec)⁻¹, effective focal length 5.4 m, and is contained within an instrument of length 1.9 m. The design, tolerance specification and fabrication techniques are described. The performance of the system at X-ray wavelengths has been determined experimentally and is compared with theoretical results produced by ray tracing.

Introduction

The field of X-ray astronomy has developed rapidly over the past quarter century spurred by technical advances in the fabrication of grazing incidence optics. These optical systems have allowed the study of X-ray emission mechanisms over a range of astronomical sources from the coronae of stars, including the sun, to supernovae remnants, galaxies and quasars. Although the structure of many of the more distant sources remain unresolved, imaging has revealed a wealth of detail for objects which are relatively close (like the sun) or extend over a large angular extent (e.g., supernovae remnants). In general the structures that are observed reflect the interaction between a high temperature plasma and a magnetic field. For the solar corona the visual identification of a diverse population of coronal structures has provided a new framework for the reformulation of the more classical concepts of solar physics. However, many of the theoretical descriptions involve processes which occur over very small spatial scales. Therefore, future advances will require the acquisition of even higher resolution observations.

In practice the resolution in astronomical observations depends on both the intrinsic resolution of the optical system and the relationship of the size of the image to that of the detector. In the past nearly all X-ray images have been detector limited¹ even when the recording medium was photographic emulsion. The situation is worse when solid state detectors are used. However, for most space missions, electronic imaging has to be used since there is no opportunity to recover film. Consequently there are strong incentives for the development of imaging systems, optics and detectors, in which the performance of each element is optimized for maximum system performance.

When the system angular resolution is limited by the detector, the instrument designer has produced a mismatch between the instrument's focal length and the dimensions of the detector pixel. Although efforts continue to improve the latter, electronic detectors are unlikely to surpass the spatial resolution of photographic film. Therefore it is essential to simultaneously explore the second factor, namely increasing the focal length of the X-ray telescope.

To quantify these statements, we establish a requirement for a system spatial resolution of 1 arc second. If features on this scale are to be resolved, they must subtend an angle greater than 1 pixel, and we use the quantity of $2\sqrt{2}$ pixel size to define limiting resolution. Taking the pixel size as 15 microns, the best that is currently available in CCDs, the instrument focal length would have to be 8.75 m. This results in an instrument size which is impractical for any but major programs. The solution to this problem in normal incidence optical systems would be to use secondary optics to increase the effective focal length, i.e., magnify the primary image. Until recently this approach had not

* Present Address: NASA/Marshall Space Flight Center, Code ES-52
Huntsville, Alabama 35812

been followed for X-ray imaging because of the difficulties associated with the figuring of small grazing incidence optical elements and the increased scattering from four reflections instead of the customary two. However, recent advances in fabrication technology, in particular in the in-process metrology and the preparation of low-scatter surfaces, have combined to make their development possible. Consequently, under NASA sponsorship, we have designed and fabricated a grazing incidence magnifier to be used in conjunction with an existing grazing incidence primary for solar studies.

Design considerations

Two options for the design of the secondary magnifier are possible. In the first option the secondary optic acts as a microscope and is located behind the primary focal plane. It is known as a converging magnifier and has internally reflecting hyperboloid and ellipsoid surfaces. The second design places the mirror in front of the focal plane where it acts as a Barlow lens. This configuration is known as a diverging magnifier and the mirror has externally reflecting hyperboloid-hyperboloid surfaces².

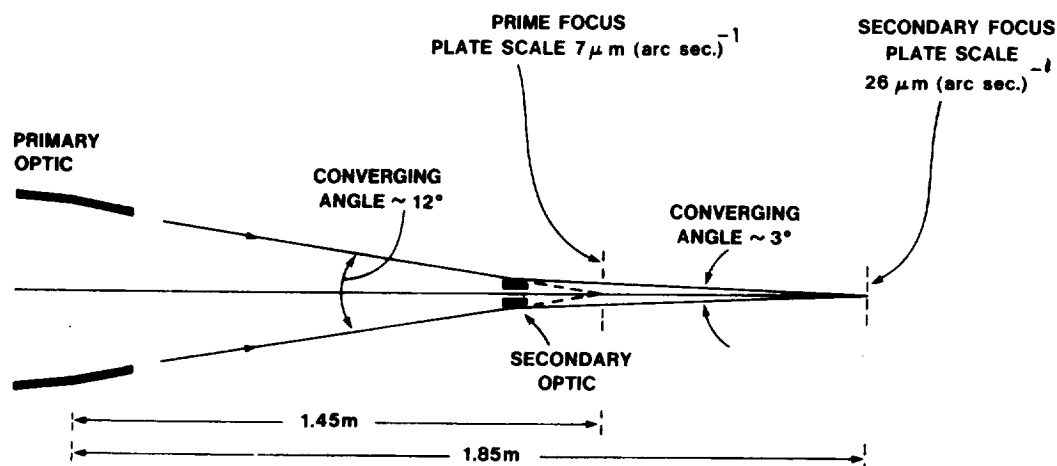


Figure 1. Diagram of the design for the grazing incidence relay optic system.

In the present program, the total length of the system is of critical importance because the telescope will be flown as a sounding rocket payload. For a given object distance and magnification, the diverging magnifier (Figure 1) is the shorter of the two designs. It was selected for this project. An additional benefit of this design is that the primary focused X-rays are bent through a smaller angle to reach the secondary focus, thus minimizing reflection losses and maximizing collecting area.

The design is fixed by choosing the magnification and the object distance (where object distance is the separation between the principle plane of the secondary and the primary focus). In practice increasing magnification lowers the system's speed. Increasing object distance, for a given magnification, lengthens the overall instrument and also increases the physical size of the polished area. A compromise design was chosen¹ which has a magnification of 3.7, corresponding to a plate scale of $26 \mu\text{m (arc sec)}^{-1}$ while retaining reasonable exposure times. The object distance was set at 14.5 cm. This leads to an overall length for the imaging system of 185 cm which is within the 2 m limit established for the experiment. The general properties of the primary and secondary mirror design are summarized Table 1.

Table 1. Design Requirements of the X-Ray Mirrors

| | Primary | Secondary |
|-------------------------|------------------------------------|--------------------------------------|
| Figure | Wolter Schwarzschild | Hyperboloid Hyperboloid |
| Material | Fused Silica | Nickel Coated Beryllium |
| Principal Diameter | 30.48 cm | 3.15 cm |
| Focal Length | 144.9 cm | -19.9 cm |
| Geometrical Area | | |
| On-axis | 42.4 cm^2 | 34.3 cm^2 |
| 2 arc minutes | 39.6 cm^2 | 5.8 cm^2 |
| Plate Scale | $7.0 \mu\text{m (arc sec)}^{-1}$ | $26.0 \mu\text{m (arc sec)}^{-1}$ |
| Field of View | $60 \times 60 \text{ (arc min)}^2$ | $2.5 \times 2.5 \text{ (arc min)}^2$ |
| Resolving Power (X-Ray) | 1 arc sec | 1 arc sec |

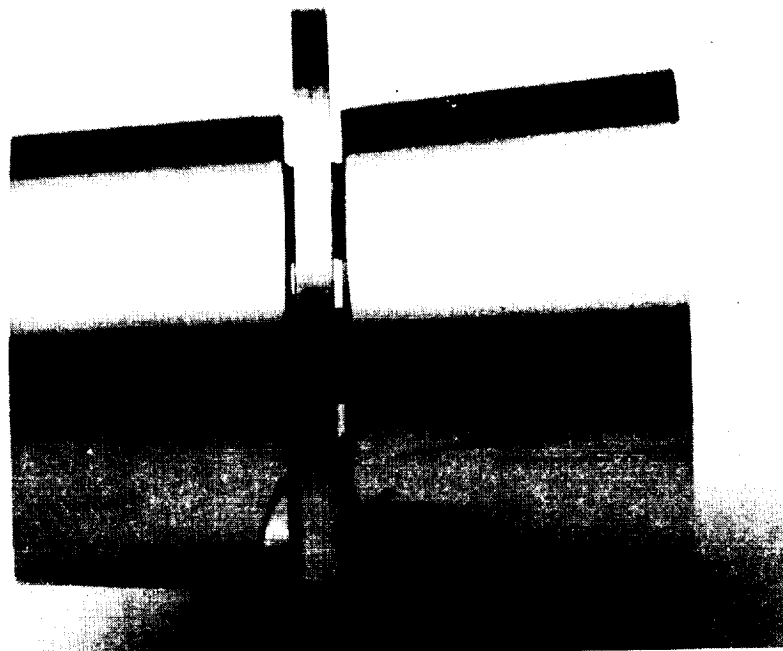


Figure 2. Photograph of the nickel coated hyperboloid-hyperboloid diverging magnifier.

Specification and fabrication

A photograph of the completed diverging magnifier is presented in Figure 2. The equations for the external mirror surfaces of the diverging magnifier are:

$$\text{First Hyperboloid: } \frac{(Z + c)^2}{c^2 - b^2} - \frac{X^2}{b^2} = 1$$

$$\text{Second Hyperboloid: } \frac{(Z + 2c + f)^2}{f^2 - e^2} - \frac{X^2}{e^2} = 1$$

$$\text{where } c = 1.981416 \quad b = 0.167138 \\ e = 0.261239 \quad f = 6.157995$$

The first hyperboloid is located so that its first focus is co-spatial with the focus of the primary mirror. Its second focus is made confocal with the first focus of the second hyperboloid. The second focus of this surface forms, in turn, the secondary focus of the telescope. Since hyperboloids have two foci, small deviations from the design surface can be compensated for by axial displacements with no drawbacks other than a slight change in the overall focal length.

The surface profile was measured in-situ using a laser beam which is scanned over the surface in a controlled way. The local slope is determined from the reflected beam using a position-sensitive detector. The difference between the slope of the required surface and the best fit circle is corrected optically before display. In performing this operation one has to be careful to remember that the geometry established to generate a surface with a given radius will measure a surface with twice that radius and therefore it is necessary to reconfigure the equipment when changing between a polishing and a measuring mode. Typically the best fit spheres have radii on the order of several thousand inches. The error in establishing these radii is on the order of one part in a thousand. This error is acceptable since it can be accommodated during the assembly of the optic by adjustment of the spacer. The signal can also be integrated electronically to obtain the sagittal depth as a function of position. Once a satisfactory surface has been obtained the end pieces are removed from the finished mirror and the radial dimensions measured. As a cost savings measure, the end pieces were made from cast iron. This turned out to be a mistake since it was more difficult to remove this material during polishing. This caused the surfaces near the edges to roll up and the removal of this effect was both difficult and time consuming. Finally, the surfaces were superpolished to provide a low-scatter finish. The mirror was fabricated, in two pieces, from optical grade beryllium.

ORIGINAL PAGE

BLACK AND WHITE PHOTOGRAPH

The selected blanks were diamond turned to their approximate dimensions using a numerically controlled lathe. Since the polished area is relatively small, it is important to minimize roll over at the ends and the blanks were turned and lapped with removable end pieces in place. The machined blanks were then nickel plated which was applied to a depth of 0.13 mm over all the surfaces of the two elements. The nickel reflecting surfaces were again single point diamond turned and lapped to the required profile. The work was performed on a modified Random machine utilizing linear, air bearing slides to define tangents to the best fit circle. This circle is used to guide the lathe head which holds the mirror during both the diamond turning and polishing. The radii of curvature, which in our case are on the order of 40 m, are determined with an accuracy of 2 cm and the location of the center of curvature with respect to the surface is known to be better than 1 part in 4000.

Each section is separately mounted to a central plate made of high-strength stainless steel. The plate is supported by four fingers which together intercept less than 3% of the open aperture. The steel chosen, 17-4PH, heat treated to condition H1150, provides a very close thermal match to the beryllium, which is essential to avoid radial distortions of the mirror surfaces under changing temperature conditions. This central plate, in addition to providing support for the two hyperbolas, also acts as the spacer. Adjustment of its thickness allows the two hyperbolas to be made confocal.

The measured dimensions of the individual hyperbolas are compared to the design values in Table 2. The differences are a result of the sequence of operations followed during fabrication. As a result of various technical difficulties, the second hyperbola was completed first. Measurements of the front and back radii were made and the surface profile derived from the measured differences between the actual surface and the best fit circle. An updated hyperbola was calculated to fit these data and the first hyperbola modified to match. The tolerances placed on the reflecting surfaces are shown in Table 3. We identified as the most demanding tolerances that had to be met during the fabrication of the mirror as the roundness of the elements and the deviation of the local slope from that predicted by the design curve. The principal roundness criterion is the variation in the difference between the forward and aft radii of each piece as a function of azimuth. This tolerance is referred to as $\Delta(\Delta R)$, and for this mirror we established a goal of 6 micro-inches. This is a tighter specification than usual for grazing incidence

Table 2. Secondary Mirror Dimensions (Note: Dimensions Are in Inches)

| | Design | Measured |
|--------------------------------------|-----------|----------|
| Diameter at front of 1st hyperboloid | = 1.40804 | 1.40846 |
| Diameter at rear of 1st hyperboloid | = 1.24878 | 1.25209 |
| Calculated diameter at mid-plane | = 1.24000 | |
| Diameter at front of 2nd hyperboloid | = 1.23527 | 1.23346 |
| Diameter at rear of 2nd hyperboloid | = 1.16433 | 1.16485 |
| Length of 1st hyperboloid | = 0.91006 | 0.9131 |
| Length of 2nd hyperboloid | = 0.74605 | 0.7433 |
| Gap for center plate | = 0.10000 | 0.1400 |

Table 3. Secondary Mirror Tolerances

| Optical Tolerance | Definition | Specification (inches or as stated) | Achieved |
|-------------------------|--|-------------------------------------|-----------------------------|
| Average Radius | $R = \bar{R}_a - R_d$ | 200×10^{-6} | 100×10^{-6} |
| Out of Roundness | $\Delta R = (\bar{R}_f - R_{fd}) - (\bar{R}_r - R_{rd})$ | 40×10^{-6} | 8×10^{-6} |
| Variation in ΔR | $\Delta(\Delta R) = (R_{f\phi} - \bar{R}_f) - (R_{r\phi} - \bar{R}_r)$ | 6×10^{-6} | 5×10^{-6} |
| Axial Figures | Sagittal Depth Deviation from Design Curve | 3×10^{-6} | 5×10^{-6} |
| Axial Slope Error | $\left(\frac{dR}{dz}\right)_a - \left(\frac{dR}{dz}\right)_d$ | 5×10^{-6} radians | 15×10^{-6} radians |
| Surface Finish | RMS Roughness | 5 - 15 A | 15 - 20 A |

Subscripts: a = actual f = forward radius
d = design r = rear radius
 ϕ = angular position around circumference

mirrors and is a consequence of their small size. In practice this tolerance depends on the precision of the spindle used during the diamond turning and figuring processes and these proved to be more than adequate. The axial slope error was set at five microradians (1 arc second) and this proved difficult to meet. The final figuring was performed manually and the tendency was to remove material too quickly which, while correcting the slope, adversely affected the figure (sag). Because of program constraints, this deviation from the design requirement was accepted.

X-ray testing

All measurements of the grazing incidence relay optic telescope system performance in the X-ray regime have been conducted in the 89.5 meter vacuum facility at American Science and Engineering, Inc. An Advanced Metals Research X-ray source provides either a point source 30 micrometers in diameter (0.07 arc seconds) or a line source 100 micrometers in width and 1000 micrometers in length (0.2 x 2.3 arc seconds) which can be tilted with respect to the telescope optical axis to produce a 0.2 x 0.2 arc second spot. Since the 5.4 m effective focal length of the compound telescope is a significant fraction of the collimation tube length, the approximation of the laboratory source to a point source at infinity must be evaluated for each quantity measured. The effects of a finite source distance have significant implications for the point response function.

Telescope resolution on-axis

The point response function (PRF) of an optical system describes the radial dependence of the focused image of a point source at infinity. Experimentally, the PRF is derived from an Abel inversion of slit scan data obtained with proportional counters masked by 0.051, 0.254, and 1.270 mm wide slit windows and translated across the image plane. The counting rate of the image plane counter is normalized by comparison to the simultaneous counting rate of a cross-calibrated monitor counter masked with a circular, 0.321 cm² aperture and located directly in front of the telescope mirror.

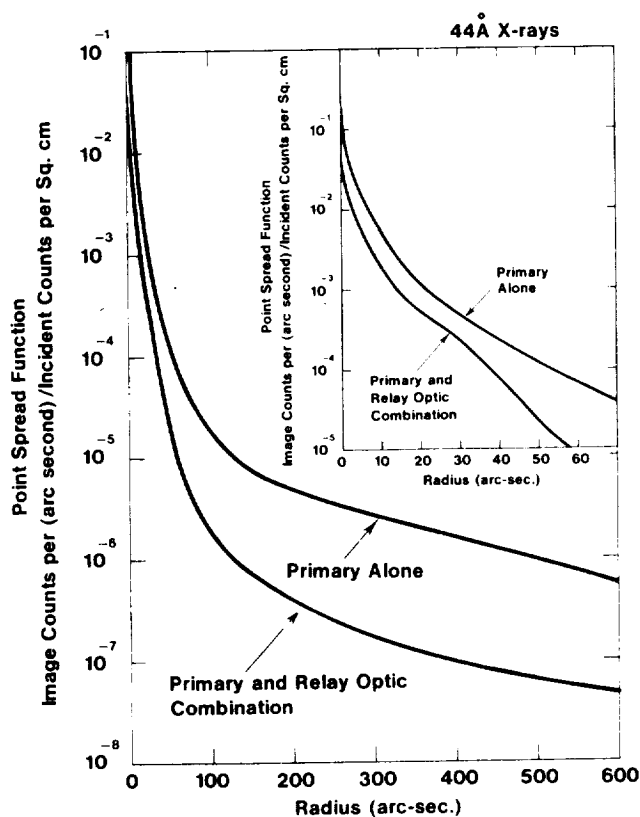


Figure 3. A comparison of the point response function of the compound telescope and the primary mirror alone at 44.5 Å.

The compound telescope PRF of a 44.7 Å (carbon K-alpha) source located on the axis of the optical system is presented in Figure 3. For comparison purposes the PRF of the primary mirror alone² is also plotted in Figure 3. The most significant effect of the addition of the secondary optic is a reduction in the overall efficiency of the system. The PRF is not degraded. In fact, the relative PRF of the compound telescope becomes more narrow than the primary mirror alone at radii greater than 35 arc seconds.

The negligible contribution of scattering from the secondary to the overall PRF has more to do with geometrical optics than with the quality of the secondary. An on-axis ray which undergoes a net scatter from the primary mirror of 1 arc second and is then specularly reflected by the secondary will intersect the compound telescope image plane 26 micrometers from the optical axis because the effective focal length is 5.37 m. An on-axis ray which is specularly reflected by the primary but which undergoes a net scatter from the relay optic of 1 arc second will intersect the image plane 3 micrometers (corresponding to one-ninth of an arc second) from the optical axis because the distance from the relay optic to the image plane is only 0.61 m. Therefore, at the image plane the scattering due to the secondary mirror is completely masked by the scattering due to the primary mirror.

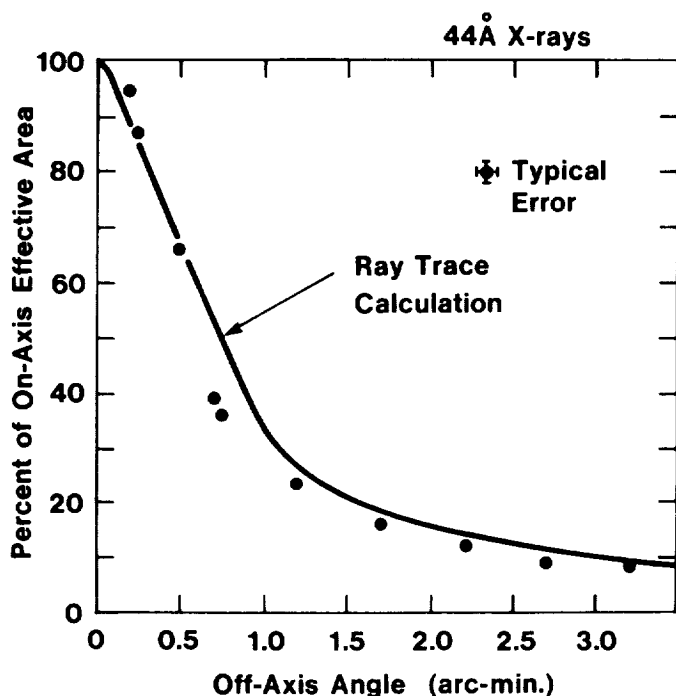


Figure 4. A comparison of the calculated and observed off-axis decline in energy throughput of the compound telescope, expressed as a fraction of the on-axis effective collecting area, for a 89.5 meter source distance.

The apparent narrowing of the compound telescope PRF at large scattering angles is due to vignetting of off-axis rays by the relay optic. The length of the hyperboloid mirrors of the relay optic were chosen to maximize on-axis resolution. Many off-axis rays which are reflected by the primary miss the reflecting surfaces of the secondary. A plot of the relative decrease in effective area with off-axis angle is presented in Figure 4. The solid line is a theoretical curve which is obtained from a ray tracing program which does not include scattering. The measured data points are obtained by removing the slit mask on the image plane proportional counter and rotating the optical bench of the telescope relative to the source. If the field of view is defined as the position where the effective area is 10% of its on-axis value, then the field of view of the compound telescope is restricted to a radius of 2.5 arc minutes.

Integration of the PRF in Figure 3 which yields the percent of total energy in the focal plane within a given radius of the optical axis is presented in Figure 5. The improvement in percent encircled energy of the compound telescope relative to the primary is due to vignetting of off-axis rays by the relay optic. Because of vignetting, rays at large scattering angles are lost so that a higher fraction of the rays that do reach the focal plane are close to the image center.

Vignetting of off-axis rays by the relay optic reduces the total energy throughput of the compound telescope relative to the primary alone. If the energy in the secondary focus image plane within a given radius of the image center were plotted as a fraction of the total energy in the prime focus image plane, each point of the Primary and GIRO Combination curve in Figure 5 would be reduced by a factor of 2.6 and the curve would asymptotically approach the value of 38.5%. Therefore, the improvement in the percent encircled energy of the compound telescope is achieved with a reduction in total energy throughput.

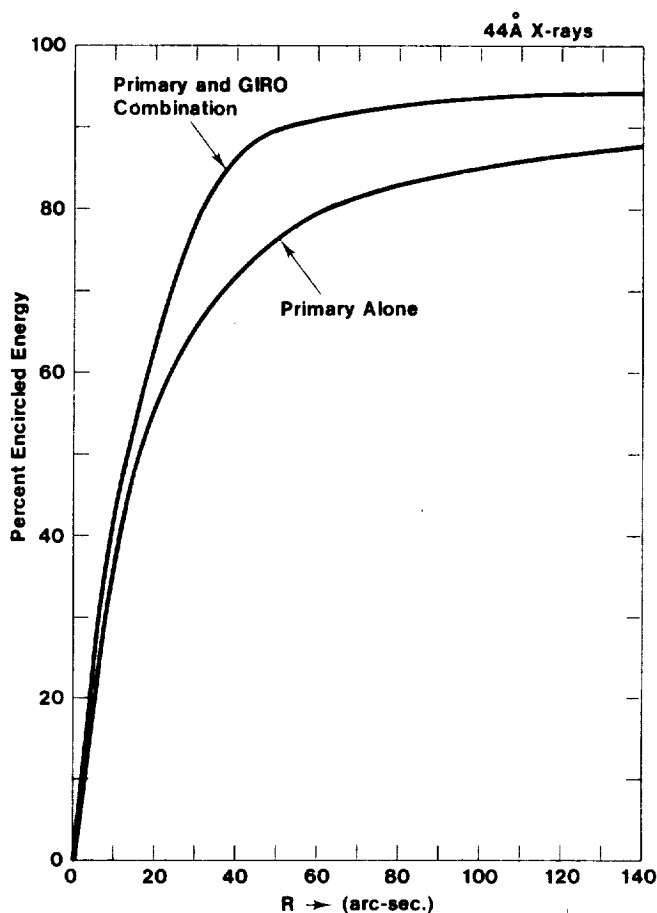


Figure 5. A comparison of the integrated point response function of the compound telescope and the primary mirror alone at 44.5 Å.

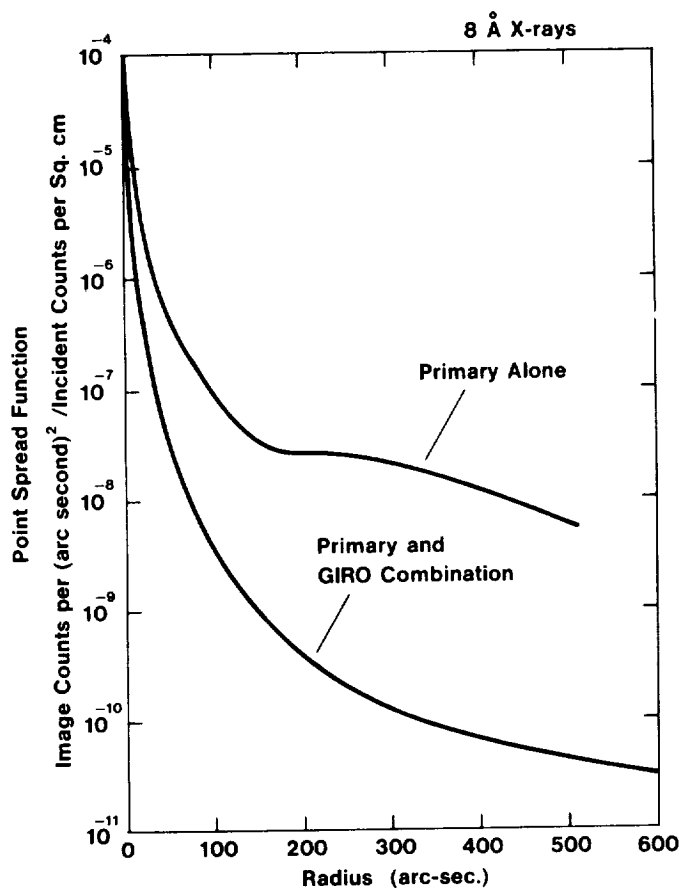


Figure 6. A comparison of the point response function of the compound telescope and the primary mirror alone at 8.3 Å.

Finite source distance effects and off-axis resolution

Geometrical ray tracing (without scattering) of the compound telescope image blur diameter for an on-axis point source as a function of source distance is presented in Figure 7. Because the optical elements of the relay optic were shortened to maximize resolution, the energy throughput of the compound telescope is very sensitive to the position of the relay optic. The calculations displayed in Figure 7 are constrained to maximize the energy throughput of the system by adjustment of the relay optic position. At object distances less than 600 m, the goals of zero blur diameter and maximum energy throughput become mutually exclusive and at object distances less than 100 m, it is impossible to achieve zero blur diameter with any relay optic position. Even at infinite source distance, the relay optic position for maximum energy throughput is slightly different from that for zero blur diameter although the resulting blur is small compared to the effect of scattering. While it has not been possible to experiment with different vacuum tube lengths to test these calculations, the experimentally determined relay optic position for maximum energy throughput in the 89.5 m facility corresponds to the 21 mm displacement from infinity focus position predicted by the calculations. The 1 arc second RMS blur diameter predicted by ray tracing for a 89.5 m source distance is significant in comparison to the 1 arc second half width-half maximum of the observed PRF.

All off-axis images of the compound telescope have some level of geometrical blurring which is greater in the direction perpendicular to the displacement of image from the on-axis point. The degree of the blur in the X and Y secondary focal plane directions for an image which is displaced in the X direction from the on-axis point is shown by the geometrical ray trace calculation presented in Figure 8. This aberration is independent of scattering and will limit the practical field of view for high resolution imaging to a 1.25 arc minute radius.

At shorter wavelengths, the PRF of the primary mirror is distinguished from its PRF at 44.7 Å by an increase in the large angle scattering². Because these scattered off-axis rays miss the relay optic, the 8.3 Å (aluminum K-alpha) PRF of the compound telescope presented in Figure 6 is similar to the 44.7 Å PRF of the compound telescope. Integration of PRFs of the compound telescope at both 44.7 Å and 8.3 Å yield 50% encircled energy radii at 17 arc seconds. In contrast, the 50% encircled energy radii of the prime focus are 18 arc seconds at 44.7 Å and 31 arc seconds at 8.3 Å.

Photographs of a pinhole array illuminated by a diffuse source provide another indication of the on-axis resolution of the compound telescope. A pinhole array with 1 arc second diameter pinholes on 2 arc second centers was illuminated with 44.7 Å X-rays from the defocused AMR source. The 6 pinholes which were illuminated are resolved. Although detailed film calibration and densitometry have not been conducted for these photographs, the film developing and printing were conducted in a manner consistent with that used in previous rocket flights.

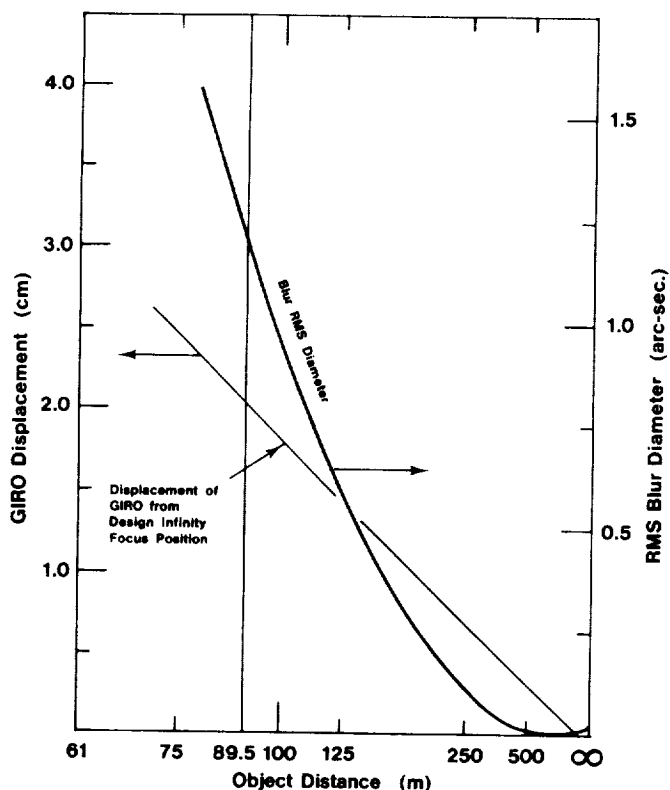


Figure 7. Ray trace calculation of the position of the secondary optic which maximizes the on-axis energy throughput and the resulting blur (not including scatter) for a range of source distances.

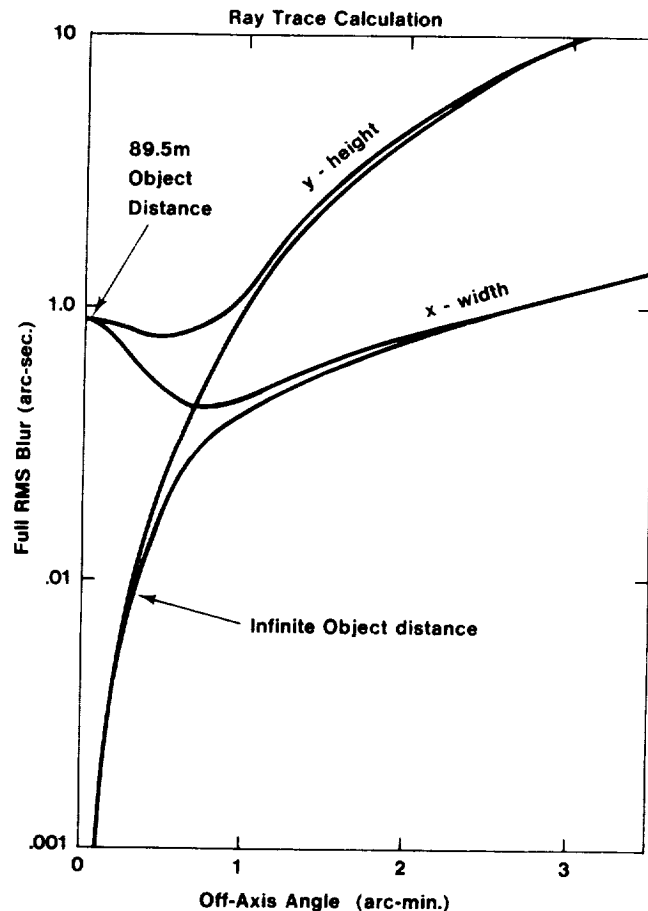


Figure 8. Ray trace calculations of blur (not including scattering) in the two dimensions of the compound telescope image plane for a point source off-axis in the X direction

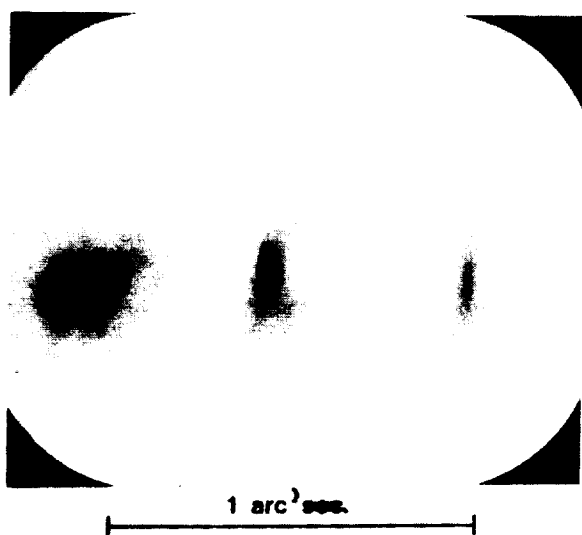


Figure 9. Photograph of X-ray source imaged by the compound telescope for the off-axis displacements (from left to right) of 0 arc seconds, 30 arc seconds, and 60 arc seconds.

Since the off-axis blur is not a circular intensity pattern, a slit scan along one axis is not sufficient to determine the response function. Accordingly, we used photographic X-ray photometry to measure the two-dimensional structure of the off-axis blur. A composite photograph of three exposures of a 44 Å X-ray source taken at the on-axis point, 30 arc seconds off axis, and 60 arc seconds off axis is presented in Figure 9. Although the tasks of film calibration and densitometry have not been completed at the time of this writing, the three exposures were taken on the same roll of film to the same level of monitor counts at the entrance aperture of the telescope and printed as a negative "sandwich" to eliminate any relative enhancements. Although the line source was utilized to generate a counting rate sufficient for reasonable exposures, the ratios of the height to width in the photograph agree with the ray trace calculation. The elongated geometrical blurring pattern is not obscured by scatter because the majority of the scatter seen in the image plane is due to scatter of the primary

(see above). Since the scattering angle is small (50% in less than 18 arc seconds), the rays scattered by the primary are subject to approximately the same aberration as those not scattered—yielding an overall X-Y asymmetry in the total blur.

Conclusion

The goal of increasing the plate scale of a soft X-ray solar telescope over that of previous optical systems while retaining a physical size less than 2 meters has been achieved with the use of a grazing incidence relay optic. The design and fabrication of the relay optic produced a system with on-axis resolution equal to that of the primary alone. However, the drawback of the compound telescope system is an increase in geometrical aberration and decrease in effective area with off-axis angle. Limits in field of view are 1.25 arc minutes in radius for 1 arc second resolution and 2.5 arc minutes in radius for acceptable effective area. Use of a CCD detector instead of photographic film reduces the problem of effective area because of the higher quantum efficiency of CCDs. Additionally, the larger plate scale of the compound telescope compensates for the larger pixel size of CCDs. It is anticipated that this system will provide a useful tool to study small scale structure in the solar corona.

Acknowledgements

It is a pleasure to acknowledge the help of the staffs of the Applied Optics Center and of Research Optics and Development, Inc., who participated in the fabrication of the secondary optic. We would also like to thank Alan DeCew who as both a consultant and as President of Research Optics and Development contributed to the development of the fabrication procedures. Tireless effort in gathering X-ray performance data was contributed by Daniel O'Mara of AS&E. The work was performed under NASA contract NAS5-25496.

References

1. J.M. Davis, A.S. Krieger, J.K. Silk and R.C. Chase, Proc. Soc. Photo-Opt. Instrum. Eng. **184** (1979) 96.
2. R.C. Chase, A.S. Krieger and J.H. Underwood, Appl. Opt. **21** (1982) 4446.
3. Fabrication was started at the Applied Optics Center, Burlington, MA 01803 USA. When the Burlington facility was closed, the work was transferred to Research Optics and Development, Inc., Waltham, MA 02154 USA.
4. Random Devices Inc., Newbury, Massachusetts 01950, USA.

4.17 The Plasma and Magnetic Field Properties of Coronal Loops Observed at High Spatial Resolution

D.F. Webb

American Science and Engineering, Inc.
Cambridge, Massachusetts 02139

and

Emmanuel College
Boston, Massachusetts

G.D. Holman

Laboratory for Astronomy and Solar Physics
NASA/Goddard Space Flight Center
Greenbelt, Maryland 20771

J.M. Davis

American Science and Engineering, Inc.
Cambridge, Massachusetts 02139

and

NASA/Marshall Space Flight Center
Huntsville, Alabama 35812

and

M.R. Kundu and R.K. Shevgaonkar

Astronomy Program
University of Maryland
College Park, Maryland 20771

ORIGINAL PAGE IS
OF POOR QUALITY

THE PLASMA AND MAGNETIC FIELD PROPERTIES OF CORONAL LOOPS OBSERVED AT HIGH SPATIAL RESOLUTION

D. F. WEBB

American Science and Engineering, Inc., Cambridge, Massachusetts; and Emmanuel College, Boston, Massachusetts

G. D. HOLMAN

Laboratory for Astronomy and Solar Physics, NASA Goddard Space Flight Center, Greenbelt, Maryland

J. M. DAVIS

American Science and Engineering, Inc.; and NASA Marshall Space Flight Center, Huntsville, Alabama

AND

M. R. KUNDU AND R. K. SHEVGAONKAR¹

Astronomy Program, University of Maryland, College Park

Received 1986 May 22; accepted 1986 October 6

ABSTRACT

We compare coordinated, high spatial resolution observations obtained in 1979 and 1981 in soft X-rays in microwaves at 1.45 GHz (20 cm) and 4.9 GHz (6 cm) and with photospheric magnetograms, of six coronal loops. The loops were found to have plasma parameters typical of quiescent active region loops. Each loop had a compact microwave source with $T_b = 1-2.5 \times 10^6$ K cospatial with or near the loop apex. Contrary to some interpretations, no complete loops (as determined by the X-ray observations) were imaged in microwaves. Model loops using the derived observational plasma and magnetic parameters are constructed, and the predicted distribution of thermal microwave emission compared with observations. The loop emission observed at 4.9 GHz is best described by fourth harmonic gyroresonance emission from a dipole loop model, but with less field variation along the loop than in the models of Holman and Kundu. The 1.45 GHz emission is likely to be free-free, since the X-ray loops are optically thick to free-free emission. The modeling results require the existence of an external plasma around the X-ray loops with a temperature of $\sim 10^5$ K or less. We are also able to deduce or place constraints on the magnetic field strengths within and their variations along the loops.

Subject headings: plasmas — Sun: corona Sun: magnetic fields Sun: radio radiation Sun: X-rays

1. INTRODUCTION

High spatial resolution observations over more than a decade have revolutionized studies of active regions and coronal loops. In particular, microwave observations have revealed broad, diffuse areas coincident with plage emission and small, intense components associated with sunspot penumbrae and satellite spots, transverse fields over neutral lines or filaments (Kundu *et al.* 1977; Kundu, Schmahl, and Gerassimenko 1980), and emerging flux regions (Kundu and Velusamy 1980). Observations with the Very Large Array (VLA) have revealed looplike structures reminiscent of those observed in soft X-rays and EUV (e.g., Lang, Willson, and Rayrole 1982; Lang and Willson 1983; Kundu and Velusamy 1980), suggesting that some of this microwave emission arises in individual coronal loops.

Most of the coronal plasma in an active region is at high temperature (i.e., $T_e > 10^6$ K) and has its dominant emission in the soft X-ray regime (e.g., Webb 1981). In the radio regime, the slowly varying component of emission over active regions has a spectral maximum at centimeter wavelengths. Therefore, coordinated high-resolution observations in X-rays and microwaves can provide physical insights into coronal loop structures. The X-ray observations provide information on the three-dimensional distribution of plasma and the overall topology of the coronal magnetic field in a loop. The microwave observations provide details on the scale height, strength,

and direction of the loop magnetic field and the relative contribution of magnetic and gas pressure, while photospheric magnetograms measure the strength of the field in the feet of the loop.

At low spatial resolution (~ 0.5), quiescent active region microwave emission has been interpreted as either thermal, low-harmonic gyroresonance (gr) emission associated with strong sunspot fields, or thermal bremsstrahlung from plage regions. Recent combined, high-resolution X-ray and microwave observations reveal a more complicated picture. Some observers (Chiuderi-Drago *et al.* 1982; Lang, Willson, and Gai-zaukas 1983; Shibasaki *et al.* 1983; Strong, Alissandrakis, and Kundu 1984) have found good agreement between the X-ray and microwave observations and the accepted emission mechanisms for quiescent features. Others (Schmahl *et al.* 1982; Webb *et al.* 1983, hereafter Paper I; Kahler *et al.* 1984, hereafter Paper II) have observed significant differences between the detailed locations of these sources. We will emphasize that the detailed correspondence in active regions between X-ray and microwave emission is poor, and that a major problem with interpreting loop microwave emission is that this emission is often compact and restricted to the loop top.

Comparisons between models and observations of active region loops have been inconclusive because of the lack of high spatial resolution data at different wavelengths and information on the three-dimensional structure of the magnetic field in the corona. Recently, comparisons have been attempted between X-ray, EUV, and radio observations of loops and

¹ Also Indian Institute of Astrophysics, Bangalore.

static loop models, but these suffered from either a lack of high-resolution radio data (e.g., Pallavicini, Sakurai, and Vaiana 1981) or a lack of simultaneous X-ray or EUV and microwave data (e.g., McConnell and Kundu 1983). Our results demonstrate the importance of simultaneous high spatial resolution microwave and soft X-ray (and EUV) observations for the testing and refinement of coronal magnetic loop models.

This paper is the third of a series studying the detailed plasma and magnetic field properties of active region loops, with the goal of constraining models of the structure and heating of active regions. The first two papers (Paper I and Paper II) described combined soft X-ray rocket and 6 cm VLA observations on 1979 November 16 and 7 respectively and were primarily observational. In this paper we first describe new results from the comparison of a third set of X-ray rocket and 20 cm VLA observations of an active region on 1981 February 13, and then analyze six loops from these data sets observed to have significant cospatial soft X-ray and microwave emission. Based on this set of observations and the dipole loop models of Holman and Kundu (1985), we then construct model loops and compare the predicted distribution of thermal microwave emission with observations.

In the next section we describe the comparative analysis of the 1981 February 13 observations of Hale region 454 and briefly review the analysis and results from Paper I of the two active regions observed on 1979 November 16. In § III we discuss the derivation of the plasma and magnetic properties of the six loops observed on these two dates to have cospatial soft X-ray emission and microwave sources. Comparison of these data with the loop models are described in § IV, and the results are summarized and discussed in the last section.

II. COMPARATIVE ANALYSIS OF ACTIVE REGIONS

a) 1981 February 13 Observations and Results

i) Observational Data

Instrumental details of the AS&E rocket payloads have appeared in Kahler, Davis, and Harvey (1983) and Webb and Davis (1985). The 1981 February 13 flight payload utilized the fused-quartz grazing-incidence mirror, four different filters (with bandpasses over the range 8–65 Å), a moderate-speed film emulsion (SO-212), and a fine-grain emulsion (SO-253). Full-disk X-ray coronal images with an on-axis spatial resolution of $\sim 2''$ were obtained between 1916 and 1921 UT. Examples of these images are shown in the aforementioned papers.

Radio observations were made with the VLA of the National Radio Astronomy Observatory² between 1600 and 2330 UT. Twenty-six antennas were available in the B-configuration during the observations, providing good UV coverage. The system was sensitive to structures smaller than 1/5 because the shortest spacing used for these maps was $\sim 2000\lambda$. Observations were obtained at 4.9 GHz (6.1 cm) and 1.45 GHz (20.75 cm), and the phase center for continuous tracking was N11W37 at 1915 UT. This was centered on one of the leading sunspots in Hale region 454. A reliable synthesized map of total intensity at 1.45 GHz was produced with a synthesized beam of $4.7'' \times 4.7''$. Unfortunately, reliable 5 GHz maps and polarization data at both wavelengths were not obtained

because the sources were not bright enough at 5 GHz. The observing procedure, calibration, and cleaning methods were similar to that of McConnell and Kundu (1983).³

A full-disk photospheric magnetogram was obtained at the National Solar Observatory⁴ (NSO) Kitt Peak at 1507 UT, and a video magnetogram at Big Bear Solar Observatory (BBSO) at 2009 UT. (It was cloudy at BBSO earlier in the day.) We obtained contour plots and printouts of the NSO magnetogram for use in the analysis. A high-resolution H α image of H454 was obtained at BBSO at 2008 UT. A cine version of the daily full-disk H α patrol film from 1428 to ~ 2000 UT was obtained from NSO-Sacramento Peak Observatory and used to study the evolution of the active centers on this day.

The X-ray and visible light images, the microwave map, and the magnetogram were co-aligned and compared in the same manner as discussed in Papers I and II. Briefly, the major sunspots in H454 were used to co-align the X-ray image, the 20 cm map and the magnetograms. The alignment accuracy was within $\sim 10''$.

ii) Comparative Results

Since we are interested in studying only the quiescent features of the active region corona, each radio map was synthesized from several hours of observations which excluded periods with fluctuations exceeding $\sim 10\%$ of the total intensity signal (i.e., bursts). Therefore, flarelike periods were excluded, but not necessarily slower or evolutionary changes in the active region. In addition, the 1.45 GHz beam included nearly the full Sun, so that contributions to the signal from activity in distant regions were possible.

For the two active regions studied on 1979 November 16 (Paper I), we are confident that the data were obtained during a quiescent period. However, this was not the case on 1981 February 13, when there were three main active region complexes on the Sun: H454 in the northwest, H461/67 in the northeast, and H465 in the southeast. All these regions were active during the VLA observing period, with flares sometimes occurring nearly simultaneously in two or three of the regions. To aid in identifying this activity, we examined Sagamore Hill Radio Observatory fixed-frequency records from 1600 to 2000 UT, NOAA GOES plots and lists of X-ray events, and Solar Geophysical Data (SGD) lists of H α flares and radio bursts (SGD 1981).

The evolution of H454 is important to an understanding of the X-ray observations. H454 was a new region that appeared at the east limb on February 4 on the trailing side of H391. It grew steadily in area and complexity. On February 13 it had roughly equal areas of east-west plage and contained 41 sunspots balanced between polarities (SGD 1981). There were three large spots: two separate symmetrical, positive-polarity spots, and one large negative spot complex. This large spot had peak fields exceeding 2100 G and an area of 1000 millionths of a solar hemisphere.

³ Radio interferometric observations of H454 were also obtained at Owens Valley Radio Observatory (OVRO) at 10.6 GHz (2.8 cm) (Hurford 1986). A single strong, unresolved source ($T_b \approx 10^5$ K) was detected at a location of $137''$ north and $542''$ west of Sun center in celestial coordinates. The source was $\sim 50\%$ circularly polarized and cospatial with the largest sunspot in H454. Its high polarization, intensity, and position over the strong spot fields are consistent with low harmonic, gr emission. Because this source was not detected at 1.45 GHz nor associated with X-ray emission, we will not discuss it further.

⁴ NSO is a facility of National Optical Astronomy Observatories, which is operated by the Association of Universities for Research in Astronomy, Inc., under contract with the National Science Foundation.

² NRAO is operated by Associated Universities, Inc., under contract with the National Science Foundation.

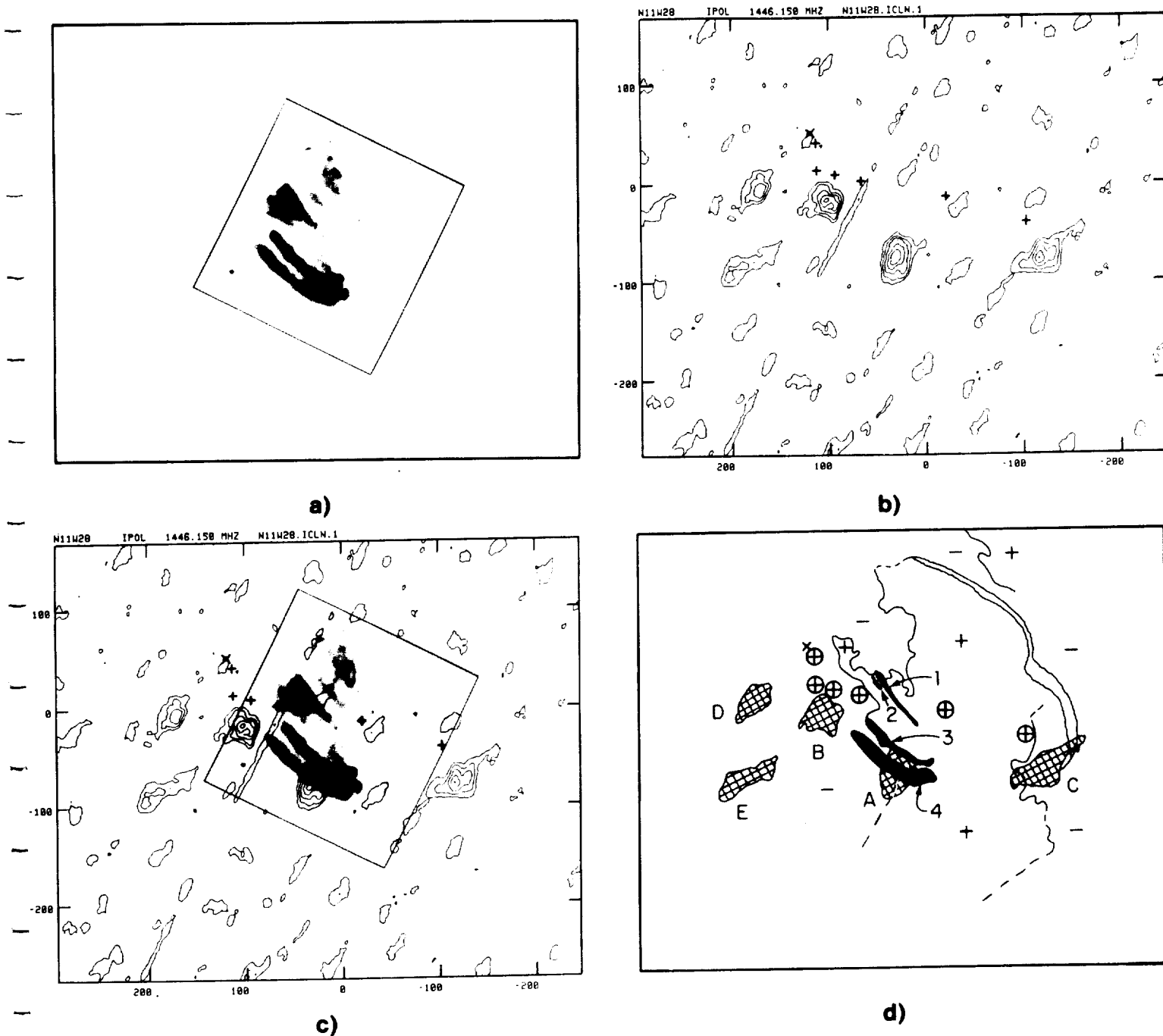


FIG. 1.—Co-aligned, high-resolution images (a) in soft X-rays and (b) at 1.45 GHz (20 cm) of active region H454 on 1981 February 13. The X-ray image is an “edge-enhanced” digitized image of a 20 s exposure on Kodak SO-253 emulsion obtained at 1920 UT. The edge-enhancement program, described in the Appendix of Kahler, Webb, and Moore (1981), essentially filters out low spatial frequencies, yielding enhanced images of coronal structures. Solar north is to the upper right of the X-ray image, and east is to the upper left. The scale unit is parallel to the border of the X-ray image, and east is to the upper left. The phase center (0, 0) of the map was at 661" west and 87" north of disk center at 1915 UT. The map is in total intensity with a synthesized clean beam of $4''.7 \times 4''.7$. The lowest contour and the contour interval are 1.72×10^5 K. The pluses (circled on the schematic) denote the centroids of six major sunspots (Fig. 4b). The cross marks the location of the single strong source observed at 10.6 GHz (see text). (c) An overlay of the X-ray and radio images. The brightest X-ray loops are denoted by numbers. The five 1.45 GHz sources with two or more contours are cross-hatched and denoted by letters. The thin solid and dashed lines are our estimate of the positions of the photospheric inversion lines separating opposite magnetic field polarities. We have drawn the outline of a long H α filament bordering the region to the northwest.

Figure 1 shows for H454 (a) a high-resolution, digitally enhanced soft X-ray image, (b) the $7\frac{1}{2}$ hr synthesis 1.45 GHz VLA map in total intensity, (c) the overlay of these two images, and (d) a schematic diagram relating the salient features from all the observations. The pluses on the 20 cm map and the circled pluses on the schematic denote the centroids of six major sunspots in the region (see Fig. 3b below—the large negative spot had a double umbra). The schematic drawing compares the locations of the brightest 1.45 GHz (and single 10.6 GHz) sources with the brightest X-ray loop, our estimate of the location of the photospheric inversion line(s), and the photospheric magnetic field polarities, both from the Kitt Peak magnetogram at 1507 UT.

As observed in Figure 1a, the dominant X-ray emission was confined to generally east-west-directed loops spanning the negative (east) and positive (west) bright plage areas between the eastern negative and middle positive spots (Fig. 1d). The northern loop systems, including the shorter, bright loop systems 1 and 2 in the center of the region, did not change during the rocket observations. However, the long southern loops, labeled "3" and "4" in Figure 1d, did evolve during this period. Since these loops are the subject of our comparison with 1.45 GHz emission in the next section, we examine this evolution more closely.

Figure 2 shows the NOAA GOES 1–8 Å and 0.5–4 Å soft X-ray flux plots around the period of the rocket flight. Two major events are evident starting at 1910 and 1933 UT. The first event involved a compact H α flare and surge in H454 that was homologous with an earlier H α event at ~1700 UT. It occurred in the northern penumbra of the large spot. This subflare appeared in the rocket images during its decay as a small, bright X-ray kernel which faded at 1918 UT. The images used in our quantitative analysis were obtained at about 1917 and 1919 UT and were not affected by this tiny flare.

After about 1920 UT, nearly simultaneous events occurred in the southeast region H465 and in H454. The relatively long duration GOES X-ray signature commencing at 1933 UT was probably dominated by an H α flare and mass ejection from H465. However, the SGD only listed a 1N flare in H454 with

an onset at 1929 UT and a maximum at 1938 UT. The H α movie revealed that the flare commenced about 1920 UT in the plage at the feet of the large southern X-ray loops 3 and 4. The X-ray image in Figure 1a was obtained at 1920 UT and shows the west foot of loop 3 brightening. This area did not appear in the earlier images that were used in our analysis. Therefore, we believe that the results of our X-ray analysis of those loops are representative of a fairly quiescent but preflare state of the loops.

To improve our understanding of the plasma and magnetic field properties of coronal structures, we need to identify emission at both X-ray and microwave wavelengths arising from the same volume of a coronal structure. However, as in the only previous studies involving simultaneous X-ray and microwave (5 GHz) observations at high spatial resolution (Paper I and Paper II), we find that the X-ray emission was generally not associated with the 1.45 GHz microwave sources. Only one of the five 1.45 GHz sources (source A, Fig. 1) was cospatial with X-ray emission.

Table 1 lists the brightest 1.45 GHz sources as designated on Figure 1d in decreasing order of peak brightness temperature T_b . To be considered, a source had to contain at least two contours; the other features on the map may be noise or artifacts of the CLEANing process. For each source in Table 1 we

TABLE 1
BRIGHTEST 1.45 GHz SOURCES IN ACTIVE REGION H454

| Source | Peak T_b (10^5 K) | Size* | Association |
|---------|---------------------------|---------|--|
| A | 8.6–10.3 | 22"–38" | Top of coronal loop arcade; photospheric neutral line |
| B | 8.6 | 22 32 | Large sunspot umbra or penumbra; near feet of coronal loops |
| C | 8.6 | 20 35 | Photospheric neutral lines/filament; sunspot |
| D | 5.2–6.9 | 15 30 | ? (Faint H α plage) |
| E | 3.4 | 5 30 | ? |

* The approximate FWHM dimensions of the total intensity along the short and long axis of each source. These are uncorrected for the beam shape.

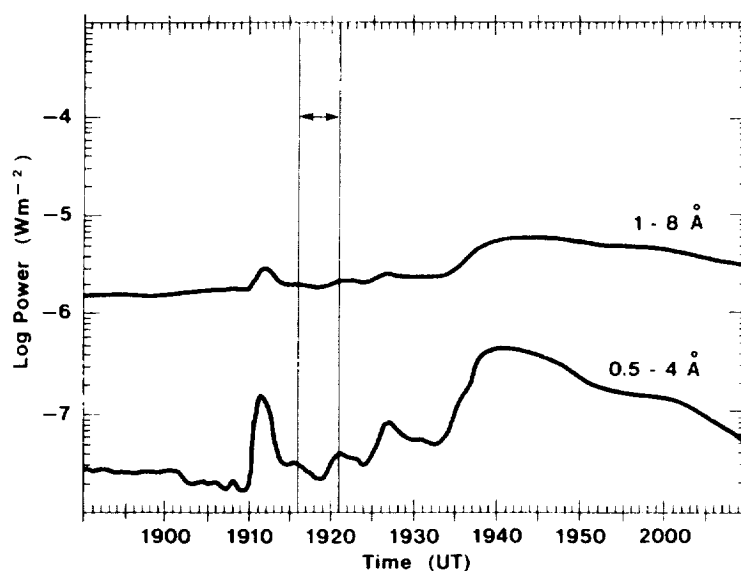


FIG. 2.—NOAA GOES2 satellite whole-Sun soft X-ray flux evolution around the time of the rocket flight on 1981 February 13. Plots from both the softer (top) and harder (bottom) channels are shown. The period of the rocket flight is denoted by the arrows. Date courtesy of S. Kahler, Emmanuel College.

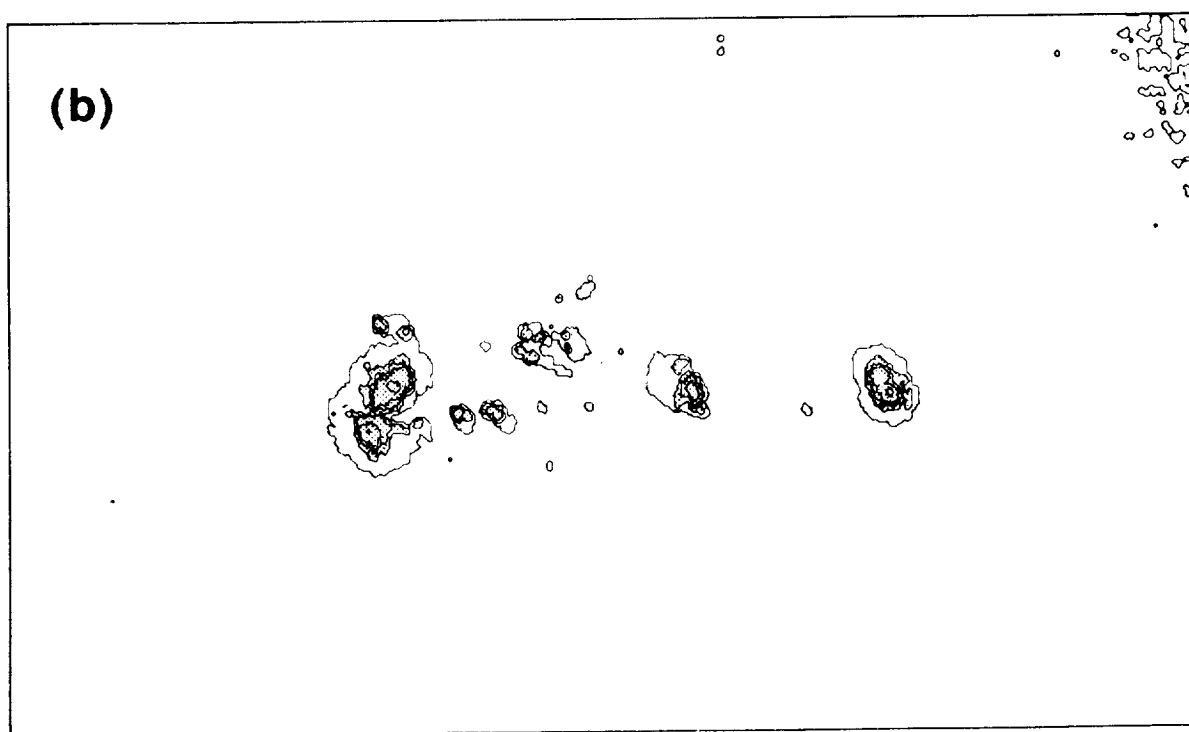
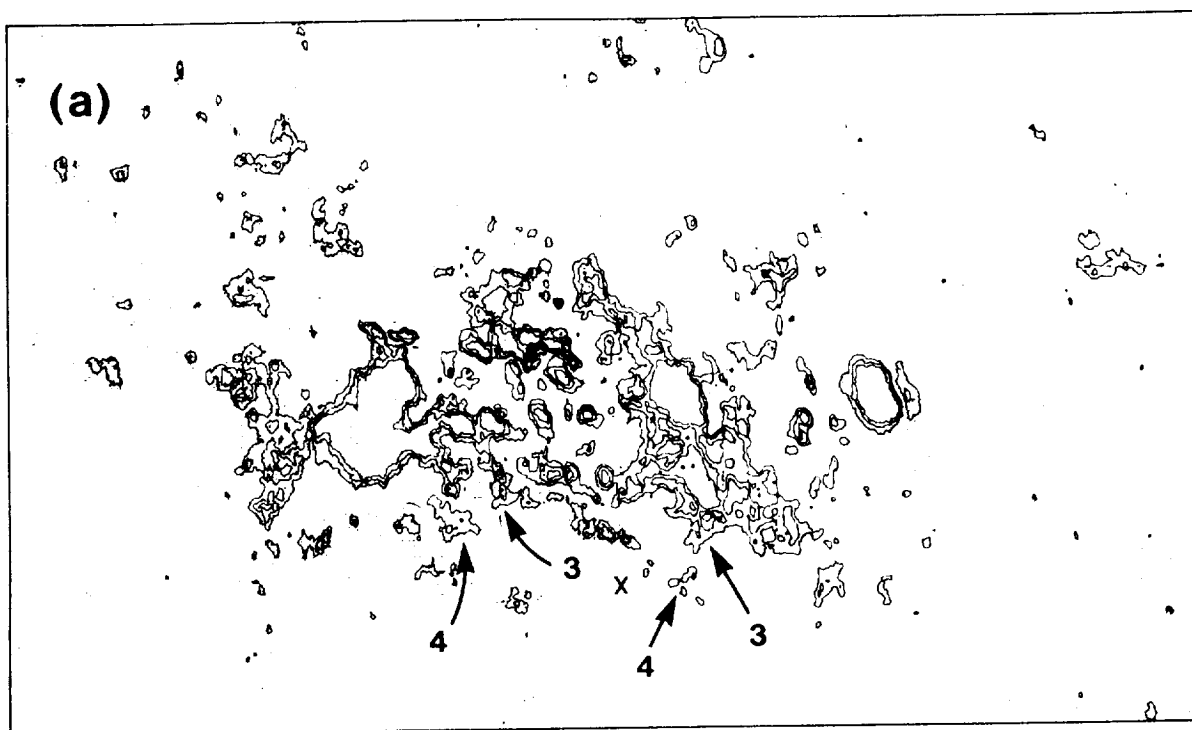


FIG. 3.—Contour map of the photospheric magnetic field in active region H454 at 1507 UT on 1981 February 13. Contours of ± 200 , 350 and 500 G are shown. Negative fields are shaded; fields less than -50 G are shown without contours. The numbered arrows point to the locations of the footpoints of X-ray loops 3 and 4 (see Fig. 1). The cross denotes the position of the peak 1.45 GHz emission from source A. (b) Co-aligned white light continuum contour map showing locations of the sunspots in H454. Solar north is up and east to the left. The horizontal dimension of the boxes is 8.5. Data courtesy of J. Harvey, NSO (Kitt Peak).

also list its size and possible physical association in the manner of Paper I.

Source A was one of the brightest and largest 1.45 GHz sources and was positioned at or near the apex of the bright southern X-ray loops (Fig. 1c). Source A also overlaid an area of moderate H α plage and was near a bend in the photospheric inversion line. But this area of the photosphere generally had magnetic fields of low strength and low gradients. Figure 3 presents Kitt Peak contour maps of (a) the photospheric magnetic field and (b) sunspots in H454 on 1981 February 13. The "X" in Figure 3a denotes the center of source A, and the arrows point to the locations of the feet of X-ray loops 3 and 4.

Source B was a strong, circular source lying near the eastern foot of loop 4. It overlaid an area of weak negative polarity field without bright H α emission. The center of the source was only 25"–30" from the southern umbra of the large spot. Given the alignment uncertainty and the possibility of projection effects, it might have been associated with the corona above this umbra or with the penumbra.

The elongated source C lay 40" west of the westernmost positive spot in an area of no H α activity and moderate magnetic field strength. The source straddled the inversion line, an area of high field gradients, and the southern end of a long-curving filament which formed the region to the west. Projection effects would be significant for this coronal source. Both sources D and E lay in areas of weak negative polarity field, with only faint H α plage and no activity. No magnetic pores or spots existed in these areas (see Fig. 3b). The reality of source E was questionable.

Finally, we note that 1.45 GHz emission was *not* detected over regions where we might have expected it based on previous results. With the possible exception of source B, no emission was detected near sunspots or other strong fields where gr emission might be expected. And other than source A, no 1.45 GHz emission was associated with the X-ray loops, the flare-active area to the northeast, nor any bright H α plage regions. Such associations have been emphasized by Lang, Willson, and Rayrole (1982), Lang, Willson and Gaizaukas (1983), and Chuderi-Drago *et al.* (1982), based on the expected dominance of bremsstrahlung radiation at 1.45 GHz. But even the associated source A did not resemble the size or shape of the X-ray loops.

b) Review of 1979 November 16 Results

Here we briefly review the main results of Paper I to provide the background necessary for the derivation of loop parameters in the next section. That study was based on a determination of the spatial correspondence in two active regions of the most intense sources of 5 GHz emission to coronal loop structures, sunspots, chromospheric structures, and photospheric magnetic fields. Some of the fainter microwave components were associated with X-ray (bandpass of 3–60 Å) loops, but the brighter components were not. Also, most of the bright 6 GHz sources were *not* associated with sunspots. In both Paper I and Paper II, the X-ray and magnetic field observations were used to constrain possible mechanisms for the centimeter radio emission.

Those authors found that free-free emission did not provide sufficient opacity to explain the 5 GHz sources (for which $T_b > 10^6$ K). Gyroresonance absorption at the third or fourth harmonic (requiring magnetic fields of 450 or 600 G; Paper I) or at the fourth or fifth harmonic (fields of 360 or 450 G, Paper II) could explain some but not all of the emission. However, in

both studies, a nonthermal mechanism was proposed to explain sources of intense emission (not associated with sunspots). This result suggests that discrete regions of continuous particle acceleration might be common in active regions, an unexpected result with potential importance to theories of loop heating.

On 1979 November 16 about one-third of the 5 GHz sources in both active regions were cospatial with the feet or upper parts of coronal loops of lengths 5×10^4 km or less. These loops were either inferred from the geometry of the magnetic field or detected directly in soft X-rays. However, only four of the loops had both cospatial X-ray and 5 GHz emission from near the top of the loop. These are summarized in Table II of Paper I and are shown here schematically in Figure 4 superposed on the VLA intensity maps. Only the microwave sources cospatial with the four X-ray loops and the sunspot locations are labeled on Figure 4. Such emission clearly arises from the lower corona. Based on the assumption that the emission in the two wavebands arises from the same volume, direct tests of microwave emission mechanisms and derivation of loop parameters, such as temperature gradients and magnetic field structure, can be made.

The two loops of interest in region H421 are shown in Figure 4a. The weak source E' was cospatial with the top of a short, bright X-ray loop. This loop bridged the main inversion line of the region in an area of high field gradient near a large sunspot (the plus). The western foot ended in or near the spot penumbra and the eastern foot was cospatial with strong ($T_b \approx 4.8 \times 10^6$ K) source E. Because source E was compact and cospatial with a magnetically complex area, we could not unambiguously associate it with the X-ray loop and will not discuss it further. The length of ($\sim 2 \times 10^4$ km), shape, and location of the X-ray loop were typical of penumbral coronal loops (Webb and Zirin 1981). North of the spot lay a classic arcade structure with X-ray loops joining opposite polarity plage divided by a weak H α filament. The X-ray loop drawn on Figure 4a was the largest diffuse arch forming the northern limit of the arcade. Cospatial with or just above the arch was the microwave source H. This source was bipolar and weakly polarized with a peak $T_b \approx 2.5 \times 10^6$ K. There were no microwave sources at the feet of the X-ray arch.

The two loops of interest in region H419 are shown in Figure 4b. The most interesting was a long, thin X-ray loop whose top was apparently fainter than its feet. Cospatial with the loop top was source M, a broad, weak microwave source with moderate polarization. Again there were no sources at the footpoints. Finally, just south of the largest sunspot in H419 lay a bright, triangular-shaped area of X-ray emission associated with H α fibrils and multiple, elongated sources, all of which were labeled source J. The north-south orientation of the radio emission, the X-ray structure, and the H α fibrils suggested that the emission was associated with an arcade of low-lying loops crossing the inversion line with their northern feet possibly in the penumbra. This source also showed significant polarization.

III. DERIVATION OF LOOP PARAMETERS

In this section we derive the pertinent coronal plasma parameters for the six X-ray loops observed (on the rocket images of 1979 November 16 and 1981 February 13) to have cospatial microwave sources at the loop top. We then use these parameters to interpret the microwave emission in terms of the thermal emission mechanisms (free-free or gr emission). For

the two flights, pairs of adjacent exposures through beryllium and aluminized polypropylene filters were converted to digitized arrays of film density. These arrays were obtained at 1702–1703 UT on 1979 November 16 and 1917–1919 UT on 1981 February 13. To determine plasma parameters of the

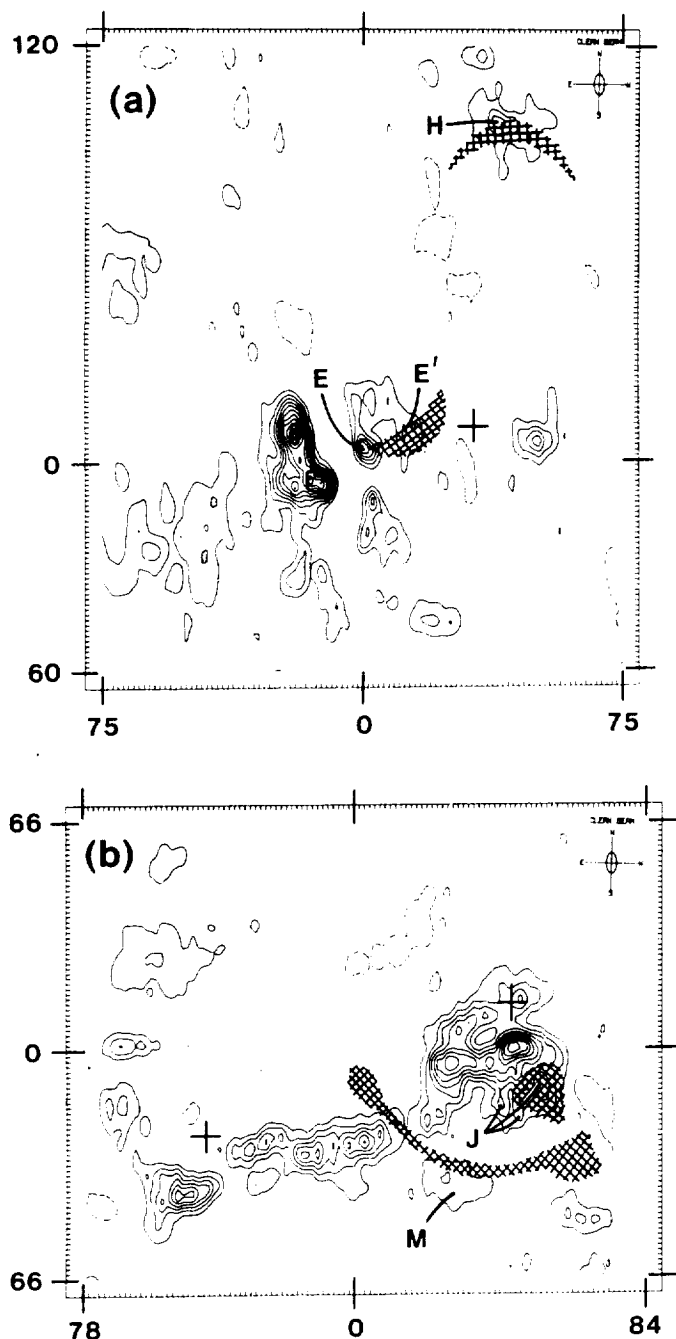


FIG. 4.—VLA intensity maps at 5 GHz (6 cm) of active regions (a) H421 and (b) H419 on 1979 November 16. The size of the synthesized beam was $6'' \times 3''$, shown in the upper right. Celestial north is at the top and east to the left. The phase centers (0, 0) of the two maps were N10W23 and N32W33 heliocentric for H421 and H419 respectively, at 00 UT. The scale units are in arcseconds. On both maps the lowest contour and the contour interval are 8×10^5 K. Large sunspot locations are denoted by plusses. The four X-ray loops with associated 5 GHz sources are overlaid and cross-hatched on the maps, and the microwave sources are labeled with letters. See text for details. This figure was adapted from Figs. 1–3 of Paper I.

X-ray loops, the density arrays were calibrated and reduced to arrays of energy flux at the film plane following procedures discussed by Vaiana *et al.* (1977) and modified by Davis and Webb (1985) for the rocket data. For the 1979 data we used the same laboratory calibrations at 8.3 and 44 Å of the SO-212 film used in Paper II, whereas for 1981 we used the modified procedure discussed by Davis and Webb (1985).

The X-ray images on the two flights were obtained with two different mirror systems, a Kanigan metal mirror on 1979 November 16 and the fused silica mirror in 1981. These mirrors have different characteristics, but both yield image-plane pixel sizes of $\sim 3''$. The mirrors also have different scattering characteristics. This scattering is characterized by point spread functions which are used to produce deconvolved energy flux arrays. These arrays were then used to obtain maps of electron temperature and linear emission measure, both integrated along the line of sight.

Table 2 summarizes the derived X-ray, microwave, and photospheric magnetic data for the six X-ray loops. Columns (3)–(6) list the plasma quantities of the loops derived from the X-ray arrays. The listed errors are those due to film calibration and do not directly include errors due to deconvolution of the spread functions. This latter factor might yield uncertainties in absolute values as great as 50%, especially for the 1979 data. Because of apparent brightness differences along each loop, these parameters were averaged over the eastern and western parts of the 1981 loops, and in 1979 over the bright loop cores near their apices and along the entire loops. Despite the brightness gradients, we see that within loop segments the actual differences in emission measure, density, and temperature were small. The electron temperatures and densities all lay within ranges typical of quiescent coronal active region loops (e.g., Webb 1981). For each flight the brightness differences between loops were due mostly to density differences, not temperature differences, as also reported before (e.g., Davis *et al.* 1975; Cheng 1980). Within the uncertainties each loop was isobaric and isothermal, at least along their axes.

Following Papers I and II, we can use the X-ray loop parameters to estimate the importance of thermal bremsstrahlung to the microwave emission. The free-free optical depth is (cf. Lang 1980)

$$\tau_{ff} = \frac{9.8 \times 10^{-3} \ln(4.7 \times 10^{10} T_e)}{v^2 T_e^3} \int n_e^2 dl,$$

where v is the frequency of radio observations, and the electron parameters are obtained from the X-ray measurements. For these conditions at 4.9 GHz (1979 data), the corona is optically thin ($\tau_{ff} \approx 0.01$ – 0.06) and $T_b(ff) = \tau_{ff} T_e$. The calculated $T_b(ff)$ (col. [7]) is factors of 10–50 too low to account for the observed T_b at the loop top (col. [8]). At 1.45 GHz (1981 data), the corona is optically thick ($\tau_{ff} \approx 2.8$ – 4.5) and $T_b(ff) = T_e(1 - e^{-\tau_{ff}})$. For these conditions the calculated $T_b(ff)$ is about a factor of 2.5 greater than the observed T_b for source A, and optically thick bremsstrahlung is a viable emission mechanism.

Average values for the photospheric magnetic field at the loop footpoints estimated from the NSO contour maps are given in the last column of Table 2. The X-ray loops cospatial with sources H421-E' and H419-J each might have had one foot in a spot penumbra where kG fields are possible. Thus significant longitudinal field gradients were possible in these loops; indeed, these loops were among the brightest in their respective active regions. The fields at the other loop feet (a few hundred G) are typical of plage fields.

TABLE 2
DERIVED PARAMETERS FOR X-RAY LOOPS WITH MICROWAVE SOURCES

| Source or Loop (1) | Region (2) | $\int N_e^2 dl^a$ (10^{28} cm^{-5}) (3) | Δl^b (10^8 cm) (4) | N_e^c (10^9 cm^{-3}) (5) | T_e^d (10^6 K) (6) | $T_e(\text{ff})^e$ (10^6 K) (7) | Peak $T_e(\text{obs})^f$ (10^6 K) (8) | Polarity ^g (9) | Percent Polarity ^h (10) | Footpoint B ^h (G) (11) |
|--------------------|------------|--|---|---|-------------------------------------|--|--|---------------------------|------------------------------------|--------------------------------------|
| 1979 November 16 | | | | | | | | | | |
| H421-E' | Core | 3.9 ± 0.3 | 6.5 | 7.8 ± 0.2 | 3.0 ± 0.2 | 0.15 | 1.5 | L | ... | 50-200 East |
| | Loop | 3.6 ± 0.3 | 6.0 ± 0.8 | 7.8 ± 0.8 | 2.9 ± 0.3 | 0.15 | | | | <1000 West |
| H421-H | Core | 4.2 ± 0.4 | 8.7 | 6.9 ± 0.3 | 2.8 ± 0.2 | 0.17 | 2.5 | R | 33% | 350-500 |
| | Loop | 3.4 ± 0.2 | 13 ± 4.2 | 5.4 ± 1.1 | 2.9 ± 0.2 | 0.14 | | | | |
| H419-M | Top | 0.74 ± 0.06 | 7.0 ± 1.8 | 3.4 ± 0.6 | 2.9 ± 0.2 | 0.03 | 1.5 | R | 50 | 50-200 |
| H419-J | Core | 2.5 ± 0.2 | (10) | (5.0 ± 0.2) | 3.0 ± 0.2 | 0.10 | 1.5-2.5 | R | 33-100 | >500 |
| | Loops | 2.2 ± 0.2 | (10) | (4.7 ± 0.2) | 3.0 ± 0.2 | 0.09 | | | | <1000 |
| 1981 February 13 | | | | | | | | | | |
| 3 | East | 21 ± 8.8 | 7.0 | 17 ± 3.8 | 2.5 | 2.5 | 0.9-1.0 | ... | ... | 300 |
| | West | 20 ± 8.4 | 3.5 | 23 ± 5.2 | 2.4 | 2.4 | | ... | ... | |
| 4 | East | 14 ± 6.0 | 8.7 | 13 ± 2.8 | 2.6 | 2.4 | ... | ... | ... | 250 |
| | West | 15 ± 6.4 | (12) | (11 ± 2.4) | 2.4 | 2.3 | | ... | ... | |

^a Integral emission measure along the line of sight (LOS). Errors are uncertainties due to the film calibration.

^b Loop thickness along the LOS estimated from the loop width on the fine-grain SO-253 film. Quantities in parentheses are less reliable.

^c Electron density derived by dividing the emission measure by Δl .

^d Electron temperature along the LOS from two-filter method. Errors are uncertainties due to the film calibration.

^e For 1979 values, average brightness temperature due to optically thin thermal bremsstrahlung calculated from X-ray parameters; for $\nu = 4.9 \text{ GHz}$. For 1981 values, $T_b = T_e(1 - e^{-\tau})$ because at 1.45 GHz and with these X-ray parameters corona is optically thick.

^f From Paper I, Table II.

^g From Paper I, Table I.

^h Average photospheric magnetic field strength estimated from magnetogram contour maps (e.g., Fig. 3).

Following Kundu, Schmahl, and Gerassimenko (1980) and Papers I and II, curves of unit optical depth are plotted in Figure 5. Figure 5a is for an observation frequency of 4.9 GHz, and Figure 5b is for 1.45 GHz. The pairs of curves running from upper left to lower right are for second to fifth harmonic, extraordinary mode gr absorption. The lower (*dashed*) curve of each pair is for an angle $\theta = 60^\circ$ between the line of sight and the magnetic field, while the upper (*solid*) curve is for an angle of 30° . The curves are computed from the absorption coefficients given by Takakura and Scalise (1970).

In computing the optical depth, the scale length for variation of the magnetic field, $L_B = B/(dB/dl)$, was assumed to be $1 \times 10^9 \text{ cm}$. This is consistent with estimates from magnetic field models (Kundu, Schmahl, and Gerassimenko 1980; Schmahl *et al.* 1982; McConnell and Kundu 1983) and with the sizes of observed X-ray loops. The curves vary as $L_B^{1/(1-s)}$, where s is the harmonic number, and, therefore, the higher harmonics are not very sensitive to small changes in the value of L_B . The short-dashed curves represent unit optical depth for free-free absorption when the density scale length (or loop thickness) is $1 \times 10^9 \text{ cm}$. A source is optically thick to gr absorption if it lies above and to the right of the appropriate curve, and to free-free absorption if it lies below and to the right of the dotted curve. Also shown are the electron densities corresponding to the plasma frequency (*vertical line*). Gyroresonance emission is suppressed in the vicinity of and to the right of the plasma frequency line.

The small rectangles in Figures 5a and 5b encompass the range of electron temperatures and densities deduced from the X-ray observations for the six loops. Free-free emission should be an important contributor to the microwave emission of the loops observed at 1.45 GHz, since the X-ray loops are optically thick to free-free absorption. Gyroresonance emission may also have contributed to the 1.45 GHz source, but it is likely

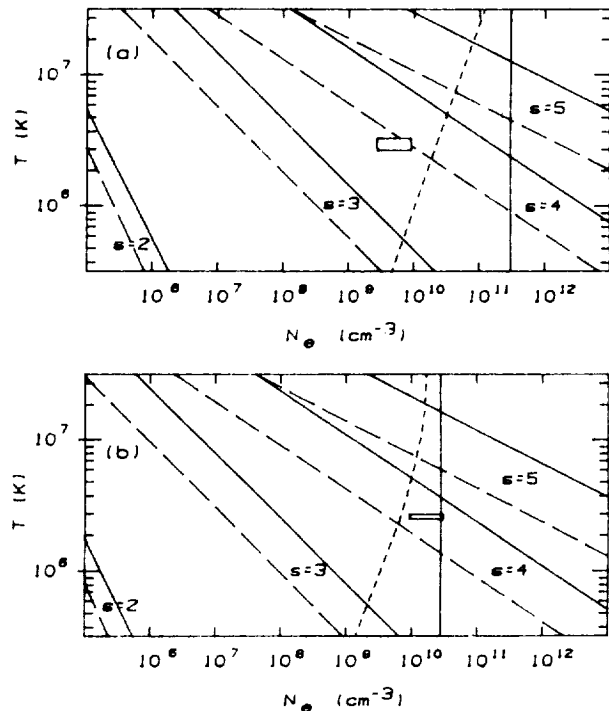


FIG. 5.—Curves of unit optical depth as a function of plasma temperature and density for the observation frequencies of (a) 4.9 GHz and (b) 1.45 GHz. The pairs of diagonal curves are for thermal gyroemission at the second through fifth harmonics. The lower (*dashed*) curve is for $\theta = 60^\circ$ and the upper (*solid*) curve is for $\theta = 30^\circ$. The short-dashed curves show unit optical depth for thermal bremsstrahlung, and the solid vertical lines show the electron densities corresponding to the plasma frequency. The box shows the range of temperatures and densities of the coronal loops determined from the X-ray data for (a) 1979 November 16 and (b) 1981 February 13.

that the observed emission was predominantly free-free. At 5 GHz free-free emission is not important and the loop sources are probably gr emission or, possibly, gyrosynchrotron emission from a more energetic population of electrons. Since the observed brightness temperatures were on the order of or slightly less than the electron temperatures, it is likely that the 5 GHz sources arose from low harmonic gr emission. The highest optically thick harmonic is the fourth, corresponding to a magnetic field strength of 440 G. Such a field strength is consistent with that found in the photosphere at the loop feet, except possibly for source H419-M. This source is consistent with fourth harmonic gr emission and the observed photospheric field strength only if either the photospheric field is directed at a high angle (60°) to the line of sight or if the photospheric field is concentrated in small, unresolved areas.

Because the solar atmosphere cannot be modeled by a simple plane parallel atmosphere, the microwave emission could have arisen from harmonic emission lower than the fourth (see Holman and Kundu 1985). The polarization data can be used to test this possibility. Following Takakura and Scalise (1970), in Figure 6 we have plotted the polarization as a function of the angle θ for the second through the fourth harmonics at 4.9 GHz (a polarization of 1.0 corresponds to 100% polarization in the extraordinary mode). Based on the X-ray data, we assumed the magnetic scale length to be 1×10^9 cm and the loop temperature and density to be 3×10^6 K and 5×10^9 cm $^{-3}$. All the 4.9 GHz sources showed some polarization, and three of the four showed polarizations of 33% or more (see Table 2). If the emitting region was essentially isothermal, as assumed, this would limit the emission to the third or fourth harmonic. Since the observations revealed single compact sources near the X-ray loop tops, high values of θ are likely, which favors fourth-harmonic emission (Fig. 6).

IV. COMPARISON WITH MICROWAVE LOOP MODELS

In the previous section we concluded that the most likely source of the microwave emission at 1.45 GHz (1981 February) was thermal bremsstrahlung, and at 4.9 GHz (1979 November) was fourth-harmonic gr emission. Now we would expect the bremsstrahlung microwave emission to be cospatial with the entire X-ray loop, since, to first order, they are isothermal and isobaric. Computations of the thermal gr emission from iso-

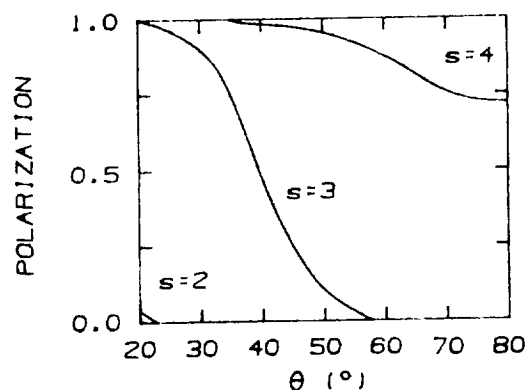


FIG. 6.—Fractional polarization (thermal gr emission in the extraordinary mode) as a function of θ , the angle between the line of sight and magnetic field, for the second, third and fourth harmonics of the gyrofrequency at 4.9 GHz. Plasma parameters consistent with the X-ray observations are assumed (see text).

thermal, two-dimensional dipole magnetic loop models have been made by Holman and Kundu (1985). In these dipole models the variation of the magnetic field strength along the length of the loop is such that several harmonics will contribute to the loop emission. However, contrary to our expectations for the thermal mechanisms, in most of the X-ray loops in our observations the microwave source appeared as a single, fairly compact region near the top of the loop. Therefore, we were forced to consider alternative models for both the 1.45 and 4.9 GHz observations.

a) 4.9 GHz: 1979 November 16

At least two of the X-ray loops observed on 1979 November 16, namely H421-H and H419-M, had a single isolated microwave source near the loop top. In the simple isothermal dipole models, it is difficult to have fourth or even third gr harmonic emission from near the top of the loop without also detecting lower harmonic emission from the legs of the loop. Source H419-J could be consistent with the dipole model if the multiple microwave peaks arose from a single east-west loop. However, the authors of Paper I interpreted the X-ray and H α data as indicating an arcade of north-south directed loops. Source H421-E' could be consistent with a large variation in field strength along an asymmetric loop if H421-E were also associated with the western side of the X-ray loop. A difficulty with such an interpretation in this case, however, is that the peak brightness temperature of source E was greater than the electron temperature deduced from the X-ray observations. Thus, for these latter two sources, direct application of the dipole models of Holman and Kundu does not seem appropriate. (We note that both 419-M and 421-E' were weak sources. The observations, however, reveal three cases of similar microwave structures coincident with X-ray loop tops, a situation unlikely to be due to chance.)

Therefore, we have examined two alternative models. In the first, the magnetic field is held constant along the loop, while in the second the field varies along the loop, though not as much as in the Holman and Kundu (1985) dipole models, and a limited temperature gradient exists in the loop. To obtain a model in which the magnetic field strength does not vary along the length of the loop, we use, instead of a dipole field, the field generated by a line current ($B \propto r^{-1}$). If the current is taken to be at the solar "surface" and hot (3×10^6 K) plasma is present only along field lines with $B \approx 400$ –500 G, a semicircular loop (or arcade) might be observed in X-rays. At 4.9 GHz only fourth-harmonic emission would be observed. If the loop were observed from a direction perpendicular to the plane containing the loop, $\theta = 90^\circ$ and the entire loop would be detected at 4.9 GHz. If the observer looked directly down upon the loop, however, θ would vary from 90° at the top to 0° at the footpoints. Since, for the observed densities and temperatures, the fourth harmonic is only optically thick at high values of θ , only the upper part of the loop would be observed. A computation of the 4.9 GHz brightness temperature (extraordinary mode) as a function of position x_0 along such a loop with average electron temperature and density is shown in Figure 7. The magnetic field strength of 440 G, corresponding to the fourth harmonic, is taken to be constant at the loop radius of $r = 2 \times 10^9$ cm. The scan is for the observer in the plane of the loop with the line of sight perpendicular to the surface ($\phi = 90^\circ$). Some corresponding values of θ are also shown ($\cos \theta = x_0/r$).

The lowest brightness temperature plotted in Figure 7

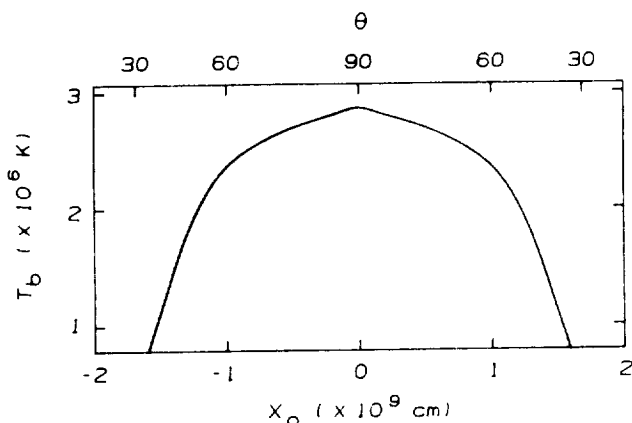


FIG. 7.—Computed 4.9 GHz brightness temperature (extraordinary model) as a function of position for a scan along the projected length of a model semicircular loop with a constant field strength of 440 G (fourth-harmonic emission) at the loop radius of 2×10^9 cm. The loop electron temperature and density are taken to be 3×10^6 K and 5×10^9 cm $^{-3}$. The angle ϕ between the line of sight and the solar surface is 90° . Representative values of θ are also shown.

(8×10^5 K) corresponds to the lowest intensity contour on the microwave maps (Fig. 4). An important conclusion is that although part of the loop is not expected to be observed, the predicted microwave emission is still too extended to explain the compactness of the observed sources. Since the line-of-sight component of the loop magnetic field changes direction at $\theta = 90^\circ$, the observed microwave polarization should change sign where the brightness temperature is greatest. It is interesting that source H421-H did show evidence for such a

polarization reversal (percentage polarization: 33%), and the lowest contour was elongated along the axis of the X-ray loop (Fig. 4 and Paper I, Fig. 1). However, the region of left-hand polarization was less intense and the total intensity contours not as elongated as predicted by this model. On the other hand, source H419-M showed neither evidence for a polarization reversal nor significant elongation along the X-ray loop. It appears that, at least for source M, some variation in field strength along the loop would be required, although not as much as in the simple dipole model.

Sources such as H421-H and H419-M can most easily be explained by a temperature gradient along the loop, with the hottest region in the upper part of the loop as in the model considered by McConnell and Kundu (1983). However, as is typical (e.g., Webb 1981), the X-ray observations revealed the loops to be essentially isothermal along their length. Such a gradient is consistent with these observations if the hot, X-ray emitting plasma is limited to an extended region in the upper part of the loop, with a thin transition zone at the ends of the hot region. For fourth-harmonic emission, the transition zone must occur above the 580 G level within the loop, so that emission from the lower harmonics is not observed.

Detailed models of the observational results are beyond the scope of this paper. Full three-dimensional loop models are presently in preparation (Holman and Brosius 1986). In Figure 8 we demonstrate how the observed 4.9 GHz loop properties can be obtained from a modified dipole loop model. In the figure the third and fourth harmonic levels are shown in a model dipole loop with a minimum magnetic field strength of 425 G (at the top of the loop where $y = 10.4 \times 10^9$ cm) (cf. Fig. 1 of Holman and Kundu 1985). The y -coordinate is measured from the position of the dipole. The transition zone must occur

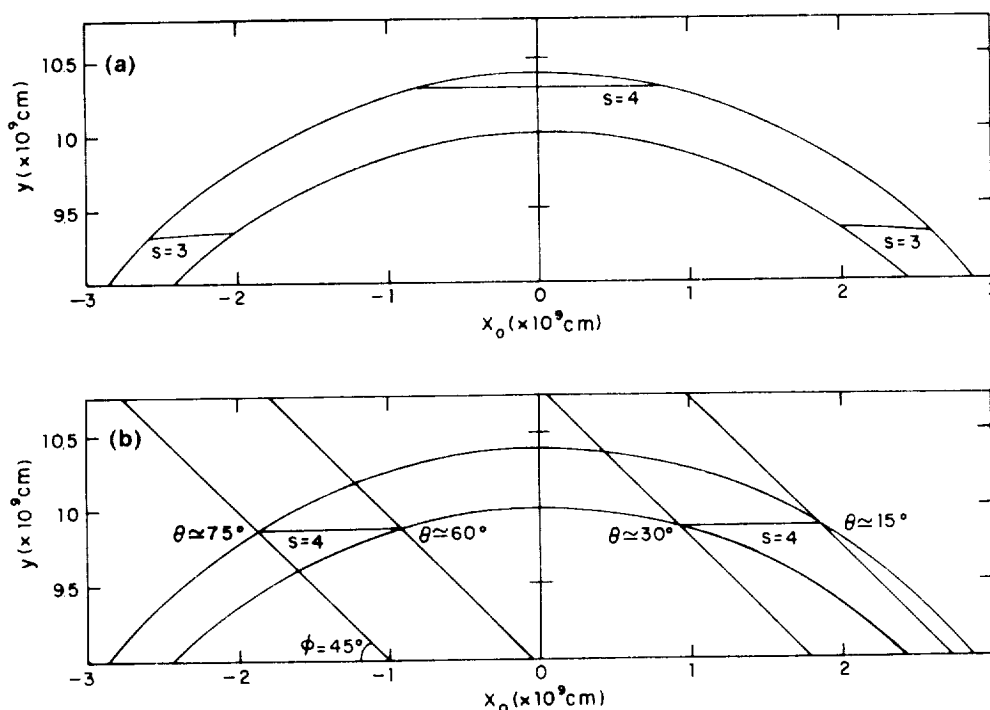


FIG. 8.—(a) A model dipole magnetic loop with a minimum magnetic field strength of 425 G at $y = 10.4 \times 10^9$ cm. The third- and fourth-harmonic thermal gr emission levels for an observation frequency of 4.9 GHz are shown. The y -axis coordinates are measured from the position of the dipole. (b) Same geometry, with a minimum magnetic field strength of 375 G at $y = 10.4 \times 10^9$ cm. Lines of sight with an inclination of $\phi = 45^\circ$ are shown at the edges of the fourth-harmonic level, and corresponding values of θ are shown.

at or above the $y = 9.4 \times 10^9$ cm level so that third harmonic emission is not observed. The level at which fourth harmonic emission occurs ($B = 440$ G) is near the top of the loop, so that only a single microwave source at the top would be observed. If the observer looked down on the loop ($\phi = 90^\circ$), a polarization reversal would be expected, as for the line-current model. A slight inclination of the line of sight at $\phi = 75^\circ$ or less, however, will give a source of uniform polarization. An inclination angle somewhat larger than 75° may in fact explain the polarization structure of source H421-H. The line of sight might also have an inclination out of the plane of the loop, as in the actual observations, without changing these basic features.

It seems unlikely that the 440 G level typically will appear just at the apex of a magnetic loop. Figure 8b shows a model loop for which the fourth-harmonic level is somewhat lower, so that it is separated into a region in each leg of the loop. The field strength at the top ($y = 10.4 \times 10^9$ cm) of this loop is 375 G, and the third harmonic level is just below the x_0 axis. If the observer looked directly down on the loop ($\phi = 90^\circ$), a microwave source would be observed in each leg. These sources are identical if $\phi = 90^\circ$ (except for sign of polarization). For smaller values of ϕ they differ, since the range of θ is no longer the same for the two regions. As an example, in Figure 8b lines of sight with an inclination of $\phi = 45^\circ$ are shown. The values of θ for the fourth-harmonic source in the left leg of the loop range from 60° to 75° . In the right leg, however, θ ranges from 15° to 30° . For the parameters of this model, the fourth harmonic is not optically thick at these small angles, and the maximum brightness temperature of the region in the right leg of the loop would be sufficiently low to be unobservable. Hence, once again, only a single, relatively compact microwave source would be observed near the top of the projected image of the loop. The same results can be obtained for an observer outside the plane of the loop, as long as $\theta \leq 30^\circ$ for the region in the right leg of the loop.

An alternative to requiring that the transition zone occur above the third harmonic level might be to have free-free absorption in the plasma external to the loop mask microwave emission from the lower parts of the loop. In the previous section the free-free optical depth at 4.9 GHz for the X-ray loops was determined to be $\tau_{ff} \approx 0.01$ –0.06. If the external medium had a similar emission measure but a temperature an order of magnitude smaller than in the loop, $\tau_{ff} \approx 0.3$ –1.6 for the external plasma. Thus, this mechanism is a possibility, particularly if the density scale length is larger than the thickness of the X-ray loop. However, if the density scale length of the external plasma is determined by gravity, it will decrease with decreasing temperature, e.g., $l = 1 \times 10^9$ cm for a 3×10^5 K plasma. Also, if the external plasma density is much lower than the loop density, the free-free optical depth will be too small for absorption to occur.

b) 1.45 GHz: 1981 February 13

We found earlier that free-free absorption was important for the loop emission at 1.45 GHz. The X-ray loops were optically thick, but, as at 4.9 GHz, only a single, compact microwave source was observed (Fig. 1). Hence, both the failure to detect in emission the entire X-ray loops or any of the other observed X-ray structures, and the compactness of the associated microwave source, must be explained. That most of the loops were not observed at 1.45 GHz suggests that absorption by an external plasma might be important. If we assume that microwave

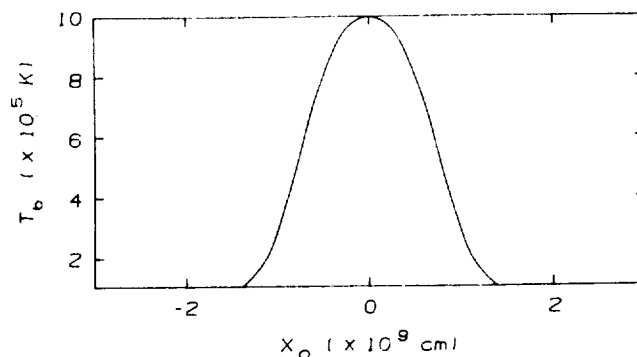


FIG. 9. — Brightness temperature at 1.45 GHz as a function of position along the loop for a scan ($\phi = 90^\circ$) of a model semicircular loop embedded in 1×10^5 K ambient plasma with density decreasing exponentially with height. The outer and inner radii of the loop are 3×10^9 (the sides of the box) and 2.5×10^9 cm respectively. The loop electron temperature and density are assumed to be 2.5×10^6 K and 1.5×10^{10} cm $^{-3}$. The microwave emission is thermal bremsstrahlung. See text for details.

source A was directly associated with X-ray loops 3 or 4 or both (Fig. 1), we can estimate the characteristics of the external plasma needed to detect the loop top but mask the emission from the sides of these loops. A plot of the free-free emission from a model demonstrating how this can occur is shown in Figure 9. The model consists of a semicircular loop with an outer radius of 3×10^9 cm and an inner radius of 2.5×10^9 cm. The loop has a uniform temperature and density of 2.5×10^6 K and 1.5×10^{10} cm $^{-3}$, like those of the observed X-ray loops. The loop is surrounded by a plasma with a uniform temperature of 1×10^5 K. The external plasma density falls off exponentially with a scale height of 3.3×10^8 cm, the gravitational scale height for a plasma of this temperature. The external plasma density at the top of the loop (height = 3×10^9 cm) is 1.6×10^9 cm $^{-3}$. Figure 9 shows a plot of 1.45 GHz brightness temperature as a function of position along the loop ($\phi = 90^\circ$). The width and peak brightness temperature of the resulting source are comparable to the observed values, as desired. (Note that the lowest contour on the 1.45 GHz map was 1.7×10^5 K [Fig. 1]. In computing the brightness temperature for Figure 9, a small contribution from the index of refraction has been neglected.)

Although the model used in Figure 9 treats the external plasma as a uniform, plane-parallel atmosphere, it could, for example, also be a more localized sheath surrounding the X-ray loop. This model is preliminary and intended only to be illustrative; it is less reliable at lower heights, which are unobservable at 1.45 GHz. The model does suffice to demonstrate how the observed structure can be obtained and indicates what properties of the external plasma are required to explain the observational results. More detailed models are in preparation (Brosius and Holman 1986). An external temperature of $\leq 10^5$ K would be required to avoid observable emission at 1.45 GHz. A temperature of the plasma this low (with its corresponding scale height) is also required to produce a microwave source that is sufficiently compact. Lower temperatures and scale heights produce more compact sources. The required emission measure of the 10^5 K plasma is estimated for the model to be $\sim 10^{27}$ cm $^{-5}$. This value is two orders of magnitude smaller than the emission measure of the hot ($> 10^6$ K) loop plasma but an order of magnitude larger than observed in active regions with the Harvard EUV Spectrometer on *Skylab*.

(Noyes *et al.* 1985).⁵ The emission measure could be an order of magnitude smaller if the plasma temperature were closer to 10^4 K.

An alternative model that does not require such a large emission measure is to have the external absorption be gyroresonance rather than free-free. Third-harmonic absorption with $T \approx 10^5$ K requires a plasma density on the order of that required for free-free absorption (see Fig. 5b), so the absorption is likely to be at the second harmonic level. In this case the magnetic field strength at the absorbing level would be 260 G, and the emission measure of the 10^5 K plasma could be as low as $\sim 10^{21}$ cm⁻⁵ (cf. Fig. 5b). The compact microwave source could be reproduced if the second harmonic level either grazed the 2.5×10^6 K loop plasma or cut through a transition zone around the loop. In this case the microwave source would likely arise from a combination of gr and free-free emission.

A third alternative is that the entire X-ray loop was masked by either second harmonic gr or free-free absorption, and the microwave source arose from gr emission from a higher, cooler ($\leq 1 \times 10^6$ K) loop. Such a loop might be part of an arcade of coronal loops, with only the lower ones being sufficiently dense or hot to be detected in X-rays. The source would likely be third harmonic emission with $B = 170$ G. Such a model is similar to that discussed for the 4.9 GHz emission, since only a single, compact source was observed. Whichever model is correct, however, one conclusion remains: the X-ray loops must have been enveloped by cooler plasma with a temperature $\leq 10^5$ K.

V. DISCUSSION

We have analyzed two data sets in order to improve our understanding of the plasma and magnetic field properties of active region coronal loops. Each of these sets consisted of co-aligned, high spatial resolution soft X-ray, microwave and magnetogram images that were used to compare observations of coronal loops and their feet in the photosphere and to constrain possible microwave emission mechanisms. Each of the VLA observations was at a single frequency; the 1979 observation was at 5 GHz (6 cm) and had suitable polarization data (Paper I), and the 1981 observation was at 1.45 GHz (20 cm) with no polarization information. Many microwave sources were detected at 5 GHz (Paper I), whereas only a few sources of lower T_b were observed at 1.45 GHz. At both frequencies the correspondence between the X-ray and microwave emission was poor. However, within the three active regions analyzed, there were six X-ray loops with cospatial microwave sources near the loop top. The plasma parameters of these loops were typical of quiescent active region loops. The microwave loop top sources had $T_b = 1\text{--}2.5 \times 10^6$ K, and three of the four 5 GHz sources were significantly polarized.

Using these results, we constructed model coronal loops and compared the predicted distribution of thermal microwave emission with the observations. At the higher frequency (4.9 GHz; 6 cm), simple isothermal, dipole loop models (i.e., Holman and Kundu 1985) do not fit the observations. The loop emission is best fitted by fourth-harmonic gr emission from a dipole loop (Fig. 8) with a magnetic field of ~ 440 G

near the loop top and with the transition zone at or above the ~ 580 G level to suppress lower harmonic emission. This model has less longitudinal field variation than the models of Holman and Kundu (1985). Alternative possibilities, such as a model where the field is generated by a line current and remains constant along the loop, or one combining gr emission from the loop top and free-free absorption from an external plasma, were considered less likely. We also found that bremsstrahlung alone could not provide sufficient opacity to explain the 5 GHz sources (for which $T_b > 10^6$ K).

At the lower frequency (1.45 GHz; 20 cm), the loops are optically thick to free-free emission. In order to explain the restriction of the 1.45 GHz emission to the top of occasional loops, it is necessary to invoke absorption by cooler material ($T_e \leq 10^5$ K) existing either as a sheath around the loops or as part of an external medium. A possible model (Fig. 9) suggests that the loop field strength would have to be below 260 G, so that the loop top emission would not be masked by second-harmonic absorption in the external medium. Other possibilities we considered include loop emission from both free-free and second harmonic gr, or third harmonic emission with $B \approx 170$ G from a higher, cooler loop invisible in X-rays. The important result is that an external plasma of $T_e \leq 10^5$ K is required in all of these models to explain the combined observations at 1.45 GHz.

In several recent studies, researchers have claimed detection of neutral hydrogen and helium in absorption over active regions (see Webb 1981 for a review). Schmahl and Orrall (1979) found column densities of such cool $N_H > 10^{17}$ cm⁻². And Foukal (1981) discussed EUV observations of opaque coronal material at $\lambda > 912$ Å that was most likely due to absorption by the neutral carbon continuum. Sufficient amounts of such cool material could easily absorb the free-free microwave emission from all or portions of coronal loops and explain the general absence of emission from the X-ray loops. However, white-light and X-ray observations during solar eclipses suggest that any material between coronal loops must be at a pressure at least 3–6 times less than in the loops (e.g., Krieger 1977).

It has been argued from recent observations that entire, large coronal loops at 5 GHz (Kundu and Velusamy 1980; Shibasaki *et al.* 1983) and at 1.45 GHz (Lang, Willson, and Rayrole 1982; Lang and Willson 1983, 1984) are being observed. In fact, Lang and Willson (1983) have suggested that such 20 cm coronal loops, whose dominant emission should be bremsstrahlung, are the radio-wavelength counterparts of X-ray coronal loops. However, none of these observations were supported by simultaneous spatially resolved X-ray imagery. In studies such as ours, where resolved X-ray and microwave images have been compared, the detailed correspondence of the emission at both wavelengths has been poor. Specifically, we have found no cases of cospatial X-ray and microwave emission outlining entire loops and therefore cannot support the interpretation that complete magnetic loops filled with coronal plasma will be imaged at any single microwave frequency.

However, although our 1.45 GHz source A was roughly circular, elongated or curvilinear microwave structures have apparently been observed by others. This suggests that at least portions of coronal loops are being detected. For instance, McConnell and Kundu (1983) observed a looplike structure at 1.45 GHz and, using both 1.45 and 5 GHz observations and

⁵ The portion of the active region discussed here is distant from sunspots and, therefore, is unlikely to be effected by so-called "sunspot plumes," which can have enhanced emission at $T_e \approx 2.6 \times 10^5$ K (e.g., Foukal *et al.* 1974; Webb 1981).

the Rosner, Tucker, and Vaiana (1978) loop model, they concluded that their data were most consistent with bremsstrahlung emission from the loop feet and gr emission from the loop top. They disputed the claims that at 20 cm the entire loop emission could be attributed to thermal bremsstrahlung. Other recent modeling results (e.g., Paper II; this paper; Strong, Alissandrakis, and Kundu 1984; Holman and Kundu 1985) support this view and imply that, at any given radio frequency, the emission from a quiescent coronal loop will be patchy and may be dominated by different mechanisms at different layers (or heights) of the loop. And our results suggest that external absorption may play a significant role in microwave loop emission. Taken together, these studies demonstrate that the physical interpretation of coronal loops requires an appropriate combination of high spatial resolution observations at several wavelengths with mature loop models.

Our observational and modeling results have revealed important differences in interpretation with other results based primarily on observations at a single microwave frequency. Further substantial progress in this field will require simultaneous imaging of coronal structures in soft X-rays, the EUV, and microwaves at several frequencies, and of the photospheric

field for comparison with improved theoretical models of coronal loops.

We are grateful for data and discussions provided by the following individuals: R. Bentley of Mullard Space Science Laboratory, UCL, England, for magnetogram contour maps; E. Cliver of AFGL, Hanscom Air Force Base, for Sagamore Hill radio data; L. Gilliam of NSO-Sacramento Peak Observatory for H α patrol film; H. Jones and J. Harvey of NSO-Kitt Peak Observatory for magnetograms; G. Hurford of OVRO for 10.6 GHz radio data; and S. Kahler of Emmanuel College for GOES X-ray plots. D. McConnell performed the initial reductions of the 1981 February 13 microwave data at the University of Maryland. We thank the AS&E Technical Publications Group for assistance with the images and figures. This study was supported at AS&E by NSF grant ATM-8314115 and at Emmanuel College by AFGL contract AF 19628-82-K-0039. G. D. H. acknowledges partial support from NASA grant 188-38-53-01. The work of M. R. K. and R. K. S. was supported by NASA grant NGR-21-002-199, NASA contract NAG 5511, and NSF grant ATM-84-15388.

REFERENCES

- Brosius, J. W., and Holman, G. D. 1986, *Ap. J.*, submitted.
 Cheng, C.-C. 1980, *Ap. J.*, **238**, 743.
 Chiuderi-Drago, F., Bandiera, R., Falciani, R., Antonucci, E., Lang, K. R., Willson, R. F., Shibasaki, K., and Slottje, C. 1982, *Solar Phys.*, **80**, 71.
 Davis, J. M., Gerassimenko, M., Krieger, A. S., and Vaiana, G. S. 1975, *Solar Phys.*, **45**, 393.
 Davis, J. M., and Webb, D. F. 1985, *A Study of the Cyclical Variations of Coronal Holes and Their Relation to Open Magnetic Fields* (AFGL-TR85-0003).
 Foukal, P. 1981, *Ap. J.*, **245**, 304.
 Foukal, P. V., Huber, M. C. E., Noyes, R. W., Reeves, E. M., Schmahl, E. J., Timothy, J. G., Vernazza, J. E., and Withbroe, G. L. 1974, *Ap. J. (Letters)*, **193**, L143.
 Holman, G. D., and Brosius, J. W. 1986, in preparation.
 Holman, G. D., and Kundu, M. R., 1985, *Ap. J.*, **292**, 291.
 Hurford, G. 1986, private communication.
 Kahler, S. W., Davis, J. M., and Harvey, J. W. 1983, *Solar Phys.*, **87**, 47.
 Kahler, S. W., Webb, D. F., Davis, J. M., and Kundu, M. R. 1984, *Solar Phys.*, **92**, 271 (Paper II).
 Kahler, S. W., Webb, D. F., and Moore, R. L. 1981, *Solar Phys.*, **70**, 335.
 Krieger, A. S. 1977, in *Proc. OSO-8 Workshop* (Boulder: University of Colorado), p. 98.
 Kundu, M. R., Alissandrakis, C. E., Bregman, J. D., and Hin, A. C. 1977, *Ap. J.*, **213**, 278.
 Kundu, M. R., Schmahl, E. J., and Gerassimenko, M. 1980, *Astr. Ap.*, **82**, 265.
 Kundu, M. R., and Velusamy, T. 1980, *Ap. J. (Letters)*, **240**, L63.
 Lang, K. R. 1980, *Astrophysical Formulae* (2d ed.; New York: Springer-Verlag).
 Lang, K. R., and Willson, R. F. 1983, *Adv. Space Res.*, Vol. 2, No. 11, p. 91.
 ———, 1984, *Adv. Space Res.*, Vol. 4, No. 7, p. 105.
 Lang, K. R., Willson, R. F., and Gaizaukas, V. 1983, *Ap. J.*, **267**, 455.
 Lang, K. R., Willson, R. F., and Rayrole, J. 1982, *Ap. J.*, **258**, 384.
 McConnell, D., and Kundu, M. R. 1983, *Ap. J.*, **269**, 698.
 Noyes, R. W., Raymond, J. C., Doyle, J. G., and Kingston, A. E. 1985, *Ap. J.*, **297**, 805.
 Pallavicini, R., Sakurai, T., and Vaiana, G. S. 1981, *Astr. Ap.*, **98**, 316.
 Rosner, R., Tucker, W. H., and Vaiana, G. S. 1978, *Ap. J.*, **220**, 643.
 Schmahl, E. J., Kundu, M. R., Strong, K. T., Bentley, R. D., Smith, J. B. Jr., and Krall, K. R. 1982, *Solar Phys.*, **80**, 233.
 Schmahl, E. J., and Orrall, F. Q. 1979, *Ap. J. (Letters)*, **231**, L41.
 Shibasaki, K., Chiuderi-Drago, F., Melozzi, M., Slottje, C., and Antonucci, E. 1983, *Solar Phys.*, **89**, 307.
Solar Geophysical Data Bulletins 1981, (Boulder: US Dept. of Commerce, NOAA)(SGD).
 Strong, K. T., Alissandrakis, C. E., and Kundu, M. R. 1984, *Ap. J.*, **277**, 865.
 Takakura, T., and Scalise, Jr., E. 1970, *Solar Phys.*, **11**, 434.
 Vaiana, G. S., Van Speybroeck, L., Zombeck, M. V., Krieger, A. S., Silk, J. K., and Timothy, A. 1977, *Space Sci. Instr.*, **3**, 19.
 Webb, D. F. 1981, in *Solar Active Regions*, ed. F. Q. Orrall (Boulder: Colorado Associated Universities Press), p. 165.
 Webb, D. F., and Davis, J. M. 1985, *Solar Phys.*, **102**, 177.
 Webb, D. F., Davis, J. M., Kundu, M. R., and Velusamy, T. 1983, *Solar Phys.*, **85**, 267 (Paper I).
 Webb, D. F., and Zirin, H. 1981, *Solar Phys.*, **69**, 99.

J. M. DAVIS: NASA/Marshall Space Flight Center, Code ES-52, Huntsville, AL 35812

G. D. HOLMAN: Laboratory for Astronomy and Solar Physics, Code 682, NASA/Goddard Space Flight Center, Greenbelt, MD 20771

M. R. KUNDU: Astronomy Program, Space Science Building, University of Maryland, College Park, MD 20742

R. K. SHEVGAONKAR: Indian Institute of Astrophysics, Bangalore 560 034, India

D. F. WEBB: AFGL/PHP, Hanscom Air Force Base, MA 01731

ERRATUM

In the paper "Neutrino Flows in Collapsing Stars: A Two-Fluid Model" by J. Cooperstein, L. J. van den Horn, and E. A. Baron (*Ap. J.*, **309**, 653 [1986]), equations (4.30) and (4.33) erroneously contain the coefficient pertaining to neutrino-proton scattering (cf. eqs. [4.31] and [4.34]) and should be corrected to read

$$\mathcal{A}_{\nu n} = -\langle z \rangle \frac{5G^2}{3\pi^3} \left(\frac{1}{4} + \frac{5}{4} g_A^2 \right) n_n T_\nu^6 F_4(\eta_\nu), \quad (4.30)$$

$$\mathcal{A}_{\nu n} = -\langle z \rangle \frac{10G^2}{3\pi} \left(\frac{1}{4} + \frac{5}{4} g_A^2 \right) n_n \epsilon_\nu T_\nu \omega_\nu. \quad (4.33)$$

4.18 The Flight Test of a Grazing Incidence Relay Optics Telescope for Solar
X-Ray Astronomy Utilizing a Thinned, Back-Illuminated CCD Detector

J. Daniel Moses

American Science and Engineering, Inc.
Cambridge, Massachusetts 02139

and

John M. Davis

Marshall Space Flight Center, Alabama 35812

ORIGINAL PAGE IS
OF POOR QUALITY



THE FLIGHT TEST OF A GRAZING INCIDENCE RELAY OPTICS TELESCOPE FOR SOLAR X-RAY ASTRONOMY UTILIZING A THINNED, BACK-ILLUMINATED CCD DETECTOR

J. Daniel Moses

American Science and Engineering, Inc.
Cambridge, Massachusetts 02139

and

John M. Davis

Marshall Space Flight Center, Alabama 35812

Abstract

The new AS&E Ultrahigh Resolution Soft X-Ray Solar Research Rocket Payload has been successfully flown twice on Black Brant IX Sounding Rockets from White Sands Missile Range. These flights, conducted on 15 August 1987 and 11 December 1987, provided the first test of the new payload which consists of 3.8X magnifying hyperboloid-hyperboloid grazing incidence relay optic used in conjunction with an existing Wolter-I primary mirror. An RCA SID 500 series CCD detector was utilized in a thinned, back-illuminated configuration for recording the images. The 5.4 m effective focal length of the compound optics system resulted in a plate scale of 1 arc second per pixel which is comparable to the inherent resolution of the primary mirror. These flights represent the first use in X-ray astronomy of either of these two new technologies. These observations are presented with comparison to laboratory measurements and theoretical expectations of the instrument performance.

Introduction

The scientific objective of the new AS&E Ultrahigh Resolution Soft X-Ray Solar Research Rocket Payload is high spatial resolution observations with short integration (exposure) times in order to search for fine scale transient coronal phenomena. The motivation for this search arises from the current interest in observations of coronal waves or nanoflares which may be associated with active region heating (e.g., Parker, 1988)¹. These observations require several arc second spatial resolution with temporal resolution of the order of a second. Such observations have not been previously available.

In order to address this observational goal of simultaneous high temporal and spatial resolution, two emerging technologies were combined each having individual applications to X-ray astronomy. X-ray sensitive CCD detector technology provides high detection efficiency so that short integration times become possible. CCD detectors also provide accurate and consistent measurement of X-ray energy deposit which is straight forward to model and calibrate. Grazing incidence relay optic technology provides the means in the soft X-ray regime (<40 Angstroms) to match a variety of focal plane instruments to the same primary mirror. The combination of a CCD detector with a magnifying grazing incidence relay optic provided a match of the plate scale of the AS&E high resolution rocket borne X-ray mirror to the spatial resolution of the CCD detector so that the high temporal resolution available with the CCD detector could be obtained with the high spatial resolution of the existing X-ray optics.

Extensive modeling and laboratory testing was conducted to determine the performance in the X-ray regime of both the compound grazing incidence optical system and the CCD detector. Flight tests of the compound telescope/CCD detector system were conducted on 15 August 1987 and 11 December 1987 as an ancillary experiment during the 1987 X-ray Bright Point Observing Campaign. A proof of the design principle was established during these flights, but initial analysis of the observations indicates a level of performance below expectation in both sensitivity and spatial resolution. The reasons for this apparent lack of performance are not understood and further research is required to explore these questions.

Instrumentation

Grazing Incidence Relay Optics Compound Telescope

The compound X-ray optics system consists of a Wolter Schwarzschild primary mirror coupled with a diverging magnifier relay optic as illustrated in Figure 1. The relay

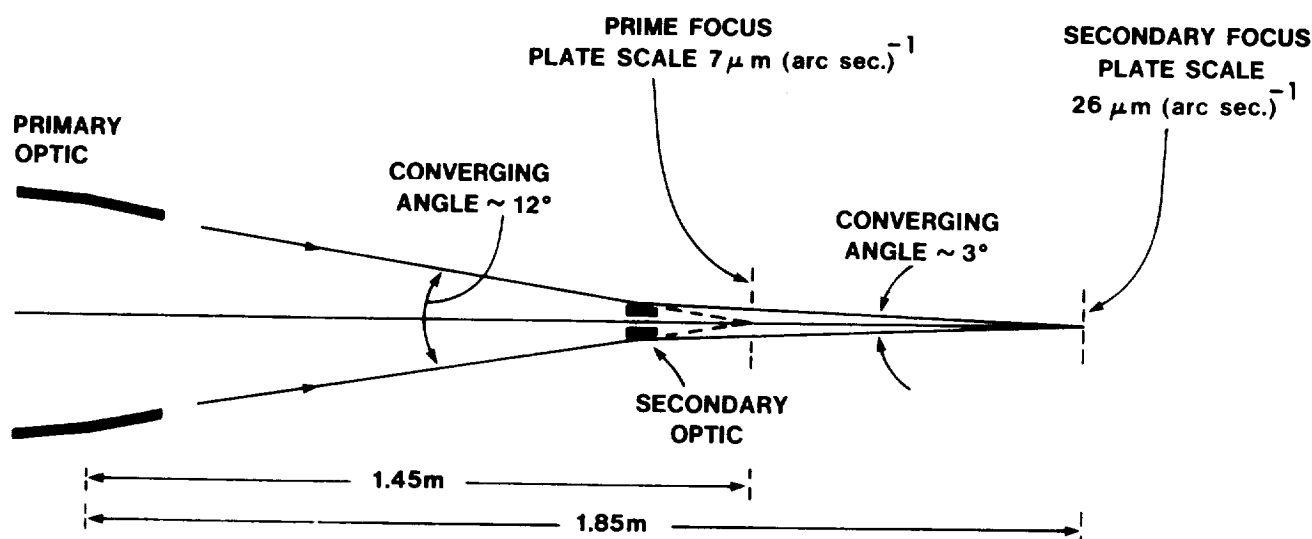


Figure 1. Diagram of the design for the grazing incidence relay optics system.

optic is an externally reflecting mirror with two hyperboloidal segments. This configuration is analogous to the well-known Barlow lens magnifier and the specific design considerations of such a grazing incidence mirror are described by Chase *et al* (1982)². The relay optic manufactured for this payload has a magnification of 3.7 which produces the desired plate scale of 26 microns (arc sec)⁻¹. Although the effective focal length is 5.4 m, the actual length of the imaging system is 1.85 m thereby fitting within the 2 m envelope available in the sounding rocket payload. The magnified plate scale matches the pixel size of the CCD used in this payload to the inherent resolution of the X-ray optical system. Table 1 summarizes the design of the primary and secondary mirrors.

The new AS&E Solar Research Rocket payload is constructed to obtain observations at both the prime focus and the secondary focus during a single flight. The secondary optic is mounted on a translation stage that can be inserted into or removed from the optical path upon command of the experiment computer. A film camera is also mounted on a separate translation stage that can be inserted into or removed from the prime focus upon computer command. At take off, the secondary optic is stowed out of the optical path and the film camera is positioned in the prime focus to accomplish the primary mission of these flights acquisition of full disk photographic images of the solar X-ray corona. Following the completion of the primary mission, the film camera is retracted from the optical path and the relay optic inserted into the optical path to form a magnified image at the secondary focus where the CCD camera image plane is located.

The performance of compound telescope in the X-ray regime has been measured utilizing the 89.5 meter vacuum collimator long-tube facility (LTF) at AS&E. A report on these measurements was made by Moses *et al.* (1986)³. The on-axis performance of the compound telescope was found to be comparable with the one arc-second level resolution of the primary mirror alone as reported earlier by Davis *et al.* (1979)⁴. Since the distance from the relay optic to the image plane is 0.61 m while the effective focal length of the primary mirror is 5.4 m, the plate scale for scattering from the relay optic (from figure error or surface roughness) is much smaller than the equivalent scattering from the primary mirror projected onto the focal plane. The off-axis performance of the compound telescope was found to be much worse than the primary mirror alone. Because the off-axis

Table 1. Design Requirements of the X-Ray Mirrors

| | Primary | Secondary |
|-------------------------|-------------------------------------|--------------------------------------|
| Figure | Wolter Schwarzschild | Hyperboloid Hyperboloid |
| Material | Fused Silica | Nickel Coated Beryllium |
| Principal Diameter | 30.48 cm | 3.15 cm |
| Focal Length | 144.9 cm | -19.9 cm |
| Geometrical Area | | |
| On-axis | 42.4 cm ² | 34.3 cm ² |
| 2 arc minutes | 39.6 cm ² | 5.8 cm ² |
| Plate Scale | 7.0 microns (arc sec) ⁻¹ | 26.0 microns (arc sec) ⁻¹ |
| Field of View | 60 x 60 (arc min) ² | 2.5 x 2.5 (arc min) ² |
| Resolving Power (X-Ray) | 1 arc sec | 1 arc sec |

ORIGINAL PAGE
BLACK AND WHITE PHOTOGRAPH

performance of the compound telescope so strongly influences the appearance of the flight images, the previously reported off-axis measurements will be summarized.

The relay optic design was optimized for maximum on-axis resolution. The resulting lengths of the relay optic hyperboloid mirrors are insufficient to reflect much of the off-axis flux. Figure 2 illustrates the consequent vignetting of off-axis rays by the relay optic both as predicted by ray trace calculation and as measured in the 89.5 m LTF. The restriction of the vignetted field of view to a circle of radius 2.5 arc minutes is essentially the same for both the 89.5 m and infinite source distance. The compound telescope also suffers from a form of astigmatism. The off-axis image blur due to geometric optics (no scattering) is greater in the direction perpendicular to the displacement of the image from the on-axis point. A ray trace calculation of the rms blur of a point source displaced in the X direction from the on-axis point is presented in Figure 3. To express the asymmetric character of the off-axis

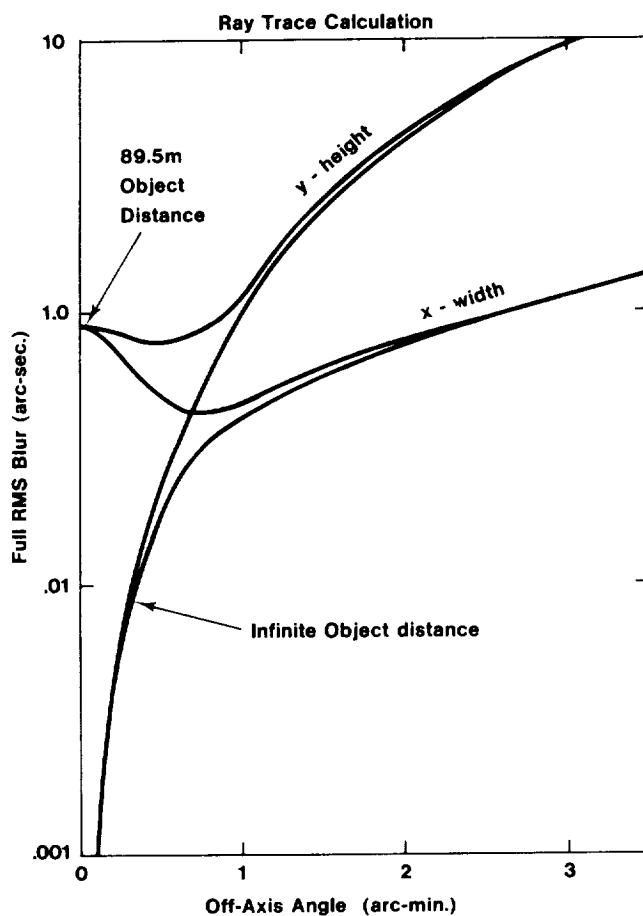


Figure 3. Ray trace calculation of blur (not including scattering) in the two dimensions of the compound telescope image plane for a point source off-axis in the X direction.

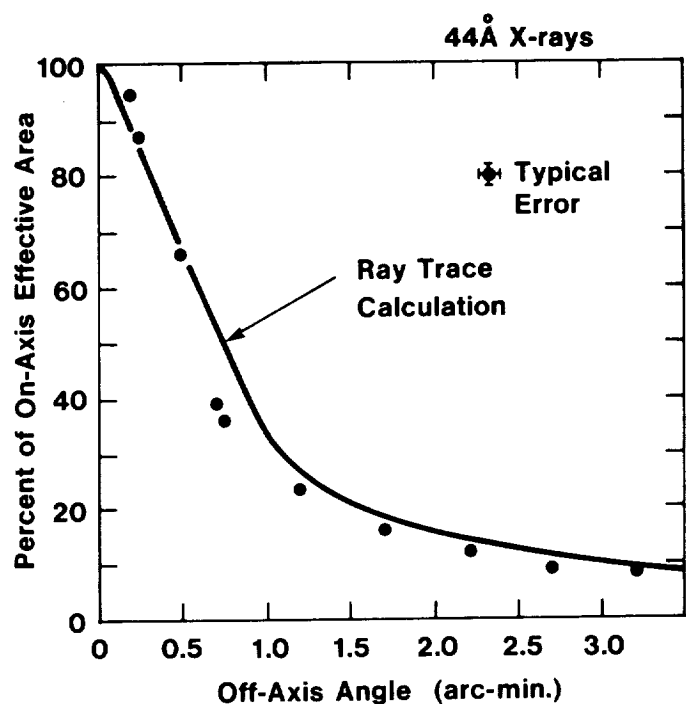


Figure 2. Ray trace calculation and observed off-axis decline in energy throughput of the compound telescope for a 89.5 m source distance.

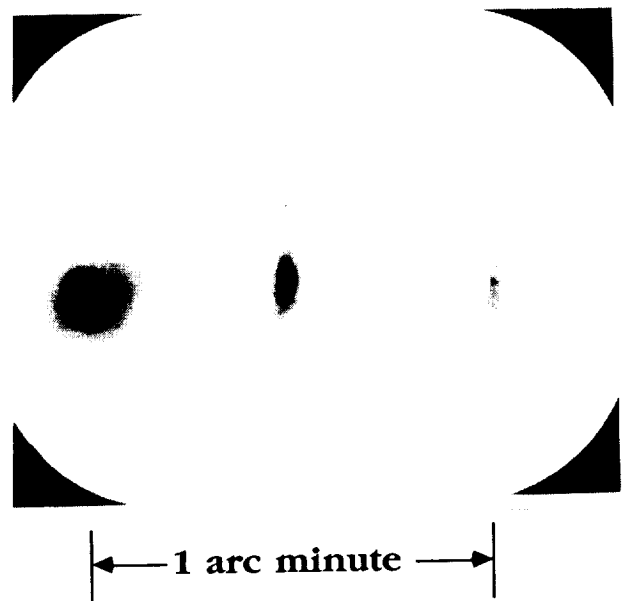


Figure 4. Photograph of X-ray source imaged by the compound telescope for the off-axis displacements (from left to right) of 0 arc seconds, 30 arc seconds, and 60 arc seconds.

aberration, the blur in the X and Y directions are plotted separately. For off-axis angles less than 2 arc min, the ray trace calculation predicts a different blur pattern for a 89.5 m and an infinite object distance, so both functions are plotted in Figure 3. This aberration is obvious in the photograph presented in Figure 4 of an X-ray point source in the AS&E 89.5 m LTF for off-axis displacements of 0, 30, and 60 arc seconds. Further, it can be seen in Figure 4 that the wings of the point response function (which are due to scattering and figure errors) clearly demonstrate the asymmetric off-axis aberration predicted by the ray trace calculations for the unscattered rays in the core of the point response function. Therefore, the net effect on the image is much greater than the several arc second blur indicated by the ray trace. A practical limit on the field of view is difficult to establish since the ray trace without scattering provides only a qualitative guide to the off-axis aberration, although a 30 arc sec radius field of view appears likely to be distortion free.

X-Ray Sensitive Charge Coupled Device Detector

The CCD detector is an RCA SID 500 series device operated in a back-side illuminated mode for soft X-ray sensitivity. This required thinning the device to a thickness of approximately 10 microns. This is a low noise, three-phase frame transfer device with 30 micron square pixels. The pixels are arranged in a 320 (H) by 256 (V) format. The CCD camera converts the X-ray imaged focussed on the CCD device into a 256 x 256 pixel array with each pixel magnitude represented by a digital word. As each pixel is sequentially clocked out of the CCD, it is analyzed, incorporated into the telemetry bit stream format, transmitted to a ground station receiver, and recorded.

The video chain of the X-ray CCD camera consists of a preamplifier, a correlated double sample and hold and an analog to digital converter (ADC). Ancillary circuits include a clock driver which provides the regulated analog clock voltages required by the CCD. It receives timing signals from a clock generator which is synchronized to the basic frequency of the PCM modulator. The clock driver also provides the digital control signals required by the correlated double sample and hold and the ADC. The preamplifier, which amplifies the analog video signal, is designed to operate with a CCD which has an on-chip source follower transistor. It is a linear amplifier with a gain of eleven, and it provides the sample and hold circuit with a low impedance source.

The correlated double sample and hold samples the difference between the video pulse generated by the CCD and a correlated null reference pulse and passes this difference signal for processing by the ADC. The reference or "background" level signal is generated, before transferring out the next pixel charge, by discharging the previous pixel charge at the CCD output transistor through a switching transistor. After the transient caused by this discharge has decayed, the output level is an indication of the "black" level of the CCD. This output level is not exactly equal to the pixel black level because of the leakage charge transferred by the switching transistor control signal. The resulting differential does not change because it depends only on the control signal voltage, which is well regulated, and the geometry of the switching transistor, which is extremely stable. It can therefore be accurately cancelled by an externally introduced offset signal. This signal is generated in the video offset control from a series of analog switches in the control register.

The circuits in the clock generator and clock driver generate the wave forms that are used to move the exposed image from the image area to the storage area in the CCD. The stored image is then moved, line by line, to a readout register and then, pixel by pixel, to the output transistor. Additional features of these circuits include:

- * Raster limit feature which allows blanking of the beginning and the end of each line to reduce the line from 320 to 256 pixels.
- * Line blanking, for the blanking of entire lines.
- * The combination of "dummy" readouts with line blanking which allows the CCD to be partially or totally cleared without undesirable and time-consuming digital readout.

The sounding rocket telemetry clock has a basic frequency (frame rate) of 1024 Hz. Since no provision is made for on-board data storage other than the storage area of the CCD, the telemetry rate determines the timing for the CCD. The minimum time for a frame transfer of a complete image into the storage area with this clock is 15.6 msec. Since it is anticipated that exposure as short as 20 msec will be required, electronic shuttering is insufficient. A mechanical shutter system was fabricated utilizing an iris shutter in combination with a feedback controlled chopper wheel.

The total time for telemetry of a complete image is approximately 10 sec (8 image pixels are contained in a frame of image data). Exposure times on the order of tens of

ORIGINAL PAGE
BLACK AND WHITE PHOTOGRAPH

seconds may also be required for some applications. Therefore, it is necessary for the CCD to be cooled to reduce thermal noise. An -80°C operating temperature is obtained through a cold strap connection to a liquid nitrogen reservoir. Active temperature control is achieved by electric heaters and a feedback circuit. The CCD and the CCD head electronics board (containing the preamplifier and logic-level clocks) are mounted inside the vacuum jacket of the LN2 dewar to prevent condensation on the CCD. A window in the dewar is opened when the payload reaches observing altitude.

A qualitative indication of the performance of the CCD camera in the X-ray regime can be seen in the shadowgraph image presented in Figure 5. Edges are clearly resolved at the 3 pixel level in this photograph with a finite mask to CCD distance. The 6-minute exposure time also indicates the high level of background suppression obtained with the cooled device.

Detailed, quantitative measurements of the quantum efficiency (QE) of the CCD have been made. The QE is defined here as the ratio of the charge at the output gate of the device to the charge which would have been collected in a pixel if all the radiation incident on that pixel had been converted into electron-hole pairs (3.6 eV per electron-hole pair). The CCD camera with flight electronics was coupled to a test vacuum chamber with filtered electron bombardment sources of either carbon or aluminum K-alpha X-rays. Dosimetry was determined with cross calibrated gas flow proportional counters. An average ADC value over a 50×50 pixel array was computed by the GSE computer for each exposure.

In order to determine a charge at the CCD output gate from the ADC value, two quantities must be well known: the capacitance of the CCD output floating diffusion charge collector and the total electronic gain between the output gate and the ADC. The value of the output gate capacitance is taken from the calibration reports provided by RCA when the device was purchased. A value of 0.19 pF was obtained by measuring the output transistor discharge current during video rate readout of white light exposure. The gains of the various stages of the video chain are:

| | |
|---------------------------------|-------|
| Sample and Hold Post Amplifier: | 5.01 |
| Sample and Hold Preamplifier: | 3.55 |
| Sample to Hold Switching: | 0.90 |
| Camera Head Preamplifier: | 11.0 |
| CCD Output: | 0.99 |
| Total | 174.3 |

The QE for the Al source (1.49 keV) and C source (0.278 keV) are plotted in Figure 6. Also plotted in Figure 6 is the theoretical efficiency of a backside illumi-

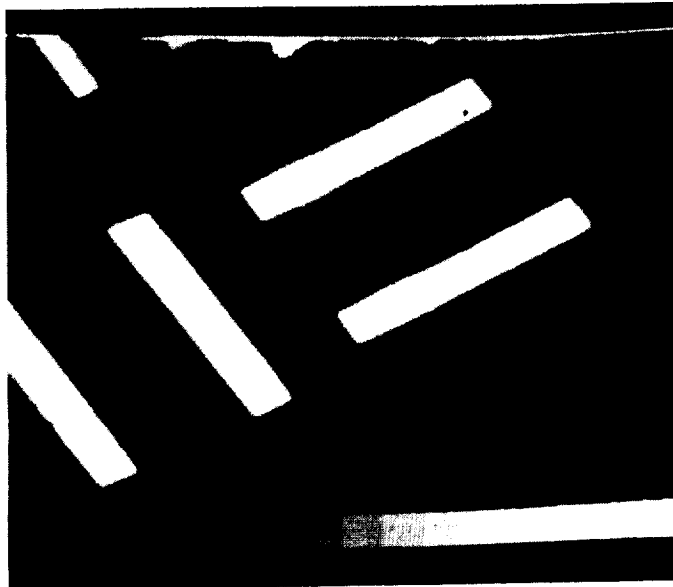


Figure 5. A shadowgraph taken at 44 Angstroms with the CCD camera. The exposure time was 6 minutes.

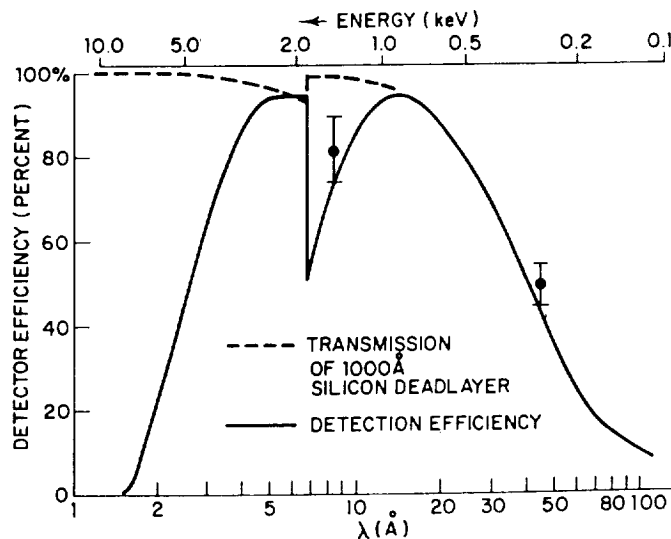


Figure 6. Measurements of the detector efficiency of the RCA SID 500 CCD detector and theoretical efficiency curve for a back-illuminated CCD thinned to 10 microns.

nated device 10 microns thick with a 1000 angstrom dead layer. Perfect charge collection and transfer are assumed. The low energy efficiency is determined by the filtering effect of the dead layer. The high energy efficiency is determined by the X-ray transmission of the 10 micron thick sensitive region. Error bars on the QE observations are representative of 10% uncertainty in output gate capacitance and electronic gains.

Flight Observations

X-ray images of the solar corona obtained during AS&E Solar Research Rocket flights on 15 August 1987 and 11 December 1987 are presented in Figures 7 and 8, respectively. The top image in each figure is a full disk photograph taken at the prime focus of the telescope. The lower image in each figure is a CCD image taken at the secondary focus of the telescope. All images are filtered through 1 micron of polypropylene and 3500 Å of aluminum. The circles drawn on the full disk photographic images are 2 arc minutes in diameter and centered on the target region of the CCD exposure. The circles drawn on the CCD images are 2 arc minutes in diameter and centered on the region of maximum compound telescope throughput. Although the optical axis of the CCD/compound telescope system cannot currently be determined after final assembly, the CCD optical axis implied by the technique utilized in Figures 7 and 8 approximately agree with the optical axis last determined before final assembly. Review of the rapid decline in throughput with off-axis angle, as illustrated in Figure 2, instills confidence in this method of locating the optical axis of the CCD system for an image of any active region larger than 2×2 (arc min)².

The first impression created by the CCD images is the lack of resolved spatial structure. The on-axis resolution of the compound telescope as measured in the laboratory leads one to expect a high resolution core to the CCD image. While the off-axis aberrations illustrated in Figures 3 and 4 could combine in a non-intuitive way with the source image, the tentative conclusion on the spatial resolution of the flight images is that they do not match that obtained in the laboratory.

A second surprise is the lack of sensitivity of the flight observations. Calculations based on a typical 2.5×10^6 °K active region emission measure of 2×10^{29} cm⁻⁵ and the measured CCD and telescope performance indicates CCD saturation should be obtained with a 0.5 second exposure. Flight measurements imply that CCD saturation by the observed active region requires approximately an order of magnitude greater exposure!

The CCD X-ray response is found to increase linearly exactly as expected. For the CCD images with pixel values significantly above background, the histograms of pixel intensity are found to map into each other simply by the factor of exposure time. Therefore, the value of the CCD detector as a calorimeter has been established in these flight tests.

Conclusions

One possible explanation for the apparent lack of both spatial resolution and system throughput of the flight observations relative to the laboratory measurements is a misalignment of the relay optic. There are several ways in which such a misalignment could occur, including a deformation of the relay optic translation stage due to launch loads, extreme sensitivity to thermally induced changes in the optical bench, and a discrepancy between the ground-based white-light alignment technique and the in-flight, free-fall X-ray observation configuration. Pre-flight environmental testing was conducted on the relay optic translation stage to determine its sensitivity to launch loads. Damage to the translation stage during the reentry and recovery phase of both flights preclude a post-flight investigation of unexpected deformation of the stage during launch.

However, at the present level of analysis, it is premature to draw many conclusions. Two calculations are in progress which will address the question of whether the discrepancy between flight observations and laboratory measurements is real or illusory: (1) Since the rocket flights occurred near solar minimum, the observed active regions may have lower emission measures than typical active regions. Quantitative analysis is underway on the film images from these flights using standard techniques in order to determine the emission measures of the target regions. (2) The true convolution of the target active region emission with the point response function and geometrical aberration of the compound telescope as measured in the laboratory may result in the observed secondary focal plane image. It is possible that the narrow compound telescope field of view will only be useful for observing bright points and isolated active regions less than an arc minute in size. The calculation required to test this possibility is a deconvolution of the prime focus photographic image followed by a convolution of that image utilizing both the point response function and geometrical off-axis aberration of the compound telescope.

Finally, since two new systems were combined in the same observation, there remains an uncertainty as to which component did not perform in flight as it did in the lab. The CCD

ORIGINAL PAGE
BLACK AND WHITE PHOTOGRAPH

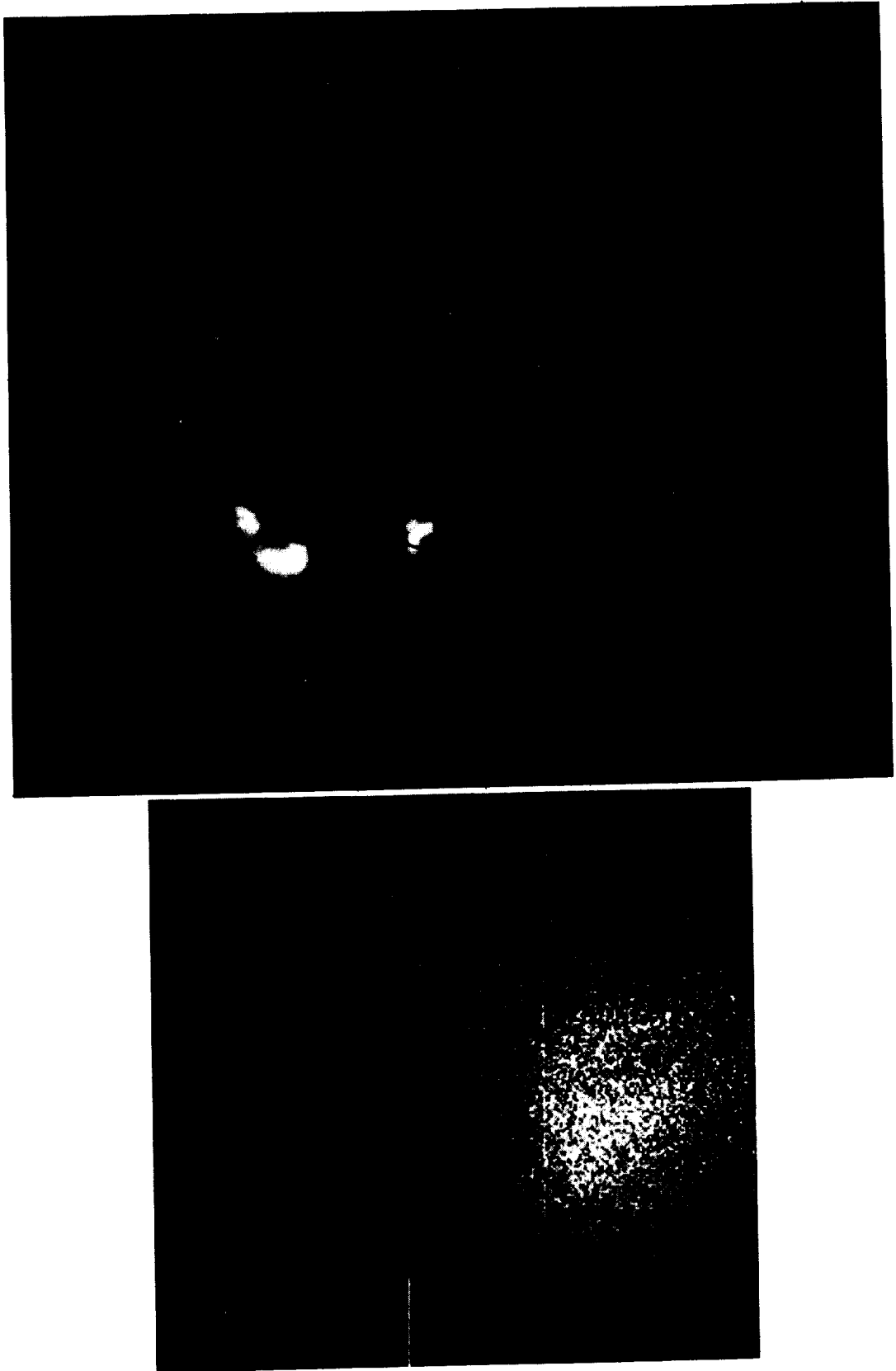


Figure 7. 15 August 1987 X-ray images of the solar corona through aluminized polypropylene filters. Both circles are 2 arc min diameter. Top: Full disk photographic image obtained at prime focus. Bottom: 0.280 second exposure CCD detector image obtained at secondary focus.

ORIGINAL PAGE
BLACK AND WHITE PHOTOGRAPH

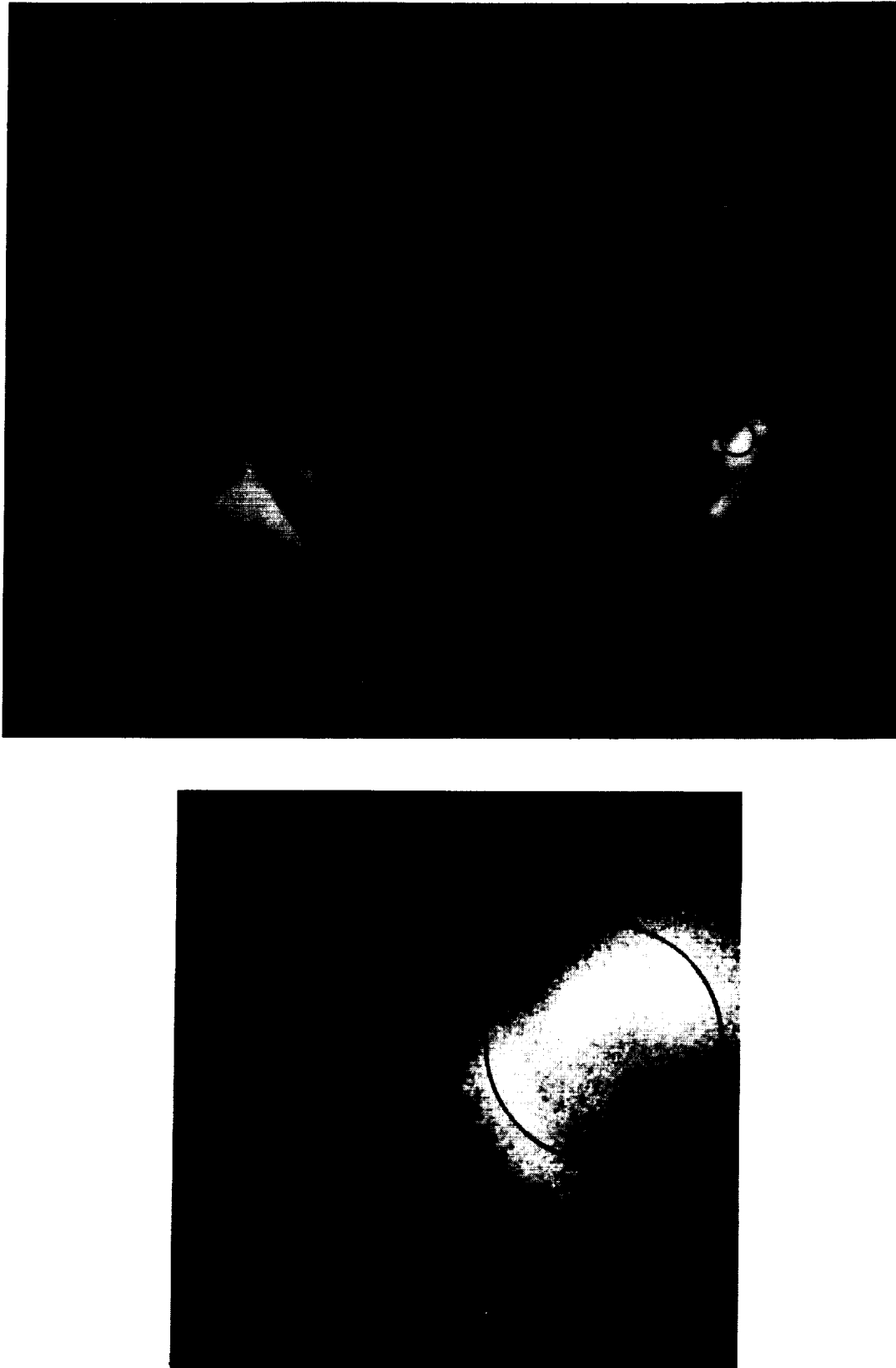


Figure 8. 11 December 1987 X-ray images of the solar corona through aluminized polypropylene filters. Both circles are 2 arc min diameter. Top: Full disk photographic image obtained at prime focus. Bottom: 1.0 second exposure CCD detector image obtained at secondary focus.

detector will be isolated with proven systems in the next planned flight of the AS&E Solar Research Rocket Payload. The payload will be configured with the CCD detector at the prime focus of the Wolter Schwarzschild mirror to obtain high precision calorimetry of large scale coronal structure. In this configuration the linearity and sensitivity (even in the worse case interpretation of the 1987 flight data as 10% of the laboratory efficiency) of the CCD detector will provide new and useful measurements of faint large scale coronal structures such as coronal holes and helmet streamers in which a 5 arc minute spatial resolution is useful. The insights gained from this flight on CCD performance can then be applied to the 1987 flight data.

Acknowledgments

We would like to acknowledge the efforts at AS&E of Ken Overoye in providing ray trace calculations and interpretations, Charles Carpenter and Frank Hills in providing electronics design, testing, and field support, and Roger Eng and Richard Schueller in providing mechanical design, testing, and field support. We would like to thank Drs. M. Annis, P. Bjorkholm, and A. Krieger for useful discussions. This work was performed under NASA contracts NAS5-25496 and NASW-3942.

References

1. E.N. Parker, Ap. J. **330** (1988) 474.
2. R.C. Chase, A.S. Krieger, and J.H. Underwood, Applied Opt. **21** (1982) 4446.
3. D. Moses, A.S. Krieger, and J.M. Davis, Proc. Soc. Photo-Opt. Instrum. Eng. **691** (1986) 138.
4. J.M. Davis, A.S. Krieger, J.K. Silk, and R.C. Chase, Proc. Soc. Photo-Opt. Instrum. Eng. **184** (1979) 96.

4.19 The Correspondence Between Small-Scale Coronal Structures and the
Evolving Solar Magnetic Field

D.F. Webb

Emmanuel College
Boston, Massachusetts 02115

and

D. Moses

American Science and Engineering, Inc.
Cambridge, Massachusetts 02139

ORIGINAL PAGE IS
OF POOR QUALITY

THE CORRESPONDENCE BETWEEN SMALL-SCALE CORONAL STRUCTURES AND THE EVOLVING SOLAR MAGNETIC FIELD

D.F. Webb* and J.D. Moses**

* Emmanuel College, Boston, MA 02115 USA,

** American Science and Engineering, Inc., Cambridge, MA 02139 USA

ABSTRACT

Solar coronal bright points, first identified in soft X-rays as X-ray Bright Points (XBPs), are compact, short-lived and associated with small bipolar magnetic flux. Contradictory studies have suggested that XBPs are either a primary signature of the emerging flux spectrum of the quiet Sun, or that they are representative of the disappearance of pre-existing flux. We present results using coordinated data obtained during recent X-ray sounding rocket flights on 15 August and 11 December 1987 to determine the correspondence of XBPs with time-series, ground-based observations of evolving bipolar magnetic structures, He-I dark points, and the network. Our results are consistent with the view that coronal bright points are more likely to be associated with the annihilation of pre-existing flux than with emerging flux.

INTRODUCTION

In the coronae of the sun and many stars, magnetic fields permeate and constrain the hot plasma such that the radiation traces, at least in a general sense, the field lines. At the visible surface of the Sun, the quiescent field consists of brighter knots of emission and stronger magnetic field that make up the "network." This network is related to supergranulation cells, which are a surface manifestation of the deeper seated convective activity of the Sun. Recent high temporal and spatial resolution imagery has shown that the network magnetic fields consist of the merging and cancellation of "ephemeral" or emerging regions, intranetwork fields, and the remnants of active region fields. Ephemeral regions are small magnetic bipoles of equal strength which appear at the surface and steadily move apart. Such regions are the most common form of flux emergence in the quiet Sun. Flux is observed to disappear from the surface at a rate which, over the short term, results in a steady-state balance of flux. Observationally, this disappearance takes the form of either cancellation of opposite-polarity elements or the gradual fading of flux. These processes involve magnetic energy conversion that have been interpreted as the reconnection and/or submergence below the surface of field lines.

In the solar corona the brightest quiet Sun structures are called bright points, because of their compact, circular form. The X-ray characteristics of coronal bright points were analyzed in detail during Skylab (see /1,2/ for reviews). These X-ray Bright Points (XBPs) are compact (typically 20-30 arc sec) and short-lived (average about 8 hours), and are associated with small photospheric magnetic bipoles. XBPs likely are small loops that connect the opposite polarity poles. A key question is how these coronal structures are related to the evolving network fields: are they the coronal manifestation of the emergence of new flux, the disappearance of older, pre-existing flux, or a combination of both? Similar bright points are also observed at other coronal wavelengths and in the transition region and chromosphere, but at lower contrast with a confusing background which consists of bright network elements.

Prior to the work presented in this paper, two approaches -- producing contradictory results -- have been taken in determining the evolution of the magnetic structure of XBPs. The approach of Golub and coworkers /1,3/ is primarily based on Skylab high resolution X-ray observations and concludes that XBPs are a consequence of emerging magnetic flux. The approach of Martin and Harvey /4,5,6/ is primarily based on high resolution magnetograms, utilizing compact absorption features in He-I 10830A images as XBP indicators, and concludes that XBPs are a consequence of cancelling or submerging magnetic flux.

The strength of the Skylab based approach was the unique time series of high spatial resolution soft X-ray data obtained during the Skylab era. From this work the fundamental characterization of XBPs was made in terms of spatial distribution, lifetime, and, in conjunction with subsequent sounding rocket flights, the solar cycle variation in XBP population /1,2,3/. The weakness of this approach was that it lacked simultaneous high time resolution, high quality magnetograms. The association of XBPs with ephemeral regions was based on study of only two simultaneous Skylab X-ray and Kitt Peak magnetogram image sets, and the correspondence between XBPs and dipoles going in either direction was only

about 50%. With the assumption that all "new" bipoles associated with XBPs were ephemeral regions, Golub and coworkers concluded that XBPs are the primary coronal signature of emerging flux in the quiet Sun.

The strength of the more recent ground-based approach is the high time and spatial resolution of the magnetogram data as well as the superior coverage of solar cycle variations. From this work Martin and Harvey /4/ found that the spatial distribution and the solar cycle variation of ephemeral regions did not match that of XBPs. The weakness of this approach was the lack of high spatial resolution soft X-ray observations. Because of this Harvey /6/ suggested that ground-based He dark point (DP) observations be used as a proxy for XBP observations. The association of XBPs and DPs is based on a single comparative study by Harvey et al. /7/ using Skylab X-ray and HeI-D3 images. That study was qualitative and did not reveal a one-to-one correspondence between XBPs and DPs. DPs exhibit the same solar cycle variation as XBPs but are more typically associated with cancelling flux regions than with ephemeral regions. Utilizing the assumption that DPs are a good proxy for XBPs, Martin and Harvey argue that XBPs are not a reliable signature of emerging flux.

The difficulty with both of the above approaches is the lack of simultaneous high spatial and high temporal resolution X-ray and ground-based observations. Partly in an attempt to correct this difficulty, two rocket flights of the AS&E high resolution, soft X-ray imaging payload were conducted in 1987. These flights were carefully orchestrated in an unprecedented campaign to coordinate key rocket and ground-based observations of small-scale solar features. Here we report on preliminary results which address primarily the problem of the correspondence of XBPs to evolving magnetic bipoles.

CORRESPONDENCE OF XBPS TO MAGNETIC BIPOLES

Three components of the XBP Observing Campaign are useful in the study of XBP-associated bipole evolution. Full-disk soft X-ray images of the solar corona were obtained from AS&E rocket flights on 15 August and 11 December 1987. Full-disk magnetogram and He-I 10830Å images were obtained by J. Harvey and K. Dere at the National Solar Observatory (NSO), Kitt Peak before and after each flight, and narrow-field video magnetograms (VMGs) were acquired by H. Zirin, S. Martin and J. Cook at Big Bear Solar Observatory (BBSO) starting about 2.5 hours before and continuing through and after each flight. The NSO and BBSO magnetogram data are of comparable spatial resolution, but the VMGs have better sensitivity and a temporal resolution of about 10 min.

The figures show examples of these data on 11 December 1987. Figure 1 is a comparison of a full-disk NSO magnetogram with the longest exposure soft X-ray rocket image. The images are to the same scale. Superimposed on each is a rectangle outlining the area of 6 of the 8 VMG fields that were observed (two of the fields covered the west limb and were not used in this study). The area of each of the fields was about 300 x 400 arc-sec; one example is shown in Figure 2.

Several steps were necessary to compare the locations of the XBPs with bipoles on the VMGs. We first coaligned the full-disk X-ray and NSO magnetogram images using common bright emission features. The VMGs were easily related to the full-disk magnetograms. In an independent, double-blind manner, the authors identified XBPs on X-ray images for each flight, and S. Martin of Caltech-BBSO identified and classified the evolving bipoles within the VMG fields. Viewing each of the fields as a movie, Martin classified the bipoles as either emerging (strengthening and moving apart) or cancelling (moving together and disappearing) (see Martin et al. /5/). All other bipoles were considered static during the several hour interval of the BBSO observations. We confirmed previous results that nearly all the XBPs corresponded to bipoles on the full-disk images. We then compared the locations of the XBPs with the bipoles within the VMG areas. As an example, Figure 2 shows one of the VMG fields shortly after the 11 December rocket flight, with the evolving bipoles and locations of four XBPs marked.

The important new results are summarized in Table 1. Because of the small number of XBPs, we summed the data from both periods. However, the majority of both of the X-ray and magnetic field structures were observed in the 11 December data. The reasons for this are: (1) The global number of XBPs, and also He DPs, was about a factor of 3 higher on 11 December. (2) The nonuniformity of the XBP spatial distributions further limited the sample within the narrow VMG field of view. (3) The VMG area we used on 11 December was well onto the disk, whereas the area on 15 August was displaced toward the northwest limb where foreshortening effects compromised the magnetic field data. (4) Computer problems compromised the motion study of the bipoles on 15 August.

The second column of the table gives the total number of each class of feature observed. From the table, several points are clearly evident: (1) Within the VMG areas there were only 15 XBPs but hundreds of bipoles. Consequently, very few bipoles have associated coronal emission. (2) Most of the bipoles were not obviously evolving during these periods

of observation. This is due to two factors: The interval of observation is short compared to the mean lifetime of an ephemeral region (approximately 1 day) and many of the apparent bipoles in the VMG images are probably unrelated, i.e., not connected by the same loop.

(3) Of the evolving bipoles, twice as many were classified as cancelling as emerging.

TABLE 1 Correspondence of X-ray Bright Points and Bipolar Magnetic Features

| Feature | Total No. Observed* | Observed XBP Assoc.* | Expected XBP Assoc. | Standard Deviation |
|--------------------|------------------------|-------------------------|------------------------|-----------------------|
| XBPs | 16 | -- | -- | -- |
| Cancelling Bipoles | 97 | 11 | 3.6 | 3.4 |
| Emerging Bipoles | 41 | 1 | 1.5 | < 1 |
| Static Bipoles | 262 | 4 | 9.8 | 2 |
| Total Bipoles | 400 | | | |

* Sum from both 1987 observations on 15 August and 11 December.

The third column of the table shows how the XBPs were apportioned among the three classes of bipoles. (One XBP could be associated with both a cancelling and an emerging bipole, hence the total number of associations as 16.) Eleven of the 15 XBPs (approximately 2/3) were associated with cancelling bipoles. The significance of this result can be checked by apportioning the 15 XBPs according to the ratios of the observed bipole distributions to yield the expected XBP associations, assuming the XBPs are randomly distributed among the three classes of bipoles (Column 4). The last column gives the standard deviation of the observed vs. expected distributions. Despite the small number of XBPs, we see that both the higher number of XBPs associated with cancelling regions and the lower number associated with static bipoles are significant at the 2-3 sigma level. On the contrary, the single association with an emerging bipole is about as expected by chance.

CORRESPONDENCE OF XBPs TO He-I DARK POINTS

As discussed in the Introduction in the context of the debate between the association of XBP with emerging or cancelling bipoles, it is important to confirm whether or not He dark points, which can be observed from the ground, can be used as proxy for the X-ray bright points. Briefly we report on a collaborative study in progress with L. Golub of the Center for Astrophysics (CFA) and K. Harvey and J. Harvey of NSO to address this question. Routine high-quality He-I 10830A images were not available until after the Skylab mission. Therefore, we have collected 5 data sets, each consisting of AS&E full-disk, soft X-ray rocket images and near-simultaneous ground-based NSO 10830A images. These include three older data sets in 1974, 1976 and 1979 and the two sets from 1987.

Independently the XBPs on each X-ray image were identified by the authors and L. Golub and the He DPs were identified by K. and J. Harvey. These identification processes are fairly subjective, but particularly so for the He DPs. This is because He images have lower contrast and He absorption features consist of both coronal and lower temperature components.

Initial DP identifications using the older method yielded the following result, which is consistent for all 5 data sets. More XBPs than DPs were always identified, and the fraction of XBPs associated with DPs was always low, typically 1/4 or 1/3. This suggests that, using the previous subjective method, most XBPs will not be identified on a He image and, further, that with these data we cannot confirm the assumption that He DPs are a good proxy for XBPs.

However, it is clear from comparison of the images that nearly all the XBPs are associated with some compact He absorption. We are presently developing a more objective method for identifying DPs from the He data. In addition, since the He features tend to evolve in brightness and size on short time scales /6/, we need to examine the temporal evolution of individual DPs and the He emission features at the XBP sites. The 1987 data is best suited for this purpose, because full-disk and narrow-field, time-series He images were obtained in the observing campaign with the X-ray data.

SUMMARY AND CONCLUSIONS

We have used coordinated coronal images obtained from X-ray rocket flights, especially in 1987 and ground-based magnetogram and helium images to address important questions on the nature of the bright, small-scale components of the quiet-Sun magnetic field. Our main goal was to address the question of whether coronal bright points as evidenced by XBPs are a primary signature of the solar emerging flux spectrum, or representative of the annihilation of pre-existing flux. Our results with this limited data set are consistent with the latter picture. This contradicts the original Skylab result suggesting that all XBPs signified ephemeral regions, and therefore emerging flux /1,3/. A recent result using

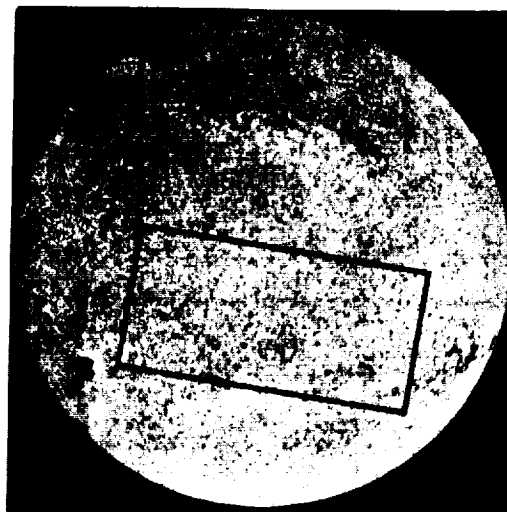


Fig. 1. Comparison of full-disk, near-simultaneous images of a photospheric magnetogram (NSO) and a soft X-ray image (AS&E). Acquisition time for the magnetogram was 40 min. The X-ray image was a 60 sec. exposure with a passband of $\sim 8-60\text{\AA}$. Solar north is at the top and east to the left. The total area covered by the six BBSO VMGs is denoted on each image by the rectangle.

ORIGINAL PAGE
BLACK AND WHITE PHOTOGRAPH

ORIGINAL PAGE
BLACK AND WHITE PHOTOGRAPH

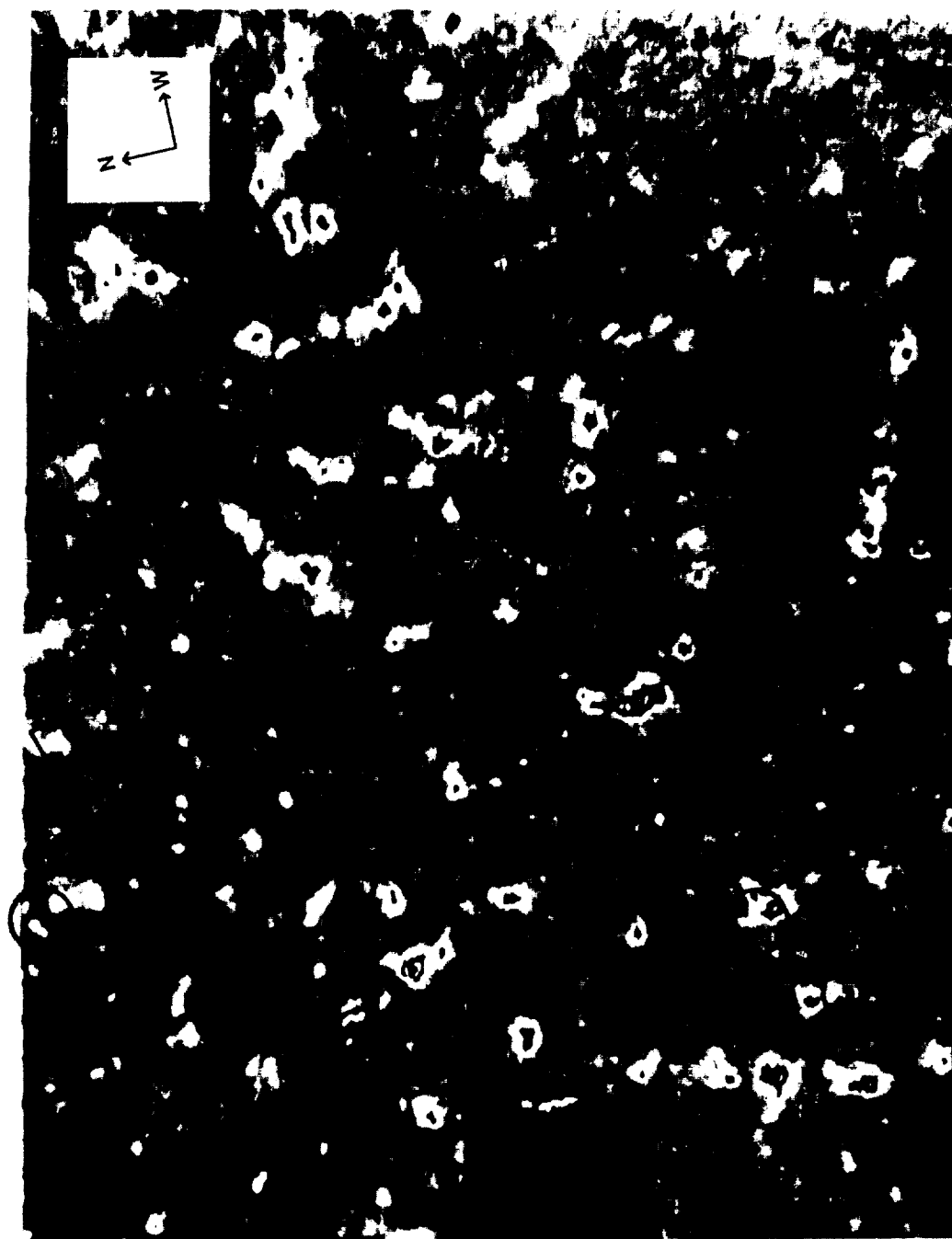


Fig. 2. An example of our comparison of the correspondence of magnetic bipoles to XBPs within one of the six VMG fields outlined by the rectangle shown in Figure 1. Square symbols identify cancelling magnetic bipoles and oval symbols identify emerging magnetic bipoles. If the evolution of the bipole occurred within one hour of the X-ray rocket flight, the symbol is marked with a solid outline, while if the evolution occurred later, the symbol is marked with a dashed outline. XBP locations are marked by the solid circles which are 20 arc sec in diameter.

older X-ray rocket images and daily NSO magnetograms falls in between these two studies, indicating that XBPs are slightly more likely to be associated with emerging than with cancelling flux /8/

Our result is consistent with Martin and Harvey's suggestion that XBPs are more likely to be associated with chance encounters of pre-existing flux than the emerging flux. This despite the fact that we have been unable to confirm one of their basic assumptions, namely that He DPs are a good proxy for coronal bright points (XBPs). We emphasize in this study, as with previous VMG studies, no distinction can be made among various mechanisms of flux disappearance.

It is possible that there are several physical classes of bright points/magnetic bipoles, and that these classes may have different solar cycle dependencies. It remains unclear where the XBPs occur with respect to the visible supergranular network. In our data most of the XBPs within the VMG fields were at sites of convergence of magnetic elements. Such convergence tends to occur at network boundaries, as do cancelling magnetic features /5/. Thus, our data provide some evidence that at least one class of XBPs occurs at network boundaries.

Finally, despite our acquisition of excellent time-series magnetic field and helium data, our comparisons were essentially static because of the short duration X-ray rocket flights. A definitive test of these correspondences and, therefore, an improved understanding of the solar small-scale magnetic flux spectrum must await the acquisition of simultaneous high spatial and high temporal resolution data at both coronal and optical wavelengths.

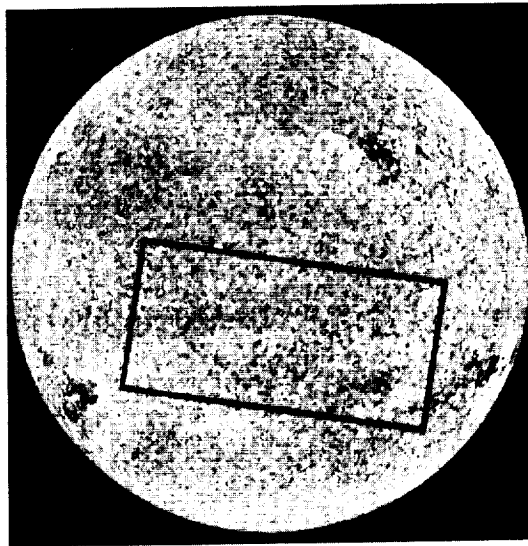
ACKNOWLEDGEMENTS

We thank S. Martin of Caltech and J. Harvey of NSO for processing and analysis of images and helpful discussions. The successful Bright Point Campaign was the result of a cooperative effort among a large group of solar researchers. Those who contributed to the data acquisition and/or planning for this study include G. Brueckner, D. Bartoe, J. Cook and K. Dere of NRL, J. Davis of MSFC, H. Zirin of Caltech, K. Harvey of SPRC/NSO, L. Golub of CFA and the AS&E launch-support team consisting of R. Eng, F. Hills, R. Schueller, and E. Smith. The work of DFW was supported at Emmanuel College by AFGL contract F19628-87-K-0033 and NRL order N00173-87-TO-06614. The work of JDM at AS&E was supported by NASA contract NAS5-25496.

REFERENCES

1. L. Golub, X-ray bright points and the solar cycle, Phil. Trans. R. Soc. Lond. 297, 595 (1980).
2. D. Webb, Small-scale coronal structure, in: Coronal and Prominence Plasmas, ed. A.I. Poland NASA CP-2442, 1986 p. 329.
3. L. Golub, A.S. Krieger, J.W. Harvey, and G.S. Vaiana Magnetic properties of X-ray bright points Solar Phys 53, 111 (1977).
4. S.F. Martin and K.L. Harvey Emerging active regions during solar minimum, Solar Phys. 64 93 (1979).
5. S.F. Martin, S.H.B. Livi, J.Wang, and Z. Shi, Ephemeral regions vs. pseudo ephemeral regions, in: Measurements of Solar Vector Magnetic Fields, ed M.J. Hagyard NASA CP-2374, 1985 p 403.
6. K.L. Harvey, The relationship between coronal bright points as seen in HeI 10830 and the evolution of the photospheric network magnetic fields Aust. J Phys. 38 875 (1985).
7. J.W. Harvey, A.S. Krieger, A.F. Timothy, and G.S. Vaiana, Comparison of Skylab X-ray and ground-based helium observations, Osserv. Mem Oss Arcetri 104 50 (1975).
8. L. Golub, K.L. Harvey and D.F. Webb, Magnetogram and soft X-ray comparisons of XBP and ER, in: Coronal and Prominence Plasmas, ed., A.I. Poland, NASA CP-2442, 1986, p. 365.

11 DECEMBER 1987



NSO MAGNETOGRAM
1504-1544 UT



AS&E X-RAYS
1815 UT

Fig. 1. Comparison of full-disk, near-simultaneous images of a photospheric magnetogram (NSO) and a soft X-ray image (AS&E). Acquisition time for the magnetogram was 40 min. The X-ray image was a 60 sec. exposure with a passband of 8-60Å. Solar north is at the top and east to the left. The total area covered by the six BBSO VMGs is denoted on each image by the rectangle.

ORIGINAL PAGE
BLACK AND WHITE PHOTOGRAPH



ORIGINAL PAGE
BLACK AND WHITE PHOTOGRAPH

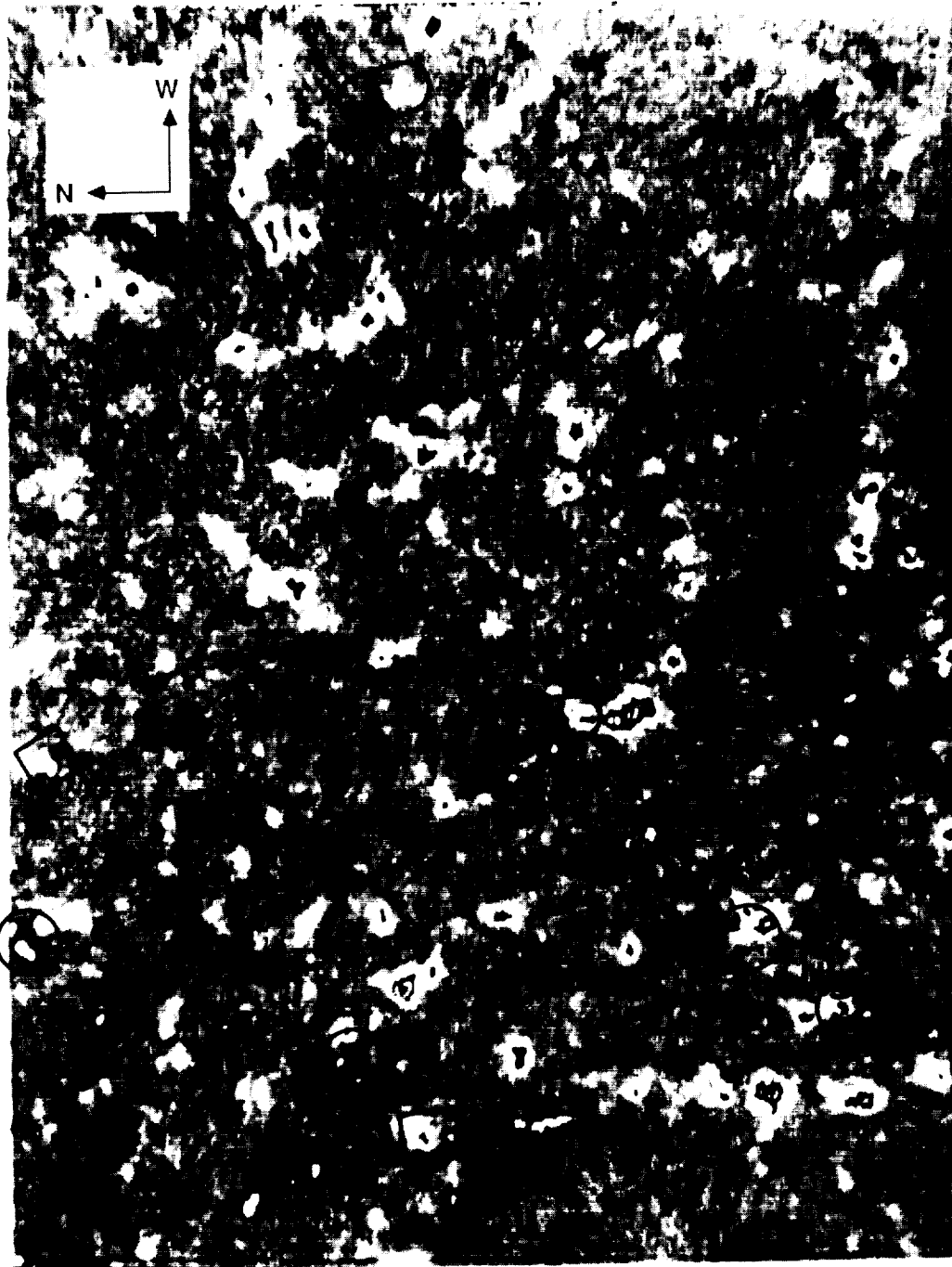


Fig. 2. An example of our comparison of the correspondence of magnetic bipoles to XBPs within one of the six VMG fields outlined by the rectangle shown in Figure 1. Square symbols identify cancelling magnetic bipoles and oval symbols identify emerging magnetic bipoles. If the evolution of the bipole occurred within one hour of the X-ray rocket flight, the symbol is marked with a solid outline, while if the evolution occurred later, the symbol is marked with a dashed outline. XBP locations are marked by the solid circles which are 20 arc sec in diameter.

4.20 The Observation of Possible Reconnection Events in the Boundary Changes
of Solar Coronal Holes

S.W. Kahler

Physics Research Division
Emmanuel College
Boston, Massachusetts 02115

and

D. Moses

American Science and Engineering, Inc.
Cambridge, Massachusetts 02139

ORIGINAL PAGE IS
OF POOR QUALITY

THE OBSERVATION OF POSSIBLE RECONNECTION EVENTS IN THE BOUNDARY CHANGES OF SOLAR CORONAL HOLES

S.W. Kahler

Physics Research Division, Emmanuel College, 400 The Fenway, Boston
MA 02115

J.D. Moses

American Science and Engineering, Inc., Ft. Washington,
Cambridge MA 02139

Abstract. Coronal holes are large scale regions of magnetically open fields which are easily observed in solar soft X-ray images. The boundaries of coronal holes are separatrices between large-scale regions of open and closed magnetic fields where one might expect to observe evidence of solar magnetic reconnection. Previous studies by Nolte and colleagues using Skylab X-ray images established that large scale ($\sim 9 \times 10^4$ km) changes in coronal hole boundaries were due to coronal processes, i.e., magnetic reconnection, rather than to photospheric motions. Those studies were limited to time scales of about one day, and no conclusion could be drawn about the size and time scales of the reconnection process at hole boundaries.

We have used sequences of appropriate Skylab X-ray images with a time resolution of about 90 min during times of the central meridian passages of the coronal hole labelled "Coronal Hole 1" to search for hole boundary changes which can yield the spatial and temporal scales of coronal magnetic reconnection. We find that 29 of 32 observed boundary changes could be associated with bright points. The appearance of the bright point may be the signature of reconnection between small-scale and large-scale magnetic fields. The observed boundary changes contributed to the quasi-rigid rotation of Coronal Hole 1.

Introduction

Coronal holes are regions of unusually low density and temperature in the solar corona. They are present at all phases of the solar cycle, but reach their maximum extent in the two or three years before solar minimum. Over a decade ago Krieger (1977) in his review of the temporal behavior of coronal holes posed several fundamental questions about the evolution of holes that have yet to be completely answered. In particular, he asked: 1) What is the relationship between the stochastic diffusion of photospheric magnetic flux and the large-scale boundary changes? 2) What is the characteristic time scale for coronal hole boundary changes? 3) What is the role of emerging flux? 4) Are the large-scale boundary shifts cases of field line reconnection or of the evacuation of previously opened field lines?

An examination of the boundary changes of coronal holes was carried out by Nolte and colleagues (Nolte et al., 1978 a,b,c) using Skylab X-ray images from the period of May to November 1973. For each central meridian passage (CMP) of the Skylab coronal holes they compared the boundaries observed in three X-ray images: an image at CMP, an image 1 day earlier, and an image 1 day later. This procedure allowed them to study boundary changes with a time resolution of 1 day. Because of a concern with the possibility that the boundaries could move as a result of the diffusive motion of the field lines, they considered two classes of changes. Small-scale changes ranged from $\approx 1.2 \times 10^4$ km, the smallest changes they could measure, to 9×10^4 km. Large-scale changes were those exceeding 9×10^4 km, ≈ 3 times the average supergranulation cell length. This criterion was used to preclude the possibility that large-scale changes could arise from the chance association of random motions. Nolte et al. (1978a) found statistically that about 38% of the boundary lengths showed a significant change over 1 day. The small-scale changes accounted for 70% of this total, and the large-scale changes for the remaining 30%.

In their second paper Nolte et al. (1978b) inferred that the large-scale changes (which they referred to as "sudden") must involve a process different from that of at least some of the small-scale changes because the large-scale changes were found to account for most of the long-term (rotation-to-rotation) changes in coronal hole areas whereas the small-scale changes seemed poorly correlated with the long-term changes.

In the third paper Nolte et al. (1978c) studied the specific coronal structures which seemed to play roles in the growth and decay of coronal holes. They found a general agreement with the hypothesis that holes are born and grow in conjunction with active regions. They also found evidence that holes decayed when the number of X-ray bright points in the longitude bands containing the holes was relatively high. X-ray bright points are pointlike X-ray emitting features associated with small bipolar magnetic features (Golub et al., 1974).

We might expect that the detailed studies of Nolte et al. (1978 a,b,c) would have explored Krieger's (1977) questions to the limit of the X-ray observations. However, those studies were based only on comparisons of X-ray images obtained at 1-day intervals. Appropriate X-ray images were regularly obtained at roughly 6-hr intervals through most of the Skylab mission and in some cases, which we discuss here, the observations were made at least once per orbit (≈ 90 min) for sequences of 3 to 7 consecutive orbits. We use these images to study coronal hole boundary changes on this substantially shorter time scale.

Analysis

The X-ray spectrographic telescope built by American Science and Engineering, Inc. flew on the Skylab spacecraft in 1973 and 1974. During the 8-month operational lifetime of the mission soft X-ray images of the sun were recorded on film with a spatial resolution of ≈ 2 arc sec. Six different broad-band filters and

a large dynamic range of exposure times were used to image various solar features and provide effective temperature diagnostics. The instrument has been described in detail by Vaiana et al. (1977), and an atlas of daily full-sun images of the X-ray corona was published by Zombeck et al. (1978).

The optimum images for studying the faint features of coronal holes are those obtained with the largest X-ray fluence. These are the 256 s exposures taken through the thinnest filter (filter 3) with passbands of 2-32 and 44-54 Å. Usable images in this mode were obtained from 1973 May 28 to November 21 (Nolte et al., 1976). We examined a catalog of all such sun-centered images obtained during 5-day periods centered on the CMPs of low-latitude coronal holes determined by Nolte et al. (1976) to look for images in three or more consecutive orbits. We restricted the images to those with coronal holes near CMP and limited the regions of interest to latitudes of $\pm 40^\circ$ to minimize the projection effects of optically thin structures at hole boundaries (Nolte et al., 1976). Since we wanted to study hole boundary changes, we sought large area holes with extensive boundaries. For that reason we eliminated the sequences of images of coronal holes 2 (on May 29 and August 18) and 3 (on August 12 and 13) because of their small areas (Nolte et al., 1976) and concentrated on Coronal Hole 1 (hereafter CH 1, following the designation used by Timothy et al. (1975) for the first coronal hole observed during the Skylab mission). The only images satisfying our requirements were obtained on 3 consecutive orbits on June 2, 7 orbits on August 19, 4 orbits on August 20, and 4 orbits on August 21.

Full-disk X-ray images of CH 1 at each CMP have been published by several authors (i.e., Figure 9 of Timothy et al. (1975); Figure 1 of Nolte et al. (1978c); and Figure 1 of Maxson and Vaiana (1977)) and will not be repeated here. It was the largest of the Skylab coronal holes, extending from the north pole to about S 20° with a width of order 15° at the equator. The extensive boundaries of the hole allow us a good opportunity to study the details of the boundary changes.

The changes of the hole boundaries were examined by a visual comparison of second-generation transparencies with a disk diameter of 10.8 cm. Since the positions of the boundaries and the changes in those positions over several consecutive orbits involves a subjective determination, we first listed all suspected boundary changes in all sets of images and then repeated the effort to get only the clearest examples. We eliminated cases where the area changes were so small as to be questionable or where the brightness change of a boundary feature was not sufficient to cause one to redraw the boundary. Although they claimed that coronal hole boundaries are sharp, Maxson and Vaiana (1977) presented cross sections of photographic density through the filter 3, 256 s images that clearly display the low spatial gradients of brightness at the boundary that render the boundary determination uncertain by perhaps 10-30 arc sec. Our boundary changes, characterized as one-dimensional features, ranged from ≈ 10 arc sec ($\approx 7 \times 10^3$ km) to ≈ 1 arc min (4.3×10^4 km). Our lower limit is slightly less than that ($\approx 1.2 \times 10^4$ km).

of Nolte et al. (1978a) who examined hole boundary shifts on a time scale of 1 day.

In the examination of the boundary changes it was immediately apparent that bright points played an important role. This can be seen in Figure 1, which shows the sequences of filter 3, 256 s images of CH 1 during the times of 7 consecutive orbits on August 19. In the figure black arrows point to the bright points associated with coronal hole expansions and white arrows point to the bright points associated with coronal hole shrinkages. One case of a hole shrinkage with no bright point association is shown with the lower white arrow at 0651 UT in Figure 1. In the images of August 20 and 21 there were two cases of coronal hole expansions without any observed associated bright point. In the images of all four dates we found 32 boundary changes of which 29 could clearly be associated with bright points.

The most common kind of boundary change is simply the appearance of a new bright point or the disappearance of a pre-existing bright point at the coronal hole boundary in such a way as to cause an apparent shift in the boundary by about the dimension of the bright point itself. Most of the boundary changes of Figure 1 are of this type. In some cases an X-ray region somewhat more extensive than just the bright point itself will brighten or dim. Two examples in Figure 1 are shown by the lower white arrow at 0226 UT, in which a relatively large X-ray structure in the hole attaches itself to the boundary, and by the black arrow at the eastern boundary at 0415 UT, where a large bright region surrounding the bright point slowly fades after the transient appearance of the bright point.

A summary of the time and size scales of the three kinds of boundary changes is given in Table 1, where we have averaged the measured sizes and the number of orbits over which the brightening or dimming of the X-ray structure was observed. Since the time resolution is ≈ 90 min, the actual time scales could be significantly less than the observed values, and we have given them as upper limits. To compare these boundary changes with those expected from supergranulation motions, we can use the time and size scales to calculate a characteristic speed for the boundary changes of $\geq 6 \times 10^3$ km hr⁻¹ for all categories of changes. Assuming a supergranulation cell size of 3.2×10^4 km and cell lifetime of 20 hr, we see that the speeds of the boundary changes exceed the supergranulation speed of 1.6×10^3 km hr⁻¹ by at least a factor of 4. These boundary changes are therefore not due to supergranulation motion.

The dimensions of the 32 observed boundary changes ranged from 7×10^3 km to 4.5×10^4 km with an average of 1.7×10^4 km; only one event exceeded 3.2×10^4 km. We therefore find no evidence for large scale boundary shifts of a size exceeding three times the supergranulation cell size ($\approx 9 \times 10^4$ km) discussed by Nolte et al. (1978a).

Most of the bright points associated with the boundary changes are much fainter than those used by Golub et al. (1974) for bright point statistics studies. Those authors used bright points visible on 4 s exposures, while we have used 256 s exposures. Comparing bright point counts in coronal holes on 4 s

and 256 s images, Golub et al. found about 100 times more bright points visible on the longer exposures. They also found a correlation between the maximum areas and the lifetimes of bright points. The bright points we have observed are generally small in area ($< 20 \times 10^7 \text{ km}^2$) and short lived (1-5 hrs), consistent with this correlation.

The tendency of CH 1 to rotate quasi-rigidly rather than to participate in the solar differential rotation was discussed by Timothy et al. (1975). To see whether the 32 boundary changes we found in the sequences of images contributed to that quasi-rigid rotation, we establish two categories of boundary changes. X-ray brightenings on the western boundary and dimmings on the eastern boundary of the hole result in an eastward shift of the hole boundary. Conversely, X-ray brightenings on the eastern boundary and dimmings on the western boundary shift the hole boundaries westward. We used Stoneyhurst disks to measure the latitude of each boundary change and then compared the eastward shifts with the westward shifts as a function of latitude. The summed results for all four dates are shown in Table 2. Coronal holes will be sheared by differential rotation as the low-latitude regions are shifted westward relative to the high-latitude regions. We see that within the limited statistics of Table 2 the observed shifts oppose the differential rotation by being predominately eastward at low ($\leq 20^\circ$) latitudes and westward at high ($> 20^\circ$) latitudes. This result may perhaps have been anticipated from our previous knowledge of the quasi-rigid rotation (Timothy et al., 1975), but it provides supporting evidence that the boundary changes associated with bright points are the changes important to the development of the coronal hole.

Discussion

Recent work on modeling coronal fields by the Naval Research Lab group (Nash et al., 1988) has provided an explanation for the rigid rotation of coronal holes near solar minimum. Using a potential field model with differential rotation, diffusion and meridional flow, they found that the outer coronal field rotates more rigidly than the underlying photospheric field because it depends on only the lowest-order harmonic components. The motion of the hole boundary is uncoupled from that of the underlying photospheric flux elements by continual reconnection of magnetic field lines. The details of the reconnection process are not specified. One possibility is that this reconnection occurs in the high corona. The time scale of the boundary changes ($\approx 1-5$ hrs) is consistent with this, but no bright point involvement would be expected.

The appearance of X-ray bright points in boundary changes suggests that we examine the weak photospheric fields for the source of the reconnection process. The structure of the magnetic fields at hole boundaries is characteristic of the quiet sun fields consisting of network clusters at supergranular cell vertices and of weaker intranetwork fields (Zwaan, 1987). The latter weak ($< 50 \text{ G}$) fields consist of mixed polarities and do not extend into the outer corona. We suggest that reconnection

occurs between the small-scale structure and the larger scale magnetic field as shown schematically in Figure 2. The X-ray bright points associated with the hole boundary changes may correspond to the small loop in A or C of the figure or to the reconnection region in B. The separatrix is drawn between the two closed field regions in C because it separated the small scale structure from the large scale structure and because the bright point will be faint either before the sequence C,B,A or after the sequence A,B,C. The size and time scales of the proposed reconnection scenario are those given in Table 1. A somewhat similar schematic was proposed by Marsh (1978) to explain the relationship between bright point flares and supergranulation network flux elements. He observed several cases of an H α brightening at the network element followed by a fibril system linking the network element with one of the poles of the bipolar region.

Nolte et al. (1978c) found a statistical relationship between the bright point density in coronal holes and the rate of shrinkage of the hole area. They suggested that this was due to two reasons. First, the hole was being filled in by X-ray-emitting closed-field remnants of the bright points. A problem with this idea is that we have no evidence that the bright points grow to the observed sizes of large-scale structures. The brightest bright points have lifetimes of less than a day (Golub et al., 1974). The second reason proposed by Nolte et al. (1978c) was that the bright points enhanced the rate of reconnection of open field lines at the hole boundaries. However, if a bright point reconnects with an open field line, one end of the bright point bipole must also be open after the reconnection process. Thus the proposed reconnection scenario will not result in a net closing of large-scale open field lines. In contrast, in our Figure 2 we see that the bright point in C interacts with adjacent closed field line flux to produce a shrinking of the hole area in the C,B,A sequence by motions of previously closed field lines. A further observational problem with the Nolte et al. idea is that a more detailed examination of the bright point densities in coronal holes by Davis (1985) showed no association between bright point density and the rates of hole growth or decay.

At the time of their discovery it was obvious that bright points were bipolar magnetic structures (Golub et al., 1974). They were interpreted as regions of emerging flux by Golub et al. (1974) and others. This view was challenged by Harvey (1985), who used He I 10830 A dark points as a proxy for X-ray bright points and found that about two-thirds of the dark points were associated with chance encounters of features of opposite magnetic polarity. In a recent study Webb and Moses (1988) compared bright points observed in rocket solar X-ray images with bipoles observed in simultaneous videomagnetograms. The great majority of bipoles were not associated with X-ray bright points, but 11 of 16 observed X-ray bright points were associated with cancelling bipoles and only one with an emerging bipole. Webb and Moses concluded that their results were consistent with the Harvey (1985) interpretation that most bright points are

associated with encounters of opposite polarity features. Our observations suggest that the bright points form due to coronal heating at some time during the reconnection process. X-ray bright points are known to flare on a time scale of minutes (Golub et al., 1974), but it is not clear how the flare event or the formation and disappearance of the bright point are related to the reconnection scenario of Figure 2.

Acknowledgements. We thank D. Webb, E. Hildner, R. Moore, A. Nash, and N. Sheeley, Jr. for helpful comments. This research was supported at Emmanuel College by AFGL contract F19628-87-K-0033 and at AS&E by NASA contract NAS5-25496.

References

- Davis, J.M., Small-scale flux emergence and the evolution of equatorial coronal holes, Solar Phys., 95, 73-82, 1985.
- Golub, L., A.S. Krieger, J.K. Silk, A.F. Timothy, and G.S. Vaiana, Solar X-ray bright points, Ap.J., 189, L93-L97, 1974.
- Harvey, K.L., The relationship between coronal bright points as seen in He I 10830 and the evolution of the photospheric network magnetic fields, Aust. J. Phys., 38, 875-883, 1985.
- Krieger, A.S., Temporal behavior of coronal holes, in Coronal Holes and High Speed Wind Streams, edited by J.B. Zirker, Colorado Associated University Press, Boulder, 71-102, 1977.
- Marsh, K.A., Ephemeral region flares and the diffusion of the network, Solar Phys., 59, 105- 113, 1978.
- Maxson, C.W., and G.S. Vaiana, Determination of plasma parameters from soft X-ray images for coronal holes (open magnetic field configurations) and coronal large-scale structures (extended closed-field configurations), Ap.J., 215, 919-941, 1977.
- Nash, A.G., N.R. Sheeley, Jr., and Y.-M. Wang, Mechanisms for the rigid rotation of coronal holes, Solar Phys., 117, 359-389, 1988.
- Nolte, J.T., A.S. Krieger, A.F. Timothy, G.S. Vaiana, and M.V. Zombeck, An atlas of coronal hole boundary positions May 28 to November 21, 1973, Solar Phys., 46, 291-301, 1976.
- Nolte, J.T., A.S. Krieger, and C.V. Solodyna, Short term evolution of coronal hole boundaries, Solar Phys., 57, 129-139, 1978a.
- Nolte, J.T., M. Gerassimenko, A.S. Krieger, and C.V. Solodyna, Coronal hole evolution by sudden large scale changes, Solar Phys., 56, 153-159, 1978b.
- Nolte, J.T., J.M. Davis, M. Gerassimenko, A.S. Krieger, C.V. Solodyna, and L. Golub, The relationship between solar activity and coronal hole evolution, Solar Phys., 60, 143-153, 1978c.
- Timothy, A.F., A.S. Krieger, and G.S. Vaiana, The structure and evolution of coronal holes, Solar Phys., 42, 135-156, 1975.
- Vaiana, G.S., L. van Speybroeck, M.V. Zombeck, A.S. Krieger, J.K. Silk, and A. Timothy, The S-054 X-ray telescope experiment on Skylab, Space Sci. Instr., 3, 19-76, 1977.
- Webb, D.F., and J.D. Moses, The correspondence between small-scale coronal structures and the evolving solar magnetic field, Advances Space Res., in press, 1988.
- Zombeck, M.V., G.S. Vaiana, R. Haggerty, A.S. Krieger, J.K. Silk, and A. Timothy, An atlas of soft X-ray images of the solar corona from Skylab, Ap.J. Supple., 38, 69-85, 1978.
- Zwaan, C., Elements and patterns in the solar magnetic field, Ann.Rev.Astron.Astrophys., 25, 83-111, 1987.

TABLE 1. Time and Size Scales of Boundary Changes

| <u>Boundary Change</u> | <u>Dimming</u> | <u>Brightening</u> |
|---|---|--|
| Bright Point Only | 11 cases 1.3×10^4 km ≤ 2.3 hr | 9 cases 1.4×10^4 km ≤ 1.8 hr |
| Bright Point and Extended Structure | 6 cases 2.2×10^4 km ≤ 3.0 hr | 3 cases 2.3×10^4 km ≤ 4.0 hr |
| Extended Structure Without Bright Point | 2 cases 2.3×10^4 km ≤ 3.0 hr | 1 case 2.0×10^4 km ≤ 3300 hr |

TABLE 2. Observed Boundary Shifts of CH 1

| <u>Shifts</u> | <u>Latitude</u> | | | |
|---------------|-----------------|----------------|----------------|----------------|
| | <u>01°-10°</u> | <u>11°-20°</u> | <u>21°-30°</u> | <u>31°-40°</u> |
| Eastward | 4 | 9 | 2 | 1 |
| Westward | 3 | 4 | 6 | 3 |

Fig. 1. Skylab X-ray images of CH 1 during seven consecutive orbits on 1973 August 19. The five bright points which were associated with expansions of the hole area are shown by black arrows; the six bright points associated with hole shrinkage by white arrows. One case of a hole shrinkage with no obvious bright point association is shown by the lower white arrow at 0651 UT.

Fig. 2. Schematic for reconnection of magnetic fields at coronal hole boundaries. Dotted regions are closed fields; the wavy line is the separatrix between open and closed fields. Reconnection occurs in B in the shaded region. The sequence A,B,C corresponds to an expansion of the hole area; C,B,A corresponds to a shrinking of the hole area.



0032 UT



0226 UT

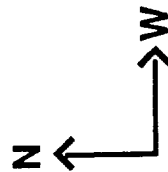


0415 UT



0512 UT

15 ARC MIN



0651 UT

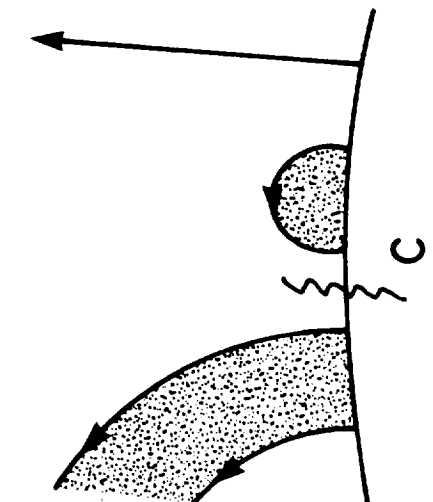
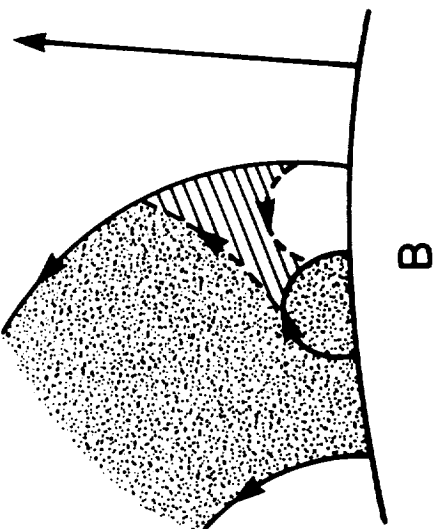
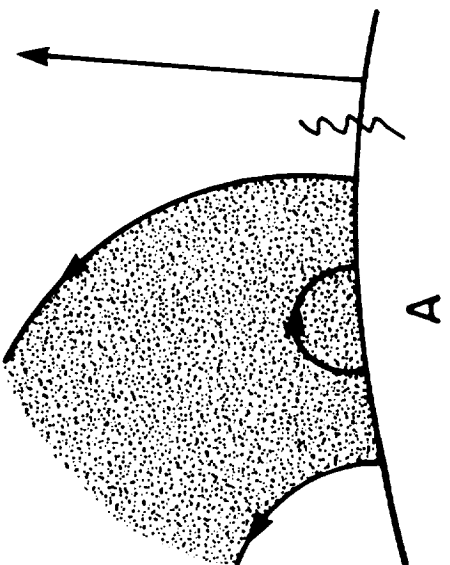


0818 UT



0952 UT

19 AUGUST 1973



4.21 X-Ray Bright Points and He I 10830 Dark Points

L. Golub

Smithsonian Astrophysical Observatory
Cambridge, Massachusetts 02138

K.L. Harvey

Solar physics Research Corporation
Tucson, Arizona

M. Herant

Harvard University
Cambridge, Massachusetts 02138

and

D.F. Webb

Emmanuel College, Boston, Massachusetts
and
American Science and Engineering, Inc.
Cambridge, Massachusetts 02139

ORIGINAL PAGE IS
OF POOR QUALITY

X-RAY BRIGHT POINTS AND He I λ 10830 DARK POINTS

L. Golub
Smithsonian Astrophysical Observatory
Cambridge, Mass.

K. L. Harvey
Solar Physics Res. Corp.*
Tucson, Ariz.

M. Herant, Harvard University
Cambridge, Mass.

and

D. F. Webb
Emmanuel College
Boston, Mass.
and
American Science & Engineering
Cambridge, Mass.

* Visitor, National Solar Observatory. National Optical Astronomy Observatories operated by the Association of Universities for Research in Astronomy, Inc. under contract with the National Science Foundation.

ABSTRACT

Using near-simultaneous full disk Solar x-ray images and He I 10830 \AA spectroheliograms from three recent rocket flights, we compare dark points identified on the He I maps with x-ray bright points identified on the x-ray images. We find that for the largest and most obvious features there is a strong correlation: most He I dark points correspond to x-ray bright points. However, about two-thirds of the x-ray bright points were not identified on the basis of the helium data alone. Once an x-ray feature is identified it is almost always possible to find an underlying dark patch of enhanced He I absorption which, however, would not *a priori* have been selected as a dark point. Therefore, the He I dark points, using current selection criteria, cannot be used as a one-to-one proxy for the x-ray data. He I dark points do, however, identify the locations of the stronger x-ray bright points.

X-RAY BRIGHT POINTS AND He I λ 10830 DARK POINTS

L. Golub
Smithsonian Astrophysical Observatory

K. L. Harvey
Solar Physics Research Corporation

M. Herant
Harvard University

and

D. F. Webb
Emmanuel College

and

American Science & Engineering

1. Introduction

The name "x-ray bright point" or XBP was given to the numerous small regions of enhanced emission which were seen on early high resolution x-ray images (Vaiana *et al.* 1970) of the Solar corona. For large, long-lived regions, whenever detailed comparison between coronal features and magnetic field maps is performed, one finds that non-flaring coronal emission is associated with closed loop structures which appear as bipoles on magnetograms and as loops in x-rays (Vaiana and Rosner 1978). For the smallest features the comparison is not as straightforward, particularly because there are many small magnetic bipoles which are not associated with any obvious x-ray emission. The XBP, which are associated with magnetic bipoles, are so numerous that if they are caused by newly emerging magnetic flux, then they could be responsible for the vast majority of the emerging magnetic flux coming to the Solar surface (Golub *et al.* 1977).

The sharp division in x-ray brightness between open and closed regions is particularly useful for identifying and studying small bipolar regions. Such studies have indicated that the vast majority of closed, compact emission features in the corona correspond to regions having lifetime τ of two days or less (Golub *et al.* 1974). For the larger ($\tau > 2$ days) regions, it is clear that they represent emerging flux; these regions generally develop arch filament systems and pores, and occasionally small sunspots. The more numerous shorter-lived regions exhibit fewer indicators of flux emergence; until now we have only established that there is a statistical correlation between magnetic bipole separation and magnetic flux, and the age of the XBP (Golub *et al.* 1977).

Unfortunately, because x-ray observations can only be obtained from instruments above the atmosphere, only infrequent sounding rocket x-ray data with sufficient spatial resolution and sensitivity to detect XBP have been obtained since the Skylab mission. On the other hand, daily groundbased full disk He I $\lambda 10830$ spectroheliograms have been available since Skylab from the National Solar Observatory (NSO) at Kitt Peak. The Helium data have been used, among other things, for studying the small regions which are called "dark points" when seen in Helium, under the working hypothesis that there is a one-to-one association between dark points and XBP. This assumption is based on a study carried out in 1973 (Harvey *et al.* 1975) using some of the earliest He I data available. This study was

a qualitative comparison of four pairs of observations in x-rays and He I D_3 , which is essentially identical to He I 10830 (Harvey and Hall 1971; Giovanelli *et al.* 1972).

The He $\lambda 10830$ absorption line is produced by He I in its triplet state. It is formed in the chromosphere, at about the same height as the Ca K and H $_{\alpha}$ lines. Goldberg (1939; see also Zirin 1975; Kahler, Davis and Harvey 1983) suggested that UV emission from the corona can overpopulate the triplet state of He I through photoionization followed by recombination. This model explains the resemblance between He I spectroheliograms and x-ray maps, as well as the presence of a faint network similar to that which can be seen in Ca K or H $_{\alpha}$.

Because of the correlation between x-ray emission and He I absorption, combined with the relative lack of x-ray data in recent years, there has been a tendency within the Solar community to use the He I $\lambda 10830$ spectroheliograms as a substitute for the unavailable coronal x-ray data. While this has been shown to be justified in the case of large, long-lived structures such as active regions and coronal holes (Kahler, Davis and Harvey 1983), quantitative comparisons of the smallest features have not until now been carried out. The purpose of this letter is to show that the validity of using He I dark points as a proxy for x-ray bright points is limited and that He I $\lambda 10830$ maps and x-ray images, despite evident similarities, cannot be used interchangeably.

2. Comparison of He I $\lambda 10830$ and X-ray Data

K. Harvey (1985) conducted an extensive survey of NSO magnetograms and He I $\lambda 10830$ spectroheliograms collected from 1970 to 1984, partly as an attempt to analyze in detail the connection between magnetic activity and small coronal features. Within the time frame of this study, three x-ray datasets which are appropriate for use in this study were obtained from flights of the A.S.&E. rocket-borne grazing incidence telescope (see Vaiana *et al.* 1973 for instrument description). Near simultaneous (i.e., within two hours) ground-based data were obtained for these flights, as summarized in Table 1. Note that full disk Helium and magnetic field scans take approximately 40 minutes each; times listed in the table are start times.

Table 1. Dates and Times of X-ray, He I and Magnetogram Data Used.

| Date | X-ray (UT) | He I 10830 | Magnetogram |
|----------|------------|------------|--|
| 6/27/74 | 1948 | 1605 | 1508 |
| | | 1657 | 1854 |
| | | 1804 | |
| 9/16/76 | 1803 | 1841 | 1532 |
| 11/16/79 | 1703 | 1646 | 1543, 1743, 1828, 1917, 2007, 2100 |
| | | | |
| | | | |

We have performed the comparison as a double-blind experiment. Using these datasets we compared the XBP as marked by one of us (L.G.) against the He I dark points identified separately (by K. L. H.). The procedures for selecting x-ray bright points have been discussed in our earlier papers, but may be summarized briefly as follows: we examine the photographs for small, compact, isolated regions of x-ray emission. This may be pointlike, or give the appearance of elongated loop structure, or they may be fairly diffuse and best described as "cloudlike". The main criterion is that the region be self-contained and clearly isolated from any larger structure. The upper limit on size is arbitrarily taken

to be one arcminute.

Dark points were selected on the basis of a visual inspection of the He I $\lambda 10830$ spectroheliograms using as criteria the size and intensity of isolated structures. Structures identified as dark points are typically less than 40 arcsec in extent, although some larger regions are included, particularly those in coronal holes, having an intensity at least 20% darker than the surrounding network. No attempt was made to eliminate filament fragments which can have a similar appearance. Consistency in the selection of features that are dark points depends strongly on the day-to-day variations of the calibration of the He I $\lambda 10830$ data and the print quality.

The result of this comparison is best illustrated visually as in Figure 1. This figure shows the central portions of the He I and x-ray images obtained on 27 June 1974, and it illustrates the result which we find in general for all of the observations. There are four categories of correspondence between the two images. These are: He I dark points which *are* and *are not* associated with XBP, and XBP which *are* and *are not* associated with dark points.

In Figure 1 only three of these categories needed to be labelled since the last category was not present. That is, there were no XBP which did not have an associated He I feature. Thus, the figure contains three types of overlay symbols: a solid circle indicates an XBP located at the place where a He dark point was identified, a dotted circle indicates an XBP which did not have a *previously* identified He dark point, and a square indicates a helium feature which did not have an XBP.

The major conclusions reached from comparison of the x-ray and He I $\lambda 10830$ data are:

1. There are, in general more XBP identified than there are He I dark points selected - 162 compared with 65;
2. Most of the dark points have corresponding XBP - 53 out of 64. In the few cases for which there is no XBP present, the helium feature tends to be a piece of filament material. Filaments appear as absorption features in He I $\lambda 10830$, much as they do in H α .
3. In essentially every case, an XBP can later be associated with a patch of He I absorption.

Results 1 and 2 are summarized quantitatively in Table 2.

Table 2. Statistics of Dark Point/Bright Point Identifications.

| Date | # d.p. | # XBP | # d.p. w/o XBP | # XBP w/o d.p. |
|----------|--------|-------|----------------|----------------|
| 6/27/74 | 31 | 58 | 1 | 27 |
| 9/16/76 | 26 | 90 | 6 | 70 |
| 11/16/79 | 9 | 14 | 5 | 10 |

Explanation of column headings:

- # d.p. = number of He I dark points identified
- # XBP = number of x-ray bright points identified
- # d.p. w/o XBP = number of He I dark points which did not have corresponding x-ray bright points
- # XBP w/o d.p. = number of x-ray bright points which did not have previously selected dark points.

The key numbers in this table is listed in the last two columns. Our comparison shows that only $\frac{1}{2}$ to $\frac{1}{3}$ of the x-ray bright points correspond to helium features which are identified on the basis of the He I data alone. It is, of course, quite possible that essentially all of the XBP correspond to helium features, which would be consistent with the small number of dark points without XBP, shown in the table's fourth column. However, the results of this study show that using present identification methods, $\frac{1}{2}$ to $\frac{1}{3}$ of the x-ray bright points may not be located on the basis of the He I $\lambda 10830$ data. On the other hand most He I dark points correspond to x-ray bright points, specifically the brighter ones (see Figure 1).

Although there are major differences apparent when comparing the two sets of small scale features, the statistical results should be viewed with caution because of two important considerations. As can be seen from Table 1, the datasets are not strictly simultaneous and it can be argued that the short lifetime and rapid variability of helium dark points and x-ray bright points may be partially responsible for the lack of correlation between the two maps. This may be particularly true for the

smaller, weaker x-ray bright points which, if they are not in the very early or very late stages of development, characteristically have shorter lifetime than the larger XBP (Golub *et al.* 1974).

The second point is that the selection criteria for x-ray bright points and helium dark points are somewhat subjective. Our analysis of the correlation between x-ray bright points and helium dark points is based on today's best effort. We do not rule out the possibility of empirically developing a reliable automated selection algorithm, perhaps in conjunction with magnetic field and H_{α} information.

3. Implications

On the basis of the assumed correlation between XBP and emerging magnetic flux certain major conclusions were reached: that the small regions contribute the majority of the emerging flux at nearly all phases of the Solar cycle (Davis, Golub and Krieger 1977), and that this would lead to an anticorrelation in the cycle behavior between the large (active regions as represented by sunspots) and the small (XBP) emerging regions (Golub, Davis and Krieger 1979; Davis 1983). By arguing that bright points are associated with small regions of emerging magnetic flux, Golub *et al.* 1979 put forward the suggestion that the Solar cycle is a variation in the size distribution of new emerging flux rather than a variation in the total quantity of flux.

Recent studies have greatly confused this proposed picture. In particular, time sequences of high resolution magnetograms show that many, if not most, of the observed small bipoles represent "chance encounters" of small opposite polarity magnetic elements which appear to come together and disappear (Martin *et al.* 1985). The work done by Harvey (1985) shows that two-thirds of the He I dark points are associated with chance encounters of opposite polarities, while the remaining one-third result from emerging new flux. If one were to assume that the He I dark points identify all of the XBP, instead of the fraction which we report here in Table 2, then we would conclude that chance encounters are mainly responsible for the XBP. The conclusions reached by Golub, Davis and Krieger (1979) would therefore be incorrect (Zwaan 1987).

Even though we have shown in this paper that there is a limit in finding from the ground-based data alone all of the XBP, this limit is largely irrelevant to the earlier bright point studies. The reason is that most of the earlier bright point studies were done using short x-ray exposures (Golub *et al.* 1977) in order to eliminate possible bias caused by the varying large scale coronal structures and coronal holes. Thus, the bright points studied were the largest and most easily seen, and those correspond quite well to the features selected in the Helium $\lambda 10830$ data. The data used in the present study were taken with a different telescope than the one used on Skylab, but we attempted to choose exposure times which would produce images as close as possible to those used in the earlier work.

In Golub, Harvey and Webb (1986) we examined the relationship between XBP and ephemeral magnetic regions, using these same x-ray data and near-simultaneous magnetograms. Our conclusion was that the separation of the ER into encounters between opposite polarity network elements and emerging bipoles makes almost no difference in the probability of seeing an x-ray feature. Thus, if two-thirds of the magnetic features are chance encounter ("reconnection") events, then two-thirds of the x-ray features will by probabilities alone also be associated with reconnection events. The XBP which we studied would then be dominated by chance encounters and should have the same Solar cycle properties as the He I dark points.

The question remaining is why the XBP show an anticorrelation with the Solar cycle, as do the dark points (Harvey 1985), while the ER do not behave the same way. Unfortunately, we are not at this time in a position to answer this crucial question. A possible answer may be provided by noticing that the fractional area coverage of mixed polarity on the Sun is anticorrelated with the Solar cycle (Giovannelli 1979). The fraction of the Sun's surface covered by mixed polarity field tracks well with the variation in XBP number as a function of phase in the Solar cycle. However, Golub *et al.* (1977) established quite clearly that the size and lifetime of an XBP correlates well with the quantity of magnetic flux in the bipolar region. It is not clear whether area coverage of mixed polarities in itself is sufficient to explain the XBP variation, as Harvey (1985) argued, since field strength or quantity of flux in the region should also be a factor. For example, if at Solar minimum the mixed polarity field on the Sun consists of relatively small bits of magnetic flux, then the distribution of XBP lifetimes should be skewed toward short-lived regions. However, since the Skylab mission we have not had any time resolved x-ray data from which to determine changes in the XBP lifetime distribution as a function of Solar cycle. Moreover, it will be possible to make such a differentiation only if the distribution of lifetimes or fluxes for the emerging regions is different than that of the chance encounters.

The detailed comparisons between x-ray and magnetic data, with time resolved sequences of both, were done during the Skylab mission. At that time the magnetograph being used had lower spatial resolution and sensitivity than the present instrument. In the intervening fifteen years, no time sequences of high resolution x-ray data have been available. A step toward an answer may be pro-

vided by future flights of x-ray telescopes with higher spatial resolution, which could provide snapshots of the detailed structure within XBP, as well as time sequence observations to study the relation between XBP and the evolving underlying magnetic field. Such data may show a difference in topology between emerging and reconnecting features, which would at least help in determining whether there are differences in the coronal behavior of these two different kinds of magnetic regions. If we can successfully differentiate between the two types of region then one would expect that the two classes would have different Solar cycle properties, as determined by time-resolved data.

4. Acknowledgements

This work was supported as SAO by NASA Grant NAGV-112, at Emmanuel College by AFGL contract F19628-87-K-0033, and at A.S.&E. by NASA Contract NAS5-25453.

5. References

- Davis, J.M., L. Golub and A.S. Krieger 1977, *Ap. J.*, **214**, L141.
- Davis, J. M. 1983, *Sol. Phys.*, **88**, 337.
- Giovannelli, R. G., D. Hall and J. W. Harvey 1972, *Solar Physics*, **22**, 53.
- Golub, L. 1980, *Phil. Trans. R. Soc. London A*, **297**, 595.
- Golub, L., A.S. Krieger, J.W. Harvey and G.S. Vaiana 1977, *Sol. Phys.*, **53**, 111.
- Golub, L., K. L. Harvey and D. F. Webb 1986, NASA CP-2442, ed. A. I. Poland, p.365.
- Harvey, J. W. and D. Hall 1971, IAU Symp. **43**, 279.
- Harvey, J. W., A. S. Krieger, A. F. Timothy and G. S. Vaiana 1975, in G. Righini (ed.), "Skylab Solar Workshop", Oss. e Mem. Osservatorio di Arcetri, **104**, 50.
- Harvey, K. 1985, *Australian J. Phys.*, **58**, 385.
- Kahler, S. W., J. M. Davis and J. W. Harvey 1983, *Sol. Phys.*, **87**, 47.
- Vaiana, G.S., A.S.Krieger and A.F. Timothy 1973, *Sol. Phys.*, **32**, 81.
- Zwaan, C. 1987, *Ann. Rev. Astron. and Astroph.*, **25**, 83.

ORIGINAL PAGE IS
OF POOR QUALITY

6. Figure Caption

Figure. 1. a) He I $\lambda 10830$ spectroheliogram taken at 1657 UT (end at -1740 UT) on 27 June 1974. Overlay indicates comparison with x-ray bright points, as follows: solid circle indicates He I dark point with corresponding XBP, dotted circle indicates location of XBP for which no He I feature was selected and squares indicate small pieces of filament material.

b) X-ray image obtained at 1948 UT on 27 June 1974.

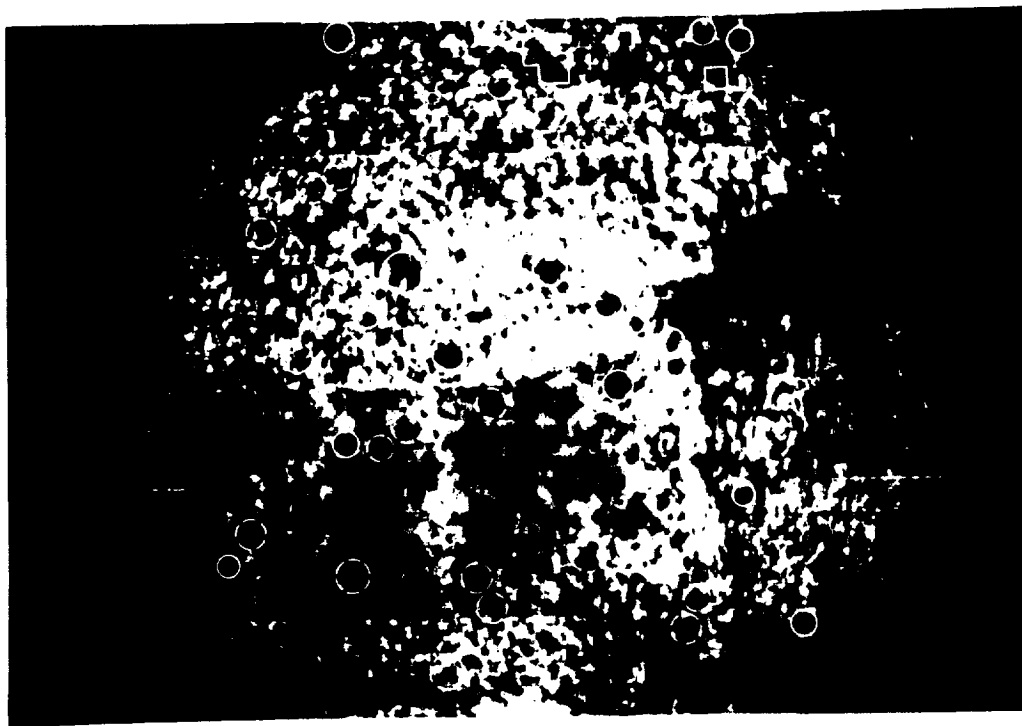


Fig. 1a

ORIGINAL PAGE
BLACK AND WHITE PHOTOGRAPH



Fig. 1b

ORIGIN: PAB
BLACK AND WHITE PHOTOGRAPH

4.22 Advanced in Photographic X-Ray Imaging for Solar Astronomy

D. Moses and R. Schueller

American Science and Engineering, Inc.
Cambridge, Massachusetts 02139

K. Waljeski

Brandeis University
Waltham, Massachusetts 02254

and

J.M. Davis

NASA/Marshall Space Flight Center
Huntsville, Alabama

ORIGINAL PAGE IS
OF POOR QUALITY

1. *Phragmites australis*
 2. *Scirpus americanus*
 3. *Spartina patens*
 4. *Distichlis spicata*
 5. *Eleocharis acicularis*
 6. *Eleocharis obtusa*
 7. *Eleocharis tenuis*
 8. *Eleocharis palustris*
 9. *Eleocharis acicularis*
 10. *Eleocharis obtusa*
 11. *Eleocharis tenuis*
 12. *Eleocharis palustris*
 13. *Eleocharis acicularis*
 14. *Eleocharis obtusa*
 15. *Eleocharis tenuis*
 16. *Eleocharis palustris*
 17. *Eleocharis acicularis*
 18. *Eleocharis obtusa*
 19. *Eleocharis tenuis*
 20. *Eleocharis palustris*
 21. *Eleocharis acicularis*
 22. *Eleocharis obtusa*
 23. *Eleocharis tenuis*
 24. *Eleocharis palustris*
 25. *Eleocharis acicularis*
 26. *Eleocharis obtusa*
 27. *Eleocharis tenuis*
 28. *Eleocharis palustris*
 29. *Eleocharis acicularis*
 30. *Eleocharis obtusa*
 31. *Eleocharis tenuis*
 32. *Eleocharis palustris*
 33. *Eleocharis acicularis*
 34. *Eleocharis obtusa*
 35. *Eleocharis tenuis*
 36. *Eleocharis palustris*
 37. *Eleocharis acicularis*
 38. *Eleocharis obtusa*
 39. *Eleocharis tenuis*
 40. *Eleocharis palustris*
 41. *Eleocharis acicularis*
 42. *Eleocharis obtusa*
 43. *Eleocharis tenuis*
 44. *Eleocharis palustris*
 45. *Eleocharis acicularis*
 46. *Eleocharis obtusa*
 47. *Eleocharis tenuis*
 48. *Eleocharis palustris*
 49. *Eleocharis acicularis*
 50. *Eleocharis obtusa*
 51. *Eleocharis tenuis*
 52. *Eleocharis palustris*
 53. *Eleocharis acicularis*
 54. *Eleocharis obtusa*
 55. *Eleocharis tenuis*
 56. *Eleocharis palustris*
 57. *Eleocharis acicularis*
 58. *Eleocharis obtusa*
 59. *Eleocharis tenuis*
 60. *Eleocharis palustris*
 61. *Eleocharis acicularis*
 62. *Eleocharis obtusa*
 63. *Eleocharis tenuis*
 64. *Eleocharis palustris*
 65. *Eleocharis acicularis*
 66. *Eleocharis obtusa*
 67. *Eleocharis tenuis*
 68. *Eleocharis palustris*
 69. *Eleocharis acicularis*
 70. *Eleocharis obtusa*
 71. *Eleocharis tenuis*
 72. *Eleocharis palustris*
 73. *Eleocharis acicularis*
 74. *Eleocharis obtusa*
 75. *Eleocharis tenuis*
 76. *Eleocharis palustris*
 77. *Eleocharis acicularis*
 78. *Eleocharis obtusa*
 79. *Eleocharis tenuis*
 80. *Eleocharis palustris*
 81. *Eleocharis acicularis*
 82. *Eleocharis obtusa*
 83. *Eleocharis tenuis*
 84. *Eleocharis palustris*
 85. *Eleocharis acicularis*
 86. *Eleocharis obtusa*
 87. *Eleocharis tenuis*
 88. *Eleocharis palustris*
 89. *Eleocharis acicularis*
 90. *Eleocharis obtusa*
 91. *Eleocharis tenuis*
 92. *Eleocharis palustris*
 93. *Eleocharis acicularis*
 94. *Eleocharis obtusa*
 95. *Eleocharis tenuis*
 96. *Eleocharis palustris*
 97. *Eleocharis acicularis*
 98. *Eleocharis obtusa*
 99. *Eleocharis tenuis*
 100. *Eleocharis palustris*

ADVANCES IN PHOTOGRAPHIC X-RAY IMAGING FOR SOLAR ASTRONOMY

D. Moses and R. Schueller
American Science and Engineering, Inc.
Cambridge, Massachusetts 02139

K. Waljeski
Brandeis University
Waltham, Massachusetts 02254

and

J.M. Davis
NASA, Marshall Space Flight Center
Huntsville, Alabama 35812

ABSTRACT

The technique of obtaining quantitative data from high resolution soft X-ray photographic images produced by grazing incidence optics was successfully developed to a high degree during the AS&E Solar Research Sounding Rocket Program and the S-054 X-Ray Spectrographic Telescope Experiment Program on Skylab. Continued use of soft X-ray photographic imaging in sounding rocket flights of the AS&E High Resolution Solar Soft X-Ray Imaging Payload has provided opportunities to further develop these techniques. The developments discussed include: (1) The calibration and use of an inexpensive, commercially available microprocessor controlled drum type film processor for photometric film development. (2) The use of Kodak Technical Pan 2415 film and Kodak SO-253 High Speed Holographic film for improved resolution. (3) The application of a technique described by Cook, Ewing, and Sutton⁽¹⁾ for determining the film characteristics curves from density histograms of the flight film. Although the superior sensitivity, noise level, and linearity of microchannel plate and CCD detectors attracts the development efforts of many groups working in soft X-ray imaging, the high spatial resolution and dynamic range as well as the reliability and ease of application of photographic media assures the continued use of these techniques in solar X-ray astronomy observations.

1. INTRODUCTION

Photographic detection of X-rays has been an essential technique in the history of X-ray applications since the discovery of the phenomena. X-ray photography has been primarily used as a position sensing (imaging) technique with only qualitative information on dosimetry. However, when sufficient effort is devoted to calibration (in all its various aspects), quantitative measurements of total energy deposit on a photographic medium have been successfully made for many applications.

One particularly successful use of quantitative measurements from photographic X-ray images was developed for the AS&E Solar Research Sounding Rocket Program and the S-054 X-Ray Spectrographic Telescope Experiment Program on Skylab. The details of this approach have been described in a series of papers and presentations⁽²⁻⁵⁾. In these programs, images of the solar soft X-ray (3-60 Angstroms) corona were formed by grazing incidence optics with angular resolution ranging from 2-5 arc seconds. Since the plate scales for these telescopes range from 7 to 10 microns

per arc second, the plate scale of the detector must be of the order of 7 to 20 microns. Furthermore, it is quite common to observe coronal structures which vary by over three orders of magnitude in soft X-ray emission within a single image; flares can generate a dynamic range of 10^6 . At the time of the design of these instruments, photographic film was the only detector suitable for space flight that possessed the required combination of sensitivity, spatial resolution, and dynamic range. Even today, this combination of performance, when coupled with the refinements in technique which are described in this paper, makes photographic media a very attractive choice for quantitative soft X-ray imaging of the solar corona.

2. PHOTOMETRIC DEVELOPMENT PROCEDURE

A large immersion-type continuous flow film processor was designed and built for the Skylab S-054 film processing. This machine was capable of maintaining variations in a test sensitometric visible light exposure to within ± 0.03 diffuse density units throughout the D log E curve for the film type used in this investigation (Kodak SO-212). Furthermore, the gamma of the test D log E curve was held to 1.50 ± 0.06 . While this machine provided excellent results with the 1300-foot rolls of 70 mm Skylab film, it is poorly suited to the 25-foot rolls of 35 mm film from the sounding rocket investigations because of the differences in the width of film, the difficulties in splicing a sufficient length of leader for the large processor, and the degradation in the machine following long periods of disuse.

Two aspects of the SO-212 film used in both the Skylab and Sounding Rocket investigations complicate the search for alternative solutions to the problem of photometric film processing: (1) The film was manufactured with a 2.5 mil base instead of the standard 4 mil base to reduce the bulk of the film rolls, and (2) the film was manufactured without the usual 1 micron gelatin topcoat to minimize absorption of low energy X-rays. The thin film base makes for serious handling difficulty in a processing system, particularly in loading reels for hand development. The lack of a topcoat makes the film very sensitive to pressure-induced developable artifacts in the handling process. Furthermore, the lack of a topcoat makes the development of the film extremely sensitive to the local concentration of developer chemistry. This difficulty made it impossible to obtain uniform development across the film with any type of hand development attempted by these investigators.

Through the suggestion of R. Haggerty of Crimson Camera Company, Cambridge, Massachusetts, the film processing needs of the sounding rocket program were met by the use of a mass produced, microprocessor controlled film processor manufactured by King Concept Corporation of Minneapolis, Minnesota. The processor is designed around a horizontally positioned light-tight drum into which the reel mounted film is placed. Under microprocessor control, chemistry is introduced and evacuated on a one-shot basis, and agitation is obtained through rotation of the drum. The temperature of the chemistry is maintained within 0.2 degrees centigrade by a water jacket, and the air temperature is controlled in the chamber where the drum is mounted. Kodak HC110 developer was used because of the ease of adjusting and repeatably obtaining the desired dilution. The greatest difficulty in the entire procedure was loading the 25-foot lengths of thin base SO-212 film on the stainless steel reels. This was finally accomplished with a modification to the King Concept Corporation device for film loading and a very practiced hand. Particular care was also devoted to monitor the temperature soak of the process, to avoid contamination effects, and to properly mix and store solutions.

The performance of the processor was monitored through the use of the same visible light sensitometric exposures (step-wedge with density increments of 1.414) as used in the Skylab effort. Visible light exposures were chosen over X-ray exposures based on the issues of ease and repeatability of exposure. The calibration effort consisted of 38 test batches conducted over a three-month interval.

The gamma of the D log E curve was found to vary along the length of the film within a given batch by no more than 0.03 from the mean. The film development batch exhibiting the greatest variation from the target gamma of 1.50 had a gamma of 1.37 (a variation of 0.13), although typical variations from the target value were of the order of 0.05. The extreme variation was obtained during a run significantly separated in time from the previous batches, indicating the need for a calibration run immediately before any flight run to test for changes in chemistry strength, temperature drifts, etc.

Measurement of variations in density throughout the sensitometric step wedges was complicated by the combination of the density structure of the step wedge, the extreme sensitivity of SO-212 film to local chemistry variations, and the direction of flow of the chemistry during agitation. Since agitation was accomplished in the drum by continuous rotation, the chemistry flow was constant and unidirectional along the length of the film. The length of the sensitometric step wedge was such that it could only be oriented with step exposures either increasing or decreasing along the length of the film. Therefore, the "downstream" density steps were always exposed to developer which was partially exhausted by the upstream density steps. While this developer exhaustion effect was never detected between two successive step wedges, the effect was always apparent within an individual step wedge. If the orientation of the sensitometric exposure was such that the more heavily exposed steps were "upstream" in the flow of the developer, the densest steps would have higher values and the less dense steps would have lower values than the case in which the least exposed steps were oriented "upstream." The two D log E curves would cross in the transition between the shoulder and straight line region with the greatest differences being restricted to the shoulder region (thus minimizing differences in gamma).

The variables of developer dilution, temperature, rotational agitation speed, rotational agitation direction (cw vs. ccw), and development time were explored and adjusted -- within the constraint of the target gamma value of 1.5 -- to minimize the effects of the developer depletion along flow direction. The resulting optimal development parameters were found to be dilution D of HC110 at 20°C for 3.75 minutes with 60 RPM rotational speed and a flow direction opposite that of the standard process. Within a single roll of film, density variations of 0.03 were found between step wedges of similar orientation with respect to developer flow direction. For step wedges of opposite orientation, the straight line portions were found to differ by less than 0.06 density units within a given roll of film while individual steps in the shoulder region could differ by as much as 0.12 density units. The density variations from roll to roll are in proportion to the variations in gamma from roll to roll.

The actual effect of depletion along the developer flow for the flight images is much less than that implied by the sensitometric step wedge measurements for two reasons: (1) The flight exposures are chosen such that the density values in the region of interest are within the straight line portion of the D log E curve to

provide energy resolution. (2) The size of the solar image on the film is much smaller than the size of the sensitometric exposure (24 mm x 18 mm vs. 121 mm x 10 mm), thus requiring much less developer for equivalent exposures. Furthermore, the size of the most dense region in a solar image, the core of a solar active region, is of the order of 0.5 mm. Since the active region spatial scale is less than the spacing between successive layers of film in the development reel, one would expect the mixing of the solution on these scales to make local developer depletion negligible. This expectation is borne out in the analysis described in the fourth section of this paper, where a local variation of the shape of the D log E curve in the longer exposures would become apparent in comparison with the shorter exposures. No localized developer depletion effects have been found in any analysis of the flight images.

Even the worst case variations in the automated film processor performance are greatly superior to performance obtained by hand development of SO-212 film, where seemingly random localized variations in density are found of the order of 0.20 density units throughout most of the D log E curve. The new automated processor does not match the consistency of performance from roll to roll of film obtained with the Skylab effort, but since all the film from a flight is developed in one load, the roll to roll variations are not as important. The consistency of performance within a given development load of film is comparable between the new processor and the Skylab machine. With careful attention to the inclusion of calibration white light and the appropriate X-ray sensitometric step wedge exposures with the development of a roll of film, excellent photometric results are obtained with the new system.

3. PHOTOGRAPHIC MEDIA

In preparation for the S-054 X-Ray Spectrographic Telescope Skylab mission, a special order photographic film was procured from Eastman Kodak in 1973. This film, labeled SO-212, is a standard aerographic emulsion with panchromatic response and was obtained without a gelatin top coat to improve its soft X-ray sensitivity. This stock of SO-212 has been used as the primary detector of the AS&E X-ray Imaging Sounding Rocket Program since its manufacture. The large volume required for a minimum special order makes it impractical to consider the manufacture of another batch of SO-212 (or an improved special order film) for the sounding rocket program. However, the considerable stock (in sounding rocket terms) left over from the Skylab mission has been kept in refrigerated storage and, other than an increase in the base density level by 0.05 to 0.07 diffuse density units, retains the same level of X-ray performance to within the uncertainty of variations in film processing and X-ray sensitometry.

Two main drawbacks exist in the use of SO-212 in the X-ray imaging sounding rocket program. The first drawback is the difficulties in handling the film which are described above. The second drawback is the level of granularity of the emulsion and the ultimate spatial resolution of the film relative to the plate scale of the telescope. Visible light tests with fine grain film show that the X-ray rocket mirror possesses angular resolution slightly better than 1 arc second, while both visible light test and X-ray flight images on SO-212 demonstrate resolution of several arc seconds at best.⁽⁶⁾

Listed in Table 1 are the candidates we have considered as supplements to the SO-212 film in an attempt to improve spatial resolution and handling. The T-Max 100

film has been used in the sounding rocket flight of an XUV telescope by Hoover et al.⁽⁷⁾, but we have not tested it. The SO-253 High Speed Holographic film was tested by AS&E during a flight on 31 January 1978.⁽⁸⁾ The Technical Pan 2415 (TP2415) was tested by AS&E during a flight on 15 August 1987.

TABLE 1 - PHOTOGRAPHIC FILM COMPARISON
(Kodak Technical Data based on visible light performance)

| <u>Film Designation</u> | <u>RMS Granularity</u> | <u>Resolution (lines/mm)</u> |
|---|-------------------------------------|------------------------------|
| * SO-253 High Speed Holographic | < 5 | 1250 |
| * Technical Pan 2415 | From < 5-8 depending on development | 320 |
| T-Max 100 | 8 | 160 |
| SO-212 Special X-Ray Emulsion Manufactured for Skylab Mission | 20 | 160 |
| * Available only with gelatin top coat. | | |

X-ray sensitometry was conducted for the films which were flown and the results are presented in Figure 1. The development parameters used in this comparison for all three films are those producing the desired speed and contrast for SO-212. It is possible to somewhat modify the characteristic curves of TP2415 and SO-253 through changes in development parameters to obtain a better suited response for a given application, but the baseline of X-ray performance in Figure 1 is useful for comparison purposes.

The X-ray sensitivity of photographic film is obviously inversely proportional to the grain size and resolution. It has not been practical at this point to obtain low energy (44 Angstrom) sensitometry of the ultra-high resolution SO-253 film because the response of this film requires a month-long exposure with our current apparatus. The effect of the top coat on the TP2415 appears to be minimal since there does not appear to be a great difference in the 8.3 Angstrom and 44 Angstrom performance relative to the SO-212 performance. Although a quantitative determination of the relative importance to soft X-ray photographic response of grain size and top coating must await parameterization of these results in terms of a model such as that of Henke et al.⁽⁹⁾, it is useful to speculate on this subject. In a film with a fine grain structure, the higher volume fraction of AgBr grains implies a photon will, on average, traverse a smaller path length of emulsion gelatin before absorption by a developable grain relative to a more coarse grain film. It seems reasonable that the disadvantage of a top coat is compensated for by the reduction in gelatin traversed by a photon in the emulsion of TP2415 in comparison to SO-212. Higher maximum density in the shoulder region is expected in the more densely packed fine grain films. At lower energies, the decrease in penetration depth may minimize this effect.

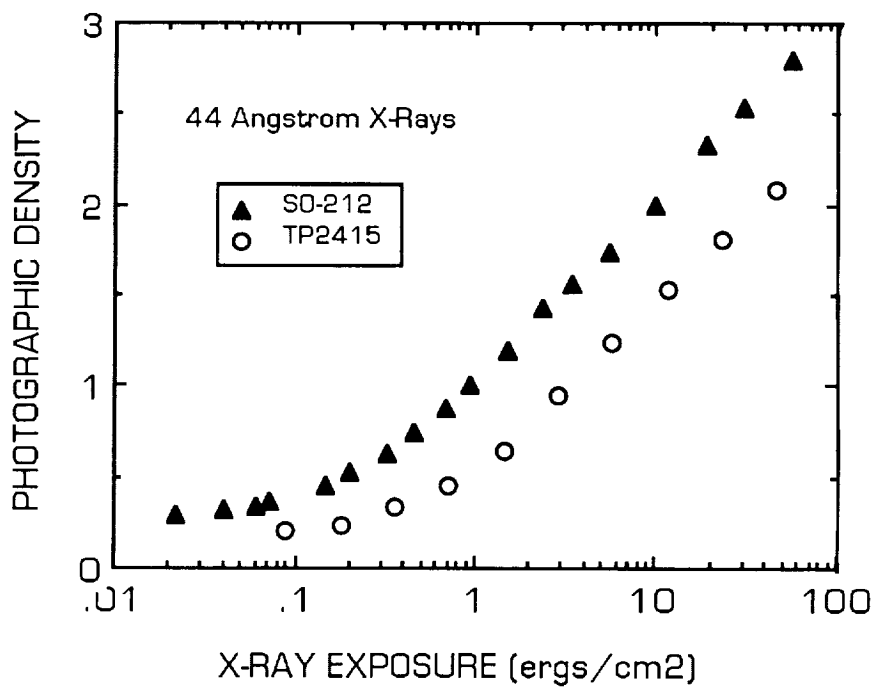
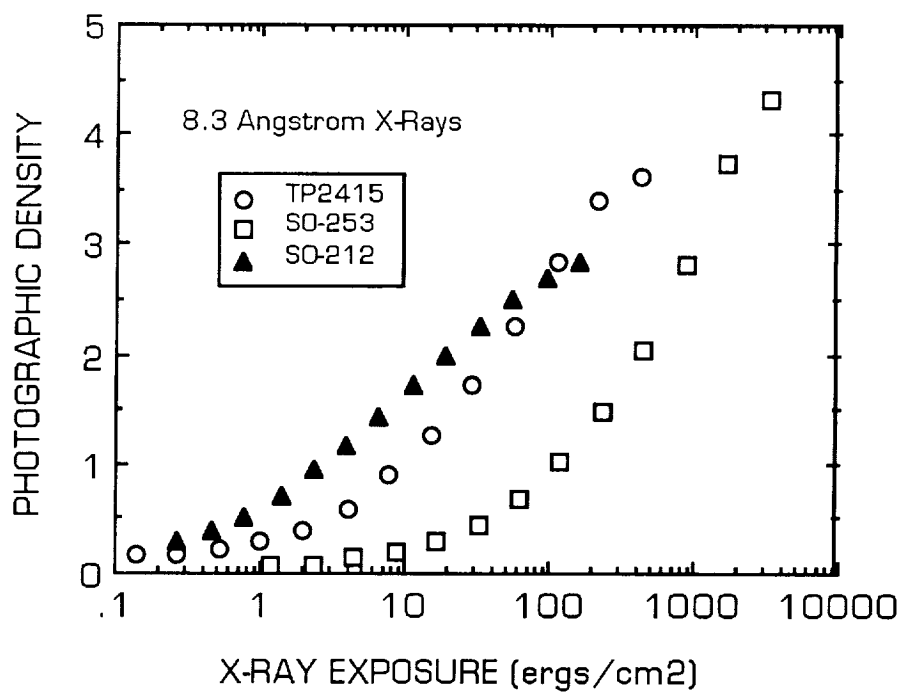


Figure 1. X-Ray Sensitometry of Photographic Film used in AS&E Solar Astronomy Soft X-Ray Imaging Sounding Rocket Program.

In practice, the target exposure times for SO-253 and TP2415 are increased relative to that of SO-212 by 5.5 and 2 stops, respectively. Since a typical sounding rocket flight provides about 5 minutes of observing time, the SO-253 is restricted to observations of bright active region cores and flares while the TP2415 can be used for everything but faint structures such as coronal holes and streamers. The SO-253 solar images show the active region cores resolved into loops in most regions with widths on the order of 1 arc second. The resolution of the TP2415 images fall midway between the resolution seen in the SO-253 images and that seen in the SO-212 images. The core regions which are resolved in the TP2415 images show complexes of loops with widths of 2 arc seconds.

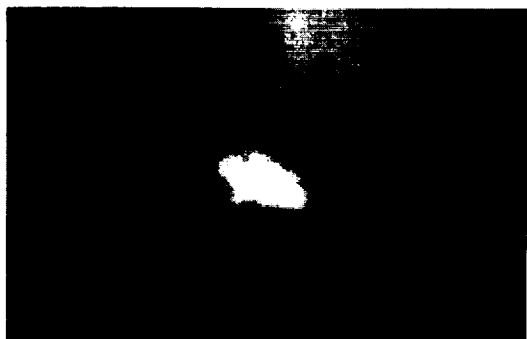
An attempt is made to reproduce examples of these images in Figures 2 and 3. The limitations of photographic reproduction in these proceedings restricts the differences which can be shown. In Figure 2, a flaring bright point is clearly resolved into a loop like structure approximately 12 arc seconds long and 1 arc second wide in the SO-253 image of frame (c). The interpretation of this feature from the best SO-212 exposure in frame (b) would be that of a small linear region. It is impossible to identify any structure in the SO-212 image in frame (a) that was taken through the same filter as the SO-253 image of frame (c). In Figure 3, the differences between the TP2415 and the SO-212 are more subtle but still quite apparent in the original prints. The grain of the TP2415 is much finer than that of the SO-212, resulting in a higher confidence in the determination of the outline of these inherently diffuse structures. The arrow in frame (b) points to one of three small loops (approximately 2 arc-seconds wide and 8 arc-seconds long) in the southern boundary of Active Region 4839 that are resolved in the TP2415 images but not in the SO-212 images. The arrow in frame (d) points to the core loop system of the arcade of Active Region 4841 that is resolved into individual loops (approximately 2 arc-seconds wide and 1 arc-minute long) in the high temperature TP2415 image but is not resolved in the corresponding SO-212 image.

These results are very encouraging. Each of the three film types has a specific advantage that will be exploited in future flights. Because it is easy to compare the results from the very well calibrated SO-212 with the considerable archival X-ray coronal images, this film will remain the baseline film for the synoptic aspect of these investigations.

4. DETERMINATION OF THE FILM CHARACTERISTIC CURVE

Quantitative information about the properties of the coronal plasma can be obtained from soft X-ray solar images only if the film characteristic curve (i.e., the relationship between the photographic density of the image and the energy incident upon the film) is known. The determination of the applicable characteristic curve is significantly complicated by the fact that the film response is wavelength dependent and the wavelength distribution of the incident broadband spectrum through a given filter is not known *a priori*. Therefore, the determination of the film characteristics curve must be an iterative process. The wavelength dependence of the X-ray response of the SO-212 was determined through an exhaustive effort conducted during the S-054 Skylab Program^(3,4). The measured wavelength response of the film is combined (through a weighted average) with a model of the X-ray emission of a plasma with assumed temperature, density, ionization state, and composition (folded with the transmission function of the telescope and filter) to produce a modeled characteristic curve. This modeled curve must be compared with the photographic data from the flight in a convenient way, as the plasma parameters

Figure 2. Flaring Bright Point
photographed on
January 31, 1978.



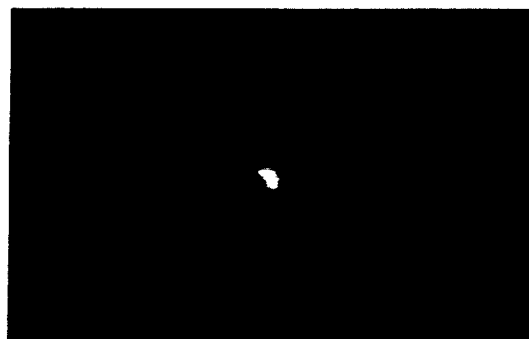
(a)

WAVEBAND 8-39, 44-64Å
FILM S0-212
EXPOSURE 0.9 sec.



(b)

WAVEBAND 8-20Å
FILM S0-212
EXPOSURE 0.7 sec.



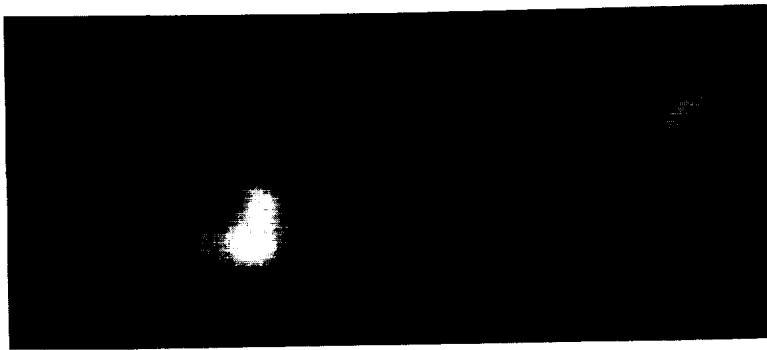
(c)

WAVEBAND 8-39, 44-64Å
FILM S0-253
EXPOSURE 20.3 sec.

—
1 arc min.

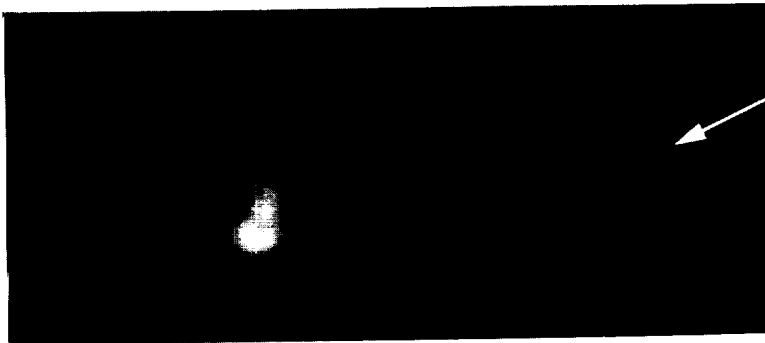
Figure 3. Active Region complexes
4842, 4841, and 4839 in the
southern hemisphere on
August 15, 1987.

(a)



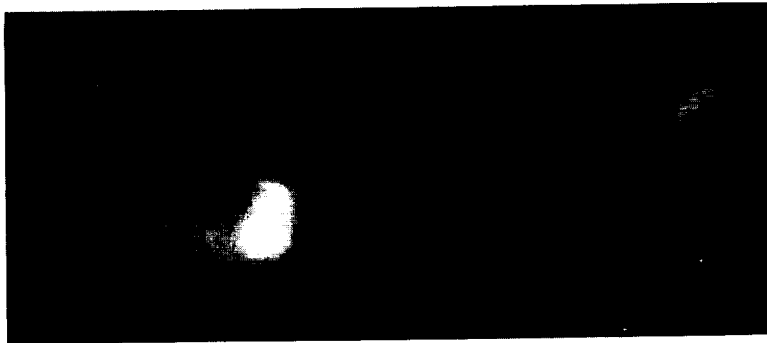
WAVEBAND 8-39, 44-60Å
FILM S0-212
EXPOSURE 3 sec.

(b)



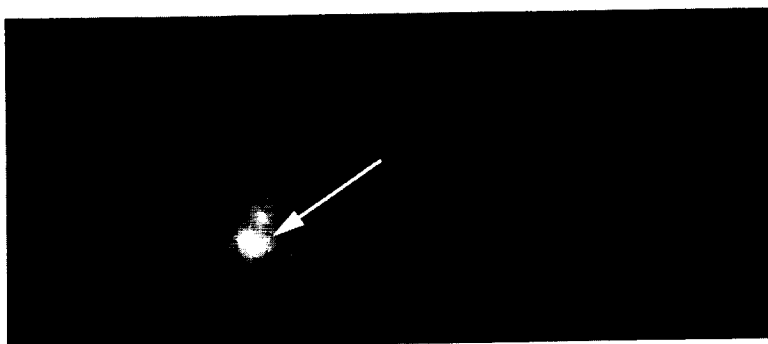
WAVEBAND 8-39, 44-60Å
FILM TP2415
EXPOSURE 9 sec.

(c)



WAVEBAND 8-20Å
FILM S0-212
EXPOSURE 9 sec.

(d)



WAVEBAND 8-20Å
FILM TP2415
EXPOSURE 20 sec.

5 arc min.

are iteratively adjusted to obtain a good fit to all the plasma diagnostics of these measurements.

For this discussion, we will use a parameterization of the film characteristic curve that was developed by VanSpeybroeck for the Skylab S-054 data analysis; it has been found to fit experimental film characteristic curves well. Other functional forms have been used to describe $D \log E$ curves (Tsubaki and Engvold⁽¹⁰⁾, Cook *et al.*⁽¹⁾); the VanSpeybroeck form is chosen for this analysis, as its parameters relate to quantities which can be easily measured from an experimental film characteristic curve. The VanSpeybroeck form of the relationship between the photographic density on the film is:

$$D = D_{base} + D_{max} + k \int_{a\mu E}^{\infty} \frac{e^{-z}}{z} dz - k \int_{a\mu E e^{-D_{max}/k}}^{\infty} \frac{e^{-z}}{z} dz$$

where: D = net density on the film
 E = power per unit area deposited on the film
 D_{base} = density of the base fog level
 D_{max} = maximum possible net density
 au = film speed parameter, proportional to the reciprocal of the energy at which the density equals D_{base} in the extrapolation of the linear portion of the curve.
 k = the slope of the linear portion of the $\ln E$ vs. D curve

The relationship between k (the slope of the characteristic curve expressed in terms of the natural logarithm of energy) and γ (the slope of the characteristic curve expressed in the traditional terms of the logarithm base-ten of energy) is

$$\gamma = 2.3 k$$

The four parameters of the characteristic curve to be determined are D_{base} , D_{max} , au , and γ . D_{base} and D_{max} do not vary with wavelength, so these values can be measured in the laboratory. The other two parameters, au and γ , are wavelength dependent and must be determined by an iterative technique.

Two methods of comparing a trial parameterized characteristic curve to the flight data have been utilized:

1. The scatter plot technique, which was developed as part of the Skylab ATM experiment data analysis of broadband soft X-ray images of the solar corona.
2. The density histogram technique, which was developed by Cook, Ewing, and Sutton⁽¹⁾ for the analysis of UV photographic spectra of the Sun.

By both of these techniques, the energy calibration is an iterative process between the laboratory calibration of the film and the flight data: The D -to- E calibration curve measured in the lab from a stepwedge, generated with monochromatic X-rays of a wavelength approximating the mean of the bandpass of the relevant filter, is used as a first approximation to the film characteristic curve. This approximation is refined iteratively by comparing image with different exposure times. The scatter plot and density histogram techniques differ in the methods used for image comparison.

The Scatter Plot Technique

By this technique, two digitalized images of differing exposure are, pixel by pixel, transformed and compared to determine the energy calibration curve. The images used must be co-aligned images of the same region, taken close enough together in time that the region can be assumed not to have changed between exposures. The trial $D \log E$ curve, taken from the monochromatic stepwedge, is used to convert the photographic densities $(D_1)_i$ and $(D_2)_i$, of each pixel, i , from each of the two exposures to powers per unit area, $(E_1)_i$ and $(E_2)_i$. A "scatter plot" is constructed by plotting E_1 vs. $(t_2/t_1) E_2$, where (t_2/t_1) is the ratio of the exposure times. If the slope of the best fit straight line to the scatter plot is unity, the film characteristic curve is correct. If not, au and γ are varied. The procedure is then repeated until no improvement in the scatter plot can be made. Note that the accuracy of this method is critically dependent upon the distribution of the points within the scatter plot. Furthermore, the scatter plot provides little sensitivity to, and feedback for, the toe region of the characteristic curve.

The Density Histogram Technique

This technique is the application of a method described by Cook *et al.*⁽¹⁾ for determining the film characteristic curve by transforming and comparing density histograms from images of differing exposures. Histograms of density are constructed from at least two digitalized images of the same region of the Sun, taken with different exposure times. One of the exposures is chosen as the base exposure, and bin-by-bin the histograms for the other exposure times are constructed from the base using the trial $D \log E$ curve, obtained from a monochromatic stepwedge. These transformed histograms are compared to the actual histograms of the appropriate exposure. The parameters of the characteristic curve, au and γ , are varied iteratively until the best match is found between the transformed histograms and the actual histograms.

This technique was used to determine the characteristic curves for film from the 11 December 1987 AS&E sounding rocket flight. The monochromatic reference stepwedge for this film is shown in Figure 4. Also plotted in Figure 4, is the fit to the stepwedge data obtained with the density histogram technique, for which $D_{base} = 0.16$, $D_{max} = 3.35$, $au = 5.70$, and $\gamma = 0.89$. It is apparent in Figure 4 that the density histogram technique provides the means to determine an excellent fit to the data of the characteristic curve parameters. Presented in Figure 5 is the characteristic curve determined by the density histogram technique using 3 s, 9 s, and 30 s exposures through the 8-39, 44-64 Angstrom bandpass filter of Active Region 4901, obtained during the 11 December 1987 flight of the AS&E Solar Rocket Payload. Also plotted for comparison in Figure 5 are the values of the monochromatic reference stepwedge shown in Figure 4. The final values of the parameters of the flight data characteristic curve were: $D_{base} = 0.16$, $D_{max} = 3.35$, $au = 7.00$, and $\gamma = 0.91$.

Although a determination of the characteristic curve by the scatter plot technique has not yet been completed for the image of Active Region 4901, in the data analysis of previous flights of this payload, the values of au and γ determined by the scatter plot technique for the comparable flight data are on the order of 10 to 20 percent greater than those determined for the reference 44 Angstrom

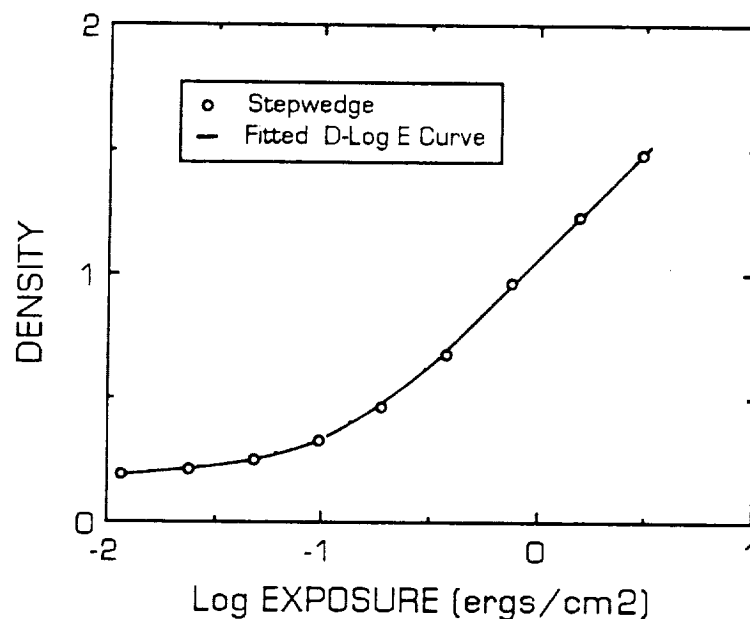


Figure 4. The 44 Angstrom monochromatic reference stepwedge for the 11 December 1987 rocket flight and the D log E curve fitted to this stepwedge data using the density histogram technique. ($D_{\text{base}} = 0.16$, $au = 5.70$, and $\gamma = 0.89$).

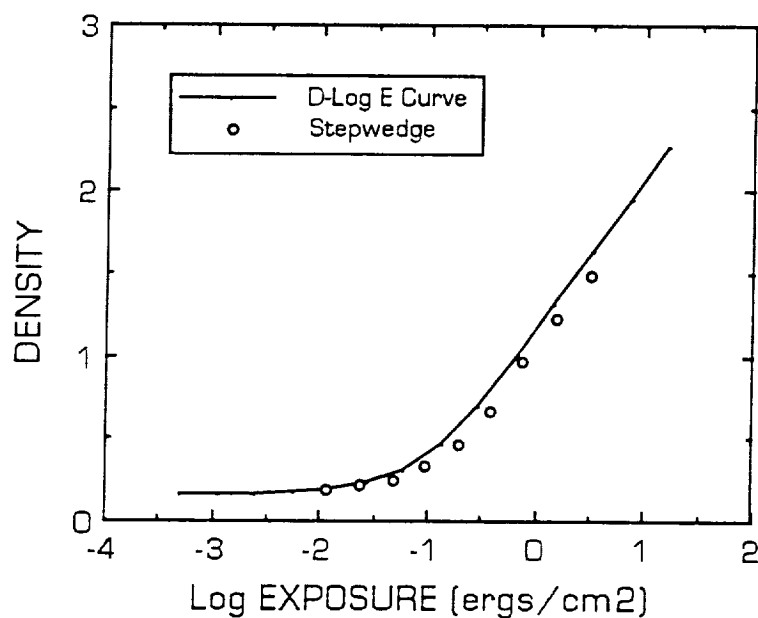


Figure 5. The characteristic curve for images from the 11 December 1987 rocket flight, as determined by the density histogram technique using 3 s, 9 s, and 30 s exposures through a polypropylene filter. ($D_{\text{base}} = 0.16$, $au = 7.00$, and $\gamma = 0.91$). The reference 44 Angstrom monochromatic stepwedge steps previously shown in Figure 4 are plotted again for comparison.

monochromatic stepwedge. Thus, both techniques find the same qualitative difference between the actual flight data and the reference monochromatic stepwedge data. As can be seen in Figure 5, making the assumption that the reference monochromatic stepwedge characteristic curve is equivalent to the flight data characteristic curve leads to an over-estimate of energy deposit in the focal plane by as much as 50 percent. The importance of this aspect of the image analysis is clear.

Discussion

The density histogram technique is expected to be the more reliable method of energy calibration for the following reasons:

1. The accuracy of the image co-alignment is less critical in the statistical approach of the density histogram technique. The pixel-by-pixel comparison of the scatter plot technique requires more exact co-alignment of the images.
2. As many exposures as are available may be used simultaneously to determine the characteristic curve by the density histogram technique. The scatter plot technique can compare two exposures only.
3. The density histogram technique is much less sensitive to the distribution of density values within a given exposure, and works well in the toe region of the characteristic curve.
4. It is easier to identify and ignore dirt, scratches, background, etc in the density histograms than in scatter plots.

We are only in the initial stages of implementing the density histogram technique in the analysis of flight data. A parallel effort with the scatter plot technique is planned for comparison. The initial results of the density histogram technique are very encouraging.

5. CONCLUSION

Three improvements in photographic X-ray imaging techniques for solar astronomy have been presented. The testing and calibration of a new film processor has been conducted, and the resulting product will allow photometric development of sounding rocket flight film immediately upon recovery at the missile range. Two fine-grained photographic films have been calibrated and flight tested to provide alternative detector choices when the need for high resolution is greater than the need for high sensitivity. An analysis technique used to obtain the characteristic curve directly from photographs of UV solar spectra has been applied to the analysis of soft X-ray photographic images, and the resulting procedure provides a more complete and straightforward determination of the parameters describing the X-ray characteristic curve than previous techniques. These improvements fall into the category of refinements instead of revolutions, indicating the fundamental suitability of the photographic process for X-ray imaging in solar astronomy. Although development of electronic detectors is the central component of our on-going development effort, photographic media will continue to be our baseline director for the near future.

6. ACKNOWLEDGEMENTS

We would like to acknowledge the crucial assistance and guidance of Robert Haggerty during all aspects of photometric film development in the AS&E Solar Physics Program. Anna Franco and Daniel O'Mara provided significant laboratory support to this project. We would like to thank S. Kahler, A. Krieger and D. Webb for useful discussions. This work builds on the strong tradition of quantitative image analysis that is a hallmark of AS&E. This work was supported by NASA contract NAS5-25496 and NASA GSRP Grant NGT-50308.

7. REFERENCES

1. Cook, J.W., Ewing, J.A., and Sutton, C.S., Pub. Astro. Soc. of the Pacific 100, 402, 1988.
2. Vaiana, G.S. VanSpeybroeck, L., Zombeck, M., Krieger, A.S., Silk, J.K., and Timothy, A.F., Space Sci. Inst. 3, 19, 1977.
3. Haggerty, R., Simon, R., Golub, L., Silk, J.K., Timothy, A.F., Krieger, A.S., and Vaiana, G.S., AAS Photo. Bull. 10, 8, 1975.
4. Simon, R., Haggerty, R., Golub, L., Krieger, A.S., Silk, J.K., and Timothy, A.F., Presented at the AAS Working Group on Photographic Materials, Rochester, NY, August 1974.
5. Krieger, A.S., SPIE, 106, 24, 1977.
6. Davis, J.M., Krieger, A.S., Silk, J.K., and Chase R.C., SPIE 184, 96, 1979.
7. Hoover, R.B., Barbee, T.W., Lindblom, J.F., and Walker, A.B.C., Kodak Tech Bits, pp. 1-6, June 1988.
8. Davis, J.M., Quarterly Progress Report No. 11, Contract NAS2-8683, 1977.
9. Henke, B.L., Kwok, S.L., Uejio, J.Y., Yamada, H.T., and Young, G.C., J. Opt. Soc. Am. B 1, 818, 1984.
10. Tsubaki, T. and Engvold, O., AAS Photo-Bulletin 9, 17, 1975.

4.23 Correspondence Between Solar Fine-Scale Structures in the Corona,
Transition Region, and Lower Atmosphere from Collaborative
Observations

D. Moses

American Science and Engineering, Inc.
Cambridge, Massachusetts 02139

J.W. Cook, J.-D.F. Bartoe, G.E. Brueckner, K.P. Dere

Naval Research Laboratory
Washington, D.C. 20375-5000

D. Webb

Emmanuel College
Boston, Massachusetts

J.M. Davis

NASA/Marshall Space Flight Center
Huntsville, Alabama

F. Recely

National Solar Observatory
Tucson, Arizona

and

S.F. Martin and H. Zirin

Big Bear Solar Observatory
Pasadena, California

ORIGINAL PAGE IS
OF POOR QUALITY.

N90-10804

CORRESPONDENCE BETWEEN SOLAR FINE-SCALE STRUCTURES
IN THE CORONA, TRANSITION REGION, AND LOWER ATMOSPHERE
FROM COLLABORATIVE OBSERVATIONS

D. Moses, J.W. Cook, J.-D.F. Bartoe, G.E. Brueckner, K.P. Dere,
D.F. Webb, J.M. Davis, F. Recely, S.F. Martin, H. Zirin

For submission to THE ASTROPHYSICAL JOURNAL

September 1989

1
2
3
4
5
6
7
8
9
10
11
12
13
14
15
16
17
18
19
20
21
22
23
24
25
26
27
28
29
30
31
32
33
34
35
36
37
38
39
40
41
42
43
44
45
46
47
48
49
50
51
52
53
54
55
56
57
58
59
60
61
62
63
64
65
66
67
68
69
70
71
72
73
74
75
76
77
78
79
80
81
82
83
84
85
86
87
88
89
90
91
92
93
94
95
96
97
98
99
100

ABSTRACT

The American Science and Engineering Soft X-Ray Imaging Payload and the Naval Research Laboratory High Resolution Telescope and Spectrograph (HRTS) instrument were launched from White Sands on 11 December 1987 in coordinated sounding rocket flights to investigate the correspondence of coronal and transition region structures, especially the relationship between X-ray bright points (XBPs) and transition region small spatial scale energetic events. We present the coaligned data from X-ray images, maps of sites of transition region energetic events observed in C IV (100,000 K), HRTS 1600 Å spectroheliograms of the T_{\min} region and ground-based magnetogram and He I 10830 Å images.

The transition region energetic events do not correspond to XBPs; in fact, they are associated with X-ray dark lanes in quiet regions. XBPs are associated with magnetic dipoles often appearing as prominent network elements, and the actual corresponding features in C IV observations are brighter, larger scale (20 arc sec) regions of complex velocity flows of order 40 km s^{-1} . However, analogously as He I 10830 Å dark points are not uniquely associated with XBPs, so also there are other similar C IV features which do correspond to an XBP in the X-ray image.

The C IV energetic events appear to be concentrated in the quiet Sun at the edges of strong network, or in weaker network regions. The X-ray image shows a pattern of dark lanes in quiet Sun areas, and the C IV events are predominantly concentrated within these dark lanes, avoiding areas of hazy, slightly brighter X-ray emission probably corresponding to unresolved loop systems seen even in quiet areas of the disk. We also find a greater number of C IV events than we would have expected from the results of a disk survey undertaken on the Space-lab 2 flight of the HRTS payload (Cook et al. 1987). This is possibly because

of the occurrence of particularly rich regions (associated with the X-ray dark lanes) in the field of view, and by an extended detection threshold from better spatial resolution with the HRTS V data.

I. INTRODUCTION

Fine scale features have been observed in the upper solar atmosphere both in the corona and in the transition region. X-ray bright points (XBPs), structures at the 10-20 arc sec spatial scale, lasting the order of 12 hours but with more transient periods of activity, have been observed from space by soft X-ray instruments viewing the corona. EUV spectrographs viewing transition region and chromospheric plasmas have observed highly transient fine scale structures down to arc second spatial scales. In particular, small scale (2 arc sec) features in transition region emission lines such as C IV 1548 A and 1550 A have been observed which show line profiles broadened to the red or blue by $50\text{--}200\text{ km s}^{-1}$ with average lifetimes of the order of 90 s or less (Brueckner and Bartoe 1983; Cook et al. 1987). We wanted to know if these C IV energetic events are related to XBPs, but the lack of near simultaneous X-ray and EUV observations left the correspondence between these coronal and transition region fine-scale transient structures unclear. In addition, we would like to know how these features are associated with lower atmospheric structures, for example, with magnetic field structures and with possible He I 10830 A counterparts.

In an effort to determine this correspondence, a collaborative "bright point campaign" of co-observations from ground and space was organized whose primary purpose was to determine the relationship of X-ray bright points, HRTS high velocity transition region energetic events, He I 10830 A dark points or other structures, and photospheric magnetic structures. Coordinated sounding rocket flights were made by the American Science and Engineering (AS&E) High Resolution Soft X-Ray Imaging Payload and the Naval Research Laboratory (NRL) High Resolution Telescope and Spectrograph (HRTS) experiment from White Sands

on 1987 December 11, with launches at 1815 UT (AS&E) and 1845 UT (NRL). The AS&E experiment obtained full disk coronal images over the wavelength range 8-64 Å, emitted by 10^6 K plasmas, with a spatial resolution of approximately 2 arc sec. The HRTS spectrograph slit of 920 arc sec length was rastered in 2 arc sec steps across an approximately 3 arc min wide area in the northeast quadrant, covering a quiet area out to the solar limb. HRTS spectra were obtained of the C IV 1548 Å and 1550 Å lines, emitted by transition region plasmas at 10^5 K. In addition, spectroheliograms covering an area of approximately 920 x 460 arc sec were taken over a 20 Å passband centered at 1600 Å.

Collaborative ground based observations were also obtained, including magnetograms (NSO/Kitt Peak and BBSO), He I 10830 Å (NSO/Kitt Peak), and H-alpha (BBSO). The HRTS spectroheliograms can be accurately registered with the magnetograms. The slit position of HRTS spectrograms covering the transition region C IV lines 1548 Å and 1550 Å can be accurately placed on the HRTS spectroheliograms. We then studied the correlation of sites of small spatial scale (2 arc sec) high velocity (100 km s^{-1}) transition region energetic events with the ground based data, and in particular the spatial relationship with the quiet Sun network.

In this paper we will present the co-registered observations from the two sounding rocket experiments and the ground-based observations, and discuss their correspondence and interpretation.

II. ROCKET INSTRUMENTATION

In this section we describe the two rocket payload experiments of the bright point collaboration.

(i) AS&E X-ray payload

The American Science and Engineering High Resolution Soft X-Ray Solar Astronomy Imaging Payload was flown on 15 August 1987 and 11 December 1987 in participation with the Collaborative Bright Point Campaign. X-ray imaging is achieved in the AS&E payload by grazing incidence optics. The AS&E payload was programmed to reconfigure the X-ray telescope during flight from an instrument based on a photographic film detector obtaining full disk images to an instrument based on an X-ray sensitive CCD camera obtaining 2 arc min x 2 arc min images. Only the full disk X-ray photographic images presented in Figure 1 are used in the collaborative Bright Point Campaign.

The primary mirror is a Wolter Schwarzschild design with principal diameter of 30.48 cm and focal length of 144.9 cm. The reflecting surfaces of the mirror are uncoated fused silica. The level of suppression of scattering which is obtained with this mirror material by the reduction in surface roughness results in a point spread function relatively independent of wavelength (particularly in comparison to the Kanigen Skylab S-054 and sounding rocket mirrors). However, the reflectivity of this surface at the grazing angles of this mirror (approximately 1.5 degrees) is strongly wavelength dependent and defines the decline of the short wavelength response of the system below 30 angstroms.

Kodak SO-212 film was chosen as the primary photographic film for this mission because of its superior sensitivity with the longer wavelength filter used to image the "cooler" coronal plasma typical of X-ray bright points. The resolution of the combination of the telescope optics and the SO-212 film is

limited by the film but is comparable to the practical level of microdensitometry which results in pixels of 3 arc sec x 3 arc sec. This film was manufactured in 1973 for the Skylab S-054 X-Ray Spectrographic Telescope Experiment Program and has since been kept in cold storage. Aging of the film has had little impact on its X-ray response and advances in the photometric process continue to make this film a valuable resource for X-ray imaging (Moses et al. 1989). Since this film has been used for almost all high resolution X-ray photographic imaging of the solar corona, comparison with prior observations in synoptic studies is greatly facilitated.

In addition to the filtering effect of the reflectivity of the imaging mirror, the X-rays are also filtered by a heat rejection prefilter of approximately 1500 Angstroms of Aluminum and one of two focal plane filters: (1) a 17.5 micron thick Beryllium filter with a bandpass of 8 to 20 Angstroms or (2) a 1 micron thick polypropylene filter coated by 2000 Angstroms of Aluminum (for visible light rejection) with a dual bandpass of 8 to 39 and 44 to 64 Angstroms. A series of exposures through each of these filters was made with exposure times of 1/2 sec, 1 sec, 3 sec, 9 sec and 30 sec. This sequence was chosen to accommodate the dynamic range of the coronal X-ray emission (which can vary from 10^3 for quiet sun to more than 10^6 for a flare) as well as provide additional control on variations induced by photographic development (Moses et al., 1989). The X-ray throughput of the instrument with the polypropylene filter is greater than with the Beryllium filter for all temperatures of X-ray emitting plasmas. Furthermore, the throughput of the polypropylene filter is proportionally much greater for low temperature plasma so that the ratio of flux through the polypropylene filter to the flux through the Beryl-

limum filter provides a good plasma temperature diagnostic over the range of $1 \times 10^6\text{K}$ to $2 \times 10^7\text{K}$ (Vaiana, Krieger and Timothy, 1973). Since the objective of the collaborative observations is small scale coronal structure and since such structures are typically cool ($1.5 - 1.8 \times 10^6\text{K}$), the primary X-ray data used in the correspondence studies are the longest available exposures through polypropylene filters which are shown in Figure 1.

The Collaborative Bright Point Campaign had been attempted previously in August 1985 during the Spacelab 2 flight of the HRTS instrument. The Collaborative AS&E Sounding Rocket Flight was aborted during boost phase by the White Sands Missile Range Safety Officer. Beyond creating the necessity of repeating the Collaborative in 1987 from two sequentially launched rocket platforms, this abort also left the legacy of a contamination coating on the X-ray mirror from the explosives used to destroy the rocket booster. An effort toward cleaning the mirror was made before the August 1987 flight. A review of the image from the August flight compared with previous coronal images compelled us to attempt a more invasive cleaning effort.

The second X-ray mirror cleaning effort was conducted with a considerably more vigorous scrubbing action coupled with particular attention to removing organic deposits during the final sequence of solvent rinses. This cleaning effort was a dramatic success and the resulting images from the December 1987 flight show details as fine as any soft X-ray image of the solar corona. As a precaution, an extra 60-second exposure through the thinnest available polypropylene filter was added to the December 1987 flight exposure sequence. With the added integration time obtained with the 60 sec exposure, the threshold

emission measure ($\int N_e^2 dl$) for detection of $1.6 \times 10^6 K$ plasma typical of small scale coronal structure became $1.2 \times 10^{25} \text{ cm}^5$. Furthermore, the contrast of the December 1987 image was improved to the extent that dark lanes between regions of diffuse, quiet coronal emission became readily apparent. These dark lanes are not associated with filament channels, neutral lines, or any other readily perceivable magnetic structure. While these features can be found on review of some previous X-ray coronal images, they do not appear as distinctly defined. It is reasonable to conclude that the intrinsic improvement in image contrast of the fused silica mirror over previous metal mirrors coupled with the reduction in scatter by contaminants removed by the cleaning has resulted in the recognition of a coronal feature which, as will be discussed in Section IV, shows a unique relationship with fine scale transition region energetic events.

(ii) The NRL HRTS experiment

The High Resolution Telescope and Spectrograph (HRTS) instrument was flown as a rocket payload for the fifth time on 11 December 1987. HRTS consists of a 30 cm cassegrain telescope, a broadband spectroheliograph which was tuned to a wavelength region around 1600 A, a stigmatic slit spectrograph which covered a wavelength range from 1520-1570 A which included the C IV lines at 1548 A and 1550 A, and an H-alpha imaging system. The spatial resolution of the instrument is potentially sub arc second, and in this flight the smallest resolved spatial features in the slit spectrograph and the spectroheliograph are approximately 1 arc sec in size. Slit spectra were recorded by film exposure using Kodak type 101 emulsion, and spectroheliograph images on Kodak type 104 emulsion. The spectrograph slit length of 920 arc sec was rastered in 1 or 2 arc

sec steps across an approximately 3 arc min wide area in the northeast quadrant, covering a quiet area out to the solar limb. In addition, spectroheliograms covering a field of 920 x 460 arc sec were taken every other raster step of the slit spectrograph.

An example of a spectroheliograph exposure can be seen in Figure 2. The spectroheliograph passband is centered at 1600 Å, with a 20 Å FWHM. The predominant flux source in this passband is the ultraviolet continuum, arising from the solar temperature minimum region (see Vernazza et al. 1976), with remaining flux contributed by chromospheric and transition region emission lines. From an integration of this passband over a representative quiet solar spectrum from the atlas of Kjeldseth Moe et al. (1976), where we have estimated the continuum level and separated the flux into emission line and continuum contributions, we find that 72% of the flux from this quiet region would arise from continuum emission if observed by the HRTS spectroheliograph. The spectroheliograph field of view is 7.5 x 15 arc min in size. The HRTS spectrograph slit passes down the approximate center of the spectroheliograph image, which is obtained from a solar image reflected from the mirrored slit jaw plates. Three fiducial wires cross the image field perpendicular to the slit.

A series of film exposures of length 2.0 s, 1.0 s, and 0.5 s was taken at every other raster step of the slit spectrograph. In practice, the longest 2.0 s exposures have been used. After initially developing a flight film sample, it was clear that the spectroheliograph instrumental efficiency was down by as much as a factor of 10. With the help of Brian Dohne, a chemical developer was devised which optimally brought out the film latent image, effectively boosting the tail and steepening the gamma of the film characteristic curve. Although

the developed images had a greater fog level than nominal, the final images were usable and photometrically reliable.

The slit spectrograph on this flight covered the 1520-1570 Å wavelength range. The slit was widened to a 1 arc sec width to bring down the exposure time and allow more exposures, covering a greater surface area. The resulting spectral resolution was 0.10 Å. This region contains chromospheric lines of Si I, Si II, C I, Fe I, and other species, and the transition region resonance lines of C IV at 1548 Å and 1550 Å; in addition, the continuum in this region arises from the temperature minimum region of the solar atmosphere. In this paper we discuss only the C IV slit spectrograph observations. An exposure time of 2.4 s was used for the raster exposures, which optimally exposed the C IV lines.

The slit spectrograph was rastered across the solar field by mechanically stepping the slit position. We wanted to raster as wide an area as possible, but with steps small enough not to miss C IV turbulent events in the field. From the size distribution for these events given in Cook *et al.* (1987), a step size of 2 arc sec was generally used, although one raster with 1 arc sec step size was performed. As noted above, a spectroheliograph exposure was taken with every second raster step. On these spectroheliograph images the slit can be seen displaced in the raster direction in successive images. Although it is possible to raster over larger fields, optical aberrations in the slit spectrograph increase beyond a distance of approximately 30 arc sec to left or right of the slit central position, and to cover a wide field four individual rasters were made, with the telescope pointing changed between rasters so that no individual raster exceeded 25 arc sec relative to the central slit position. The nominal raster layout was to have 4 individual rasters of the 920 arc sec long

slit in the following pattern: raster 1 (2 arc sec steps, 26 position); 5 arc sec inter-raster spacing; raster 2 (1 arc sec steps, 21 positions); 5 arc sec inter-raster spacing; raster 3 (2 arc sec steps, 26 positions); 10 arc sec inter-raster spacing; raster 4 (2 arc sec steps, 24 positions). The total width of the pattern is nominally 186 arc sec, or 3 arc min.

III. THE COLLABORATIVE BRIGHT POINT CAMPAIGN

The collaborative observing plan called for a morning launch of the AS&E payload, followed in one-half hour by the NRL HRTS payload, both on Black Brant IX sounding rockets. In an effort to minimize possible launch constraints which might make it harder to launch two closely timed rockets, each Black Brant was equipped with a Saab S-19 boost phase guidance system. The S-19 allows a wider tolerance for high altitude winds, and gives a lower dispersion in the re-entry trajectory and final landing spot of the rocket and payload. The morning launch time was chosen to allow ground-based observations at Kitt Peak and Big Bear Solar Observatory (BBSO) to begin an hour or more before launch, while still keeping the actual flight within a time period which would typically insure good seeing at the ground-based observing sites. Observing programs at the ground-based sites were developed which emphasized He I 10830 A images and magnetograms from Kitt Peak, and videomagnetograms and H-alpha from Big Bear. At Kitt Peak, full disk images were taken outside the actual flight period, while during the flight period a 512 x 256 arc sec field at the planned position of the HRTS field was viewed in He I 10830 A. At Big Bear, a program was devised where videomagnetograms and film H-alpha images were taken during the observing day in overlapped boxes which also covered the planned HRTS field, while other areas of the Sun where magnetograms showed bipolar regions

were also occasionally observed to further support the full disk field of the AS&E X-ray payload.

This planned program was actually attempted several times during the summer of 1987, but was unsuccessful because of difficulties in launching the first rocket because of malfunctions with the S-19 rocket guidance system. On 1987 August 15 the AS&E rocket was successfully launched, but one-half hour later the NRL rocket could not be launched because of a similar S-19 malfunction. The X-ray and ground-based data obtained on 1987 August 15 are not discussed in this paper.

Finally on 1987 December 15 both rockets were successfully launched. This time, however, another malfunction occurred which affected the pointing of the HRTS payload. Pointing information on pitch, roll, and yaw for the Lockheed SPARCS payload pointing system was uplinked by radio to the rocket after launch, and a data dropout occurred during the sending of the roll angle. Instead of the desired pointing at the southwest quadrant, covering an area including an active region at the limb, the roll received put the pointing almost 180° away, in the northeast quadrant, with HRTS observing one of the quietest areas on the disk.

[The actually desired southwest limb pointing was jointly observed by participants in the Coronal Magnetic Structures Observing Campaign (COMSTOC), and a broad additional range of data is available for this pointing. The full disk X-ray images, and the small field CCD X-ray images of this area, will be useful in a separate COMSTOC analysis.]

IV. COALIGNMENT OF THE OBSERVATIONAL MATERIAL

We have coaligned the three full disk images which were obtained: the full disk Kitt Peak magnetogram and He I 10830 A, and the X-ray image. We have processed digitized full disk data which were obtained hours before and after the rocket flights by compute to produce a rotated image for the time of flight. This is a computer constructed image in which each pixel in the constructed image is obtained by rotating that pixel position to the time of the actual full disk observation, using the full geometry of the tilted solar axis and a formula for solar differential rotation. This rotated pixel position falls on the actual image, and its numerical value is taken as a linearly weighted average of the (typically four) original observed pixels which contribute to it. Solar rotation near the disk center is 9 arc sec an hour, and in comparing observations hours apart, as we have, where we are trying to determine correspondences in features which may be only arc seconds in dimension (the C IV high velocity events, for example), solar rotation is a significant effect. This is purely a geometrical correction, and does not account for actual temporal evolution of features between the time of the actual observation and the time of the calculated rotated image. In addition, no attempt is made to further adjust the numerical value of this constructed pixel for the changed line of sight, so for example a constructed pixel in a magnetogram can have a magnetic field value from an area of the actual observed magnetogram eastward or westward of this position, with a different line of sight angle, or a He I 10830 A constructed image can have constructed pixel values which are not corrected for changed limb brightening coefficient at the new constructed pixel position.

The Kitt Peak magnetogram and He I 10830 A images are obtained at different wavelengths by the same instrument, and are at the same scale, nominally 1 arc sec per pixel; in addition, no rotation should be necessary in coaligning different images. After placing all Kitt Peak full disk images at the same center image coordinates, we compared magnetograms and He I images. In the Kitt Peak gray scale image display representation most often seen, the He I image is surrounded by a white ring at the limb, which is actually limb brightening in this chromospheric line at a numerical intensity which is represented by white in the gray scale used. As a check, we verified that the magnetogram limb falls at the inside of this white band on the He I image, as should the limb from a photospheric line.

The general problem of coaligning images from different instruments can be difficult. Besides the obvious necessity to place the two images on a similar linear scale and rotational orientation, there are often instrumental aberrations present so that to some extent the image is not flat field, perhaps in a nonlinear barrel sense. We have developed a general computer program to align two images where a number of corresponding points on each are believed to exist. This program constructs a rescaled, rotated image from one of the original images which in a least squares sense produces the best coalignment of the selected pairs of fiducial points on each original image. The rescaling can be either linear or nonlinear in x and y .

We coaligned the full disk X-ray image using this program, where as fiducial points we took XBPs and their plausible He I dark point counterparts, or other pairs of fiducial features are small spatial scale which appeared to be plausible counterparts. Although subjective to some extent, this was very straightforward to accomplish. We then checked the resulting aligned X-ray

image's limb with the limbs of the Kitt Peak He I and magnetogram images. The X-ray limb, black where silhouetted against the brighter general off disk coronal emission, fell at the magnetogram limb and the inside of the limb brightening ring at the He I limb. As a further check, we compared the full disk white light image also obtained by the AS&E experiment with the X-ray image and found that the white light and dark X-ray limb were coincident.

V. RESULTS FROM THE COALIGNED DATA

The XBPs observed are associated with magnetic dipoles in the magnetograms, and with dark points in the He I 10830 A data. However, every magnetic dipole, and every dark point, are not always associated with a corresponding XBP. Webb and Moses (1989) studied the X-ray and Big Bear videomagnetogram data from the December 11 and August 15 launch efforts in an attempt to classify the nature of the magnetic bipolar regions associated with XBPs. In quiet network regions magnetic flux appears to emerge in small bipolar ephemeral regions, spread apart with time, and disappear either by gradual fading of the two opposite polarity elements of the ephemeral region or by cancellation of one element with another existing opposite polarity element with its own previous evolution as an internetwork element, active region remnant, or ephemeral region (see Martin and Harvey 1979). A time series of magnetograph observations over several hours is necessary to classify a magnetic bipolar region observed in a snapshot observation as either an emerging flux ephemeral region, a disappearing flux cancellation, or a stationary flux element lasting an appreciable time, perhaps simply fading with time. Because of excellent temporal coverage, Webb and Moses (1989) were able to characterize the magnetic dipoles corresponding to XBPs as emerging, stationary, or disappearing flux, and found that

the most significant class of magnetic dipole signature was disappearing flux regions.

We do not have comparable temporal coverage in the HRTS field of observation. The roll error in the HRTS V pointing described in Section III oriented the HRTS field of view completely outside of the target 10 arc min x 25 arc min region of observation for the Big Bear videomagnetogram. The temporal resolution of the Kitt Peak full disk magnetograms is sufficient to show the magnetic development of some XBPs as shown in Fig. 2.

We have studied the identification in the combined data of sites corresponding to locations in HRTS spectra of the C IV 1550 Å wavelength region showing the high-velocity energetic events described before. The method is to coalign HRTS V spectroheliograms, which image a wavelength interval around 1600 Å where flux is emitted predominantly from the temperature minimum continuum, with ground-based magnetograms. The T_{\min} images are known (see Cook, Brueckner, and Bartoe 1983) to be highly correlated in their fine structure with magnetograms, and in fact we can coalign the HRTS spectroheliograms to the Kitt Peak magnetogram to around 5 arc sec accuracy. The HRTS spectrograph slit can be seen on the HRTS spectroheliograph images, and thus the location of transition region C IV energetic events from the spectra can be accurately transferred to the spectroheliograms, and thus to the magnetograms and the ground-based data.

We have measured the location of the energetic events observed in C IV from HRTS slit spectrograph data. These events appear to be located at the edges of strong field network elements, or even within network elements of weakest magnetic field; they appear to generally avoid areas away from networks such as cell centers completely. The C IV events are not X-ray bright points, which

instead occur at sites of magnetic dipoles whose corresponding features in the HRTS C IV data are larger and more intense areas instead of the small high-velocity energetic events.

In Figure 2 the HRTS data has been aligned and compared with the X-ray, magnetograph, and He I 10830 A data. An original goal of the bright point campaign was to determine the correspondence of the transition region high velocity events seen in C IV with the observations from lower atmospheric regions and with coronal XBPs. The transition region high velocity events appear to be concentrated at the edges of strong network, or in weaker network regions, in the quiet Sun. They are not the transition region counterparts of XBPs. The X-ray image shows a pattern of dark lanes in quiet Sun areas, and the C IV events appear to be predominantly concentrated within these dark lanes, avoiding areas of hazy brighter X-ray emission probably corresponding to unresolved loop systems in active region areas of the disk.

We have been unable to determine if the individual C IV events are associated with magnetic dipoles, as are the XBPs, although it is clear that such an association, if it exists, must be with much weaker dipoles than those associated with XBPs. In examining magnetograms which are displayed to bring up the weaker field regions (20-50 G), mixed polarity small scale features appear everywhere in the quiet Sun. The Kitt Peak magnetograph data is from hours before the rocket flight. We would need to obtain truly simultaneous data and, more importantly, to develop an objective criterion to claim an association with a unique dipole out of those present ubiquitously.

We also find a greater number of C IV events than we would have expected from the results of a disk survey undertaken on the Spacelab 2 flight of the HRTS payload (Cook et al. 1987). Because of the spatial distribution of the C

IV events, we are lead to interpret the X-ray dark lanes as regions of enhanced C IV population. However, this interpretation must be weighed against the possibility that the detection threshold was extended during the HRTS V flight because the spatial resolution of the data is better than that from the Space-lab 2 flight. A resolution of this question must await an increase in the set of coordinated X-ray images and EUV spectra through additional rocket flights or an orbital mission.

We have also determined the transition region spectral features which do correspond with the coronal XBPs. These were found to be larger, brighter structures in C IV than the high velocity events, with a complex velocity structure which, however, did not reach the 100 km s^{-1} velocities seen in the C IV events. Figure 4 shows the HRTS C IV feature corresponding to the prominent XBP at the right side of the raster pattern, toward Sun center. Two consecutive raster steps are illustrated. The XBP covers a raster width approximately equal to its length along the slit, and is seen in both raster steps. A prominent C IV energetic event is also seen in one raster step, but is not present on the step just 2 arc sec away. As with the He I 10830 A dark points (see Fig. 3), we also see C IV spectral features, no different than those corresponding to XBPs, which do not have an XBP corresponding X-ray feature. In the cases both of He I 10830 A dark points and the HRTS transition region C IV observations, only a fraction of all similar events are heated to temperatures where an X-ray signature is also produced.

VI. FUTURE OBSERVING PROGRAMS

The bright point campaign provides an example for the type of collaborative programs which might be attempted during the solar maximum period 1989-1991.

Although there were certainly logistical problems in coordinating multiple sounding rocket launches and simultaneous ground-based observations, the scientific return is more than correspondingly greater. Further, simultaneous observations from all levels of the solar atmosphere continues to be shown as an essential approach to obtain new insight into solar phenomena and must form the backbone of any future orbital solar observatory.

REFERENCES

- Brueckner, G.E., and Bartoe, J.-D.F. 1983, Ap. J., 272, 329.
- Brueckner, G.E., Bartoe, J.-D.F., Cook, J.W., Dere, K.P., and Socker, D.G., 1986, Adv. Space Res., 6, 263.
- Cook, J.W., Bartoe, J.-D.F., Brueckner, G.E., Dere, K.P., Recely, F., Martin, S., and Zirin, H. 1988, B.A.A.S., 20, 722.
- Cook, J.W., Brueckner, G.E., and Bartoe, J.-D.F. 1983, Ap. J. Lett., 270, L89.
- Cook, J.W., Lund, P.A., Bartoe, J.-D.F., Brueckner, G.E., Dere, K.P., and Socker, G.D. 1987, Fifth Cambridge Workshop on Cool Stars, Stellar Systems, and the Sun, ed. J.L. Linsky and R.E. Stencel (Springer-Verlag), 150.
- Martin, S.F., and Harvey, K.L. 1979, Solar Phys., 64, 93.
- Moses, J.D., Bartoe, J.-D.F., Brueckner, G.E., Cook, J.W., Dere, K.P., Davis, J.M., and Webb, D. 1988, B.A.A.S., 20, 722.
- Moses, D., Schueller, R., Waljeski, K., and Davis, J.M., 1989, SPIE 1159.
- Vaiana, G.S., Krieger, A.S., and Timothy, A.F. 1973, Solar Phys. 32, 81.
- Vernazza, Avrett, and Loeser 1976, Ap. J. Suppl., 30, 1.
- Webb, D.F., and Moses, J.D. 1988, Adv. Space Res., ____, .

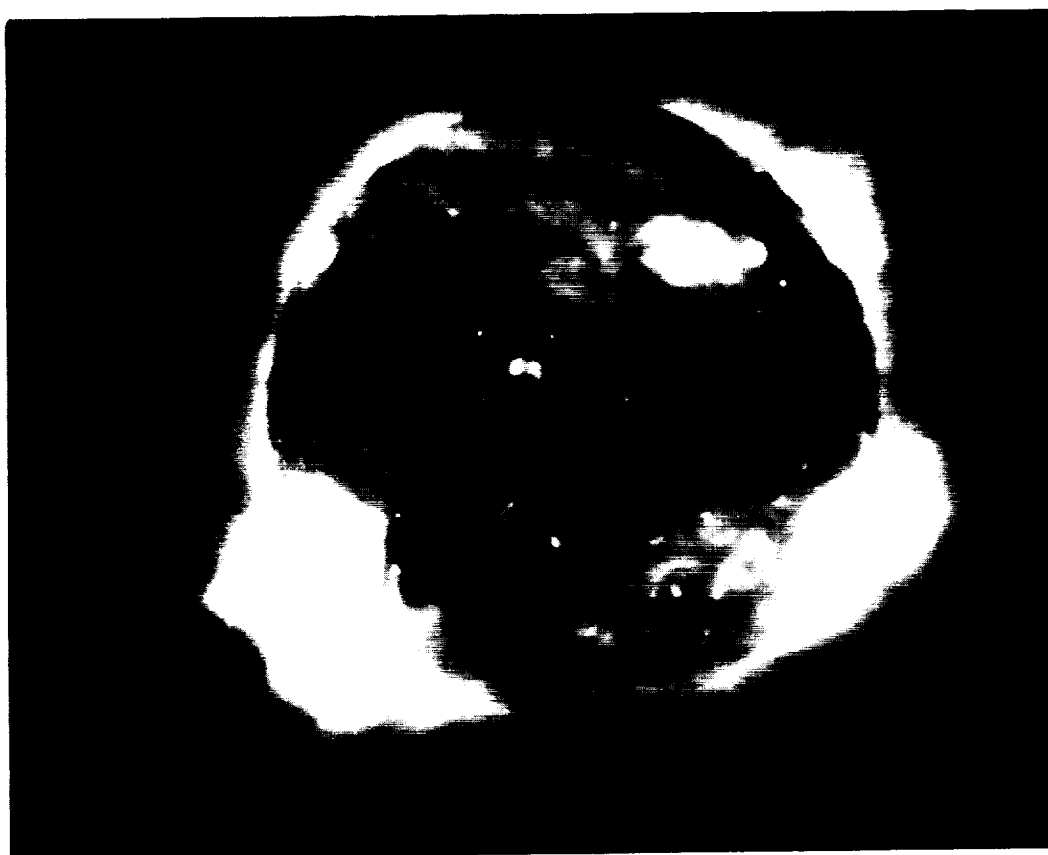
FIGURE CAPTIONS

Figure 1. Full disk soft X-ray photographic images used in the Collaborative Bright Point Observing Campaign. Top: 15 August 1987 image, 30 second exposure with organic filter. Bottom: 11 December 1987 image, 60 second exposure with organic filter.

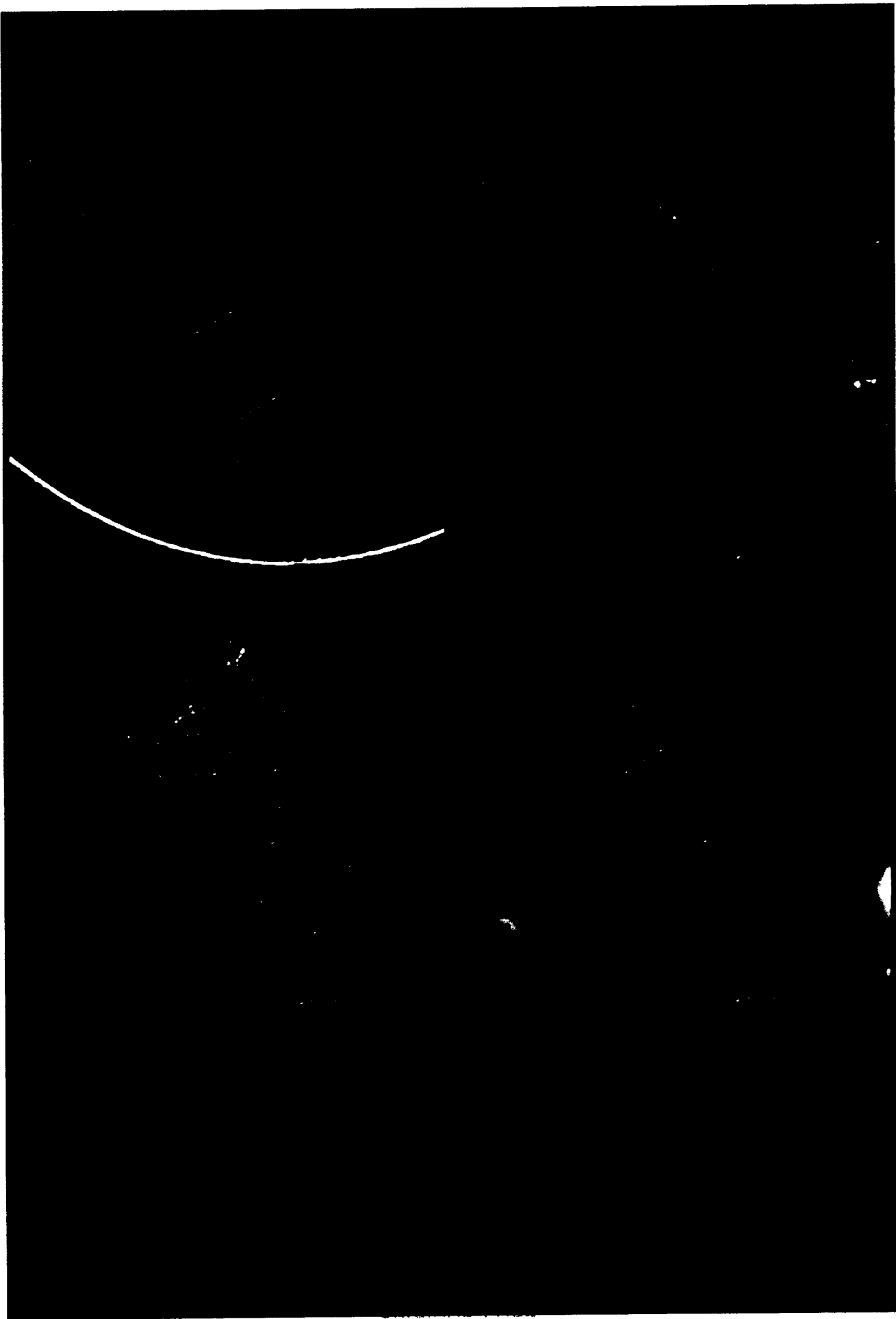
Figure 2. The section of the solar disk containing the HRTS field. North at top, east at left. The map of sites of C IV energetic events is superposed on a HRTS 1600 A spectroheliogram, and the AS&E X-ray, Kitt Peak magnetograph, and Kitt Peak He I 10830 A images.

Figure 3. Top: XBP and He I corresponding dark point compared to Kitt Peak magnetogram of the corresponding dipole from the day before, hours before flight, hours after flight, and the following day. Bottom: Comparison of X-ray image and He I 10830 A image, showing one He I dark point with an XBP corresponding to it, while a second similar He I dark point has no such XBP counterpart.

Figure 4. HRTS slit spectra of C IV 1548 A and 1550 A from two consecutive steps (24 and 25) of the third HRTS raster. The steps are 2 arc sec apart. The C IV counterpart to an XBP is shown, together with a C IV energetic event visible only in Step 25.

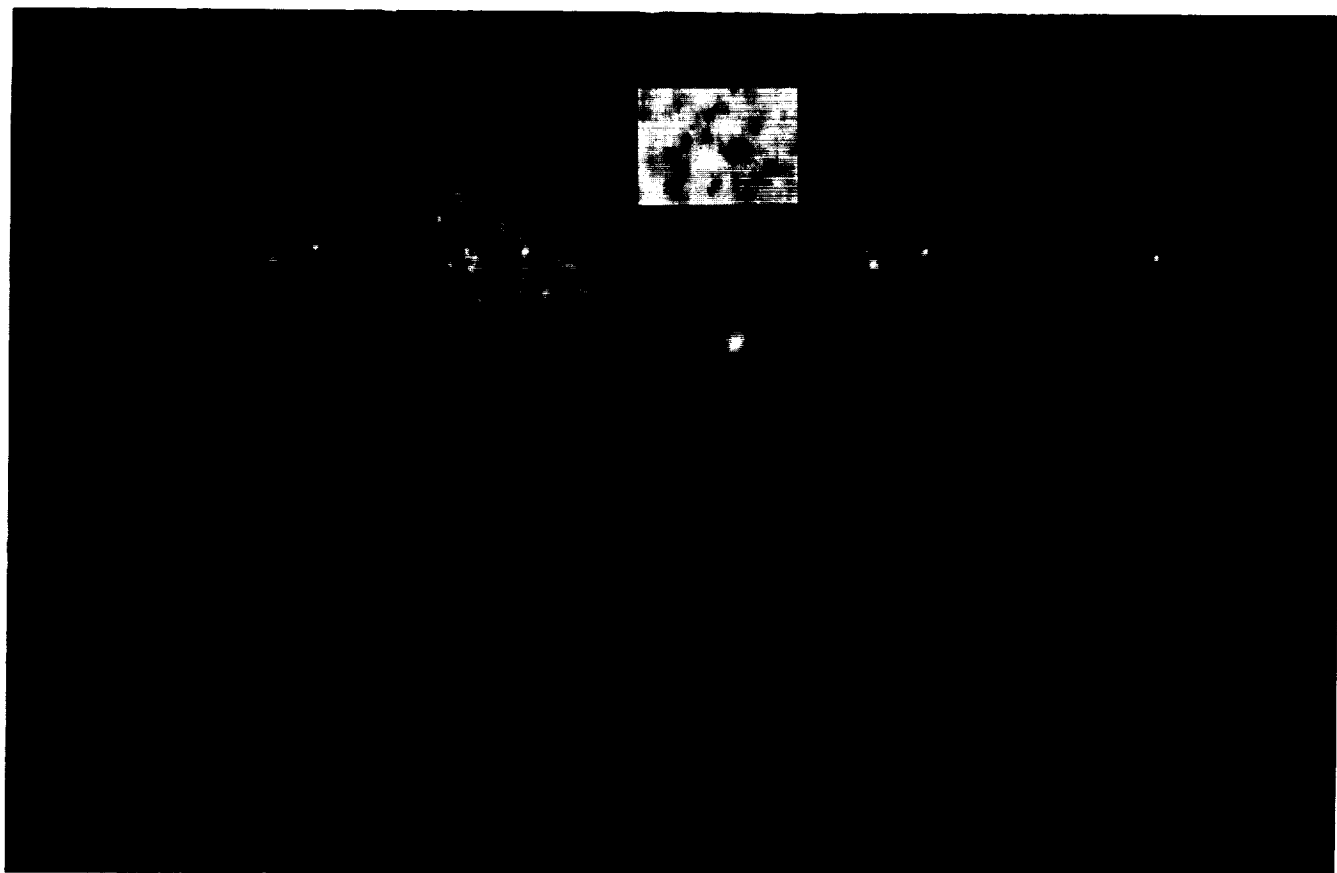


ORIGINAL PAGE
BLACK AND WHITE PHOTOGRAPH

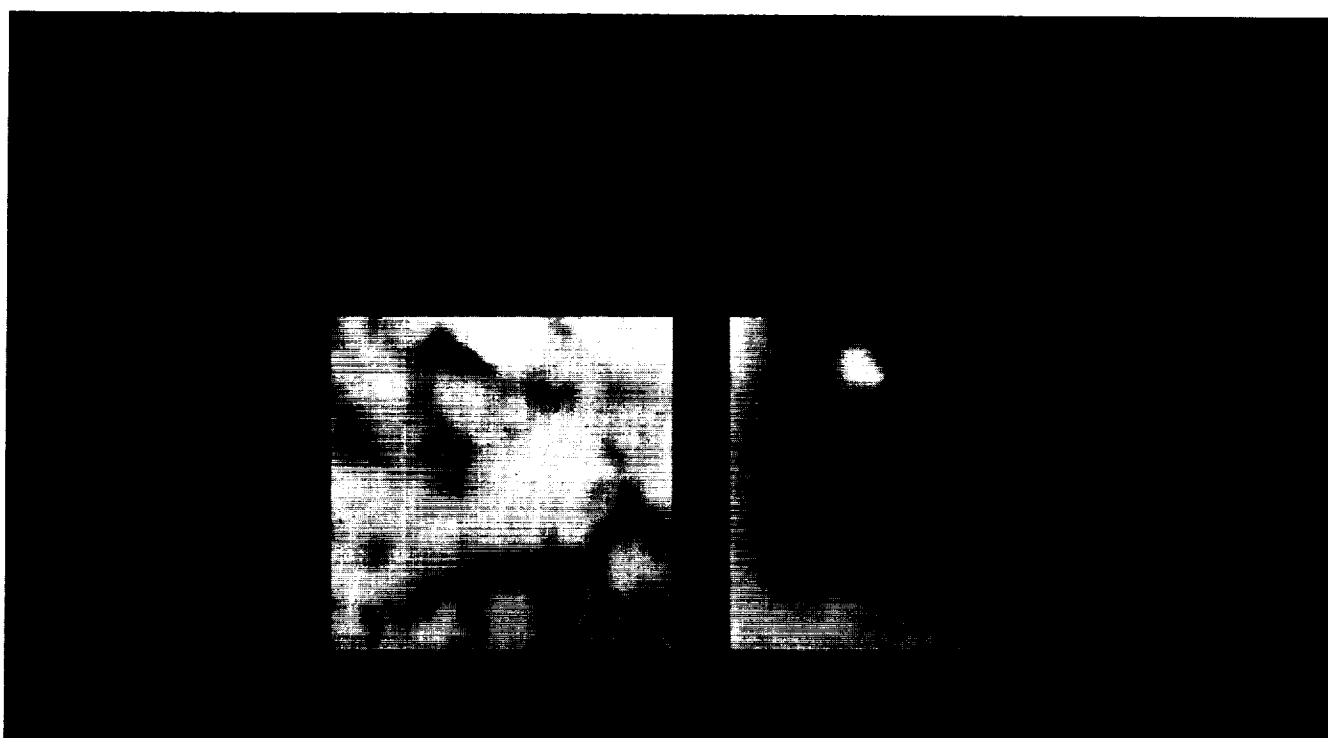


ORIGINAL PAGE
BLACK AND WHITE PHOTOGRAPH

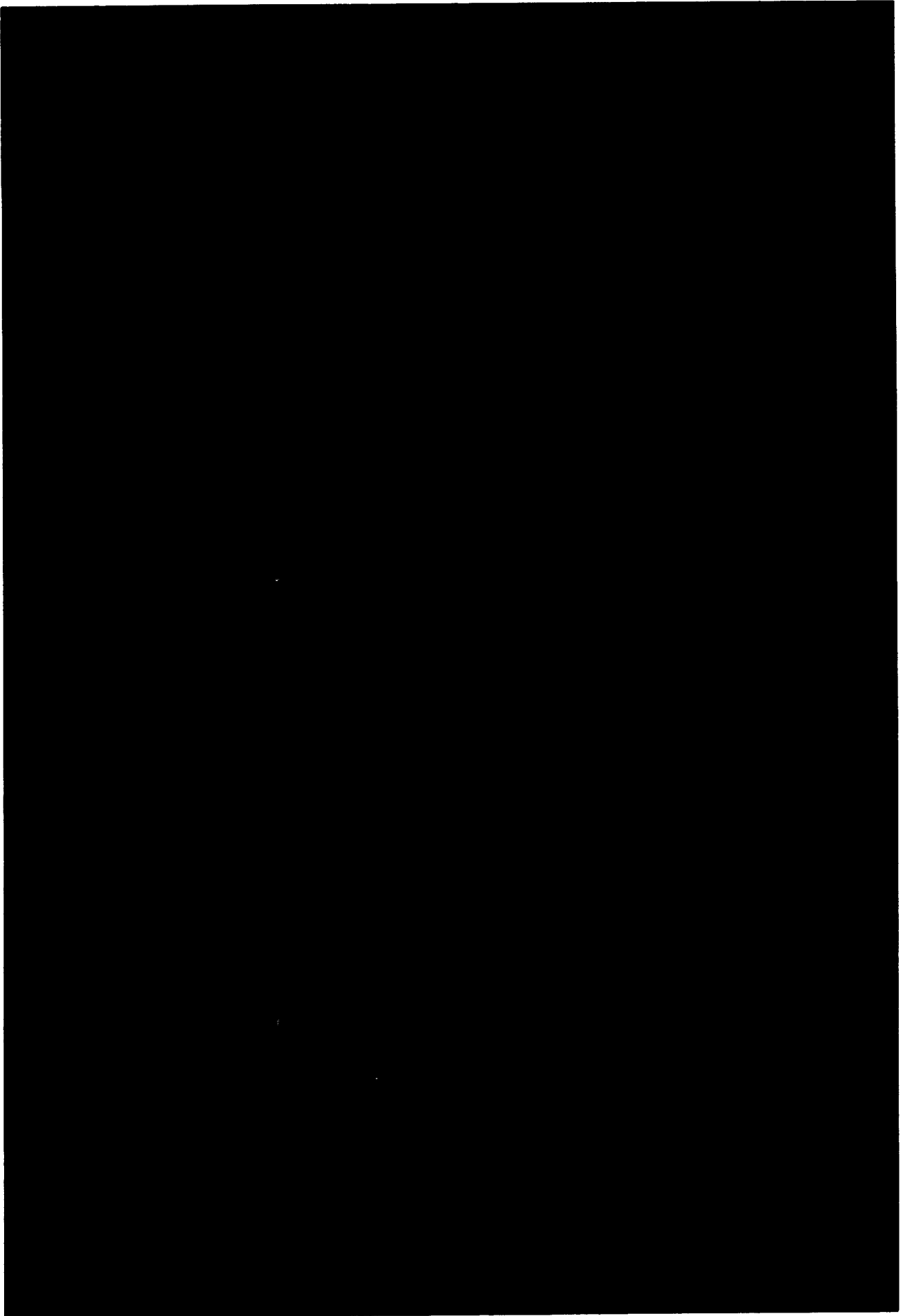
BLACK AND WHITE PHOTOGRAPH



ORIGINAL PAGE
BLACK AND WHITE PHOTOGRAPH



ORIGINAL PAGE
BLACK AND WHITE PHOTOGRAPH



1
2
3
4
5
6
7
8
9
10
11
12
13
14
15
16
17
18
19
20
21
22
23
24
25
26
27
28
29
30
31
32
33
34
35
36
37
38
39
40
41
42
43
44
45
46
47
48
49
50
51
52
53
54
55
56
57
58
59
60
61
62
63
64
65
66
67
68
69
70
71
72
73
74
75
76
77
78
79
80
81
82
83
84
85
86
87
88
89
90
91
92
93
94
95
96
97
98
99
100
101
102
103
104
105
106
107
108
109
110
111
112
113
114
115
116
117
118
119
120
121
122
123
124
125
126
127
128
129
130
131
132
133
134
135
136
137
138
139
140
141
142
143
144
145
146
147
148
149
150
151
152
153
154
155
156
157
158
159
160
161
162
163
164
165
166
167
168
169
170
171
172
173
174
175
176
177
178
179
180
181
182
183
184
185
186
187
188
189
190
191
192
193
194
195
196
197
198
199
200
201
202
203
204
205
206
207
208
209
210
211
212
213
214
215
216
217
218
219
220
221
222
223
224
225
226
227
228
229
230
231
232
233
234
235
236
237
238
239
240
241
242
243
244
245
246
247
248
249
250
251
252
253
254
255
256
257
258
259
260
261
262
263
264
265
266
267
268
269
270
271
272
273
274
275
276
277
278
279
280
281
282
283
284
285
286
287
288
289
290
291
292
293
294
295
296
297
298
299
300
301
302
303
304
305
306
307
308
309
310
311
312
313
314
315
316
317
318
319
320
321
322
323
324
325
326
327
328
329
330
331
332
333
334
335
336
337
338
339
340
341
342
343
344
345
346
347
348
349
350
351
352
353
354
355
356
357
358
359
360
361
362
363
364
365
366
367
368
369
370
371
372
373
374
375
376
377
378
379
380
381
382
383
384
385
386
387
388
389
390
391
392
393
394
395
396
397
398
399
400
401
402
403
404
405
406
407
408
409
410
411
412
413
414
415
416
417
418
419
420
421
422
423
424
425
426
427
428
429
430
431
432
433
434
435
436
437
438
439
440
441
442
443
444
445
446
447
448
449
450
451
452
453
454
455
456
457
458
459
460
461
462
463
464
465
466
467
468
469
470
471
472
473
474
475
476
477
478
479
480
481
482
483
484
485
486
487
488
489
490
491
492
493
494
495
496
497
498
499
500
501
502
503
504
505
506
507
508
509
510
511
512
513
514
515
516
517
518
519
520
521
522
523
524
525
526
527
528
529
530
531
532
533
534
535
536
537
538
539
540
541
542
543
544
545
546
547
548
549
550
551
552
553
554
555
556
557
558
559
560
561
562
563
564
565
566
567
568
569
570
571
572
573
574
575
576
577
578
579
580
581
582
583
584
585
586
587
588
589
590
591
592
593
594
595
596
597
598
599
600
601
602
603
604
605
606
607
608
609
610
611
612
613
614
615
616
617
618
619
620
621
622
623
624
625
626
627
628
629
630
631
632
633
634
635
636
637
638
639
640
641
642
643
644
645
646
647
648
649
650
651
652
653
654
655
656
657
658
659
660
661
662
663
664
665
666
667
668
669
670
671
672
673
674
675
676
677
678
679
680
681
682
683
684
685
686
687
688
689
690
691
692
693
694
695
696
697
698
699
700
701
702
703
704
705
706
707
708
709
710
711
712
713
714
715
716
717
718
719
720
721
722
723
724
725
726
727
728
729
730
731
732
733
734
735
736
737
738
739
740
741
742
743
744
745
746
747
748
749
750
751
752
753
754
755
756
757
758
759
760
761
762
763
764
765
766
767
768
769
770
771
772
773
774
775
776
777
778
779
780
781
782
783
784
785
786
787
788
789
790
791
792
793
794
795
796
797
798
799
800
801
802
803
804
805
806
807
808
809
810
811
812
813
814
815
816
817
818
819
820
821
822
823
824
825
826
827
828
829
830
831
832
833
834
835
836
837
838
839
840
84

— — — — —

1
2
3
4
5
6
7
8
9
10
11
12
13
14
15
16
17
18
19
20
21
22
23
24
25
26
27
28
29
30
31
32
33
34
35
36
37
38
39
40
41
42
43
44
45
46
47
48
49
50
51
52
53
54
55
56
57
58
59
60
61
62
63
64
65
66
67
68
69
70
71
72
73
74
75
76
77
78
79
80
81
82
83
84
85
86
87
88
89
90
91
92
93
94
95
96
97
98
99
100
101
102
103
104
105
106
107
108
109
110
111
112
113
114
115
116
117
118
119
120
121
122
123
124
125
126
127
128
129
130
131
132
133
134
135
136
137
138
139
140
141
142
143
144
145
146
147
148
149
150
151
152
153
154
155
156
157
158
159
160
161
162
163
164
165
166
167
168
169
170
171
172
173
174
175
176
177
178
179
180
181
182
183
184
185
186
187
188
189
190
191
192
193
194
195
196
197
198
199
200
201
202
203
204
205
206
207
208
209
210
211
212
213
214
215
216
217
218
219
220
221
222
223
224
225
226
227
228
229
230
231
232
233
234
235
236
237
238
239
240
241
242
243
244
245
246
247
248
249
250
251
252
253
254
255
256
257
258
259
260
261
262
263
264
265
266
267
268
269
270
271
272
273
274
275
276
277
278
279
280
281
282
283
284
285
286
287
288
289
290
291
292
293
294
295
296
297
298
299
300
301
302
303
304
305
306
307
308
309
310
311
312
313
314
315
316
317
318
319
320
321
322
323
324
325
326
327
328
329
330
331
332
333
334
335
336
337
338
339
340
341
342
343
344
345
346
347
348
349
350
351
352
353
354
355
356
357
358
359
360
361
362
363
364
365
366
367
368
369
370
371
372
373
374
375
376
377
378
379
380
381
382
383
384
385
386
387
388
389
390
391
392
393
394
395
396
397
398
399
400
401
402
403
404
405
406
407
408
409
410
411
412
413
414
415
416
417
418
419
420
421
422
423
424
425
426
427
428
429
430
431
432
433
434
435
436
437
438
439
440
441
442
443
444
445
446
447
448
449
450
451
452
453
454
455
456
457
458
459
460
461
462
463
464
465
466
467
468
469
470
471
472
473
474
475
476
477
478
479
480
481
482
483
484
485
486
487
488
489
490
491
492
493
494
495
496
497
498
499
500
501
502
503
504
505
506
507
508
509
510
511
512
513
514
515
516
517
518
519
520
521
522
523
524
525
526
527
528
529
530
531
532
533
534
535
536
537
538
539
540
541
542
543
544
545
546
547
548
549
550
551
552
553
554
555
556
557
558
559
560
561
562
563
564
565
566
567
568
569
570
571
572
573
574
575
576
577
578
579
580
581
582
583
584
585
586
587
588
589
590
591
592
593
594
595
596
597
598
599
600
601
602
603
604
605
606
607
608
609
610
611
612
613
614
615
616
617
618
619
620
621
622
623
624
625
626
627
628
629
630
631
632
633
634
635
636
637
638
639
640
641
642
643
644
645
646
647
648
649
650
651
652
653
654
655
656
657
658
659
660
661
662
663
664
665
666
667
668
669
670
671
672
673
674
675
676
677
678
679
680
681
682
683
684
685
686
687
688
689
690
691
692
693
694
695
696
697
698
699
700
701
702
703
704
705
706
707
708
709
710
711
712
713
714
715
716
717
718
719
720
721
722
723
724
725
726
727
728
729
730
731
732
733
734
735
736
737
738
739
740
741
742
743
744
745
746
747
748
749
750
751
752
753
754
755
756
757
758
759
760
761
762
763
764
765
766
767
768
769
770
771
772
773
774
775
776
777
778
779
780
781
782
783
784
785
786
787
788
789
790
791
792
793
794
795
796
797
798
799
800
801
802
803
804
805
806
807
808
809
810
811
812
813
814
815
816
817
818
819
820
821
822
823
824
825
826
827
828
829
830
831
832
833
834
835
836
837
838
839
840
84